Dissertation
submitted to the
Combined Faculties for the Natural Sciences and for Mathematics
of the Ruperto-Carola University of Heidelberg, Germany
for the degree of
Doctor of Natural Sciences

Put forward by
Dipl.-Phys.: Katja Großmann
Born in: Mannheim

Oral examination: 10.12.2014

Aircraft-borne DOAS limb observations of UV/visible absorbing trace gas species over Borneo:
Implications for the photochemistry of iodine, volatile organic oxide degradation, and lightning-produced radicals

SHIVA

Referees: Prof. Dr. Klaus Pfeilsticker

Prof. Dr. Thomas Leisner

Abstract

Tropical deep convection is one of the major mechanisms for transporting trace gases from the lower to the upper troposphere and tropical tropopause layer (TTL). From there, they further ascend to the lowermost stratosphere by diabatic heating.

Within this thesis, airborne spectroscopic measurements were carried out during the SHIVA (Stratospheric ozone: Halogen Impacts in a Varying Atmosphere) campaign at Malaysian Borneo in November and December 2011 in order to study the abundance and transport of trace gases in the lower atmosphere. Sixteen flights were performed with the research aircraft DLR-Falcon covering legs near the surface as well as in the free troposphere up to an altitude of 13 km. The measurements were evaluated using the Differential Optical Absorption Spectroscopy (DOAS) technique in limb geometry, which supports observations of UV/visible absorbing trace gases, such as O_4, BrO, IO, NO_2, HCHO, CHOCHO, HONO and H_2O.

Inferred vertical profiles of IO show mixing ratios of 0.5–1.5 ppt in the marine boundary layer decreasing to 0.1–0.3 ppt in the free troposphere. Thus, the main IO sources originate from near or at the surface. Enhanced IO concentrations occasionally occurred in the mid-troposphere, sometimes in coincidence with elevated concentrations of CO, suggesting rapid vertical transport by shallow to medium strong convection. Due to low concentrations of IO in the mid-troposphere over land together with short time scales for vertical and horizontal transport, it is concluded that efficient IO loss processes exist, preventing IO from reaching the TTL and stratosphere. BrO did not exceed the detection limit of approximately 2 ppt since in the terrestrial tropical atmosphere around Borneo the chemistry of volatile organic compounds (VOCs) acts as a large sink for reactive bromine species.

CHOCHO and HCHO frequently exceeded background concentrations. These observations indicate efficient VOC photochemistry, since CHOCHO and HCHO are mainly produced through the oxidation of VOCs emitted from the tropical rain forest of Borneo and from distinct anthropogenic sources.

Signatures of HONO, HCHO, and NO_2 in the outflow of convective clouds indicate a rapid transport of HCHO and NO_2 from polluted near surface air into the upper troposphere as well as lightning-induced production of HONO and NO_x.

Zusammenfassung

In den Tropen ist hochreichende Konvektion einer der wichtigsten Mechanismen für den Transport von Spurengasen aus der unteren in die obere Troposphäre und in die tropische Tropopausenschicht (TTL). Von dort steigen sie durch diabatische Erwärmung weiter in die unterste Stratosphäre auf.

Im Rahmen dieser Arbeit wurden während der SHIVA (Stratospheric ozone: Halogen Impacts in a Varying Atmosphere) Kampagne im November und Dezember 2011 luftgestützte spektroskopische Messungen im malaysischen Teil von Borneo durchgeführt, um die Menge und den Transport von Spurengasen im unteren Teil der Atmosphäre zu untersuchen. Sechzehn Messflüge an Bord des Forschungsflugzeugs DLR-Falcon deckten sowohl Flugabschnitte nahe der Oberfläche als auch in der freien Troposphäre bis zu einer Höhe von 13 km ab. Die Messungen, die mittels Differentieller Optischer Absorptions Spektroskopie (DOAS) in limb Geometrie durchgeführt wurden, umfassen Spurengase, welche im UV und sichtbaren Spektralbereich absorbieren, wie O_4, BrO, IO, NO_2, HCHO, CHOCHO, HONO und H_2O.

Die ermittelten Vertikalprofile von IO zeigen Mischungsverhältnisse von 0.5–1.5 ppt in der marinen Grenzschicht sowie eine Abnahme auf 0.1–0.3 ppt in der freien Troposphäre. Die Hauptquellen von IO sind somit nahe der Oberfläche zu finden. In der mittleren Troposphäre traten gelegentlich erhöhte IO Konzentrationen zusammen mit erhöhten CO Konzentrationen auf, was auf einen Transport durch flache bis mittelstarke Konvektion hindeutet. Aus den niedrigen IO Konzentrationen in der mittleren Troposphäre über Land und den kurzen Zeitskalen für vertikalen und horizontalen Transport folgt, dass es effiziente Verlustprozesse für IO gibt, die dessen Transport in die TTL und Stratosphäre verhindern. BrO lag nicht über der Nachweisgrenze von 2 ppt, da die chemischen Reaktionen mit flüchtigen organischen Verbindungen (VOCs) in der terrestrischen tropischen Atmosphäre um Borneo als Senke für reaktive Bromverbindungen dienen.

CHOCHO und HCHO überschritten häufig die Hintergrundkonzentrationen. Diese Beobachtungen weisen auf eine effiziente VOC Photochemie hin, da CHOCHO und HCHO hauptsächlich durch die Oxidation von VOCs produziert werden, die vom tropischen Regenwald in Borneo und von verschiedenen anthropogenen Quellen emittiert werden.

Die Erhöhungen von HONO, HCHO und NO_2 im Ausfluss konvektiver Wolken deuten auf einen schnellen Transport von HCHO und NO_2 aus der verschmutzten bodennahen Luft in die obere Troposphäre, sowie auf eine durch Blitzschlag bedingte Produktion von HONO und NO_x hin.

Contents

1. Introduction

Ozone plays a major role in atmospheric chemistry. The ozone layer of the stratosphere contains about 90 % of the atmospheric ozone, which absorbs solar ultraviolet (UV) radiation, thereby protecting life on the Earth's surface. The remaining ozone (about 10%) is found in the troposphere, where it has significant influence on the overall oxidation capacity, since it is a substantial source of OH radicals and acts as a greenhouse gas (WMO, 1999).

It is well-known that halogenated compounds can catalytically destroy ozone. Molina and Rowland (1974) postulated that catalytic reaction cycles involving the anthropogenically produced chlorofluorocarbons (CFCs), such as $CFCl_3$, or CF_2Cl_2, are responsible for the destruction of stratospheric ozone. The most severe ozone loss was discovered by Farman et al. (1985) over Antarctica during springtime. After the discovery of this phenomenon, which became known as the so-called ozone hole, primarily caused by the increase in ozone-destroying halogens in the stratosphere since the middle of the past century, the photochemistry of halogenated compounds became an important research topic (Solomon, 1999; WMO, 1999, 2007, 2011). This led to the Montreal Protocol in 1987 and its amendments, limiting the worldwide production of ozone-depleting substances (ODSs).

The Montreal Protocol and its amendments have successfully led to a decline in the production of halogenated ODSs over the last three decades. Today, reductions in ozone-destroying halogens are becoming obvious in the stratosphere (e.g. WMO, 2011). Nevertheless, it has been recognized that not only anthropogenically produced but also naturally emitted halogen compounds, such as the so-called Very Short Lived Species (VSLS), contribute to the stratospheric halogen load. VSLS are defined as halogen-containing substances with a lifetime smaller than six months (WMO, 2007). A major source of halogenated VSLS is the ocean (e.g. Chuck et al., 2005; Carpenter et al., 2012). Oceanic sources include for example macroalgae, such as kelp or seaweed, and phytoplankton (e.g. Quack and Wallace, 2003). Figure 1.1 summarises the processes related to the transport of halogenated compounds into the stratosphere. Despite their short lifetime, VSLS can be transported to the upper troposphere and lower stratosphere by means of deep convection. Deep convection particularly occurs over the Western Pacific, which thus represents an important source region for air masses transported from the lower to the upper troposphere and to the tropical tropopause layer (TTL), and finally to the stratosphere (e.g. Newell and Gould-Stewart, 1981; Fueglistaler et al., 2009; Ashfold et al., 2012; Rex et al., 2014). From the upper troposphere and lower stratosphere, VSLS and their decay products can be transported into higher altitudes (e.g. Aschmann et al., 2009, and references therein). In the stratosphere, VSLS are distributed worldwide via the Brewer-Dobson circulation (e.g. Bönisch et al., 2011).

Uncertainties exist with regard to the emission strengths as a function of VSLS type, location and time, their atmospheric transport and decay and loss processes, and finally their contribution to the stratospheric halogen loading. The SHIVA (Stratospheric ozone: Halogen Impacts in a Varying Atmosphere) project was initiated to address these issues through experimental and theoretical studies (Pfeilsticker, 2012). The SHIVA project was mainly aimed at reducing uncertainties with regard to the amount of VSLS that reach the stratosphere, by performing ground-, ship-, and satellite-based measurements, as well as airborne observations of different atmospheric trace gases, and photochemical transport studies. The SHIVA field campaign took place in the South China Sea and along the coastline of Peninsular Malaysia and Borneo during November and December 2011.

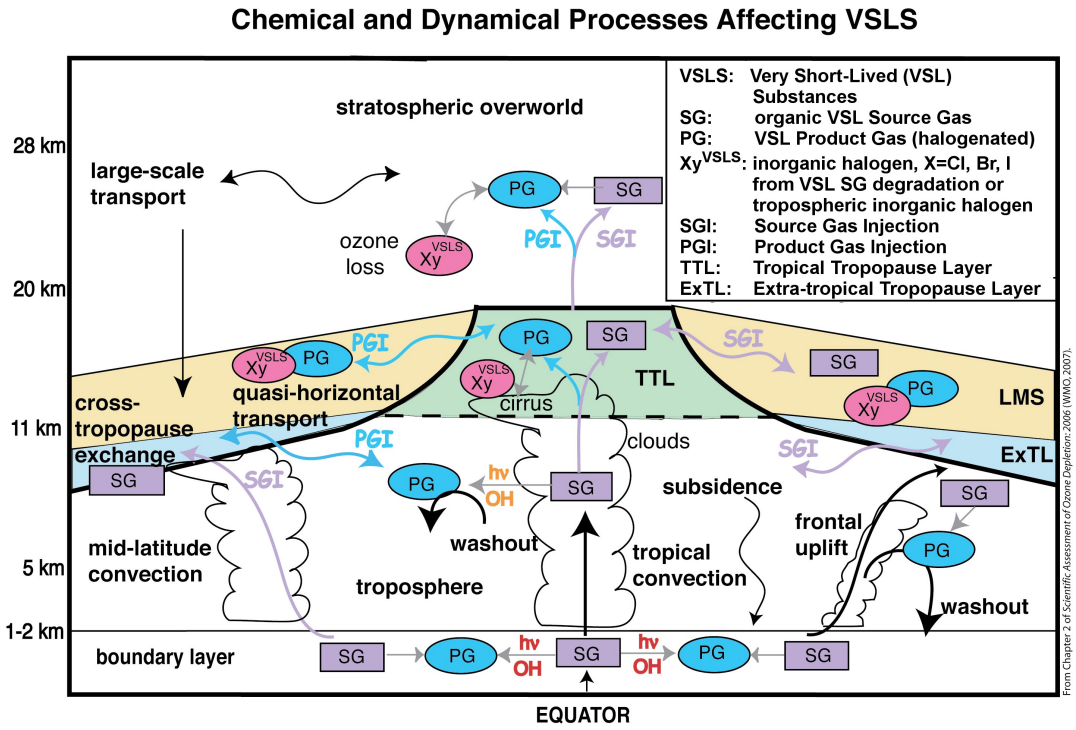

Figure 1.1: Sketch of the principle chemical and dynamical pathways of the organic very short-lived (VSL) source gases (SGs) and their product gases (PGs) between the boundary layer and the stratosphere. SGs include for example $CHBr_3$, $CHBr_2Cl$, or CH_3I, whereas PGs include for example BrO and IO, Figure adapted from WMO (2007).

The main objectives of the SHIVA campaign were (Pfeilsticker, 2012):

a) Determination of the oceanic emission strengths of different halogenated compounds;

b) Investigation of the atmospheric transport and transformation of the halogenated SGs and PGs within the tropical troposphere, TTL, and tropical lower stratosphere;

c) Analysis of the past, present, and likely future trend of the total halogen burden in the stratosphere;

d) Estimation of the impact of long- and short-lived halogenated SGs and their inorganic PGs for past, present, and future ozone within the upper troposphere, TTL, and global stratosphere.

The present thesis focuses on objective (b) of the SHIVA project. Airborne DOAS (Differential Optical Absorption Spectroscopy) (Platt and Stutz, 2008) measurements were carried out aboard the DLR-Falcon aircraft to study the abundance of the reactive halogen compounds BrO and IO in the marine boundary layer and free troposphere around and above Borneo. Further objectives of the aircraft-borne DOAS measurements were to investigate the oxidation capacity of the atmosphere, i.e. to examine the oxidation products of volatile organic compounds (VOCs), leading to formaldehyde (HCHO) and glyoxal (CHOCHO). VOCs are not only emitted by the tropical rain forests of Borneo, but also by distinct anthropogenic sources, such as fossil fuel combustion, biomass burning, oil rigs, shipping, or local traffic. Thus, local air pollution around Borneo was studied with a view to identifying the major emission sources of HCHO, CHOCHO, and nitrogen dioxide (NO_2). Finally, the composition of air masses in convective outflows of thunderstorm clouds was investigated. A challenging aspect of the interpretation of the DOAS measurements was the frequent occurrence of clouds, which significantly influence the light path length.

Outline of this thesis

The present thesis is organised as follows: Chapter 2 provides scientific background information on the relevant aspects of atmospheric physics and chemistry, including a basic overview on the photochemical processes of the different trace gas species that were measured in the scope of this thesis. Chapter 3 presents the physical fundamentals of radiative transfer in the atmosphere, followed by a description of the principles and details of the Differential Optical Absorption Spectroscopy (DOAS) measurement technique, which was used for the retrieval of trace gas differential slant column densities (dSCDs) (Chapter 4). Radiative transfer modelling is needed to infer trace gas concentrations from the measured dSCDs and is summarised in Chapter 5. Following the setting of the theoretical context of this thesis, Chapter 6 describes details of the SHIVA field campaign. Furthermore, a description of the relevant meteorological and regional characteristics is provided. Chapter 7 briefly describes the instrumental set-up and provides a characterisation of the utilised mini-DOAS instrument. In Chapter 8, the spectral retrieval steps are explained in detail, including the analysis settings of the different trace gases of O_4, O_3, BrO, IO, NO_2, HCHO, CHOCHO, HONO, and H_2O. The atmospheric conditions prevailing during the SHIVA campaign were rather complex with both horizontally and vertically varying cloud fields. Thus, in Chapter 9, different approaches are introduced to assess the influence of clouds on DOAS measurements. Chapter 10 describes two different methods (and their limitations), which are geared at deriving volume mixing ratios (VMRs) of the targeted trace gases. VMRs at flight altitude are inferred using a scaling method with a gas of known profile, whereas vertical VMR profiles are derived by an inversion method. Chapter 11 discusses the major observations made by the mini-DOAS instrument during the SHIVA aircraft campaign and the implications of these results for the tropospheric photochemistry over Borneo. These findings are further compared to simulations using chemistry transport models, as well as to previous measurements. In Chapter 12, the key results of the present thesis are summarised and discussed with respect to previous studies. Finally, open scientific issues are addressed.

In Appendix A, a detailed description of each Falcon sortie including an overview of the inferred dSCDs can be found. In Appendix B, the number of photons is estimated, for which the root mean square (RMS) of the DOAS spectral fit does not further decrease. Appendix C describes two possible methods to infer 3D cloud fields from 2D webcam images. In Appendix D, the reaction rate coefficients are determined, which are required for the estimation of the OH concentration. Based on the experience gained during the SHIVA campaign, Appendix E finally summarises several recommendations for future aircraft missions.

2. Physics and chemistry of the Earth's atmosphere

The atmosphere is a thin gaseous layer surrounding the Earth attracted by the planet's gravity. It protects the surface from harmful solar ultraviolet (UV) radiation and provides oxygen, which makes life on Earth in the present form possible. This chapter gives an overview of the relevant properties of the atmosphere and its most important trace gas species. In addition, the global circulation patterns located in the troposphere and stratosphere are addressed.

2.1 Vertical structure of the atmosphere

The Earth's atmosphere has a vertical structure that can be divided into different layers. The layers are either defined according to their thermal structure, their motion mechanism or their degree of ionisation. Based on its temperature profile (Figure 2.1), the atmosphere can be divided into several layers with distinct boundaries, the so-called *-pauses*. The pressure within the atmosphere decreases with increasing altitude z according to the barometric height formula (e.g. Roedel, 2000):

$$p(z) = p_0 \cdot e^{-\frac{Mgz}{RT}}, \tag{2.1}$$

with $p_0 = 1013$ mbar representing the surface pressure for standard conditions, M being the mean molecular mass of air ($M = 0.029\ \frac{\mathrm{kg}}{\mathrm{mol}}$), g the acceleration due to gravity ($g \approx 9.81 \frac{\mathrm{m}}{\mathrm{s}^2}$), and $R = 8.314\ \frac{\mathrm{J}}{\mathrm{mol \cdot K}}$ representing the universal gas constant. In contrast to the pressure profile the temperature profile shows local minima and maxima where the aforementioned pauses are located.

The lowermost atmospheric layer is the *troposphere* which extends from the surface to the tropopause. In the troposphere, the temperature decreases with height according to the decreasing pressure from Equation 2.1 with an average moist adiabatic lapse rate of approximately 7 K/km. Due to heating of the surface by solar radiation hot air masses can rise from the surface leading to a vertical mixing of the troposphere. As soon as these air masses cool down, water vapour can condense and form clouds (Section 5.6). The troposphere contains the largest part of the mass of the atmosphere and can be further subdivided into the boundary layer (BL), which is directly affected by friction at the surface, the free troposphere (FT), and the upper troposphere (UT). Due to heating from the surface and friction, the BL is often governed by turbulence and hence well-mixed. The height of the BL is influenced by surface temperature, surface roughness, wind speed and relative humidity and ranges between some hundreds of metres up to 2 km over land. As the surface temperature over the ocean is more constant than over land the height of the marine boundary layer (MBL) is with a few hundred metres also more constant than over land.

The *tropopause* marks the border between the troposphere and the stratosphere. Here the sign of the temperature gradient changes from negative to positive, i.e. a temperature inversion occurs. The tropopause is located between 17 and 18 km in the tropics and between 9 and 13 km in polar regions (Roedel, 2000). The *stratosphere* is characterised by a maximum ozone concentration located between 20 and 25 km (Chapter 2.4.1). The temperature in the stratosphere increases with altitude since the lower stratosphere is cooled by the infrared emission of water vapour and CO_2

and the upper stratosphere is heated due to the absorption of solar radiation by the ozone layer. Due to the positive temperature gradient there is a thermally stable stratification with almost no convection in the stratosphere. The stratosphere extends to a height of approximately 50 km where the *stratopause* separates it from the mesosphere.

The *mesosphere* lies between the stratopause and the mesopause at approximately 85 km. Here, the temperature decreases again with increasing altitude because of decreased solar heating and increased cooling by CO_2 emission. The mesosphere is terminated by the *mesopause*, which represents the coldest region of the atmosphere with temperatures as low as 190 K. The *thermosphere*, located above the mesopause, is strongly influenced by solar wind (charged particles emitted from the sun). In this layer, the temperature increases again due to absorption of solar radiation by mainly O_2, and reaches values of up to approximately 1500 K.

Another way to vertically differentiate atmospheric behaviour is to look at molecule mixture. Above 100 km the atmospheric constituents start to separate according to their mass, as the effectivity of diffusion increases with increasing altitude. This region is called *heterosphere*. The *homosphere* corresponds to the lower part of the atmosphere below 100 km where turbulent mixing dominates over molecular diffusion. The transition zone at approximately 100 km is called *turbopause* and is often regarded as the boundary between the Earth's atmosphere and outer space. The degree of ionisation allows a further division of the atmosphere into the *neutrosphere* and the *ionosphere*. The transition zone is located at an altitude of approximately 65 km and distinguishes the layer where the atmospheric constituents are ionised by solar radiation (ionosphere) from the neutrosphere.

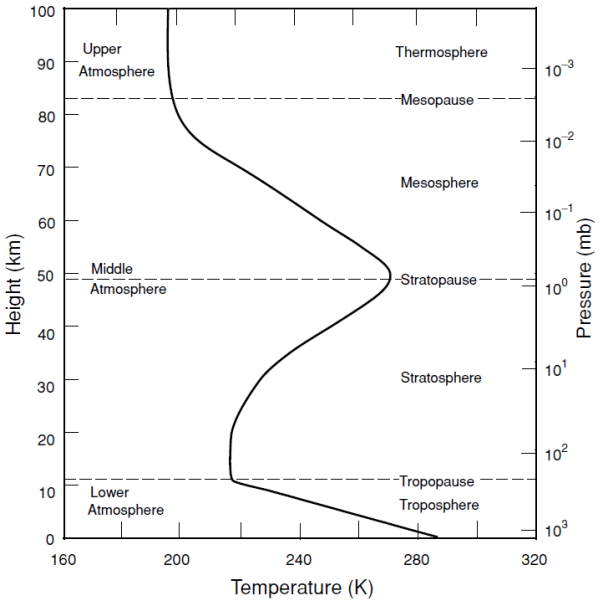

Figure 2.1: Vertical temperature profile of the atmosphere according to the U.S. Standard Atmosphere and the corresponding layers. Adapted from Liou (2002).

2.2 Global circulation systems

The tropospheric circulation system is mainly driven by the difference between the incident solar radiation between the tropics (30°N to 30°S) and the higher latitudes. In the equatorial zone, the intensity of the incident solar radiation and hence the temperature at the surface is highest as the direction of the radiation is almost perpendicular to the ground. This region with rather low air pressure, where hot humid air is lifted up to the tropopause, is called the intertropical convergence zone (ITCZ). Its exact position shows a seasonal variation due to the tilted rotational axis of the

Earth and the stronger distribution of land masses in the northern hemisphere. On a global scale, three major tropospheric circulation patterns can be observed, which are depicted in Figure 2.2:

1. Hadley cell: The Hadley circulation pattern forms a loop, which starts at the ITCZ where warm and moist air is lifted up into the low pressure regions of the tropopause. There, it moves poleward. It descends again in a high pressure system at a latitude of about 30°, where many of the Earth's deserts are located. The surface winds towards the ITCZ are deflected by the Coriolis force, resulting in a constantly blowing component from the north-east direction on the northern hemisphere and from the south-east direction on the southern hemisphere. Due to their large impact on maritime navigation these winds are called trade winds.

2. Ferrel cell: The Ferrel circulation cell occurs in the mid-latitudes (30° to 60°) between the Hadley and the Polar cell. On the northern hemisphere, the average air flow near the surface moves eastwards to the poles due to the Coriolis force. Hence, the Ferrel cell is also called the west wind zone.

3. Polar cell: Warm air rises at about 60° and moves towards the poles through the upper troposphere. When the polar regions are reached, the air has cooled considerably and descends as a cold and dry high pressure area and moves away from the poles along the surface. Again influenced by the Coriolis force, the air is twisting westward to produce the Polar easterlies.

As a consequence of the horizontal temperature differences between the circulation cells, at latitudes of 30° and 60° strong winds occur in the tropopause, the so-called jet streams (Figure 2.2b).

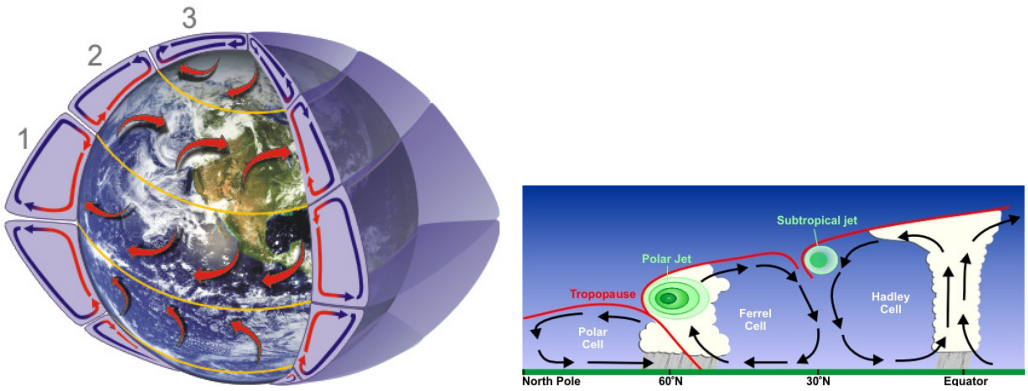

(a) (b)

Figure 2.2: (a) Overview of the global circulation patterns: 1. Hadley cell, 2. Ferrel cell and 3. Polar cell, adapted from `http://www.srh.noaa.gov/jetstream/global/circ.htm` (March 2014). (b) Cross-section of the tropospheric circulation in the northern hemisphere, adapted from `http://www.srh.noaa.gov/jetstream/global/jet.htm` (March 2014).

Figure 2.3 shows characteristic time scales for the horizontal and vertical transport of air in the atmosphere. The long-range transport of air parcels is faster in longitudinal direction than in meridional direction due to the westerlies, the geostrophic wind along the longitudinal bands. According to Jacob (1999), air parcels need a few weeks to circumnavigate the globe in longitudinal direction, whereas it takes approximately one to two months for an air parcel at mid-latitudes to reach the tropics or polar regions. The transport across the Equator is even slower due to the low temperature differences, and an air parcel in the northern hemisphere needs about a year to reach the southern hemisphere.

The time scales for vertical transport of air from the surface to the tropopause depend on the turbulent atmospheric flow. The Einstein diffusion equation to derive the time Δt an air parcel

needs to travel along a certain vertical height Δz can be expressed as:

$$\Delta t = \frac{(\Delta z)^2}{2 \cdot K_z} \tag{2.2}$$

with a tropospheric turbulent diffusion coefficient K_z of about $2{\cdot}10^5$ cm^2s^{-1} (Jacob, 1999). Hence, vertical mixing up to the tropopause happens on a time scale of approximately one month. Due to the temperature inversion in the stratosphere (Section 2.1), the time needed for the exchange of air between the troposphere and the stratosphere is greater and can be on the order of years.

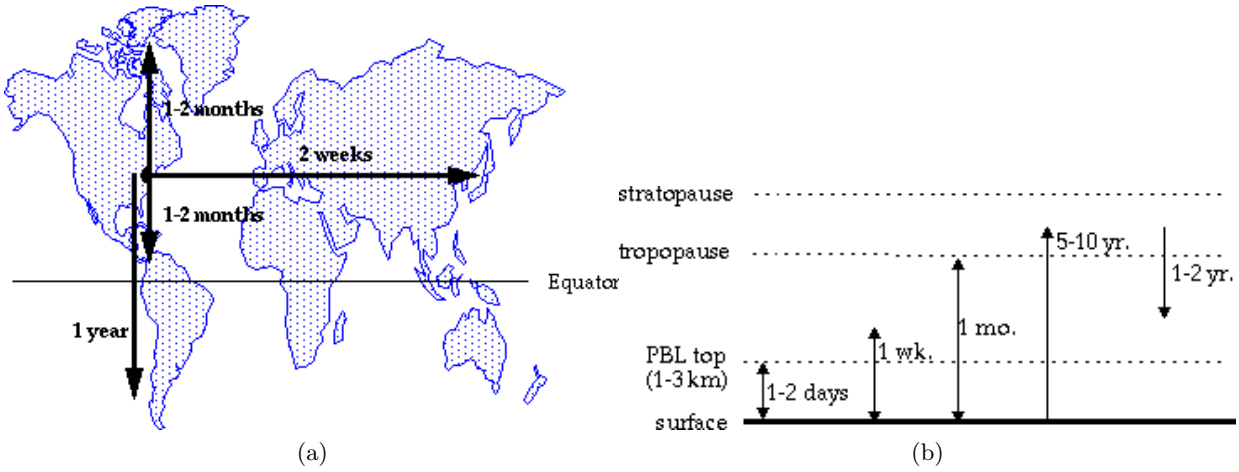

Figure 2.3: Time scales which are typically needed for (a) global horizontal transport in the troposphere and (b) vertical transport up to the stratosphere, reproduced from Jacob (1999) with kind permission of Princeton University Press (August 2014).

2.3 Composition of the atmosphere

Table 2.1 provides a list of the main constituents of the Earth's atmosphere. With more than 99% of dry air, molecular nitrogen (N_2), oxygen (O_2) and the noble gas argon (Ar) are the most abundant species in the atmosphere. All other species and many other compounds not listed here add up to less than 1% of the atmosphere. Hence, those species are referred to as trace gases. In Section 2.4, the chemistry of some of these trace gases measured within this work is described. Another important component of the atmosphere are aerosols. With a diameter of a few nanometres to tens of micrometres, aerosols are small liquid or solid particles which are dispersed and suspended in the air. Aerosol particles are emitted from natural or anthropogenic sources, for example from combustion processes like biomass burning or from industrial processes, volcanic eruptions, dust transported by the wind, or from sea spray. They are further specified in Section 2.4.10. In order to quantify the different atmospheric gases, two fundamental descriptions are used: The concentration c and the mixing ratio x. The concentration of a trace gas indicates the amount of a trace gas per volume of air (Platt and Stutz, 2008):

$$c = \frac{\text{amount of tracegas}}{\text{volume of air}}. \tag{2.3}$$

The amount can either refer to the number of molecules, the number of moles or to the mass yielding the number concentration c_n, the molar concentration c_M, and the mass concentration c_m, respectively. In general, the unit of c_n is given in molecules per cm^3. Another quantity is given by the mixing ratio, which describes the ratio of the amount of a trace gas and the amount of air including the trace gas (Platt and Stutz, 2008):

$$x = \frac{\text{amount of tracegas}}{\text{amount of air} \;+\; \text{trace gas}} \approx \frac{\text{amount of tracegas}}{\text{amount of air}}. \tag{2.4}$$

In this case, the amount frequently refers to a volume, yielding volume mixing ratios (VMRs). Typically, atmospheric trace gas VMRs are of the order of 10^{-6}, 10^{-9} or 10^{-12}, which corresponds to ppm (parts per million), ppb (parts per billion) or ppt (parts per trillion), respectively. In order to convert a concentration c_n into VMR, the following equation can be applied according to the ideal gas law:

$$x_v = c_n \cdot \frac{R \cdot T}{N_A \cdot p}, \tag{2.5}$$

with p and T being the pressure and temperature, R the gas constant and N_A the Avogadro number.

Table 2.1: Main constituents of the unpolluted dry atmosphere. Numbers adapted from Platt and Stutz (2008).

element	chemical formula	mixing ratio by volume [%]
Nitrogen	N_2	78.09
Oxygen	O_2	20.95
Argon	Ar	0.93
Carbon dioxide	CO_2	0.037
Neon	Ne	0.0018
Helium	He	0.00052
Methane	CH_4	0.00017
Krypton	Kr	0.00011
Xenon	Xe	0.00009
Hydrogen	H_2	0.00005
Nitrous oxide	N_2O	0.00003

2.4 Atmospheric chemistry

This section provides an overview of the chemical processes of the different trace gas species that are addressed in this thesis. In the following, a short introduction to these trace gas species is given, as well as a summary of their sources, sinks, and relevant processes in the atmosphere.

2.4.1 Ozone chemistry

Ozone (O_3) plays a major role in the chemical and radiative budgets of the atmosphere.

Stratospheric ozone

More than 90 % of the total atmospheric ozone is located in the stratosphere where it forms a layer between 20 and 25 km altitude (Fahey and Hegglin, 2010). This ozone layer is crucial for life on Earth, since it absorbs the solar UV radiation ($\lambda < 320$ nm) before it can reach the surface. This high energy UV radiation can cause skin cancer or DNA changes. Figure 2.4 shows a sketch of the ozone distribution in the atmosphere.

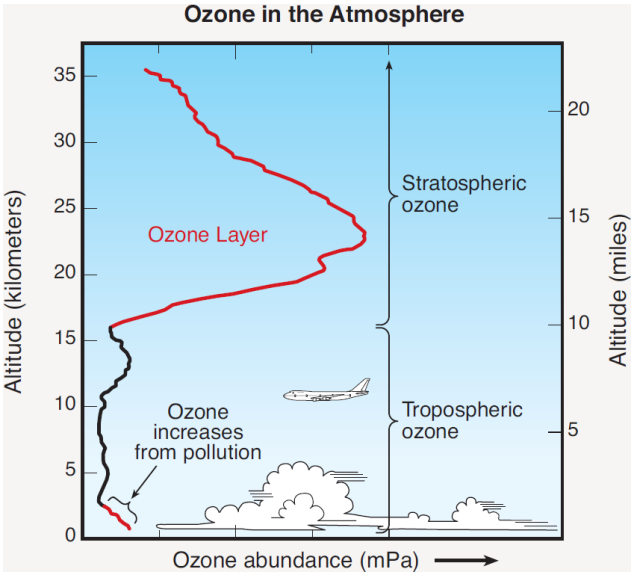

Figure 2.4: Vertical profile of the ozone concentration in the atmosphere, adapted from [Fahey and Hegglin (2010)].

The first theory of the formation and destruction of O_3 in the stratosphere was reported by Chapman (1930). The Chapman cycle includes the following steps:

$$O_2 + h\nu \longrightarrow 2\ O(^3P) \qquad \lambda < 242\ \text{nm} \tag{2.6}$$

$$O(^3P) + O_2 + M \longrightarrow O_3 + M \tag{2.7}$$

$$O_3 + h\nu \longrightarrow O_2 + O(^1D) \qquad \lambda < 320\ \text{nm} \tag{2.8}$$

The production of ozone is initiated by the photolysis of molecular oxygen (O_2) yielding two oxygen atoms (Equation 2.6), which can then react with another oxygen molecule and a collision partner M (typically N_2 or O_2) to form ozone (Equation 2.7). Loss of O_3 happens due to photolysis (Equation 2.8) or via the reaction with atomic oxygen:

$$O(^1D) + M \longrightarrow O(^3P) + M \tag{2.9}$$

$$O_3 + h\nu \longrightarrow O_2 + O(^3P) \qquad \lambda < 1180\ \text{nm} \tag{2.10}$$

$$2\ O(^3P) + M \longrightarrow O_2 + M \tag{2.11}$$

$$O(^3P) + O_3 \longrightarrow 2\ O_2 \tag{2.12}$$

Reaction (2.12) is the main loss process for odd oxygen (O, O_3) in the Chapman cycle, whereas reaction (2.11) is known to be too slow to be important for stratospheric chemistry. However, as it turned out that the Chapman cycle would balance at an ozone concentration that is higher than observed values, additional ozone destroying mechanisms had to be considered. These additional loss reactions are mainly catalytic cycles according to the following reaction scheme:

$$X + O_3 \longrightarrow XO + O_2 \tag{2.13}$$

$$XO + O \longrightarrow X + O_2 \tag{2.14}$$

$$\text{net} : O_3 + O \longrightarrow 2\ O_2, \tag{2.15}$$

with X either being the hydroxyl radical OH, nitrogen monoxide (NO), or a halogen radical (Cl, Br, I) (Crutzen, 1970; Johnston, 1971; Molina and Rowland, 1974). These radicals can be of natural origin or from anthropogenic sources, one example being the industrially produced chlorofluorocarbons (CFCs), which are mainly used as freezing agents. Due to their extremely long tropospheric

lifetime, they can easily reach the stratosphere and act as ozone depleting substances (ODEs). Farman et al. (1985) discovered the so-called ozone hole over the Antarctic, where a dramatic loss of ozone can be observed during the Antarctic spring. Recent studies show that a similar ozone loss close to that found in some Antarctic winters was observed during the Arctic winter 2010/2011 (Kuttippurath et al., 2012).

Tropospheric ozone

Only approximately 10% of the total atmospheric ozone is located in the troposphere. Possible sources for tropospheric ozone are, on the one hand, the transport processes from the stratosphere to the troposphere and, on the other hand, the reaction of atomic with molecular oxygen. The atomic oxygen can be formed via photolysis of tropospheric NO_2. Fishman and Crutzen (1978) proposed these reactions involving sufficient amounts of NO_x:

$$NO_2 + h\nu \longrightarrow NO + O(^3P) \qquad \lambda < 420 \text{ nm} \tag{2.16}$$

$$O(^3P) + O_2 + M \longrightarrow O_3 \tag{2.17}$$

$$NO + O_3 \longrightarrow NO_2 + O_2 \tag{2.18}$$

O_3 is formed when an oxygen radical that is produced by the photolysis of NO_2 (Equation 2.16) reacts with O_2 (Equation 2.17). Since O_3 can be destroyed by NO again, no net O_3 is produced and a photo-stationary steady state between NO_2, NO and O_3 is reached during daytime. This can be expressed by the *Leighton ratio L* (Leighton, 1961), which is the ratio of NO and NO_2:

$$L \equiv \frac{[NO]}{[NO_2]} = \frac{J_{NO_2}}{[O_3] \cdot k_{NO}} \tag{2.19}$$

with k_{NO} being the reaction rate for Equation (2.18) and with J_{NO_2} representing the photolysis frequency of NO_2 (Equation 3.5).

Another important source of tropospheric ozone is the oxidation of CH_4, which results in the formation of HCHO (Equation 2.38).

2.4.2 Nitrogen oxides

In atmospheric chemistry, the nitrogen oxides (NO_x) nitrogen monoxide (NO) and nitrogen dioxide (NO_2) are both radicals and highly reactive, thus having a strong impact on the oxidation capacity of the atmosphere. In the troposphere NO_x enables the production of O_3, while the depletion of the stratospheric ozone layer is enhanced by NO_2. Natural sources of NO_x include emissions from biomass burning, lightning or soil. Nowadays, the majority of the NO_x emissions originates from anthropogenic sources such as fossil fuel combustion, traffic, and industrial activities. According to Lee et al. (1997), this anthropogenic contribution makes up more than half of the global NO_2 emissions.

Stratospheric nitrogen oxides

The most important stratospheric source of NO_x is nitrous oxide (N_2O). N_2O is emitted in the troposphere by both natural sources like the oceans or soil, and by anthropogenic sources like artificial fertilizers from chemical industries. It is a rather inert molecule and has a long lifetime ($\tau \approx 120$ years), which makes it stable enough to reach the stratosphere. After its transport to the stratosphere, N_2O reacts with atomic oxygen to N_2, O_2 or NO:

$$N_2O + O(^1D) \longrightarrow 2\ NO. \tag{2.20}$$

NO can then further react with ozone to form NO_2:

$$NO + O_3 \longrightarrow NO_2 + O_2. \tag{2.21}$$

The further photolysis of NO and the subsequent reactions of N with NO act as a sink for NO_x in the upper stratosphere.

As the catalytic cycles involving NO_x depend on solar radiation, NO and NO_2 have a strong diurnal variation. From sunrise on, NO_2 is photolysed to NO according to Equation (2.16). During daytime, there is a photochemical equilibrium between NO and NO_2 described by the *Leighton ratio* L (Equation 2.19). According to laboratory measurements by Atkinson et al. (2004), the reaction rate results in $k_{NO} = 1.8 \cdot 10^{-14} cm^3 molec^{-1} s^{-1}$, depending on the solar zenith angle (SZA). Thus, L changes during the course of the day with a maximum photolysis rate of approximately $J_{NO_2} = 8 \cdot 10^{-3} s^{-1}$ at noon time for clear sky conditions, resulting in an average NO_2 lifetime of the order of two minutes (e.g. Junkermann et al., 1989). L typically lies between 0.5 and 1 in the lower troposphere, depending on the ozone concentration and daytime. With increasing altitude, L is shifted towards NO due to the increasing photolysis frequency of NO_2. After sunset, NO is rapidly converted to NO_2 due to the missing NO_2 photolysis. NO_2 is then oxidised to NO_3 by O_3 according to the following equation:

$$NO_2 + O_3 \longrightarrow NO_3 + O_2. \tag{2.22}$$

Since NO_3 photolyses quickly in the sunlit atmosphere, it has a very short lifetime during the day. However, at night it reacts with NO_2 and builds the night time reservoir species dinitrogen pentoxide (N_2O_5):

$$NO_3 + NO_2 + M \longrightarrow N_2O_5 + M. \tag{2.23}$$

When the Sun rises again, all NO_3 is destroyed very quickly yielding NO, and N_2O_5 reacts back to NO_2 and NO_3 by collisional decomposition or photolysis:

$$N_2O_5 + M \longrightarrow NO_3 + NO_2 + M \tag{2.24}$$

$$N_2O_5 + h\nu \longrightarrow NO_2 + NO + O_2. \tag{2.25}$$

Since the photolysis of NO_2 proceeds some orders of magnitude faster than that of N_2O_5, the observed NO_2 concentration decreases in the morning until a photochemical steady state between NO and NO_2 is reached according to the Leighton ratio. Due to its reduced photolysis, the NO_2 concentration increases in the evening. Additionally, the slow photolysis of N_2O_5 leads to a further increase of the NO_2 concentration throughout the day.
One important sink for NO_x is the formation of long-lived reservoir species like N_2O_5 or nitric acid (HNO_3), which originate from oxidation processes such as:

$$NO_2 + OH + M \longrightarrow HNO_3 + M. \tag{2.26}$$

Tropospheric nitrogen oxides

As already mentioned in Section 2.4.1, tropospheric NO_x is strongly involved in ozone production. Combustion processes mainly lead to the emission of NO and to a lesser extent to NO_2 (Lee et al., 1997). NO is converted to NO_2 via the reaction with O_3 (Equation 2.18). During the day, Reactions 2.16 to 2.18 lead to a photo-stationary state between NO, NO_2 and O_3 according to the Leighton ratio L (Equation 2.19). No net ozone is produced in this reaction cycle (Figure 2.5a), except if any other reaction occurs that converts NO into NO_2 without consuming an O_3 molecule. In the troposphere, this is the case for reactions with the hydrogen oxide radical HO_x ($HO_x = OH + HO_2$) or organic compounds RO_2 (R = CH_3 or larger hydrocarbons) and reaction 2.18 can for example be replaced by:

$$NO + HO_2 \longrightarrow NO_2 + OH \tag{2.27}$$

$$NO + RO_2 \longrightarrow NO_2 + RO. \tag{2.28}$$

Since the photolysis of NO_2 again yields NO and O_3, the formation of O_3 can be quite efficient and leads to the so-called photochemical smog in polluted areas. The reaction scheme of NO_2 is illustrated in Figure 2.5.

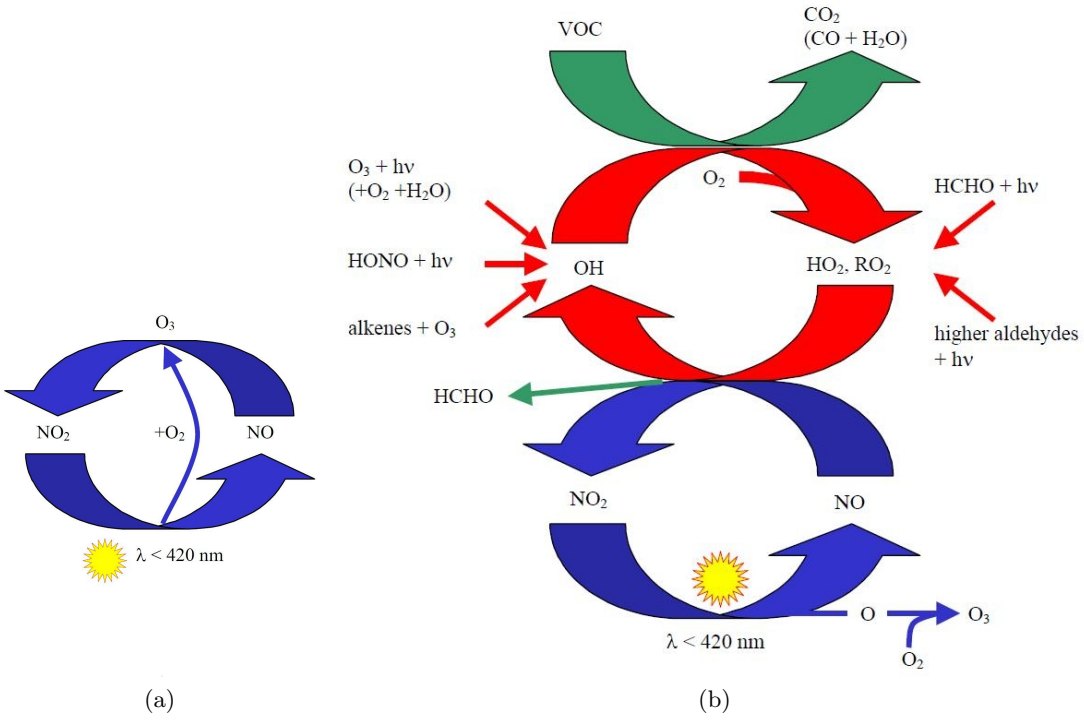

Figure 2.5: (a) Schematic summary of the reactions yielding the photo-stationary steady state of NO_2. (b) O_3 formation in the presence of HO_x or volatile organic compounds (VOCs). Adapted from Trick (2004).

2.4.3 Water vapour (H_2O)

Water vapour belongs to the natural atmospheric greenhouse gases and is expected to have a significant influence on climate change due to an increase of the water vapour concentration in a warmer world (e.g. Held and Soden, 2000). In the atmosphere, water can occur in all three phases and is therefore an extremely variable trace gas. In the troposphere, water vapour is the major source of hydroxyl radicals (Section 2.4.4) (e.g. Rohrer and Berresheim, 2006), and can thus have an indirect influence on the lifetime of several atmospheric trace gases. It is the main component of clouds and can affect the transport of latent heat and the radiative transfer in the atmosphere. In the lower troposphere, the water vapour mixing ratio usually reaches values around 3 %, whereas in the stratosphere the mixing ratios are much smaller, typically between 2 and 4 ppm. The absorption cross-section of water vapour is for example provided by the absorption line data base HITRAN (Rothman et al., 2013). However, especially in the UV and visible wavelength range below 500 nm, experimental data is sparse and several absorption lines are only calculated and not validated by measurements (Lampel, 2014). Thus, uncertainties might exist in the UV and visible wavelength range when significant amounts of water vapour are present in the atmosphere. The atmospheric water vapour content has been inferred by satellite measurements in the blue spectral range by Wagner et al. (2013b) as well as by ground-based measurements providing H_2O vertical profiles (Wagner et al., 2013a).

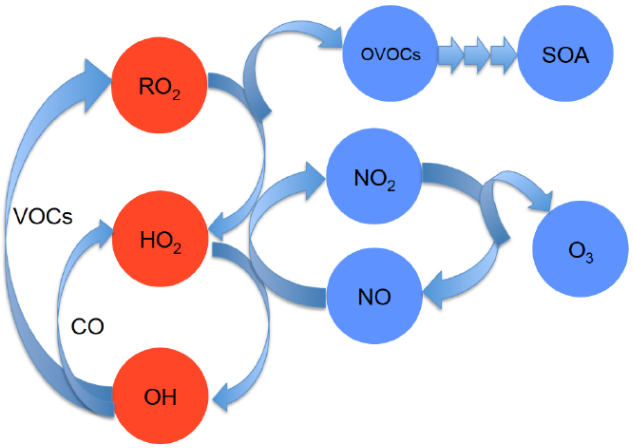

Figure 2.6: Schematic diagram of the hydrogen oxide radical reactions in the troposphere, adapted from Kim et al. (2014).

2.4.4 Hydrogen oxide radicals

The hydroxyl radical OH and the hydroperoxy radical HO_2 (also summarised as the hydrogen oxide radical HO_x = OH + HO_2) are key species in the oxidation chemistry of the atmosphere. OH acts as the dominant daytime oxidant in the troposphere and initiates the removal of several atmospheric trace gases. OH is primarily formed by the photodissociation of O_3 in the presence of water vapour (Levy, 1971). Since solar irradiation and humidity are highest in the tropics, the formation rate of OH is highest in the tropics (e.g. Lelieveld et al., 2002, 2008). Due to its high reactivity, it has a short photochemical lifetime of approximately 1 second (Heard and Pilling, 2003; Stone et al., 2012), leading to highly variable concentrations with a global mean in the order 10^6 molec cm^{-3} (Lelieveld et al., 2004). The lifetime of HO_2 is approximately 100 seconds, with a typical concentration of the order of 10^8 molec cm^{-3} during daytime. Figure 2.6 shows an overview of the HO_x radical cycle that is influenced by NO_x and volatile organic compounds (VOCs). Further reactions of HO_x with peroxy radicals (RO_2) and NO_x initiate the production of tropospheric ozone and oxygenated VOCs (OVOCs), which are precursors for secondary organic aerosols (SOA). In environments with high NO_x levels where the reaction of OH and NO_2 dominates the loss processes of OH, the chemistry of HO_x is well-understood (e.g. Edwards et al. (2013) and references therein). Discrepancies between HO_x measurements and models occur under low NO_x conditions, especially in the presence of large amounts of VOCs, as e.g. in tropical rain forests. In these remote forested regions, considerably higher values of OH radicals are found than can be simulated by well-established chemical models (e.g. Lelieveld et al., 2008; Kubistin et al., 2010; Edwards et al., 2013). In order to compensate for the discrepancies between measurements and models, these studies have led to the development of alternative chemical mechanisms. According to Taraborrelli et al. (2012) the oxidation of isoprene over tropical forests can act as both sink and source, i.e. as a buffer for hydroxyl radicals.

2.4.5 The O_2-O_2 collision complex O_4

The collision of two oxygen molecules (O_2) leads to the formation of the O_2-O_2 collision complex (henceforth referred to as O_4) according to the following formula:

$$2\ O_2 \longrightarrow O_4 \quad \text{and} \quad k_{eq} = [O_4]/[O_2]^2 \tag{2.29}$$

with k_{eq} being the equilibrium constant. The existence of a weak chemical bond between two oxygen molecules was first proposed by Lewis (1924), who studied the magnetic susceptibility of liquid oxygen. He further stated that oxygen is a mixture of O_2 and O_4 with O_2 being paramagnetic, whereas O_4 is not paramagnetic, since it is chemically and magnetically saturated (Aquilanti et al.,

1999). However, the nature of the molecular interactions in the O_2-O_2 collision complex are still uncertain and the equilibrium constant k_{eq} is not known (Sinreich et al., 2006).

O_4 has several broad absorption bands throughout the ultraviolet (UV), visible (vis) and near-infrared region of the electromagnetic spectrum. In the UV/vis spectral range (300 - 630 nm) they are caused by simultaneous transitions of the two O_2 molecules from their ground states to electronically excited states. The UV wavelength range comprises three absorption bands at 343 nm, 360 nm, and 380 nm that correspond to the transition from the ground state ${}^3\Sigma_g^- + {}^3\Sigma_g^-$ to the excited state ${}^1\Sigma_g^+ + {}^1\Sigma_g^+$ with the vibrational quantum numbers $\nu = 2$, 1, and 0, respectively. The visible wavelength range includes five absorption bands, which are due to simultaneous transitions of the two O_2 molecules to excited states. The absorption bands at 446 nm and 477 nm are caused by the transition ${}^3\Sigma_g^- + {}^3\Sigma_g^-$ to the excited state ${}^1\Sigma_g^+ + {}^1\Delta_g$ with the vibrational quantum numbers $\nu = 1$ and $\nu = 0$, respectively. The bands at 532 nm, 577 nm, and 630 nm are caused by the simultaneous transition from the ground state ${}^3\Sigma_g^- + {}^3\Sigma_g^-$ to the excited state ${}^1\Delta_g + {}^1\Delta_g$ with the vibrational quantum numbers $\nu = 2$, 1, and 0, respectively (Platt and Stutz, 2008).

The atmospheric concentration of O_4 is proportional to the square of the O_2 concentration and is hence exponentially decreasing with altitude (e.g. Frieß et al., 2006). It can be calculated according to the ideal gas law:

$$[O_4] = k_{eq} \cdot \left(\frac{0.21 \cdot p \cdot N_A}{R \cdot T} \right)^2 \tag{2.30}$$

with p and T being the pressure and temperature, R the gas constant and N_A the Avogadro number. The scale height of O_4, i.e. the height where the O_4 concentration has decreased by a factor of e, corresponds to approximately 4 km. According to Thalman and Volkamer (2013), the integral of the stronger absorption lines is independent of temperature, while the line shape and peak O_4 absorption cross-section exhibit a temperature dependence, i.e. the peak O_4 absorption cross-section increases at lower temperatures. The absorption cross-section σ_{O_4} is usually specified in units of $cm^5 molec^{-2}$. Since the vertical profile of O_4 is known (Equation 2.30), O_4 can be used as indicator for the effective light path in the atmospheric radiative transfer. Changes in the absorption of O_4 are induced by respective changes in the light path. Therefore, together with radiative transfer simulations and inversion methods, O_4 measurements can be used to gain information on the light path through the atmosphere (Chapter 3).

2.4.6 Formaldehyde (HCHO)

Formaldehyde (HCHO) is the most abundant organic carbonyl compound in the atmosphere and belongs to the family of oxygenated volatile organic compounds (OVOCs). On a global scale, it is mainly produced from the oxidation of methane (CH_4) (60 %) and non-methane volatile organic compounds (NMVOCs), such as isoprene (C_5H_8) (30 %) (Stavrakou et al., 2009a). Isoprene is the most abundant biogenic VOC emitted into the atmosphere and accounts for about half of the total biogenically emitted VOCs (Guenther et al., 1995) (Section 6.3). During several studies, HCHO vertical column densities obtained from satellite observations have been used to constrain isoprene fluxes, for example over Africa (Marais et al., 2012) or over China and South-East Asia (Fu et al., 2007; Stavrakou et al., 2009c, 2014). For a sufficient amount of NO_x, the oxidation of CH_4 follows

the reaction scheme:

$$\begin{aligned}
CH_4 + OH &\longrightarrow CH_3 + H_2O && (2.31)\\
CH_3 + O_2 + M &\longrightarrow CH_3O_2 + M && (2.32)\\
CH_3O_2 + NO &\longrightarrow CH_3O + NO_2 && (2.33)\\
CH_3O + O_2 &\longrightarrow HCHO + HO_2 && (2.34)\\
HO_2 + NO &\longrightarrow OH + NO_2 && (2.35)\\
2\ (NO_2 + h\nu) &\longrightarrow 2\ (NO + O(^1D)) && (2.36)\\
2\ (O(^1D) + O_2 + M) &\longrightarrow 2\ (O_3 + M) && (2.37)\\
\hline
\text{net}: CH_4 + 4\ O_2 &\longrightarrow HCHO + H_2O + 2\ O_3. && (2.38)
\end{aligned}$$

Hence, the oxidation of CH_4 results in the production of HCHO, O_3, and H_2O. In the absence of NO_x, the reaction scheme changes according to the following equations:

$$\begin{aligned}
CH_4 + OH &\longrightarrow CH_3 + H_2O && (2.39)\\
CH_3 + O_2 + M &\longrightarrow CH_3O_2 + M && (2.40)\\
CH_3O_2 + HO_2 &\longrightarrow CH_3O_2H + O_2 && (2.41)\\
CH_3O_2H + h\nu &\longrightarrow CH_3O + OH && (2.42)\\
CH_3O + O_2 &\longrightarrow HCHO + HO_2 && (2.43)\\
\hline
\text{net}: CH_4 + O_2 &\longrightarrow HCHO + H_2O. && (2.44)
\end{aligned}$$

In contrast to the situation in a high NO_x environment, only HCHO and H_2O are produced under low NO_x levels. In the remote marine atmosphere the global HCHO background reaches values between 0.2 and 1 ppb at the surface (Weller et al., 2000; Peters et al., 2012). Further sources of HCHO are emissions from fossil fuel combustion (e.g. Luecken et al., 2012), biomass burning (e.g. Yokelson et al., 2013), or from vegetation (e.g. DiGangi et al., 2011). In addition to deposition via washout during rain fall, the major sinks of HCHO are the degradation by OH radicals and the photolysis at wavelengths below 365 nm:

$$\begin{aligned}
HCHO + OH &\longrightarrow HCO + H_2O && && (2.45)\\
HCHO + h\nu + O_2 &\longrightarrow HCO + HO_2 && \lambda < 330\ \text{nm} && (2.46)\\
HCHO + h\nu &\longrightarrow H_2 + CO && \lambda < 365\ \text{nm}. && (2.47)
\end{aligned}$$

The HCO radical reacts rapidly with O_2 resulting in HO_2 and CO, which is in turn eventually converted to CO_2 on a longer timescale (several months). The lifetime of HCHO with respect to the two photolysis reactions (Equation 2.46 and 2.47) is 9 and 7 hours, respectively, while it is 31 hours against the reaction with OH (De Smedt, 2011). The overall HCHO lifetime is relatively short and lies around a few hours (Arlander et al., 1995; De Smedt et al., 2008). Thus, HCHO is present close to its sources, such as rain forests, industries or shipping emissions (Marbach et al., 2009; Stavrakou et al., 2009c; MacDonald et al., 2012). Figure 2.7 gives an overview of the reaction mechanisms involving HCHO in the troposphere.

2.4.7 Glyoxal (CHOCHO)

Glyoxal (CHOCHO) is the smallest possible α-dicarbonyl compound and is produced in the atmosphere by the oxidation of volatile organic compounds (VOCs). These VOCs can be biogenic, e.g. isoprene and monoterpenes (Stavrakou et al., 2009b), or anthropogenic, e.g. aromatics like benzene or toluene, produced by biomass burning, fossil fuel combustion or anthropogenic activities (Volkamer et al., 2001, 2005a). The largest source of CHOCHO is estimated to be the oxidation

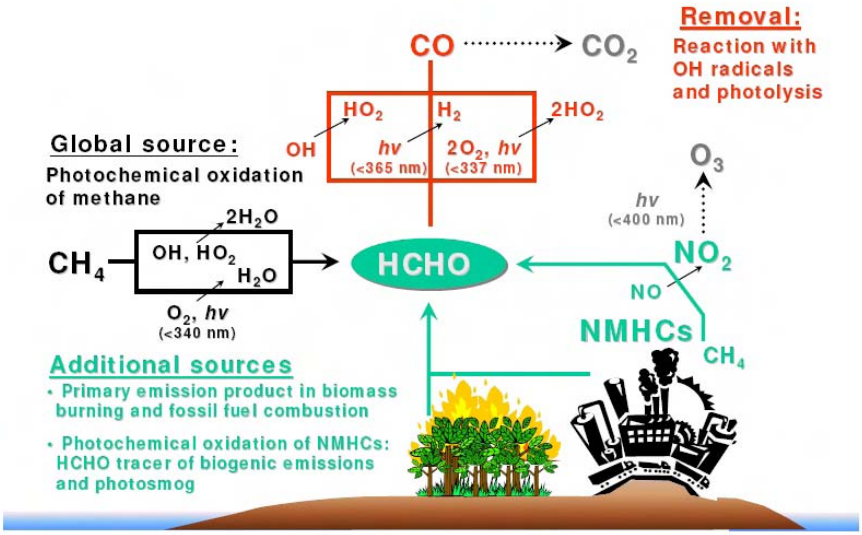

Figure 2.7: Diurnal cycle of formaldehyde during daylight, adapted from Marbach et al. (2007).

of biogenic VOCs, particularly of isoprene (C_5H_8, 2-methyl-1,3-butadiene) (Vrekoussis et al., 2009; Stavrakou et al., 2009b).

In analogy to HCHO, glyoxal is destroyed in the atmosphere by photolysis (63 %), oxidation by OH (23 %), and to a lesser extent by wet (8 %) and dry (6 %) deposition (Fu et al., 2008; Myriokefalitakis et al., 2008). Since the photolysis and the reaction with OH proceeds very quickly, the lifetime of CHOCHO in the atmosphere is about 1.3 hours for overhead sun conditions in urban air (Volkamer et al., 2005a), and 2 to 3 hours on a global scale (Fu et al., 2008; Myriokefalitakis et al., 2008). Since glyoxal is highly soluble, it might play a role in the formation of secondary organic aerosol (SOA) and might explain the considerable amount of SOA missing in model simulations (Volkamer et al., 2007). During the last years, measurements from satellite instruments have been used to infer global maps of CHOCHO as well as to run long-term studies of its temporal and spatial distribution (e.g. Wittrock et al., 2006; Vrekoussis et al., 2010; Alvarado et al., 2014). Glyoxal was also observed under open ocean condition during several ship campaigns (Mahajan et al., 2014), which showed a large variability in the amount of CHOCHO (approximately between 25 and 140 ppt). However, observations of CHOCHO, especially above the open ocean, have to be treated with care due to overlaying effects of liquid water absorption and scattering or vibrational Raman scattering (Lampel, 2014). As an example, Sinreich et al. (2010) reported CHOCHO mixing ratios of up to 140 ppt over the open ocean of the Eastern Pacific, whereas recent measurements above the equatorial Pacific showed lower mixing ratios between 25 and 80 ppt (Coburn et al., 2014).

2.4.8 Nitrous acid (HONO)

Nitrous acid (HONO) is an important precursor for OH radicals through its photolysis into OH and NO (Stockwell and Calvert, 1978; Platt et al., 1980; Stutz et al., 2000):

$$\mathrm{HONO} + \mathrm{h}\nu \longrightarrow \mathrm{OH} + \mathrm{NO} \qquad (300\ \mathrm{nm} < \lambda < 405\ \mathrm{nm}) \tag{2.48}$$

According to Alicke et al. (2002), the photolysis of HONO is the most important source for OH formation in the early morning hours, surpassing the OH production from O_3 photolysis on certain days. The diurnal variation of HONO typically shows a maximum before sunrise, followed by a rapid decrease in the concentration due to photolysis with low concentrations during the day. HONO accumulates during the night via heterogeneous disproportionation of NO_2 (Equation 2.49),

or via reaction of NO with OH (Equation 2.50) (Sörgel et al., 2011):

$$2\ NO_2 + H_2O \longrightarrow HONO + HNO_3 \quad (2.49)$$

$$NO + OH + M \longrightarrow HONO + M. \quad (2.50)$$

The dominant sinks for HONO are photolysis (Equation 2.48) and reaction with OH:

$$HONO + OH \longrightarrow NO_2 + H_2O. \quad (2.51)$$

Equations 2.48, 2.50 and 2.51 lead to a photo-stationary state where no net OH radical is produced. The OH radical is finally destroyed by a reaction with NO_2:

$$OH + NO_2 + M \longrightarrow HNO_3 + M. \quad (2.52)$$

Hence, the overall production and destruction processes of the OH radical strongly depend on the ratio between NO and NO_2 (*Leighton ratio* L, Equation 2.19). As mentioned in Section 2.4.2, L lies below 1 in the lower troposphere and reaches higher values of up to 10 in the upper troposphere due to the enhanced photolysis frequency at higher altitudes. Brasseur et al. (2002) found enhanced OH concentrations (120 - 200 %) over clouds in the upper troposphere. This leads to an increased production rate of HONO on top of clouds. Dix et al. (2009) and Heue et al. (2014) detected HONO aboard the CARIBIC aircraft while flying through a convective cloud system over a polluted region in central Asia and over the Caribbean islands of Guadeloupe, respectively. Several studies further observed increased amounts of HONO during dust events, especially where enhanced concentrations of mineral oxide aerosols occur (e.g. Saliba et al., 2014, and references therein). Saliba et al. (2014) propose two mechanism for the formation of HONO during dust events, which depend on the relative humidity of the air. If the relative humidity is high, the hydrolysis according to Equation 2.49 will predominate the production of HONO, whereas for regions with low relative humidity a combined mechanism of adsorption and reaction between NO_2 and SO_2 on dust particles can be responsible for the increased formation of HONO. However, the sources of HONO in the troposphere as well as its vertical profile are still not fully understood. Ground-based HONO measurements during daytime showed much larger concentrations than the values calculated from the above-mentioned reactions, indicating the existence of a large unexplained source of HONO (e.g. Kleffmann et al., 2005). Recent studies of HONO onboard a Zeppelin airship provide evidence for a strong gas-phase source of HONO that dominates the overall HONO production in the lower troposphere and that requires nitrogen oxides and possibly hydrogen oxide radicals (Li et al., 2014). They further state that the previously assumed impact of HONO on the formation of OH might be overestimated.

2.4.9 Reactive halogen species (RHS)

In the stratosphere halogens (F, Cl, Br or I) are well-known for their potential to catalytically destroy ozone (Section 2.4.1). In tropospheric chemistry, however, they also play an important role. Besides the influence on the ozone chemistry, RHS can further disturb the partitioning of NO_x and HO_x, oxidise dimethyl sulphide (DMS), transform elemental mercury (Hg^0) into reactive mercury ($Hg^{I}I$), and lead to the formation of ultrafine particles. A detailed overview of halogen chemistry in the troposphere is given by Saiz-Lopez and von Glasow (2012).

Figure 2.8 shows an overview of the most important RHS-related processes in the troposphere. There are several processes that can lead to the release of RHS into the atmosphere, for example through the release from:

a) sea spray or sea salt particles (e.g. Hönninger, 2002),

b) biogenic sources, such as halogenated hydrocarbons (halocarbons), which are emitted by macroalgae (seaweed) at coastal sites or microalgae (phytoplankton) in the ocean and are photolysed in the troposphere to form RHS (Huang et al., 2010),

c) abiotic sources, e.g. methyl iodide (CH_3I) can be released from sea water containing dust aerosols and photolyses forming iodine radicals (Williams et al., 2007; Martino et al., 2009),

d) sea salt surfaces, for example during the polar bromine explosions due to an autocatalytic release of reactive bromine from sea salt water deposits or from frost flowers on sea ice (e.g. Frieß et al., 2004),

e) anthropogenic precursors, such as chlorofluorocarbons (CFCs),

f) volcanoes (Bobrowski et al., 2003).

Loss processes of RHS in the atmosphere include for example the reaction with hydrocarbons (RH, with R representing an organic molecule, e.g. CH_4), with HO_2 to form hydrogen halides (HX), and with hypohalous acids HOX. A further sink of RHS is the reaction with NO_2 forming $XONO_2$.

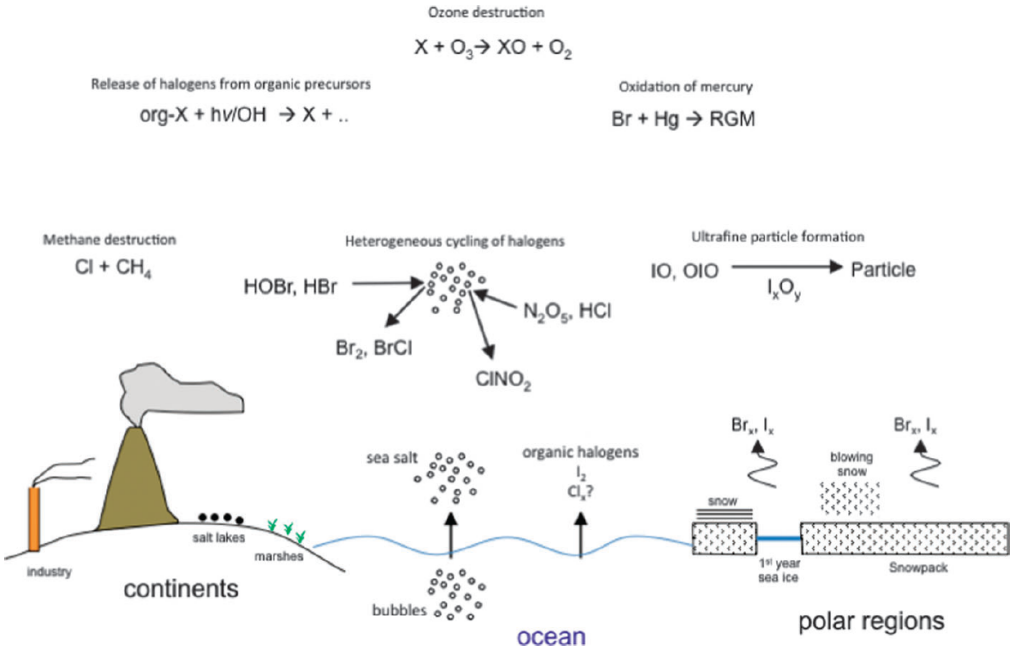

Figure 2.8: Sketch of the major release mechanism of RHS in the troposphere, adapted from Saiz-Lopez and von Glasow (2012).

Bromine monoxide (BrO)

The dominating source of reactive bromine in the MBL is the heterogeneous bromine activation on aerosol surfaces, such as on sea-salt aerosols (e.g. Fickert et al., 1999). A further source of BrO is the emission from brominated halocarbons, such as bromoform ($CHBr_3$) or dibromomethane (CH_2Br_2). The lifetimes of the different brominated halocarbons are given in Table 2.2.

Table 2.2: Typical lifetimes of brominated halocarbons in the free troposphere.

	Life time [days]	Reference
$CHBr_3$	24	Montzka et al. (2011)
$CHBr_2Cl$	59	Montzka et al. (2011)
$CHBrCl_2$	78	Montzka et al. (2011)
CH_2Br_2	123	Montzka et al. (2011)
CH_2BrCl	137	Montzka et al. (2011)

These brominated halocarbons mainly originate from oceanic sources including macroalgae or phytoplankton, especially at coastal sites or upwelling regions (e.g. Quack and Wallace, 2003). An overview of the emissions of brominated halocarbons by tropical macroalgae can be found in Leedham et al. (2013).

A typical sink for reactive bromine species in the tropical MBL is the reaction with VOCs, forming HBr or HOBr. Possible pathways involve the reactions with HCHO (Hansen et al., 1999) or NO_2:

$$\mathrm{BrO + NO_2} \longrightarrow \mathrm{BrONO_2} \tag{2.53}$$

$$\mathrm{BrO + HCHO} \longrightarrow \mathrm{HOBr + CHO} \tag{2.54}$$

$$\mathrm{Br + HCHO + O_2} \longrightarrow \mathrm{HBr + CO + HO_2}. \tag{2.55}$$

Lampel (2014) estimated loss rates of BrO for typical concentrations of various atmospheric compounds occurring at the Cape Verde Islands, assuming a BrO concentration of 1 ppt. According to Lampel (2014), the dominating sink for bromine in the tropical MBL is the reaction with VOCs to form HBr. Among the chosen compounds, ethanal (CH_3CHO) and methanol (CH_3OH) seem to be the compounds responsible for the strongest BrO loss rate with approximately 9–36 ppt/h and 15–60 ppt/h, respectively. Isoprene, HCHO, and NO_2 represent further BrO sinks with BrO loss rates of approximately 4–20 ppt/h, 4.5 ppt/h, and 2.4–6.9 ppt/h, respectively. Thus, in order to maintain BrO mixing ratios of approximately 1–3 ppt in the MBL, strong sources for reactive bromine species are needed.

Iodine monoxide (IO)

Reactive iodine species (I, I_2, IO and OIO) can have a strong influence on different atmospheric processes. Iodine atoms are released by the photolysis of iodine-containing substances like molecular iodine (I_2) or iodocarbons (RI, with R representing an organic molecule). Very short-lived iodocarbons include e.g. methyl iodide (CH_3I), chloroiodomethane (CH_2ClI), bromoiodomethane (CH_2BrI) or diiodomethane (CH_2I_2). The lifetime of these iodocarbons ranges from several minutes to days (Table 2.3). They can be emitted by biotic and photochemical processes from the ocean (Carpenter et al., 2012; Saiz-Lopez et al., 2012, 2014). Macroalgae are known to produce iodine containing precursor species, such as I_2 or iodocarbons (e.g. Carpenter et al., 2012; Leedham et al., 2013). The kelp *Laminaria* and related brown macroalgae thereby represent the strongest iodine source in coastal regions (Küpper et al., 1998).

Table 2.3: Typical lifetimes of iodocarbons and I_2 in the MBL.

	Life time	Reference
CH_3I	6 days	Bell et al. (2002)
CH_2ClI	0.1 days	Rattigan et al. (1997)
CH_2BrI	$\approx$ 1 h	Mössinger et al. (1998)
CH_2I_2	2–10 min	Mössinger et al. (1998)
I_2	10 sec	Saiz-Lopez and von Glasow (2012)
HOI	10 sec	Paquette et al. (1986)

The photolysis of these organic and inorganic precursors leads to the formation of reactive iodine atoms, which further react with O_3 to produce IO. After the rapid photolysis of IO, a steady state

is generated between IO and I atoms, which has no net effect on O_3 (Vogt et al., 1999):

$$I_2 + h\nu \longrightarrow 2\ I \quad (2.56)$$
$$RI + h\nu \longrightarrow R + I \quad (2.57)$$
$$I + O_3 \longrightarrow IO + O_2 \quad (2.58)$$
$$IO + h\nu \longrightarrow I + O \quad (2.59)$$
$$O + O_2 + M \longrightarrow O_3 + M. \quad (2.60)$$

Destruction of O_3 occurs if IO further reacts with other species. For low IO concentrations, the following reactions dominate the O_3 destruction cycle (Chameides and Davis, 1980; Vogt et al., 1999):

$$I + O_3 \longrightarrow IO + O_2 \quad (2.61)$$
$$I + HO_2 \longrightarrow HI + O_2 \quad (2.62)$$
$$IO + HO_2 \longrightarrow HOI + O_2 \quad (2.63)$$
$$HOI + h\nu \longrightarrow OH + I \quad (2.64)$$
$$\text{net}: O_3 + HO_2 \longrightarrow OH + 2\ O_2. \quad (2.65)$$

When higher concentrations of IO are present, the IO self-reaction becomes more crucial and the photolysis of the formed OIO and I_2O_2 leads to a further O_3 destruction (e.g. Ashworth et al., 2002):

$$IO + IO \longrightarrow I_2O_2 \quad (2.66)$$
$$IO + IO \longrightarrow I + OIO \quad (2.67)$$
$$OIO + h\nu \longrightarrow I + O_2 \quad (2.68)$$
$$I_2O_2 + h\nu \longrightarrow 2\ I + O_2. \quad (2.69)$$

Recent modelling studies suggest that, among the reactive halogen species, iodine species are responsible for at least 70 - 85 % of the total halogen-mediated O_3 destruction in the troposphere (Saiz-Lopez et al., 2014). Furthermore, the ratio of HO_2 and OH can be disturbed by the influence of iodine species (e.g. McFiggans et al., 2000; Bloss et al., 2005). Due to the reaction with HO_2 (Equation 2.62 and 2.63) and the further photolysis of HOI, the ratio of HO_2 and OH is reduced. IO can also react with NO_x according to the following equations (McFiggans et al., 2000; Saiz-Lopez et al., 2012) leading to a modulation of the ratio of NO_2 and NO:

$$IO + NO_2 + M \longrightarrow IONO_2 + M \quad (2.70)$$
$$IO + NO \longrightarrow I + NO_2. \quad (2.71)$$

$IONO_2$, which is produced in Equation 2.70, is further photolysed and forms iodine atoms. This reaction with the subsequent photolysis can contribute to the depletion of O_3 (McFiggans et al., 2000). Equation 2.71 limits the O_3 destruction cycle and thus leads to a null cycle as the produced NO_2 is able to photolyse to NO, which can again form an O_3 molecule (Equations 2.16 - 2.18).

Several studies indicate that reactive iodine is related to the formation of ultrafine particles in coastal areas (e.g. Hoffmann et al., 2001; O'Dowd et al., 2002). In coastal regions, iodine atoms can be formed by the photolysis of molecular iodine (I_2) or iodocarbons, which are emitted by macroalgae (e.g. Seitz et al., 2010; Huang et al., 2010; Commane et al., 2011; Leedham et al., 2013) (Equation 2.56 and 2.57). Measurements of IO at coastal sites, e.g. in Mace Head, yielded mixing ratios of up to 50 ppt (Commane et al., 2011). With such high values the self-reaction of IO (Equation 2.66 and 2.67) can be sufficient for the formation of new particles. After this self-reaction of IO, the products OIO and I_2O_2 can continue polymerising to higher iodine oxides (I_xO_y, with x and y generally being of the order of x = 2 and y = 2 - 4), leading to the formation of iodine

oxide nuclei (Hoffmann et al., 2001; Saunders et al., 2010). However, despite several field studies, the mechanism for the formation of particles is still quite uncertain (Sommariva et al., 2012). An overview of the different reaction pathways of iodine species can be found in Saiz-Lopez et al. (2014).

Iodine species have already been detected by a number of ground-, ship-, and satellite-based measurements in coastal and open ocean regions (e.g. Read et al., 2008; Schönhardt et al., 2008; Mahajan et al., 2012; Großmann et al., 2013). Measurements of IO in the marine boundary layer (MBL) over the remote open ocean indicate mixing ratios of 1-2 ppt (Mahajan et al., 2012; Großmann et al., 2013). However, the measured halocarbon precursors such as CH_3I, CH_2I_2, CH_2ClI, or CH_2BrI are not sufficient to reproduce these amounts of IO in the remote MBL. Recent laboratory studies proposed a possible pathway via the reaction of aqueous iodide (I^-_{aq}) with O_3, leading to the formation of I_2 and hypoiodous acid (HOI) (Carpenter et al., 2013; MacDonald et al., 2014):

$$H^+ + I^- + O_3 \longrightarrow HOI + O_2 \tag{2.72}$$

$$H^+ + HOI + I^- \longrightarrow I_2 + H_2O. \tag{2.73}$$

I_2 and HOI quickly photolyse (lifetimes see Table 2.3) and release iodine atoms, which further react with O_3 finally forming IO. Inorganic processes in sea salt spray could be also an important source of HOI and I_2 (Pillar et al., 2013). The emission of I_2 and HOI over the open ocean further depends on the wind speed, the sea surface temperature (SST) and on the deposition of tropospheric O_3 (MacDonald et al., 2014) and can vary geographically (Pillar et al., 2013; Prados-Roman et al., 2014). According to model simulations by Carpenter et al. (2013), the emission of HOI and I_2 can explain approximately 75 % and thus the majority of the observed IO concentrations in the MBL.

Information regarding the vertical distribution of IO is sparse. Butz et al. (2009) reported upper limits of IO and OIO in the tropical upper troposphere and stratosphere being below 0.1 ppt. Puentedura et al. (2012) inferred vertical profiles of IO from MAX-DOAS measurements at Izaña, Canary Islands, with the majority of IO being located in the MBL, but also small amounts in the overlaying free troposphere. Dix et al. (2013) presented the detection of IO with mixing ratios of approximately 0.1 ppt in the tropical free troposphere (FT) over the Pacific Ocean. It is argued that, in contrast to the IO detected in the MBL, the IO amounts found in the FT cannot mainly be explained by I_2 with its short lifetime. Iodocarbons or aerosols with a sufficient lifetime are suggested as precursors to carry iodine up into the FT through tropical deep convection (Dix et al., 2013). As the iodine-containing di-halocarbons, such as CH_2I_2, CH_2ClI, or CH_2BrI, are mainly photolysed within the MBL, CH_3I is the predominant iodocarbon species that is present in the FT (Saiz-Lopez et al., 2014). According to model studies by Saiz-Lopez et al. (2014), the combined release of iodine atoms from the photolysis of CH_3I and the photolytic recycling of higher iodine oxides (I_xO_y) can be responsible for the IO levels in the FT. They further propose a tropical ring of atomic iodine extending from 30 °N to 30 °S with maximum iodine atom abundances at an altitude of approximately 11 km and 14 km, depending on the considered photochemical scheme.

2.4.10 Aerosol particles and clouds

Aerosols are defined as colloidal systems or suspensions composed of fine solid or liquid particles in the air or in another gas (e.g. Seinfeld and Pandis, 2006). Examples for atmospheric aerosols are biogenic particles, haze, dust, fog, smoke, liquid or ice cloud particles, and volcanic ash. They can influence the radiation budget of the Earth by absorbing, scattering and reflecting solar radiation and by modifying the formation of clouds as they can act as cloud condensation nuclei (CCN) (IPCC, 2013). Thus, aerosols can cause radiative forcing (RF) of the climate system. However, large uncertainties concerning the quantification of this aerosol-related RF exist. The correctness of aerosol impact on the RF in climate models mainly depends on knowledge of the vertical distribution of aerosols (e.g. Kaufman et al., 2002).

Aerosols can be divided into primary and secondary aerosols. Primary aerosols (75 %) are injected into the atmosphere mechanically by natural or anthropogenic processes, such as sea spray

emitted from the sea surface and soot released by biomass burning or fossil fuel combustion processes. Aerosols are further classified into secondary aerosols (25 %), which are formed chemically by gas-to-particle conversion, such as e.g. sulphates, organics or nitrates. Secondary aerosols that are emitted from gas-phase organic precursors are referred to as secondary organic aerosols (SOA) (e.g. Riipinen et al., 2012). Most of the primary aerosols are coarse particles with a diameter larger than 1 µm, while secondary aerosols are rather fine particles with a diameter smaller than 1 µm. Figure 2.9 illustrates the different production and removal processes of atmospheric aerosols.

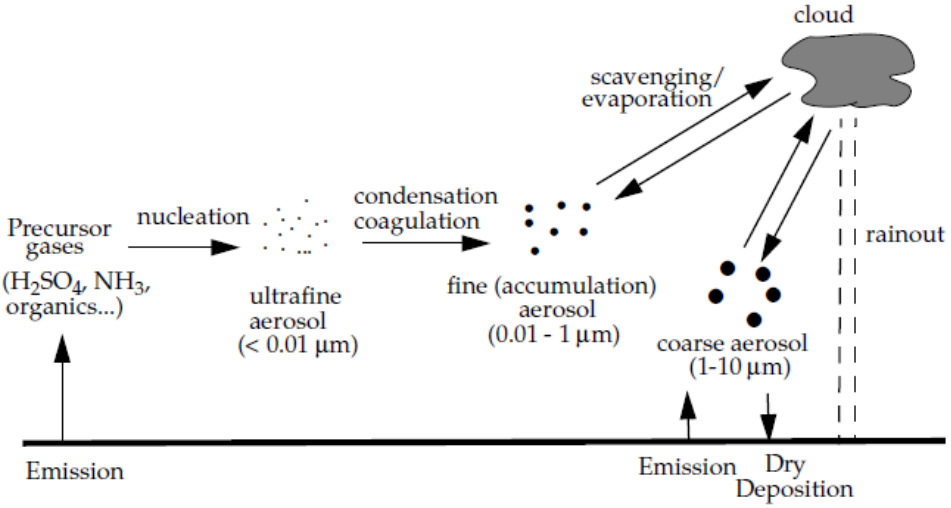

Figure 2.9: Production and removal processes of aerosols, adapted from Jacob (1999) with kind permission of Princeton University Press (August 2014).

Nucleation of precursor gases such as sulphuric acid (H_2SO_4), which is produced by the oxidation of sulphur dioxide (SO_2) emitted during combustion processes or volcanic eruptions, leads to the formation of ultrafine particles with a diameter smaller than 0.01 µm. Through condensation of gases or coagulation, these ultrafine particles rapidly form larger particles with a size of up to 1 µm (fine particles). The average lifetime of these particles ranges from several days for particles close to the surface up to one year for stratospheric particles (e.g. Jaenicke, 2007). They are removed again from the atmosphere by scavenging by clouds or rainout. Coarse particles, which are emitted by mechanical processes and distributed by the wind, are also removed by rainout from clouds. Hence, increased aerosol loads which act as CCN can change the cloud properties and thus change precipitation processes.

Clouds cover approximately 70% of the surface of the Earth (Hamann et al., 2014). They are very complex atmospheric components consisting of water droplets or ice crystals with a size of the order of microns to millimetres, which are affected by convective and turbulent processes (Battaglia et al., 2014). In general, aerosol particles are smaller than cloud particles. Clouds are usually formed in rising air masses, which expand and cool, thereby activating aerosol particles to transform into cloud droplets and ice crystals in supersaturated air (IPCC, 2013). They have a strong influence on the Earth's radiation budget. On the one hand, they reflect the incoming short-wave solar radiation back into space leading to a cooling effect (the albedo effect). On the other hand, they absorb the long-wave infrared radiation from the surface and lower atmosphere leading to a warming effect (IPCC, 2013). In addition, clouds have a major impact on the atmospheric part of the global water cycle since they are responsible for latent heat transport.

Clouds can be classified according to their location in the atmosphere. Table 2.4 shows an overview of the different cloud types, which occur in the atmosphere, following the classifications of the World Meteorological Organisation's (WMO) International Cloud Atlas (WMO, 1975, 1987).

Table 2.4: Overview of the ten cloud types according to the classifications of the World Meteorological Organisation's (WMO) International Cloud Atlas (WMO, 1975, 1987).

	altitude [km]	cloud type	abbreviation
high-level clouds	6–13	cirrus	Ci
		cirrocumulus	Cc
		cirrostratus	Cs
mid-level clouds	2–6	altocumulus	Ac
		altostratus	As
low-level clouds	0–2	stratocumulus	Sc
		stratus	St
vertical clouds	0–13	cumulonimbus	Cb
		nimbostratus	Ns
		cumulus	Cs

Clouds with a base altitude of approximately 6 km and higher are referred to as high-level clouds or cirrus clouds. Cirrus clouds have a thin and fibrous appearance. At altitudes between 2 km and 6 km the mid-level clouds are composed of altocumulus and altostratus clouds, while at altitudes lower than 2 km stratus and stratocumulus clouds occur. Shallow cumulus and stratiform clouds occur over essentially all oceans but are most prevalent over cooler subtropical oceans and in polar regions (IPCC, 2013). Cumulus as well as nimbostratus clouds can be present at different altitude layers since they have a large vertical extent. Nimbus clouds usually indicate precipitating clouds. Deep convective cloud systems often occurring in the tropics (Section 6.4) are defined as cumulonimbus (Cb) clouds (e.g. Liou, 2002). Convective clouds normally develop in an unstable atmosphere with a large vertical temperature gradient. In general, the low and mid-level clouds consist of spherical water droplets ranging from 1 to 20 µm, while the higher cirrus clouds are composed of ice crystals. Figure 2.10 displays the different shapes of ice crystals, which depend on temperature and relative humidity as well as on collision processes within the cloud. The most abundant types are bullet rosettes, hollow columns, and plates.

Since aerosols can act as cloud condensation nuclei, the formation and development of clouds strongly depends on the amount of aerosols present in the atmosphere, i.e. aerosols and clouds are closely linked to each other. Aerosol particles can have different effects on clouds and precipitation. Aerosols are able to suppress precipitation by decreasing the amount of solar radiation reaching the surface, which lowers water the evaporation rates (IPCC, 2013). Furthermore, large amounts of anthropogenically produced aerosols have been reported to both decrease and increase rainfall (Rosenfeld et al., 2008).

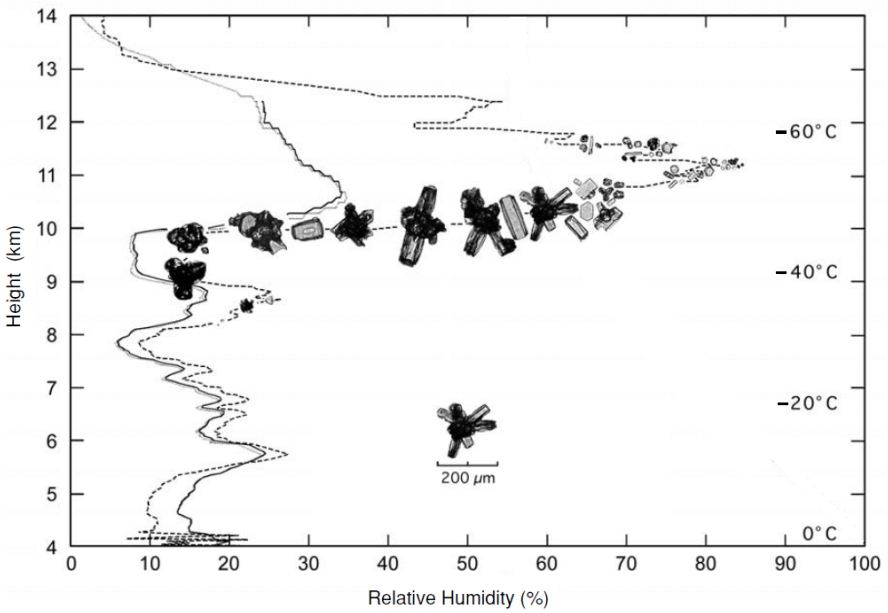

Figure 2.10: Ice crystal size and shape as a function of height and relative humidity, adapted from Liou (2002).

3. Radiative transfer in the atmosphere

This chapter focuses on radiative transfer (RT) in the atmosphere, which is a key process in the retrieval of atmospheric trace gas concentrations. The interpretation of the differential slant column densities (dSCDs) of the trace gas of interest, the basic quantity obtained from a DOAS measurement (Section 4), depends on the length of the atmospheric light path. The light path depends on the interaction of solar radiation with clouds, aerosols, and air molecules. The chapter starts with the basic principles of solar radiation (Section 3.1) and continues with general concepts of atmospheric absorption (Section 3.2.1) and scattering (Section 3.2.2), which influence the incoming radiation budget. The resulting radiative transfer equation is introduced in Section 3.3. This equation describes the interactions of photons with atmospheric molecules mathematically.

3.1 Solar radiation

The Sun emits electromagnetic radiation ranging from X-rays ($\lambda_{\mathrm{X-rays}} \approx 0.01$ - 10 nm), ultraviolet (UV) ($\lambda_{\mathrm{UV}} \approx 10$ - 400 nm), visible (vis) ($\lambda_{\mathrm{vis}} \approx 400$ - 700 nm) and infra-red (IR) light ($\lambda_{\mathrm{IR}} \approx 700$ nm - 1 mm) to radio waves ($\lambda_{\mathrm{radio}} \approx 1$ mm - 100 km). The solar spectrum can be approximated as a black body radiator with a surface temperature of T $\approx$ 5800 K. Planck's law describes the spectral distribution of the black body radiation emissions:

$$R(\lambda, T) = \frac{2hc^2}{\lambda^5} \cdot (e^{\frac{hc}{\lambda k T}} - 1)^{-1}, \tag{3.1}$$

with $h = 6.63 \cdot 10^{-34}$ Js being the Planck constant, $k = 1.38 \cdot 10^{-23}$ JK^{-1} the Boltzmann constant and $c = 3.0 \cdot 10^{8}$ m s^{-1} representing the speed of light. The spectral radiance is defined as the incident radiation energy per time and wavelength, also referred to as spectral flux $\Phi(\lambda)$, on the area element A and the solid angle Ω. The spectral radiance is given in Wnm^{-1}m^{-2}sr^{-1} and can be expressed as:

$$I(\lambda) = \frac{\Phi(\lambda)}{\Omega \cdot A}. \tag{3.2}$$

Another quantity that is often used in this context is the spectral irradiance $E(\lambda)$ which is defined as:

$$E(\lambda) = \int_{\Omega} I(\lambda, \phi, \theta) \cdot \cos\theta d\Omega = \frac{\Phi(\lambda)}{A}. \tag{3.3}$$

The spectral irradiance can be obtained by integrating the spectral radiance over the solid angle Ω with units of Wnm^{-1}m^{-1}. The actinic flux $F(\lambda)$ is calculated by integrating the radiance (Equation 3.2) over all angles θ and ϕ, i.e. over the solid angle Ω and is also given in Wnm^{-1}m^{-1} (e.g. Madronich, 1987):

$$F(\lambda) = \int_{\Omega} I(\lambda, \phi, \theta) d\Omega. \tag{3.4}$$

The photolysis frequency J_i of a gas i can be derived by integrating the product of the actinic flux F(λ) (Equation 3.4), the absorption cross-section $\sigma(\lambda)$, and the quantum yield $\Phi(\lambda)$ over the wavelength λ:

$$J_i = \int F(\lambda) \cdot \sigma(\lambda)\Phi(\lambda)d\lambda. \tag{3.5}$$

Wien's displacement law can be derived from Planck's law and specifies the wavelength position of the maximum of the black body emission:

$$\lambda_{\max} \cdot T = 2897.8\ \mu\text{m} \cdot \text{K}. \tag{3.6}$$

For a Sun surface temperature of $T \approx 5800$ K, the irradiance peaks at $\lambda \approx 500$ nm. However, the Sun is not an ideal black body radiator. Superimposed on the broad-band component of the solar spectrum are several characteristic absorption lines of chemical elements present in outer layers of the Sun's atmosphere. These are called Fraunhofer lines (Section 4.3.3) and can be seen in the solar spectrum in Figure 3.1. Absorbers in the Earth's atmosphere further attenuate the solar radiation depending on the wavelength. Thus, the solar spectrum shows additional structures, for example due to the absorption by ozone.

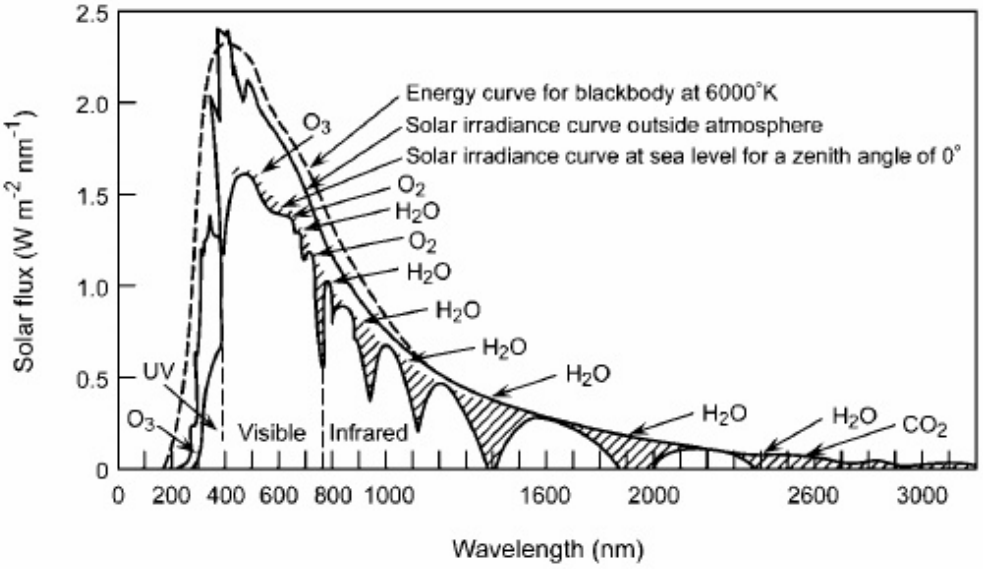

Figure 3.1: Spectrum of a black body radiator at 6000 K (dashed curve), of the solar irradiance at the top of the atmosphere (TOA) (solid curve) and at sea level for a solar zenith angle (SZA) of 0° showing absorption structures of different atmospheric gases, adapted from Finlayson-Pitts and Pitts Jr. (2000).

3.2 Interaction processes of radiation in the atmosphere

A photon that travels through the atmosphere can interact with molecules in various ways. It can be scattered or absorbed by air molecules, aerosol particles or cloud droplets. The following section describes these processes.

3.2.1 Absorption

The interaction between a photon and a molecule can change the state of the molecule and lead to absorption or emission of the photon. The absorption and emission spectra of molecules have

characteristic band structures due to their different energy levels. The state of molecules can be characterised by the time-independent Schrödinger equation (e.g. Demtröder, 2010):

$$H\Psi = E\Psi, \tag{3.7}$$

with the molecule wave function Ψ and the Hamilton operator H that consists of a kinetic energy operator and the potential energy V:

$$H = -\frac{\hbar^2}{2m}\nabla^2 + V, \tag{3.8}$$

with $\hbar$ being the reduced Planck constant $\hbar = \frac{h}{2\pi}$ and m being the mass of the particle. Since molecules consist of several nuclei, the results of the Schrödinger equation can only be approximated, e.g. with the Born-Oppenheimer approach (Demtröder, 2010). In principle, the Born-Oppenheimer approximation assumes that the motion of an electron is much faster than the motion of the nucleus since the nucleus has a much larger mass relative to the mass of the electron. Thus, the problem can be separated into nuclei and electron motion. The resulting wave function Ψ can thereby be divided into an electronic (Ψ_{el}), a rotational (Ψ_{rot}) and a vibrational component (Ψ_{vib}). Electronic transitions occur if the configuration of the electron shell changes. For small atoms, such as the hydrogen atom, the energy of a particular electronic state n can then be approximated by the Rydberg formula:

$$E_n^{el} = -\frac{R_{Ry}}{n^2}, \tag{3.9}$$

with the Rydberg constant of $R_{Ry} = 1.097{\cdot}10^7$ m^{-1}. The transition energy is quantised according to ΔE = hc/λ with a wavelength interval covering the UV, visible and near-infrared region. In contrast to atoms, molecules consist of at least two atoms, leading to a three-dimensional structure and therefore to rotational and vibrational transitions. A molecule that consists of N atoms generally has 3N degrees of freedom for translation, rotation and vibration according to 3N = f_{trans} + f_{rot} + f_{vib}. The absorption of photons with wavelengths in the far infrared to-microwave range (typically 1 mm to 1 cm) can lead to rotational transitions. The allowed energy eigenvalues for rotations are then given to first order neglecting centrifugal distortion by:

$$E_j^{rot} = \frac{\hbar^2}{2\Theta}J(J+1), \tag{3.10}$$

with the quantum number J and the moment of inertia Θ. Transitions between purely rotational states follow the transition rule of ΔJ = $\pm$1. Transitions with ΔJ = -1 are referred to as P-branch, while transitions with ΔJ = 1 belong to the R-branch. Vibrations of a molecule can be approximated by a harmonic oscillator. Thus, the energy eigenvalues can be expressed as:

$$E_\nu^{vib} = (\nu + \frac{1}{2})\hbar\omega \quad \text{with} \quad \nu = 0, 1, 2, 3..., \tag{3.11}$$

with ν representing the vibrational quantum number. Vibrational transitions mostly occur in the infrared wavelength range. However, in general, the absorption of a photon is a combination of electronic, vibrational and rotational states with $E^{el} > E^{vib} > E^{rot}$. All these assumptions are valid as a first approximation. More details can e.g. be found in Haken and Wolf (2004), and Haken and Wolf (2006).

3.2.2 Scattering processes

There are three main types of scattering processes in the atmosphere: Rayleigh, Mie and Raman scattering. Elastic scattering processes by air molecules (Rayleigh scattering) or atmospheric aerosol particles (Mie scattering) change the propagation direction of light, but the photon wavelength is unchanged. Inelastic Raman scattering also changes photon energy in addition to the propagation direction and therefore shifts the wavelength. For inelastic Raman scattering, the photon energy can either be reduced (Stokes scattering) or increased (anti-Stokes scattering).

Rayleigh scattering

Rayleigh scattering corresponds to elastic scattering of light where no energy is exchanged between the photon and the particle. It occurs when the scattering particles are dielectric and their radius r is much smaller than the wavelength of the incoming radiation ($r \ll \lambda$). This is the case for air molecules or small aerosol particles with sizes below ≈ 1 µm. The incoming light induces an oscillating dipole with a Hertz dipole radiation pattern in the dielectric particle, leading to the emission of the same frequency at which is was polarized (e.g. van de Hulst, 1981). The wavelength dependency of the Rayleigh scattering cross-section is very strong:

$$\sigma_R \propto \lambda^{-4}. \tag{3.12}$$

Thus, light with a small wavelength is scattered to a greater extent than light with a large wavelength, i.e. Rayleigh scattering is particularly effective in the UV wavelength range. Blue light, with its shorter wavelength ($\lambda \approx 425$ nm), is scattered more strongly than red light ($\lambda \approx 650$ nm). Hence, the colour of the sky appears to be blue, whereas the colour of the Sun during sunrise and sunset is red because the red component of the sunlight is scattered less by air molecules relative to the blue component. The Rayleigh extinction coefficient ϵ_R for a number density of air molecules N_{air} can be determined according to:

$$\epsilon_R = N_{air} \cdot \sigma_R. \tag{3.13}$$

Compared with scattering on large particles (Section 3.2.2), the angular dependency of the Rayleigh phase function Φ is relatively small (Figure 3.2). For unpolarised light, it is proportional to $1+\cos^2\theta$ and is given by (e.g. Platt and Stutz, 2008):

$$\Phi_R(\cos(\theta)) = \frac{3}{4} \cdot (1 + \cos^2(\theta)), \tag{3.14}$$

where θ is the scattering angle between the directions of incoming and scattered light/photons. Considering the anisotropic polarisability (red dashed line in Figure 3.2) according to Penndorf (1957), Equation 3.14 can be changed to:

$$\Phi_R(\cos(\theta)) = 0.76 \cdot (0.93 + \cos^2(\theta)). \tag{3.15}$$

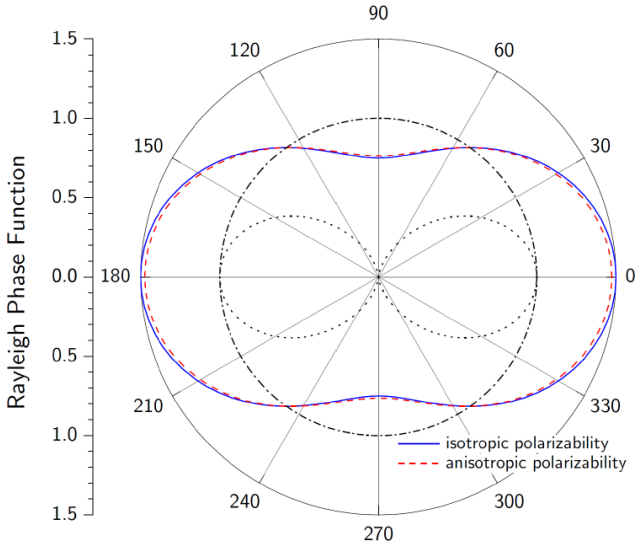

Figure 3.2: Polar diagram of the Rayleigh phase function Φ_R for unpolarised incoming light. The dotted line represents the contribution of light that is polarised parallel to the scattering plane and the dash dotted line shows the contribution of light that is polarised perpendicular to the scattering plane, adapted from Hönninger (2002).

Mie scattering

Mie scattering is an elastic process during which the light is scattered by particles (assumed to be spherical) with a diameter d comparable to or larger than the wavelength of the incoming light ($d \geq \lambda$). In the atmosphere, these particles are aerosols, e.g. dust particles, sea salt droplets or particles emitted by biomass burning or volcanoes (Section 2.4.10). Their size ranges from 0.1 to 10 µm. The Mie scattering phase function depends on the aerosol size parameter x:

$$x = \frac{2 \cdot \pi \cdot r}{\lambda} \tag{3.16}$$

with the radius r of the particle and the wavelength λ of the incident radiation. For $x \ll 1$, , the scattered electromagnetic radiation corresponds to that of an oscillating dipole and the scattering process can be approximated by Rayleigh scattering. For $x \gg 1$, the problem can be described by classic geometrical optics, as e.g. during the scattering on water droplets. Between these two possibilities, scattering processes are referred to as Mie scattering. In contrast to Rayleigh scattering, Mie scattering has a much weaker wavelength dependency. The Mie scattering cross-section for a typical distribution of particles in the atmosphere is given by:

$$\sigma_M \propto \lambda^{-1.3}, \tag{3.17}$$

which causes the white colour of clouds and the whitening of the colour of the sky if aerosols are present (Roedel, 2000). Figure 3.3 shows some examples of Mie scattering phase functions for water droplets at a wavelength of 550 nm. Obviously, as the aerosol size parameter x increases, forward scattering begins to dominate. However, as the size, shape and composition of aerosols in the atmosphere can differ strongly, the determination of σ_M can be very complex. Using numerical models, the Mie scattering phase function can be approximated by only a few observable parameters. A common method is the Henyey-Greenstein parameterisation (Henyey and Greenstein, 1941) where the Mie scattering phase function is expressed as:

$$\Phi_{HG}(\cos(\theta)) = \frac{1 - \mathrm{g}^2}{4\pi \cdot (1 + \mathrm{g}^2 - 2\mathrm{g} \cdot \cos(\theta))^{\frac{3}{2}}}, \tag{3.18}$$

with the asymmetry parameter g, which is defined as the intensity-weighted average cosine of the scattering angle θ: $g = \langle \cos(\theta) \rangle$ (Andrews et al., 2006). The asymmetry parameter g ranges between -1 and 1. For $\mathrm{g} = 0$ the scattering is isotropic, for $\mathrm{g} = 1$ complete forward scattering dominates, whereas for $\mathrm{g} < 0$ backward scattering occurs (e.g. van de Hulst, 1981). Typically, the values for g for tropospheric aerosols at ambient relative humidity lie between 0.59 and 0.72 (Andrews et al., 2006).

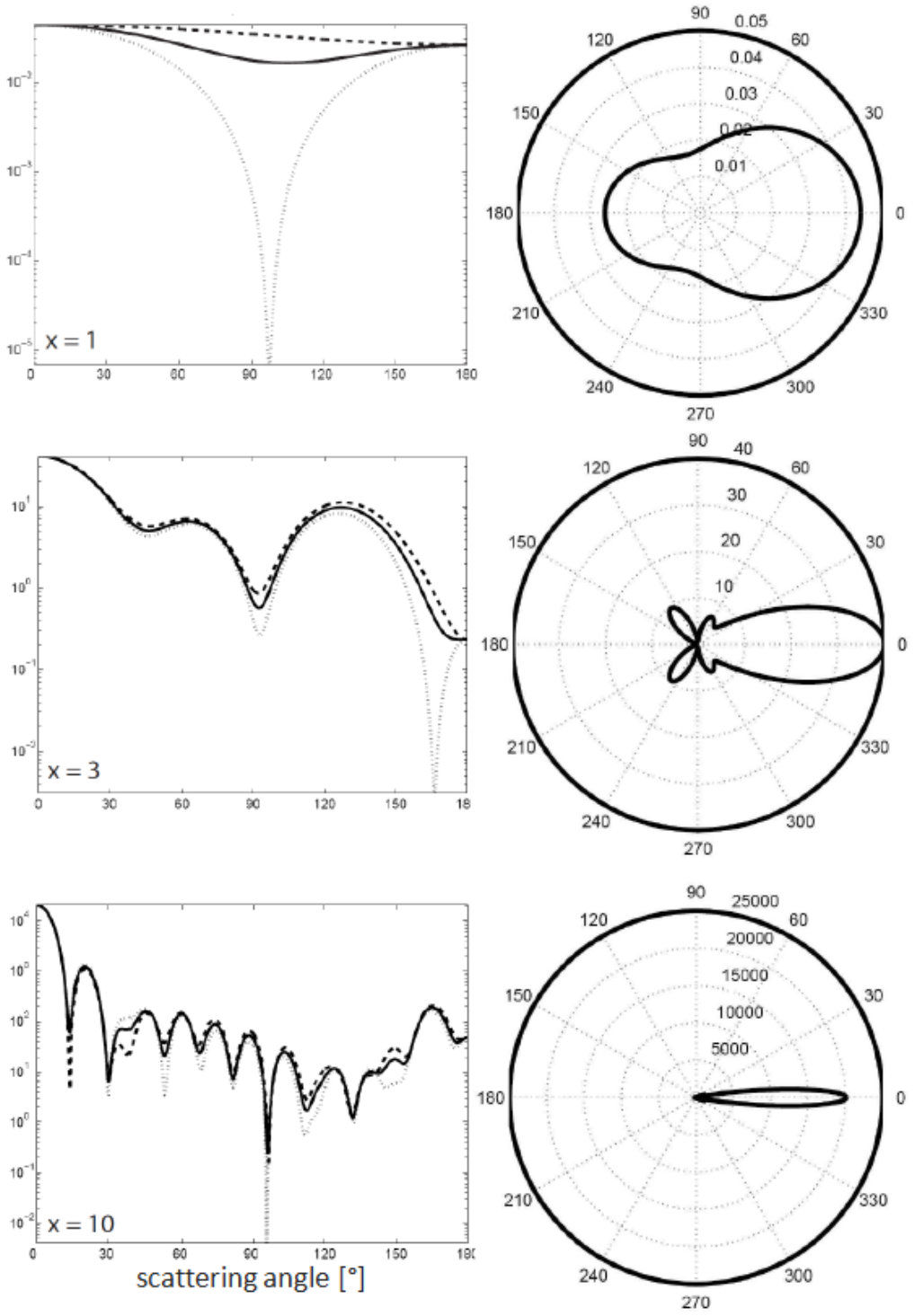

Figure 3.3: Examples of phase functions for Mie scattering at 550 nm for water droplets at x = 1, 3, 10. The left panels represent the phase function on a logarithmic scale. The dotted and dashed lines represent the two orthogonal polarisation states, whereas the solid lines represents unpolarised light. The right panels show polar diagrams of the respective phase function on a linear scale, adapted from Sanghavi (2003).

Raman scattering

Inelastic scattering of photons by air molecules is referred to as Raman scattering, named after the Indian physicist C.V. Raman, who discovered the effect in 1928 (Raman, 1928). Raman scattering

changes the energy of the scattering photon in addition to the change in the propagation direction. Raman scattering leads to two possible states:

- Stokes-Raman scattering: The air molecule absorbs a part of the photon's energy and the emitted photon has a lower energy than the absorbed photon,
- Anti-Stokes-Raman scattering: The photon takes over part of the excitation energy of the air molecule and the emitted photon has a higher energy than the absorbed photon.

In general, Anti-Stokes-Raman lines are weaker than Stokes Raman lines since the excited state has to be occupied. Figure 3.4 shows the position of the rotational and vibrational Raman lines in the spectrum. The rotational Raman lines are arranged around the vibrational Raman lines and the Rayleigh line.

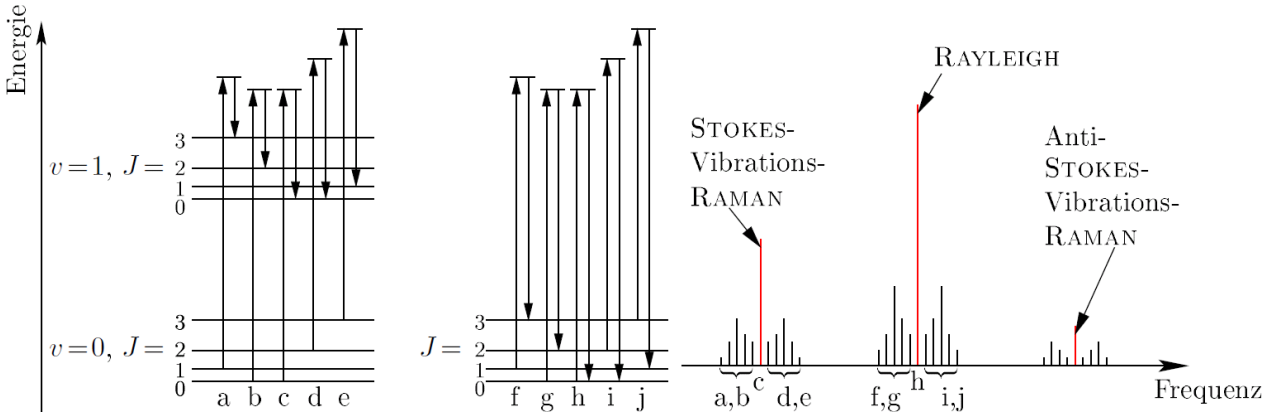

Figure 3.4: Schematic drawing of rotational and vibrational Raman lines of a diatomic molecule, adapted from Dinter (2005).

If there is no change in the vibrational state ($\nu = 0$), the term rotational Raman scattering (RRS) is used. Otherwise, if the vibrational state is also affected ($\nu = \pm 1$), the scattering process is called rotational-vibrational Raman scattering (VRS). The RRS is approximately one order of magnitude stronger than the VRS but still weaker than Rayleigh scattering. Raman scattering may be observed in atmospheric measurements of scattered sunlight as a filling-in of the Fraunhofer lines. This so-called Ring effect (Grainger and Ring, 1962) (Section 4.3.4) is considered to be caused by RRS and has to be accounted for in the spectral retrieval.

3.2.3 Aerosol optical properties

Aerosols may absorb as well as scatter the incident radiation. In addition to the scattering phase function, aerosols can be characterised by their extinction coefficient ϵ, which is the sum of the scattering coefficient ϵ_s and the absorption coefficient ϵ_a:

$$\epsilon(\lambda) = \epsilon_s(\lambda) + \epsilon_a(\lambda). \tag{3.19}$$

ϵ is given in units of 1/length. The Ångström exponent α further describes the wavelength dependency of ϵ:

$$\epsilon(\lambda) = \epsilon(\lambda_0) \cdot \left(\frac{\lambda}{\lambda_0}\right)^{-\alpha}, \tag{3.20}$$

with λ_0 being the reference wavelength. α is often used as a quantity to estimate the particle size, since the smaller the aerosol particles, the larger α. α typically reaches values between 0.5 and 2.5,

with an average value of approximately 1.3 (Angström, 1930). Integrating the extinction profile along the light path of length z provides the aerosol optical thickness (AOT) τ:

$$\tau(\lambda) = \int_0^z \epsilon(\lambda, z')dz'. \tag{3.21}$$

Typically, passive satellite remote-sensing instruments, such as MODIS (Section 6.2.3), are used to infer the total column AOT. As aerosols reduce visibility, the aerosol extinction coefficient can be further used to estimate the visibility distance L_{vis} according to Roedel (2000):

$$L_{vis} = \frac{3.9}{\epsilon(\lambda_{eye})}, \tag{3.22}$$

with λ_{eye} being the wavelength at which the human eye has the highest sensitivity. Another quantity to describe aerosol properties is the unit-less single scattering albedo (SSA) ω_0, which is defined as the ratio of the scattering and the extinction coefficient. It quantifies the fraction of scattering relative to the total extinction. The SSA is calculated by:

$$\omega_0(\lambda) = \frac{\epsilon_s(\lambda)}{\epsilon_s(\lambda) + \epsilon_a(\lambda)}. \tag{3.23}$$

The value of the SSA lies between 0 and 1, with SSA = 0 meaning that the particle completely absorbs light and no scattering occurs (black particle), while for SSA = 1 all light is scattered (white particle).

3.3 The radiative transfer equation

Taking into account the processes above, the propagation of light through the atmosphere can be described by the radiative transfer equation (RTE). A change of the radiance $I(\lambda)$ at a given wavelength λ while travelling through an absorbing layer of the thickness ds is given by:

$$\frac{dI(\lambda)}{ds} = -I(\lambda) \cdot \epsilon_a(\lambda) = -I(\lambda) \cdot \sigma_a(\lambda) \cdot N_a, \tag{3.24}$$

with the absorption coefficient ϵ_a, the absorption cross-section σ_a and the number of absorbing molecules per unit volume N. Integration of Equation 3.24 over the layer thickness L results in the well-known Lambert-Beer law (Equation 4.1). Analogous to the absorption process, the attenuation of the incoming radiance due to scattering is given by:

$$\frac{dI(\lambda)}{ds} = -I(\lambda) \cdot \epsilon_s(\lambda) = -I(\lambda) \cdot \sigma_s(\lambda) \cdot N_s, \tag{3.25}$$

with ϵ_s being the scattering coefficient and σ_s the scattering cross-section. Often, a dimensionless scattering function $S(\theta, \phi)$ is used, which depends on the zenith angle θ and on the azimuth angle ϕ:

$$S(\theta, \phi) = \frac{4\pi}{\sigma_s(\lambda)} \cdot \frac{d\sigma_s(\lambda)}{d\Omega}. \tag{3.26}$$

If thermal emission is neglected, the total RTE can be expressed as:

$$\frac{dI(\lambda)}{ds} = -[\epsilon_a(\lambda) + \epsilon_s(\lambda)] \cdot I(\lambda) + \epsilon_s(\lambda) \int_0^{\pi} \int_0^{2\pi} I(\lambda, \theta, \phi) \cdot \frac{S(\theta, \phi)}{4\pi} d\phi \cdot \sin\theta d\theta. \tag{3.27}$$

The first part of this equation describes the attenuation of incoming radiation by absorption and scattering processes. The second part of the equation describes the radiance that is added to the propagation direction by scattering. The radiation field can be further separated into a direct and diffusive radiance.

As the length of the light path through the atmosphere is a result of a multitude of different overlaying processes, the RTE (Equation 3.27) cannot be solved analytically. Thus, different radiative transfer modelling (RTM) approaches have to be applied which solve the RTE numerically (Section 5).

4. Absorption spectroscopy

In this chapter the theory of absorption spectroscopy, a method to determine atmospheric trace gas abundances, is described starting with fundamentals and ending with the final data retrieval. For the retrieval of different atmospheric trace gas species, the method of Differential Optical Absorption Spectroscopy (DOAS) is applied (Platt and Stutz, 2008). This method, introduced by Perner and Platt (1979), is a remote-sensing technique that uses scattered skylight attenuated along its light path in the atmosphere according to the Lambert-Beer law. In contrast to passive DOAS measurements, where the light from the Sun is used, active DOAS measurements require an artificial light source that sends light through the atmosphere along a well-defined light path. The DOAS technique allows simultaneous measurements of different trace gas species, thereby providing a high time resolution. DOAS is used in the ultraviolet (UV) and visible (vis) wavelength range, where a large number of atmospheric trace gases can be detected, such as OH, HONO, NO_2, O_3, SO_2, CHOCHO, HCHO, water vapour, or halogen compounds like IO or BrO. An overview of the absorption spectra of various molecules detectable with the DOAS method is shown in Figure 4.1. During the last years several airborne DOAS measurements were performed aboard different research aircrafts and at different flight altitudes (e.g. Wahner et al., 1990; Pfeilsticker and Platt, 1994; Dix et al., 2009; Merlaud et al., 2011; Prados-Roman et al., 2011; Baidar et al., 2013; Heue et al., 2014; General et al., 2014b). The scientific goals of these measurements ranged from studies of stratospheric air masses to tropospheric trace gas emissions.

A detailed description of the DOAS method and its applications can be found in Platt and Stutz (2008), which represents the foundation for this chapter.

4.1 The DOAS principle

The DOAS method is based on the Lambert-Beer law and can be used to describe the attenuation of scattered sunlight along its atmospheric light path through the atmosphere. The attenuation of the incident light intensity I_0 due to absorption by an absorber with the concentration c along the light path L can be expressed as:

$$I(\lambda, L) = I_0(\lambda) \cdot e^{-c \cdot \sigma(\lambda) \cdot L}, \tag{4.1}$$

with $\sigma(\lambda)$ being the wavelength-dependent absorption cross-section of the absorber. For measurements in the atmosphere, the Lambert-Beer law has to be expanded since the absorption cross-sections do not only depend on temperature and pressure, but the trace gas concentration c is also a function of altitude and varies along the light path L. Elastic Rayleigh and Mie scattering on molecules and aerosols further influence light intensity attenuation, as does inelastic Raman scattering via the Ring effect (Section 3.2.2). Thus, the resulting Lambert-Beer Law has a more complex form:

$$I(\lambda, L) = I_0(\lambda) \cdot \exp\left(- \int_0^L \left(\sum_i c_i(l) \cdot \sigma_i(\lambda, T, p) + \epsilon_R(\lambda, l) + \epsilon_M(\lambda, l) \right) dl \right). \tag{4.2}$$

$\epsilon_R(\lambda, l)$ and $\epsilon_M(\lambda, l)$ denote the extinction coefficients due to Rayleigh and Mie scattering processes, respectively, while $\sigma_i(\lambda, T, p)$ represents the absorption cross-section of the molecule i.

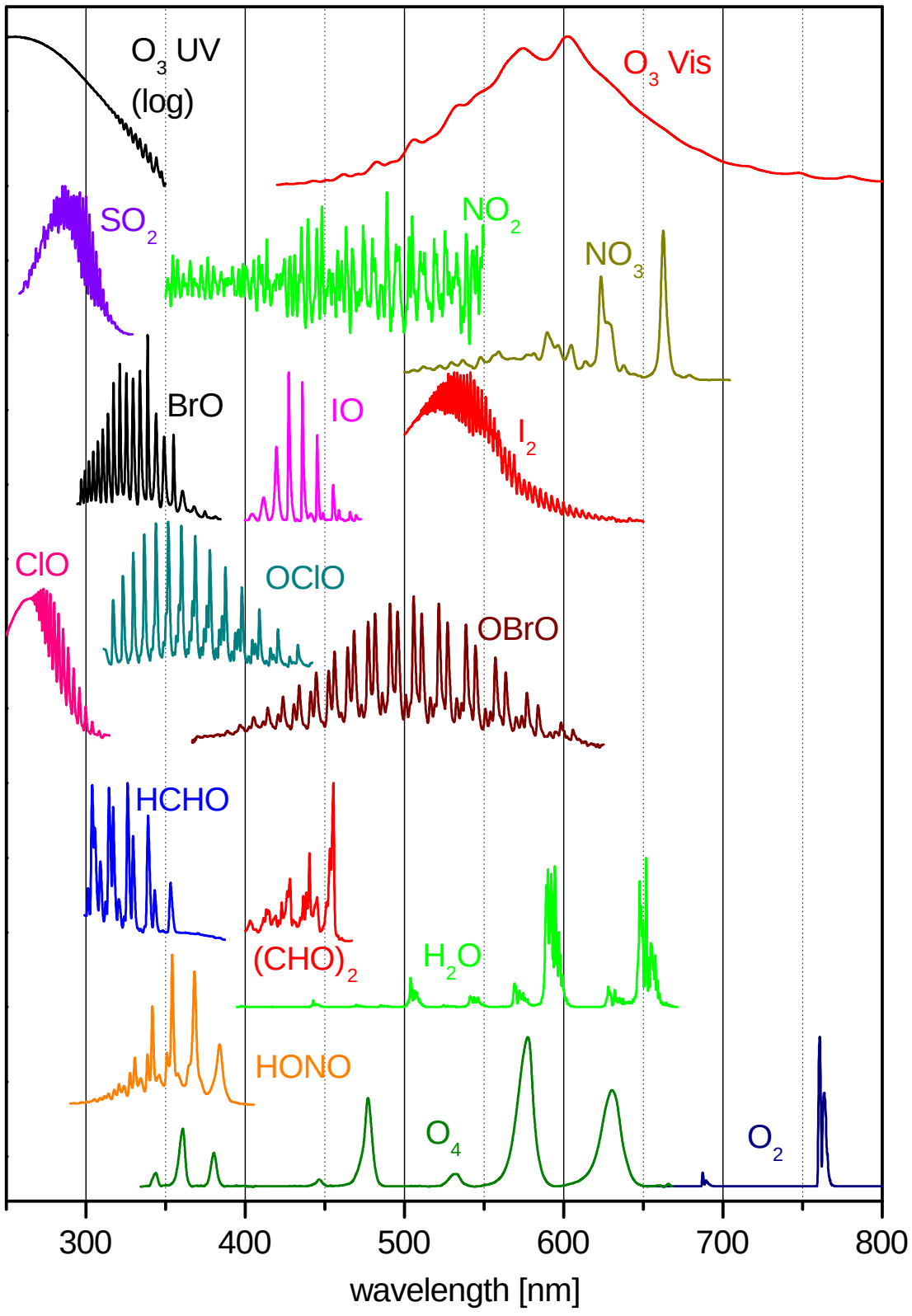

Figure 4.1: Differential absorption cross-sections of several atmospheric trace gas species measurable with the DOAS technique in arbitrary units in the wavelength range from 250 to 800 nm [Udo Frieß, personal communication, 2010]. The data can be found in the MPI-Mainz UV/vis spectral atlas of gaseous molecules of atmospheric interest (`www.uv-vis-spectral-atlas-mainz.org`), which is a comprehensive database containing numerous absorption cross-sections of different species.

The logarithmic ratio of the incident and attenuated intensity is defined as the optical density τ:

$$\tau(\lambda) \equiv \ln\left(\frac{I_0(\lambda)}{I(\lambda,L)}\right) = \int_0^L \left(\sum_i c_i(l)\cdot\sigma_i(\lambda,T,p) + \epsilon_R(\lambda,l) + \epsilon_M(\lambda,l)\right) dl \tag{4.3}$$

As mentioned above, the absorption cross-sections are usually temperature and pressure dependent and thus depend on altitude. However, Equation 4.3 requires the exact knowledge of Rayleigh and Mie scattering processes in the atmosphere on the light intensities $I_0(\lambda)$ and $I(\lambda,L)$, which cannot be easily determined. The basic idea of the DOAS method is to avoid this problem by separating the absorption structures into a narrow-band component σ', accounting for the absorption structures of the different trace gas molecules, and a broad-band component σ_b that describes the scattering effects as well as instrumental properties:

$$\sigma(\lambda) = \sigma'(\lambda) + \sigma_b(\lambda) \tag{4.4}$$

This can be achieved by applying a high-pass filter to both the measured spectra and the absorption cross-sections or by including an additional polynomial into the DOAS spectral fit, the so-called DOAS polynomial. $\sigma'(\lambda)$ strongly depends on wavelength whereas $\sigma_b(\lambda)$ varies slightly with wavelength. As the polynomial accounts for the influences of Rayleigh and Mie scattering on the spectrum, the narrow-band (also referred to as differential) trace gas absorption structures can be isolated. Hence, trace gas species with differential absorption structures in the observed spectral wavelength range can be retrieved with the DOAS method, whereas the rather broad-band structures of scattering processes can be accounted for by the DOAS polynomial. Equation 4.2 can then be written as:

$$\begin{aligned} I(\lambda,L) = I_0(\lambda)\cdot\exp\left(-\int_0^L\left[\sum_i c_i(l)\cdot\sigma_i'(\lambda,T,p)\right]dl\right) \\ \cdot\exp\left(-\int_0^L\left[\sum_i c_i(l)\cdot\sigma_{b,i}(\lambda,T,p) + \epsilon_R(\lambda,l) + \epsilon_M(\lambda,l)\right]dl\right). \end{aligned} \tag{4.5}$$

The first exponential term represents the differential component, while the second exponential term describes the broad band part. Equation (4.5) can also be displayed in the following way:

$$I(\lambda,L) = I_0'(\lambda)\cdot\exp\left(-\int_0^L\left[\sum_i c_i(l)\cdot\sigma_i'(\lambda,T,p)\right]dl\right) \tag{4.6}$$

with

$$I_0'(\lambda) = I_0(\lambda)\cdot\exp\left(-\int_0^L\left[\sum_i c_i(l)\cdot\sigma_{b,i}(\lambda,T,p) + \epsilon_R(\lambda,l) + \epsilon_M(\lambda,l)\right]dl\right), \tag{4.7}$$

where $I_0'(\lambda)$ includes $I_0(\lambda)$ as well as the broad-band component. In analogy to Equation 4.3, the differential optical density τ' can be expressed as:

$$\tau'(\lambda) = \ln\left(\frac{I_0'(\lambda)}{I(\lambda,L)}\right) = \int_0^L \sum_i c_i(l)\cdot\sigma_i'(\lambda,T,p)\cdot dl. \tag{4.8}$$

Figure 4.2 illustrates this basic principle of the DOAS method. In the following, the temperature and pressure dependence of the absorption cross-sections is assumed to be constant along the light path. The Slant Column Density (SCD) S_i of a particular trace gas i is the concentration integrated along a light path L, given in units of molec cm^{-2}:

$$S_i \equiv \int_0^L c_i(l)dl = \frac{\tau_i'}{\sigma_i'}. \tag{4.9}$$

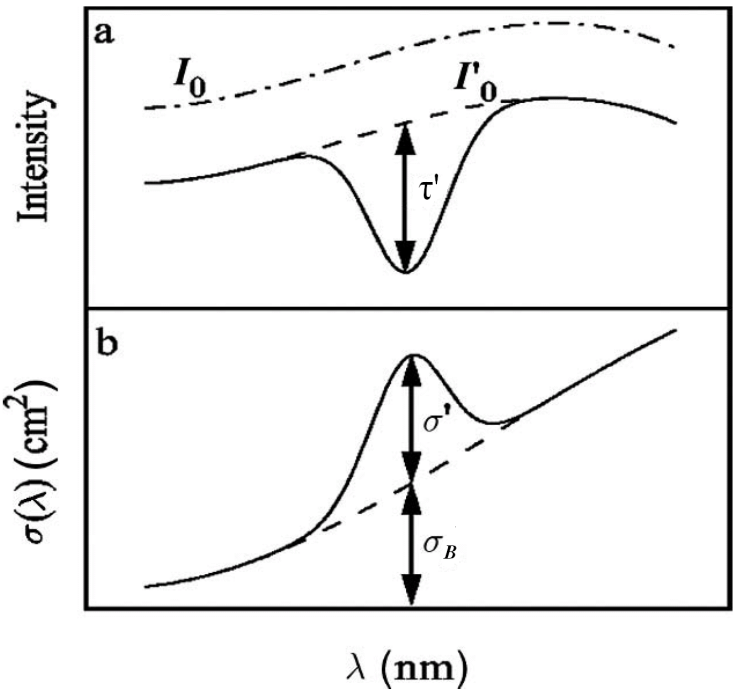

Figure 4.2: Sketch of the DOAS principle: The intensity I_0 and the absorption structures σ are separated into a narrow-band (τ', σ') and broad-band part (I'_0, σ_B) , adapted from Platt and Stutz (2008).

If the concentration is homogeneous along the light path or if the average concentration shall be calculated, the following equation can be applied:

$$\overline{c}_i = \frac{S_i}{L} = \frac{\tau'_i}{\sigma'_i \cdot L}. \tag{4.10}$$

However, the DOAS method requires a reference spectrum I_0 and can only yield the difference between the measured and the reference spectrum. The differential Slant Column Densities (dSCDs) dS for each fitted trace gas is therefore the primary output quantity of the DOAS method and is defined as:

$$dS_i(\alpha) = S_i(\alpha) - S_{ref,i}, \tag{4.11}$$

with $S_i(\alpha)$ being the SCD at a certain elevation angle α and S_{ref} being the SCD of the Fraunhofer reference spectrum (FRS). The elevation angle α is defined as the angle between the horizon and the telescope line of sight. Zenith sky measurements have an elevation angle of 90°, whereas measurements towards the horizon have an elevation angle of 0°. The FRS is usually measured at higher altitudes or is a zenith measurement with an elevation angle of 90°. Multi-Axis DOAS (MAX-DOAS) measurements generally record spectra at different elevation angles α between 0° and 90°. The radiation reaching the DOAS instrument further depends on the Solar Zenith Angle (SZA) θ. The SZA is the angle between the position of the Sun and the zenith on a vertical plane. When the Sun is in the zenith, the SZA is very small depending on the geolocation, whereas during sunrise and sunset, the SZA is large. Moreover, the light reaching the DOAS instrument also depends on the Solar Relative Azimuth Angle (SRAA) ϕ. The SRAA is defined as the angle between the azimuth of the telescope viewing direction and the solar azimuth angle (SAA) of the Sun.

So far, this is only valid for infinitely-high resolved spectra. The DOAS method only works for small optical densities τ. If the optical densities are small enough, the following equation can be applied:

$$I^* = I * H \approx I_0 \cdot e^{-S_i \cdot (\tau * H)}, \tag{4.12}$$

with H being the instrument function (Section 4.3.1) and S_i the SCD of a particular trace gas i.

4.2 The DOAS fitting routine

The core principle of DOAS is to account for the broad-band structures σ_b by including an additional polynomial $P(k)$ in the fit, the so-called DOAS polynomial. The choice of polynomial order depends on the shape of the broad-band structures but is typically between 2 and 5. The resulting modelled spectrum can be expressed as:

$$F(\lambda) = \ln(I_0) - (\sum_k P_k \lambda^k + \sum_{i=1}^{m} \sigma(\lambda)_i^* \cdot S_i), \tag{4.13}$$

with S_i corresponding to the SCD of the specific trace gas i. The optimal retrieval is performed in a wavelength rage where the trace gas of interest exhibits strong and characteristic absorption structures. Some trace gases exhibit similar absorption bands in the same wavelength region, e.g. O_3, BrO, HCHO and HONO between 330 and 360 nm. Thus, interferences might occur, i.e. the fitting scenario does not correctly attribute the spectral features of the trace gas of interest to that specific gas but to another gas with similar absorption bands. Including a greater number of absorption bands in the fitting range reduces the likelihood of interference by or correlations with the features of other trace gases. However, larger wavelength ranges may require inclusion of more trace gases, which can lead to interferences by the other trace gases. Another complication can arise from the wavelength dependency of the light path and thus the SCD. The retrieval interval mapping method according to Vogel et al. (2013) is used to find the optimal wavelength intervals for this thesis and is described in Section 8.2.

In order to retrieve the trace gas dSCDs in the DOAS analysis, a least-squares fit is applied (Stutz and Platt, 1996). This fitting algorithm uses the Levenberg-Marquard algorithm (Levenberg, 1944; Marquardt, 1963) in order to minimise χ^2:

$$\chi^2 = \sum_{j=1}^{n} (\ln(I'_j) - F_j)^2 \stackrel{!}{=} \min, \tag{4.14}$$

where j corresponds to a specific spectral point and n to the total number of spectral points in the analysed wavelength interval. I' is the wavelength-calibrated measurement spectrum (with the lower resolution of a real instrument). χ^2 is defined as:

$$\chi^2 = \sum_{j=1}^{n} R_j^2 \tag{4.15}$$

with R_j being the residual:

$$R_j = \ln(I'_j) - F_j. \tag{4.16}$$

In addition to χ^2, the residual R_j (Equation 4.16) or the root mean square (RMS) of R_j are good quality criteria of the fit results. From Equation 4.16 it is obvious that the residual R_j has the meaning and unit of an optical density while the RMS corresponds to χ^2 normalised by the number of spectral points n:

$$\mathrm{RMS} = \sqrt{\frac{\chi^2}{n}} = \sqrt{\frac{1}{n}\sum_{j=1}^{n} R_j^2}. \tag{4.17}$$

Ideally, the residual of the resulting fit is small ($< 10^{-3}$) and unstructured, containing only random noise. However, systematic structures in the residual can occur due to various reasons, for example due to absorbers missing in the fit (but present in the light path), inaccurate literature absorption cross-sections, or wavelength shifts due to temperature instabilities. Since the linear fitting process

cannot account for these effects, a non-linear component can be included in the fit that allows the spectrum to be shifted and squeezed based on a numerical solution of the Levenberg-Marquard algorithm.

4.3 Corrections for the spectral fit

The DOAS principle described above is based on ideal measurements. In reality, several effects occur that have to be considered before starting the analysis. Firstly, any spectrometer has a finite spectral resolution and the highly resolved absorption cross-sections have to be convolved to the same spectral resolution as the instrument used to acquire the measurements. Furthermore, measurements of scattered sunlight require application of several corrections in the spectral analysis, which are described in the following section.

4.3.1 Spectral resolution and wavelength calibration

The limited optical and spectral resolution of the spectrograph spectrally degrades the incident, highly resolved absorption spectrum $I(\lambda, L)$. The limited resolution is caused by optical components such as the grating properties and the entrance slit. Hence, the spectrum $I^*(\lambda, L)$ arriving at the spectrograph can be described as the convolution of the incident, highly resolved absorption spectrum $I(\lambda, L)$ with the instrument function $H(\lambda)$:

$$I^*(\lambda, L) = I(\lambda, L) * H(\lambda) = \int I(\lambda', L) \cdot H(\lambda - \lambda') d\lambda'. \tag{4.18}$$

The different highly resolved literature absorption cross-sections have to be downgraded to the spectral resolution of the instrument. According to Equation 4.18, the absorption cross-sections have to be convolved with the instrument function $H(\lambda)$ yielding:

$$\sigma^*(\lambda) = \sigma(\lambda) * H(\lambda) = \int \sigma(\lambda') \cdot H(\lambda - \lambda') d\lambda'. \tag{4.19}$$

As mentioned above, this equation is only valid for small optical densities with $\tau \ll 1$. The instrument function $H(\lambda)$ can be determined by measuring a discrete atomic emission line, such as from a mercury, neon or krypton spectrum. The width of these discrete emission lines usually lies around a few picometres, whereas the resolution of the instruments used in this work is approximately 0.5 nm (Section 8.1). As the spectrum recorded by the detector is mapped to discrete pixels, it has to be wavelength-calibrated. In general, the wavelength-pixel mapping C_J for a detector with q channels can be approximated by a polynomial:

$$C_J : \lambda(j) = \sum_{k=0}^{q-1} c_k \cdot j^k. \tag{4.20}$$

The wavelength-pixel mapping is further specified in Section 8.1.

4.3.2 Electronic offset and dark current

The electronic offset is an artificial signal that is added to each measured spectrum because negative signals, which may occur due to detector noise, cannot be interpreted by the analogue-digital converter of the spectrograph. The analogue-digital converter transforms the analogue signal from the spectrograph into a digital signal that can be read by the computer. The offset signal has to be subtracted from all spectra prior to the execution of the DOAS spectral fitting procedure. The measured spectra have to be corrected according to the following equation:

$$I_O(n) = I(n) - \frac{j_s}{j_O} \cdot O(n), \tag{4.21}$$

where $I(n)$ and $I_O(n)$ refer to the signal of a particular channel n of the measured spectrum I before and after the offset correction, respectively. O(n) corresponds to the offset spectrum recorded with j_O co-added scans and j_s indicates the number of co-added scans of the measured spectrum. The offset is proportional to the number of performed scans. In order to obtain an offset spectrum, a short integration time is used to minimise dark current, as well as a high number of scans for statistical reasons.

Dark current is caused by thermal excitation. This occurs when electrons have sufficient kinetic energy to move from the valence band to the conducting band. The probability of the electrons receiving enough energy, and thus the amount of dark current, is proportional to the Boltzmann factor $e^{-\Delta E/k_B T}$. Thus, to reduce the dark current signal, the detector has to be thermally stabilised at a constant, low temperature. Dark current spectra are obtained by recording one scan with a long integration time under dark conditions. All the spectra have to be corrected by subtracting the time-weighted and offset-corrected dark current spectrum. The measured spectra are corrected for the dark current signal according to:

$$I_{DC}(n) = I(n) - \frac{t_{\text{meas}}}{t_{DC}} \cdot D_O(n) \tag{4.22}$$

with t_{meas} and t_{DC} being the integration times of the measured spectrum and the dark current spectrum D_O, respectively. $D_O(n)$ corresponds to the dark current signal of a particular channel n and is corrected for the offset signal.

4.3.3 Fraunhofer lines

Fraunhofer lines are absorption lines that can be observed in the solar spectrum and are named after the German physicist Joseph von Fraunhofer (1787 - 1826) (Fraunhofer, 1817; Kirchhoff, 1860a,b). They originate from the absorption of sunlight by chemical elements such as hydrogen (H), iron (Fe), nickel (Ni), calcium (Ca), magnesium (Mg) or natrium (Na), which are present in the upper layers of the solar atmosphere. These lines are observed as 'dark' solar spectrum regions with relatively low radiation intensity. The optical density of these Fraunhofer lines is two or three orders of magnitude higher than the optical density of atmospheric trace gases in the UV/vis spectral range. Hence, these lines have to be considered in the spectral retrieval of atmospheric trace gas species. This effect can be accounted for by including a Fraunhofer reference spectrum (FRS) in the retrieval procedure, which serves as the I_0 spectrum. As the DOAS retrieval can only yield the difference between a measured spectrum and the FRS (Equation 4.11), the FRS should ideally contain no trace gas absorption features. Thus, the choice of the FRS is both important and also not always straightforward. The Fraunhofer reference spectra used in this analysis are taken from the same instrument as the measurements and are described in Section 8.1.

4.3.4 Ring effect

Grainger and Ring (1962) first observed that the depth of the Fraunhofer lines in spectra of scattered sunlight is reduced compared to direct sunlight spectra. This "filling-in" of Fraunhofer lines is called the Ring effect. It arises due to inelastic scattering processes in the atmosphere, mainly rotational Raman scattering (RRS) (Section 3.2.2) of photons by air molecules like oxygen (O_2) and nitrogen (N_2) (Bussemer, 1993). As a result, measured spectra exhibit broadened solar and atmospheric spectral features. The broadening typically reduces the optical density of the Fraunhofer lines by a few per cents. Thus, the Ring effect has a strong impact on DOAS measurements and requires an appropriate correction in the spectral retrieval. The intensity of scattered sunlight measured by the DOAS instrument can be expressed as:

$$I_{\text{measured}} = I_{\text{Rayleigh}} + I_{\text{Mie}} + I_{\text{Raman}}, \tag{4.23}$$

with I_{Rayleigh}, I_{Mie} and I_{Raman} being the intensities due to elastic Rayleigh, Mie and inelastic Raman scattering, respectively. The logarithm of the above Equation yields:

$$\begin{aligned} \ln(\mathrm{I_{measured}}) &= \ln(\mathrm{I_{elastic}} + \mathrm{I_{Raman}}) && (4.24)\\ &= \ln(\mathrm{I_{elastic}}) + \ln(1 + \frac{\mathrm{I_{Raman}}}{\mathrm{I_{elastic}}}) && (4.25)\\ &\approx \ln(\mathrm{I_{elastic}}) + \frac{\mathrm{I_{Raman}}}{\mathrm{I_{elastic}}} = \ln(\mathrm{I_{elastic}}) + \mathrm{I_{Ring}}. && (4.26) \end{aligned}$$

The Ring spectrum, which can be accounted for by inclusion of a pseudo absorption cross-section in the DOAS spectral fitting procedure, is hence defined as:

$$I_{\mathrm{Ring}} = \frac{I_{\mathrm{Raman}}}{I_{\mathrm{elastic}}}. \tag{4.27}$$

In this work, the Ring effect is determined using the software *DOASIS* (Kraus, 2006b). In *DOASIS* the Ring spectrum is calculated according to Bussemer (1993) by dividing a Raman-smoothed skylight spectrum with the original skylight spectrum (i.e. the FRS), both being wavelength-normalised. The Raman spectrum is calculated from a skylight spectrum using input knowledge about the atmospheric concentrations of N_2 and O_2 (Bussemer, 1993; Chance and Spurr, 1997).

4.3.5 Solar $\mathrm{I_0}$ effect

As mentioned above, spectra of scattered sunlight show the typical Fraunhofer lines, which lead to variations in the intensity of the solar spectrum. However, the limited spectrograph resolution can cause an incomplete removal of Fraunhofer lines, since these structures are usually too narrow to be resolved by the spectrograph. This can result in errors in the spectral analysis if the narrow Fraunhofer lines overlap with trace gas absorption lines. Since this effect has its origin in the spectrum from the Sun, it is called the "solar I_0 effect" (e.g. Platt et al., 1997; Aliwell et al., 2002). Assuming simplified conditions with only one absorber of constant concentration, the Lambert-Beer law (Equation 4.1) can be written as:

$$I = I_0 \cdot e^{-\sigma \cdot S} \tag{4.28}$$

where I_0 denotes a high resolution FRS, σ a highly resolved absorption cross-section and S the SCD of a particular trace gas. According to Equation (4.18), the spectra have to be convolved with the instrument function H to simulate the spectrum as measured by the spectrograph:

$$\begin{aligned} I^*(\lambda) &= I * H = (I_0(\lambda) \cdot e^{-\sigma \cdot S}) * H && (4.29)\\ I_0^*(\lambda) &= I_0(\lambda) * H. && (4.30) \end{aligned}$$

During the DOAS spectral fitting procedure, the optical density $\tau^* = \ln(I_0^*/I^*)$ is determined. After several transformations, including a Taylor expansion, τ^* can be approximated by $\tau^* \approx S \cdot \sigma^*$. Finally, the I_0-corrected absorption cross-section can be calculated according to the following equation (e.g. Wagner et al., 2002c):

$$\sigma_{I_0}(\lambda, S) = \frac{\tau^*}{S} = \frac{1}{S} \cdot \ln\left(\frac{I_0 * H}{(I_0 \cdot e^{-S\sigma}) * H}\right). \tag{4.31}$$

The solar I_0 effect has to be considered for strong absorbers but can be neglected for weak absorbers.

4.3.6 Stray light polynomial

Another factor that can cause systematic residual structures in the spectrum is stray light in the spectrometer housing. This can be compensated for by including an additional polynomial in the

DOAS spectral fit that is added to the intensity. Assuming that the amount of stray light is independent of the wavelength, it can be approximated by a constant C. The optical density τ would thus look like this:

$$\begin{aligned}\tau(\lambda) &= \ln\left(\frac{I_0(\lambda)+C}{I(\lambda)}\right) && (4.32)\\ &= \ln\left(\frac{I_0(\lambda)}{I(\lambda)}+\frac{C}{I(\lambda)}\right) && (4.33)\\ &= \ln\left(\frac{I_0(\lambda)}{I(\lambda)}\right)+\ln\left(1+\frac{C}{I_0(\lambda)}\right) && (4.34)\\ &\approx \ln\left(\frac{I_0(\lambda)}{I(\lambda)}\right)+\frac{C}{I_0(\lambda)}. && (4.35)\end{aligned}$$

The last term of Equation 4.34 is approximated by a first order Taylor expansion. Together with a scaling factor, the amount of stray light can then be implemented as an additional pseudo absorption cross-section in the DOAS spectral fit. Due to the dependence on $1/I_0$, the spectral structures of this additive polynomial resemble the shape of the Ring spectrum (Section 4.3.4). Thus, this additional polynomial can potentially compensate for small-band structures such as structures due to vibrational Raman scattering (VRS) (Vountas et al., 2003; Peters et al., 2014). Assuming that the amount of stray light depends linearly on the wavelength, the optical density τ changes to:

$$\tau(\lambda) = \ln\left(\frac{I_0(\lambda)+C+D(\lambda)}{I(\lambda)}\right). \quad (4.36)$$

$D(\lambda)$ is proportional to the fraction $\frac{\lambda_{\text{end}}-\lambda}{\lambda_{\text{end}}}$ with λ_{end} being the upper wavelength limit of the applied wavelength interval of the DOAS spectral fit. In this thesis, the polynomial order of this stray light polynomial is set to 1.

4.4 The air mass factor concept

The primary output of DOAS measurements is the differential slant column density (dSCD) of a particular trace gas, which is defined as the gas concentration integrated along a light path L (Equation 4.9):

$$S(\lambda,\vartheta,\alpha,\phi) = \int_0^L c(l)dl, \quad (4.37)$$

with the wavelength λ, the elevation angle α, the SZA ϑ and the SRAA ϕ. As the light path L cannot be easily determined due to its dependence on scattering events or variations in the meteorological conditions, the SCDs cannot be easily interpreted and only contain indirect information on their vertical distribution. It is useful to introduce the vertical slant column density (VCD), which is independent of the viewing geometry:

$$V = \int_0^\infty c(z)\cdot dz, \quad (4.38)$$

with V corresponding to the concentration $c(z)$ integrated along the height z. The ratio of SCD and VCD is defined as the Air Mass Factor (AMF) and is introduced to convert VCDs into SCDs:

$$A(\lambda,\vartheta,\alpha,\phi) = \frac{S(\lambda,\vartheta,\alpha,\phi)}{V}. \quad (4.39)$$

The AMF can be approximated geometrically by assuming that there is just one single scattering event before the photon reaches the instrument. In the case of tropospheric absorbers, where the trace gas is assumed to be located in the lower troposphere, the scattering event occurs above the

trace gas layer (Figure 4.3a). In the case of stratospheric absorbers, the scattering should occur below the trace gas layer (Figure 4.3b).

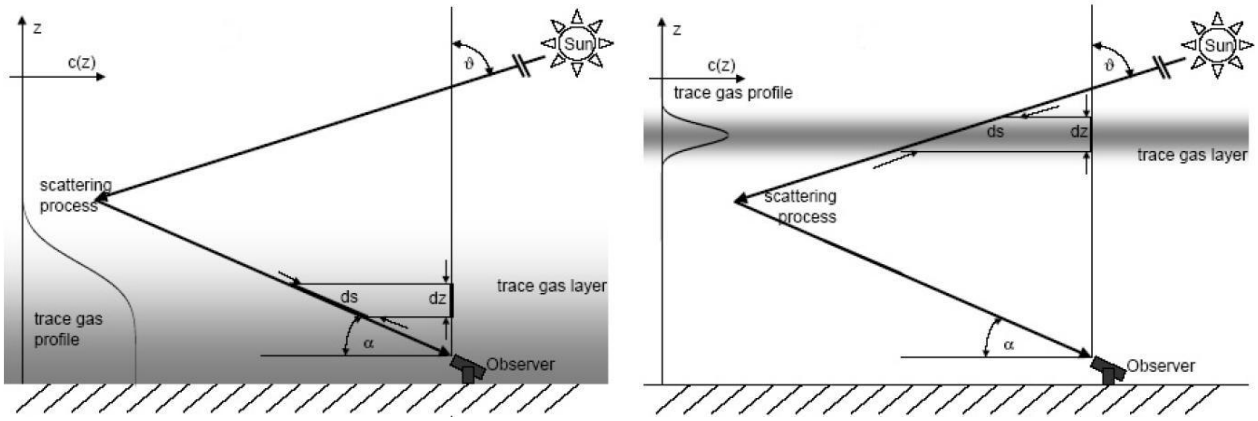

Figure 4.3: Sketch of a DOAS observation of (a) a tropospheric layer, (b) a stratospheric layer (Hönninger et al., 2004).

For the tropospheric case, the scattering height h can be calculated according to the following equation:

$$h = l \cdot \sin\alpha. \tag{4.40}$$

Assuming that the trace gas layer is below the scattering event, the measured slant column density S is only dependent on α and can be written as:

$$S_{\text{trop}} = \int c(l)dl = \int c(z) \cdot \frac{dz}{\sin\alpha} = V \cdot \frac{1}{\sin\alpha}. \tag{4.41}$$

Thus, the AMF is given by:

$$A_{\text{trop}}(\alpha) = \frac{1}{\sin\alpha}. \tag{4.42}$$

For the stratospheric case, the slant column density can be assumed to be independent of α and can be expressed as:

$$S_{\text{strat}}(\vartheta) = \int c(l)dl = \int c(l) \cdot \frac{dz}{\cos\vartheta} = V \cdot \frac{1}{\cos\vartheta}. \tag{4.43}$$

The AMF can be then written in the following way:

$$A_{\text{strat}}(\vartheta) = \frac{1}{\cos\vartheta}. \tag{4.44}$$

For a trace gas that is distributed in the troposphere and the stratosphere the combination of both approximations yields:

$$S(\alpha,\theta) = S_{\text{trop}}(\alpha) + S_{\text{strat}}(\vartheta) = \left(\frac{V_{\text{trop}}}{\sin(\alpha)} + \frac{V_{\text{strat}}}{\cos(\vartheta)}\right). \tag{4.45}$$

However, this approach has serious limitations. The AMF is influenced by geometric parameters (e.g. SZA) as well as meteorological conditions during the measurements such as pressure, temperature, aerosols, clouds or surface albedo. Aerosols or clouds can change the light path significantly due to multiple scattering. In addition, the surface albedo or the absorption by strong absorbers

can also influence the light path and thus the AMF. Hence, this approximation is only valid for SZAs smaller than 75° and for clear viewing conditions. For more accurate calculations of the AMF, radiative transport models have to be applied to simulate the height-dependent atmospheric radiation field.

One approach is to divide the atmosphere into discrete vertical height layers, the so-called boxes or clusters. The Box Air Mass-Factor (Box-AMF) B_{ij} is defined as the sensitivity of the measured slant column density S_i at elevation α_i with respect to the partial vertical column density v_j:

$$B_{i,j} = \frac{\partial S_i}{\partial v_j} \qquad \text{with} \qquad v_j = \int_{z_j}^{z_{j+1}} c(z)dz, \tag{4.46}$$

with v_j being the partial VCD of the altitude layer j that has a height of $\Delta z = z_{j+1} - z_j$. $B_{i,j}$ quantifies the change in the measured SCD at a particular elevation angle α_i when the gas amount at altitude z_j is varied. For weak absorbers, the problem can be solved with linear inversion as the Box-AMFs are constant. For strong absorbers, the Box-AMFs $A_{Box}(V(z_j))$ depend on the VCD of the trace gas, leading to a non-linear inversion problem that has to be solved numerically.

The total AMF is the sum of the Box-AMFs over the whole atmosphere over all layers and weighted with the partial VCD:

$$A = \frac{\sum_j B_{i,j} \cdot V(z_j)}{\sum_j V(z_j)}. \tag{4.47}$$

5. Radiative transfer modelling

Various radiative transfer modelling (RTM) approaches can be applied to numerically solve the RTE (Equation 3.27). One approach uses a statistical method where Monte-Carlo simulations calculate the individual photon paths through the atmosphere. The radiative transfer model McArtim (Deutschmann et al., 2011) is an example of this approach. Another method includes numerical methods that calculate the radiation field, for example the Discrete Ordinate Method (DOM), which applies a discretisation for the directions. This method is implemented in the radiative transfer model SCIATRAN 2 (Rozanov et al., 2005). Within this thesis, McArtim is used for different case studies, e.g. for cloud sensitivity studies (see Section 9.2). Vertical profiles of aerosols and trace gases are derived using SCIATRAN 2 together with an IDL program provided by Yilmaz (2012). This profile retrieval tool (henceforth referred to as 'HEIPRO' for Heidelberg Profile Retrieval) was used to derive aerosol profiles and different trace gas profiles during several ground-based and ship-borne campaigns (e.g. Yilmaz, 2012; Holla, 2013; Lampel, 2014) and has been adjusted for airborne measurements (Nasse, 2014) (Selami Yilmaz, personal communication, IUP Heidelberg, April 2012). This chapter describes the details of radiative transfer modelling, the two RT models used in this thesis as well as the different steps of the profile retrieval procedure including retrieval errors. In the last Section 5.6 the effect of clouds on remote-sensing measurements like the DOAS method is discussed.

5.1 The radiative transfer model McArtim

The Monte Carlo Atmospheric Radiation Transport Inversion Model (McArtim) is a backward model based on Monte-Carlo simulations, developed by Deutschmann et al. (2011). It solves the radiative transport equation in a spherical three-dimensional atmosphere. In Monte Carlo models, scattering and extinction processes are regarded as random phenomena, which can be sampled according to their probability distribution. Photon paths through the atmosphere are modelled for a certain amount of photons including multiple scattering events. The occurrence of a certain scattering process is determined by random numbers and their outcome is weighted with a probability distribution determined by the phase function and scattering coefficient. A time reversal operator in the RTE leads to the adjoint RTE, which has the same solution as the regular RTE (Deutschmann et al., 2011). Thus, the photon trajectories can be modelled forwards or backwards. In this case, the photon trajectories are modelled backwards, since the probability that a single photon hits the detector is very low. The trajectories are therefore calculated starting from the detector into a given direction through the atmosphere and back to the Sun. A sufficient number of photons has to be chosen in order to achieve reasonable statistics. According to sensitivity studies performed by Kreycy (2012), at least 30 000 photons should be used to reduce variances of the model while the computation time should be kept within an acceptable time frame. For a number of 30 000 photons the relative error of the modelled SCDs is typically between 0.5 and 2 % for the RT settings chosen in this study. The model divides the atmosphere into several altitude clusters (one-dimensional or three-dimensional) where each cluster is assumed to have homogeneous atmospheric properties. The larger the spatial variation in these atmospheric properties, the more layers are needed. For each cluster, McArtim calculates derivatives of the radiance with respect to the different optical

properties. The basic output of McArtim contains the simulated radiances with their absolute and relative error as well as the different derivatives with respect to optical properties such as the aerosol extinction or the single scattering albedo. In a one-dimensional atmosphere with n altitude clusters, the contribution S_j of one single cluster j to the total slant column density S measured at the detector altitude is determined by the multiplication of the Box-AMF B_j (Equation 4.46) with the trace gas concentration $[x]_j$ in this cluster (Raecke, 2013):

$$S_j = B_j \cdot [x]_j \cdot z_j, \tag{5.1}$$

with z_j being the height of the altitude cluster. The sum over the contributions S_j from all altitude clusters then corresponds to the SCD S measured at the detector:

$$S = \sum_{j=1}^{n} B_j \cdot [x]_j \cdot z_j. \tag{5.2}$$

The input parameters that are required for the description of the atmosphere and the observation geometry are specified in Table 5.1.

Table 5.1: Overview of the different variables and parameters required for the model atmosphere in McArtim.

variable name	description	unit
SZA (solar zenith angle)	angle between the position of the Sun and the zenith	°
SAA (solar azimuth angle)	azimuth angle of the Sun with respect to the North	°
north azimuth	azimuth viewing direction of the telescope (= viewing direction) towards the north pole meridian; north azimuth = heading direction of the aircraft - 90°	°
SRAA (sun relative azimuth angle)	angle between the azimuth angle of the Sun and the azimuth viewing direction of the telescope; SRAA = SAA - north azimuth	°
elevation angle α	angle between the horizon and the line of sight of the telescope	°
colatitude	90° - latitude	°
longitude		°
altitude	altitude of the telescope/ observer	km
ground albedo	wavelength dependent ground albedo	-
SSA (single scattering albedo)	fraction of scattering relative to the total extinction; between 0 and 1 with an SSA of 0 meaning that the particle completely absorbs light and no scattering occurs (black particle), whereas for an SSA of 1, all light is scattered (white particle)	-
ϵ (extinction)	vertical extinction profile of aerosol or cloud particles	km^{-1}
g	asymmetry parameter of the Henyey-Greenstein parametrisation of the phase function	-
Ångström exponent	describes the wavelength dependency of ϵ	-
air data	vertical profiles of temperature and pressure of the air obtained from radiosondes or from the Falcon standard aircraft parameters during ascents and descents	hPa, K
strong absorbers	trace gases with strong absorption bands (e.g. O_3, O_4, NO_2) have an influence on the light path and their absorption cross-section and vertical concentration profile have to be included in the RTM	cm^2, molec cm^{-3}
FOV	field of view of the instrument	°
λ	a fixed wavelength needs to be chosen for the model atmosphere, preferably, the middle wavelength of the analysed wavelength interval	nm

5.2 The radiative transfer model SCIATRAN 2

As mentioned above, the radiative transfer model SCIATRAN 2 uses the DOM approach to calculate the radiation field in a spherical atmosphere (Rozanov et al., 2001, 2005). The model applies the combined differential-integral (CDI) approach (Rozanov et al., 2001). The RTE (Equation 3.27) is thereby divided into components that deal with single scattering and multiple scattering. The resulting RTE is then solved numerically using the Finite Difference Method and the Picard iterative approximation (Rozanov et al., 2000, 2001). Compared to Monte-Carlo radiative transfer models (e.g. McArtim), this model has the advantage of greater computational efficiency (Rozanov et al., 2001) and is hence faster. Similar to McArtim, the atmosphere is subdivided into altitude layers with each layer is assumed to have homogeneous atmospheric properties. The climatological data

base implemented in SCIATRAN 2 was developed at the Max Planck Institute (MPI) for Chemistry in Mainz and uses a 2D chemo-dynamical model (Brühl and Crutzen, 1993). It contains monthly and latitudinal dependent vertical distributions of atmospheric trace gases, pressure and temperature in the altitude range between 0 and 60 km (Rozanov, 2007). The relevant vertical profiles can also be replaced by user-defined profiles. All vertical profiles are interpolated on the altitude grid using a cubic interpolation as described in Akima (1970). The input parameters for the description of the atmosphere have to be chosen accordingly to the input parameters of McArtim (see Table 5.1). In addition to the difference in the computational efficiency, a key difference between McArtim and SCIATRAN is the fact that McArtim solves the RTE in a 3D atmosphere, whereas SCIATRAN calculates the radiation field in a 1D atmosphere according to the DOM approach.

5.3 Profile inversion

The atmosphere is generally probed indirectly using remote-sensing methods such as the DOAS technique. Inversion methods have to be applied in order to retrieve information about the vertical distribution of trace gases in the atmosphere from the measured dSCDs. Inversion techniques have already been applied to DOAS measurements from different platforms, e.g. Frieß et al. (2011) used the optimal estimation method to infer vertical aerosol extinction and BrO profiles in the Arctic boundary layer. Kritten et al. (2010) retrieved NO_2 from balloon-borne measurements using a modified optimal estimation approach and Prados-Roman et al. (2011) inferred BrO profiles from airborne DOAS measurements using a regularisation method. The basics of inversion can be derived from Bayes' theorem (see Rodgers, 2000). The concept of profile inversion, the notation as well as the equations used in this thesis, are based on Rodgers (2000). The atmospheric radiative transfer is approximated by an appropriate model function $\mathbf{F}$, in this case the radiative forward model McArtim or SCIATRAN 2:

$$\mathbf{y} = \mathbf{F}(\mathbf{x}, \mathbf{b}) + \epsilon \tag{5.3}$$

with $\mathbf{y}$ being an n-dimensional vector containing the measurements and ϵ the measurement error. The m-dimensional vector $\mathbf{x}$ defines the state of interest within the measured system. The parameter $\mathbf{b}$ quantifies other properties of the system, which are not measured, but which are necessary for the model description. The values of $\mathbf{b}$ have to be specified by the user using reasonable assumptions. A main requirement for the model producing accurate results is that the forward model $\mathbf{F}$ describes the physical processes in an appropriate way. When applying this technique to DOAS measurements, $\mathbf{y}$ represents the measured dSCDs of a particular trace gas and the radiative transport model $\mathbf{F}$ depends on parameters $\mathbf{b}$ such as e.g. temperature, pressure or aerosol profiles. The aim of this method is to retrieve the state of interest $\mathbf{x}$, which is in this case the vertical profile of the respective trace gas. This state $\mathbf{x}$ is found using the least-squares method where the error weighted square of the deviation of the simulated measurement and the real measurement is minimised:

$$\chi^2(\mathbf{x}) = \sum_{m=0}^{M} \left(\frac{\mathbf{F}_m(\mathbf{x}, \mathbf{b}) - \mathbf{y}_m}{\epsilon_m} \right)^2 \overset{!}{\rightarrow} \min. \tag{5.4}$$

Usually the information content of the measurements is smaller than the information content of the quantities that will be retrieved. Since the information content of the measurements is usually limited, an additional constraint is introduced by an a priori profile $\mathbf{x_a}$ with a certain a priori error $\sigma_\mathbf{a}$. The a priori represents the best guess of the state to be retrieved prior to the measurement and defines the initial conditions of the atmosphere. The so-called optimal estimation method is based on the minimisation of the following cost function:

$$\chi^2(\mathbf{x}) = \sum_{m=0}^{M} \left(\frac{\mathbf{F}_m(\mathbf{x}, \mathbf{b}) - \mathbf{y}_m}{\epsilon_m} \right)^2 + \sum_{n=0}^{N} \left(\frac{\mathbf{x}_n - \mathbf{x}_{a,n}}{\sigma_{a,n}} \right)^2 \overset{!}{\rightarrow} \min, \tag{5.5}$$

which can be rewritten in matrix notation with the measurement covariance matrix $\mathbf{S}_\epsilon$ and the a priori covariance matrix $\mathbf{S}_a$, which contains the square of the dSCD errors and the a priori profile errors, respectively:

$$\chi^2(\mathbf{x}) = [\mathbf{F}(\mathbf{x},\mathbf{b}) - \mathbf{y}]^T \mathbf{S}_\epsilon^{-1} [\mathbf{F}(\mathbf{x},\mathbf{b}) - \mathbf{y}] + [\mathbf{x} - \mathbf{x}_a]^T \mathbf{S}_a^{-1} [\mathbf{x} - \mathbf{x}_a] \overset{!}{\rightarrow} \min, \tag{5.6}$$

with T denoting the transposed matrix and with the superscript -1 representing the inverse matrix. The solution of this problem, i.e. the optimal state vector $\widehat{\mathbf{x}}$ can be derived according to:

$$\nabla_{\mathbf{x}} \chi^2(\widehat{\mathbf{x}}) = 0. \tag{5.7}$$

In the case of a linear forward model,

$$\mathbf{F}(\mathbf{x},\mathbf{b}) = \mathbf{K}(\mathbf{b}) \cdot \mathbf{x} \tag{5.8}$$

the problem can be solved analytically and the state vector that minimises χ^2 is given by

$$\widehat{\mathbf{x}} = [\mathbf{K}^T \mathbf{S}_\epsilon^{-1} \mathbf{K} + \mathbf{S}_a^{-1}]^{-1} [\mathbf{K}^T \mathbf{S}_\epsilon^{-1} \mathbf{y} + \mathbf{S}_a^{-1} \mathbf{x}_a] \tag{5.9}$$

with $\mathbf{K}$ being the weighting function matrix or Jacobian matrix, i.e. each element of the $\mathbf{K}$-matrix is given by the partial derivative of the measurement vector element F_i with respect to the state vector element x_j:

$$K_{i,j} = \frac{\partial F_i}{\partial x_j}. \tag{5.10}$$

In the case of a trace gas profile retrieval, the Box-AMFs (see Equation 4.46) serve as elements of the weighting function matrix $\mathbf{K}$ with $K_{i,j} = B_{i,j}$. The Jacobian matrix can be regarded as the sensitivity of the measurement to the state of the atmosphere. For non-linear inversion problems, the weighting function $\mathbf{K}$ depends on the state vector. Iterative methods like the Levenberg-Marquardt method (Levenberg, 1944; Marquardt, 1963) have to be applied to solve the minimisation problem. The aerosol profile retrieval represents a non-linear inversion problem, whereas the trace gas profile retrieval is assumed to be a linear case. For a detailed discussion see Rodgers (2000) or Deutschmann (2008) and Deutschmann et al. (2011).

The sensitivity of the retrieved state vector with respect towards changes in the measured quantities can be described by the retrieval gain function $\mathbf{G}$ and can be calculated according to:

$$\mathbf{G} = \frac{\partial \widehat{\mathbf{x}}}{\partial \mathbf{y}} = [\mathbf{K}^T \mathbf{S}_\epsilon^{-1} \mathbf{K} + \mathbf{S}_a^{-1}]^{-1} \mathbf{K}^T \mathbf{S}_\epsilon^{-1}, \tag{5.11}$$

containing the error covariance matrix. The gain function indicates whether the retrieved information is a priori or can be derived from the measurement. A further useful retrieval quantity is the averaging kernel matrix $\mathbf{A}$. It quantifies the sensitivity of the retrieved state vector $\widehat{\mathbf{x}}$ towards changes in the true state $\mathbf{x}_{true}$. Hence, it indicates how much the retrieved state depends on the true state of the atmosphere:

$$\mathbf{A} = \mathbf{GK} = \frac{\partial \widehat{\mathbf{x}}}{\partial \mathbf{y}} \frac{\partial \mathbf{y}}{\partial \mathbf{x}_{true}} = \frac{\partial \widehat{\mathbf{x}}}{\partial \mathbf{x}_{true}} = [\mathbf{K}^T \mathbf{S}_\epsilon^{-1} \mathbf{K} + \mathbf{S}_a^{-1}]^{-1} \mathbf{K}^T \mathbf{S}_\epsilon^{-1} \mathbf{K}. \tag{5.12}$$

The retrieved vertical profile is equal to the real atmospheric profile, smoothed with the averaging kernel matrix:

$$\widehat{\mathbf{x}} = \mathbf{x}_a + \mathbf{A}(\mathbf{x}_{true} - \mathbf{x}_a) + c \cdot \epsilon. \tag{5.13}$$

Ideally, when the retrieved profile is the true profile ($\widehat{\mathbf{x}} = \mathbf{x}_{true}$), the averaging kernel matrix $\mathbf{A}$ corresponds to the identity matrix. In this case, the a priori does not contribute to $\widehat{\mathbf{x}}$. In reality, the elements of $\mathbf{A}$ are usually smaller than 1 or close to 1. In general, the averaging kernels are used to determine the quality of the profile retrieval. The number of independent pieces of information that

can be retrieved from the measurement is given by the degrees of freedom (DOFs) and is determined by the trace of the averaging kernel matrix (Rodgers, 2000):

$$d_s = \text{trace}(\mathbf{A}). \tag{5.14}$$

For ground-based DOAS measurements of scattered skylight d_s typically reaches values between 2 and 4.

5.4 Retrieval errors

The error of the retrieved profile $\widehat{\mathbf{x}}$ is given by the total retrieval error $\widehat{\mathbf{S}}$. According to Rodgers (2000), the total retrieval covariance matrix $\widehat{\mathbf{S}}$ results from the Bayes' theorem and is defined as the sum of the smoothing error covariance $\mathbf{S_s}$ and the retrieval noise covariance $\mathbf{S_m}$:

$$\widehat{\mathbf{S}} = \mathbf{S_s} + \mathbf{S_m}. \tag{5.15}$$

The covariance matrix of the smoothing error can be expressed as:

$$\mathbf{S_s} = (\mathbf{A} - \mathbf{I}_n)\mathbf{S}_a(\mathbf{A} - \mathbf{I}_n)^T. \tag{5.16}$$

Rodgers (2000) defines $\mathbf{S_s}$ as the smoothing error since this covariance matrix includes elements of the profile space that the measurements cannot identify due to smoothing, e.g. small scale variations that are masked by the limited altitude resolution. However, von Clarmann (2014) states that the concept of the smoothing error is questionable since it is not compliant with Gaussian error propagation. The smoothing error cannot be linearly related to another grid with a different resolution. According to von Clarmann (2014), the smoothing error instead specifies the difference between the retrieved state and an arbitrary representation of the true state, which itself has its own implicit smoothing error. The averaging kernel should be provided instead of the smoothing error.

The covariance matrix of the retrieval noise can be quantified by the measurement error and the gain function according to:

$$\mathbf{S_m} = \mathbf{G}\mathbf{S}_\epsilon\mathbf{G}^T. \tag{5.17}$$

$\mathbf{S_m}$ describes the propagation of the measurement error into the profile retrieval. Different sources of measurement errors are given in Section 8.3. Furthermore, the forward model itself also contains errors that have to be added to the total retrieval covariance matrix $\widehat{\mathbf{S}}$. The forward model error $\mathbf{S_f}$ is not calculated analytically. The magnitude of this error is estimated by performing sensitivity studies. Possible systematic errors that propagate into the profile retrieval are for example uncertainties in the a priori profile, changes in the surface albedo or pointing inaccuracies due to the changing roll angle of the aircraft within one measurement point. Sensitivity studies concerning the forward model error are specified in Section 10.2.3. A detailed error analysis can for example be found in Yilmaz (2012).

5.5 Retrieval procedure

Yilmaz (2012) developed a retrieval algorithm for DOAS measurements based on the inversion principle described by Rodgers (2000). Figure 5.1 shows the retrieval procedure steps according to Yilmaz (2012). The procedure is based on a two-step approach: The non-linear inversion of the aerosol extinction profile and the linear inversion of different trace gas profiles. The length of the light paths strongly depends on the amount, distribution and properties of aerosols present in the atmosphere. O_4 can be used to derive information about the atmospheric aerosol load since the profile of the oxygen collision complex O_4 is proportional to the square of the profile of O_2 and only depends on meteorological parameters like the temperature and pressure (Equation 2.30), (e.g.

Wagner et al., 2004; Sinreich et al., 2005; Frieß et al., 2006). In a first step, the measured spectra are analysed using the DOAS technique to derive dSCDs of O_4 and, optionally, the radiances at a certain wavelength relative to a certain reference radiance. In this study, the measurement vector for the aerosol profile retrieval only consists of O_4 dSCDs while the relative radiances are not used. The respective O_4 dSCD errors are the input for the measurement covariance matrix. The optimal estimation method is applied using radiative transfer simulations, in order to retrieve aerosol extinction profiles. Therefore, the aerosol extinction profile is optimised iteratively until the difference between modelled and measured O_4 dSCDs is within a predetermined limit. As an additional constraint, a priori profiles of the aerosol extinction are used. A selection of predetermined a priori profiles are available. These include linearly decreasing profiles, exponentially decreasing profiles, a smoothed box-shaped profile, which is similar to a Boltzmann distribution, or a profile peaking at a distinct altitude similar to a Gauss distribution. Alternatively, an a priori profile can be provided by the user. Optionally, further aerosol optical properties, such as the Ångström exponent, the aerosol single scattering albedo or the asymmetry parameter of the Henyey-Greenstein parametrisation g can be retrieved. In this work, either McArtim (Section 5.1) or SCIATRAN 2 (Section 5.2) are used as a radiative transfer model.

In a second step, these retrieved aerosol extinction profiles, together with the trace gas dSCDs obtained from the DOAS method, serve as input for the optimal estimation retrieval of vertical trace gas profiles. Similar to the non-linear retrieval, a priori trace gas profiles can be either generated from a list of predefined profiles or provided by the user. More details of the retrieval algorithm and procedure are provided by Yilmaz (2012).

In this thesis, the HEIPRO retrieval is used to infer vertical profiles of HCHO, CHOCHO, NO_2, H_2O, and IO (see Section 10.2.2). The profile retrieval MaRS (Bodo Werner, IUP Heidelberg, personal communication, January 2014) that uses McArtim as a forward model is only used for sensitivity studies and synthetic tests (Section 10.2.1), as the computational costs of McArtim are too high, and is not further described in this context.

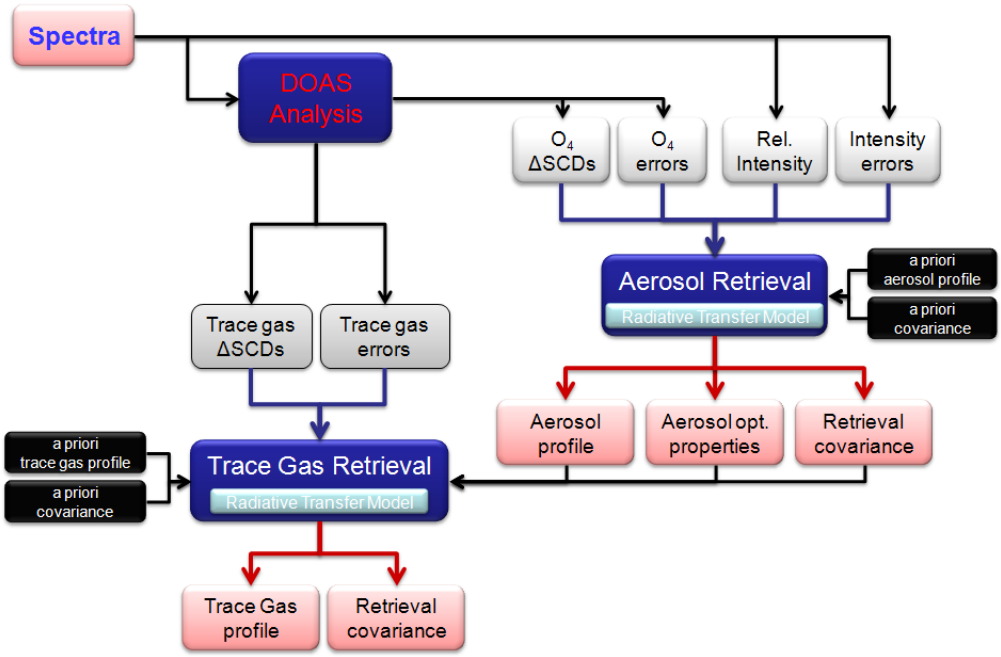

Figure 5.1: Flowchart of the aerosol and trace gas profile retrieval procedure using DOAS measurements, adapted from Yilmaz (2012).

5.6 The effect of clouds

Clouds strongly influence the Earth's radiation budget (Ramanathan et al., 1989). As mentioned in Section 2.4.10, clouds can either have a warming effect as they absorb the long-wave infrared radiation from the surface or they cool the Earth by reflecting the incoming solar radiation back to space. In the presence of clouds, actinic flux measurements indicate large variabilities as clouds reflect and diffuse the incident solar flux inhomogeneously throughout the atmosphere (e.g. Brasseur et al., 2002; Palancar et al., 2011, and references therein). In general, clouds reduce the actinic flux that reaches the surface of the Earth (e.g. Palancar et al., 2011). Under certain conditions, for example in the presence of a discontinuous cloud cover, local enhancements in the actinic flux can be observed. According to Brasseur et al. (2002), the actinic flux can be enhanced by a factor of two to five above and around a cloud when compared to a clear sky scenario. This modified actinic flux can therefore have an influence on the photolysis frequencies of different atmospheric trace gas species. Consequently, clouds have a major influence on the retrieval of atmospheric trace gas species derived from DOAS measurements. The RT in the atmosphere not only depends on the cloud fraction and height but also on the liquid water content, the droplet size and the single scattering albedo of the cloud.

There are two major cloud effects, which are crucial for DOAS measurements: The diffusing screen effect and multiple scattering (Wagner et al., 2011).

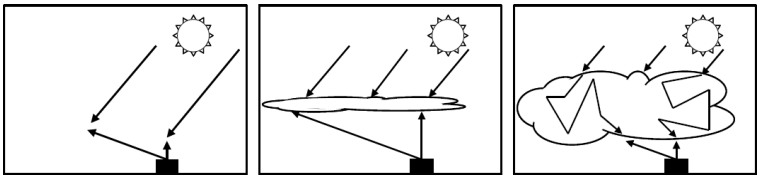

Figure 5.2: Sketch of the influence of clouds on DOAS observations for a clear sky condition (left panel), for the presence of thin clouds (centre panel) and for optically thick and vertically extended clouds, adapted from Wagner et al. (2011).

In the presence of thin clouds, a large fraction of photons is scattered by the cloud, leading to an increase in the light path length relative to clear sky conditions. According to Wagner et al. (2011), this diffusing screen effect can result in an underestimation as well as an overestimation of the retrieved trace gas concentration and has thus a rather complex influence on the interpretation of DOAS measurements. Within optically thick and vertically extended clouds, the length of the light path is strongly increased due to multiple scattering (e.g. Wagner et al., 1998). The length of the light path within such clouds often shows a high temporal variability. In order to investigate the effect of cloud-related changes on O_4 SCDs, sensitivity studies are performed for different artificial cloud scenarios in a 3D geometry (Section 9.2).

In the HEIPRO retrieval algorithm described above, the possibility of an iterative a priori profile is implemented (Udo Frieß, personal communication, March 2014). After every iteration step, the resulting profile is used as an a priori for the next iteration. The new a priori profile is smoothed to avoid instabilities of the retrieval algorithm. An iterative a priori is useful for cases with large aerosol extinctions and clouds as the algorithm is now able to retrieve vertical aerosol profiles with sharp gradients due to an aerosol or cloud layer. However, it must be noticed that using an iterative a priori profile is not "optimal estimation" in a strict sense. Results of the application of this method will be presented in Section 10.2.2.

However, for 1D vertical profile retrievals, it is impossible to identify whether the decrease in visibility is due to clouds, aerosols or a combination of both. Thus, the non-linear profile retrieval does not provide vertical aerosol extinction profiles but rather a combined aerosol-cloud extinction profile, which is further referred to as particle extinction profile.

6. The SHIVA campaign in Borneo during November and December 2011

The SHIVA (Stratospheric ozone: Halogen Impacts in a Varying Atmosphere) project (EU project reference: SHIVA-226224-FP7-ENV-2008–1) mainly aimed to reduce uncertainties in the amount of halogenated very short-lived substances (VSLS) that reach the stratosphere, leading for example to ozone depletion. The SHIVA project comprised an extensive measurement campaign, including ground-, ship-, and satellite-based measurements as well as airborne observations, together with photochemical transport studies. The SHIVA field campaign took place in the South China Sea and along the coastline of Peninsular Malaysia and Borneo during November and December 2011. Figure 6.1 shows an overview map of the different activities during the SHIVA campaign. The activities comprised the following investigations:

1. Ground-based measurements at Sabah Park Facilities on Bohey Dulang Island (17 - 28 November 2011)

2. Field and laboratory studies at Pangkor Island, Port Dickson and the Morib along the Western coast of Peninsular Malaysia (5 September - 30 November 2011)

3. Local boat cruises, leading from Kuching (19 November 2011), Kota Kinabalu (23 November 2011) and Semporna (26 November 2011)

4. Ship-based measurements aboard the German research vessel (RV) Sonne, leading from Singapore to Manila, Philippines (15 - 29 November 2011)

5. Airborne measurements aboard the Falcon aircraft from the German Aerospace Center (DLR) (16 November - 11 December 2011)

6. Satellite observations from the European satellites MERIS, MODIS, GOME-2 and SCIAMACHY

7. Transport and photochemical modelling using FLEXPART, HYSPLIT, CCATT-BRAMS, and TOMCAT.

A more detailed description of the overall campaign activities can be found in Pfeilsticker (2012) as well as on the website `http://shiva.iup.uni-heidelberg.de/`.

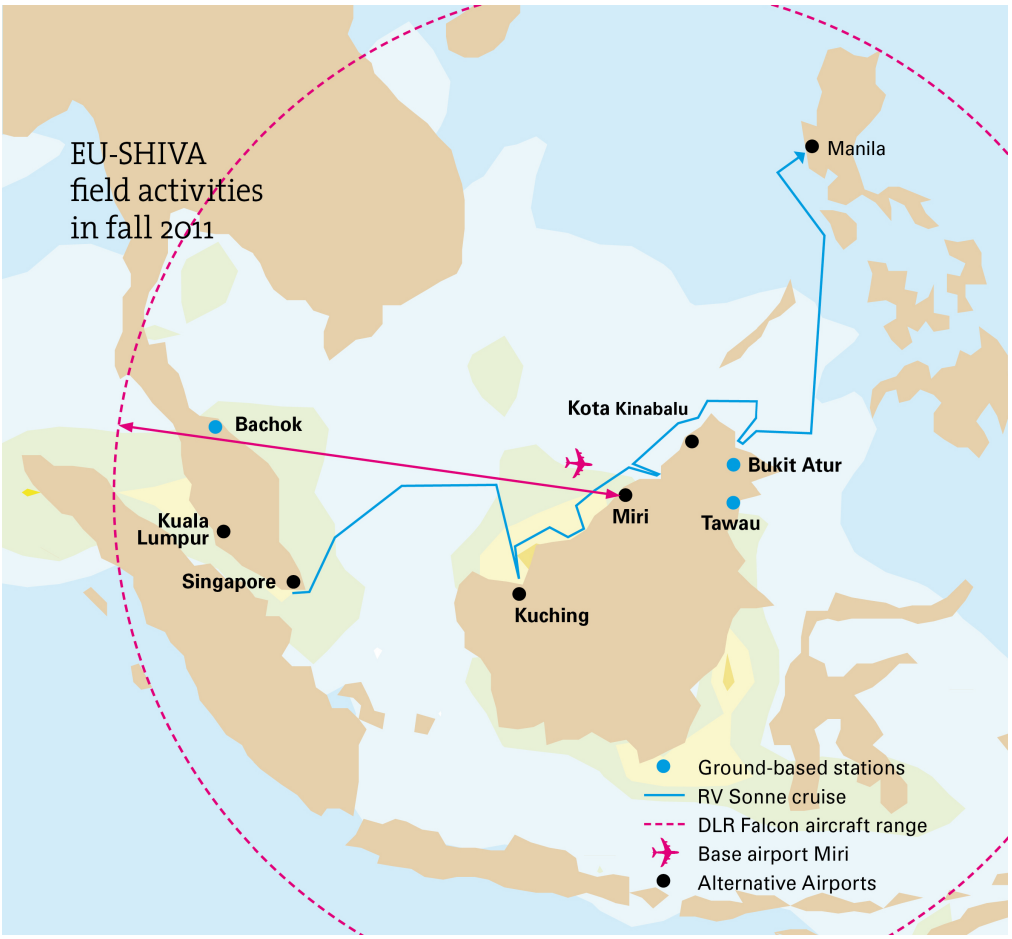

Figure 6.1: Overview of the SHIVA campaign field activities during November and December 2011 (Adapted from the SHIVA campaign leaflet `http://shiva.iup.uni-heidelberg.de/dl/shiva_leaflet_print.pdf`).

6.1 The SHIVA aircraft campaign

The major objectives of the DLR Falcon deployments from Miri Airport, Sarawak (4.3°N/ 114.0°E) were to investigate the:

a) Extent and source strength of various VSLS sources,

b) Atmospheric transport of VSLS and of an artificially released tracer,

c) Atmospheric transformation of VSLS,

d) Impact of halogen radicals on the oxidation capacity of the tropical atmosphere,

e) Entrainment rate of convectively lifted air masses into the upper troposphere (12 km), and

f) Import and impact of Asian pollution, e.g. SO_2 (Pfeilsticker (2012)).

The flight tracks of the 16 different sorties are shown in Figure 6.2 and the measured atmospheric parameters are listed in Table 6.1. If two sorties of the Falcon aircraft were performed on one day, the first sortie was termed 'a' and the second sortie was termed 'b'. In addition, Table 6.2 gives an overview of the objectives of the different DLR Falcon sorties together with the trace gas species that could be detected by the mini-DOAS instrument during each sortie. A detailed description of each DLR Falcon sortie including an overview of the inferred dSCDs can be found in Appendix A.

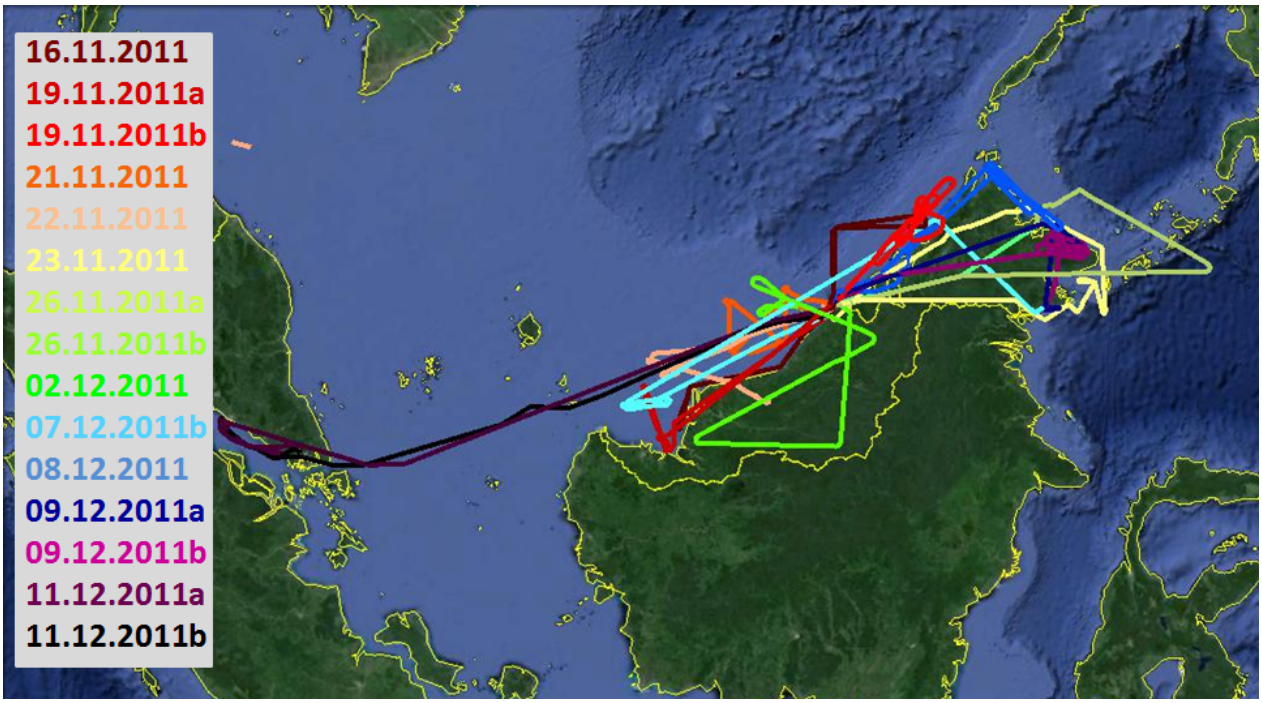

Figure 6.2: Overview of the 16 different sorties during the SHIVA campaign. The flight track of sortie 10 (07.12.2011a) is missing, since no standard aircraft parameters were available during this sortie due to a failure of the data storing process. Map adapted from Google Earth, October 2013.

The mini-DOAS operated during every sortie, except for sortie 15 (11.12.2011 a), where only the first ascent was available due to a measurement script error. The different sorties covered the marine boundary layer (MBL) at low altitudes down to 100 m as well as outflow sampling flights at a maximum altitude of approximately 13 km. Specific objectives of the aircraft-borne DOAS measurements during the field campaign were to study the:

a) Abundance of halogenated compounds in the MBL and mid-troposphere via bromine (BrO) and iodine monoxide (IO) measurements,

b) Oxidation capacity of the atmosphere, i.e. investigations of the oxidation products of volatile organic compounds (VOCs), leading to formaldehyde (HCHO) and glyoxal (CHOCHO),

c) Regional air pollution, i.e. emissions by biomass burning, oil rigs, or anthropogenic combustion, and

d) Composition of air masses in convective outflows of thunderstorms.

For the interpretation of the DOAS measurements, the measurements obtained from the other instruments on board the aircraft are used (Table 6.1). The dataset includes e.g. in-situ measurements of reactive gases like carbon monoxide (CO), ozone, and sulphur dioxide (SO_2).

Table 6.1: Overview of the instruments aboard the DLR Falcon and the atmospheric parameters and species measured during the SHIVA aircraft campaign.

Partner	Instrument	Instrument description	chemical species
DLR	UV ozone monitor[a]	slightly modified commercial ozone monitor	O_3
DLR	CI-ITMS[b]	chemical ionisation ion trap mass spectrometry	SO_2
CNRS	SPIRIT[c]	portable infrared laser absorption spectrometer	N_2O, CO, CO_2, CH_4
GUF	GhOST-MS[d]	GC/MS system operated in negative chemical ionization mode for the fast analysis of halocarbons	halocarbons (H_{1301}, H_{1211}, CH_3Br, H_{1202}, H_{2402}, CH_2ClBr, CH_2Br_2, $CHBrCl_2$, $CHBr_2Cl$, $CHBr_3$, CH_3I)
UEA	WASP[d]	whole air sample pack with subsequent ground-based state-of-the-art GC/MS analysis	hydrocarbons (isoprene, benzene, CCl_4, hexane, i-butane, n-butane, pentane, toluene, m-xylene, p-xylene, o-xylene), halocarbons (CH_3Br, CH_2ClBr, CH_2Br_2, $CHBrCl_2$, $CHBr_2Cl$)
UHEI	mini-DOAS	spectral analysis of limb scattered sunlight	O_3, NO_2, BrO, IO, HONO, CHOCHO, HCHO, H_2O, O_4
DLR	standard aircraft parameters		temperature, pressure, wind speed/direction, humidity, altitude, position, heading

[a]Schlager et al. (1997)
[b]Speidel et al. (2007)
[c]Guimbaud et al. (2011)
[d]Sala et al. (2014b)

Table 6.2: Overview of the different sorties during the SHIVA aircraft campaign. The time marks the take-off and landing. The MBL heights are estimated by Steffen Fuhlbrügge, personal communication, October 2013. As there were no Falcon data available for 7 December 2011a due to a failure in the data storing process, no MBL height could be determined for that day.

no	date	time [UTC]	SZA [°]	objective	region	MBL height [m]	mini-DOAS results
1	16.11.11	04:12 - 07:30	23 -54	MBL sampling	Miri-Kuching	≈ 300	NO_2,HCHO,CHOCHO,IO
2	19.11.11a	03:08 - 06:25	28 - 41	MBL sampling	Miri-Kuching	≈ 400	NO_2,HCHO,CHOCHO,IO
3	19.11.11b	07:45 - 10:10	58 - 92	outflow sampling	coast north of Brunei	≈ 400	NO_2,HCHO,HONO
4	21.11.11	06:33 - 10:24	43 - 95	Lagrangian experiment	coast near Bintulu	≈ 500	NO_2,HCHO
5	22.11.11	03:04 - 06:00	29 - 36	Lagrangian experiment	coast near Sibu	≈ 700	NO_2,HCHO,CHOCHO,IO
6	23.11.11	03:08 - 06:25	29 - 41	MBL sampling	Semporna - Sandakan	≈ 300	NO_2,HCHO,CHOCHO,IO
7	26.11.11a	04:09 - 06:17	25 - 44	deep profile	Sulu Sea	≈ 500	NO_2,HCHO,CHOCHO,IO
8	26.11.11b	08:52 - 09:43	78 - 85	transfer back to Miri	Sandakan-Miri	≈ 500	NO_2,HCHO
9	02.12.11	07:02 - 09:30	49 - 82	outflow sampling	south-west of Miri	≈ 400	NO_2,HCHO
10	07.12.11a	03:05 - 04:30	32 - 28	MBL sampling	Semporna-Tawau	-	NO_2,HCHO,CHOCHO,IO
11	07.12.11b	06:22 - 09:17	44 - 78	deep profile, UTLS	Kuching Bay	≈ 400	NO_2,HCHO,IO
12	08.12.11	02:07 - 05:11	41 - 30	outflow sampling	Kudat-Sandakan	≈ 400	NO_2,HCHO
13	09.12.11a	03:57 - 06:42	27 - 48	MBL sampling	NE coast of Borneo	≈ 500	NO_2,HCHO,CHOCHO,IO
14	09.12.11b	08:12 - 10:46	67 - 99	outflow sampling	NE coast of Borneo	≈ 400	NO_2,HCHO,CHOCHO,IO
15	11.12.11a	03:01 - 06:14	33 - 31	MBL & outflow sampling	Strait of Malacca	≈ 400	only data until 03:30
16	11.12.11b	07:41 - 10:18	47 - 92	MBL & outflow sampling	Strait of Malacca	≈ 500	NO_2,HCHO

6.2 Complementary data

The DOAS measurements are supported by different measurement techniques and instruments to analyse and better understand the results of the SHIVA campaign. In the following, these complementary datasets are described.

6.2.1 FLEXPART simulations

The Lagrangian particle dispersion model FLEXPART (Stohl et al., 2005) developed at the Norwegian Institute for Air Research is used to simulate the horizontal distribution of air masses. Based on the Falcon flight tracks, FLEXPART backward simulations are performed (Sabine Eckhardt, personal communication, March 2012) to determine the source region of the air masses along the flight track and to calculate estimated emission contributions for SO_2, CO, NO_2, or biomass burning tracers. The trajectories for each flight are calculated using two meteorological input data sets from the European Centre for Medium Range Weather Forecasts (ECMWF) and the Global Forecast System (GFS). The emissions of SO_2, CO and NO_2 are based on the EDGAR version 3.2 emission inventory for the year 2000 (fast track) on a 1 x 1 degree grid. This inventory has a resolution of 4 km and includes a list of point sources as well. Furthermore, FLEXPART can be run in the so-called tracer mode or in the aerosol mode, the latter including washout. The horizontal resolution of the output grid is 1 x 1 degree globally, with a 0.5 x 0.5 degree resolution nest over the area of most interest. The contribution from biomass burning is obtained daily from measurements of MODIS aboard the AQUA and TERRA satellites and processed using the MOD14 (MYD14) algorithm described by Giglio (2010).

6.2.2 HYSPLIT airmass trajectories

In order to analyse the history of air masses, the freely available Hybrid Single Particle Lagrangian Integrated Trajectory Model (HYSPLIT) (Draxler and Rolph, 2013; Rolph, 2013) is used (`http://ready.arl.noaa.gov/HYSPLIT.php`). For the model runs, different meteorological input data can be selected. In the present thesis, the backward trajectories are based on the Global Data Assimilation System (GDAS) model from the National Weather Service's National Centers for Environmental Prediction (NCEP). The trajectories can be calculated on isobaric or isentropic vertical motion or by using the modelled vertical velocity given by the meteorological input data. The latter one is used within this thesis.

6.2.3 Satellite trace gas observations

The results obtained from the mini-DOAS instrument made from aboard the Falcon aircraft can be compared to tropospheric VCDs retrieved from passive DOAS observations aboard different satellites. The satellite data of NO_2, HCHO, CHOCHO, and IO was prepared for the SHIVA campaign by the satellite group of the Belgian Institute for Space Aeronomy (IASB-BIRA), Brussels, Belgium (Francois Hendrick, Isabelle DeSmedt, Yu Huan, and Christophe Lerot) and the Institute of Environmental Physics, Bremen, Germany (Anja Schönhardt).

SCIAMACHY

The Scanning Imaging Absorption Spectrometer for Atmospheric Chartography (SCIAMACHY) is mounted aboard the Environmental Satellite (ENVISAT) of the European Space Agency (ESA). It was launched in March 2002 and operational until April 2012. Its spectrometer covers the UV to near-infrared wavelength range and has a ground pixel size of approximately 60 x 40 km^2. The overpass time across the Equator is at about 10:00 in the morning. The details of the retrieval algorithm for BrO and IO are described in Schönhardt et al. (2008) and Schönhardt et al. (2012).

GOME-2

The Global Ozone Monitoring Experiment 2 (GOME-2) instrument (Callies et al., 2000) is a nadir scanning spectrometer mounted on the MetOp-A satellite of ESA launched in 2006 to detect atmospheric trace gases in the UV, visible and near infrared (NIR) wavelength range (λ = 240 - 790 nm). The overpass time across the Equator is at about 09:30 am LT. The ground pixel size of GOME-2 amounts to approximately 80 x 40 km^2 (across-track x along-track). The retrieval of NO_2 VCDs (and of other UV/vis absorbing gases) is based on the KNMI modelling approach (http://www.temis.nl/airpollution/no2.html). The retrieval of HCHO VCDs is performed as described in De Smedt et al. (2008), De Smedt et al. (2010), and De Smedt et al. (2012).

MODIS

TERRA is a polar-orbiting satellite operated by NASA (`http://terra.nasa.gov/`). It was launched in 1999 and is the flagship of the Earth Observing System (EOS). Its payload includes five remote-sensing instruments, e.g. the Moderate-resolution Imaging Spectroradiometer (MODIS) (`http://terra.nasa.gov/MODIS/`), which captures data in the spectral range from 0.4 µm to 14.4 µm with a varying spatial resolution (2 times 250 m, 5 times 500 m, and 29 times 1 km). With its viewing swath of approximately 2300 km and altitude of roughly 700 km, MODIS can see every point on the world every one to two days. MODIS can for example monitor the frequency, distribution, and properties of clouds.

6.2.4 TOMCAT model

TOMCAT is a global 3D chemical transport model and has already been used by Hossaini et al. (2013) to simulate the brominated very short-lived substances (VSLS) bromoform ($CHBr_3$) and dibromomethane (CH_2Br_2) using aircraft observations from the SHIVA campaign. TOMCAT is run with a horizontal resolution of ≈2.8° longitude and ≈2.8° latitude. The number of vertical levels corresponds to 60 sigma-pressure levels and the vertical domain is between 0 and approximately 30 km. Further details on the model can be found in Chipperfield (2006). Contrary to Hossaini et al. (2013), TOMCAT is run with full tropospheric chemistry, including CO emissions and production from VOCs for this thesis. The following additional inventories are used for these model runs:

- Anthropogenic - The Streets v1.2 inventory basically combines numerous regional inventories and uses the EDGAR emission inventory to fill in the gaps. These inventories were updated in 2008 to account for the latest regional inventories and they used the Regional Emission inventory in ASia (REAS) for Asian emissions (Kurokawa et al., 2013).
- Biogenic/Natural - MACCity biogenic emissions calculated by MEGAN v2 model.
- Biomass Burning - Yearly specific emissions for 2011 from the Global Fire Emissions Database (GFEDv3) (`http://www.globalfiredata.org/`). This was the latest inventory available at the time.

The emitted species in the latest full chemistry of TOMCAT are: Butane, HCHO, methanol, monoterpenes, propane, propene, ethane, ethene, isoprene, NO_x, acetaldehyde, toluene, CO, and acetone. All emissions for all species are taken from these inventories and they are all monthly mean estimates. CO has emissions from all three sources with a total of 952.74Tg/yr for 2011, whereas HCHO has a total emission of 10.64Tg/yr. The model output presented in this study is kindly provided by Ryan Hossaini (Institute for Climate and Atmospheric Science, School of Earth and Environment, University of Leeds, personal communication, July 2013).

6.2.5 CCATT-BRAMS model

The Chemistry-Coupled Aerosol and Tracer Transport model to the Brazilian developments on the Regional Atmospheric Modelling System (CCATT-BRAMS) is an on-line regional chemical transport model to study local and regional atmospheric chemistry from the surface to the lower stratosphere (Longo et al., 2013). CCATT-BRAMS is based on the Regional Atmospheric Modelling System version 6 (RAMS) (Walko et al., 2000), which is a fully compressible non-hydrostatic model consistent with TRIPOLI (1982). RAMS is able to simulate meteorological processes, such as turbulence, shallow cumulus convection, deep convection, surface-air exchanges, cloud microphysics, and radiation (Hamer et al., 2013). The model BRAMS is built upon RAMS and includes further improvements for tropical regions, such as an ensemble implementation of the deep and shallow convection.

CCATT-BRAMS has already been used to study the transport and chemistry of bromoform ($CHBr_3$) and its product gases during a convective outflow event that occurred on sortie 3 (19 November 2011) of the SHIVA campaign (Hamer et al., 2013). A detailed description of CCATT-BRAMS can be found in Hamer et al. (2013).

The model output presented in this study is kindly provided by Paul Hamer (Centre National de Recherches Météorologiques, Chimie Atmosphérique Recherches en Modélisation et Assimilation, Météo-France and CNRS, France, personal communication, March 2013). The emitted species provided by the CCATT-BRAMS model include HCHO, CO, NO_2, and a lumped chemical species called 'BIO', which is mostly isoprene plus some other terpenes. The model was spun up for 2 weeks prior to the SHIVA campaign and was run for 6 weeks in total. The model ran at a horizontal resolution of 50 km x 50 km. The vertical grid consisted of 53 vertical levels with a varying resolution using a finer resolution of 50 to 500 m within the boundary layer, and a coarser resolution of 300 to 500 m between an altitude of 13 and 20 km. Further, the model was initialised, has boundary conditions from, and is forced by ECMWF wind, temperature, geopotential height, and humidity fields. Biogenic emissions were derived from the MEGAN model similar to the inventory included in TOMCAT (see Section 6.2.4). The photolysis rates were calculated on-line using the Fast-TUV radiative model of Tie et al. (2003).

6.3 Regional characteristics

Borneo is the largest island of Asia and is located at the centre of Maritime South-East Asia (`http://en.wikipedia.org/wiki/Borneo`). The island of Borneo is politically divided into three parts, which belong to the countries Malaysia, Indonesia, and Brunei (Figure 6.3).

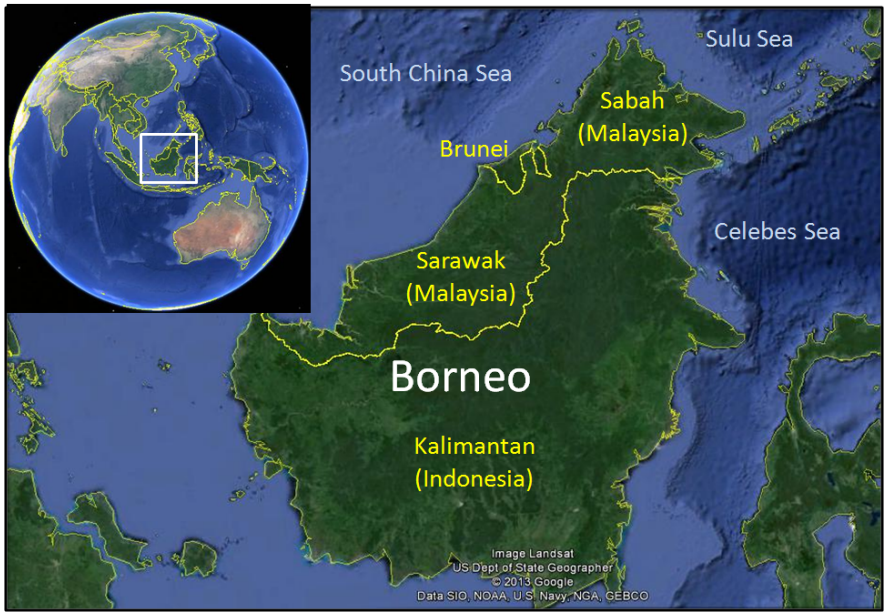

Figure 6.3: Map of Borneo, adapted from Google Earth, October 2013.

During the SHIVA campaign an overflight permission over the Indonesian part of Borneo (Kalimantan) could not be obtained, and hence, air over Kalimantan could not be probed. Brunei and the Malaysian states of Borneo (Sarawak and Sabah) are surrounded by the South China Sea in the north, the Sulu Sea in the northeast and the Celebes Sea in the east. Borneo owns one of the oldest tropical rain forests in the world. Tropical rain forests are known to emit large amounts of volatile organic compounds (VOCs) (e.g. Guenther et al., 1995, 2006). Ground-based and airborne measurements carried out during the "Oxidant and particle photochemical processes above a South-East Asian tropical rain forest" (OP3) campaign in Borneo in 2008 (Hewitt et al., 2010) show that VOCs over the rain forest of Borneo are dominated by isoprene and its oxidation products, with a significant contribution from monoterpenes (MacKenzie et al., 2011). Isoprene is one of the most abundant biogenic VOCs naturally emitted into the atmosphere (Guenther et al., 2006). It reacts rapidly with OH and can not only enhance the formation of tropospheric ozone in polluted areas, but it can also lead to the formation of secondary organic aerosols (SOA), which can act as cloud condensation nuclei (CCN) (Kiendler-Scharr et al., 2009; Robinson et al., 2011). However, there is a strong deforestation in Borneo especially due to the development of the oil palm industry (Pyle et al., 2011). The expansion of oil palm plantations has increased rapidly in Malaysia between 1975 and 2010 (Miettinen et al., 2012a,b). Figure 6.4 shows the extent of oil palm plantations on peatland in South-East Asia for 1990 and 2010. Especially in the state of Sarawak an immense increase of palm oil plantations ($\approx$ 40 %) is observed between 1990 and 2010 (Miettinen et al., 2012a). According to Fowler et al. (2011), VOC emissions from oil palm plantations are substantially larger than from the rain forest by roughly a factor of 3. Furthermore, a change in land-use also leads to an increase in NO_x through the use of fertilisers or pollution from industry and transport, thus, potentially having a major influence on the air quality (Warwick et al., 2013). Stavrakou et al. (2014) examined the isoprene emissions over Asia between 1979 and 2012, particularly regarding the impact of land-use change on climate. They claim that due to the warming trend over Asia with approximately 0.24°C per decade, the isoprene emissions in Asia may have increased by approximately 0.2 % per year since 1979. For example in Malaysia the isoprene emissions may have increased by 1.5 % from 1979 to 2005. Contrary to that but confirmed by measurements during the OP3 campaign in Borneo as well as by satellite measurements, Stavrakou et al. (2014) further state that the tropical rain forests of Indonesia and Malaysia have much lower isoprene emissions than those previously used in model calculations.

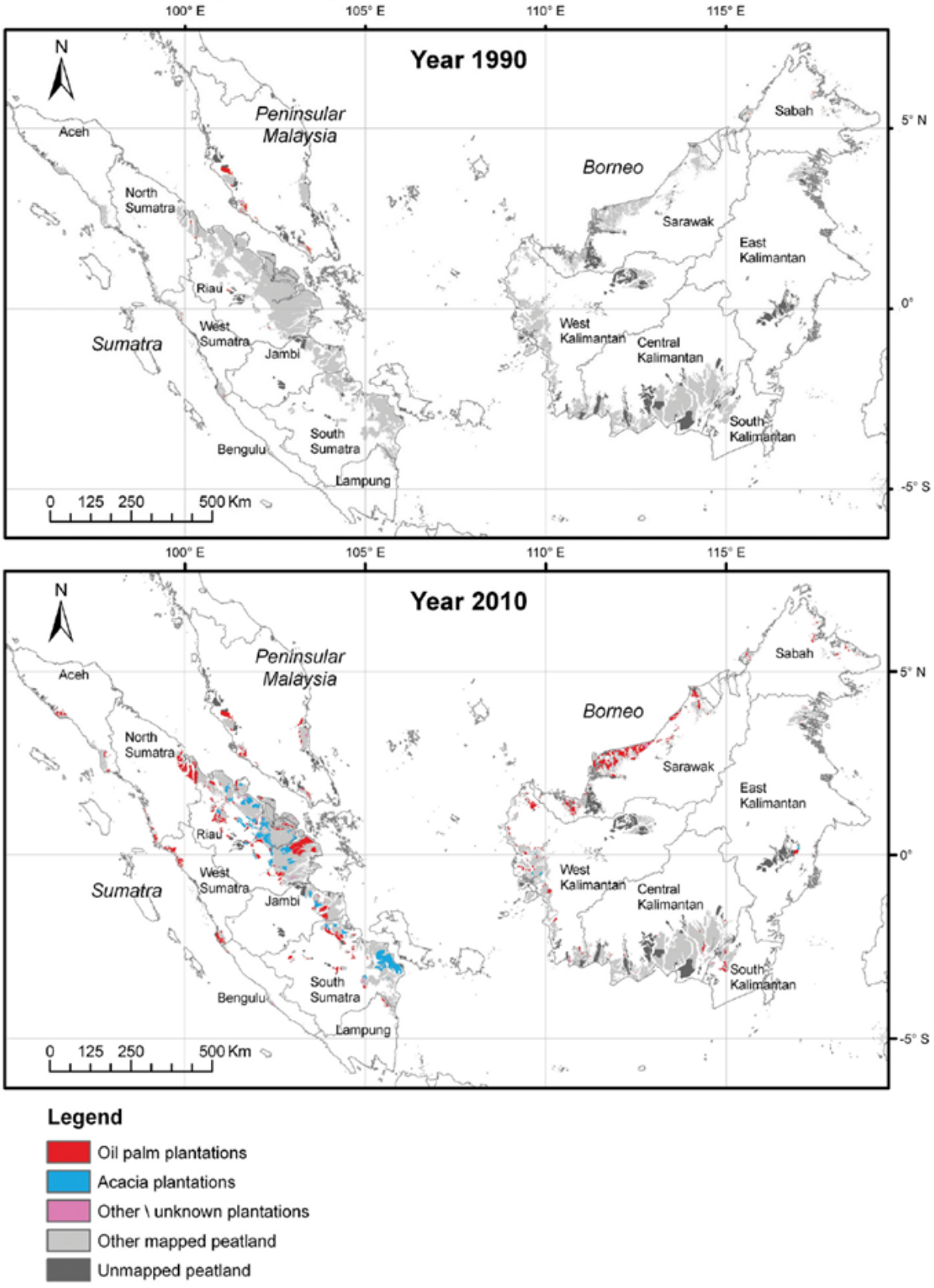

Figure 6.4: Distribution of oil palm plantations on peatland in South-East Asia in 1990 and 2010, respectively (adapted from Miettinen et al. (2012a)). It is important to note that the map only shows oil palm plantations on peatland. The number of oil palm plantations on peatland does not necessarily correspond to the total number of oil palm plantations in this region.

Land clearing especially for oil palm plantations results in anthropogenic burning of the rain forest and the degradation of peatlands. Zender et al. (2012) applied a fire and smoke detection algorithm to investigate biomass burning plumes as detected by the MODIS (Moderate Resolution Imaging Spectroradiometer) and MISR (Multi-angle Imaging Spectroradiometer) satellite data over Borneo between 2001 and 2009. The identified Borneo smoke plumes have a mean length of 41 km, a mean height of 708 m, and a mean width of 27 % of their length, and follow the orientation of the prevailing southeasterly winds. Zender et al. (2012) further expect that the orientation and plume width are representative for all Borneo smoke plumes. Figure 6.5 shows fire maps for the time period of the SHIVA campaign, detected by MODIS on board the TERRA and AQUA satellites. The red dots indicate the location where MODIS found at least one fire during the specified period. The fire detection algorithm is described in Giglio et al. (2003). Several fire events occurred along the coastline of Sarawak during November 2011, where several oil palm plantations are located (Figure 6.4). However, the number of fire events decreased in December 2011. During several take-offs and landings, the Falcon aircraft passed on occasion these plumes. Table 6.3 provides an overview of the fire events, which occurred in the vicinity of the different sorties of the Falcon aircraft. The fire events are simulated with the Lagrangian particle dispersion model FLEXPART (Stohl et al., 2005) (Section 6.2.1).

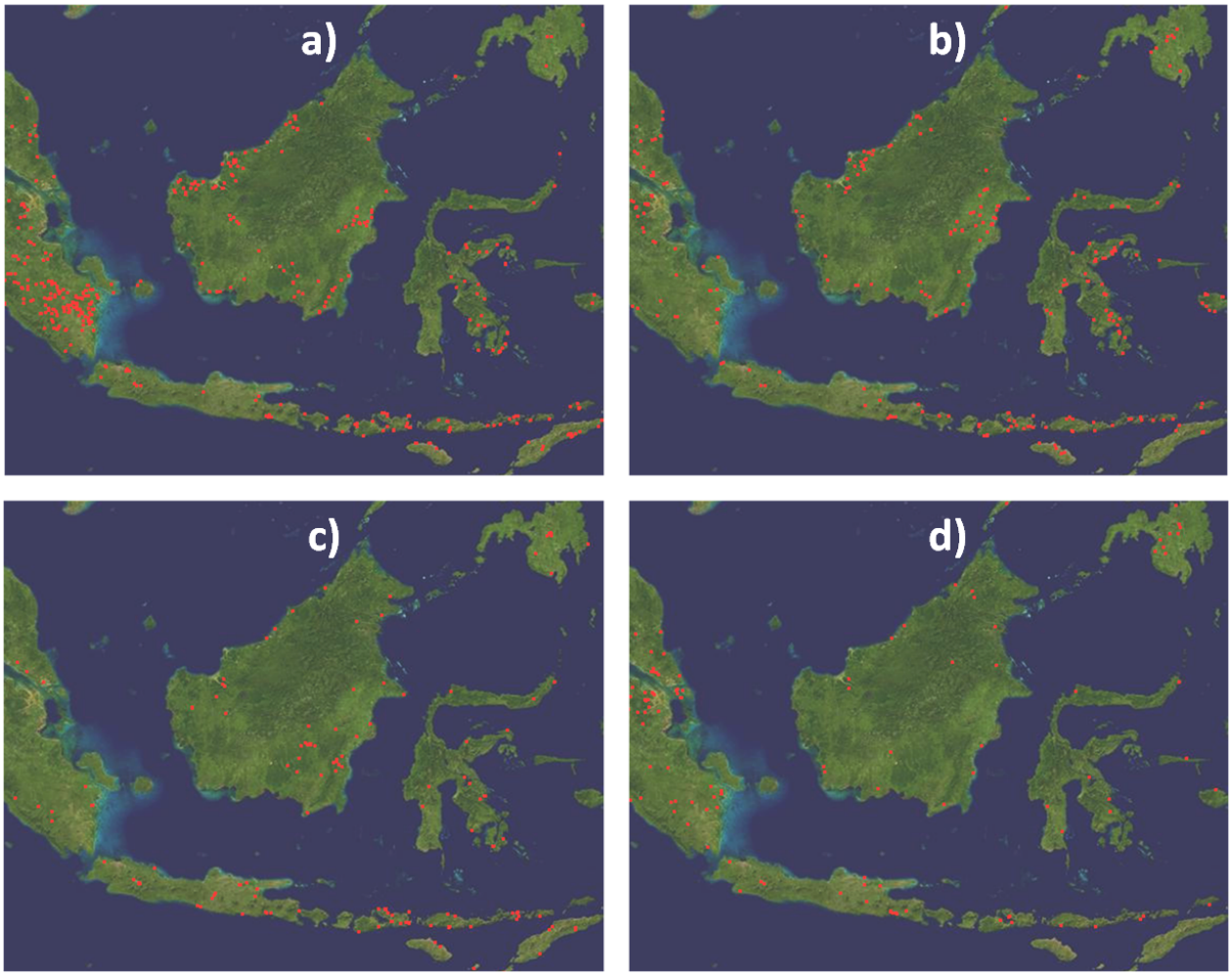

Figure 6.5: MODIS fire maps for a) 08.11.-17.11.2011, b) 18.-27.11.2011, c) 28.11.-07.12.2011, and d) 08.12.-17.12.2011 (`http://lance-modis.eosdis.nasa.gov/imagery/firemaps/`).

Table 6.3: Overview of the contribution of CO to fire events. The data was compiled by Gisèle Krysztofiak (CNRS, Université d'Orléans, France, personal communication, June 2013) from FLEXPART simulations provided by Sabine Eckhardt.

date	origin	emission age [days]	CO from fires [ppb]
16.11.11	North Borneo	7	10-14
19.11.11a	North Borneo, North Australia	<10	19-25
19.11.11b	North Borneo, Philippines	1-8	>2
21.11.11	North Borneo	0-3	35
22.11.11	North Borneo	0-3	12-95
23.11.11	North Borneo	0-1	70
26.11.11a	North Australia, Celebes	<6	>6
26.11.11b	North Australia, Celebes	<6	>6
02.12.11	Borneo, Indonesia	<5	>2
07.12.11a	North Borneo	0-1	140
07.12.11b	North Borneo	0-3	22-43
08.12.11	-	< 3	>2
09.12.11a	North Borneo	2-3	5-16
	Vietnam, China	<8	>2
09.12.11b	North Borneo	2-3	5-16
	Vietnam, China	<8	>2
11.12.11a	North Australia	<8	3-10
11.12.11b	North Australia	<8	3-10

Apart from biomass burning, other potential sources for pollution in Borneo are the emissions from oil and gas rigs and refineries. Numerous offshore oil platforms can be found along the coast of Sarawak. In addition to the emissions due to flares, process gas or oil is burned on the platforms. Figure 6.6 shows the distribution of offshore oil rigs around Borneo. Several offshore oil rigs are located off the coast of Miri and Brunei, but also at the north-western coast close to Bintulu. The technical report of the Texas Commission on Environmental Quality Air Quality Division (TCEQ, 2007) summarises the different emissions from oil and gas production facilities. They state that the potential pollutants are mainly SO_2, NO_x, VOCs, CO, and particulate matter (PM). The largest source for SO_2, NO_x, CO, and PM is represented by the drilling rig engines and compressor engines, whereas the largest sources for VOCs can be assigned to glycol dehydrators, condensate storage tanks, or gas production wellheads.

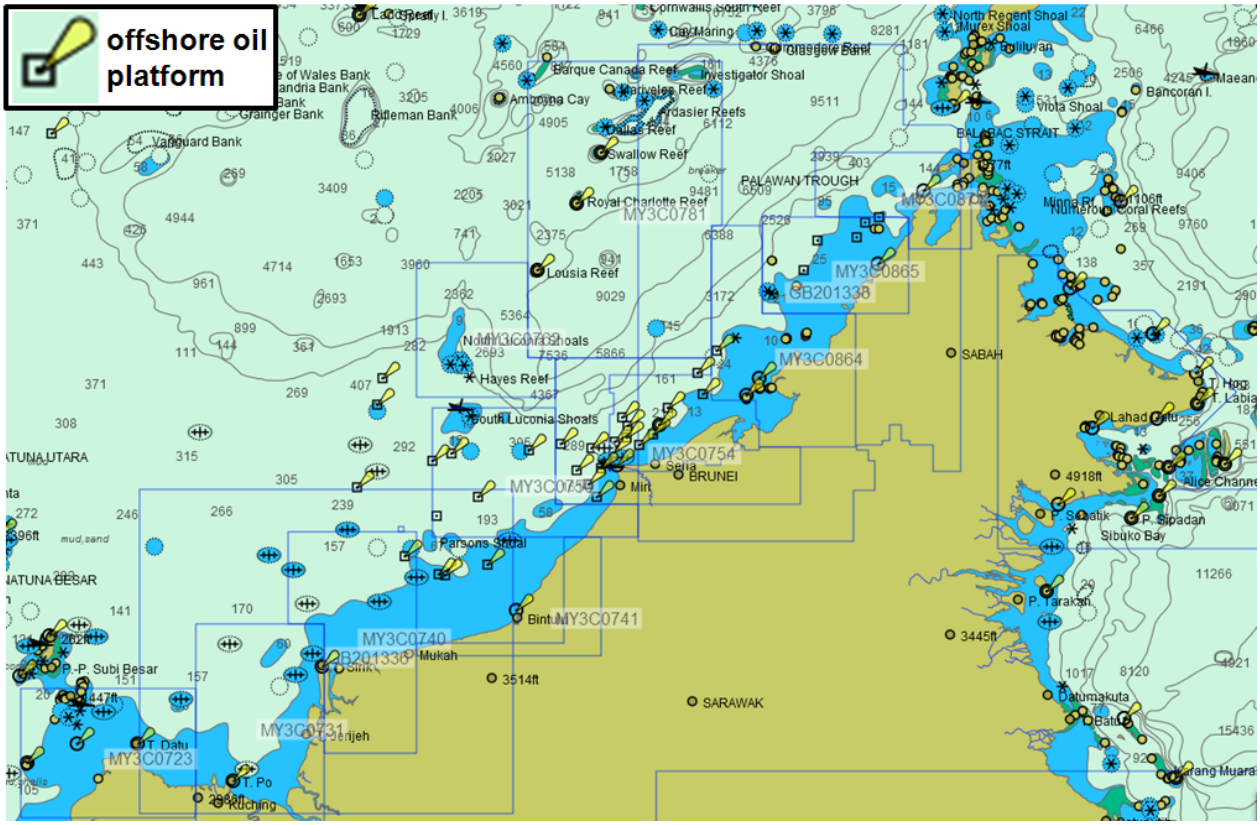

Figure 6.6: Distribution of oil platforms around Borneo. The offshore oil platforms are marked with a yellow buoy pinned to a black square. There are many other symbols in the map representing e.g. wrecks, rocks, underwater obstructions, light towers, pile beacons, water buoys, or installation buoys, which are not relevant for this study. Extracted from the software PolarView NS Version 1.8.41 (`http://www.polarnavy.com`).

Further, Malaysia has an extensive coastline surrounded by mangroves or coral reefs, which are increasingly used for seaweed production (Phang, 2006). Seaweeds are macroalgae and can be classified into brown, red, and green macroalgae, based on their type of pigmentation (McHugh, 2003). They are naturally growing or farmed for food or commercial products, e.g. as a renewable source of fuel (McHugh, 2003; John et al., 2011). Particularly in the northeastern part of Sabah and the archipelagos between Sabah and the Philippines, areas with enhanced seaweed farming exist, which have grown quickly over the last two decades (Phang, 2006). Several studies in the past years have shown that macroalgae have the potential to emit halocarbons like bromoform ($CHBr_3$) or methyl iodide (CH_3I), as they concentrate halides from the sea water, which then act as antioxidants (e.g. Leedham et al. (2013) and references therein). Figure 6.7 shows seaweed and seaweed farms close to Semporna in the northeastern part of Borneo, recorded during sortie 4 of the SHIVA aircraft campaign. However, according to long-term halocarbon measurements (2008 - 2010) at a coastal and an inland site in Sabah, Borneo, South-East Asia does not represent a hot spot for the emission of halocarbons, as has been suggested before (Robinson et al., 2014).

Figure 6.7: Seaweed and seaweed farms close to Semporna on 23 November 2011. The pictures were taken out of the window next to the ozone monitor on the starboard side of the Falcon aircraft.

6.4 Meteorology

The SHIVA campaign took place within the tropical belt, close to the ITCZ and within the upwelling branch of the Hadley circulation (Section 2.2). The South-East Asian maritime continent is known where deep convection often occurs in the wet season. Tropical deep convection is one of the primary mechanisms by which tropospheric trace gases and aerosols are lofted from the surface to the upper troposphere and lowermost stratosphere (e.g. Fueglistaler et al., 2009). Convection is particularly strong over the Western Pacific, which therefore represents an important source region for air masses, which are transported from the troposphere into the stratosphere (e.g. Newell and Gould-Stewart, 1981; Gettelman et al., 2002; Fueglistaler et al., 2009; Rex et al., 2014). Hence, this region is regarded as the main entrance gate into the stratosphere for naturally emitted halocarbons (e.g. Bonazzola and Haynes, 2004; Krüger et al., 2008; Fueglistaler et al., 2009). Figure 6.8 sketches the vertical structure of the atmosphere in the tropics including the processes related to the tropopause layer (TTL) and deep convection. The TTL is defined as the region between the level of zero radiative heating (LZRH) and the cold point tropopause (CPT), often found close to the level of maximum convective outflow (e.g. Fueglistaler et al., 2009; Randel and Jensen, 2013). The CPT is a sharp bend in the vertical temperature profile. Deep convective outflow in the upper troposphere typically occurs between 10 km and 18 km with a local maximum typically near 12 - 14 km. Deep convection mostly occurs over land, whereas shallow cumulus clouds often develop over the tropical ocean.

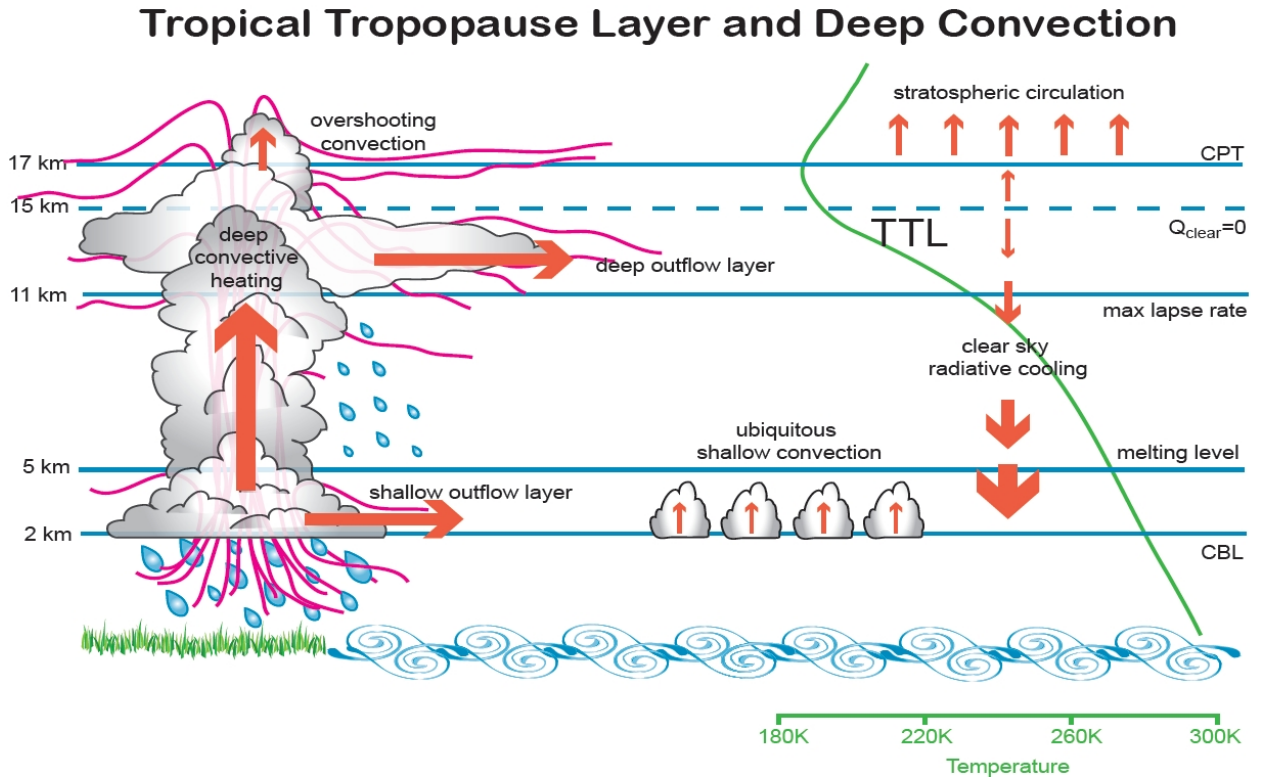

Figure 6.8: Sketch of the processes related to the TTL and deep convection in the tropics. The red arrows represent the circulation of mass and the pink lines represent typical particle advection by deep convection in the TTL; CPT = cold point tropopause; Q_{clear} = clear-sky component of the radiative heating; CBL = convective boundary layer; Figure adapted from McFarlane and Pendlebury (2007).

From November to March, the equatorial South China Sea and parts of the coastline of Borneo are strongly influenced by the Asian winter monsoon (Lim and Samah, 2004). During the winter monsoon season, cold and dry north-easterly winds prevail over the South China Sea originating from the land-sea thermal contrast between the cool air masses from the Siberian continent and the warm sea surface temperature of the underlying South China Sea (Koseki et al., 2014). These north-easterly blowing cold surges can occasionally intensify, leading to the so-called cold surge, which can result in heavy rainfall over the South China Sea for about a week (e.g. Tangang et al., 2008; Koseki et al., 2014). Cold surges can further spin up to a cyclonic circulation referred to as the Borneo vortex, occurring close to the island of Borneo (e.g. Braesicke et al., 2012, and references therein). Koseki et al. (2014) analysed the formation and development of the Borneo vortex over the South China Sea during the Asian winter monsoon (Figure 6.9). 24 hours after model initialisation (panel (b)), the wind blows southward and the Borneo vortex has not developed yet. Between 48 and 72 hours (panels (c) - (d)), a cyclonic circulation pattern forms, which intensifies to the Borneo vortex within the next days. Between 144 and 192 hours (panels (g) - (i)) after initialisation, the Borneo vortex has reached its mature stage and moves slowly in north-western direction, having a spatial dimension of approximately 100 - 1000 km (also referred to as meso-α cyclone). As soon as the cyclone reaches the Peninsula of Malaysia, its intensity weakens.

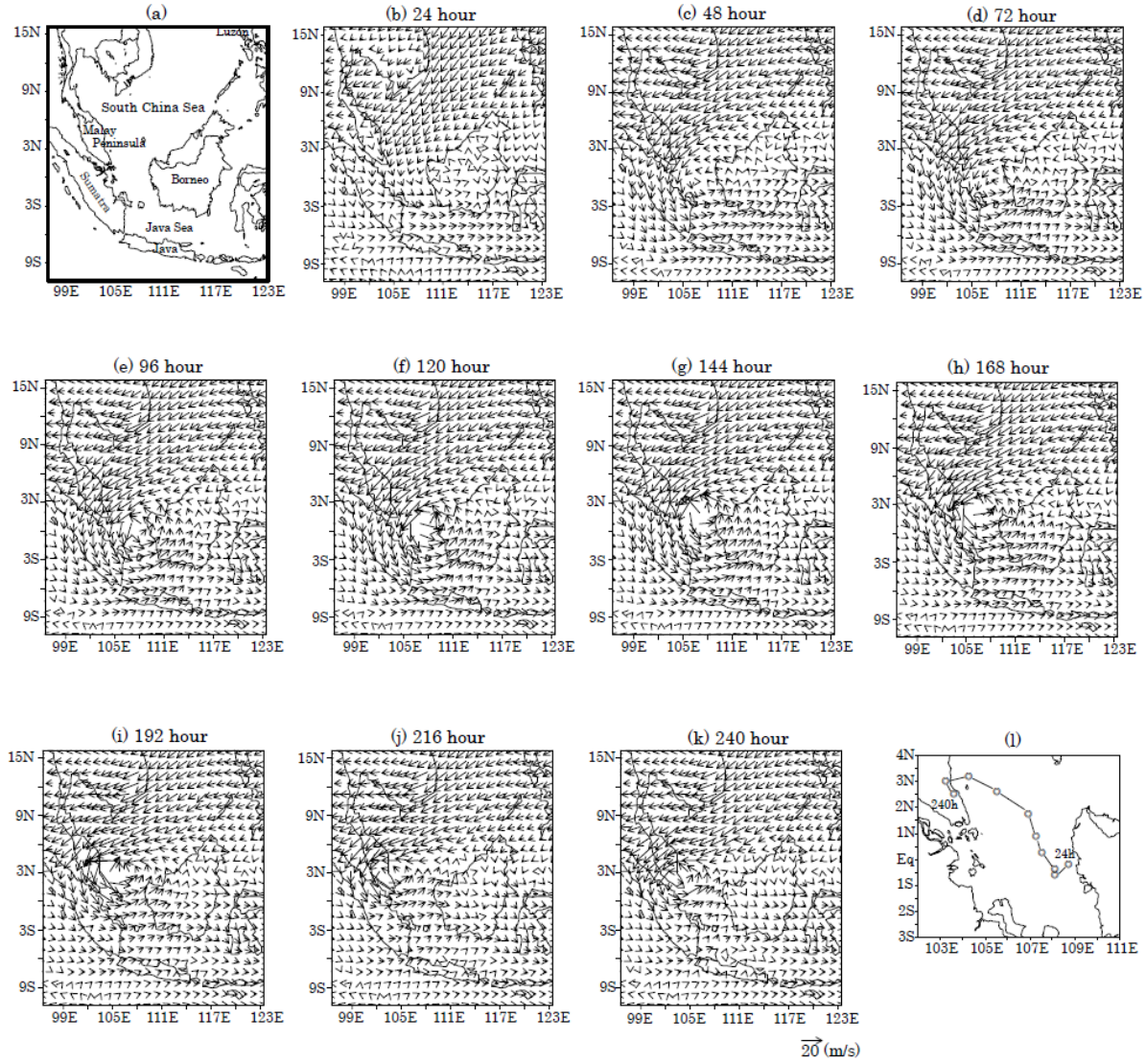

Figure 6.9: Semi-idealised experiment of the Borneo vortex: (a) map of the experiment domain, (b) - (k) 24-hourly evolution of the simulated Borneo vortex for a horizontal wind at 850 hPa from 24 to 240 hours after initialisation, (l) 24-hourly cyclone track; Figure adapted from Koseki et al. (2014).

Embedded into the circulation around Borneo are convective cells, which preferably form a regular diurnal cycle during the Asian winter monsoon (Houze et al., 1981).

Over land and along the coastline of Borneo it is mainly driven by the oscillation of the land-sea breeze (e.g. Mak and Walsh, 1976; Joseph et al., 2008). Approximately at midnight, the convection cycle is initiated when an offshore low-level wind begins. Convective cells are formed as long as the land breeze continues and converge to cloud clusters with large areas of precipitation. When the heating over Borneo has caused a sea breeze, the large cloud system shifts from the sea towards the land. Typically from midday on this convective system starts to dissipate again and has usually almost evaporated by late evening.

For the following discussion, the altitude of the top of the marine boundary layer (MBL) during the campaign is roughly estimated from the potential temperature, relative humidity, and wind speed data from the different ascents and descents of the Falcon aircraft (Steffen Fuhlbrügge, GEOMAR, Kiel, Germany, personal communication, October 2013). This estimation is based on Fuhlbrügge et al. (2013) using the approach of Seibert et al. (2000), determining the MBL height

from radiosoundings. The height of the MBL, i.e. the transition layer between the MBL and the FT, is marked by an increase in the potential temperature with altitude, whereas the relative humidity and the wind speed rather decrease with altitude. This estimation of the top of the MBL has already been used in Sala et al. (2014b) and is on average in agreement with the MBL height derived from the different radiosondes that were launched from the RV Sonne during the SHIVA campaign. In Table 6.2 the MBL height is estimated for each sortie. The average MBL height results in 450 m, which is a very low value. However, the assignment of one single boundary layer height to each flight might not be appropriate. Each vertical profile is recorded at a different time of the day and location, and the MBL height is expected to change along the flight track. Thus, the MBL height given here is only indicative.

7. Instrumental set-up

7.1 The mini-DOAS instrument

The mini-DOAS instrument deployed on the Falcon aircraft consists of a telescope unit, a housing with two Ocean Optics spectrometers (QE6500/ USB2000 for UV/ vis) and a PC as control unit. Furthermore, a commercial webcam is installed next to the mini-DOAS instrument. Figure 7.1 shows the position of the mini-DOAS instrument together with the webcam aboard the Falcon aircraft. Since the instrument was built in 2007 by Simmes (2007), it has already been used during other campaigns on different platforms, e.g. on balloon gondolas in 2009 and 2011 (Werner, 2009; Kreycy, 2012), on the Russian aircraft Geophysica in 2010 and on the Falcon aircraft in 2007 and 2008 (O'Brien, 2008; Prados-Roman et al., 2011). As the mini-DOAS instrument was already certified for flying aboard the Falcon aircraft in 2007, no instrumental changes were possible prior to the SHIVA campaign. Based on the experience gained during the SHIVA campaign, several restrictions can be identified that limit the analysis and interpretation of the data set presented in this study. A list of the different restrictions together with recommended instrumental changes for future applications can be found in Appendix E. While details on the construction and characterisation of the instrument can be found in Simmes (2007), this chapter provides a basic overview of the mini-DOAS instrument.

(a) (b)

Figure 7.1: (a) Image of the Falcon aircraft on the apron in front of the Hornbill Skyways hangar at the airport in Miri. The red circle marks the location of the mini-DOAS instrument and the webcam on the portside of the aircraft. (b) In the left aircraft window the telescope of the QE6500 (left slit) and the USB2000 (right slit) are integrated, whereas the webcam is mounted behind the second window.

The telescope unit

The telescope unit includes two telescopes with spherical quartz lenses (diameter $d = 12.7$ mm, focal length $f = 30$ mm) that are mounted on two stepper motors to perform scans from -35° to +10° elevation angle. The telescopes and stepper motors are mounted on an aluminum air-tight window, which is located on the portside of the aircraft. The viewing direction is oriented perpendicular to the heading of the aircraft. During the SHIVA campaign, both telescopes were fixed parallel to the ground. Hence, the roll angle of the aircraft (rotation of the aircraft along the heading axis)

corresponds to the elevation angle of the telescopes. An image of the interior view of the telescope unit and the mini-DOAS rack including the computer and a resin box with the spectrometer unit is shown in Figure 7.2.

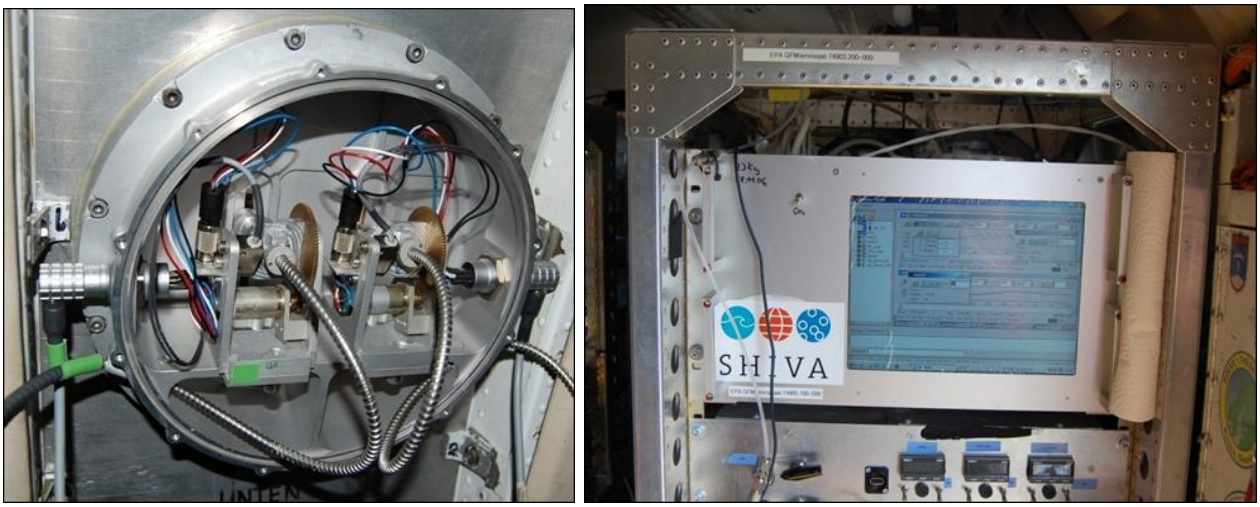

(a) (b)

Figure 7.2: Interior view of the telescope unit (a) and the mini-DOAS rack (b) including the computer and a resin box with the spectrometer unit.

The glass fibre bundles

Two quartz glass fibre bundles transmit the light from the two telescopes to the spectrographs. The individual fibres of the two fibre bundles are arranged linearly in a column at both ends. The UV fibre bundle consists of 8 individual fibres with a diameter of 200 µm for each individual fibre. An additional slit with a width of 150 µm is mounted on the spectrograph end of the UV fibre bundle to compensate for the large slit of the QE6500 (Section 7.1). The vis fibre bundle consists of 10 individual fibres with a diameter of 100 µm each. Both fibre bundles have a length of 2 m and a numerical aperture (NA) of 0.22. Figure 7.3 shows a microscopic image of the two fibre bundles. One single fibre of the UV fibre bundle is broken. A substitute fibre bundle had been ordered before the campaign. However, as it was not possible to fix the additional slit on the fibre ending without damaging the fibre bundle, the old fibre bundle had to be used. Since the blind single fibre is at the end of the column at the spectrograph end, the horizontal field of view is reduced (Section 7.2.1).

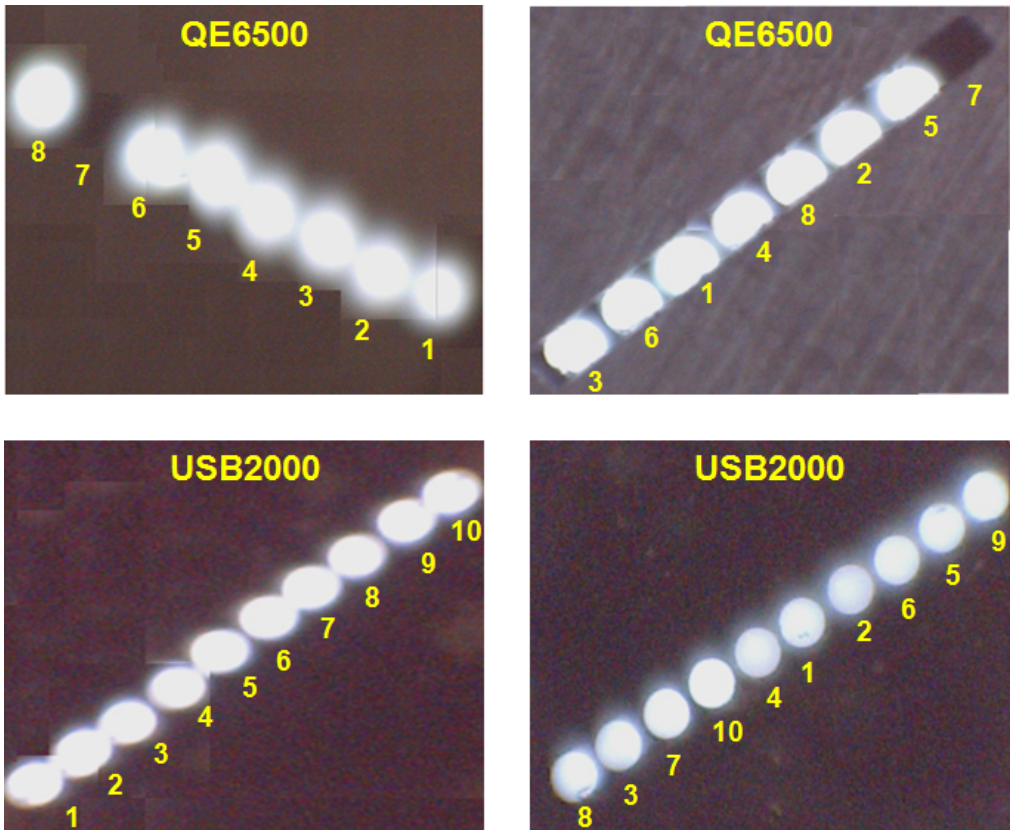

Figure 7.3: Picture of the fibre bundles at the telescope end (left panels) and the spectrograph end (right panels) of the QE6500 spectrograph and the USB2000 spectrograph taken with a microscopic camera.

The spectrographs

The two spectrographs are built by Ocean Optics with a QE6500 (henceforth referred to as 'QE') for the UV and a USB2000 (henceforth referred to as 'USB') for the visible wavelength range. The arrangement of the optical bench of the spectrometer is based on the cross Czerny-Turner principle and the incoming signal can be detected by a linear/array CCD detector, which digitizes it in a binary number that is stored on the computer memory (Figure 7.4). The QE is equipped with a Hamamatsu S7031 detector with 1024 pixels in dispersion direction, whereas the USB has a Sony ILX511 detector with 2048 pixels. The optical spectrometers cover a wavelength range of 320 - 400 nm and 409 - 530 nm, respectively with a mean full-width-at-half-maximum (FWHM) averaged over all emission lines of 0.49 nm (5.74 detector pixels) for the UV and 0.54 nm (7.00 detector pixels) for the visible instrument (Section 8.1). Figure 7.5 shows a picture of the entrance slit of both spectrographs. Originally, the slit of the QE had a size of 100 µm (Prados-Roman et al., 2011). However, after the instrument had been revised by the manufacturer Ocean Optics in 2008, a wrong slit with a width of 400 µm was integrated, which is too large for the UV fibre bundle. Instead, an additional slit with a width of 150 µm was then added to the UV fibre bundle. This slit can be identified in the microscopic picture of the QE spectrograph in Figure 7.3. As it can be seen from Figure 7.5, the surface of the slit of the QE is partly corroded and the uppermost right edge is missing. However, as the effective entrance slit of 150 µm is much smaller than the slit of the QE, this will not affect the light transmittance.

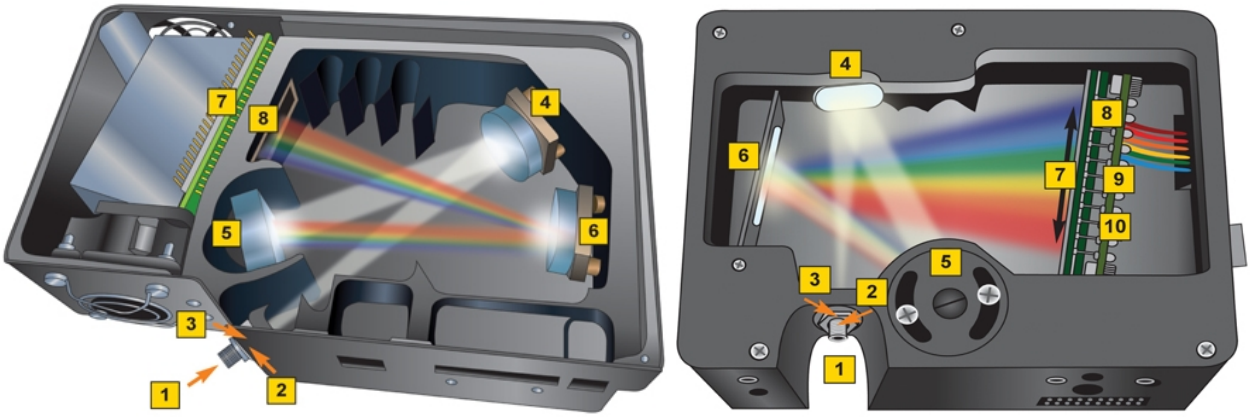

(a) (b)

Figure 7.4: Sketch of the (a) QE and (b) USB spectrograph from Ocean Optics. (1) SMA 905 connector, (2) entrance slit, (3) longpass absorbing filter (optional), (4) collimating mirror, (5) grating, (6) focussing mirror, (7) collection lenses, (8) detector, (9) longpass order-sorting filter (optional), (10) UV2 and UV4 detector upgrades (optional). Images adapted from Ocean Optics, 2013 (http://www.oceanoptics.com/).

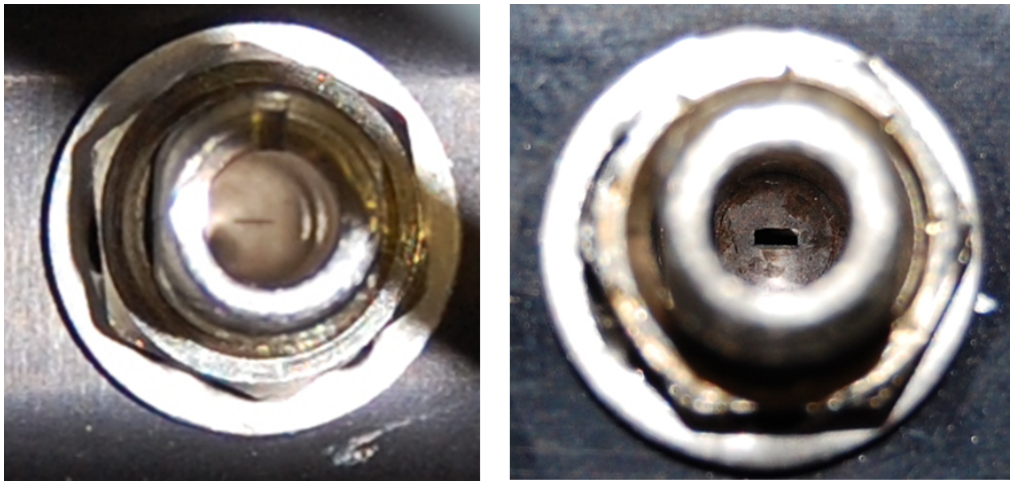

Figure 7.5: Picture of the entrance slits of the USB (50 µm x 1 mm) (left panel) and the QE (400 µm x 1 mm) (right panel) spectrographs.

Furthermore, after the QE had been revised by Ocean Optics in 2008, the shape of the spectra changed. Figure 7.6 shows spectra of scattered skylight recorded before and after the revision of the QE. Obviously, the intensity now strongly decreases starting at approximately 370 nm. Either the manufacturer built in an additional slit or the optical components within the Czerny-Turner set-up were changed. Unfortunately, the reason for this change remains unclear and the wavelength range above 370 nm is not implemented in the further spectral analysis.

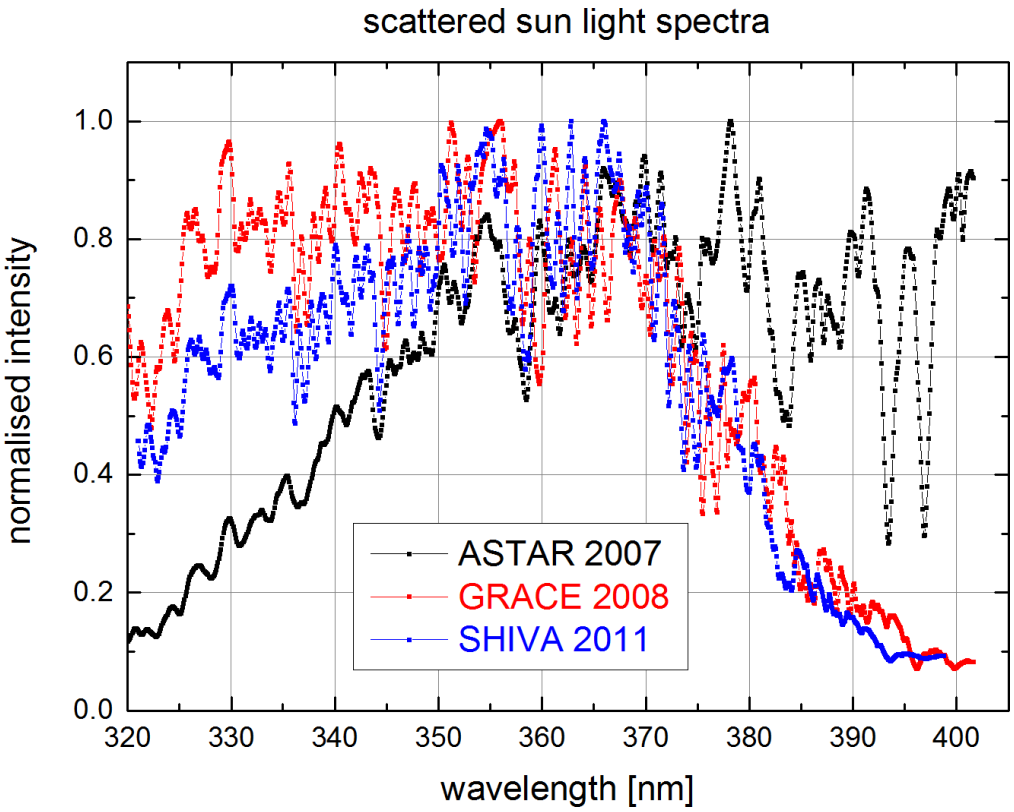

Figure 7.6: Spectra of scattered skylight recorded before the revision of the QE during the ASTAR campaign in 2007 (black) and after the revision during the GRACE campaign in 2008 (red) (Prados-Roman et al., 2011) as well as during the SHIVA campaign in 2011 (blue). the wavelength calibration is different for the three spectra.

The webcam

A commercial webcam is installed in the second window on the portside of the Falcon aircraft (Figure 7.1b) with a viewing direction minus 90° orthogonal to the heading direction of the aircraft. The distance between the first window where the telescopes of the mini-DOAS instrument are located and the second window with the webcam is 83 cm. The webcam (A4 Tech model: PK-810G, http://www.a4tech.com/) has an automatic focus range from 10 cm to infinity with an image sensor of 640x480 pixels with a horizontal FOV of $\alpha_{\text{horizontal}} = 39 \pm 1°$ and a vertical FOV of $\alpha_{\text{vertical}} = 29.5 \pm 1°$. The recording of images is restricted due to the processing power of the embedded PC. A webcam image is recorded every five seconds with a resolution of 320 x 240 pixel (16 - 19 November 2011) and 352 x 288 (21 November - 11 December 2011) stored in a colour JPEG format (24 bit). The webcam images can be used for post-flight cloud cover analyses.

The measurement routine

The measurements are performed using the software MS DOAS (developed by Udo Frieß, Institute of Environmental Physics, Heidelberg, personal communication). This software allows the simultaneous operation of several different instrument units. The individual units are controlled by scripted commands.

Aboard the Falcon aircraft no connection to the inertial navigation system (INS) is available that records the attitude of the aircraft, i.e. the standard aircraft parameters such as the roll or the pitch angle. Due to this missing delivery, a direct correction of the roll movement and thus an active pointing of the telescopes is not feasible. Hence, during the SHIVA campaign the limb measurements are performed with an elevation angle fixed horizontally relative to the aircraft

(parallel to the ground). Thereby, the elevation angle is represented by the roll angle of the aircraft. The maximum integration time for one spectrum is set to 5 seconds, both for the QE and USB spectrograph. The saturation is set to 75%. The recorded spectra are displayed graphically (Figure 7.2b) and stored to the embedded PC. Before or after each sortie of the Falcon aircraft offset, dark current and mercury-cadmium (Hg-Cd) spectra are recorded manually. Between the telescope unit and the Hg-Cd lamp a diffuser plate is inserted to guarantee a homogeneously illuminated entrance slit. A temperature sensor is mounted on the detector of the QE. The detector temperature of the QE is stored for each spectrum in a text file by MS DOAS (Section 7.2.4).

7.2 Instrumental characterisation

7.2.1 Determination of the field of view

The theoretical field of view (FOV) can be calculated according to the following equation:

$$\alpha_{\mathrm{FOV}} = 2 \cdot \arctan\left(\frac{d}{2f}\right), \tag{7.1}$$

with d being the diameter of the fibre entrance and with the focal length of f = 30 mm, i.e. the distance between lens and fibre ending. For the QE spectrograph with 8 single fibres each having a diameter of 200 µm and a cladding of 10 µm d is given by: $d_{\mathrm{horizontal}} = 8 \cdot$ 200 µm + 6 ·10 µm = 1.66 mm and $d_{\mathrm{vertical}} = 0.2$ mm. However, in an earlier configuration the slit of the UV fibre bundle was changed to a slit of a width of 150 µm (Prados-Roman et al., 2011). Thus, d_{vertical} reduces to 0.15 mm. The FOV results in: $\alpha_{\mathrm{horizontal}} = 3.17°$ and $\alpha_{\mathrm{vertical}} = 0.29°$. Since the last single fibre of the fibre bundle is blind (Figure 7.3), the horizontal FOV reduces to $\alpha_{\mathrm{horizontal}} = 2.79°$. For the USB spectrograph with 10 single fibres each having a diameter of 100 µm and a cladding of 10 µm d is given by: $d_{\mathrm{horizontal}} = 10 \cdot 100$ µm + 8 ·10 µm = 1.08 mm and $d_{\mathrm{vertical}} = 0.1$ mm. The FOV results in: $\alpha_{\mathrm{horizontal}} = 2.06°$ and $\alpha_{\mathrm{vertical}} = 0.19°$.

The FOV of the mini-DOAS instrument is measured by scanning over a halogen lamp, which is installed in a distance of 3 m to the telescope at the telescope entrance height. The halogen lamp is integrated into an aluminium housing with a slit in front of the lamp. The instrument scans over the halogen lamp in steps of 0.04° and determines the average intensity at constant integration time and scan number. A Gauss function is fitted to the resulting curve and the received line width corresponds to the FOV. Figure 7.7 shows the measured average intensities for the QE and USB spectrograph, respectively. The measured vertical FOV for the QE yields 0.27° and for the USB 0.23°. The theoretical vertical FOV of 0.29° and 0.19° for the QE and USB, respectively are in good agreement with the measurements (Table 7.1). This confirms that the fibre entrance is located in the focal point of the entrance lens. Additionally, this measurement set-up is used to determine the zero position of the stepper motor. The centre position of the Gauss fits corrected with the roll angle of the Falcon aircraft while standing in the hangar (≈ 0.5°) yields the offset. This offset is entered into the settings of the measurement routine.

Table 7.1: Summary of the theoretical and measured FOV of the mini-DOAS instrument in vertical and horizontal direction.

	QE (UV channel)			USB (vis channel)	
	vertical	horizontal		vertical	horizontal
$\mathrm{FOV_{theo}}$	0.29	2.79	$\mathrm{FOV_{theo}}$	0.19	2.06
$\mathrm{FOV_{meas}}$	0.27	-	$\mathrm{FOV_{meas}}$	0.23	-

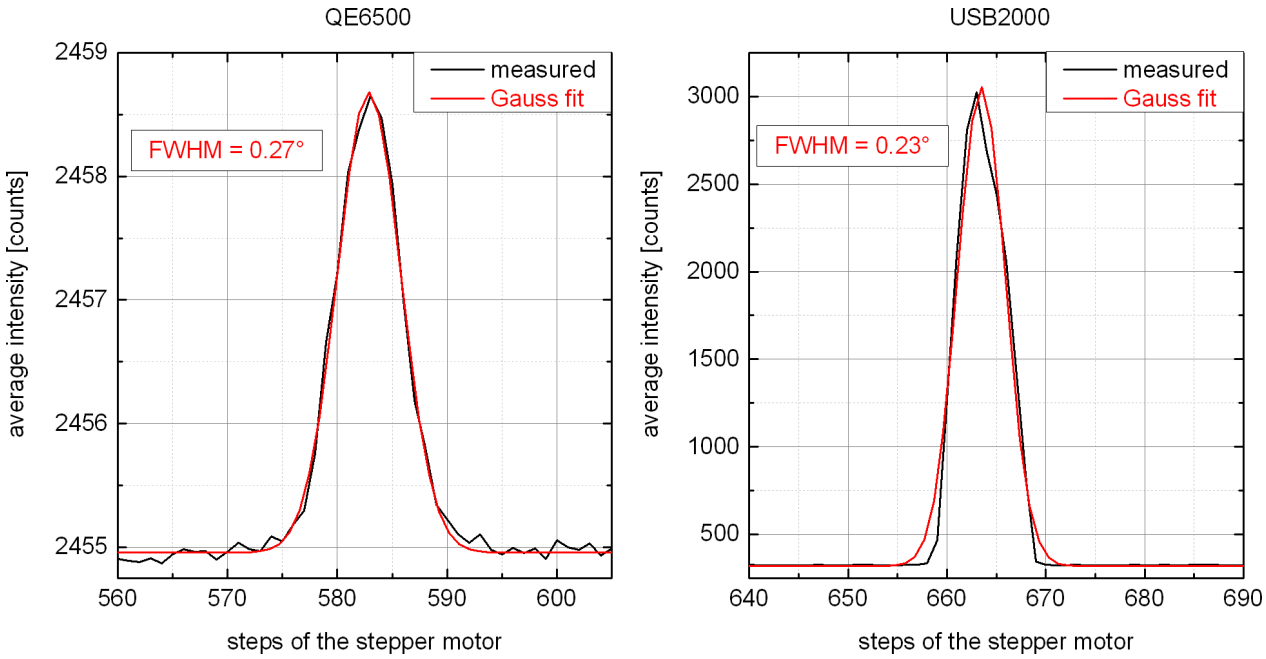

Figure 7.7: Determination of the FOV. The red line indicates a Gauss function fitted to the measured average intensities (black line). The FWHM represents the FOV.

7.2.2 Linearity

Ideally, the signal received from a detector pixel should be linear to the amount of incoming photons over the whole intensity range. However, in reality, the sensitivity to incident photons usually decreases when approaching the maximum saturation of a pixel. This non-linearity in the recorded intensities can result in residual structures in the DOAS spectral retrieval. The linearity of the detector of the QE and the USB is tested by recording spectra of a temperature-stabilised LED with a peak wavelength at approximately 365 nm (LZ1-00UV00 UV LED Gen 2 Emitter, LED Engin) and 446 nm (Cree XP-E LED Royal Blue), respectively (Figure 7.8). The LED is stabilised at $T_{LED} = 20°C$.

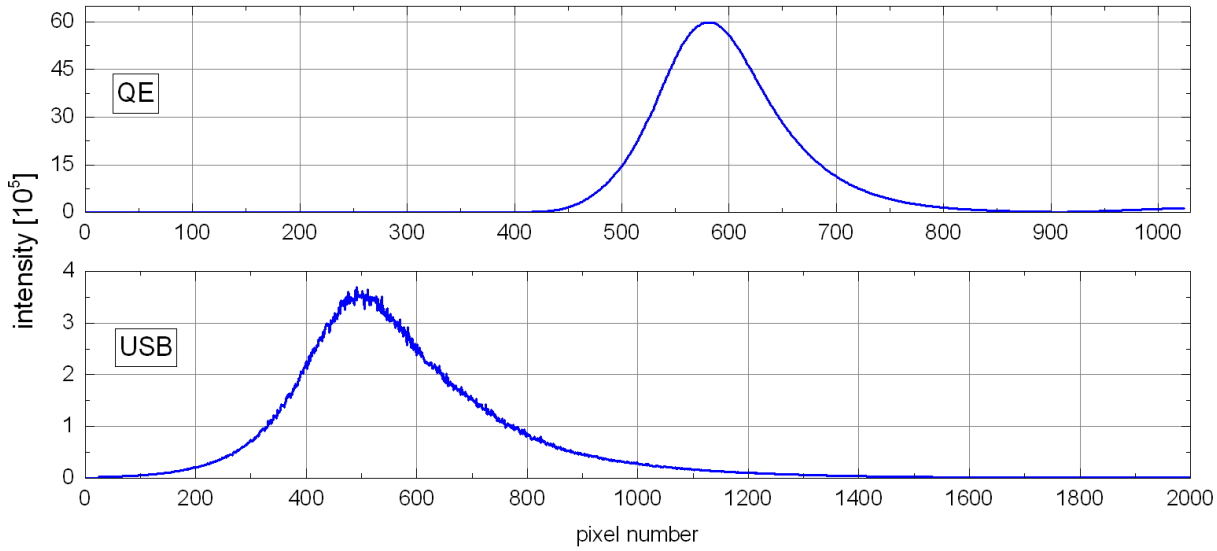

Figure 7.8: Spectrum of the temperature-stabilised LED at 365 nm recorded with the QE (upper panel) and at 435 nm recorded with the USB (lower panel).

A quartz glass diffuser is inserted between the mounting of the fibre bundle and the LED, in order to ensure a homogeneous illumination. Furthermore, a grey filter is added to avoid saturation at the minimal exposure time (QE: $t_{exposure_{min}} = 8$ ms; USB: $t_{exposure_{min}} = 3$ ms). Spectra of the LED are recorded with slowly increasing exposure time starting from the minimal exposure time up to an exposure time where saturation starts. The measurement routine is provided by Martin Horbanski (IUP Heidelberg, personal communication, March 2014). The analogue-to-digital converter (ADC) of the QE has a 16-bit resolution yielding $2^{16} = 65536$ counts at saturation, whereas the ADC of the USB has a 12-bit resolution yielding to maximum of $2^{12} = 4096$ counts. Figure 7.9 (upper panel) shows the normalised signal in counts per ms of each pixel plotted versus the corresponding intensity for the QE and USB, respectively. The linearity curves of both the QE and the USB can be described by a 6^{th}-order polynomial. The QE shows a non-linearity of approximately 2 % for less than 20000 detector counts (saturation level < 30 %) and is highly non-linear close to the maximum saturation. Between 20000 and 60000 counts the response of the detector to incident photons shows an almost linear behaviour. After the correction with a 6^{th}-order polynomial, the remaining non-linearity is less than $4 \cdot 10^{-3}$. The non-linearity of the USB is stronger with approximately 10 % for less than 1500 detector counts (saturation level < 37 %). After the correction with a 6^{th}-order polynomial, the remaining non-linearity is less than 10^{-2}. As the maximum intensity of the measured spectra during the SHIVA campaign ranges between 20000 and 60000 counts for the QE and between 2000 and 3500 counts for the USB, the areas of non-linearity are only reached in exceptional cases. Hence, for the further data processing, the measured spectra are not corrected with the non-linearity polynomial.

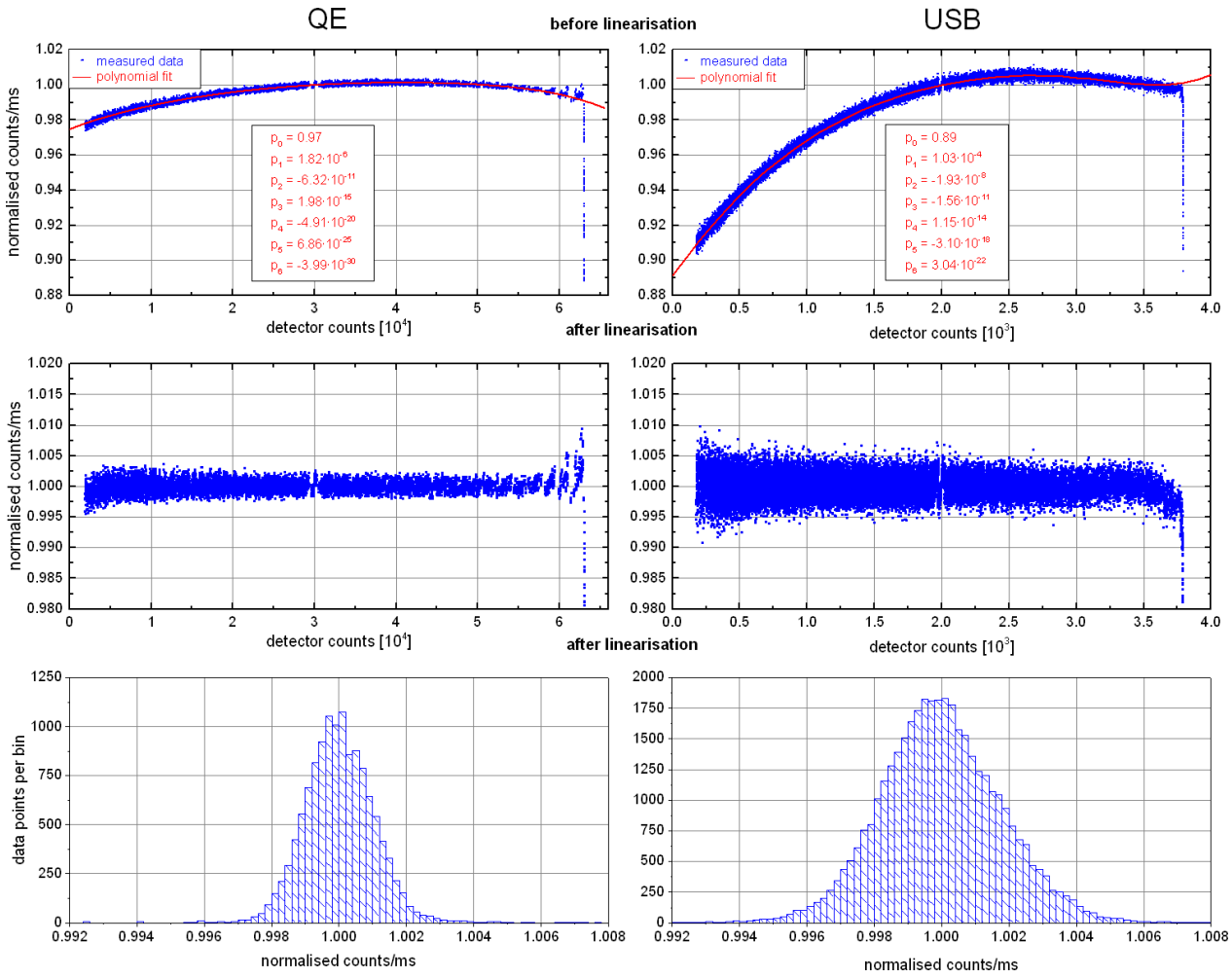

Figure 7.9: Determination of the linearity of the QE (left panels) and the USB (right panels). Upper panels: Measured counts per millisecond normalised to a reference value at an intensity level of 30000 counts for the QE and 2000 counts for the USB; middle panels: Linearity of the analysed pixels after the correction by a 6^{th}-order polynomial; lower panels: Histogram of the corrected measurements.

7.2.3 Spectrometer stray light

Spectrometer stray light is light detected at a certain wavelength range of the measured spectrum, although it is not directly projected onto the detector. It can originate e.g. from grating diffraction maxima of higher orders or from reflections due to imperfect matching of the optical components within the Czerny-Turner set-up of the spectrograph. The intensity I_{meas} measured at the detector can be expressed as the sum of the signal I and the stray light I_S:

$$I_{\text{meas}}(\lambda) = I(\lambda) + I_S(\lambda). \tag{7.2}$$

In order to assess the impact of stray light on the optical density, Equation 7.2 is inserted into Equation 4.8:

$$-\tau(\lambda) = \ln\left(\frac{I_{\text{meas}}(\lambda)}{I_0'(\lambda)}\right) = \ln\left(\frac{I(\lambda) + I_S(\lambda)}{I_0'(\lambda) + I_S(\lambda)}\right). \tag{7.3}$$

According to Platt and Stutz (2008), it can be assumed that the stray light contribution is small as compared to $I(\lambda)$ and $I_0'(\lambda)$ and that $\ln(1+x) \approx x$, i.e. the Taylor expansion is stopped after the

term of first order. Equation 7.3 can thus be rewritten in the following way:

$$
\begin{aligned}
-\tau(\lambda) &= \ln\left(\frac{I(\lambda)}{I_0'(\lambda)}\right) + \ln\left(1+\frac{I_S(\lambda)}{I(\lambda)}\right) - \ln\left(1+\frac{I_S(\lambda)}{I_0'(\lambda)}\right) && (7.4)\\
&\approx \ln\left(\frac{I(\lambda)}{I_0'(\lambda)}\right) + \frac{I_S(\lambda)}{I(\lambda)} - \frac{I_S(\lambda)}{I_0'(\lambda)} && (7.5)\\
&= \ln\left(\frac{I(\lambda)}{I_0'(\lambda)}\right) + \frac{I_S(\lambda)}{I_0'(\lambda)} \cdot \left(\frac{I_0'(\lambda)}{I(\lambda)} - 1\right) && (7.6)\\
&\approx \ln\left(\frac{I(\lambda)}{I_0'(\lambda)}\right) + \frac{I_S(\lambda)}{I_0'(\lambda)} \cdot \ln\left(\frac{I_0'(\lambda)}{I(\lambda)}\right) && (7.7)\\
&= \ln\left(\frac{I(\lambda)}{I_0'(\lambda)}\right) \cdot \left(1 - \frac{I_S(\lambda)}{I_0'(\lambda)}\right). && (7.8)
\end{aligned}
$$

Hence, stray light reduces the optical density of Fraunhofer lines by the ratio $\frac{I_S(\lambda)}{I_0'(\lambda)}$ (Platt and Stutz, 2008). As a first stray light test the Fraunhofer lines of measured scattered skylight spectra in the UV and visible wavelength are compared to a high-resolution solar reference spectrum that is convolved to the resolution of the instrument.

In order to quantify the spectrometer stray light, spectra of a halogen lamp and of scattered sunlight are recorded with and without different optical filters. Figure 7.10 shows the internal transmittance of the different filters that are used for these measurements. In the following, for the QE, a GG420 filter is used, which cuts off light between 200 and 400 nm and has a throughput close to 1 at wavelengths above approximately 500 nm. For the USB a UG11 filter is used, which prevents light between 400 and 650 nm from reaching the detector.

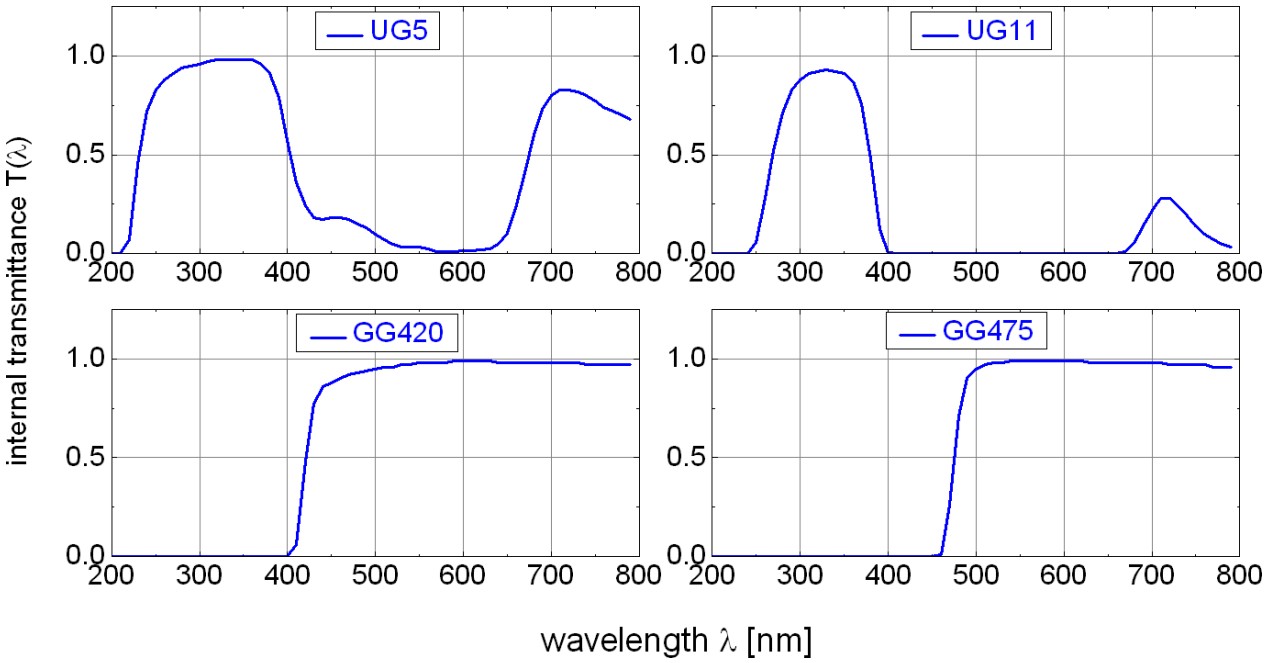

Figure 7.10: Internal transmittance of the SCHOTT filters used for the stray light measurements, adapted from `http://www.schott.com/advanced_optics/german/download/index.html`).

After offset and dark current, the ratio of stray light and light can be calculated according to the following equation:

$$
S = \frac{\text{straylight}}{\text{light}} = \frac{I_S}{I_{\text{meas}} - I_S} = \frac{I_{\text{filter}}}{I_{\text{nofilter}} - I_{\text{filter}}}. \qquad (7.9)
$$

Figure 7.11a shows the results of the stray light measurements using a halogen lamp, whereas Figure 7.11b presents the results using scattered skylight as a light source. The halogen lamp spectra of the QE show a large fraction of stray light, which increases towards higher wavelengths where the overall intensity of the QE is reduced due to an unknown reason (Section 7.1). Although the GG420 filter completely blocks the light in the wavelength range of the QE, a stray light socket of approximately 40 to 80 % is left. As the halogen lamp has its maximum intensity in the near-infrared region, the stray light test is also performed with solar scattered light where the contribution of stray light from the near-infrared region is smaller due to the solar spectrum with T = 5800 K. Except for the wavelength range between 380 and 400 nm, the solar stray light reaching the QE results in values between 5 and 10 %. This number is quite large in comparison to the specifications of the manufacturer (0.4 % at 435 nm (`http://www.oceanoptics.com/technical/QE65000.pdf`)), but comparable to other spectrometers as e.g. the OMT spectrometers (Hüneke, 2011).

In comparison to the QE, the USB shows very little stray light, both for the halogen lamp spectra (Figure 7.11a) and the scattered skylight spectra (Figure 7.11b). The mean value for S amounts to less than 0.1 %, which is in line with the specifications of the manufacturer ($<$ 0.1 % at 435 nm (`http://www.oceanoptics.com/technical/engineering/USB2000%20OEM%20Data%20Sheet.pdf`)). Obviously, the USB already has a built-in stray light trap.

A possible reason for the large stray light amount of the QE might be the wrong f-number. If the f-number of the fibre bundle or lens exceeds the f-number of the spectrograph, the incoming light overfills the collimating mirror, which can then lead to reflections at the interior walls of the spectrograph. Both fibre bundles have a numerical aperture of NA = 0.22, respectively. This results in an f-number of:

$$f/\# = \frac{1}{2 \cdot NA} \approx f/2.27. \tag{7.10}$$

The telescopes of the mini-DOAS instrument further include quartz lenses with a focal length f of 30 mm and a diameter d of 12.7 mm, respectively. This leads to an f-number of:

$$f/\# = \frac{f}{d} \approx f/2.36. \tag{7.11}$$

The f-number of the lens should match to the f-number of the spectrographs, which corresponds to f/4, both for the QE and USB. The f-number of the spectrographs is approximately 40 % larger than the f-number of the lens. Hence, the detector is overexposed leading to additional stray light. Unfortunately, this feature was not considered in the original set-up by Simmes (2007). For further deployments, it is recommended to include a special cover plate in front of the quartz lens to avoid overexposure. Furthermore, an optical bandpass filter should be implemented, e.g. the U-340 filter (`http://www.hoyaoptics.com/pdf/U340.pdf`), which completely removes light coming from the infrared wavelength region.

Stray light can be accounted for in the DOAS fitting procedure by including an additional stray light polynomial (Section 8.3.1). Hence, it is assumed, that the effect of stray light is corrected during the DOAS fitting procedure and the accuracy of the results of the DOAS evaluation are not strongly affected by the stray light.

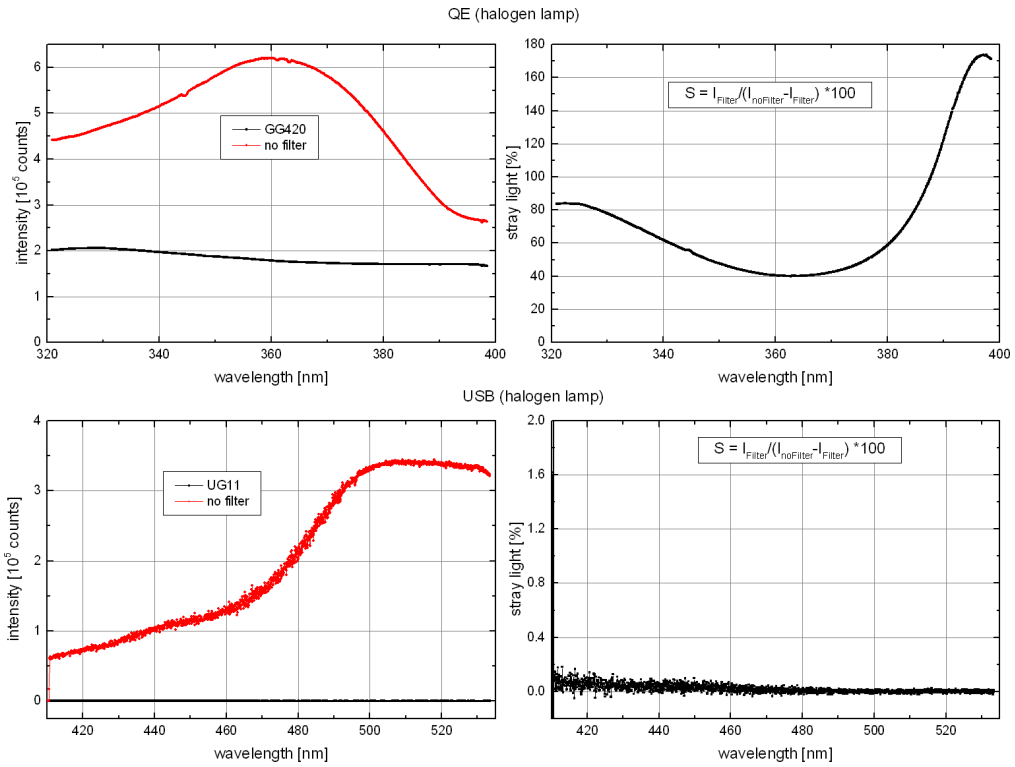

(a)

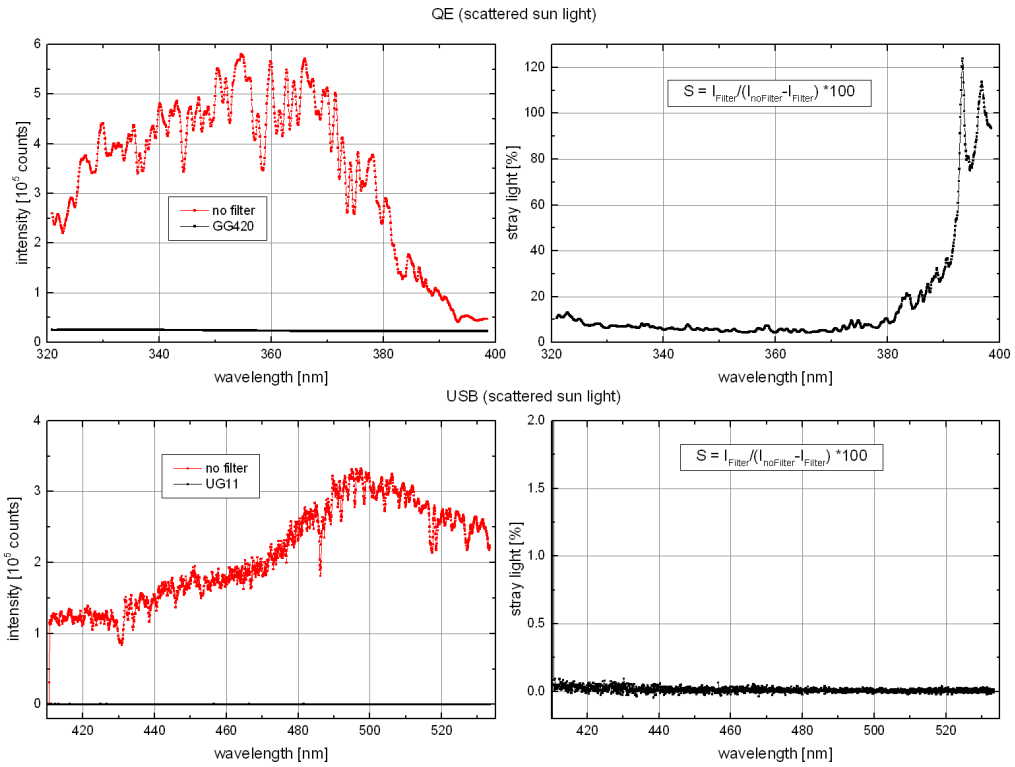

(b)

Figure 7.11: Stray light measurements using (a) a halogen lamp and (b) scattered skylight for the QE (upper panels) and the USB (lower panels), respectively. The left panels show the intensities without filter (I_{nofilter}, red line) and including a filter (I_{filter}, black line). The right panels show the ratio S according to Equation 7.3.

7.2.4 Stability of the set-up

Reliable and precise DOAS measurements require a stable optical imaging of the instrument. For airborne measurements, this requirement is a rather challenging task, since the variation of atmospheric parameters such as pressure and temperature can cover a large range. Possible changes of the wavelength alignment can be compensated in the spectral analysis by allowing a wavelength shift, whereas the quality of the spectral retrieval is very sensitive to any changes of the instrumental resolution. In order to guarantee a stable optical imaging, the housing of the spectrometers is evacuated and temperature stabilised with an ice-water bath. Before every sortie of the Falcon aircraft the housing of the spectrometer unit is evacuated. At least 12 hours before take-off a turbomolecular pump is connected to the housing until the pressure reaches 10^{-5} to 10^{-6} mbar. The temperature of the spectrographs is stabilised with an ice-water mix that is filled into a container that surrounds the housing of the spectrometer unit. At least one hour before roll-out the container is filled with as much as ice and water as possible to ensure a good thermal contact to the housings of the spectrometer unit during the whole sortie. Directly before take-off, the ice-water mix is again filled up with new ice.

Shape and position of the emission lines

In order to examine possible changes of the emission lines during the campaign the shape and position of the emission lines is investigated. Figure 7.12 shows the shape and position of four mercury and cadmium emission lines for the different spectra recorded before or after every sortie of the Falcon aircraft. In the UV, the shape of the mercury emission lines does not change significantly. However, in the visible wavelength range the shape and position does change slightly. In order to further analyse the different emission lines, a Gauss function is fitted to every emission line and the respective centre wavelength and FWHM is displayed in Figure 7.13 and 7.14. Except for the peaks at 346 nm, 361 nm and 365 nm, which are double lines (Table 8.1), the centre wavelength in the UV only changes slightly with a maximum difference of 0.02 nm. The FWHM varies between 0.43 and 0.45 nm for the single emission lines at 326 nm, 334 nm and 340 nm and is larger for the double emission lines (between 0.45 and 0.52 nm). In the visible wavelength, the centre wavelength of the different emission lines varies more than in the UV. The difference between the centre positions yields values between 0.03 and 0.07 nm. Furthermore, the FWHM of every peak is changing between 0.05 nm and 0.1 nm during the campaign. The position of the peak changes due to the temperature shift of the detector temperature. Later in the analysis (Section 8.1) the more precise Fraunhofer calibration is able to partly compensate for this spectral shift.

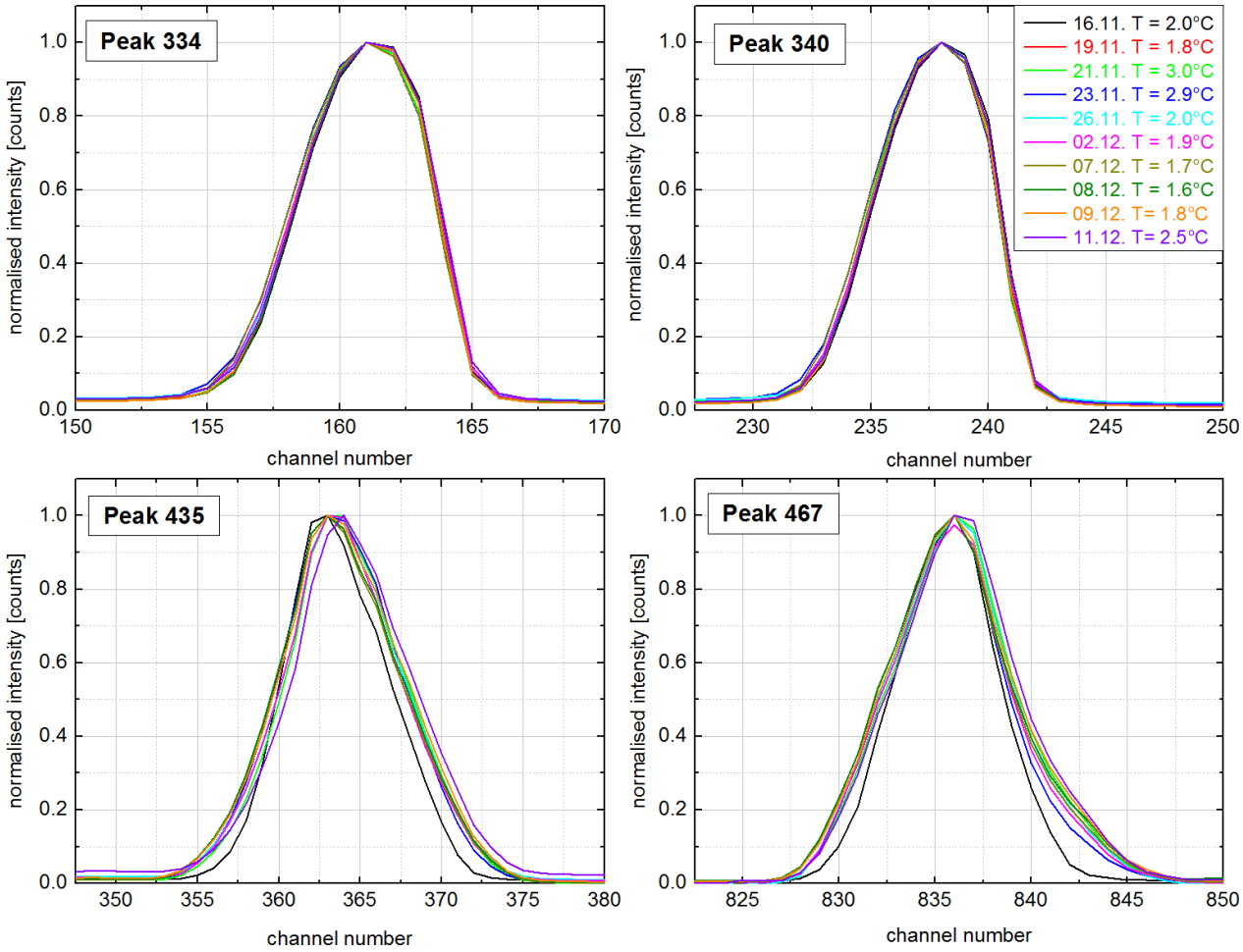

Figure 7.12: Comparison of the shape and position of two mercury and cadmium lines in the UV (upper panels) and two lines in the visible wavelength range (lower panels) colour-coded with the recording date and temperature.

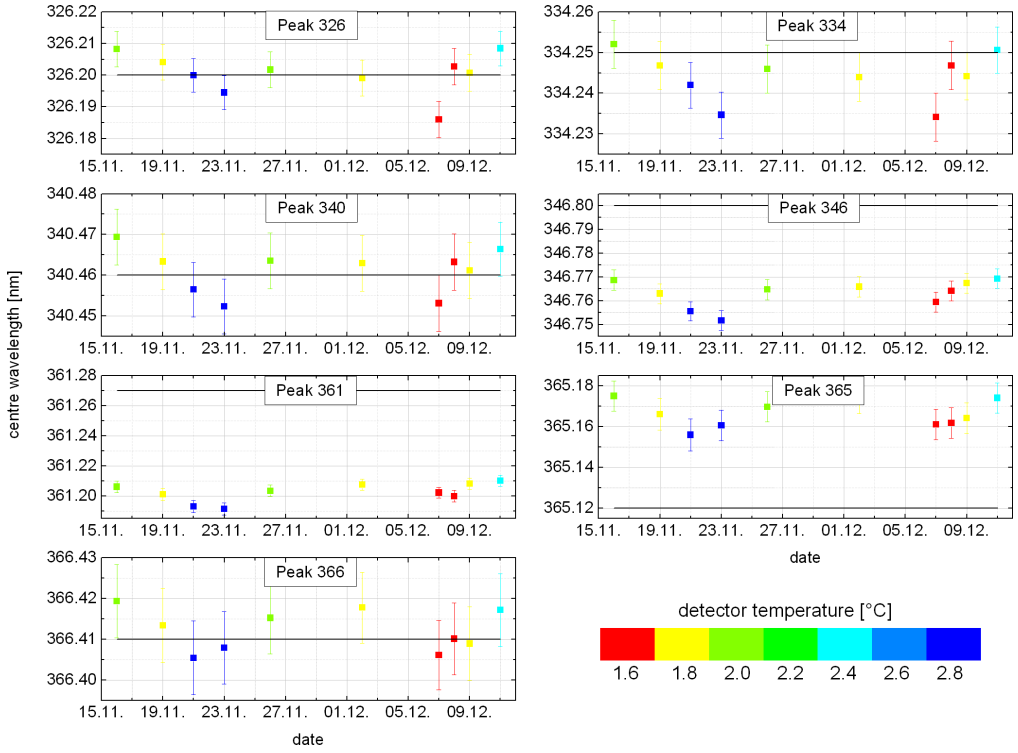

(a)

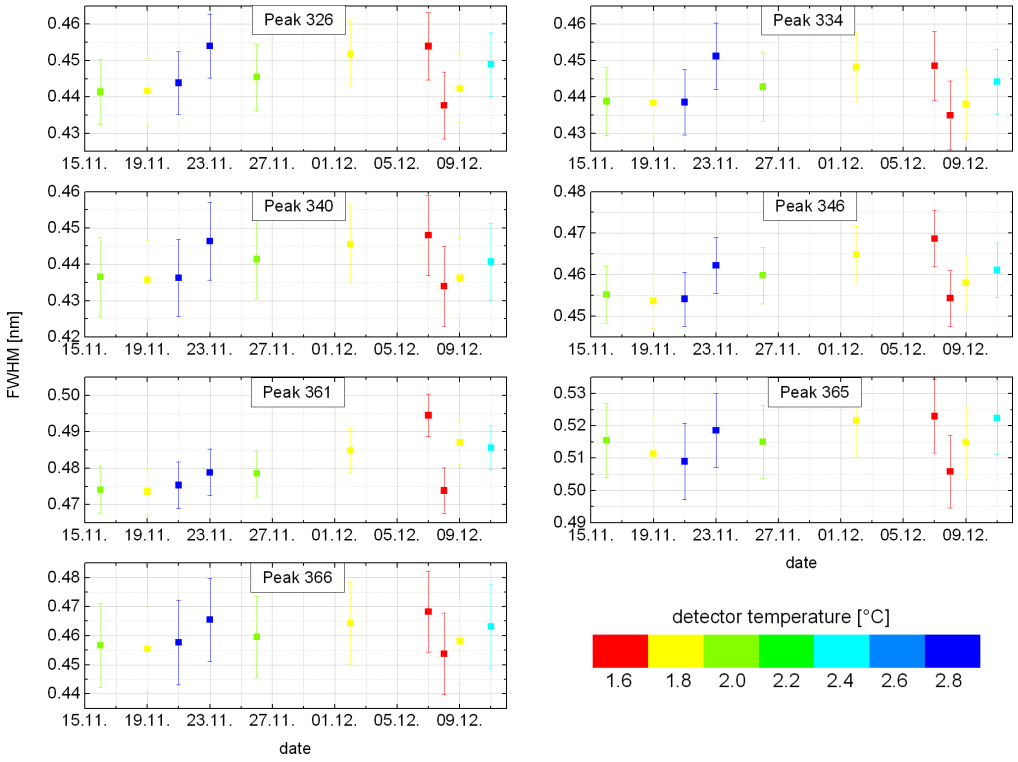

(b)

Figure 7.13: (a) Centre wavelength and (b) FWHM of the different emission lines in the UV during the campaign colour-coded with the detector temperature. The black line marks the literature position of the emission lines (Table 8.1).

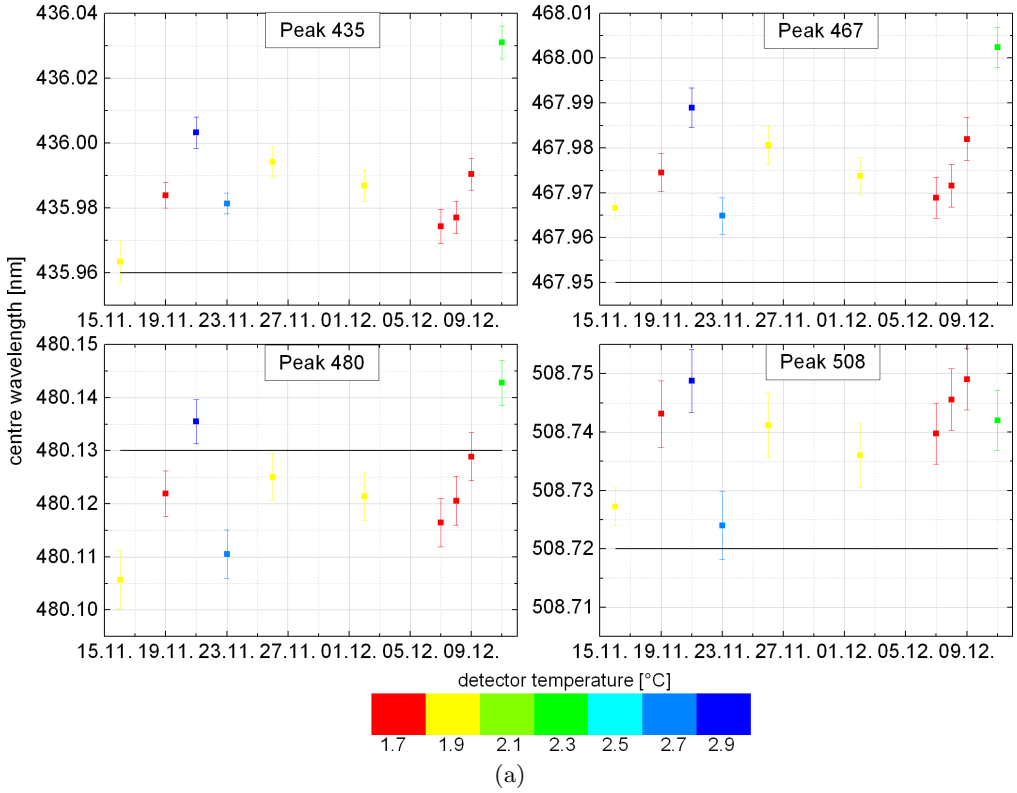

(a)

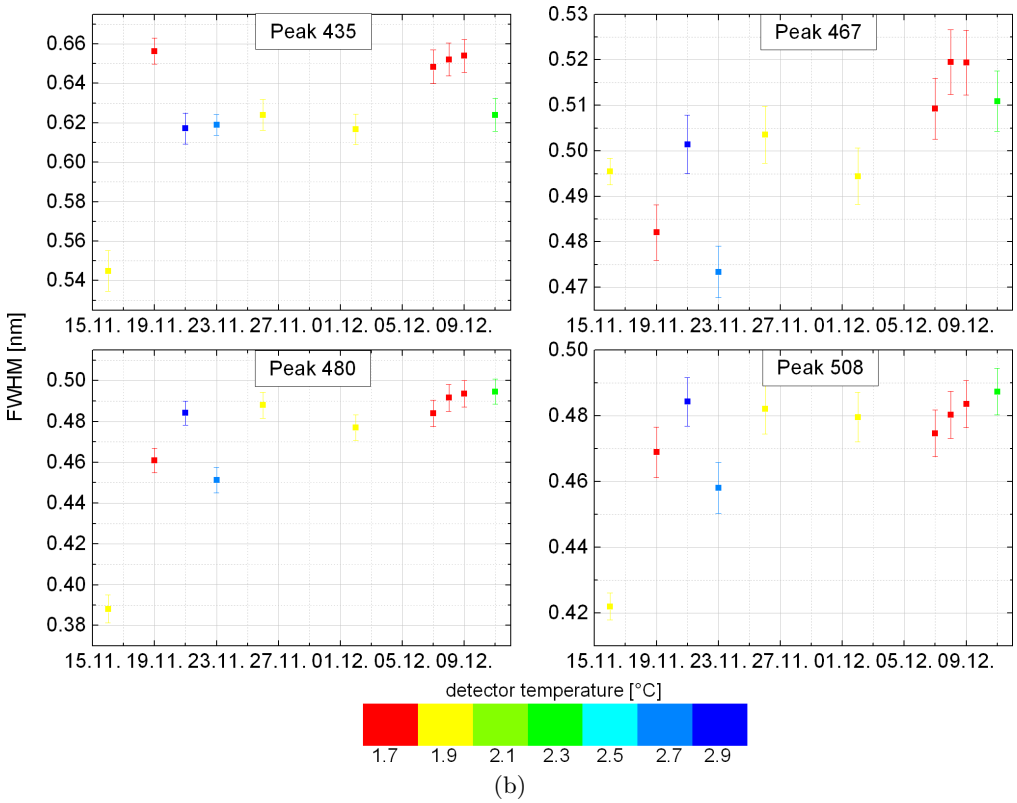

(b)

Figure 7.14: (a) Centre wavelength and (b) FWHM of the different emission lines in the visible wavelength range during the campaign colour-coded with the detector temperature. The black line marks the literature position of the emission lines (Table 8.1).

Temperature of the spectrographs

Figure 7.15 shows the detector temperature of the QE during all sorties of the Falcon aircraft. The starting temperature varies slightly and lies approximately between 1.5°C and 2°C. During the flights the detector temperature slowly increases as the ice is melting. The maximum temperature difference during one sortie is Δ T $\approx$ 1°C on 16 November and 21 November 2011. During the other sorties Δ T is smaller than 1°C and amounts to 0.3 - 0.5°C. This temperature increase can be compensated by a wavelength shift in the spectral retrieval. Typical values for a wavelength shift of the analysis in the UV are of the order of 10^{-4} nm.

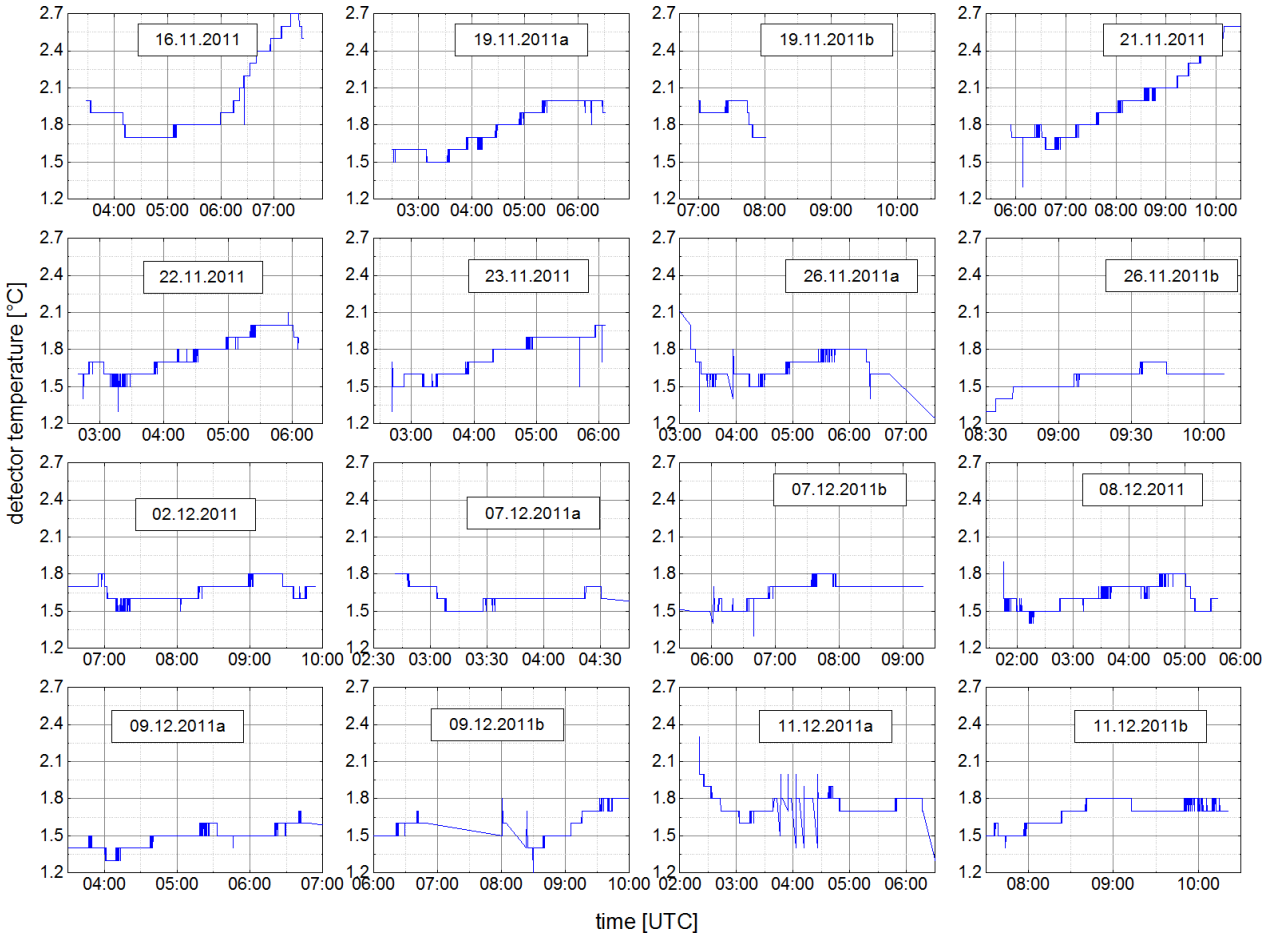

Figure 7.15: Temperature of the detector of the QE for all sorties of the Falcon aircraft during the SHIVA aircraft campaign. On 19.11.2011b the recording of the temperature stopped at 08:00 UTC due to a software failure. Hence, the data for this flight intersect is missing.

8. DOAS data analysis

8.1 Analysis settings

The limb scattered skylight spectra measured by the mini-DOAS instrument are analysed for the absorption of NO_2, HCHO, CHOCHO, IO and O_4 using the software *WinDOAS* provided by the IASB/BIRA (Belgian Institute for Space Aeronomy) (Van Roozendael and Fayt, 2001). The *WinDOAS* code is also used for the convolution of all absorption cross-sections reported in the literature (Section 8.1), whereas the Ring spectrum is calculated using the software *DOASIS* (Kraus, 2006b) (Section 8.1). The Ring spectra are calculated from the measured Fraunhofer reference spectra. The *WinDOAS* software only provides a Ring calculation tool where the Ring spectrum is derived from a highly resolved solar spectrum and not from a measured reference spectrum. Thus, the Ring spectrum is calculated in *DOASIS* and not in *WinDOAS*. The general retrieval procedure includes several steps.

Electronic offset and dark current

First, each recorded spectrum is corrected for offset and dark current according to Equations 4.21 and 4.22. For each sortie of the Falcon aircraft offset and dark current spectra were recorded directly before roll-out or after landing. An example of an offset and dark current spectrum recorded during the SHIVA campaign is shown in Figure 8.1 for the QE and the USB, respectively.

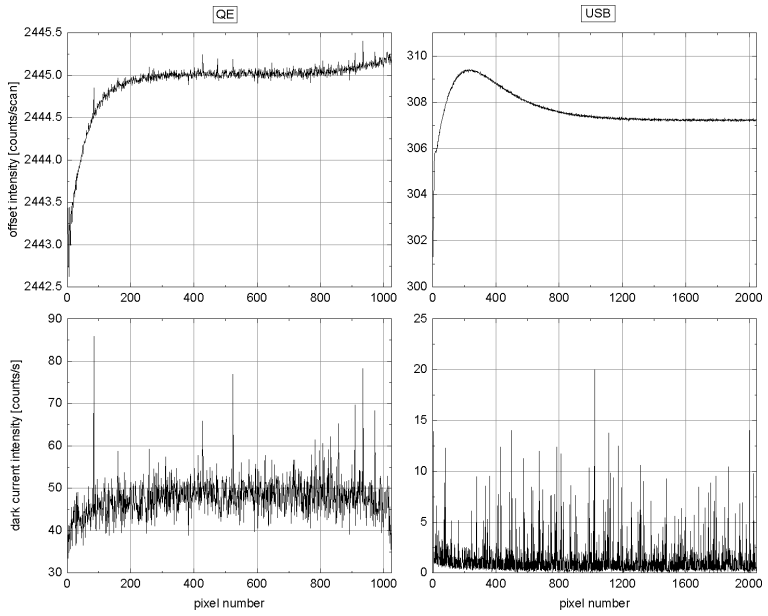

Figure 8.1: Offset (upper panels) and offset-corrected dark current spectra (lower panels) for the QE (left panels) and USB (right panels) spectrograph, respectively, recorded during the SHIVA campaign on 16 November 2011 at a detector temperature of 1.9°C.

The offset spectra were recorded by measuring 10000 scans at a minimal integration time of 8 ms for the QE and 3 ms for the USB, whereas the dark current spectra were recorded for one scan using an integration time of 60000 ms. The offset and dark current spectra should be recorded at the same temperature as the measurement spectra during the respective sortie of the Falcon aircraft. However, offset and dark current measurements are only possible before and after each sortie and not during the flight. Since the temperature changed during the flight (Section 7.2.4), the offset and dark current might have changed, leading to possible residual structures.

Wavelength calibration

In a next step the spectra need to be wavelength-calibrated. In order to roughly calibrate the two spectrometers, a mercury and cadmium spectrum with known spectral emission lines is used. The actual line width of a single atomic mercury emission line is approximately 2 pm (e.g. Sansonetti et al., 1996; Wilbur Kaye, 1997), which is significantly smaller than the resolution of the instrument. A Gauss function is fitted to the emission lines to define the centre channel and width and the line positions are assigned to the known centre wavelengths of the mercury and cadmium emission lines (Table 8.1). Some double emission lines cannot be spectrally resolved by the mini-DOAS instrument. For these emission lines the average peak wavelength is calculated. Other double emission lines are dominated by the stronger one of them. Hence, only the wavelength of the strong emission line is indicated.

Table 8.1: Line type, pixel number, vacuum wavelength, and FWHM of the mercury and cadmium emission lines. The different line positions can be found in Sansonetti et al. (1996), Pen-Ray catalogue (Wilbur Kaye, 1997), Platt and Stutz (2008) and on the webpage of the National Institute of Standards and Technology (NIST) (http://physics.nist.gov/PhysRefData/Handbook/Tables/mercurytable2.htm). The line positions can differ by some picometres.

		UV					vis		
element	line type	channel [pixel]	λ [nm]	FWHM [pixel]	element	line type	channel [pixel]	λ [nm]	FWHM [pixel]
cadmium	single	62.47	326.20	5.24	mercury	double	362.45	435.96[b]	7.47
mercury	single	160.08	334.25	5.28	cadmium	single	834.68	467.95	6.21
cadmium	single	236.81	340.46	5.35	cadmium	single	1029.70	480.13	6.31
cadmium	double	315.67	346.80[a]	5.69	cadmium	single	1535.10	508.72	8.00
cadmium	double	501.35	361.27[a]	6.20					
mercury	double	553.51	365.12	6.46					
		-	365.59	-					
mercury	double	570.45	366.41[a]	5.95					

[a] Average wavelength of the double emission line
[b] Wavelength of the dominating stronger emission lines of the double emission line

In order to wavelength-calibrate the measured spectra, a polynomial of 2^{nd} degree is fitted to this wavelength-pixel mapping according to:

$$\lambda(i) = \lambda_0 + a \cdot i + b \cdot i^2, \tag{8.1}$$

with i being the pixel number. The constant parameters that determine the wavelength calibration are specific for every instrument. For instance, a change in the parameter λ_0 leads to a spectral shift in the wavelength range of the spectrum, whereas changing parameter a causes a linear stretch or squeeze of the spectrum. Parameter b and higher polynomial orders can scale spectral distortions due

to possibly unequal spectral pixel widths (Platt and Stutz, 2008). For a more precise calibration, a so-called Fraunhofer calibration is applied according to a script written by Johannes Lampel (IUP Heidelberg, personal communication, September 2011). It is based on a high-resolution solar reference spectrum (Kurucz et al., 1984; Chance and Kurucz, 2010) that is convolved with one of the mercury or cadmium emission lines to the wavelength resolution of the instrument. The convolved Fraunhofer reference spectrum is then fitted to a randomly chosen measured spectrum together with the Ring spectrum and the absorption cross-sections of the strong absorbers O_3 and O_4. Thereby, the spectral interval is divided in a number of sub-windows with a width of 200 pixels in which a fitting algorithm is applied to fit the measured intensities to the Kurucz spectrum. The final wavelength calibration results in:

$$\lambda(i)_{\mathrm{QE}} = (320.99 + 0.08i - 7.94 \cdot 10^{-6} i^2)\ \mathrm{nm} \quad (8.2)$$

$$\lambda(i)_{\mathrm{USB}} = (408.92 + 0.08i - 8.17 \cdot 10^{-6} i^2)\ \mathrm{nm}, \quad (8.3)$$

with 0.08 nm/pixel being the wavelength dispersion. The quadratic term is small, indicating that the focal plane is not completely flat but slightly bent. The resulting wavelength ranges lie between 321.0 and 398.8 nm for the UV and between 408.9 and 533.5 nm for the visible instrument. Figure 8.2 shows the final wavelength calibration of the mercury cadmium spectra for the UV and the visible spectrometers, respectively.

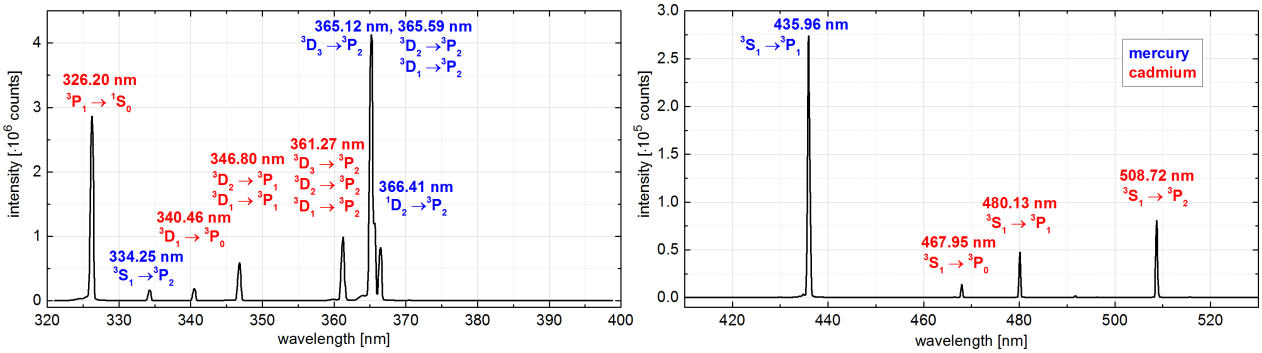

Figure 8.2: Hg-Cd spectrum from 16 November 2011 including the final calibration of the QE (left panel) and the USB (right panel). The term symbols of the transitions of the different emission lines are given in the form $^{2S+1}L_j$ with L being the total orbital angular momentum quantum number, j the total angular momentum quantum number, and S the total spin quantum number (Kramida et al., 2014).

Slit function

The high resolution and wavelength-pixel mapping of the literature reference absorption cross-sections has to be adjusted to match the measured spectra. Therefore, all highly resolved literature absorption cross-sections have to be convolved with the corresponding slit function. The convolution is performed with the software *WinDOAS*. Thus, the (wavelength-dependent) slit function of each spectrometer has to be determined. A single atomic emission line from the offset and dark current corrected mercury cadmium spectrum is selected. Ideally, it should be chosen an emission line that lies within or close to the analysed wavelength range, since the slit function is usually not constant over the entire wavelength range due to the optical properties of the spectrometer. However, some of the mercury and cadmium lines are not single lines, but double or triple lines (Table 8.1). The mean full-width-at-half-maximum (FWHM) averaged over all emission lines, including the double lines, is 5.74 pixel for the UV and 7.00 pixel for the visible instrument, which corresponds to a FWHM resolution of 0.49 nm and 0.54 nm, respectively. Figure 8.3 shows the slit functions used in this thesis. Basically, for the spectral analysis in the UV, the slit function of the mercury emission

line at 334 nm with an FWHM of 0.43 nm is used. For some cases also the cadmium line at 340 nm with an FWHM of 0.43 nm is used. For the spectral retrieval in the visible wavelength range the cadmium line at 467 nm is used for which the FWHM = 0.50 nm. Since this line is quite weak and far away from the IO spectral fit interval, instead the mercury line at 435 nm with an FWHM of 0.53 nm is used as a slit function to convolve the absorption cross-sections for the spectral retrieval of IO. Although this line consists of two emission lines, it can be regarded as a single line since its emission is dominated by its strongest transition ($^3S_1 \longrightarrow ^3P_1$).

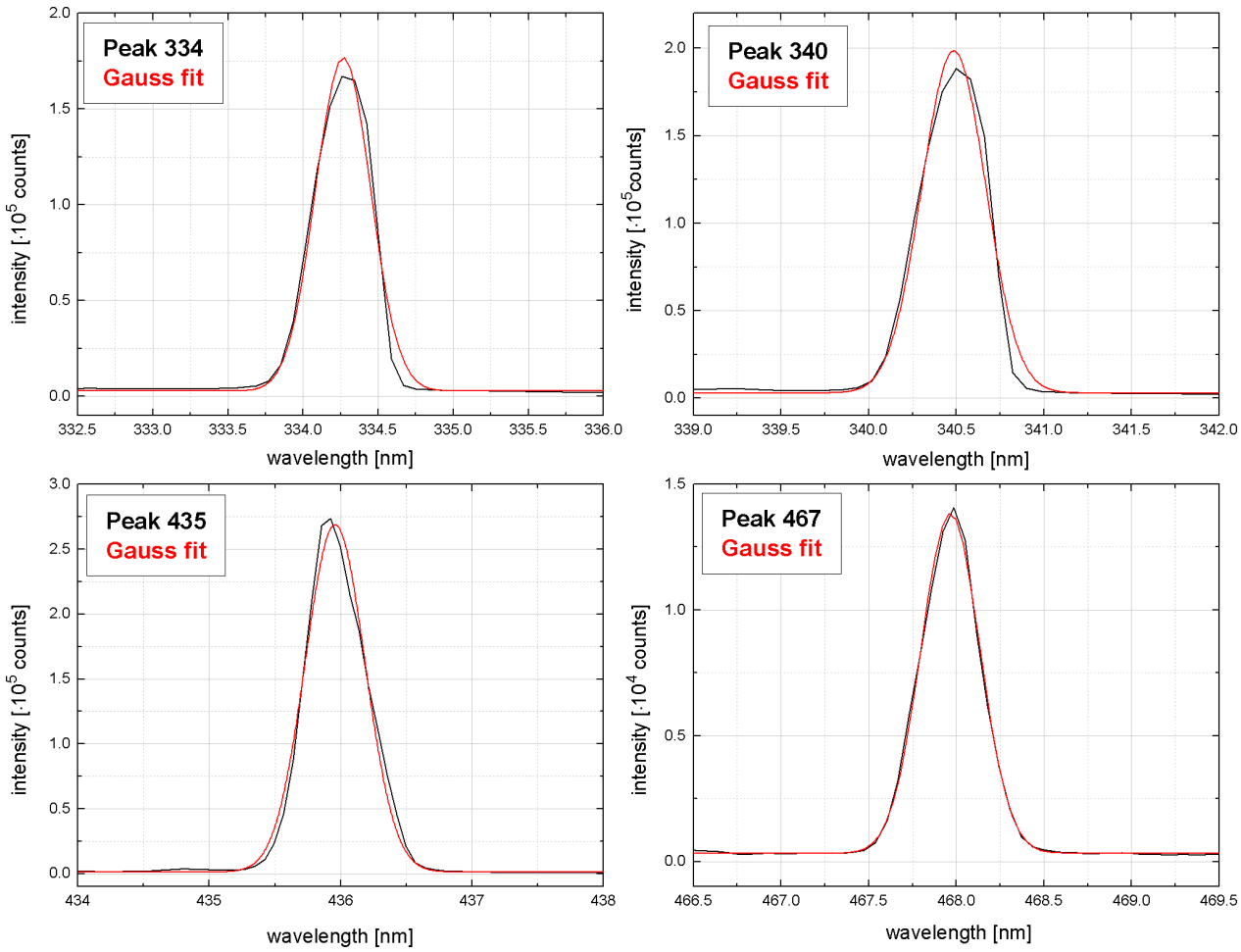

Figure 8.3: Slit functions of the emission lines used in this thesis (black) and the Gauss function fitted to the respective emission line (red).

Pixel to pixel variations

Systematic errors can arise due to the different sensitivities of the individual detector pixels (Platt and Stutz, 2008) (regarding the CCD that has been used see Werner, 2009). If the spectra were recorded with an ideal instrument having a stable optical set-up, each individual pixel would be divided exactly by the same pixel of the reference spectrum. However, if optical changes due to a varying temperature or pressure inside the instrument occur, the spectrum wavelength calibration is shifted. Consequently, the pixels of the measured spectrum are not one-to-one mapped onto the respective pixels of the reference spectrum. Therefore, the pixel to pixel sensitivity can cause large residual structures in the DOAS retrieval. All measured spectra are thus divided by a halogen lamp spectrum, which varies weakly with wavelength, in order to remove these pixel to pixel variations (e.g. Platt and Stutz, 2008). This leads to an improvement of the spectral retrieval of trace gases. The pixel to pixel variations of the USB are larger than for the QE. Thus, all spectra recorded with

the USB are divided by a high-pass-filtered halogen lamp spectrum recorded during the measurement campaign to further improve the spectral retrieval. Figure 8.4 shows a scattered skylight spectrum from 16 November 2011 before and after the correction with a high-pass-filtered halogen lamp spectrum. After the division by the lamp spectrum the pixel to pixel variations especially between detector pixel number 600 and 1100 are significantly reduced.

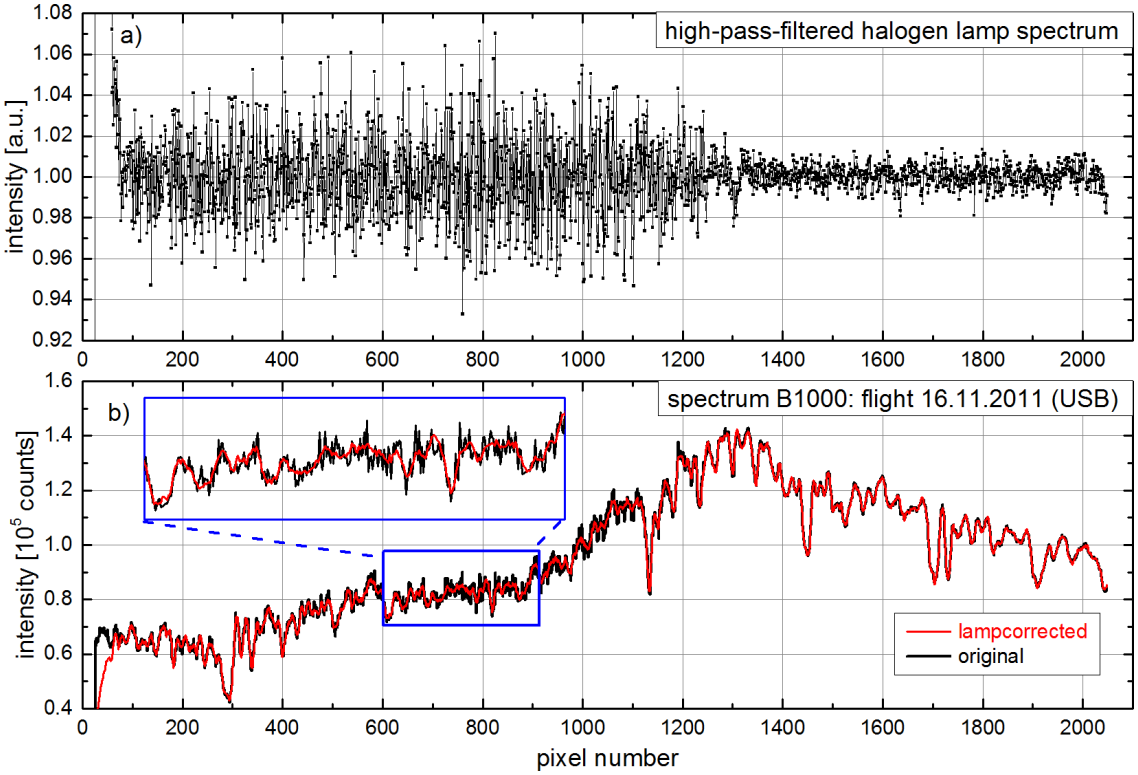

Figure 8.4: a) High-pass-filtered halogen lamp spectrum recorded with the USB, and b) a scattered skylight spectrum recorded with the USB at 05:11:36 UTC on 16 November 2011 before (black) and after (red) the division by the high-pass-filtered halogen lamp spectrum from above.

Choice of Fraunhofer reference spectra

Fraunhofer reference spectra (FRS) have to be chosen carefully, and ideally, the FRS should not contain a significant absorption of the target trace gas. In this thesis either a single FRS from the same sortie, preferably recorded at highest altitude, or a high-resolution solar FRS is used.

- All spectra of each Falcon sortie are analysed against a single FRS from the same sortie. Therefore, an appropriate FRS has to be chosen for each sortie. The FRS are taken from the highest altitude of each sortie avoiding large yaw and roll angles, i.e. when the aircraft turned. In Table 8.2 the details of each FRS are given and the respective webcam images of the sky are shown in Figure 8.5. The cloud cover during the acquisition of the FRS is quite different for the different sorties. Situations occurred when the line of sight pointed into clear sky, partially or totally cloudy skies, or when the aircraft flew within a cloud.

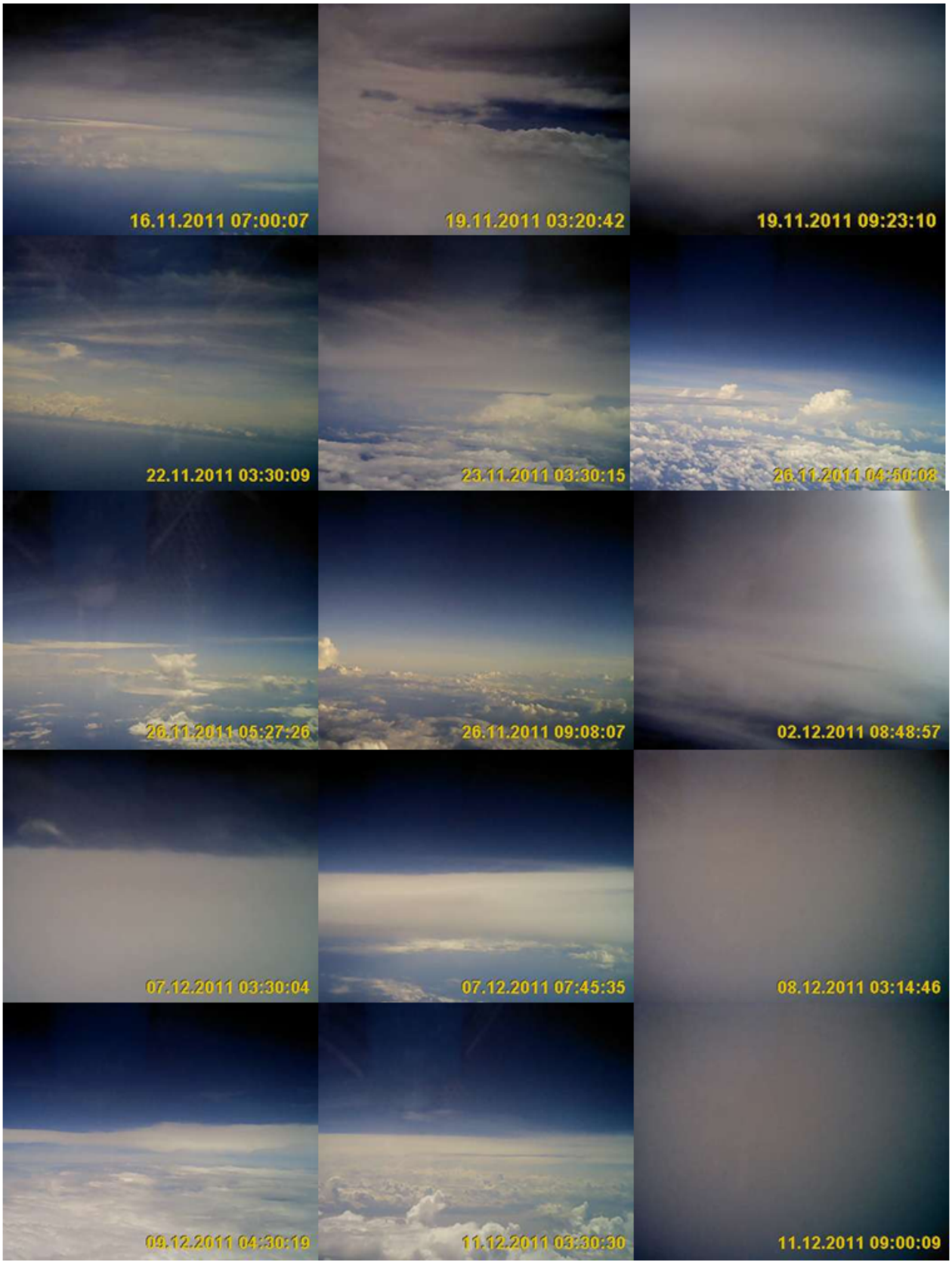

Figure 8.5: Webcam images for the time of the FRS for each flight according to Table 8.2.

- Instead of using a FRS recorded with the same instrument, a high-resolution solar FRS from Chance and Kurucz (2010) (henceforth referred to as "Kurucz spectrum") can be used as a

FRS for the evaluation. This has the advantage that the DOAS spectral fitting procedure directly yields SCDs instead of dSCDs. The Kurucz spectrum is inferred from information gained from high spectral resolution ground-based (Kitt Peak National Observatory, Arizona, USA) and balloon-based measurements of solar radiation together with lower spectral resolution but higher accuracy irradiance measurements (Kurucz et al., 1984; Chance and Kurucz, 2010). Absorption features due to O_4 and O_3 are computed and removed and the Ring effect is also corrected for the 2010 Kurucz spectrum. Prior to the DOAS spectral fitting procedure, the Kurucz spectrum is convolved with the respective instrument function of the QE and USB, which considerable degrade their spectral resolution. However, using the Kurucz spectrum instead of a measured spectrum as a reference, the effect on the spectrum due to the inter-pixel quantum efficiency of the CCD or the wavelength dependent transmission of the spectrometer do not cancel out. Overall, this may lead to increased residual structures in the DOAS spectral fitting procedure (Lübcke, 2014). Hence, only strong absorbers like O_4 and O_3 with relatively broad absorption bands are evaluated from a spectral fit of a measured against the Kurucz spectrum. For sensitivity studies, H_2O is also evaluated from a spectral fit of a measured spectrum against the Kurucz spectrum, in order to receive the reference SCD S_{H_2O} (Section 10.1.2). In order to analyse the residual spectral structures, a principal component analysis (PCA) (Pearson, 1901) of the residual structure is performed according to Lampel (2010) and Lampel (2014). Figure 8.6 shows the first principal component of the residual of an O_4 evaluation for two Kurucz FRS taken by the QE and USB spectrometer during two exemplary flights, respectively. The structures for these two exemplary flights are very similar. During both flights, the residual spectral structures of the QE show broad-band variations, whereas the USB spectrometer only shows narrow band residual spectral structures. The latter is possibly because all spectra recorded with the USB are divided by a halogen lamp spectrum to account for pixel-to-pixel variations (Section 8.1). The division by the lamp spectrum might cancel out possible instrumental effects like different sensitivities due to the quantum efficiency of the USB. Implementing the first principal component of the residual spectral structures into the DOAS spectral fit as suggested by Lübcke (2014) strongly reduces the RMS (approximately by a factor of 10). The resulting O_4 SCDs do not change significantly and only decrease by less than approximately 2 % for the QE and less than approximately 5 % for the USB spectrometer. Unlike Lübcke (2014), the first principle component of the residual is not included in the DOAS spectral fit to avoid fitting errors due to possibly remaining absorbing structures in the residual.

Figure 8.7 shows a flight by flight comparison of the inferred O_4 dSCDs and SCDs for the UV and visible wavelength range, respectively. The O_4 SCDs are enhanced by a constant offset as compared to the dSCDs. The difference between the O_4 SCDs and the dSCDs yields the SCD of the FRS S_{ref} according to Equation 4.11. Furthermore, the O_4 SCDs and dSCDs have an identical distribution. The correlation coefficient R of the O_4 dSCDs and SCDs yields values of approximately 0.99 (Figure 8.8). The O_4 SCDs are used for the O_4 scaling method in Section 10.1.

Table 8.2: Overview of the FRS spectra that were used for the UV and visible spectral analysis. The respective webcam images are shown in Figure 8.5.

	UV				vis			
date	No	time	altitude [km]	description	No	time	altitude [km]	description
16.11.11	A1754	07:00:06	12.9	cloudy	B2209	07:00:05	12.9	cloudy
19.11.a	C349	03:20:40	8.4	cloudy	D520	03:20:41	8.4	cloudy
19.11.b	C1077	09:23:11	12.9	within clouds	D1534	09:23:09	12.9	within clouds
21.11.		analogue 22.11.					analogue 22.11.	
22.11.	G399	03:30:09	5.8	cloudy	H504	03:28:02	5.8	cloudy
23.11.	I360	03:30:14	8.8	cloudy	J460	03:28:47	8.7	cloudy
26.11.a	K444, K799	04:50:11, 05:27:23	12.1, 11.4	broken clouds below	L520	04:50:09	12.1	broken clouds below
26.11.b	K1745	09:08:08	9.1	broken clouds below	L2246	09:08:05	9.1	broken clouds below
02.12.	M1262	08:48:54	12.9	cloudy	N1469	08:48:57	12.9	cloudy
07.12.a	O606	03:30:06	10.7	cloudy	P801	03:30:04	10.7	cloudy
07.12.b	O1882	07:45:33	12.6	cloudy	P2999	07:45:33	12.6	cloudy
08.12.	Q805	03:14:08	12.7	within clouds	R968	03:14:48	12.7	within clouds
09.12.a	S494	04:30:18	11.4	broken clouds below	T631	04:30:05	11.4	broken clouds below
09.12.b		analogue 09.12.a					analogue 09.12.a	
11.12.a	U507	03:30:03	11.0	broken clouds below			-	
11.12.b	U2184	09:00:09	10.7	within clouds	V2650	09:00:04	10.7	within clouds

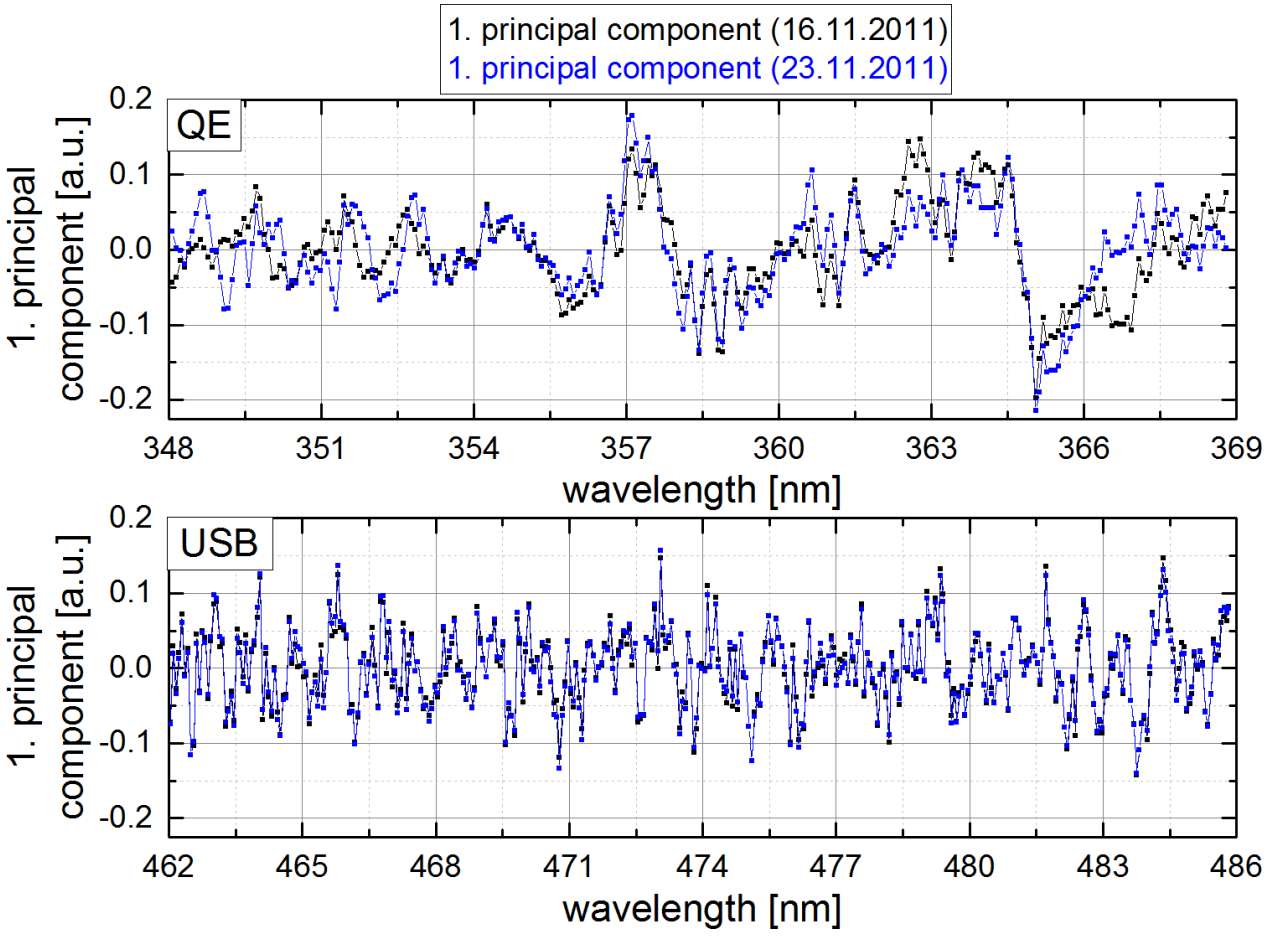

Figure 8.6: First principal component of the residual spectral structures for the O_4 evaluation in the UV (upper panel) and the visible wavelength range (lower panel) for the Falcon flights on 16 and 23 November 2011, respectively.

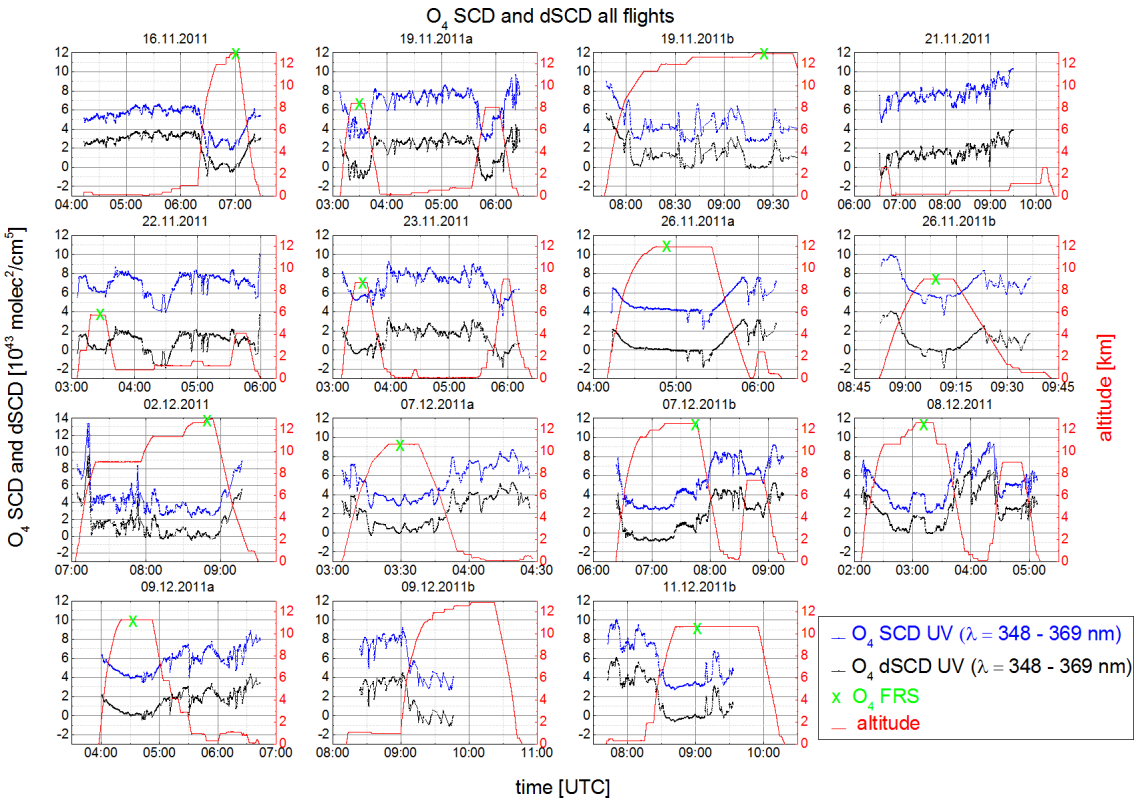

(a)

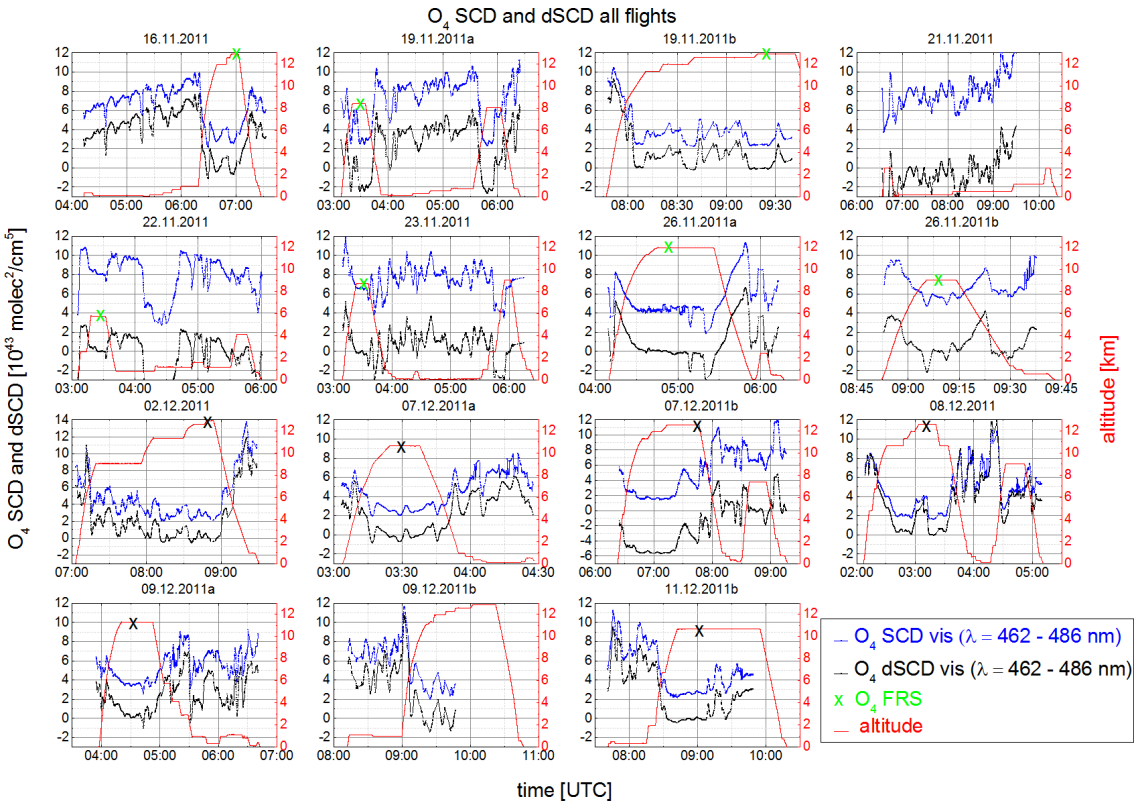

(b)

Figure 8.7: O_4 dSCDs (black) and SCDs (blue) inferred in the (a) UV and (b) visible wavelength range for the different sorties during the SHIVA campaign. In all panels, the altitude of the aircraft is indicated by the red curve. The green crosses highlight the FRS that are used for the evaluation of the dSCDs. Data points with a roll angle larger than $\pm 1\,^\circ$ are excluded.

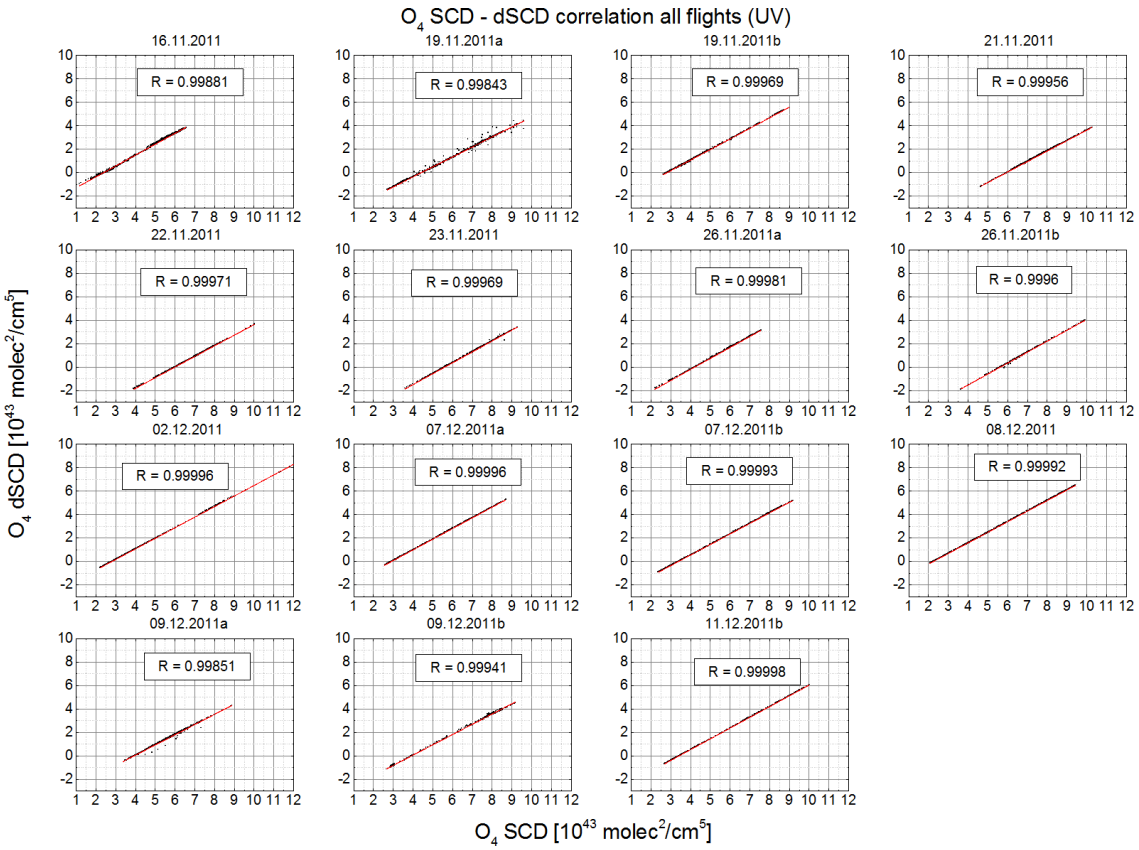

(a)

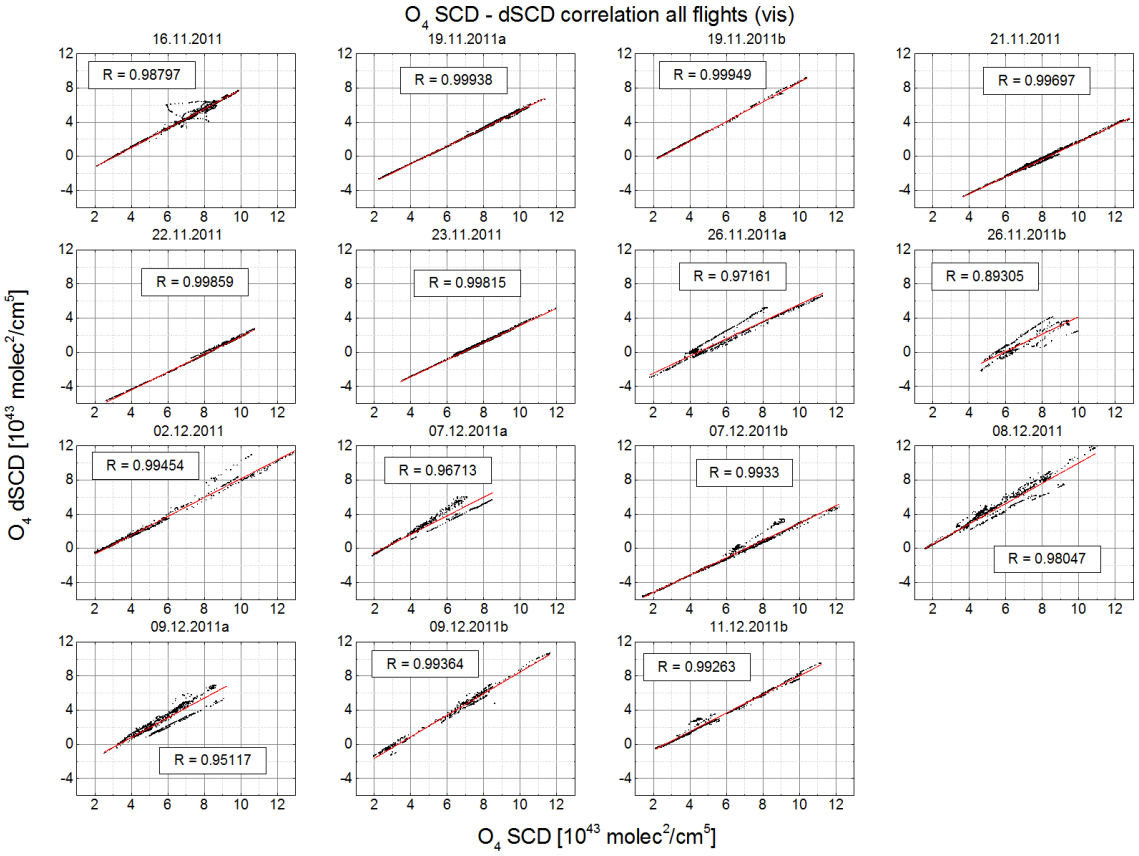

(b)

Figure 8.8: Correlation of the O_4 dSCDs and SCDs (black) for the (a) UV and (b) visible wavelength range for the different sorties during the SHIVA campaign. The red curve represents a linear fit. R specifies the Pearson correlation coefficient of the linear fit.

Ring spectrum and polynomial order

The Ring spectrum accounts for the filling-in of the solar Fraunhofer lines by rotational Raman scattering of air molecules (Section 4.3.4). The atmospheric Ring spectrum is calculated in the software *DOASIS* from the respective Fraunhofer reference spectrum measured during each sortie according to Bussemer (1993) and Chance and Spurr (1997). Figure 8.9 shows Ring spectra for the QE and the USB, respectively, calculated from a measured reference spectrum and from the convolved Kurucz spectrum. Except for the wavelength edges, the deviation of each channel between both Ring spectra averaged over the entire wavelength range is smaller than 1 % for both the QE and the USB, respectively.

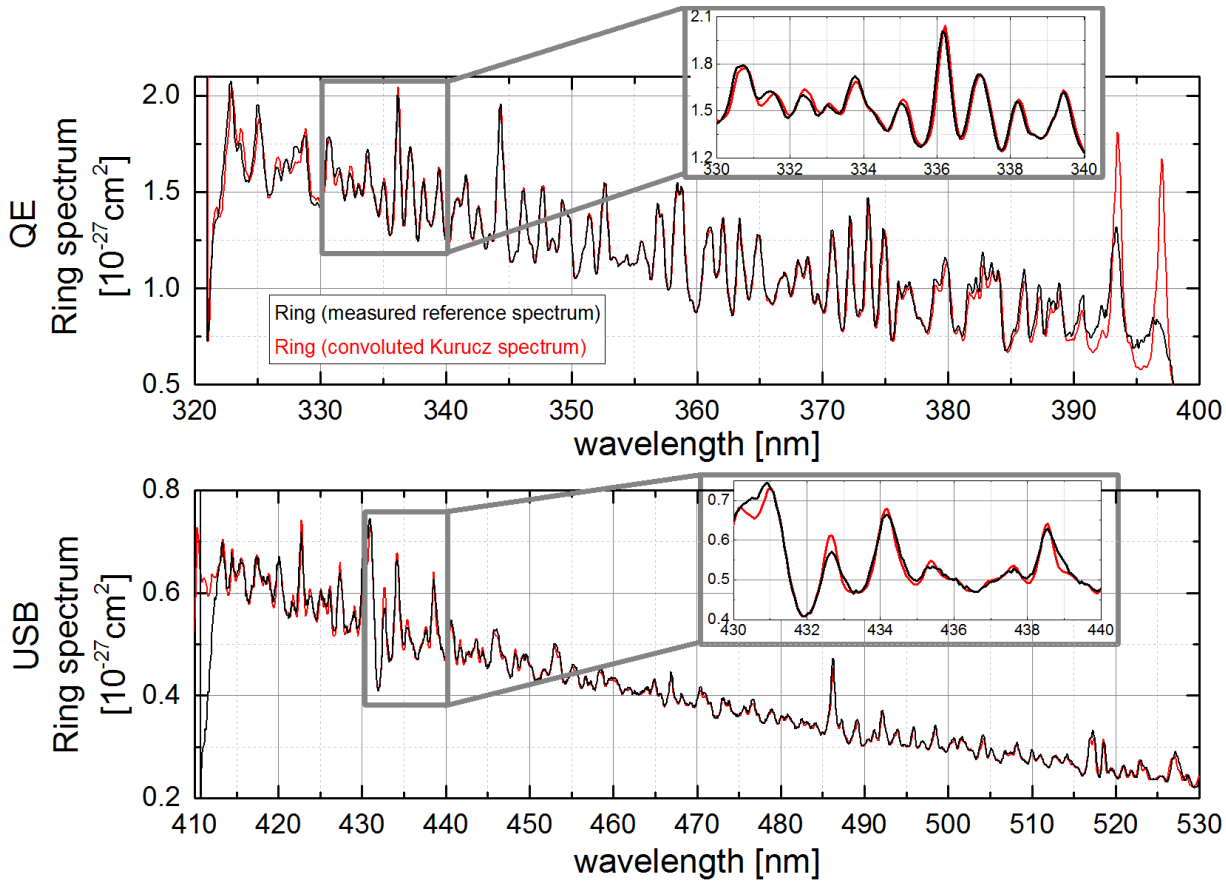

Figure 8.9: Ring spectra for the QE (upper panel) and the USB (lower panel) calculated with *DOASIS* from a measured FRS recored in limb direction for a flight altitude of h = 12.87 km on 16 November 2011 (black line). Ring spectra calculated from the convolved Kurucz spectrum for the slit functions at 334 nm and 467 nm, respectively (red line).

For multiple Rayleigh scattering events or scattering on cloud and aerosol particles, the wavelength dependency of the amplitude of the Ring spectrum can be different (Wagner et al., 2009). Thus, a second Ring spectrum is included in the spectral retrieval, which is calculated by multiplying the intensity of the original Ring spectrum with the wavelength to the power of four:

$$I_{\text{Ring 2}} = I_{\text{Ring}} \cdot \lambda^4. \tag{8.4}$$

The degree of four is chosen to compensate for the difference between the wavelength dependencies of Rayleigh scattering and scattering on cloud particles (Wagner et al., 2009). In the DOAS spectral fit, this second Ring spectrum (Ring 2) is orthogonalised with respect to the original Ring spectrum.

The DOAS polynomial accounts for the broadband spectral structures due to atmospheric Rayleigh and Mie scattering. In this study, a DOAS polynomial of 3^{rd} order is included in the spectral retrieval. Spectrometer stray light (Section 7.2.3) is accounted for by using an additional stray light polynomial of 1^{st} order (i.e. assuming a linear wavelength dependence of the stray light) in intensity space. The whole package of reference and Ring spectra is allowed to be wavelength-shifted relative to the ratio of measured atmospheric spectra.

Number of co-added spectra

The total spectral noise consists of the photoelectron shot noise, the optical noise and the instrumental noise (e.g. Platt and Stutz, 2008). Ideally, the photoelectron shot noise dominates the total noise and limits the signal-to-noise ratio of the DOAS evaluation. The photoelectron shot noise is purely statistical and scales proportional to the square root of the number of sampled photons N ($\propto \sqrt{N}$), whereas the signal-to-noise ratio scales inversely proportional to the number of sampled photons ($\propto \frac{1}{\sqrt{N}}$) (e.g. Platt and Stutz, 2008). Hence, by accumulating more photons or co-adding consecutive spectra the signal-to-noise ratio can be reduced. In order to reach a reasonable signal-to-noise ratio and hence a lower RMS several spectra are co-added.

Figure 8.10a shows the mean dSCD error and the mean RMS for a different number of co-added spectra for the spectral retrieval of HCHO in the UV and for NO_2 in the visible wavelength range, respectively. The resulting curve for the UV deviates significantly from the $\frac{1}{\sqrt{N}}$-curve. Obviously, for the QE, summing up more than five spectra even leads to an increase in the dSCD error and RMS. In contrast to the QE, the USB rather follows the $\frac{1}{\sqrt{N}}$-curve and the mean dSCD error and mean RMS decrease for an increasing number of co-added spectra. However, the curve does not reach the $\frac{1}{\sqrt{N}}$-curve indicating that systematic errors dominate. The difference to the $\frac{1}{\sqrt{N}}$-curve might be further due to a temperature increase related spectral shift as the ice-water mix is melting during the flight. A change of the detector temperature can lead to a shift in the spectra. Hence, the Fraunhofer calibration mentioned above is applied to every single spectrum to account for possible spectral shifts. The coefficients of the resulting solar-calibration polynomials are shown in Figure 8.11. After the Fraunhofer calibration of each spectrum, the course of the mean HCHO dSCD error and RMS improves significantly, whereas the results for NO_2 do not change at all (Figure 8.10b). For the QE, adding spectra up five spectra leads to approximately the same results than without the Fraunhofer calibration. However, adding up more than five spectra now leads to a further decrease in the HCHO error and RMS. This indicates that the QE is more sensitive to temperature changes of the instrumental set-up than the USB. Thus, for the USB no Fraunhofer calibration of each single spectrum is required before the spectral analysis. In order to reach a very small RMS and thus a small detection limit in the spectral analysis of the QE, the Fraunhofer calibration has to be applied to every single spectrum, e.g. for the spectral retrieval of BrO. Since adding up several spectra decreases the spatial resolution of the measurements, a compromise between a reasonable detection limit and the spatial resolution has to be determined depending on the trace gas of interest. In order to reach a reasonable detection limit for HCHO, co-adding up to five spectra seems to be sufficient. Finally, in the UV five spectra are co-added ($t_{\text{exp}} \approx 30$ s), whereas in the visible wavelength range 20 spectra are co-added ($t_{\text{exp}} \approx 2$ min) without applying a Fraunhofer calibration to every single spectrum. Assuming an average aircraft ground speed of approximately 120 m/s, which is a typical value for low level flights, co-adding five spectra corresponds to a horizontal distance of 600 m, whereas co-adding 20 spectra results in a horizontal distance of 2.4 km. At higher altitudes the aircraft reaches values of 250 m/s for the ground speed. Thus, co-adding spectra also means averaging over a large (possibly varying) horizontal distance.

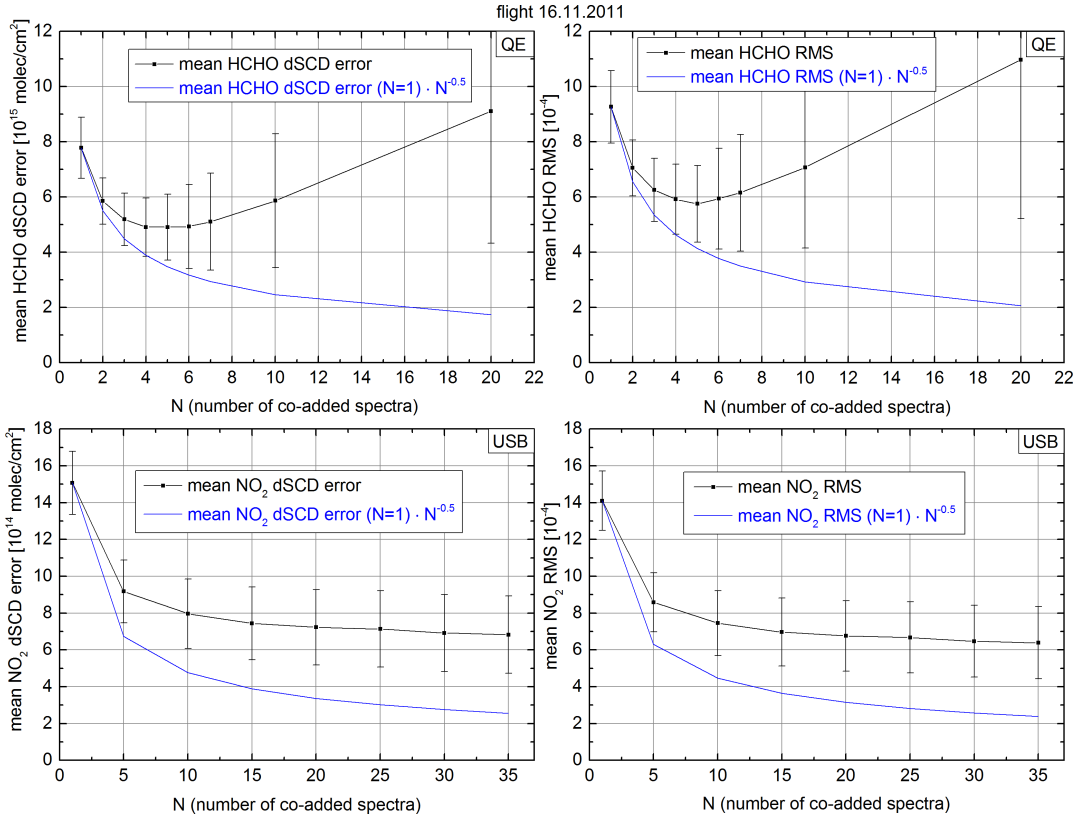

(a)

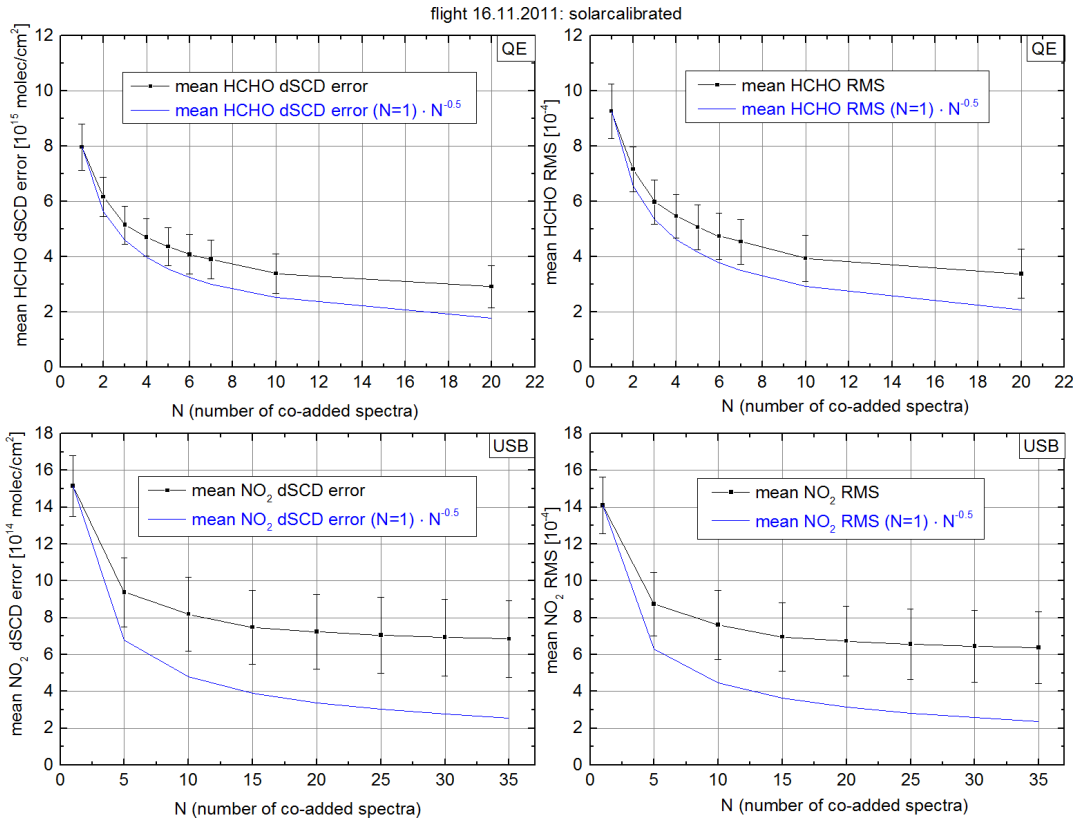

(b)

Figure 8.10: (a) dSCD error and RMS in the spectral retrieval of HCHO (upper row) and NO_2 (lower row), respectively as a function of the number of co-added spectra N averaged for the flight on 16 November 2011, and (b) the same as above but for solar-calibrated spectra. The blue line represents the $\frac{1}{\sqrt{N}}$-curve normalised to N = 1. The error bars correspond to the standard deviation of the mean value.

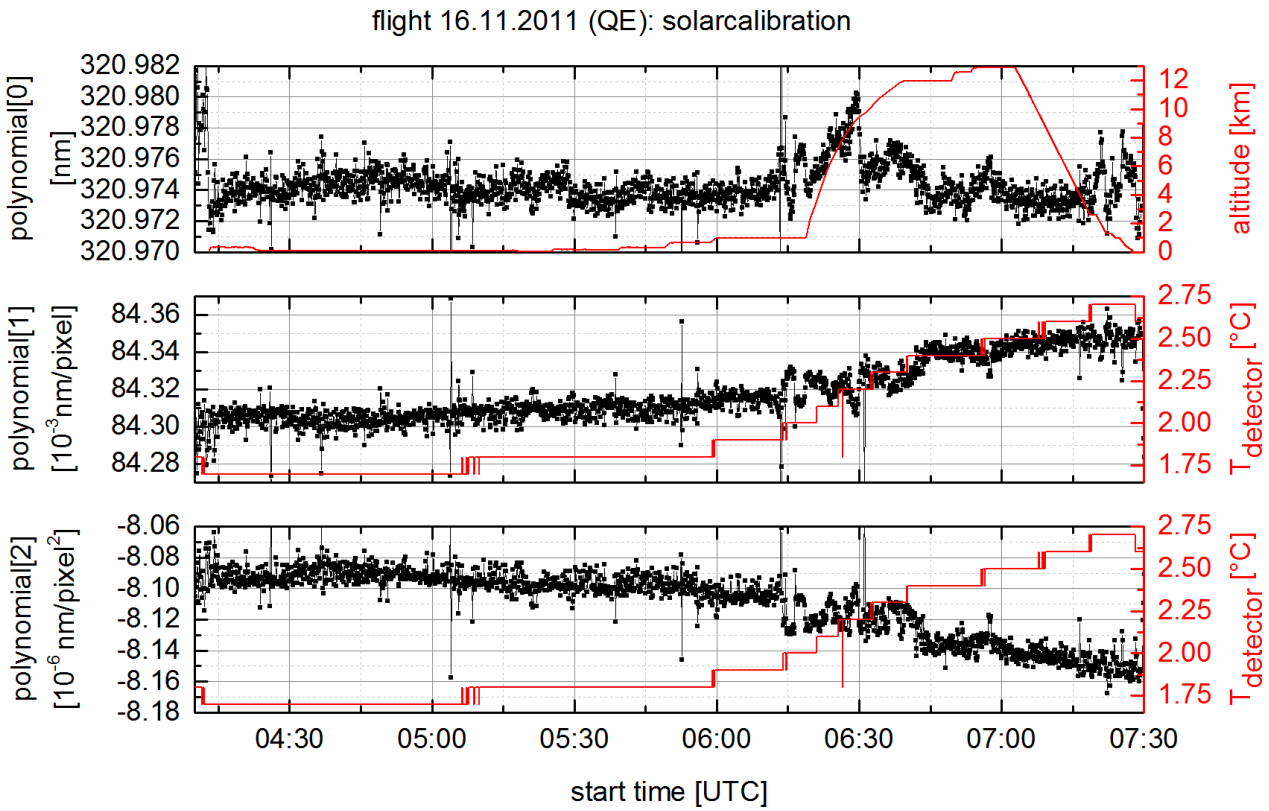

(a)

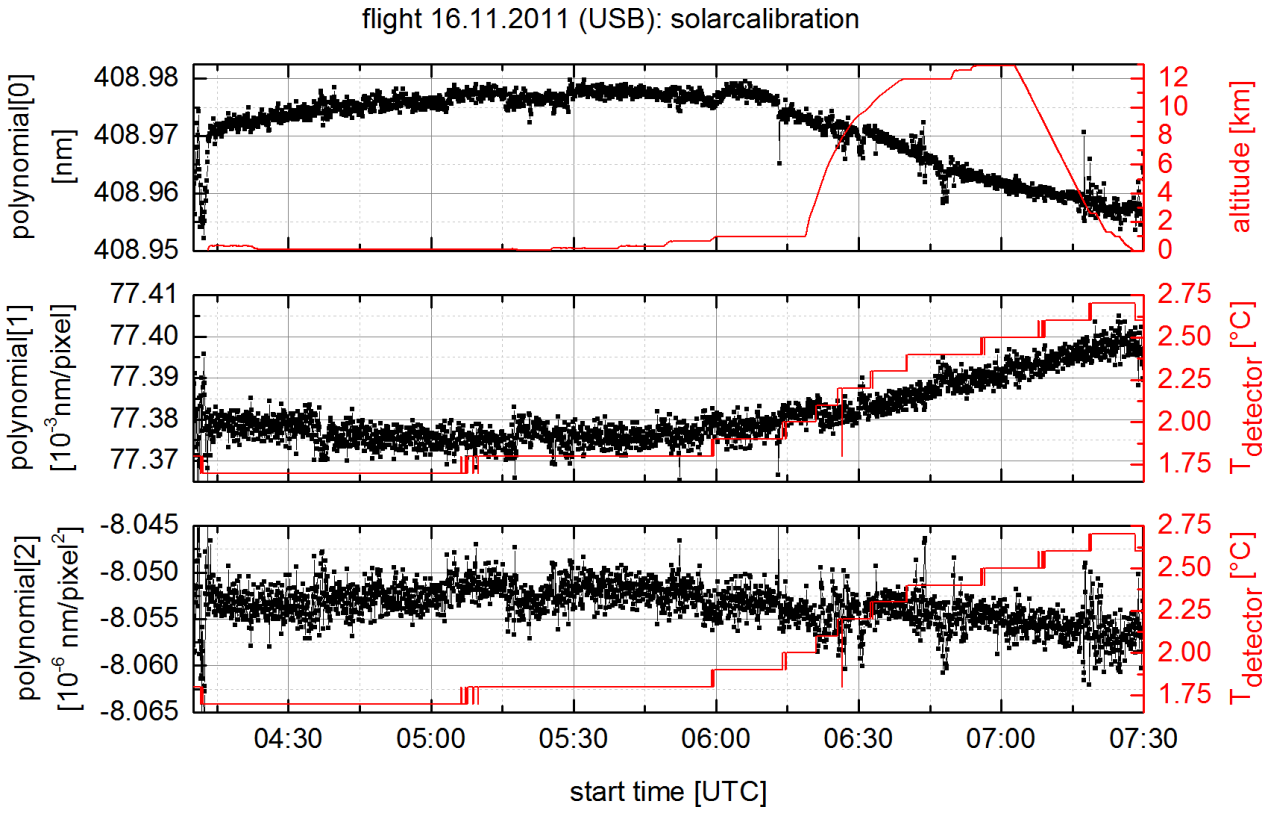

(b)

Figure 8.11: Coefficients of the dispersion polynomial obtained by the Fraunhofer calibration of each recorded spectrum for the (a) QE and (b) the USB for the flight on 16 November 2011.

8.2 Spectral retrieval

This section describes the final retrieval settings for each trace gas. In order to obtain a robust spectral analysis, parameters such as the wavelength fitting range, the number of fitted absorption cross-sections, the polynomial order, and the order of the polynomial offset are investigated. A stable spectral fit should (a) ideally include strong absorption structures of the respective trace gas to maximise its sensitivity, (b) minimize the spectral fit error and residual spectral structures and (c) reduce the interferences with other absorbers. In order to find the optimal wavelength fitting range for each trace gas, the retrieval interval mapping method according to Vogel et al. (2013) is applied. In this method, synthetic spectra are used and the lower and upper wavelength limits of the fit interval are varied systematically and a contour plot visualises the fit results. For this study, real measurement spectra are chosen and the colour plots are generated for the respective fit coefficient, fit error and RMS (Kenntner, 2013). Table 8.3 gives an overview of the absorption cross-sections used in the DOAS data analysis. Table 8.4 summarises the spectral retrieval settings for each trace gas species together with the chosen wavelength fitting range.

Table 8.3: Overview of the literature trace gas absorption cross-sections used in this study.

number	molecule	temperature [K]	resolution [nm]	reference
1	O_4	203, 296	0.02	Thalman and Volkamer (2013), Hermans et al. (1999)
2	O_3	223, 293	0.21 (UV), 0.52 (vis)	Bogumil et al. (2000)
3	H_2O	273	0.001	Rothman et al. (2009)
4	NO_2	220, 298	0.01	Vandaele et al. (1998)
5	HCHO	298	0.01	Meller and Moortgat (2000)
6	CHOCHO	296	0.001	Volkamer et al. (2005b)
7	HONO	296	0.02	Stutz et al. (2000)
8	BrO	228, 298	0.02	Wilmouth et al. (1999)
9	IO	298	0.03	Spietz et al. (2005)

Table 8.4: Overview of the spectral retrieval settings of the different trace gas species. The respective references are listed in Table 8.3.

analysis	interval [nm]	molecules
O_4 (360 nm)	348 - 369	O_4 (296 K), O_3 (223 K, 293 K), NO_2 (298 K), HCHO, BrO (228 K)
O_4 (477 nm)	462 - 486	O_4 (296 K), O_3 (223 K), NO_2 (298 K), H_2O, CHOCHO
O_3 (UV)	332 - 357	O_4 (296 K), O_3 (223 K, 293 K), NO_2 (298 K), HCHO, BrO (228 K)
O_3 (vis)	450 - 500	O_4 (296 K), O_3 (223 K), NO_2 (298 K), H_2O, CHOCHO
NO_2 (UV)	337 - 357	O_4 (296 K), O_3 (223 K, 293 K), NO_2 (298 K), HCHO, BrO (228 K)
NO_2 (vis)	450 - 485	O_4 (296 K), O_3 (223 K), NO_2 (298 K), H_2O, CHOCHO
HCHO	337 - 357	O_4 (296 K), O_3 (223 K, 293 K), NO_2 (298 K), HCHO, BrO (228 K)
HONO	337 - 372	O_4 (203 K), O_3 (223 K, 293 K), NO_2 (220 K), HCHO, HONO, BrO (228 K)
CHOCHO	447 - 465	O_4 (296 K), O_3 (223 K), NO_2 (298 K), H_2O, CHOCHO
BrO	337 - 357	O_4 (296 K), O_3 (223 K, 293 K), NO_2 (298 K), HCHO, BrO (228 K, 298 K)
IO	415 - 439.5	O_3 (223 K), NO_2 (298 K), H_2O, CHOCHO, IO
H_2O	440 - 485	O_4 (296 K), O_3 (223 K), NO_2 (298 K), H_2O, CHOCHO

All absorption cross-sections are convolved to the spectral resolution of the instrument using the mercury emission line located at 334 nm for the UV and at 467 nm for the visible wavelength range, respectively. In the case of the spectral retrieval of HONO and IO, the mercury emission lines located

at 340 nm and 435 nm are used, respectively, since these lines are closer to the chosen wavelength range. As mentioned in Section 8.1, a DOAS polynomial of 3^{rd} order is chosen. Spectrometer stray light is accounted for by using an additional stray light polynomial of 1^{st} order. The whole package of reference and Ring spectra is allowed to be wavelength-shifted relative to the ratio of measured atmospheric spectra.

8.2.1 Spectral retrieval of O_4

The O_4 analysis is performed in the wavelength interval ranging from 348 to 369 nm (UV) and from 462 to 486 nm (vis), where single absorption bands are located. Absorption cross-sections of O_4 are available from Greenblatt et al. (1990), Hermans et al. (1999) and Thalman and Volkamer (2013) with a spectral resolution of 0.6 nm, 0.03 nm and 0.3 nm, respectively. The other absorption cross-sections included in the spectral retrieval are listed in Table 8.3 and 8.4. In order to decide which O_4 absorption cross-section leads to the best spectral retrieval, an example flight (16 November 2011) is evaluated using the different absorption cross-sections and a PCA is performed. Figure 8.12 shows the three different convolved O_4 absorption cross-sections together with the first principal component of the spectral residual for the UV analysis. The absorption cross-section of Greenblatt et al. (1990) shows a spectral shift of approximately 0.4 nm towards lower wavelengths. For all absorption cross-sections, a large residual structure remains at the wavelength of the O_4 peak. This spectral residual can be observed for all O_4 absorption bands and has already been detected by Lampel (2014). The first principal component does not provide an unambiguous hint as to which absorption cross-section leads to the smallest residual structures. Using the absorption cross-section from Hermans et al. (1999) results in the smallest average RMS, whereas the absorption cross-section from Greenblatt et al. (1990) leads to the largest RMS values for this flight (Figure 8.13). Using the absorption cross-section of Thalman and Volkamer (2013) leads to RMS values similar to those using the absorption cross-section from Hermans et al. (1999). However, the RMS values for the Hermans et al. (1999) absorption cross-section are slightly smaller than the RMS values using the Thalman and Volkamer (2013) absorption cross-section. The O_4 dSCDs inferred with the absorption cross-section from Hermans et al. (1999) are approximately 10 % smaller than the dSCDs retrieved with the Greenblatt et al. (1990) absorption cross-section.

In the visible wavelength range (Figure 8.14 and 8.15), the shape of the absorption cross-sections of Hermans et al. (1999) and Thalman and Volkamer (2013) seem to be very similar to the UV spectral range. Although the absorption cross-section of Greenblatt et al. (1990) has a slightly different shape compared to the other two absorption cross-sections, the first principal component of the residual shows a similar shape for all three absorption cross-sections. The resulting average RMS and O_4 dSCDs only vary by less than 2 % for the different absorption cross-sections. Thus, choosing a different O_4 absorption cross-section does not change the O_4 dSCDs significantly in the visible wavelength range. In this study, the O_4 absorption cross-section of Hermans et al. (1999) is used, as it results in the smallest RMS values in the UV. However, as the absorption cross-section of Hermans et al. (1999) shows similar structures and results as compared to the most recent absorption cross-section of Thalman and Volkamer (2013), it is recommend to use the absorption cross-section of Thalman and Volkamer (2013) in further DOAS applications. A systematic error of approximately 10 % can be assumed for the spectral retrieval of O_4 in the UV and approximately 2 % in the visible wavelength range. Further uncertainties in the spectral analysis of O_4 can exist e.g. due to the lack of knowledge about the temperature and pressure dependence of the O_4 absorption cross-section and band shape (Aquilanti et al., 1999; Pfeilsticker et al., 2001).

It has to be noted that the quantity received by the DOAS spectral retrieval of O_4 does not really correspond to an SCD, since the concentration of O_4 is not known. It is only known that the absorption of O_4 is proportional to the square of the O_2 concentration. The measured quantity corresponds to an optical density and together with the known collisional absorption cross-section and the square of the O_2 concentration an extinction can be calculated. However, in the present study, for simplicity reasons, this quantity is nevertheless referred to as O_4 SCD.

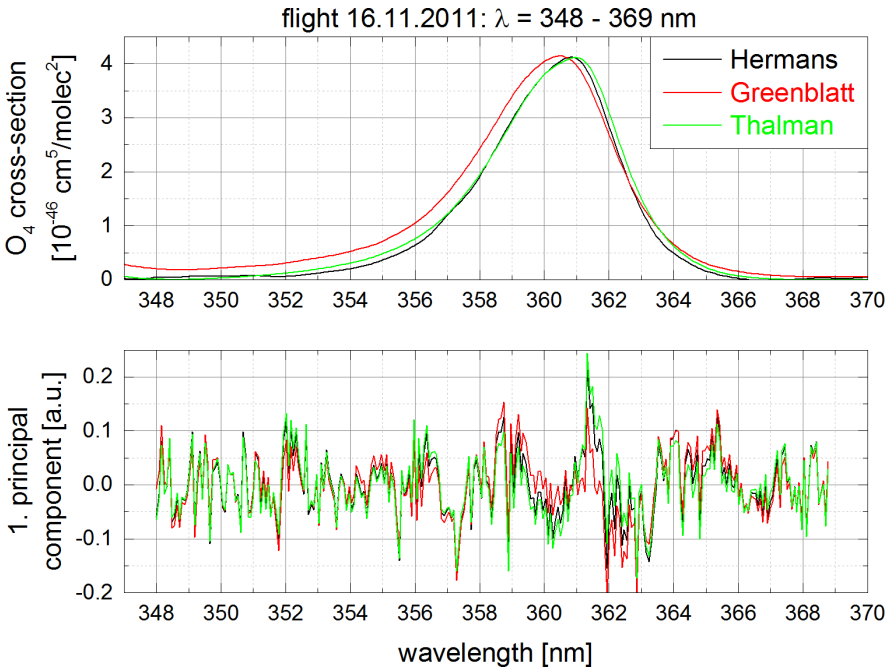

Figure 8.12: Upper panel: Convolved O_4 absorption cross-sections from Hermans et al. (1999) (black), Greenblatt et al. (1990) (red) and Thalman and Volkamer (2013) (green) for the O_4 peak at 360 nm, lower panel: First principal component of the PCA of the residuals from the O_4 spectral retrieval using the three different absorption cross-sections from the upper panel for the flight on 16 November 2011.

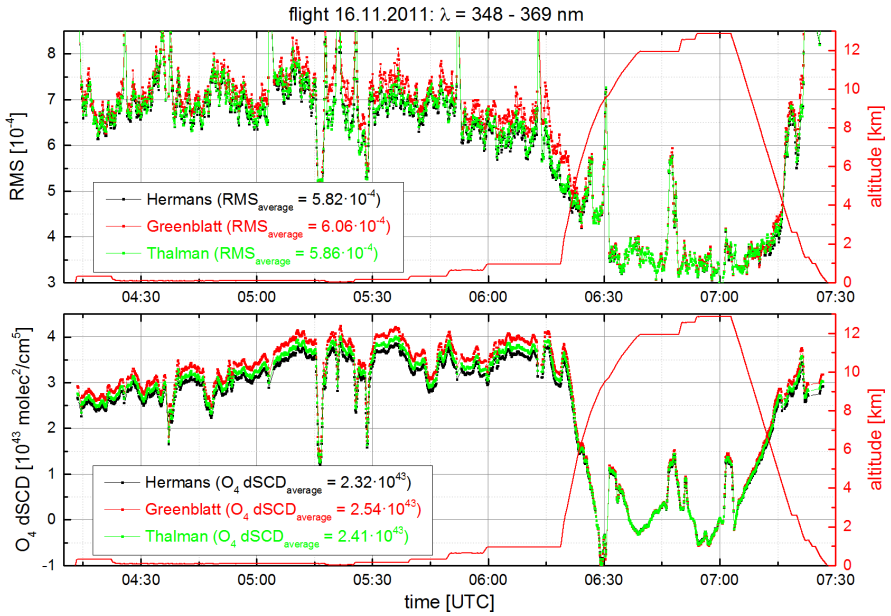

Figure 8.13: RMS of the O_4 spectral analysis (upper panel) and inferred O_4 dSCDs (lower panel) in the UV using the absorption cross-sections of Hermans et al. (1999) (black), Greenblatt et al. (1990) (red) and Thalman and Volkamer (2013) (green) for the flight on 16 November 2011.

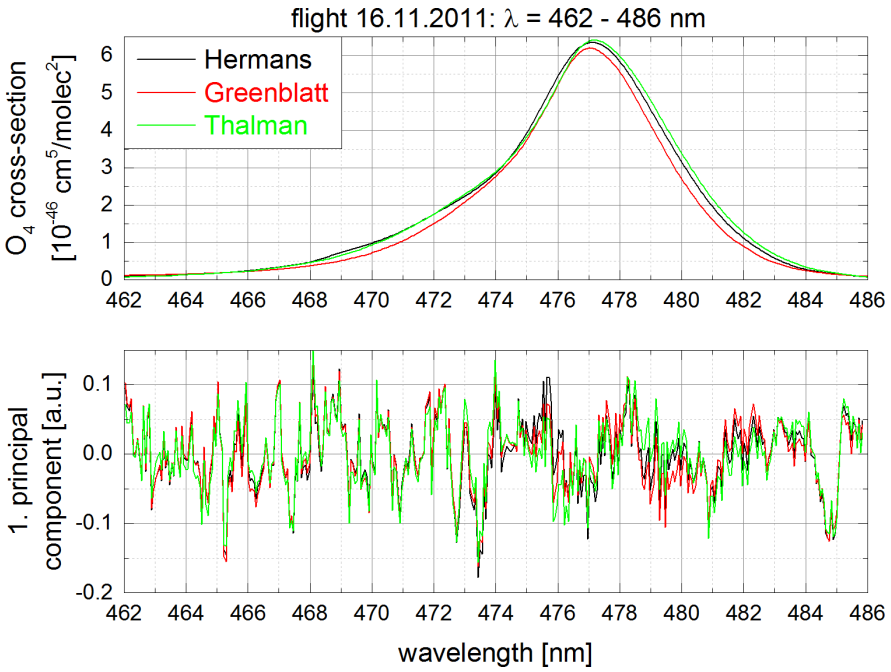

Figure 8.14: Upper panel: Convolved O_4 absorption cross-sections from Hermans et al. (1999) (black), Greenblatt et al. (1990) (red) and Thalman and Volkamer (2013) (green) for the O_4 peak at 477 nm, lower panel: First principal component of the PCA of the residuals from the O_4 spectral retrieval using the three different absorption cross-sections from the upper panel for the flight on 16 November 2011.

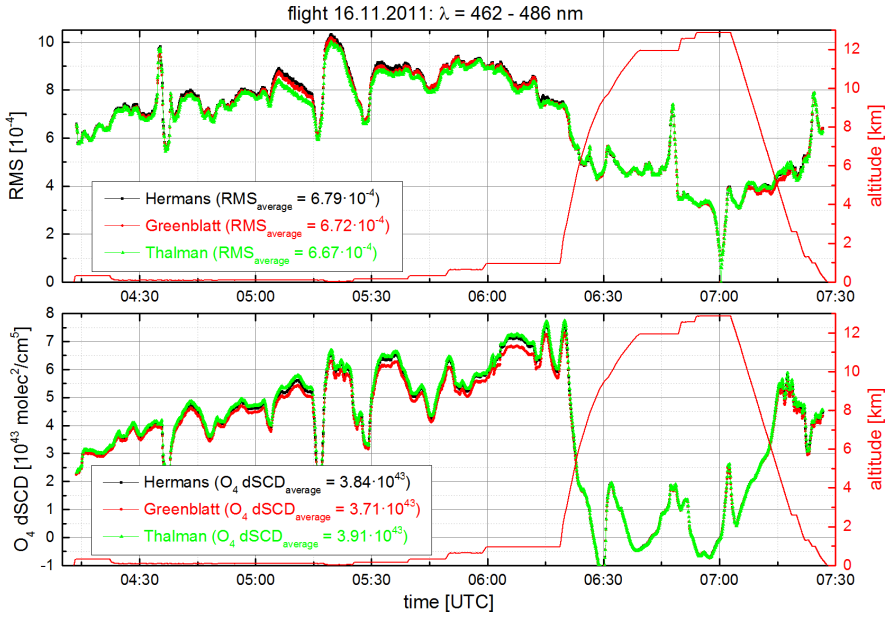

Figure 8.15: RMS of the O_4 spectral analysis (upper panel) and inferred O_4 dSCDs (lower panel) in the visible wavelength range using the absorption cross-sections of Hermans et al. (1999) (black), Greenblatt et al. (1990) (red) and Thalman and Volkamer (2013) (green) for the flight on 16 November 2011.

Figure 8.16 shows an example of an O_4 spectral retrieval in the UV and in the visible wavelength range. The average O_4 dSCD error, which is given by the *WinDOAS* software, adds up to

approximately 3 % in the UV and 10% in the visible spectral range.

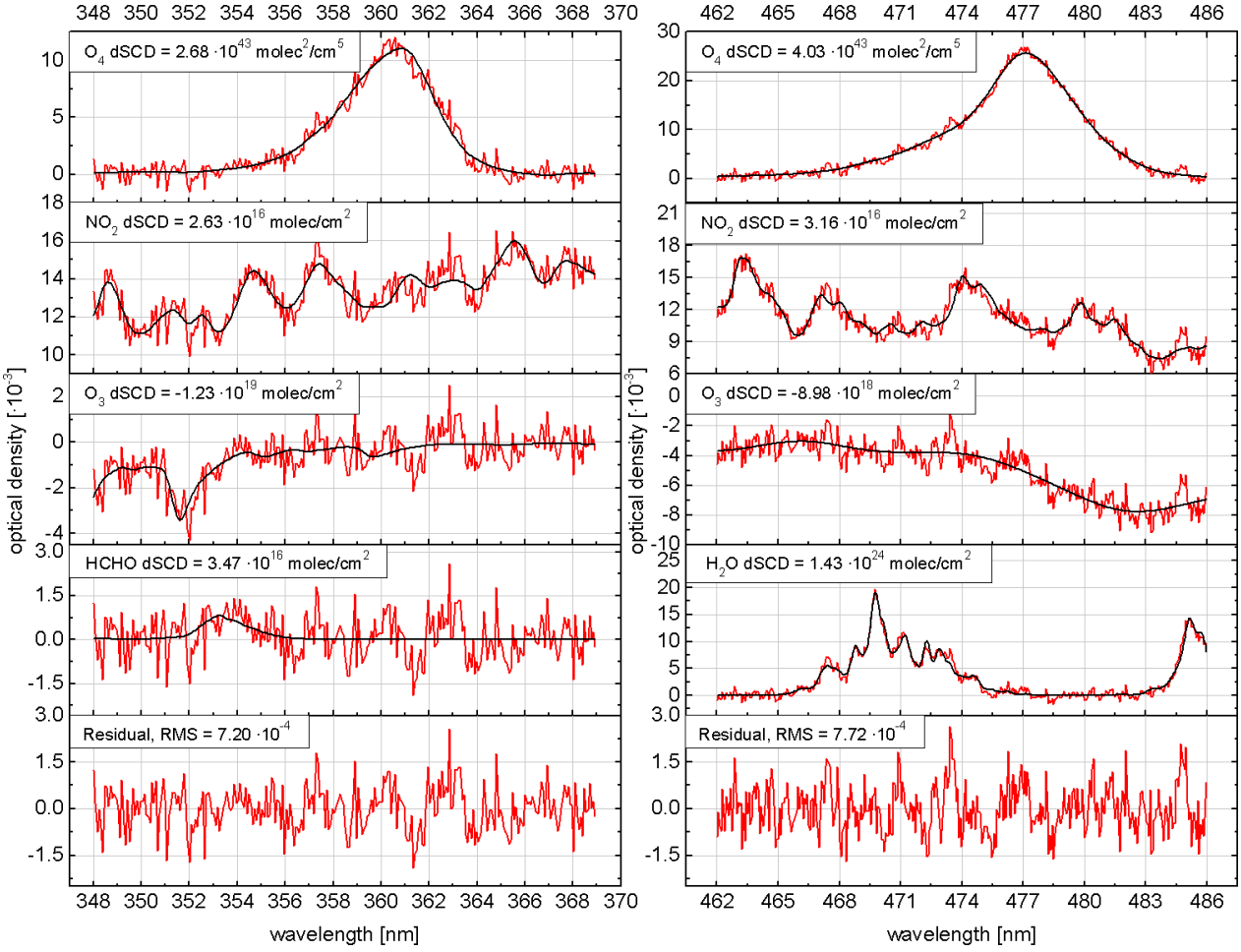

Figure 8.16: Example for an O_4 spectral fit in UV (left panel) and in the visible wavelength range (right panel). The UV spectrum was recorded at 04:34:38 (UTC) and the visible spectrum was recorded at 04:34:35 on 16 November 2011 at 3.3°N and 113.1°E at a height of 90 m and an SZA of 22.6°. The retrieved spectral signatures are indicated in red and the fitted absorption cross-sections in black.

8.2.2 Spectral retrieval of O_3

In the UV region, O_3 is a strong absorber and the spectral retrieval can be problematic, since the DOAS approach is only valid for small optical densities (Platt and Stutz, 2008). For large optical densities, Equation 4.12 cannot be applied anymore. Thus, the wavelength interval has to be chosen carefully. The analysis of O_3 is performed in the wavelength interval, ranging from 332 to 359 nm (UV) and from 450 to 500 nm (vis). The absorption cross-sections included in the spectral retrieval are given in Table 8.3 and 8.4.

Figure 8.17 shows examples for an O_3 spectral retrieval in the UV and in the visible wavelength range for the same spectra as in Figure 8.16. The O_3 dSCDs both for the UV and the visible spectral range are negative. This is because the reference spectra at higher altitudes (h = 12.9 km for 16 November 2011) are subject to stronger absorption by O_3 than the analysed spectra at lower altitudes. Since in this study for the O_3 DOAS measurements, no separation of the tropospheric and stratospheric signal is possible, the inferred O_3 dSCDs are not further used.

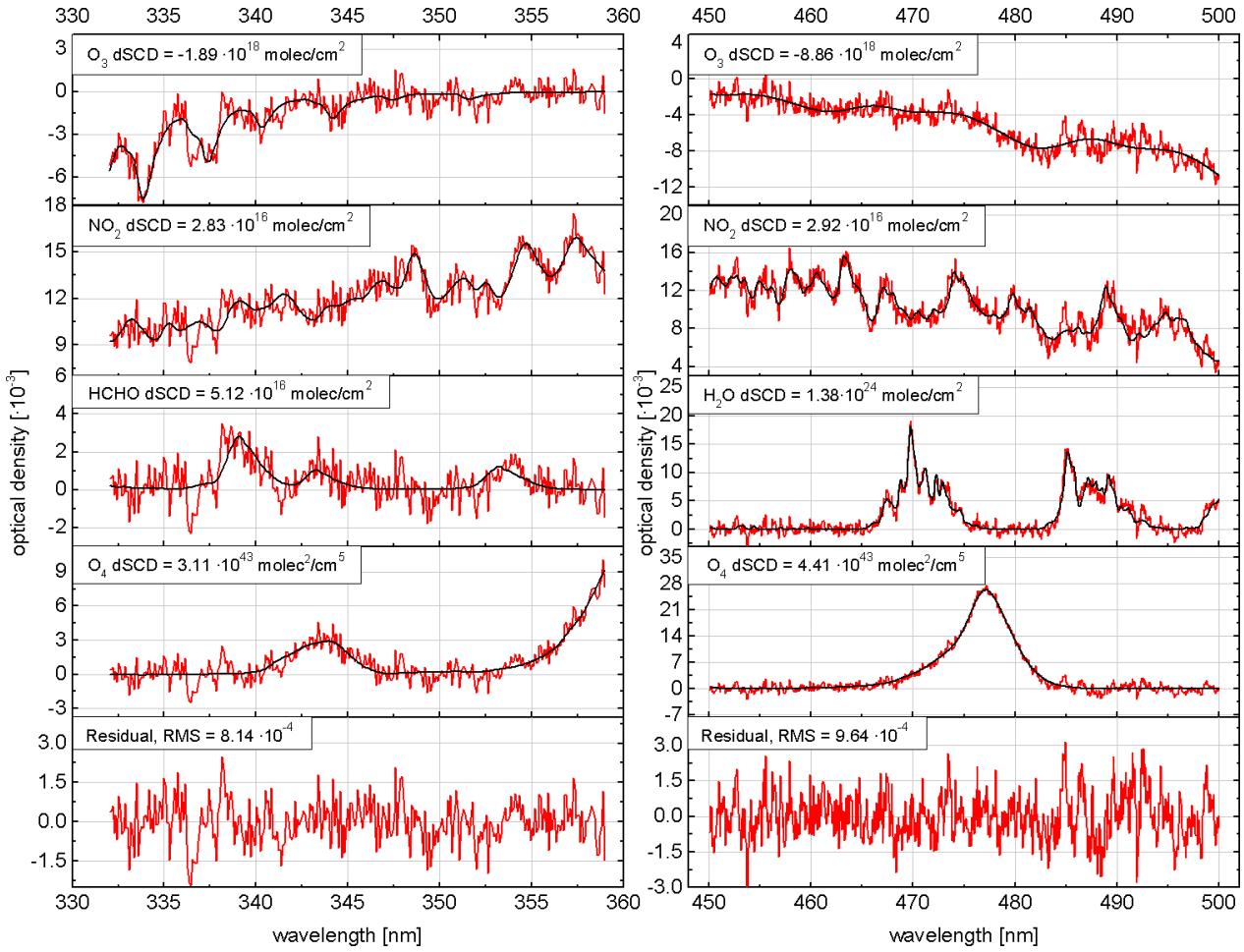

Figure 8.17: Example for an O_3 spectral fit in the UV (left panel) and in the visible wavelength range (right panel) applied on the same spectra as in Figure 8.16. The retrieved spectral signatures are indicated in red and the fitted absorption cross-sections in black.

8.2.3 Spectral retrieval of HCHO, NO_2, and BrO

In the UV, the analyses of HCHO, NO_2, and BrO are performed in the wavelength range from 337 to 357 nm (UV), encompassing three HCHO absorption bands and four BrO absorption bands. NO_2 is further analysed in the visible wavelength range from 450 to 485 nm. The absorption cross-sections included in the spectral retrieval are listed in Table 8.3 and 8.4. For the flights at low altitudes in the MBL, an HONO absorption is not included in the spectral retrieval, as it is below the detection limit. HONO can only be observed occasionally during some flights at high altitudes, when the aircraft was passing through the outflow of a thunderstorm cloud (see next Section 8.2.4). Including HONO in the spectral retrieval when it is below the detection limit can lead to instabilities in the DOAS spectral fit due to possible cross-correlations between HCHO, BrO, O_3 and HONO in this wavelength region. During all sorties BrO never exceeded the detection limit. The average BrO dSCD detection limit (assumed to be 2σ) amounts approximately to $S_{det} = 5{\cdot}10^{13}$ molec cm^{-2}.

Examples for the retrieved HCHO and NO_2 absorption in the UV and for the retrieved NO_2 absorption in the visible wavelength range are shown in Figure 8.18 for the same spectra as in Figure 8.16. Figure 8.19 depicts the retrieval interval mapping for HCHO. The resulting HCHO dSCD amounts to $(6.3 \pm 0.6) \cdot 10^{16}$ molec cm^{-2} with an RMS of $7.3 \cdot 10^{-4}$. Including a fifth HCHO absorption band at 329 nm would reduce the dSCD error. However, the RMS increases for smaller wavelengths approaching the low wavelength end of the spectrograph. Furthermore, the HCHO band at 329 nm directly coincides with an O_3 band leading to a possible cross-correlation

of the spectral signatures of HCHO and O_3. Hence, the wavelength interval ranging from 337 to 357 nm is chosen for the spectral retrieval of HCHO. A similar wavelength range encompassing these three HCHO absorption bands was also used by Pinardi et al. (2013) during a MAX-DOAS intercomparison campaign in 2009, however with a slightly different starting and ending wavelength (λ = 336.5 - 359 nm). The smaller wavelength interval edges are chosen to reduce the RMS.

Figure 8.20 illustrates the retrieval interval mapping for NO_2 in the UV and in the visible wavelength range. During the MAX-DOAS intercomparison campaign mentioned above, an NO_2 wavelength interval between 425 and 490 nm was chosen (Roscoe et al., 2010). As it can be seen in Figure 8.20, the RMS strongly increases for a start wavelength smaller than 445 nm, probably due to the strong water vapour absorption band at 443 nm. Furthermore, the RMS increases for an upper wavelength larger than 485 nm. Thus, for the evaluation of NO_2 in the visible wavelength range a fit interval between 450 and 485 nm is chosen. For the further data processing, only the NO_2 dSCDs inferred in the visible wavelength range are used.

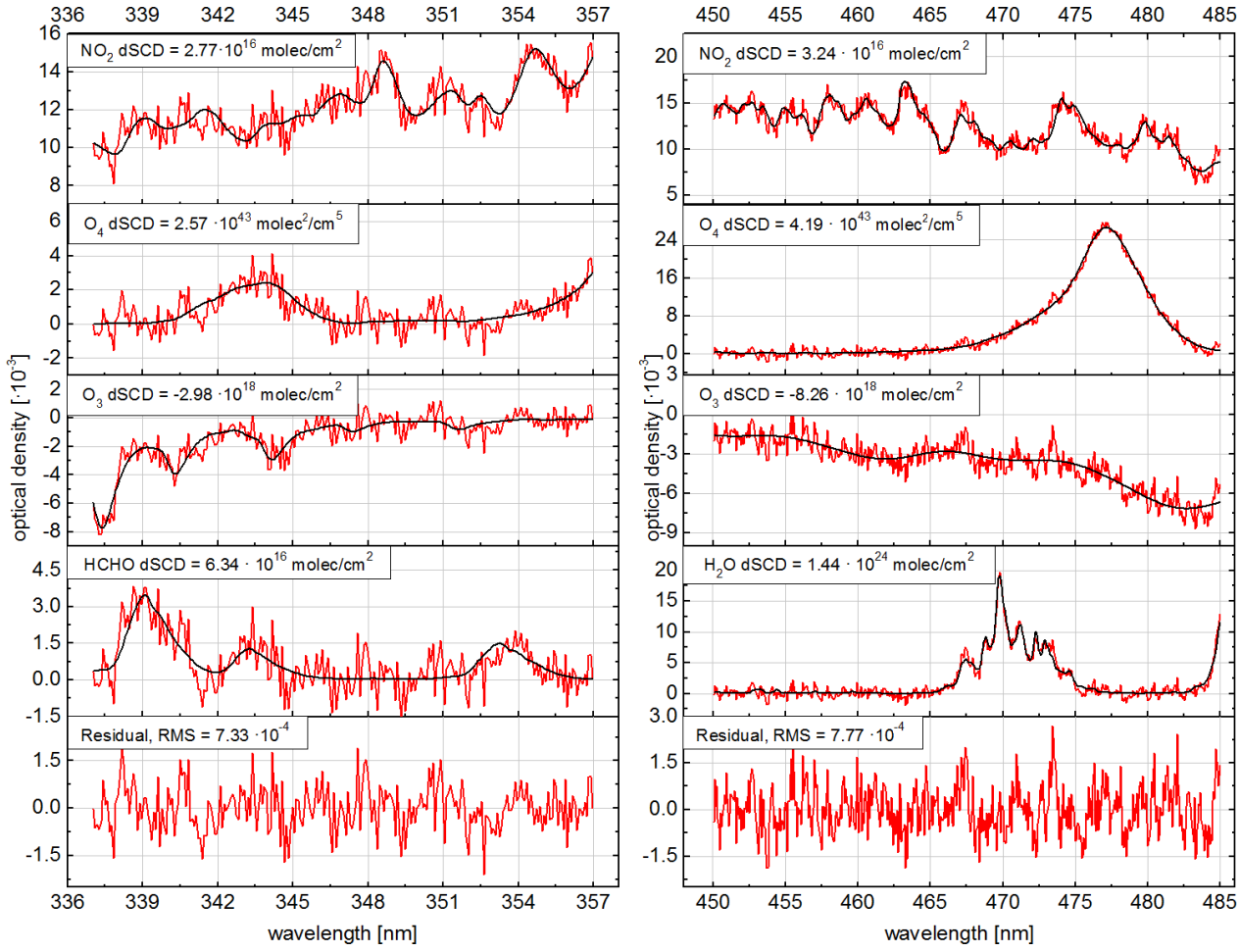

Figure 8.18: Example for an NO_2 spectral fit in UV (left panel) and in the visible wavelength range (right panel) applied on the same spectra as in Figure 8.16. The retrieved spectral signatures are indicated in red and the fitted absorption cross-sections in black. BrO is not shown in the fit, since it does not exceed the detection limit.

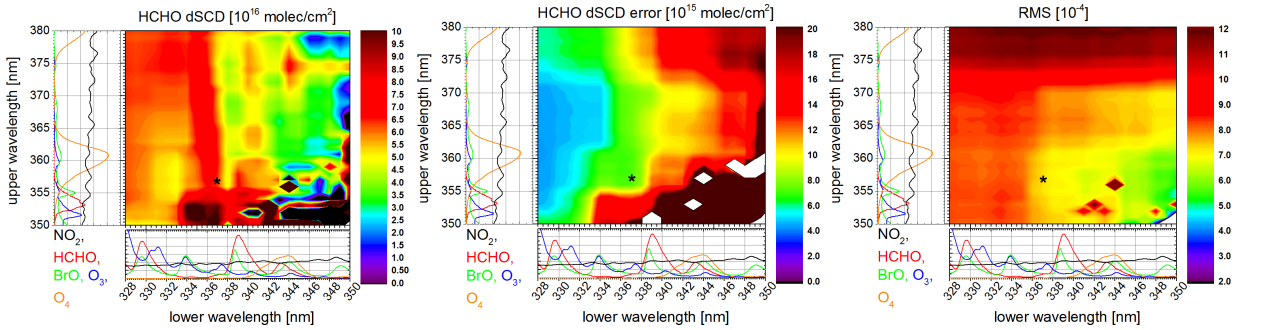

(a) (b) (c)

Figure 8.19: Retrieval interval mapping for HCHO for the same spectrum used in Figure 8.18. The colour bar in each panel corresponds to the (a) HCHO dSCDs, (b) HCHO dSCD errors, and (c) RMS, respectively. The black star highlights the chosen wavelength range. The absorption cross-sections included in the DOAS spectral fit are shown in the smaller panels.

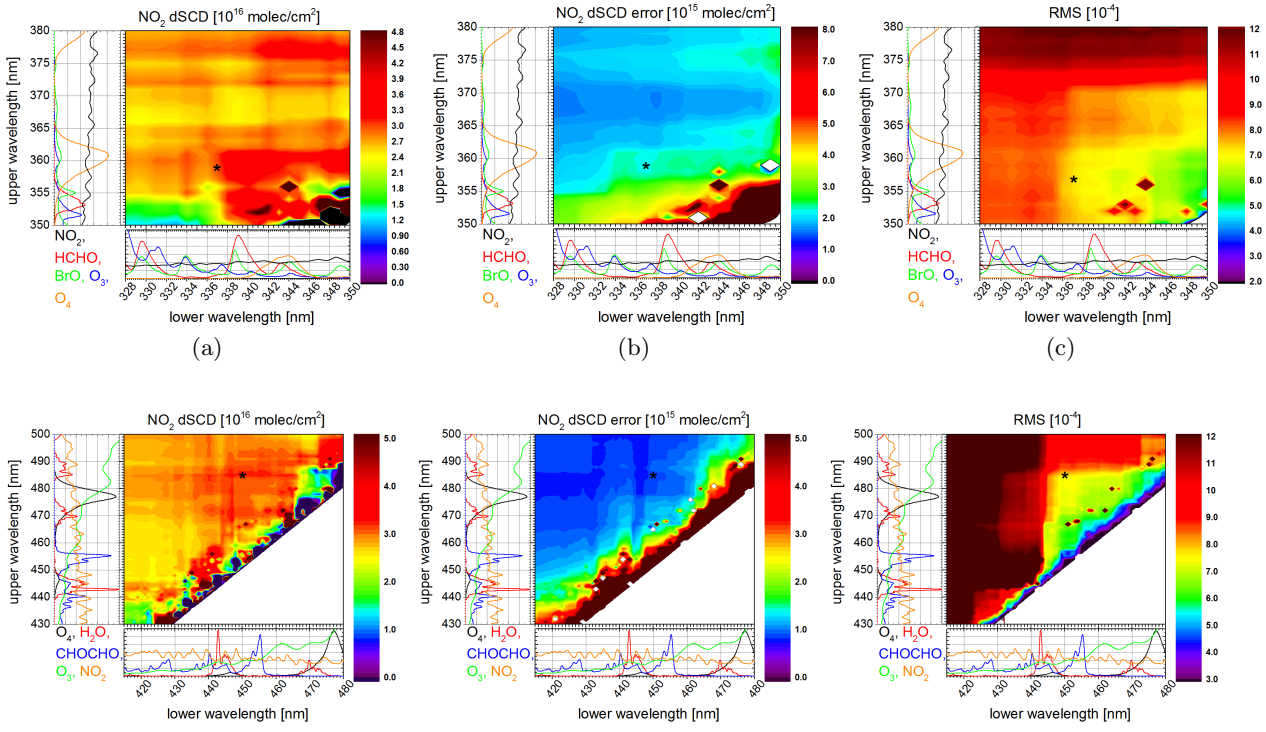

(a) (b) (c)

(d) (e) (f)

Figure 8.20: Retrieval interval mapping for NO_2 in the UV (a - c) and in the visible wavelength range (d - f) for the same spectra used in Figure 8.18. The colour bars in the panels (a) and (d) correspond to the NO_2 dSCDs, (b) and (e) to the NO_2 dSCD errors, and (c) and (f) to the RMS, respectively. The black star highlights the chosen wavelength range. The absorption cross-sections included in the DOAS spectral fit are shown in the smaller panels.

8.2.4 Spectral retrieval of HONO

The analysis of nitrous acid (HONO) is performed in the wavelength interval ranging from 337 to 372 nm, encompassing three major HONO absorption bands. The absorption cross-sections

included in the spectral retrieval of HONO are listed in Table 8.3 and 8.4. All absorption cross-sections are convolved to the spectral resolution of the instrument using the emission line located at 340 nm. However, in this wavelength region the absorption structures of O_3, HCHO, HONO, and BrO can possibly lead to spectral interferences, especially in the wavelength range between 337 and 357 nm. A typical example of the retrieved HONO absorption is shown in Figure 8.21 for the chosen HONO evaluation range (λ = 337 - 372 nm) (right panel) and for the HCHO wavelength interval from Section 8.2.3 (λ = 337 - 357 nm) (left panel). The resulting HONO dSCD amounts to $(3.8 \pm 0.4) \cdot 10^{15}$ molec cm^{-2} for the wavelength interval encompassing three major HONO absorption bands and $(5.2 \pm 0.6) \cdot 10^{15}$ molec cm^{-2} for the smaller wavelength range encompassing two major absorption bands. Figure 8.22 shows the retrieval interval mapping for HONO for a spectrum with enhanced HONO and for another spectrum with less HONO. 8.23 further shows the retrieval interval mapping for the different trace gas species included in the HONO fit. The wavelength range from 337 to 357 nm yields larger HONO dSCDs and dSCD errors than the interval from 337 to 372 nm. As the RMS of both ranges is quite similar and the HONO dSCDs are more stable for the larger interval, the final retrieval wavelength range is set from 337 to 372 nm. Heue et al. (2014) used a fitting window from 332 to 378 nm including four HONO absorption bands. However, this range cannot be applied here, as this low wavelength is too close to the lower wavelength limits of the spectrograph and the RMS increases.

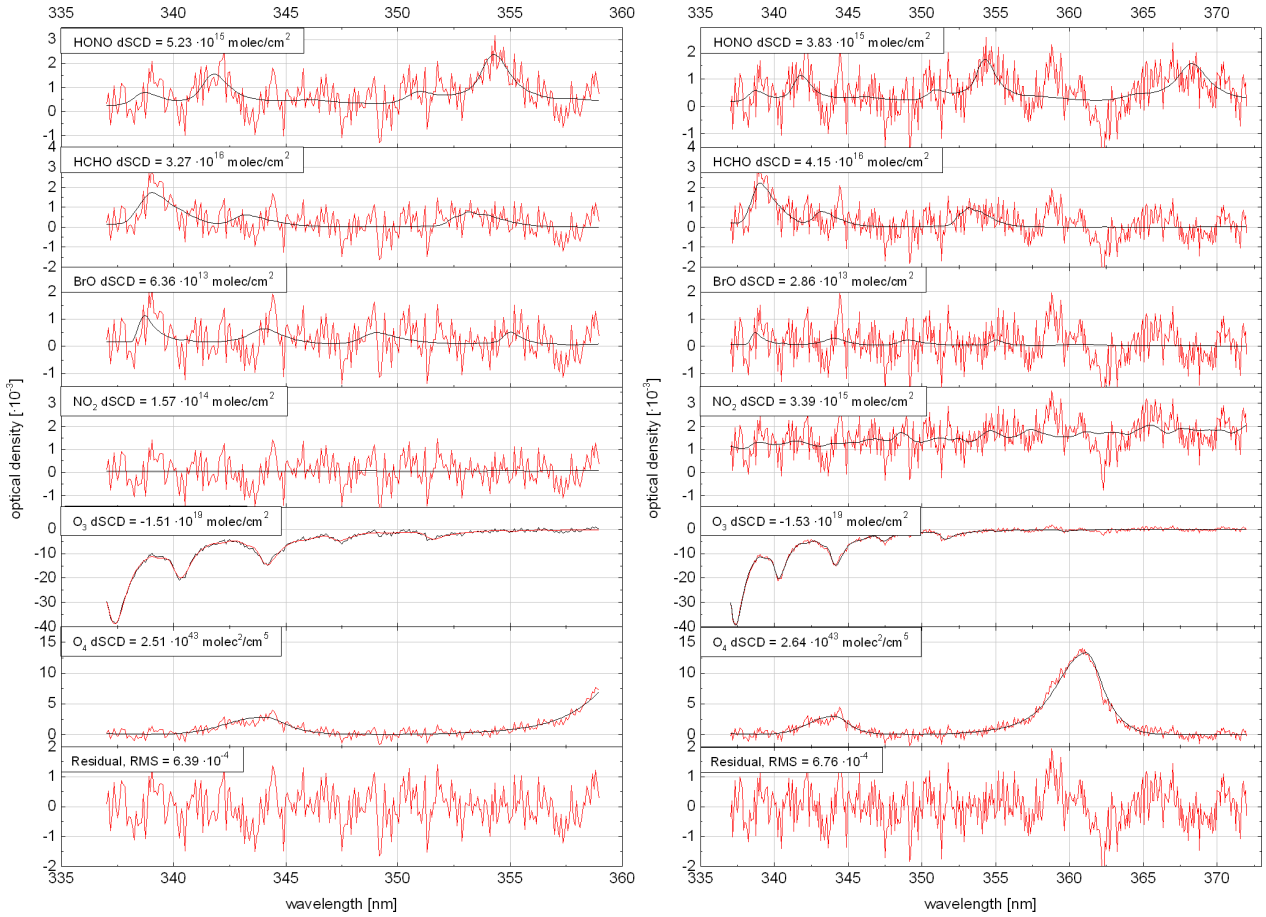

Figure 8.21: Example for a HONO spectral fit in a wavelength range of 337 - 359 nm (left panel) and 337 - 372 nm (right panel) for a spectrum recorded at 5.9°N and 115.6°E at a height of 12.6 km and an SZA = 73.6° at 08:43:49 on 19 November 2011 b. The retrieved spectral signatures are indicated in red and the fitted absorption cross-sections in black.

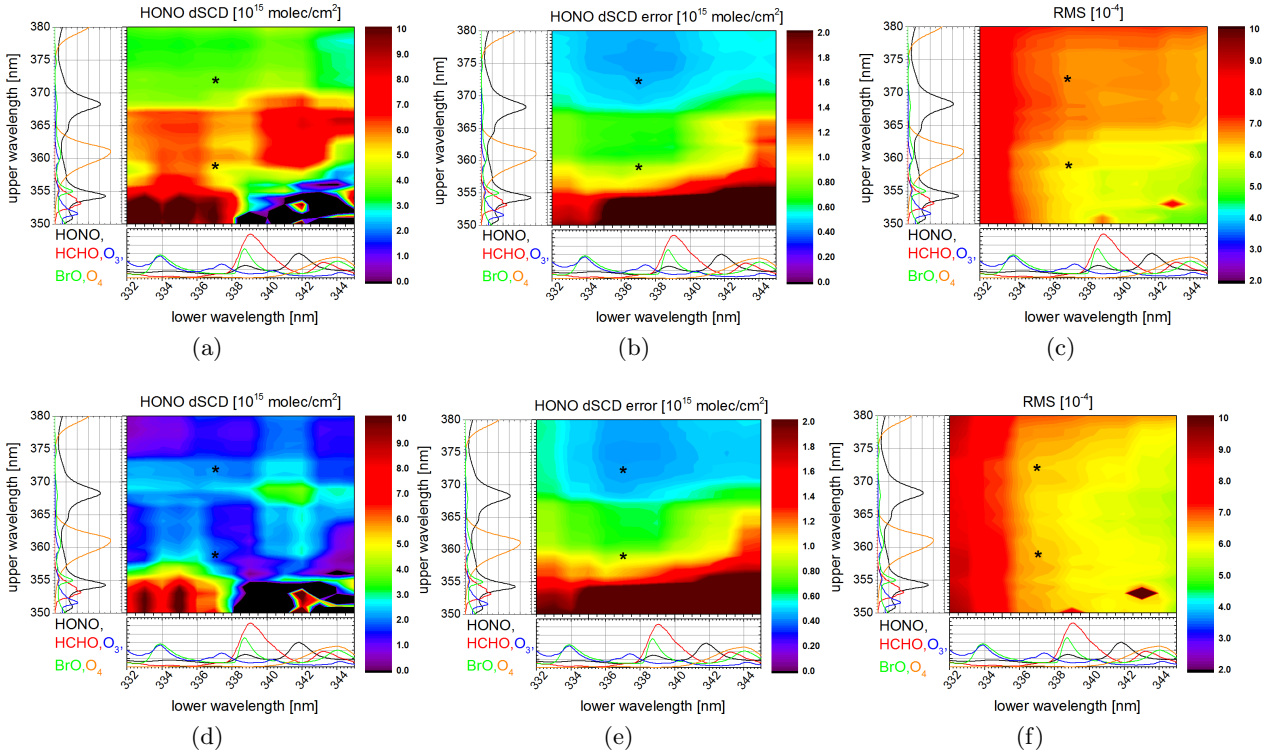

Figure 8.22: Retrieval interval mapping for HONO for the same spectrum used in Figure 8.21 (upper panels) and for a spectrum with less HONO (lower panels). The colour bars in the panels (a) and (d) correspond to the NO_2 dSCDs, (b) and (e) to the NO_2 dSCD error, and (c) and (f) to the RMS, respectively. The black star highlights the chosen wavelength ranges. The absorption cross-sections included in the DOAS spectral fit are shown in the smaller panels.

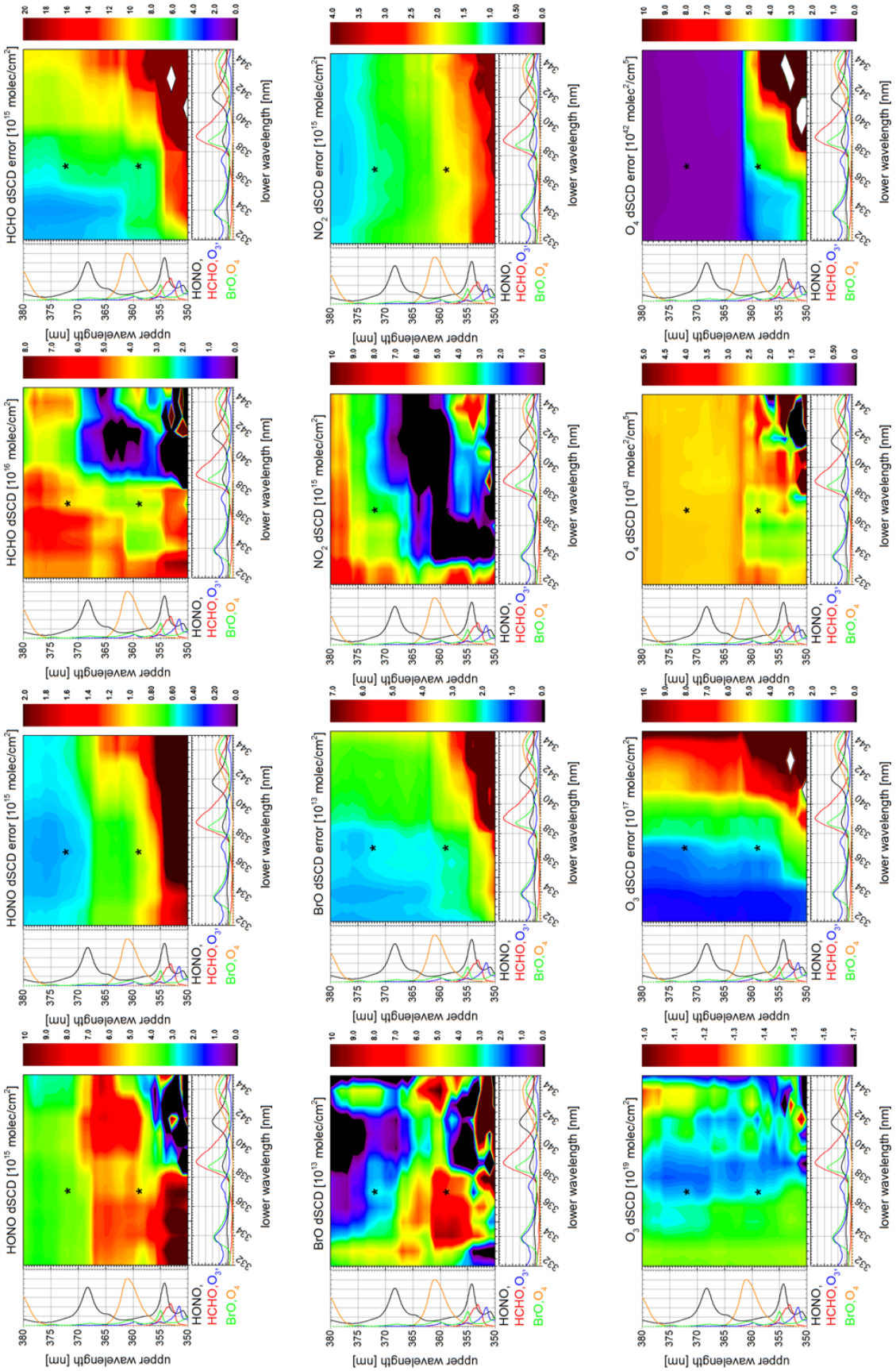

Figure 8.23: Retrieval interval mapping of the dSCDs and respective dSCD errors of all absorbers included in the HONO spectral fit for the same spectrum used in Figure 8.21. The colour bar in each panel corresponds to the dSCDs and dSCD errors of the respective trace gas. The black star highlights the chosen wavelength ranges. The absorption cross-sections included in the DOAS spectral fit are shown in the smaller panels.

8.2.5 Spectral retrieval of CHOCHO

Several studies have shown that the spectral retrieval of CHOCHO is highly sensitive to the chosen retrieval settings, especially to the wavelength range chosen for the evaluation (e.g. Sinreich et al., 2013). In this study, the CHOCHO analysis is performed in the wavelength interval ranging from 447 to 465 nm, encompassing the largest CHOCHO absorption band and avoiding the absorption band of H_2O at approximately 443 (polyad number: 7ν) nm. The absorption cross-sections included in the spectral retrieval are given in Table 8.3 and 8.4. All absorption cross-sections are convolved to the spectral resolution of the instrument using the mercury emission line located at 467 nm. As the chosen wavelength range only encompasses the largest and rather broad CHOCHO band, another retrieval scenario is tested including the same absorption cross-sections. The wavelength range is set from 415 to 465 nm with a gap from 439.5 to 447 nm to avoid the H_2O band at approximately 442 nm. Spectral structures remain in the residual at wavelengths connected to the strong absorption of H_2O. The H_2O literature absorption cross-section is extracted from the HITRAN database (Rothman et al., 2009). This database contains H_2O absorption lines that are both modelled and measured (Section 8.2.7). Hence, the absorption signatures are possibly not reproduced accurately by the H_2O absorption cross-section. This is for example the case for the H_2O absorption bands at 416 (polyad number: $7\nu + \delta$), where changes in the relative absorption band strength can be observed by MAX-DOAS and LP-DOAS measurements on the Cape Verde Islands (Lampel, 2014). Alvarado et al. (2014) recommended to avoid using a lower wavelength limit below 435 nm for the spectral retrieval of CHOCHO due to possible interferences from the Ring effect or errors in the absorption cross-sections of H_2O and NO_2. They further determine an optimal fitting range between 435 nm and 461 nm for CHOCHO measurements from satellite.

Figure 8.25 shows an exemplary DOAS spectral fit for CHOCHO in the chosen wavelength range as well as for the wavelength interval from 415 to 465 nm with a gap between 439.5 and 447 nm. The resulting CHOCHO dSCD is larger for the smaller wavelength interval than for the wider wavelength interval, whereas for the resulting RMS it is the other way around. This can be also seen in the retrieval interval mapping for CHOCHO (Figure 8.24). The wavelength range from 447 to 465 nm yields larger CHOCHO dSCDs but at the same time larger dSCD errors than the second interval. However, as the RMS almost doubles for the larger wavelength range and since the CHOCHO absorption structures at 426 nm are rather small and might be affected by the H_2O absorption band at this wavelength, the final wavelength interval for CHOCHO is set to 447 to 465 nm.

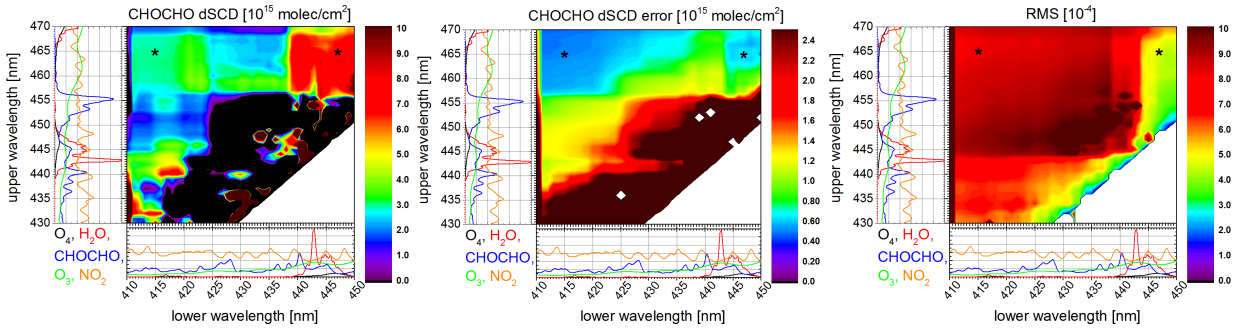

(a) (b) (c)

Figure 8.24: Retrieval interval mapping for CHOCHO for the same spectrum used in Figure 8.25. The colour bar in each panel corresponds to the (a) CHOCHO dSCDs, (b) CHOCHO dSCD errors, and (c) RMS, respectively. The black star highlights the chosen wavelength range. The absorption cross-sections included in the DOAS spectral fit are shown in the smaller panels.

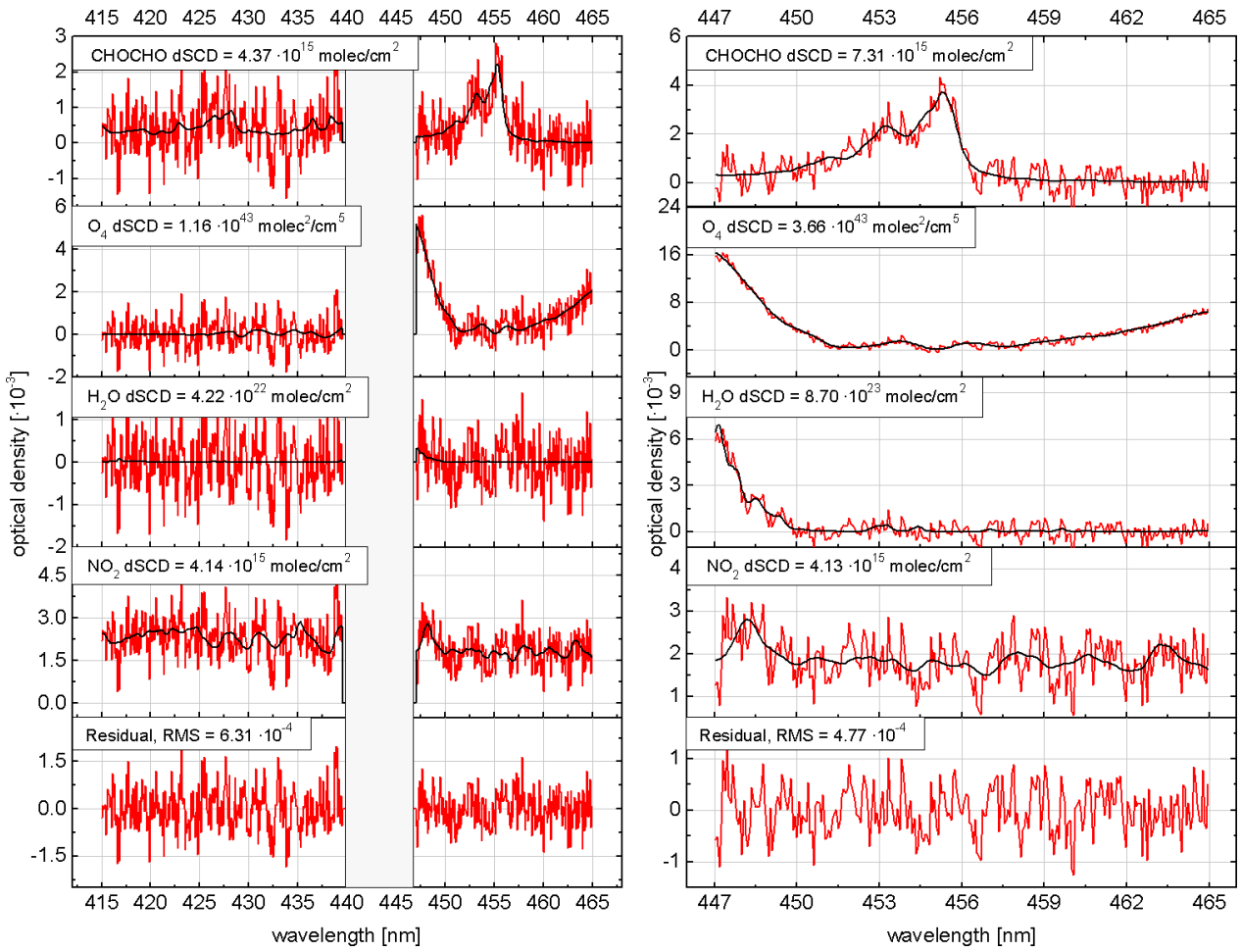

Figure 8.25: Example for an CHOCHO spectral fit in a wavelength range from 415 to 465 nm but leaving a gap from 439.5 to 447 nm (left panel) and from 447 to 465 nm (right panel). The spectrum was recorded at 5.6°N and 118.8°E at a height of 0.32 km and an SZA of 41.3° at 05:59:37 on 9 December 2011. The retrieved spectral signatures are indicated in red and the fitted absorption cross-sections in black.

8.2.6 Spectral retrieval of IO

The IO analysis is performed in the wavelength interval ranging from 415 to 439.5 nm, encompassing three vibrational IO absorption bands. The absorption cross-sections included in the spectral retrieval are listed in Table 8.3 and 8.4. CHOCHO has a small absorption band in the IO fit interval, which coincides with the second IO absorption band at approximately 427 nm. In order to avoid unrealistic large or negative CHOCHO dSCDs or cross-correlations with IO, it is recommended to fix the CHOCHO dSCDs with the values inferred from the CHOCHO spectral retrieval between 447 and 465 nm. All absorption cross-sections are convolved to the spectral resolution of the instrument using the mercury emission line located at 435 nm. Basically, this mercury emission line is a multiple emission line consisting of three emission lines. However, as the visible spectrometer is not able to resolve the three emission lines, it can be regarded as one single emission line. The effect of inelastic vibrational Raman scattering (VRS) by oceanic water on the spectral retrieval of IO has been discussed in Großmann et al. (2013) where the inclusion of a VRS compensation spectrum resulted in approximately 25 % smaller IO dSCD errors and a 10 % smaller RMS. However, including a VRS compensation spectrum into the SHIVA IO DOAS retrieval does not significantly affect the spectral fit result (RMS changes less than 1 %). As the VRS effect cannot be observed within the optical capabilities of the instrument, the VRS compensation spectrum is not included in

the IO spectral retrieval. Figure 8.27 shows the retrieval interval mapping for IO. It is obvious that the IO dSCD error is smallest within the chosen wavelength range and the RMS does not change significantly in this region. Two examples for an IO DOAS spectral fit are shown in Figure 8.26 for two spectra at different altitudes. For the lower altitude (h = 0.33 km) the resulting IO dSCD amounts to $(4.6 \pm 0.7) \cdot 10^{13}$ molec cm^{-2}, which corresponds to a relative dSCD uncertainty (dSCD error/dSCD) of 15 %. For the higher altitude (h = 2.45 km) the resulting IO dSCD amounts to $(5.2 \pm 0.6) \cdot 10^{13}$ molec cm^{-2}, which corresponds to a relative dSCD uncertainty of about 9 %.

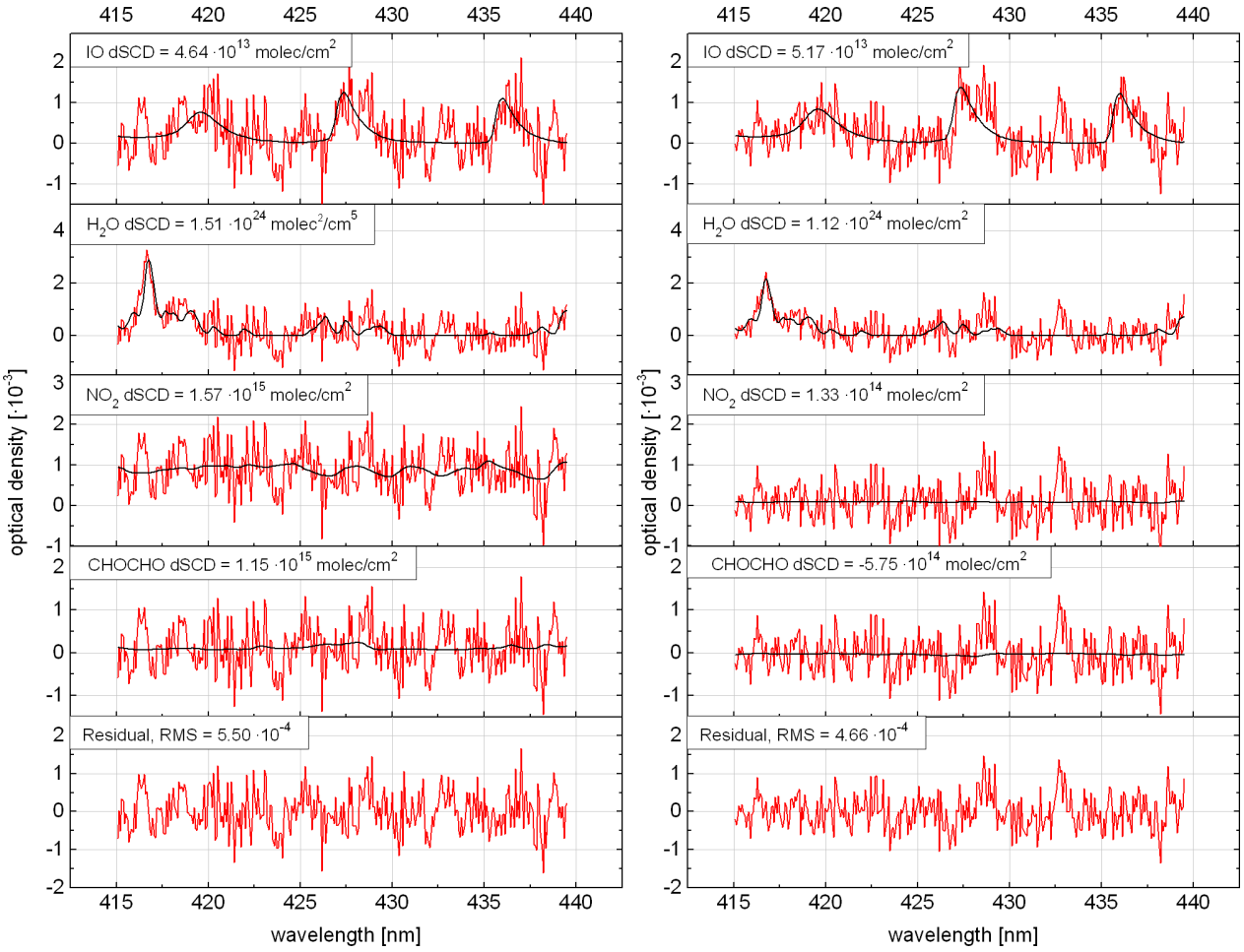

Figure 8.26: Two examples for an IO spectral fit for a spectrum recorded at a height of 0.33 km, an SZA of 39.8°, at 5.6°N and 118.7°W and 05:51:10 UTC (left panel) and for a spectrum recorded at a height of 2.45 km, an SZA of 36.3°, at 5.6°N and 118.8°W and 05:29:49 UTC (right panel) on 9 December 2011 a. The black lines indicate the fitted absorption cross-sections, whereas the red lines indicate the retrieved spectral signatures.

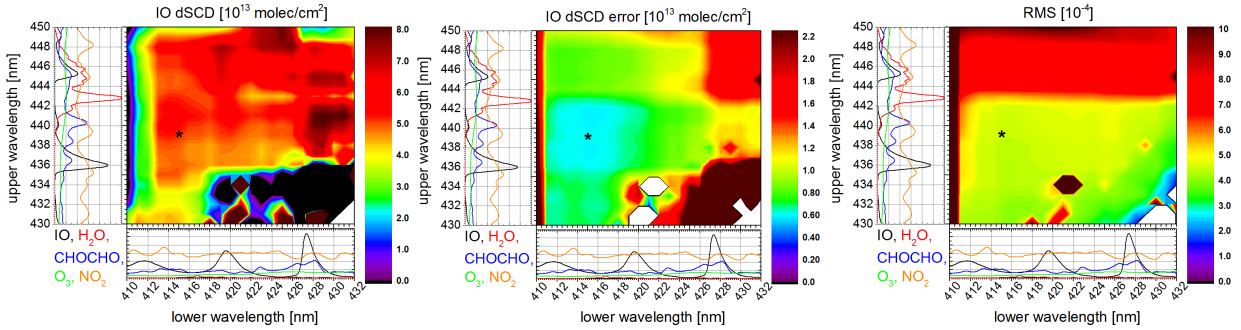

(a) (b) (c)

Figure 8.27: Retrieval interval mapping for IO for the spectrum analysed in the right panel of Figure 8.26. The colour bar in each panel corresponds to the (a) IO dSCDs, (b) IO dSCD errors, and (c) RMS, respectively. The black star highlights the chosen wavelength range. The absorption cross-sections included in the DOAS spectral fit are shown in the smaller panels.

8.2.7 Spectral retrieval of H_2O

The H_2O analysis is performed in the wavelength interval ranging from 440 to 485 nm, encompassing two strong H_2O absorption bands at approximately 443 nm (polyad number: 7ν) and 470 nm (polyad number: $6\nu + \delta$). The absorption cross-sections included in the spectral retrieval are listed in Table 8.3 and 8.4.

A typical example of the retrieved H_2O absorption is shown in Figure 8.28 for the same spectra as in Figure 8.16. The resulting H_2O dSCD amounts to $(1.18 \pm 0.01) \cdot 10^{24}$ molec cm^{-2}, which corresponds to a signal-to-noise ratio of approximately 100. However, large residual structures remain especially between 440 and 445 nm where the first strong H_2O band is located. The RMS with approximately 1 $\cdot 10^{-3}$ is therefore quite large. This is possibly because some lines of the H_2O absorption cross-section from the HITRAN database (Rothman et al., 2009) are calculated and do not coincide with real measurements. An incorrect assignment of even weaker water vapour lines is particularly relevant for measurements in the tropics where water vapour concentrations are large. Lampel (2014) performed sensitivity studies for different H_2O absorption cross-sections. Apparently, in the updated H_2O absorption cross-section from the 2012 HITRAN database (Rothman et al., 2013) the absorption bands at 416 nm and 424 nm have changed compared to the 2009 HITRAN version. According to Lampel (2014), who fitted these absorption lines in a separate DOAS evaluation, the absorption lines of the 2012 absorption cross-section are probably too large, but their shape seems to be better reproduced by the DOAS spectral fit than the 2009 version. Although the updated H_2O absorption cross-section from 2012 shows a better shape for the single lines, the HITRAN H_2O absorption cross-section from 2009 results in an overall better DOAS spectral fit. In this study, the H_2O absorption cross-section from 2009 is chosen for the retrieval. Switching from the HITRAN 2009 to the HITRAN 2012 H_2O absorption cross-section yields a 7 % lower dSCD and a slightly higher dSCD error (2 %). Figure 8.29 shows the retrieval interval mapping for H_2O. Including the strong H_2O band at around 443 nm into the DOAS spectral fit clearly enlarges the RMS by about 20 %, whereas the dSCD error is reduced by a factor of about 4. Hence, the strong absorption band at 443 nm is included in the DOAS spectral fit. Wang et al. (2014) use an almost similar wavelength range from 430 to 480 nm for evaluating H_2O from the OMI satellite where the median fitting uncertainty of the H_2O SCDs yields 1.2 $\cdot 10^{22}$ molec cm^{-2}, which corresponds to a relative SCD uncertainty of 11 %.

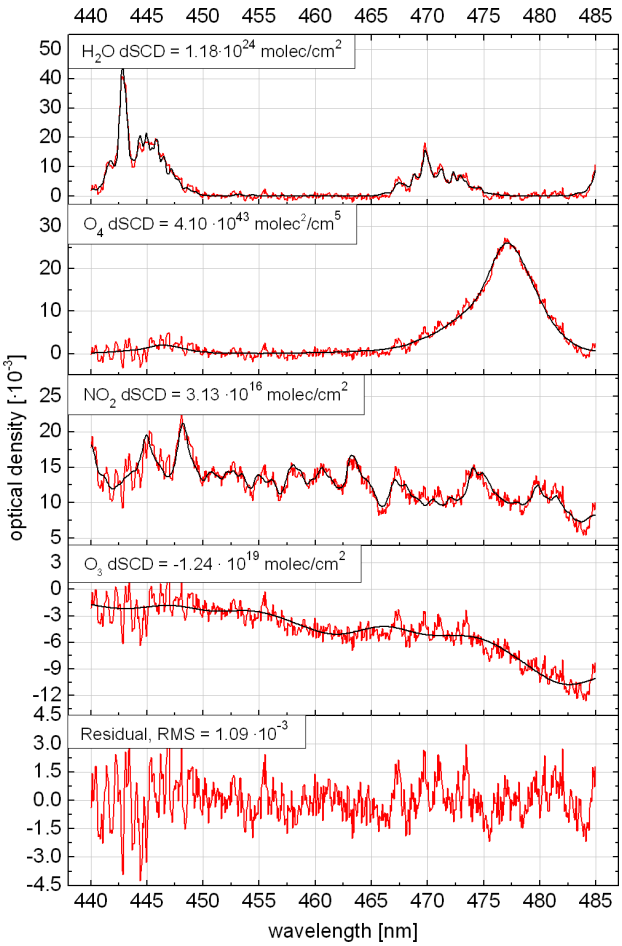

Figure 8.28: Example for an H_2O spectral fit applied on the same spectrum as in Figure 8.16. The retrieved spectral signatures are indicated in red and the fitted absorption cross-sections in black.

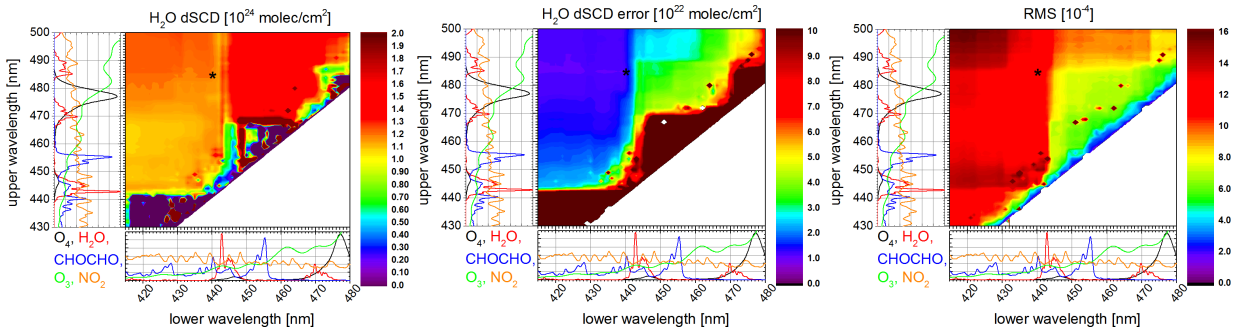

(a) (b) (c)

Figure 8.29: Retrieval interval mapping for H_2O for the spectrum analysed in Figure 8.28. The colour bar in each panel corresponds to the (a) H_2O dSCDs, (b) H_2O dSCD errors, and to the (c) RMS, respectively. The black star highlights the chosen wavelength range. The absorption cross-sections included in the DOAS spectral fit are shown in the smaller panels.

Figure 8.30a shows the optical density of H_2O derived from a high resolution literature absorption cross-section from the HITRAN database (Rothman et al., 2009) and from the absorption cross-section convolved with the slit function located at 467 nm. The optical density τ is calculated

according to the following equation:

$$\tau = -\ln(\exp^{-\sigma(\lambda)\cdot S} * H(\lambda)), \tag{8.5}$$

with $\sigma(\lambda)$ being the literature absorption cross-section of H_2O, S the H_2O SCD typically observed during the SHIVA campaign ($\approx 1 \cdot 10^{24}$ molec cm^{-2}), and $H(\lambda)$ being the slit function. It can be seen that the maximum optical density of the convolved spectrum is much lower than the maxima of the high resolution literature absorption cross-section. Curves of growth are thus calculated for each water vapour peak that is located in the wavelength range of the USB spectrograph, i.e. for λ = 442.73 nm, 469.72 nm, 485.13 nm, 503.78 nm (Figure 8.30b). The H_2O line of the 525 nm band is not used, since they are close to the upper limit of the available wavelength range of the spectrograph. For this analysis the H_2O SCDs are varied between 0.1 and 5 $\cdot 10^{24}$ molec cm^{-2}. The H_2O SCDs typically observed during the SHIVA campaign are lower than approximately 1.5 $\cdot 10^{24}$ molec cm^{-2}. The spectral analysis of H_2O is performed in the wavelength region below 485 nm, i.e. the line at 503 nm is not used. Thus, it can be concluded that the H_2O absorption is linear for the chosen SCD range and does not suffer from saturation problems.

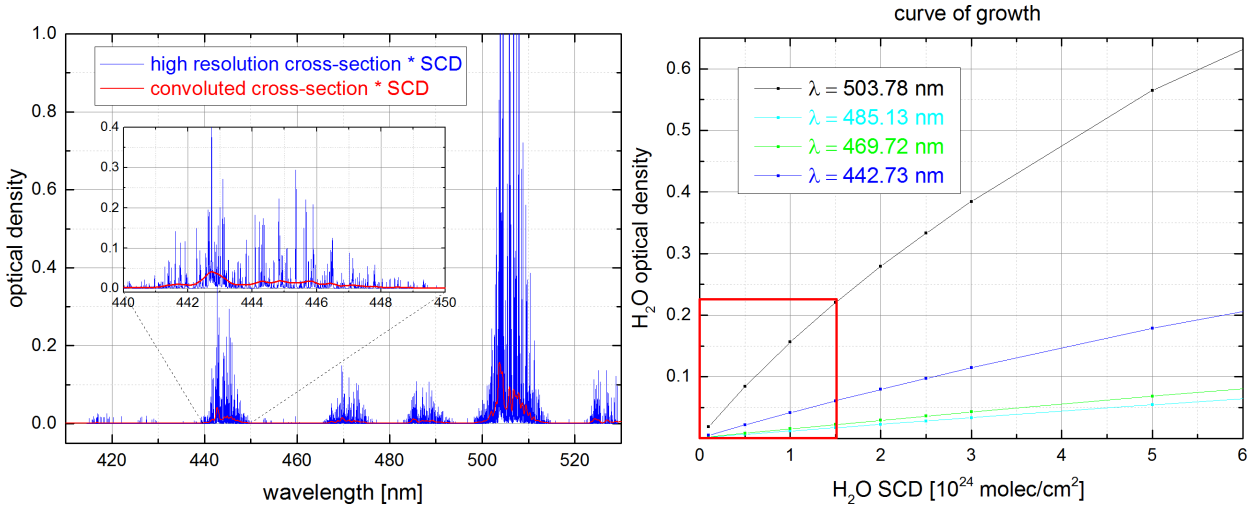

(a) (b)

Figure 8.30: (a) Comparison of the high resolution optical density and convolved apparent optical density of water vapour calculated for an SCD of $1 \cdot 10^{24}$ molec cm^{-2}. (b) Curves of growth for four different wavelengths.The red box highlights the region that represents the conditions encountered during the SHIVA campaign.

8.3 Error sources and detection limit

DOAS measurements and the spectral retrieval of dSCDs are subject to statistical as well as systematic errors. The main statistical error is due to photoelectron shot noise, which can be reduced by co-adding several spectra (Section 8.1). For an ideal DOAS instrument, this photoelectron shot noise is the limiting factor of the signal-to-noise ratio (e.g. Platt and Stutz, 2008). At a certain number of photons ($n_{\mathrm{phot_{QE}}} \approx 5.5 \cdot 10^7$ and $n_{\mathrm{phot_{USB}}} \approx 2.8 \cdot 10^8$, Appendix B) or co-added scans ($n_{\mathrm{QE}} \approx 60$ and $n_{\mathrm{USB}} \approx 900$, Appendix B), the noise does not further decrease. As the main statistical error is dominated by photoelectron shot noise, the number of photons recorded within a certain time interval is Poisson-distributed. At a large number of photons, this Poisson distribution can be approximated by a Gaussian distribution with the standard deviation σ.

Systematic structures in the residual can occur e.g. due to unknown absorbers or inaccurate absorption cross-sections. Cross-correlations between different absorption cross-sections that exhibit

absorption structures at similar wavelengths can cause further residual structures. In addition, instrumental effects as e.g. errors in the wavelength calibration or changes of the slit function due to instabilities of the instrument can lead to systematic errors (e.g. Platt and Stutz, 2008). The basic DOAS spectral fit error calculated e.g. with the software *WinDOAS* does not take into account any systematic errors and is determined under the assumption that the residual only consists of random noise. The standard deviation σ of a Gaussian distribution is used as the spectral fit error of the DOAS evaluation. Thus, the spectral fit error might underestimate the real measurement error depending on the shape of the residual structures. A correction factor $C(\tau, W)$ for a random residual spectrum is introduced by Stutz and Platt (1996), which is determined by Monte-Carlo simulations and has to be applied to the spectral fit error. It depends on the width of the absorption structures τ and the width of the residual structures W (Figure 8.31).

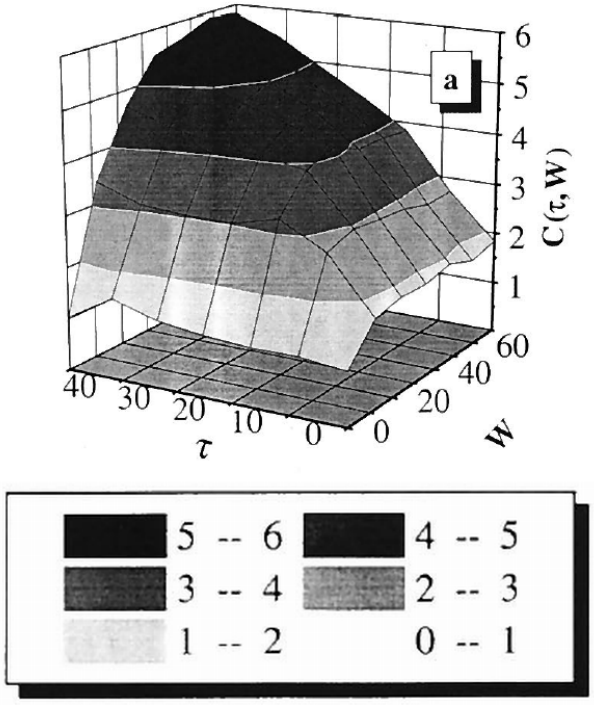

Figure 8.31: Correction factor $C(\tau, W)$ to obtain the measurement error from the spectral fit error calculated by Monte Carlo experiments. C depends on the width of the absorption structures τ and the width of the residual structures W, adapted from Stutz and Platt (1996).

If the parameter W is larger than 1, the residual is dominated by structures other than noise. Typically, the correction factor is two, i.e. the fit error underestimates the measurement error by a factor of two. If the residual is dominated by pure photoelectron shot noise, the factor can reach values smaller than 1. This correction factor is only valid for randomly generated Gaussian residuals. However, assuming a Gaussian distributed error is usually not the case for real measurements. Therefore, residual structures should be analysed thoroughly, e.g. with a principal component analysis (PCA) of the residual (Section 8.1). For measurements where a constant concentration of an absorber is expected, Holla (2013) and Lampel (2014) proposed to compare histograms of the measured dSCDs to receive an alternative estimate for this correction factor. In the following, different systematic errors are analysed.

8.3.1 Systematic errors

Uncertainties in the literature absorption cross-sections

Different literature absorption cross-sections exist for each absorber. The systematic error that arises when using different literature absorption cross-sections can be estimated to be approximately up to 10 % (e.g. for the spectral retrieval of O_4 in the UV, see Section 8.2.1).

Temperature dependence of the literature absorption cross-sections

The shape and absolute values of the various literature absorption cross-sections show a strong dependence on temperature due to the temperature-dependent occupation of the vibrational and rotational bands and since absorption occurs at different altitudes in the atmosphere and thus at different temperatures (e.g. Platt and Stutz, 2008). This effect can be accounted for by including several absorption cross-sections of the same trace gas species in the DOAS retrieval measured at different temperatures. The absorption cross-sections of the same species have to be orthogonalised to each other, in order to avoid correlations (Van Roozendael and Fayt, 2001). In this thesis, a correction for the temperature dependence of the O_3 absorption cross-section is implemented in the DOAS retrieval, i.e. O_3 absorption cross-sections at two different temperatures are included in the DOAS spectral retrieval.

Influence of the slit function

It is typically assumed in DOAS evaluations that the slit function is constant over the whole wavelength range. Figure 8.32 shows a comparison of the shape of the different mercury and cadmium emission lines that can be detected by the present instrument.

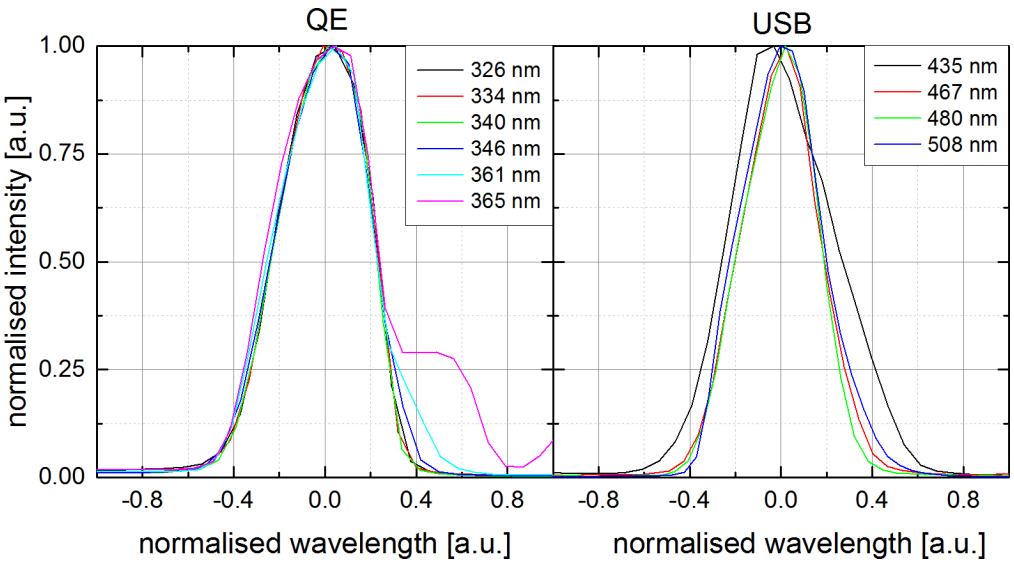

Figure 8.32: Comparison of the shape of the mercury and cadmium lines in the UV (left panel) and in the visible wavelength range (right panel) for a spectrum recorded on 16 November 2011. The wavelength and intensity axes are normalised and given in arbitrary units.

The background intensity is subtracted from each line, i.e. the minimum intensity in the wavelength range around the emission line. If the background signal below the emission line is not correctly subtracted, an offset in the inferred dSCDs might occur. A Gauss function is further fitted to the emission line to define the centre wavelength. The wavelength range of the line is then shifted to this centre position. The intensity of each emission line is then area-normalised as well

as normalised to one. It has to be noticed that not all lines are single emission lines, some emission lines are double emission lines (Table 8.1), which are not fully resolved by the instrument. The shape and FWHM of the single emission lines in the UV (326 nm, 334 nm, 340 nm, 346 nm) and in the visible wavelength range (467 nm, 480 nm, 508 nm) do not change significantly over the total spectral range, respectively. The double emission lines in the UV (361 nm, 365 nm) are slightly broader than the single emission lines, whereas the double emission line at 435 nm has a different shape and is significantly broader than the single emission lines in the visible wavelength range. The baseline of the background signal below each slit function is not always identical on both sides of the emission line. The minimum signal of the emission line might not be representative for the total range of the peak. A possible reason for small changes in the convolved absorption cross-sections and thus in the inferred dSCDs might be due to this remaining baseline in the background signal after subtracting the minimum signal. Thus, for further applications, it is recommended to fit a straight line to the background baseline and subtract this line from the intensity instead of simply subtracting the minimum intensity.

Figure 8.33 shows the absorption cross-sections of O_4, HCHO and NO_2 convolved with the different slit functions. In the UV, the absorption cross-sections of O_4 and HCHO convolved with a single emission line are almost identical, whereas the absorption cross-sections convolved with a double emission line are much smaller. In the visible wavelength range, the absorption cross-sections of O_4 and NO_2 convolved with the slit function at 480 nm and 508 nm are almost identical. The absorption cross-section convolved with the slit function at 467 nm shows a smaller absorption structure than the other absorption cross-sections convolved with a single emission. The absorption cross-sections convolved with the double emission line at 435 nm shows a similar shape than the absorption cross-sections convolved with the slit function at 467 nm.

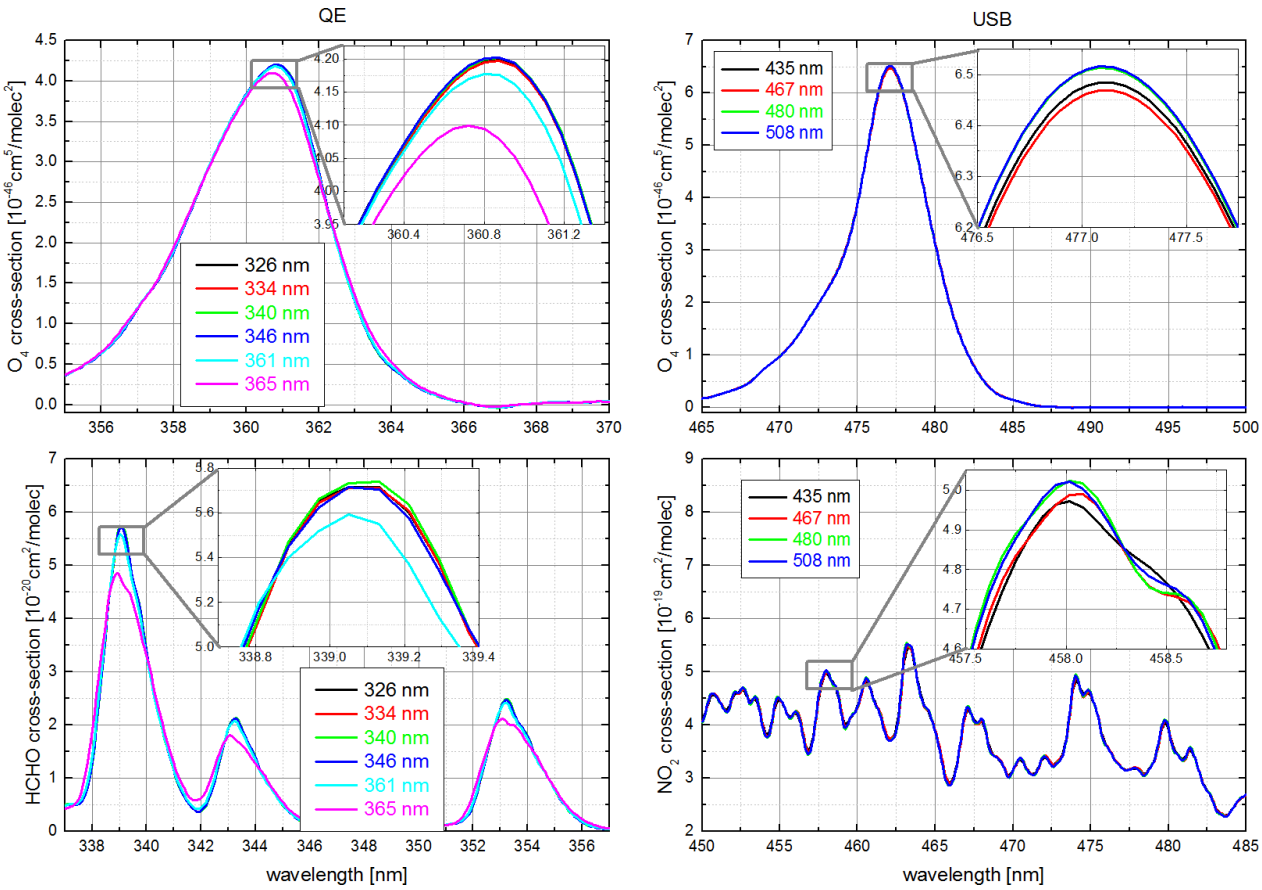

Figure 8.33: Cross-sections of O_4, HCHO and NO_2 convolved with the different slit functions from Figure 8.32.

In Figure 8.34, the different slit functions are used to evaluate O_4 and HCHO in the UV as well as O_4 and NO_2 in the visible wavelength range. Obviously, the resulting dSCDs differ depending on the slit function that is used to convolve the absorption cross-sections. It can be expected that for a broad slit function, the differential structures are smaller and thus the resulting dSCDs are larger than for a narrow slit function. The O_4 and HCHO dSCDs in the UV convolved with a single emission line agree very well with each other with an average deviation of less than 1 %. When using a double emission line as a slit function (361 nm, 365 nm), the dSCDs increase showing the largest values for the slit function at 365 nm. The O_4 dSCDs in the UV show a maximum deviation of approximately $(0.1-0.2)\cdot 10^{43}$ molec^2 cm^{-5} ($\approx$ 7 %) and the HCHO dSCDs result in a maximum deviation of approximately $1\cdot 10^{16}$ molec cm^{-2} ($\approx$ 30 %) between the dSCDs evaluated with a single emission and a double emission line. In the visible wavelength range, the difference between the dSCDs convolved with a single emission line is larger than in the UV and results in a maximum deviation of roughly $0.1\cdot 10^{43}$ molec^2 cm^{-5} ($\approx$ 3 %) for O_4 and approximately $(0.5)\cdot 10^{15}$ molec cm^{-2} ($\approx$ 4 %) for NO_2. Largest dSCDs are received for the slit function at 435 nm, which is a double emission line. However, the NO_2 dSCDs evaluated with the slit function at 467 nm are almost as large as the dSCDs evaluated using the double emission line at 435 as a convolution kernel. The reason for this remains unclear. It is recommended to only use single emission lines as a slit function. The dSCD variations due to a different slit function are smaller or of the order of the dSCD error. Thus, the influence of the shape of the slit function on the inferred dSCDs can be neglected in the analysis.

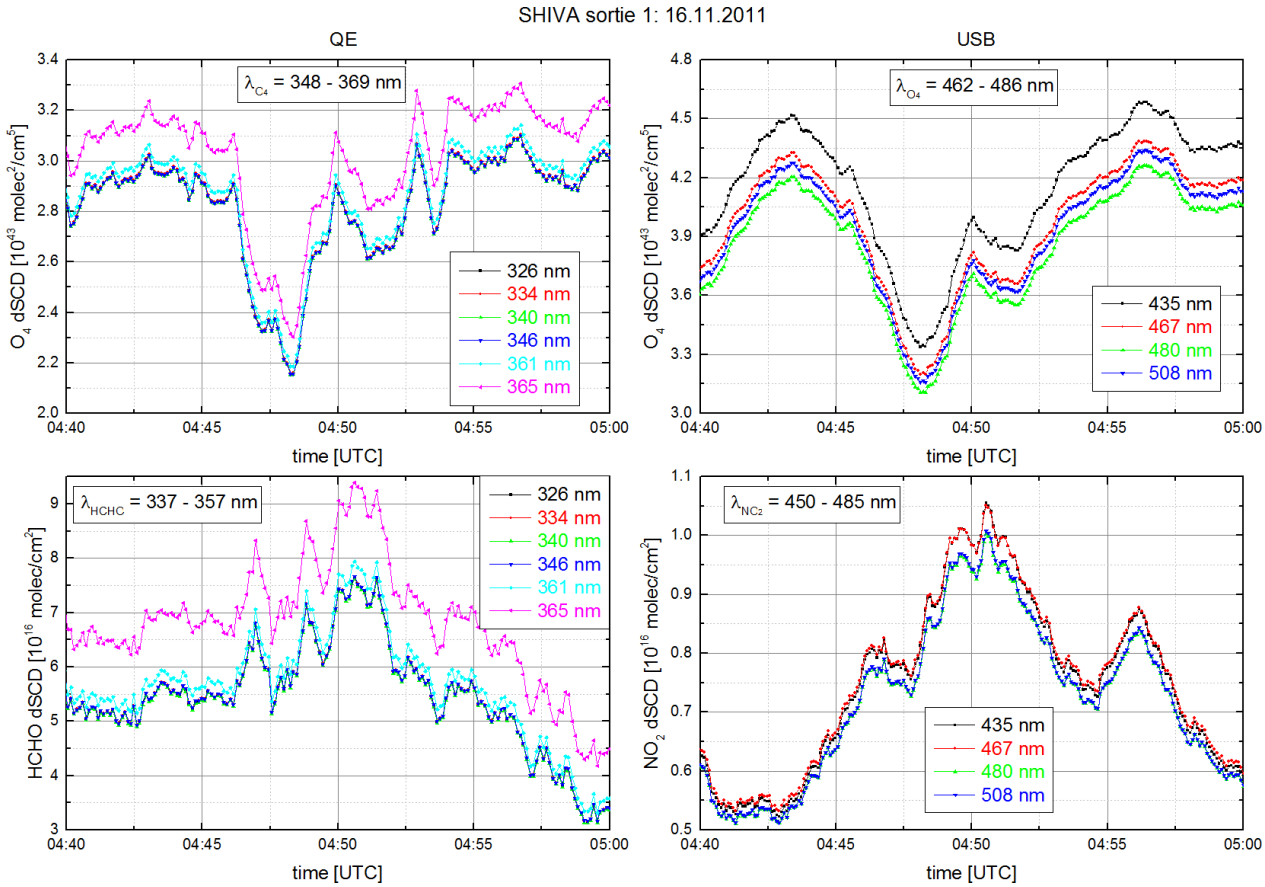

Figure 8.34: Inferred dSCDs of O_4, HCHO and NO_2 for the different slit functions from Figure 8.32 for a period of 20 minutes on 16 November 2011.

Influence of the *WinDOAS* convolution tool

A minor error has been detected in the convolution tool of the software *WinDOAS* (Caroline Fayt, IASB/BIRA, Brussels, personal communication June 2014). This error has been fixed in the software *QDOAS*, which is the successor of *WinDOAS*. In order to estimate the systematic error of this error, the absorption cross-sections are convolved with *WinDOAS*, *QDOAS* and *DOASIS*, respectively and compared to each other (Figure 8.35). Obviously, the absorption cross-sections convolved with *QDOAS* and *DOASIS* agree very well with each other, whereas the absorption cross-sections convolved with *WinDOAS* are slightly shifted to higher wavelengths by approximately 0.08 nm. In order to assess the total dSCD error that results from the error in the *WinDOAS* convolution, the dSCDs of an exemplary flight (16 November 2011) are inferred in *WinDOAS* using the absorption cross-sections convolved with *WinDOAS*, *QDOAS* and *DOASIS*, respectively. Figure 8.36 shows a section of five minutes of that flight. Overall, the dSCDs inferred with absorption cross-sections that are convolved with *QDOAS* and *DOASIS* are similar. For the O_4 dSCDs, the average deviation between the dSCDs inferred with the *WinDOAS* convolution tool and retrieved with the *QDOAS*/*DOASIS* convolution tool vary by less than 1 % and can thus be neglected. The HCHO dSCDs inferred with the *WinDOAS* convolution are approximately 6 % smaller than the dSCDs inferred with the *QDOAS* convolution tool, whereas the NO_2 dSCDs are approximately 2 to 3 % larger. The dSCD error divided by the dSCD average over the whole flight results in approximately 2 % for O_4 in the UV and visible wavelength range, 13 % for HCHO and 12 % for NO_2. The variations due to the error in the *WinDOAS* convolution tool are smaller than the averaged dSCD errors and lie within the error bars of the dSCD error. Nevertheless, for future DOAS evaluations, the software *WinDOAS* should be replaced by the software *QDOAS* to avoid this systematic error.

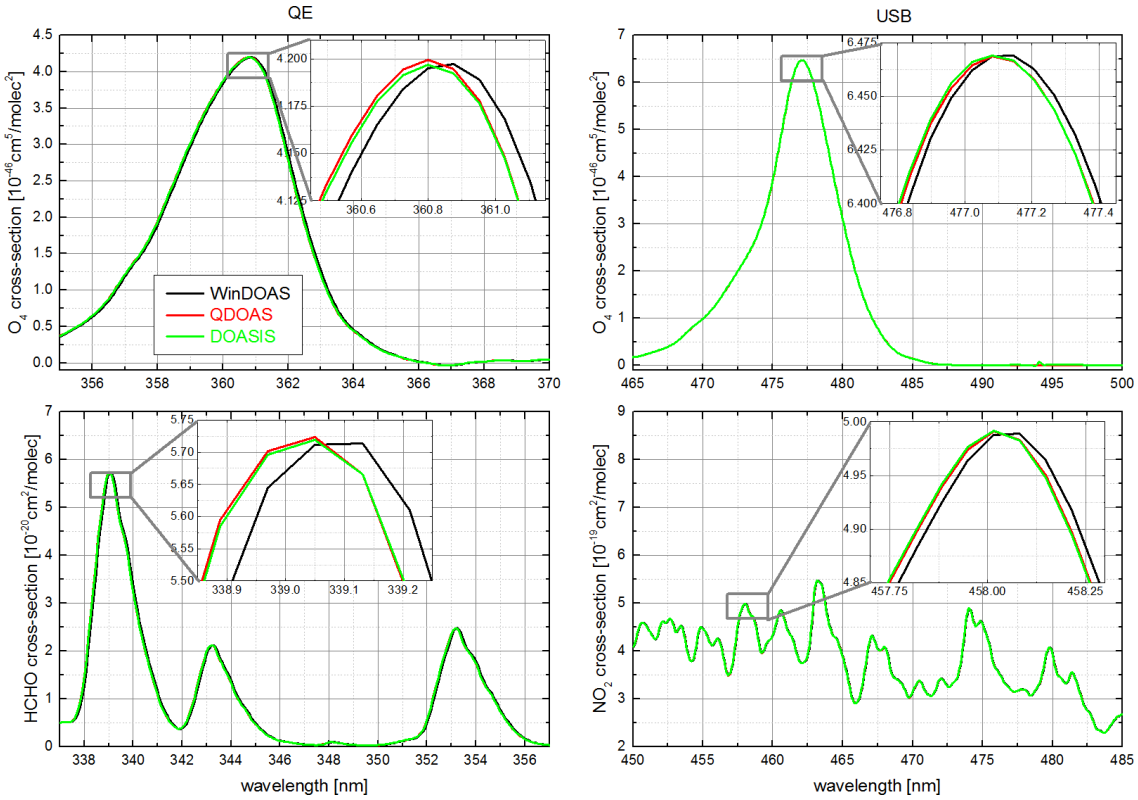

Figure 8.35: Absorption cross-sections of O_4, HCHO and NO_2 convolved with *WinDOAS*, *QDOAS* and *DOASIS* using the slit function at 334 nm for the UV (left panels) and at 467 nm for the visible wavelength range (right panels).

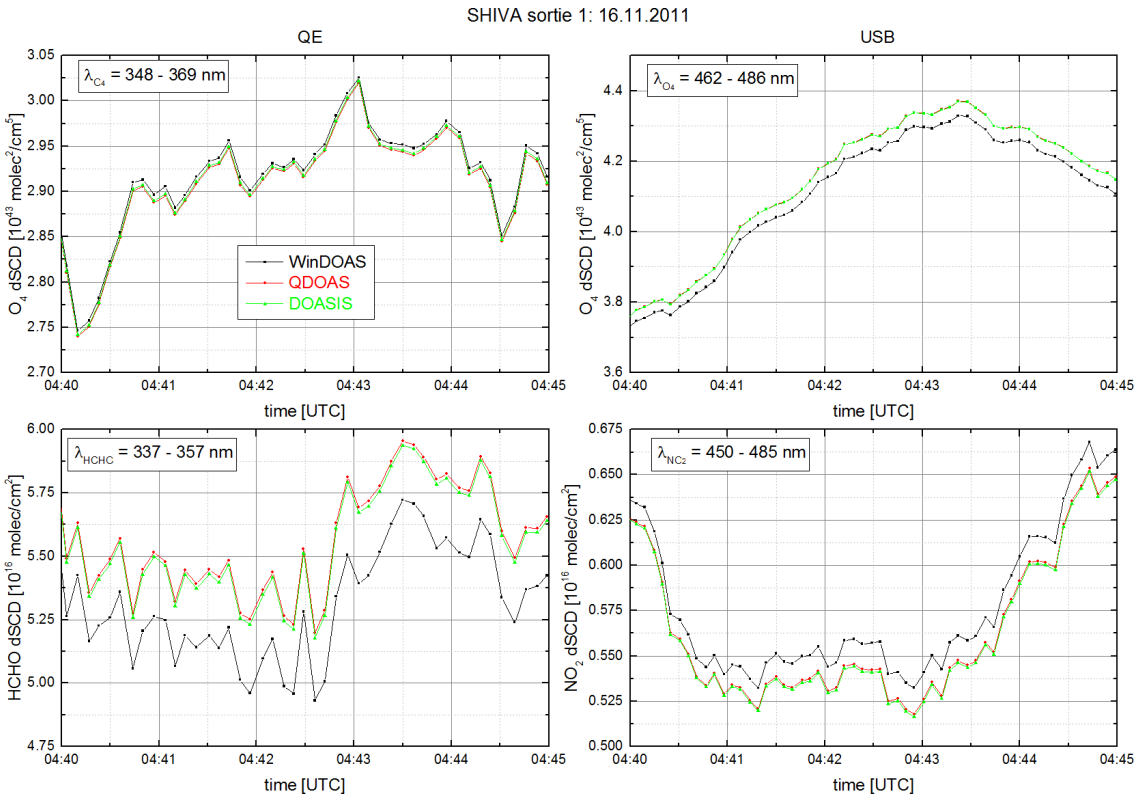

Figure 8.36: O_4 and HCHO dSCDs in the UV (left panels) and O_4 and NO_2 dSCDs in the visible wavelength range (right panels) inferred with the *WinDOAS* programme and using the absorption cross-sections convolved with *WinDOAS*, *QDOAS* and *DOASIS* programmes from Figure 8.35, respectively.

Influence of spectrometer stray light

Possible stray light of the instrumental set-up can be accounted for in the DOAS spectral fitting procedure by including an additional stray light polynomial. In order to estimate the systematic error that arises due to instrumental stray light, an exemplary flight (sortie 1 on 16 November 2011) is evaluated without using a stray polynomial, including a constant stray light polynomial as well as a polynomial of first and second order. Figure 8.37 shows the results of this analysis for O_4, HCHO and NO_2. As it can be seen from this Figure, the RMS is largest when no offset is included. In the UV, including a stray light polynomial reduces the RMS by approximately (0.5 - 1) $\cdot 10^{-4}$, i.e. by approximately 10 - 15 %, whereas in the visible wavelength range the RMS is only reduced by approximately 0.2 $\cdot 10^{-4}$, i.e. by approximately 2 - 6 %, excluding the stray light polynomial of the order of two. For O_4 in the UV as well as in the visible wavelength range, the order of the polynomial is rather not relevant, as a constant polynomial leads to almost the same dSCDs as a polynomial of the order of one or two. For HCHO, the RMS and dSCDs slightly change when using a different order of polynomial with the lowest RMS values for the case using a stray light polynomial of first order. For NO_2 it is not unambiguous, which polynomial order leads to the optimal result. Basically, the order of the polynomial should be as small as possible and as large as necessary. In this study, a polynomial of the order of one is chosen for the spectral analysis.

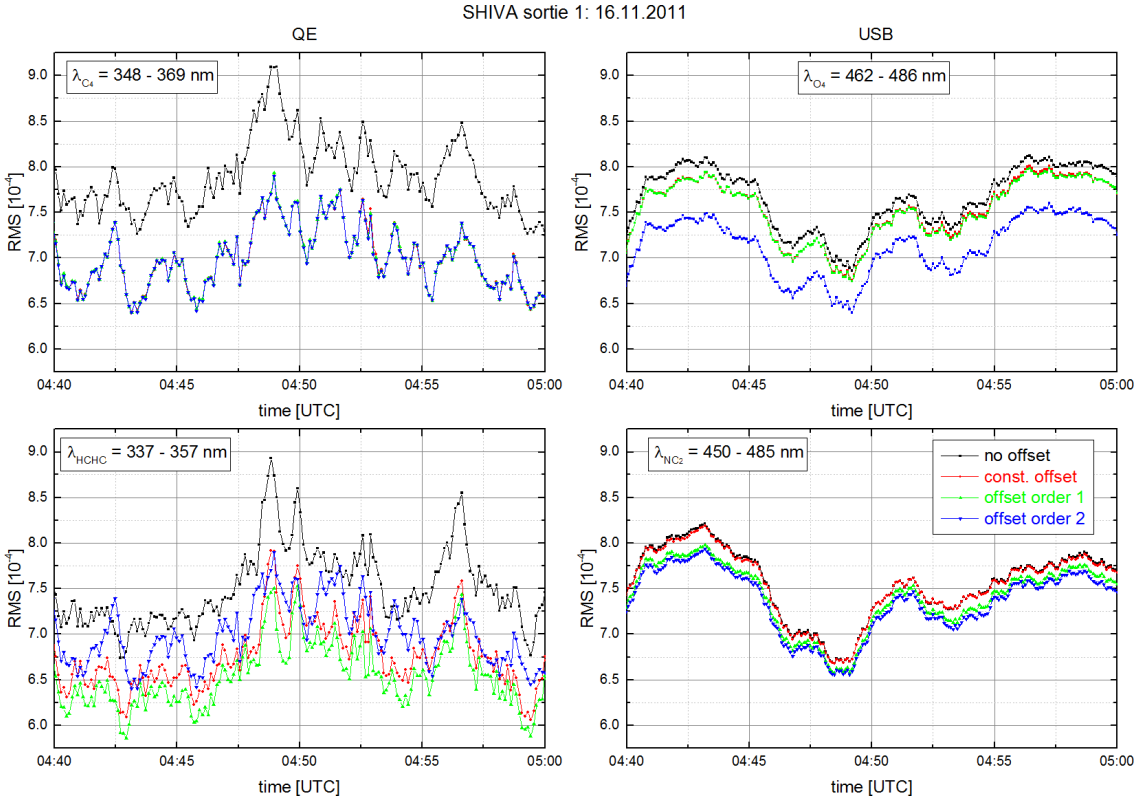

(a)

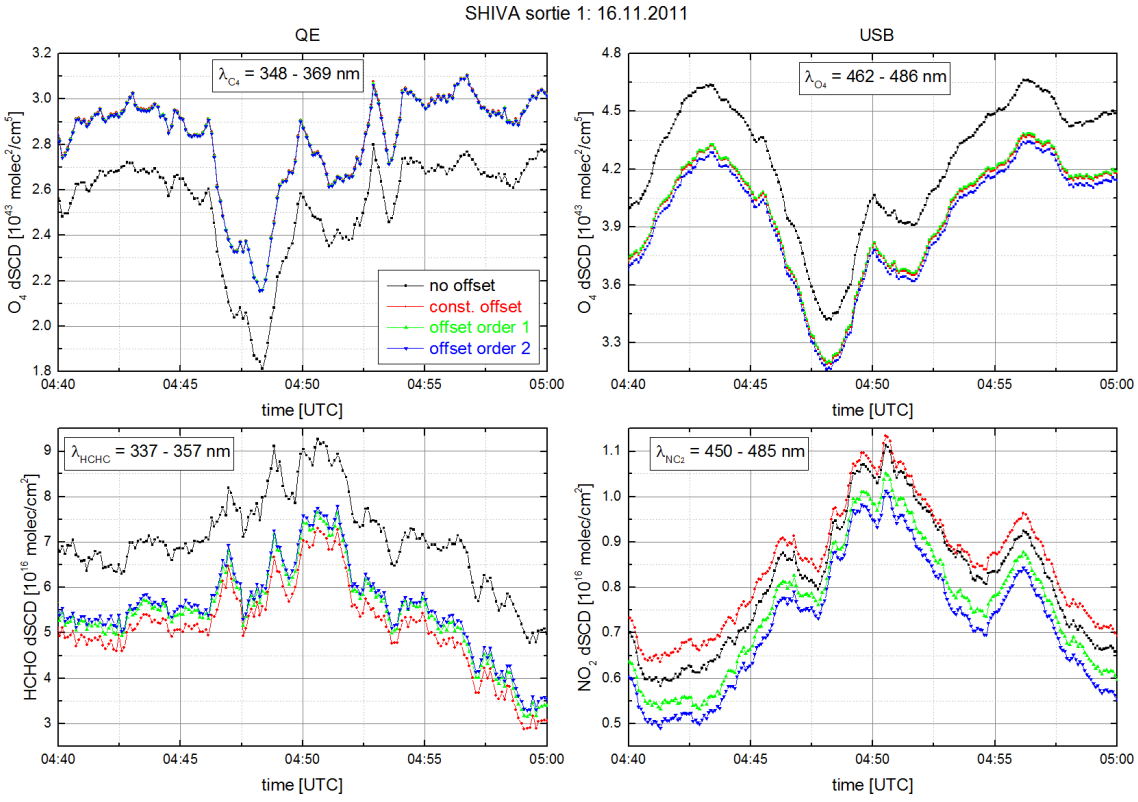

(b)

Figure 8.37: Influence of the stray light polynomial (a) on the RMS and (b) on the inferred dSCDs of O_4 and HCHO in the UV (left panels) and of O_4 and NO_2 in the visible wavelength range (right panels), respectively for sortie 1 on 16 November 2011.

8.3.2 Detection limit

The detection limit specifies the value above which the concentration of an absorber can be regarded to be significantly above the background noise. The detection limit of a dSCD depends on the quality of the measurement and can be defined by two different methods. If the differential optical density of a trace gas is larger than the noise, it is above the detection limit and can be detected. Thus, the detection limit can be calculated by dividing the peak-to-peak value Δ of a typical residual by the maximum value of the respective absorption cross-section:

$$S_{dl,i} = \frac{2 \cdot \Delta}{\sigma_i}. \tag{8.6}$$

The second method to derive the detection limit is based on the standard deviation σ of the inferred dSCDs of the respective trace gas (Stutz and Platt, 1996). The detection limits used in this study refer to a 2σ measurement error. That means, if the 2σ range of an ensemble of measured dSCDs is entirely above zero, the measured dSCDs can be regarded to be significant, having a probability of more than 95.4 %. As mentioned above, it is assumed that the distribution of the fit error is Gaussian and only consists of noise. Thus, the detection limit that is specified here, is rather a well-tempered detection limit ignoring any remaining systematic structures in the residual.

9. Quantification of the influence of clouds on trace gas measurements

The atmospheric conditions prevailing during the SHIVA campaign were rather complex with both horizontally and vertically varying cloud fields. Typically, these cloud fields comprised different cumulus cloud layers in the MBL and large convective cloud cells reaching from the ground to the free troposphere. Obviously, for the atmosphere encountered during the SHIVA a 1D parameterisation of the RT is not sufficient, since 3D effects due to the horizontally and vertically inhomogeneous atmosphere might play a role.

Information about cloudiness can be obtained from several satellites, such as from MODIS (Section 6.2.3). Figure 9.1 shows satellite images of Borneo from the MODIS instrument for the different flight days during the SHIVA campaign. As it can be seen from the satellite images, clouds are present over Borneo during every day. The distribution of the cloud cover varies from small cloud patterns to large cloud cells covering several degrees of latitude and longitude. Since clouds have a strong influence on the radiative transport in the atmosphere (Section 5.6), it is important to receive information about the altitude of the cloud cover, the spatial distribution and patchiness of clouds as well as their properties like the cloud extinction or single scattering albedo.

In this chapter, different approaches are introduced to learn more about the influence of clouds on DOAS measurements. Section 9.1 deals with cloud identification from DOAS observations and the different DOAS observables that are influenced by clouds. Section 9.2 presents cloud sensitivity studies using the RT model McArtim to assess the impact of different cloud scenarios on O_4 SCDs. Section 9.3 introduces the attempt to identify clouds from webcam images including recommendations for future applications. Identifying clouds from webcam images requires different image processing tools. Firstly, the position of the mini-DOAS FOV within the webcam images is determined via the maximum correlation coefficients between the DOAS intensity and the colour values of the webcam images (Section 9.3.1). In the next section, the distance between the aircraft and the different cloud fields is estimated using optical flow methods (Section 9.3.2).

Several methods exist in order to derive 3D cloud fields from 2D webcam images. One method is based on the transformation and projection of 2D images in space. If the transformation matrix is known, different techniques can be further applied to infer 3D cloud structures from the webcam images. Prior to the transformation, a cloud mask has to be generated for each webcam image, in order to distinguish between cloud-free and cloudy pixels. Structure from motion (SfM) represents a further tool to derive 3D structures from a sequence of 2D images. However, due to the complexity of the cloud structures, these methods have several restrictions and are not used in this study. The two methods that can be applied to infer 3D cloud fields from 2D webcam images are therefore described in Appendix C.

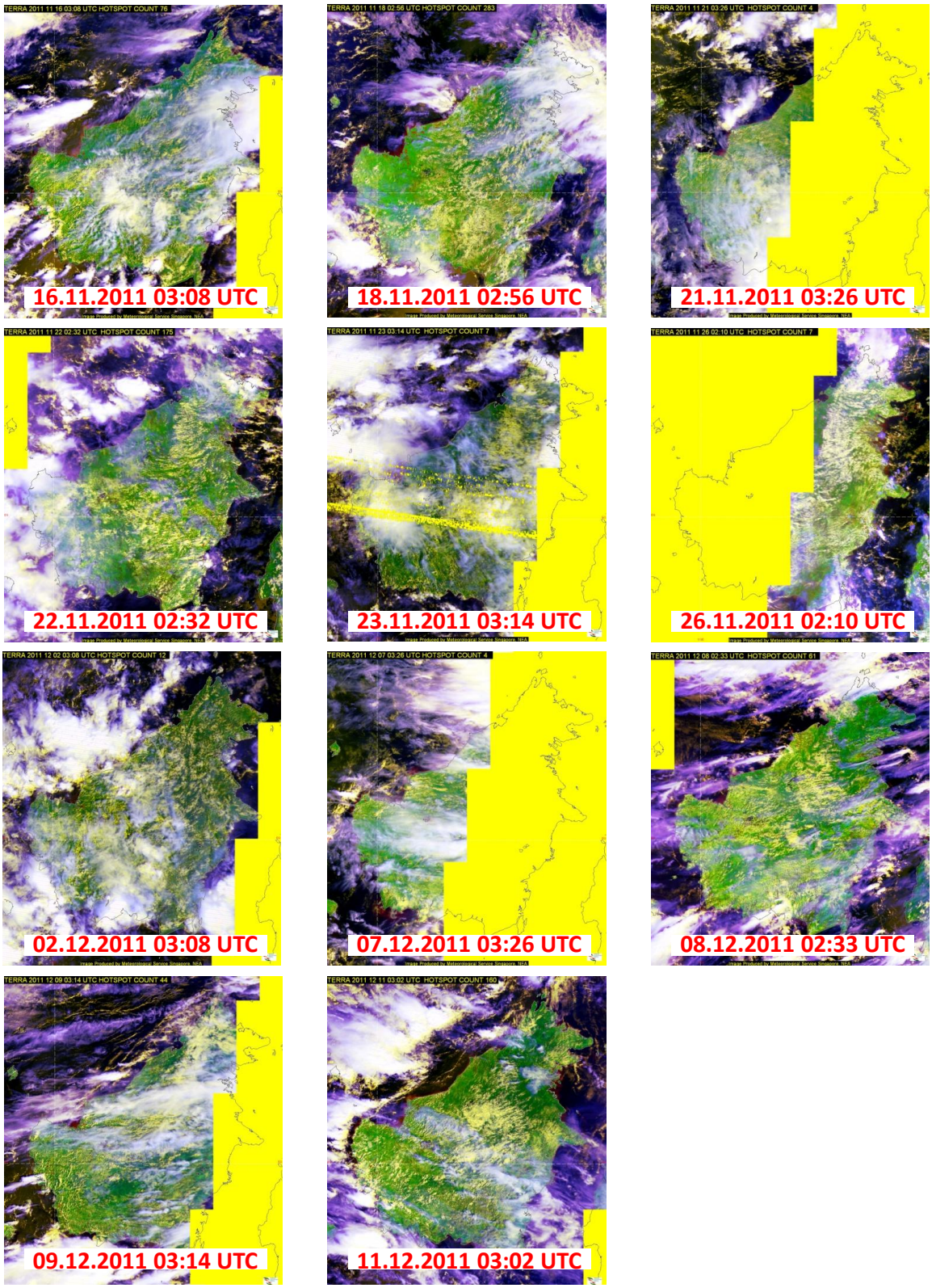

Figure 9.1: Satellite images of Borneo from the TERRA satellite provided by the Meteorological Service Singapore (`http://www.weather.gov.sg/wip/c/portal/layout?p_l_id=PUB.1003.511`) for each flight day during the SHIVA campaign (personal communication Andreas Dörnbrack, DLR, February 2014). For the sortie on 19 November, no satellite image is available, thus, an image from 18 November is shown.

9.1 Cloud identification from DOAS observations

DOAS observations of tropospheric trace gases are strongly affected by aerosols and clouds, since they modify the radiative transport in the atmosphere (e.g. Marshak and Davis, 2005). This influence on the DOAS measurements has been recognized in the late 1990s and used to improve the understanding on the RT due to clouds (e.g. Erle et al., 1995; Pfeilsticker et al., 1998,a; Veitel et al., 1998; Wagner et al., 1998, 2004, 2011). However, the influence of clouds on the measured radiances is not always unambiguous (Nakajima and King, 1990; Nakajima et al., 1991). According to radiative transfer simulations by Wagner et al. (2014), optically thin clouds can lead to an increase in the radiance, whereas optically thick clouds with an OD > 50 can decrease the radiance to values even smaller than for clear sky conditions (zenith viewing direction). In order to determine the aerosol load and the cloudiness of the sky, Wagner et al. (2014) suggest a cloud-screening method based on different quantities that can be derived from the DOAS measurements:

- colour index (CI)
- brightness of the sky
- O_4 absorption
- Ring effect.

The colour index was originally used in astronomy, where it is has been applied to determine the temperature of a star (Gray, 1992, e.g.). It is defined as the ratio of the radiance at two different wavelengths (e.g. Enell et al., 1999). In most cases, the radiance at higher wavelength is divided by the radiance at lower wavelength. Due to the strong wavelength dependency of Rayleigh scattering and the rather less wavelength-dependent Mie scattering (Section 3.2.2), the CI decreases for blue sky conditions where Rayleigh scattering dominates and increases with increasing aerosol load or cloudiness. The absolute values of the colour index depend on the chosen wavelength range. In this work, the colour index is calculated from the measured detector signal at 510 nm and 420 nm according to:

$$\mathrm{CI} = \frac{\mathrm{S}_{\lambda_{\mathrm{high}}}}{\mathrm{S}_{\lambda_{\mathrm{low}}}} = \frac{\mathrm{S}_{510\mathrm{nm}}}{\mathrm{S}_{420\mathrm{nm}}}. \tag{9.1}$$

The wavelengths correspond to the edges of the wavelength range of the USB and are chosen to have the largest possible spectral contrast. The CI is often used for DOAS evaluations to remove data points, which exceed a certain CI threshold, i.e. to remove cloudy data points (Wagner et al., 1998; Takashima et al., 2009; Sinreich et al., 2010; Wagner et al., 2014; Gielen et al., 2014). A characterisation of the magnitude of the cloudiness is only possible if enough observations are available including both clear sky and also completely cloudy conditions, e.g. Gielen et al. (2014) introduced different flags to distinguish between conditions with clear sky, broken clouds with a slightly decreased visibility as well as thick clouds with a low visibility. However, this classification cannot be applied to the SHIVA data set, as completely cloud-free conditions did never occur during the entire campaign.

Besides the CI, also the brightness of the sky can be a measure for the cloudiness of the sky (Kenntner, 2013). Changes in the brightness can be observed by a change in the exposure time and number of scans used to record the spectra. The brightness is given in counts/ ms and is determined according to the following equation:

$$\mathrm{brightness} = \frac{\text{average counts}}{\text{number of scans} \cdot \text{exposure time}}. \tag{9.2}$$

As a third criterion, O_4 dSCDs inferred from the DOAS analysis can be used to detect aerosols and clouds from DOAS observations. Examining these three quantities together yields an impression of the current atmospheric conditions during the measurements. Wagner et al. (2014) applied these

criteria to DOAS measurements in the Netherlands in 2009 to develop a cloud classification scheme and found good agreement with webcam images recorded from the ground. Figure 9.2 shows the colour index, the brightness and the O_4 dSCD in the visible wavelength range for the flight on 16 November 2011. Turns of the Falcon aircraft can be easily detected as all three quantities show increased/decreased values depending on the direction of the roll movement and thus the viewing direction of the mini-DOAS instrument towards the sky or the ground. The O_4 dSCDs decrease both for a positive roll angle with an upward viewing direction of the mini-DOAS towards the sky and for a negative roll angle with a downward viewing direction towards the ground.

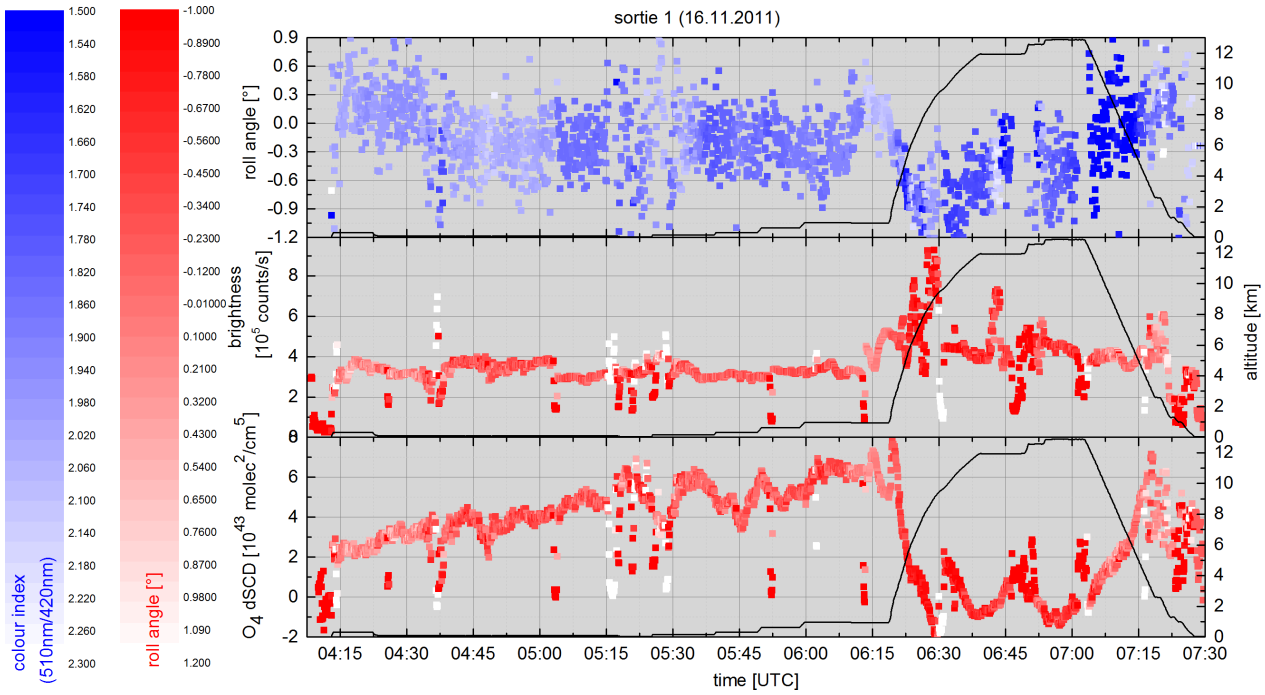

Figure 9.2: The roll angle colour-coded with the colour index (510 nm/ 420 nm), the brightness and O_4 dSCDs colour-coded with the roll angle during sortie 1 on 16 November 2011.

9.2 Cloud sensitivity studies

The effect of cloud-related changes on O_4 SCDs is systematically examined in this study. Different artificial scenarios are generated in McArtim in a spherical 3D geometry in order to test the sensitivity of the O_4 SCDs towards changes in the atmospheric parameters. An overview of the different scenarios that are studied is given in Table 9.1 and in Figure 9.3. Two major cloud scenarios are constructed: A vertical opaque cloud layer with a geometrical thickness of 10 km and a horizontal opaque cloud layer with a geometrical thickness of 1 km. The distance between the observer and the vertical cloud layer is varied from d = 2, 8, 19, 30, 38, 59, 130, and 191 km. The height of the horizontal cloud layer is 1 km with a cloud top height (CTH) of 1, 2, 3, 4, 5, 6, and 12 km, respectively. Furthermore, the structure of the vertical and horizontal cloud layer is changed from opaque to a chequerboard pattern with cells of 1 x 1 km. In addition to the influence of these different clouds, changes of the cloud properties, the aerosols, the albedo, the wavelength and the geometry are investigated.

The choice of the of geometries is based on the set-up of the mini-DOAS instrument during the first sortie of the SHIVA campaign (16.11.2011) where the Falcon aircraft cruised along the coastline of Borneo. A standard set of 20 artificial geometries is generated with fixed values (SZA = 28°, SRAA = 230°, latitude = 3.2°, height = 0.1 km, elevation angle = 0° and North azimuth (viewing direction) = 11°) except for the longitude, which varies from 112° to 113° in 0.05° steps, which

corresponds to a step size of 6 km. Figure 9.4 illustrates the viewing direction of the telescope, the position of the Sun as well as the relative azimuth angle between the Sun and the telescope.

The height grid used in this study has a vertical resolution of 0.5 km. The horizontal grid has a size of 400 x 400 km with a resolution of 1 x 1 km for each cell. The model atmosphere is set up with a vertical pressure and temperature profile as well as trace gas concentration profiles of O_4, O_3 and NO_2. The pressure and temperature profiles are extracted from one typical descent during the SHIVA campaign (sortie 7 on 26.11.2011a). The O_4 concentration is calculated from these pressure and temperature profiles according to Equation 2.30. The aerosol profile has an exponentially decreasing shape according to $e^{-z+0.25} + 0.005$, whereas the NO_2 and O_3 profiles are based on SAGE II profiles. Figure 9.5 shows the profiles used in this sensitivity study. The number of photons is set to 30000 for all model runs (Section 5.1). The Monte-Carlo noise due to the number of photons can be estimated from the standard deviation among the 20 geometries.

Table 9.1: Overview of the different scenarios used in this sensitivity study. Each scenario is simulated for a wavelength of 360.8 nm, and 477.1 nm, respectively. The distance between the observer and the vertical cloud layer is varied from d = 2, 8, 19, 30, 38, 59, 130, and 191 km. The height of the horizontal cloud layer is 1 km with a cloud top height (CTH) of 1, 2, 3, 4, 5, 6, and 12 km. The cloud extinction coefficient of the vertical cloud layer varies between ϵ = 0, 2, 10, and 20 km^{-1} and for the horizontal cloud layer additionally of: ϵ = 0, 0.5, 1, 2, 5, 10, 20 km^{-1}.

scenario	albedo	aerosol	SZA [°]	SRAA [°]	α [°]	detector altitude [km]	cloud layer type	cloud ssa	cloud altitude [km]
1	0.05	no aerosol	28	230	0	0.1	vertical, opaque	0.999	0-1
2	0.6	no aerosol	28	230	0	0.1	vertical, opaque	0.999	0-1
3	0.05	no aerosol	5	230	0	0.1	vertical, opaque	0.999	0-1
4	0.05	no aerosol	80	230	0	0.1	vertical, opaque	0.999	0-1
5	0.05	no aerosol	28	0	0	0.1	vertical, opaque	0.999	0-1
6	0.05	no aerosol	28	230	-1	0.1	vertical, opaque	0.999	0-1
7	0.05	no aerosol	28	230	1	0.1	vertical, opaque	0.999	0-1
8	0.05	no aerosol	28	230	0	0.1	vertical, opaque	0.7	0-1
9	0.05	no aerosol	28	230	0	1.51	vertical, opaque	0.999	1-2
10	0.05	no aerosol	28	230	0	2.51	vertical, opaque	0.999	2-3
11	0.05	no aerosol	28	230	0	5.51	vertical, opaque	0.999	5-6
12	0.05	no aerosol	28	230	0	10.51	vertical, opaque	0.999	10-11
13	0.05	no aerosol	28	230	0	0.1	vertical, chequerboard	0.999	0-1
14	0.05	no aerosol	28	230	0	1.51	horizontal, opaque	0.999	
15	0.05	no aerosol	28	230	0	1.51	horizontal, opaque	0.999	
16	0.05	exp., AOT = 0.1	28	230	0	0.1	vertical, opaque	0.999	0-1
17	0.05	exp., AOT = 0.3	28	230	0	0.1	vertical, opaque	0.999	0-1
18	0.05	exp., AOT = 0.6	28	230	0	0.1	vertical, opaque	0.999	0-1
19	0.05	exp., AOT = 1.0	28	230	0	0.1	vertical, opaque	0.999	0-1
20	0.05	exp., AOT = 2.0	28	230	0	0.1	vertical, opaque	0.999	0-1

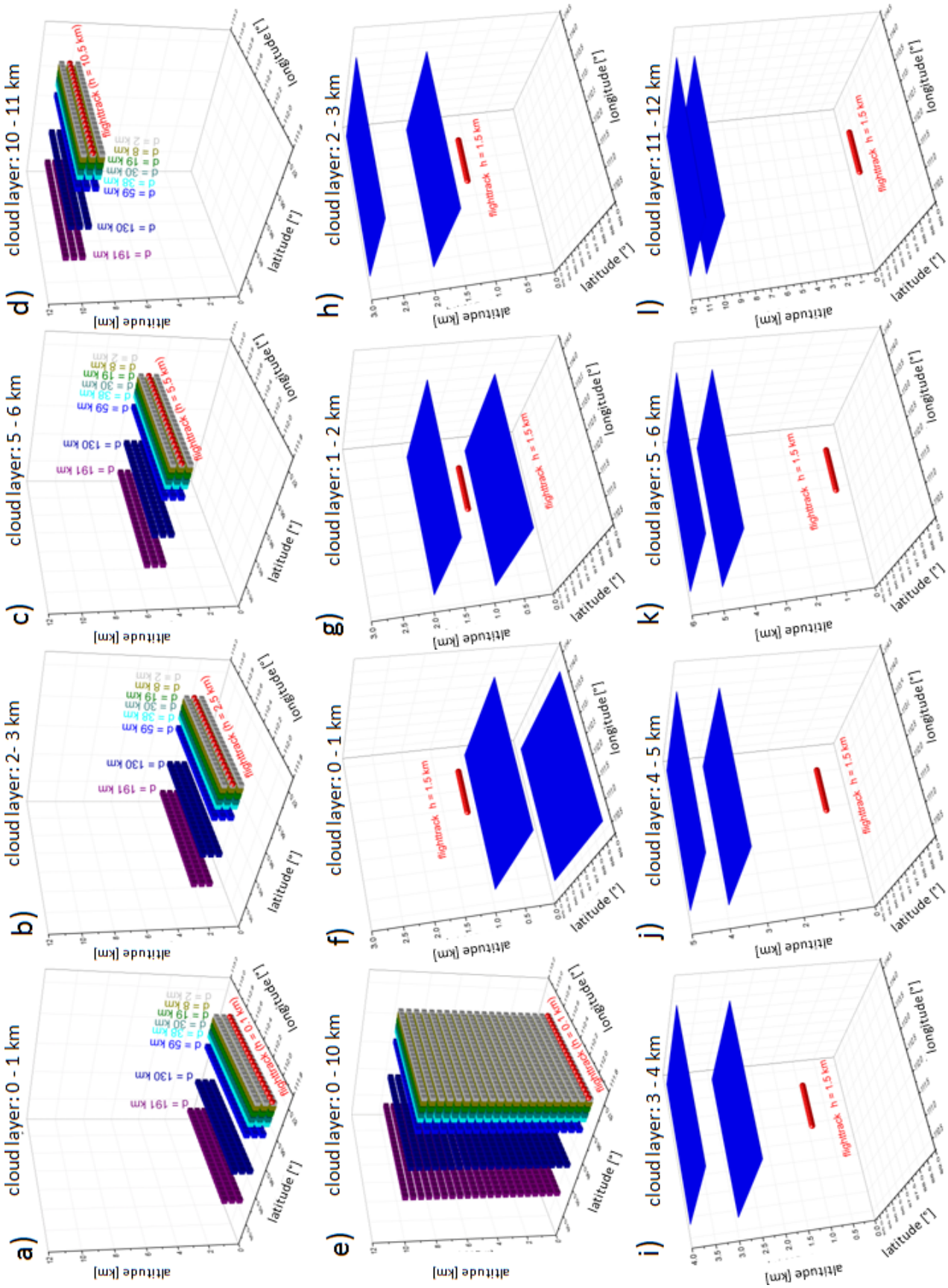

Figure 9.3: Sketch of the different scenarios used in this sensitivity study. The red dots sample the artificial flight track at different altitudes and the cloud layers are represented by coloured walls. Panels a) to e) show vertical cloud layers with a thickness of 10 km each for different distances to the flight track. Panels f) to l) show horizontal cloud layers with a thickness of 1 km each at different heights. The blue surfaces mark the edges of the cloud layer, the interior of the horizontal cloud layer is not coloured for clarity reasons.

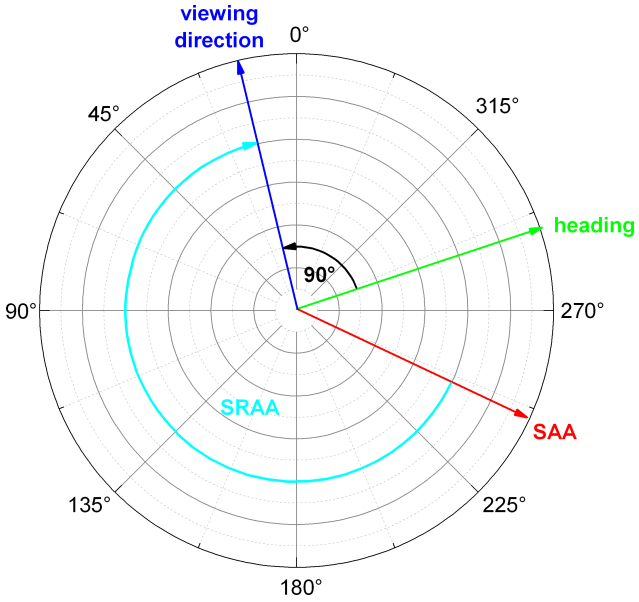

Figure 9.4: Sketch of the geometries in mathematical rotation direction used in this sensitivity study: SAA = 241°, North azimuth (viewing direction of the telescope) = 11° and SRAA = 230°.

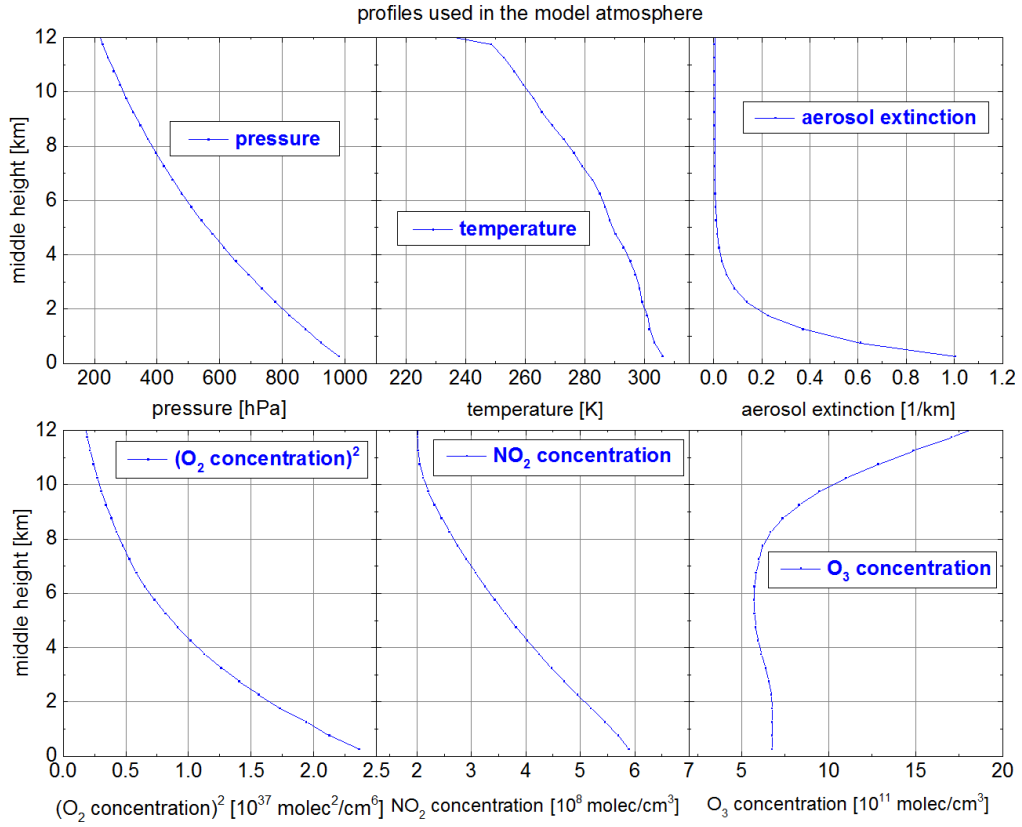

Figure 9.5: Profiles used in the McArtim simulation.

9.2.1 Influence of the wavelength

For this investigation, two wavelengths are examined, one in the UV at 360.8 nm and the other in the visible wavelength range at 477.1 nm. These wavelengths mark the middle of the two O_4

absorption bands, respectively. In Figure 9.6a the O_4 SCDs of scenario 1 (Figure 9.3a)) are displayed for 360.8 nm and 477.1 nm, respectively. In the following, a systematic error of 10 % is assumed, which defines the relevant distance d_{rel} between the flight track and the cloud layer. If the deviation between the O_4 SCDs with and without a cloud (i.e. Rayleigh atmosphere) is less than $\approx$ 10 %, the cloud layer is assumed to have an insignificant effect on the O_4 SCDs.

In the UV an opaque vertical cloud layer starts to be relevant at a distance of approximately $d_{rel} \approx 33$ km to the flight track. For a vertically extended cloud layer located at a distance $d > 33$ km the O_4 SCDs deviate from the O_4 SCDs without a cloud (i.e. Rayleigh atmosphere) by less than $\approx$ -10 %. This value increases up to approximately -60 % for a cloud layer distance of $d = 2$ km. Overall, the difference between the deviations in O_4 absorption for a cloud extinction ϵ of 10 and 20 km^{-1}, respectively, is small. This is mostly due to the shielding of the horizontal photon path by the cloud. If d is larger than approximately 20 km, the deviation of the O_4 SCDs is larger ($\approx$ 2 %) for a cloud extinction of 2 km^{-1} than for 10 or 20 km^{-1}, respectively. This is possibly because the photons are able to penetrate more deeply into the cloud for smaller than for larger extinctions (e.g. David and Marshak, 2002). However, for $d < 20$ km, the deviation of the O_4 SCDs is almost similar for the three example extinctions.

In the visible wavelength range an opaque vertical cloud layer already starts to be relevant for a distance of $d_{rel} \approx 100$ km with a deviation from the Rayleigh case of $\approx$ -10 % for $\epsilon = 2$ km^{-1}. The deviation increases up to $\approx$ -83 % for $d = 2$ km. Hence, the influence of clouds in the visible wavelength range is much stronger ($\approx$ 20 - 30 %) than in the UV. As for the UV the deviations for an ϵ of 10 or 20 km^{-1} are also very similar. For $d < 20$ km the deviations for $\epsilon = 2$ km^{-1} are also close to the deviations for $\epsilon = 10$ or 20 km^{-1}. However, for $d > 20$ km the difference between the O_4 SCDs for $\epsilon = 2$ km^{-1} and $\epsilon = 10$ or 20 km^{-1} is larger than in the UV. The course of the curves follows the rules of exponential decay with O_4 SCD $\propto e^{\frac{-d}{\tau}}$ with $\tau \approx 12$ km for the UV and $\tau \approx =$ 59 km for the visible wavelength range (for $\epsilon = 2$ km^{-1}). Varnai et al. (2013) states that near-cloud relative enhancements in particle scattering observed by MODIS and CALIOP over oceans between 60°N and 60°S at $\lambda = 550$ nm are not relevant as long as the 3D cloud has a distance of more than 20 km from the FOV.

The influence of the cloud distance on simulated O_4 dSCDs is illustrated in Figure 9.6b for the two wavelengths, respectively. The O_4 references are simulated using the same geometries as described above, but for an altitude of 12.1 km (Figure 9.7). Obviously, the O_4 references at h = 12.1 km are also affected by the different cloud layers below. The simulated O_4 references including a cloud layer below deviate from the O_4 references without a cloud by approximately up to 15 % in the UV and 20 % in the visible wavelength range, respectively, depending on the cloud distance and the cloud extinction. Thus, the influence of the cloud distance on simulated O_4 dSCDs is slightly stronger than on O_4 SCDs.

In the UV, an opaque vertical cloud layer starts to be relevant at a distance of approximately $d_{rel} \approx 40$ km. In the visible wavelength range, the relevant distance results in approximately $d_{rel} \approx$ 105 km. Thus, the cloud distance that is relevant for the observer at h = 0.1 km increases by approximately 15 % in the UV and 5 % in visible wavelength range, when considering O_4 dSCDs instead of SCDs.

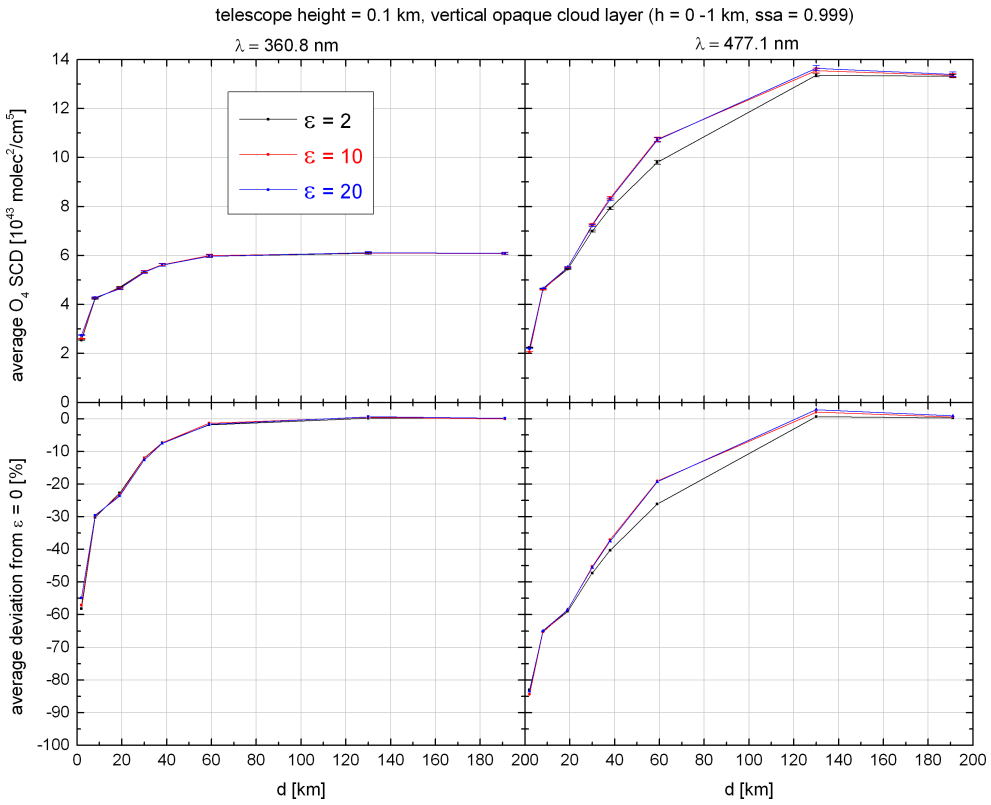

(a)

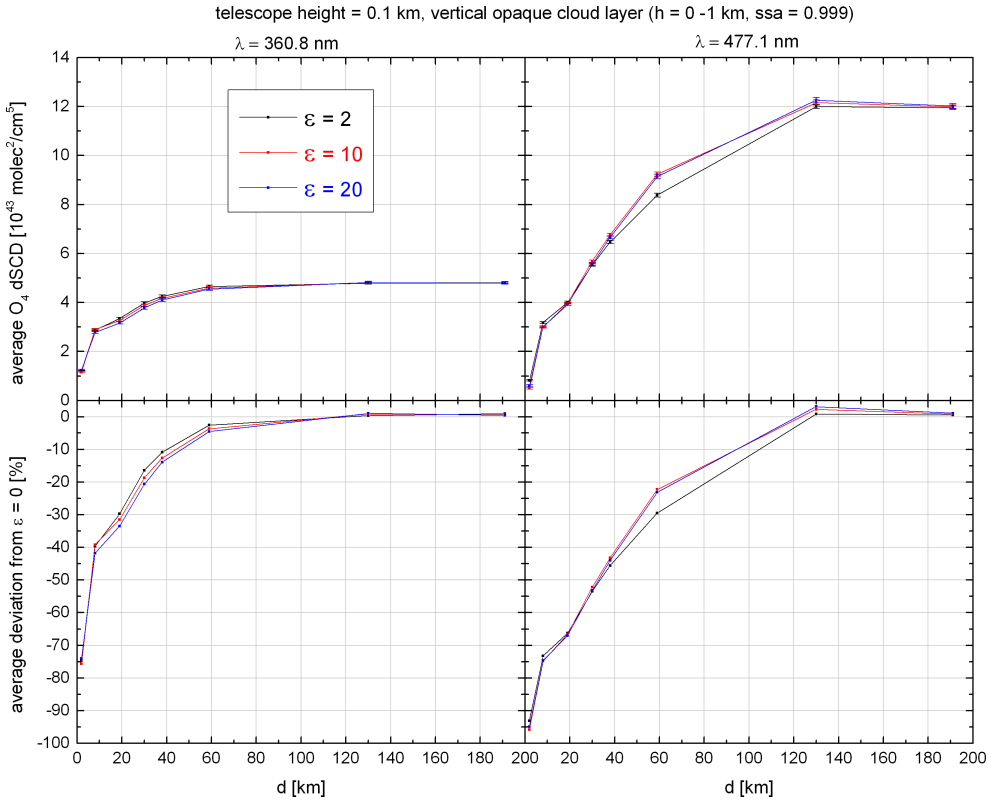

(b)

Figure 9.6: Upper panels: Simulated (a) O_4 SCDs and (b) dSCDs (upper panels) for vertical cloud layers with a varying distance to the flight track. Lower panels: Respective deviation from the cloud-free case ($\epsilon = 0$).

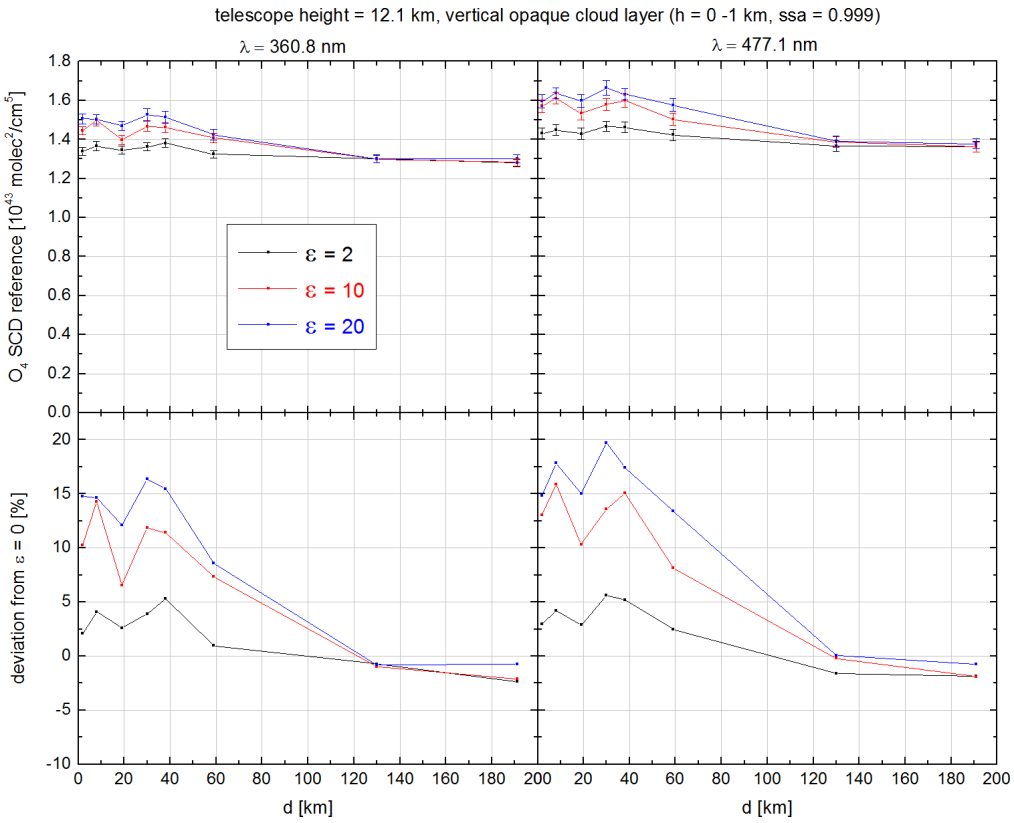

Figure 9.7: Upper panels: Simulated O_4 references at an altitude of h = 12.1 km for vertical cloud layers with a varying distance to the flight track. Lower panels: Respective deviation from the cloud-free case ($\epsilon = 0$). The height of the flight track is h = 0.1 km.

9.2.2 Influence of the albedo and geometry

A higher surface albedo results in multiple scattering of radiation in the lowest parts of the troposphere due to the increased amount of reflected photons (e.g. Barker et al., 2002). In order to examine the influence of the albedo, an albedo of 0.05 (scenario 1) is assumed, which is typical for open ocean conditions and an albedo of 0.6 (scenario 2), which is typical for bare ice or snow-covered ice (Perovich et al., 1998). Figure 9.8a shows the simulated O_4 SCDs for vertical cloud layers with a varying distance to the flight track for the two different albedo values. The O_4 SCDs increase for larger albedo values, both for the UV and the visible wavelength. The closer the vertical cloud layer to the flight track, the larger is the difference in O_4 SCDs between the albedo values. In the UV, the difference in O_4 SCDs between the albedo values increases from 10 to 18 % for a decreasing cloud layer distance, whereas in the visible wavelength range the difference increases from approximately 1 to 13 %. Although the O_4 SCDs are more increased for larger than for smaller albedo values, the relevant cloud layer distance only changes slightly, both for the UV and visible wavelength range.

In order to investigate the influence of the chosen geometries on the distance of the cloud to the observer that is relevant for O_4 SCDs, the different geometries are modified. Figure 9.8b shows a comparison between the O_4 SCDs simulated for different geometries. The relevant cloud distance does not change significantly for the modified geometries, except for the case where the roll angle is set to -1°. For a roll angle of -1°, the relevant cloud distance even yields very small values.

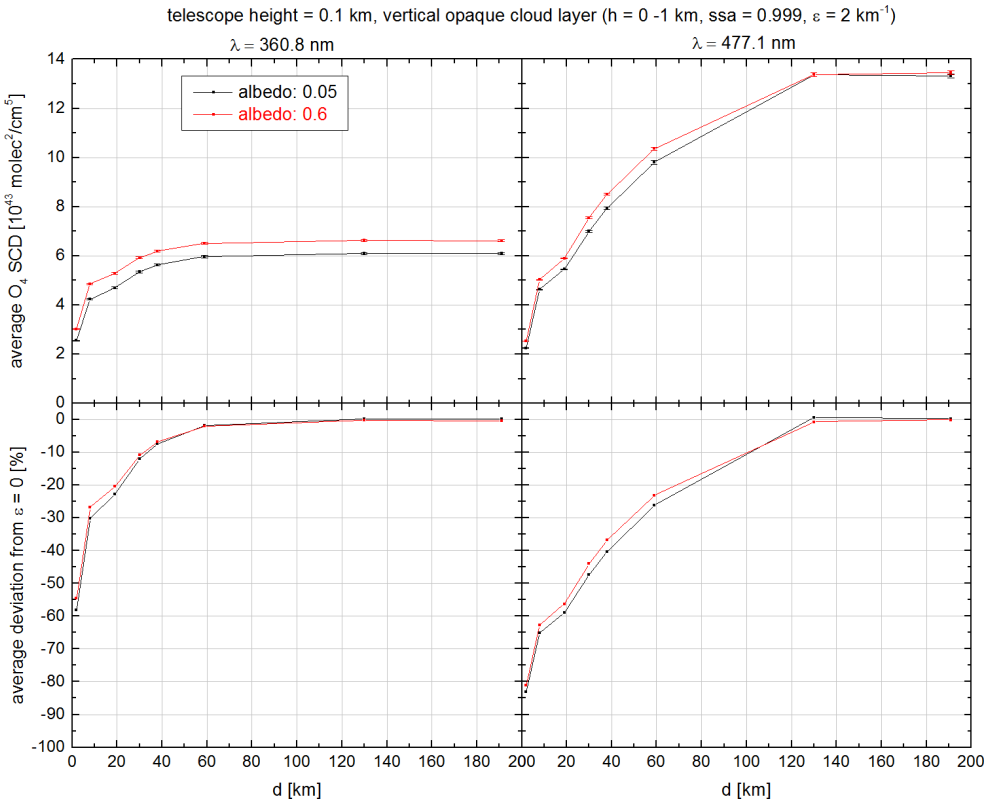

(a)

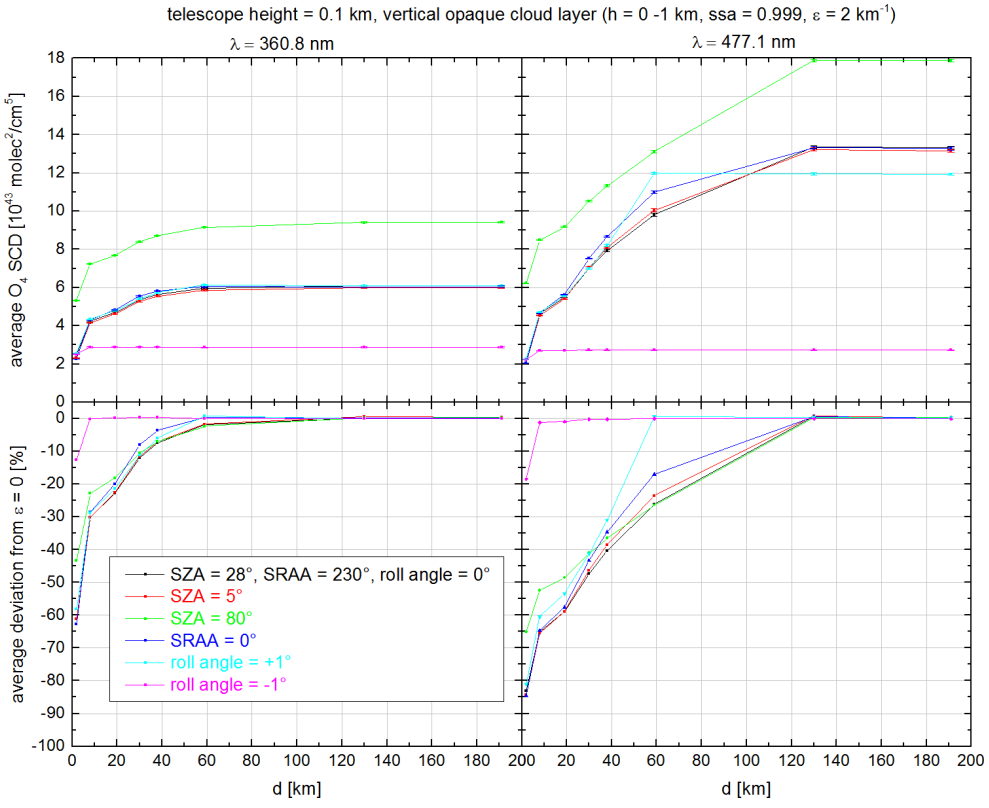

(b)

Figure 9.8: Upper panels: Simulated O_4 SCDs for vertical cloud layers with a varying distance to the flight track for (a) a different albedo values (scenario 1 and 2), and for (a) different geometries (scenario 3 - 7). Lower panels: Respective deviation from the cloud-free case ($\epsilon = 0$).

9.2.3 Influence of the cloud properties

Influence of the SSA

For the standard case, a single scattering albedo (SSA) of the cloud of 0.999 is assumed. A further SSA value of 0.7 is chosen, which represents a rather dark cloud. Low SSA values can for example occur during regional air pollution events and can indicate a high abundance of light absorbing carbon (e.g. Garland et al., 2008). These two SSA values are chosen, in order to examine the full range of the influence of the cloud SSA on the simulated O_4 SCDs. Furthermore, for both SSA values, the cloud extinction is varied between ϵ = 2, 10, 20 km^{-1}. Figure 9.9 shows the resulting O_4 SCDs and the respective deviation from the cloud-free case. The O_4 SCDs are smaller for an SSA of 0.7 than for an SSA of 0.999. In the UV, the O_4 SCDs reach up to approximately 25 % smaller values for an SSA of 0.7 than for an SSA of 0.999, whereas in the visible wavelength range the O_4 SCDs yield approximately 30 to 35 % smaller values.

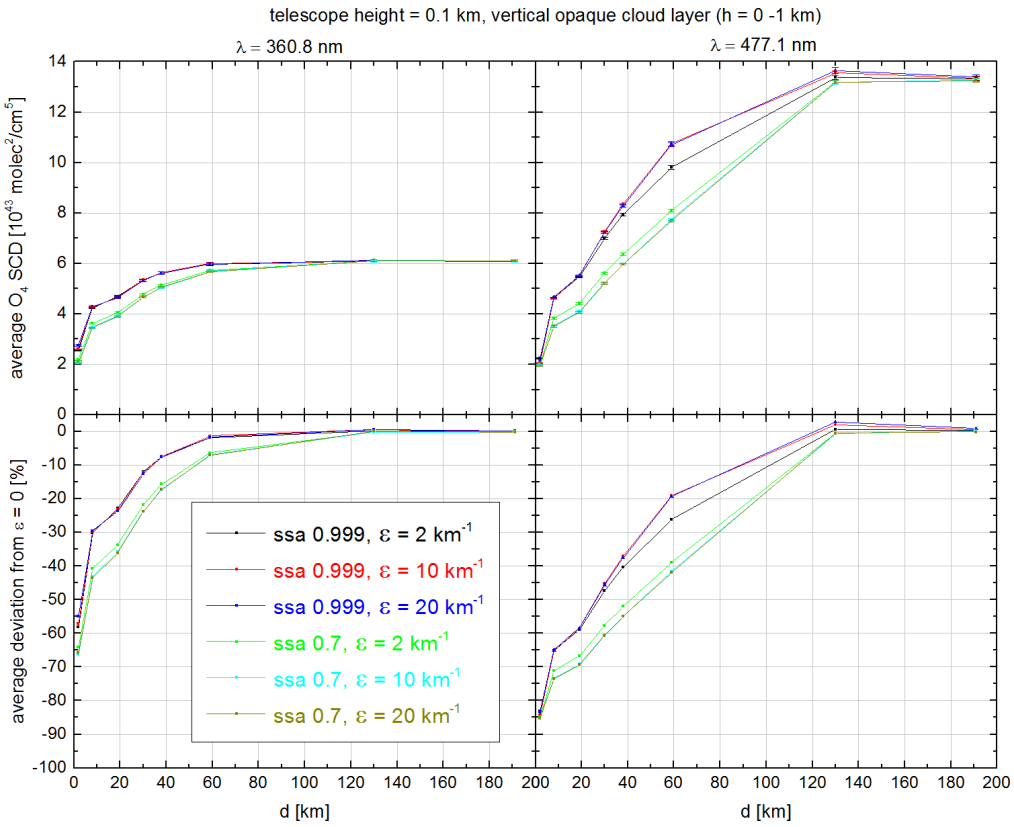

Figure 9.9: Upper panels: Simulated O_4 SCDs for vertical cloud layers with a varying distance to the flight track for a cloud SSA of 0.999 (scenario 1) and 0.7 (scenario 8). Lower panels: Respective deviation from the cloud-free case (ϵ = 0). The height of the flight track is h = 0.1 km.

Influence of the cloud height

For this study, the vertical height of the cloud deck is changed and set to different altitudes varying between h = 0 - 1 km (scenario 1), h = 1 - 2 km (scenario 9), h = 2 - 3 km (scenario 10), h = 5 - 6 km (scenario 11), and h = 11 - 12 km (scenario 12). The cloud extinction is set to ϵ = 20 km^{-1}. For each case, the height of the flight track is set to the respective middle height of the cloud layer. It has to be noted, that in McArtim altitudes have to be avoided, which directly correspond to boundary values of one altitude grid cell. Since for this study an altitude grid resolution of 0.5 km is chosen, observer altitudes at 0.5 km, 1.0 km, 1.5 km etc. have to be omitted. Therefore, 10

m are added artificially to the chosen altitudes, i.e. the observer altitudes are set to h = 0.1 km, 1.51 km, 2.51 km, 5.51 km, and 10.51 km.

Figure 9.10 shows the simulated O_4 SCDs for different altitudes of the flight track and vertical cloud layer. The simulated O_4 SCDs decrease with increasing altitude due to the exponentially decreasing O_4 concentration profile. The relevant cloud distance, where changes in the O_4 SCDs become obvious, increases for higher altitudes. In the UV, the relevant cloud distance d_{rel} increases from approximately 33 km for a cloud layer between 0 and 1 km to approximately 83 km for a cloud layer between 10 and 11 km. In the visible wavelength range, d_{rel} increases from approximately 88 km to 105 km. Thus, the relevant cloud distance d_{rel}, below which changes in the O_4 SCDs occur, is larger for observers at higher altitudes than for observers at lower altitudes.

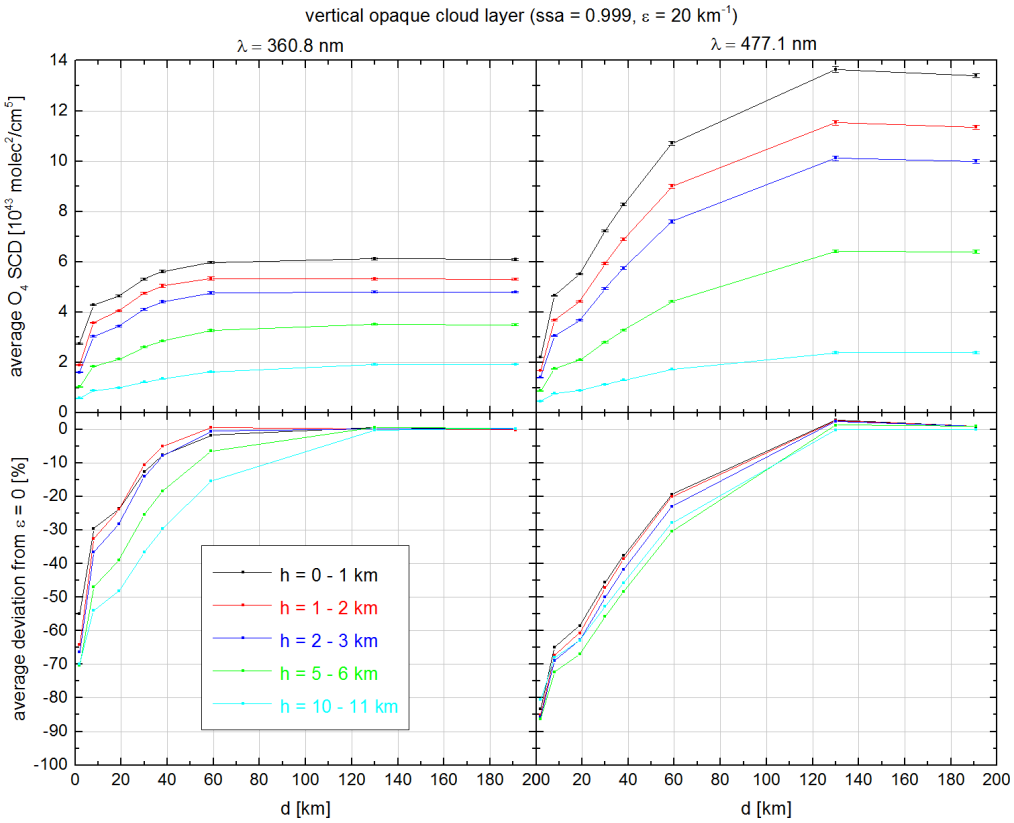

Figure 9.10: Upper panels: Simulated O_4 SCDs for vertical cloud layers at different heights (scenario 1 and scenario 9 to 12). Except for scenario 1, the height of the flight track is set to the middle height of each cloud layer, i.e. to h = 0.1 km, 1.51 km, 2.51 km, 5.51 km, and 10.51 km. Lower panels: Respective deviation from the cloud-free case ($\epsilon = 0$).

Influence of the cloud structure (opaque cloud, chequerboard cloud)

In this study, the potential influence of different 3D cloud structures on O_4 SCDs is examined. Instead of opaque cloud layers, cloud layers with a chequerboard pattern are assumed having cell sizes of 1 x 1 km. The chequerboard cloud pattern is applied both on vertical and horizontal cloud layers (scenario 13 to 15).

Figure 9.11 shows a comparison between O_4 SCDs simulated both for vertical opaque and chequerboard cloud layers for cloud extinctions of ϵ = 2, 10, and 20 km^{-1}, respectively. The chequerboard cloud layers lead to slightly smaller O_4 SCDs than the opaque cloud layers. The difference in the O_4 SCDs simulated for the opaque and chequerboard case increases with decreasing cloud distance. For small cloud layer distances of 2 km, the simulated O_4 SCDs in the UV for a chequerboard cloud layer with ϵ = 2 km^{-1} yield approximately up to 13 % smaller values than for

the opaque case. In the visible wavelength range this difference results in approximately 17 %. For larger cloud extinction coefficients this difference decreases. In comparison to opaque cloud layers, the relevant cloud distance d_{rel} slightly increases to approximately 35 km in the UV and 104 km in the visible wavelength range for the chequerboard cloud pattern. From this it follows that patchy cloud structures, such as a regularly shaped chequerboard cloud pattern, lead to a slight increase in the cloud distance where changes in the O_4 SCDs become relevant, i.e. the sensitivity to clouds is smaller if the clouds are structured.

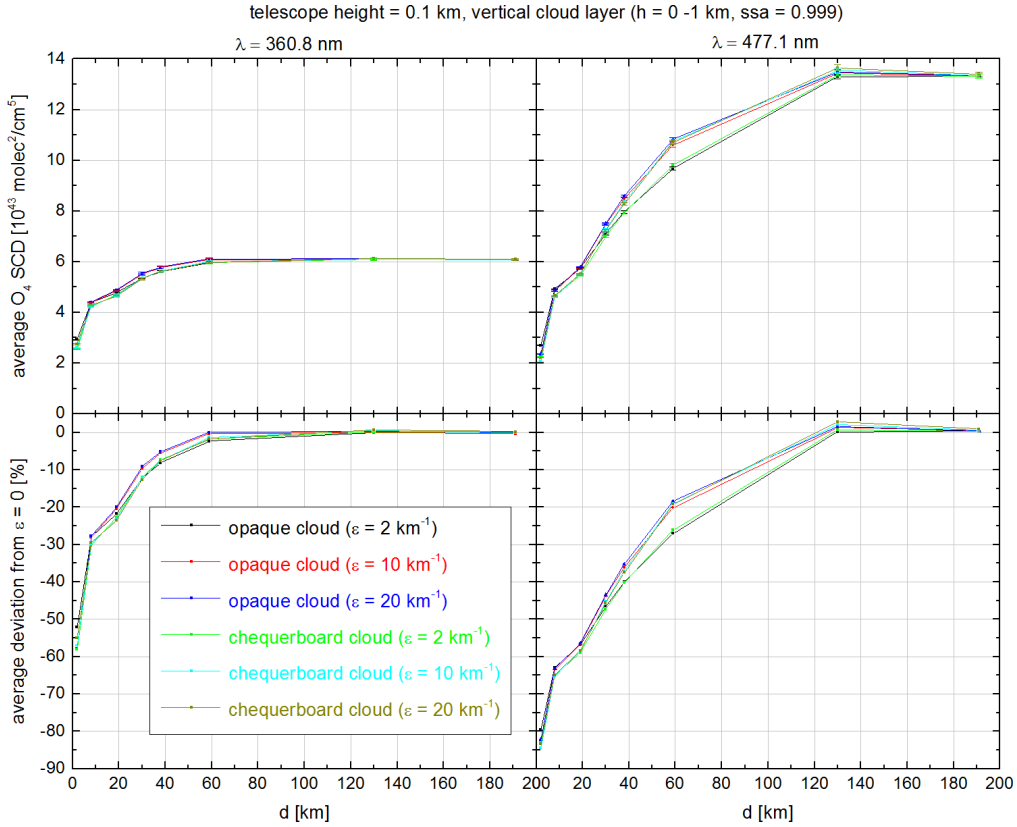

Figure 9.11: Upper panels: Simulated O_4 SCDs for vertical opaque (scenario 1) and chequerboard (scenario 13) cloud layers with a varying distance to the flight track. Lower panels: Respective deviation from the cloud-free case ($\epsilon = 0$). For the two scenarios different cloud extinction coefficients are chosen with ϵ = 2, 10, and 20 km^{-1}.

A horizontal opaque cloud layer with a thickness of 1 km is included in the model atmosphere at different heights (scenario 14). Figure 9.12a shows the dependency of the O_4 SCDs on the cloud extinction coefficient ϵ for horizontal cloud layers at different heights for the UV and visible wavelength range, respectively. The telescope height is at 1.51 km. When flying within the cloud layer, the O_4 SCDs are quite similar for 360.8 and 477.1 nm and approximately lie within the numerical error of approximately 2 %. Figure 9.12b shows the same scenario, but for horizontal chequerboard cloud layers with cells of 1 x 1 km (scenario 15). Overall, the chequerboard cloud layers lead to slightly smaller O_4 SCDs than the opaque cloud layers. Except for the case when the flight track is within the cloud layer (h = 1 - 2 km), the deviation between the opaque and the chequerboard scenario is smaller than 10 % and decreases down to some per cent for a decreasing extinction (Figure 9.13).

When the flight track is within the cloud layer, the deviation between opaque and chequerboard cloud layer increases from ≈ -17 % for ϵ = 20 km^{-1} up to ≈ -25 % for ϵ = 1 km^{-1} in the UV and from ≈ -20 % for ϵ = 20 km^{-1} up to ≈ -38 % for ϵ = 0.5 km^{-1} in the visible wavelength

range. Thus, as long as the horizontal cloud layer is located below or above the observer, the O_4 SCDs for an horizontally opaque cloud layer result in similar values than for a cloud layer with chequerboard pattern with cells of 1 x 1 km. Deviations of up to 25 % in the UV and 35 % in the visible wavelength range occur between the O_4 SCDs for an opaque and a chequerboard cloud, if the flight track lies within the cloud layer.

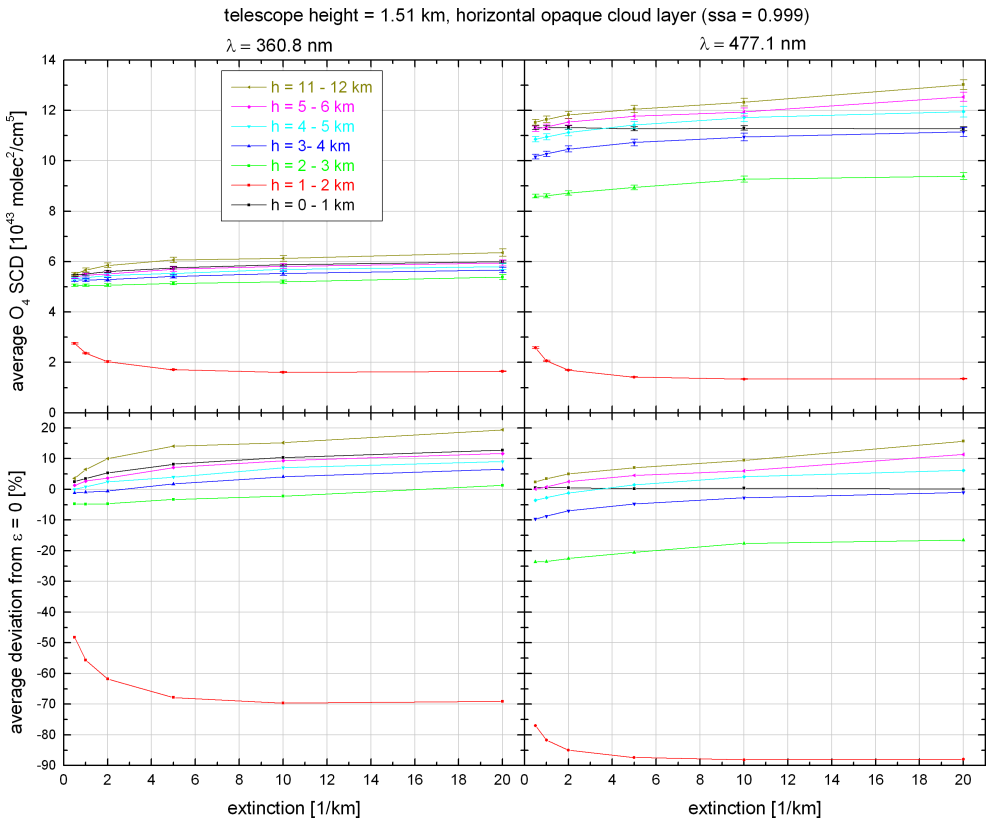

(a)

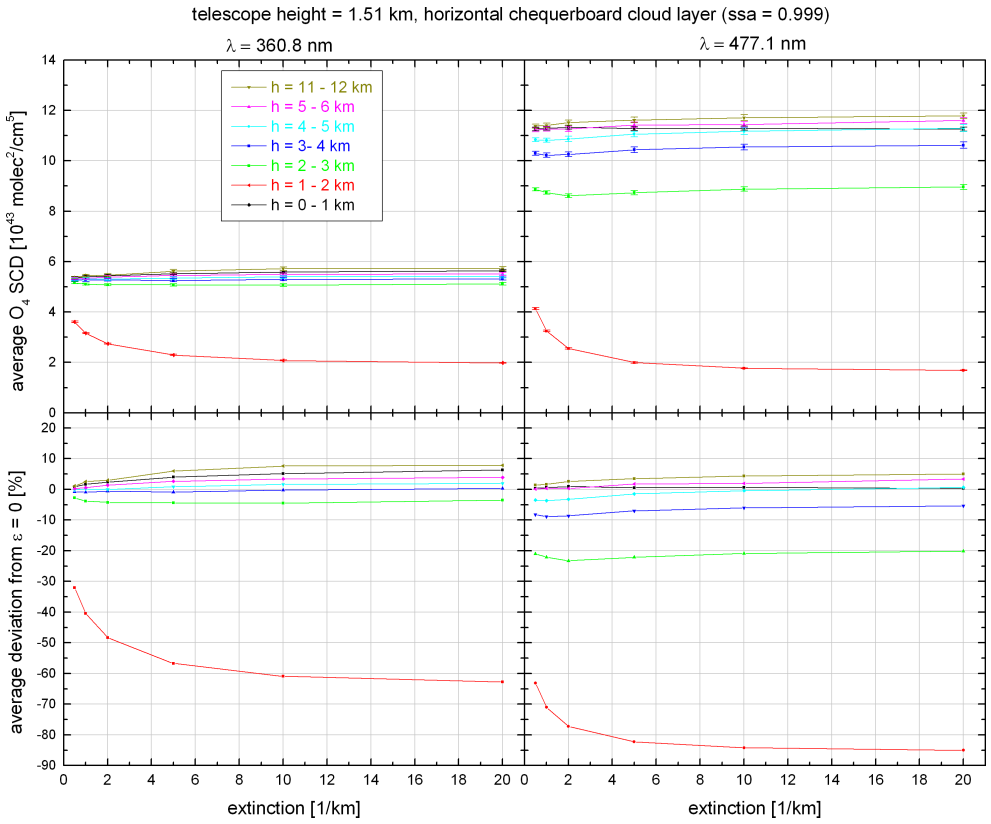

(b)

Figure 9.12: Upper panels: Simulated O_4 SCDs for horizontal cloud layers at different altitudes with (a) an opaque cloud structure (scenario 14, flight track f) to l)) and (b) for a chequerboard cloud structure (scenario 15, flight track f) to l)). Lower panels: Respective deviation from the cloud-free case ($\epsilon = 0$). The altitude of the observer is set to 1.51 km.

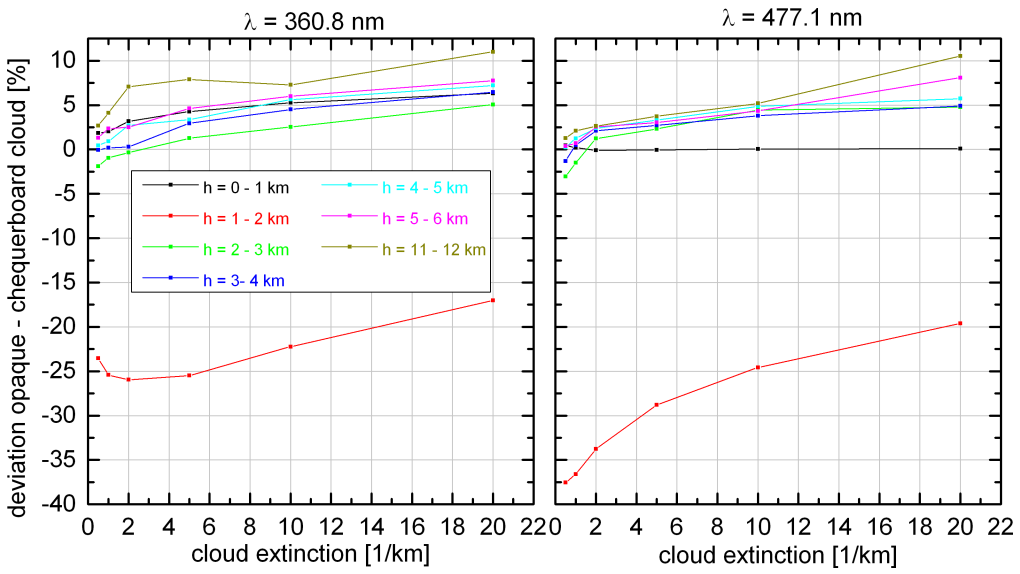

Figure 9.13: Deviation between the horizontal opaque and chequerboard cloud from Figure 9.12 in per cent.

9.2.4 Influence of clouds in the presence of aerosols

Aerosols are small solid and liquid particles occurring in the atmosphere, e.g. sea salt, dust, volcanic ash, smoke or pollution particles (e.g. Seinfeld and Pandis, 2006). Aerosols not only cause a scattering of the sunlight, but they also absorb radiation (Section 2.4.10). Multiple scattering of light due to aerosols can increase the total light path, which leads to an increase in the measured SCDs. For high aerosol concentrations the radiation is absorbed leading to a reduced radiation at the surface. Furthermore, aerosols can act as condensation nuclei, altering the formation of clouds. Aerosols can therefore modify the radiative properties of clouds.

In this study, the influence of aerosols on the O_4 SCDs in a cloudy atmosphere is investigated. An exponentially decreasing aerosol profile is assumed (Figure 9.5) for different AOTs (AOT = 0, 0.1, 0.3, 0.6, 1, 2). The SSA is set to 0.999 and the asymmetry parameter g to 0.7 (scenarios 17 - 26). Figure 9.14 shows the AERONET AOTs measured with a sun photometer at the airport of Kuching for November and December 2011 (`http://aeronet.gsfc.nasa.gov/`). There are two other AERONET stations on the island of Borneo: Pontianak (0.08°N/109.19°E) and Palangkaraya (2.23°S/113.95°E) on the Indonesian part of Borneo, but no data is available for 2011. Occasionally, the AOT exceeds 1 in the unscreened data. However, the average AOT for the Level 2 data (cloud-screened and quality assured) lies approximately between 0.1 and 0.2. According to the overview table of Smirnov et al. (2001) the mean AOT at 550 nm in the South China Sea for two unspecified measurement days corresponds to 0.2.

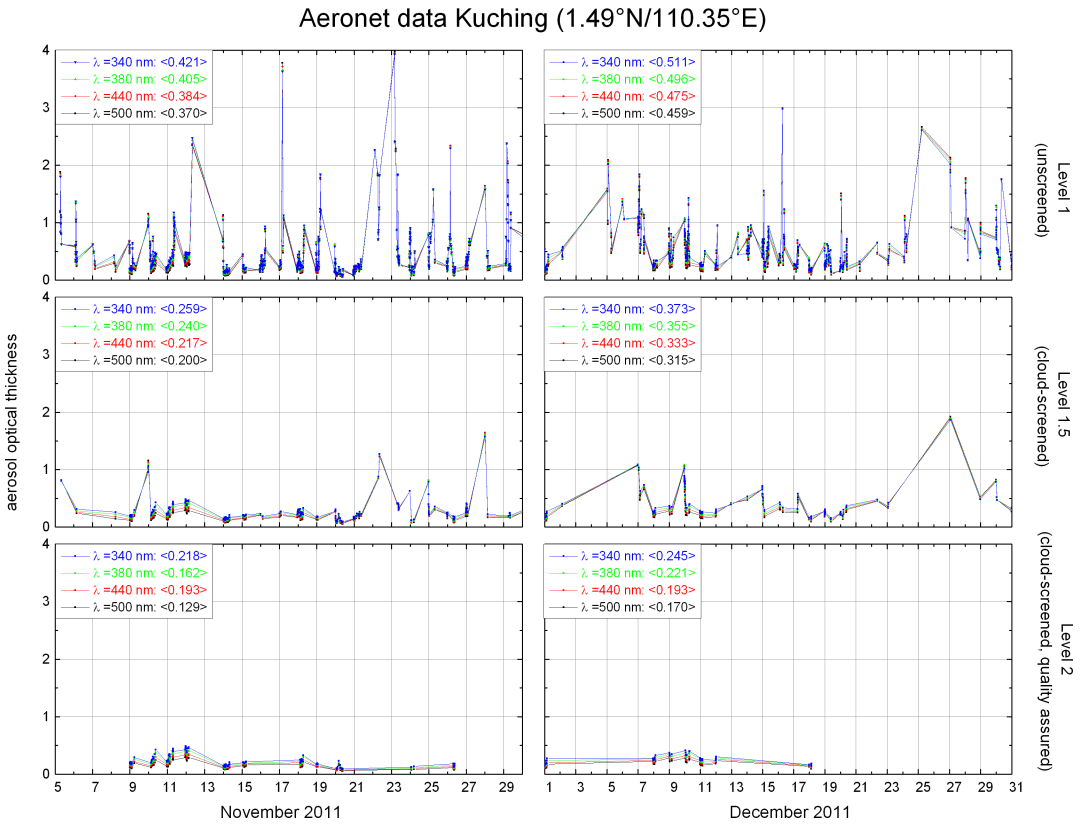

Figure 9.14: AERONET data (`http://aeronet.gsfc.nasa.gov/cgi-bin/type_one_station_opera_v2_new?site=Kuching&nachal=2&level=1&place_code=10`) from Kuching (1.45°N/110.35°E) for November and December 2011. The sun photometer of the site of Kuching is mounted on the observation tower of Kuching Meteorological Station located at the Kuching International Airport, Sarawak.

Figure 9.15 displays scenario 16 - 20 for an aerosol profile with different AOTs and a vertical opaque cloud layer with h = 0 - 1 km, SSA = 0.999 and ϵ = 2 km^{-1}. For an aerosol profile with an AOT larger than 1.0, the effect of clouds on O_4 SCDs is very small (deviation < 10 %) and can therefore be neglected, both for λ = 360.8 nm and 477.1 nm. This is possibly because for such high aerosol concentrations the cloud is not visible. For an aerosol profile with an AOT of 0.1 the relevant cloud distance decreases to $d_{rel} \approx$ 15 km in the UV compared to $\approx$ 33 km without any aerosols (Section 9.2.1). In the visible wavelength range, d_{rel} drops to $\approx$ 30 km compared to $d_{rel} \approx$ 100 km without any aerosols. Thus, in the presence of a certain amount of aerosols, the relevant cloud distance decreases, i.e. clouds, which have a certain distance to the observer, will not have a significant influence on the measured O_4 SCDs.

According to the Aeronet AOTs from Figure 9.14, an average AOT of 0.1 represents a reasonable average value for that region. Therefore, it can be concluded, that in general a cloud distance larger than approximately 15 km for the UV and approximately 30 km for the visible wavelength range will have an insignificant effect on the O_4 SCDs measured at an altitude of h = 0.1 km.

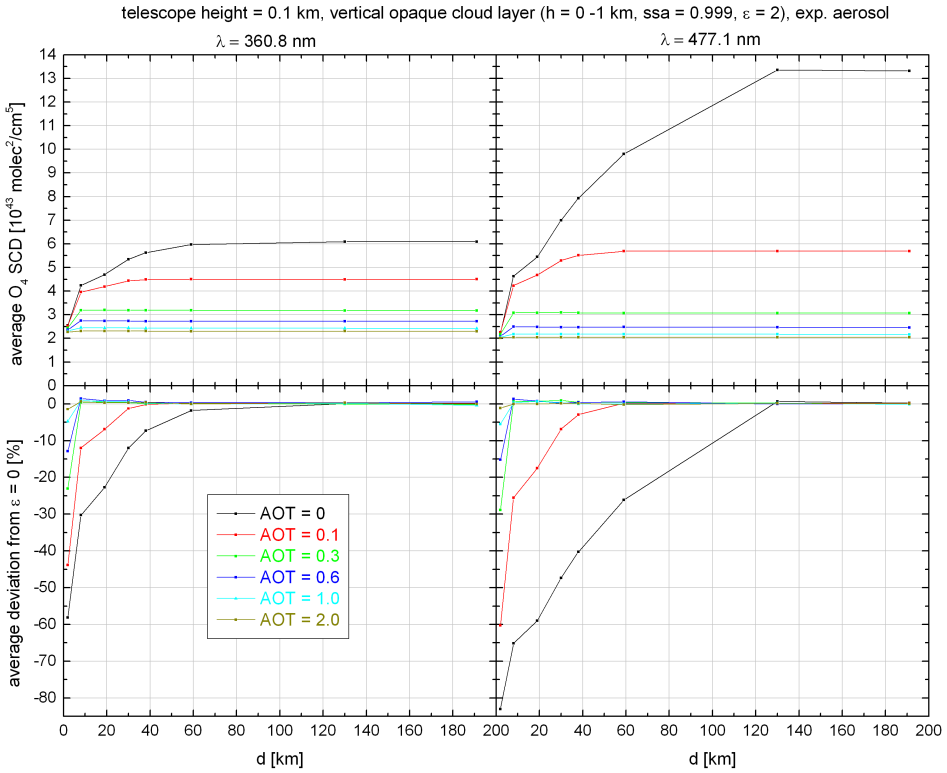

Figure 9.15: Upper panels: Simulated O_4 SCDs for vertical cloud layers with a varying distance to the flight track for different aerosol profiles (scenario 16 - 20). Lower panels: Respective deviation from the cloud-free case including aerosols.

Table 9.2 summarises the results for d_{rel} for the different scenarios of vertical cloud layers. The influence of clouds on the measured O_4 SCDs is smaller for the UV than the visible wavelength range. For an observer altitude of 0.1 km, d_{rel} results in approximately 33 km in the UV and in approximately 100 km in the visible wavelength range, excluding any aerosol amounts. Changing the cloud extinction coefficient does not lead to a significant change in d_{rel}, both for the UV and the visible wavelength range. Since the FRS is also affected by clouds, d_{rel} for simulated O_4 dSCDs is slightly larger than for SCDs and increases by approximately 15 % in the UV and 5 % in the visible wavelength range. The albedo and the observer geometry do not have a strong influence on d_{rel}. For roll angles minus 1°, the instrument is likely detecting the ground before it can detect the vertical cloud layer. Further, d_{rel} increases with increasing observer altitude and decreases with increasing aerosol load, i.e. clouds, which have a certain distance to the observer, will not have a significant influence on the measured O_4 SCDs. The influence of vertical cloud layers already disappears for an exponentially decreasing aerosol profile with an AOT of 1 both for the UV and visible wavelength range, respectively. For an AOT of 0.1, which represents a reasonable value for the region of Borneo (Figure 9.14), d_{rel} results in approximately 15 km for the UV and approximately 30 km for the visible wavelength range for an observer altitude of h = 0.1 km.

Table 9.2: Overview of the results for d_{rel} for the different scenarios of vertical cloud layers used in this sensitivity study. Each scenario is simulated for a wavelength of 360.8 nm (UV), and 477.1 nm (vis), respectively. d_{rel} is specified for a cloud extinction coefficient of $\epsilon = 2$ km^{-1}. The base run corresponds to scenario 1 from Table 9.1 and includes the following settings: Vertical opaque cloud layer, no aerosols, albedo = 0.05, SZA = 28°, SRAA = 230°, $\alpha = 0°$, observer altitude of 0.1 km, a cloud ssa of 0.999, and a cloud altitude between 0 and 1 km. The changed parameters are specified in the first column.

changed parameter	d_{rel} UV [km]	d_{rel} vis [km]
base run	33	100
O_4 dSCDs	40	105
albedo = 0.6	31	100
SZA = 5°	33	98
SZA = 80°	30	100
SRAA = 0°	27	87
$\alpha = 1°$	31	51
α = -1°	3	6
ssa = 0.7	50	110
h_{cloud} = 1-2 km	38	103
h_{cloud} = 2-3 km	55	103
h_{cloud} = 5-6 km	60	104
h_{cloud} = 10-11 km	70	105
chequerboard structure	35	104
aerosol AOT = 0.1	**15**	**30**
aerosol AOT = 0.2	6	7
aerosol AOT = 0.3	5	6
aerosol AOT = 0.6	3	4
aerosol AOT = 1.0	-	-
aerosol AOT = 2.0	-	-

9.3 Cloud identification with webcam images

In order to further interpret the DOAS measurements, knowledge about the current cloudiness is required. Therefore, it is essential to receive information about the altitude of the cloud cover, the spatial distribution and patchiness of clouds as well as their properties like the cloud extinction or single scattering albedo. Information about the spatial distribution of clouds is e.g. available from satellites measurements. In general, the satellite cloud validation is based on evaluating the O_4 and the oxygen A-band. However, the satellite data is provided in a rather low resolution with a spatial resolution e.g. for MERIS of 250 m in the horizontal. In order to support the satellite studies several ground-based whole sky imaging devices are currently used (e.g. Pfister et al., 2003; Shields et al., 2003; Souza-Echer et al., 2006; Heinle et al., 2010; Klebe et al., 2014). Different algorithms are applied to the recorded images to automatically detect clouds, to estimate the cloud cover, and also to recognize the cloud type.

In order to further estimate the current cloudiness during the different sorties of the SHIVA campaign, the images from the commercial webcam installed aboard the Falcon aircraft (Section 7.1) are used. Firstly, the position of the mini-DOAS FOV within the webcam images is determined via the maximum correlation coefficients between the DOAS intensity and the colour values of the webcam images (Section 9.3.1). This tool gives a first idea, which part of the webcam image is most relevant for the analysis of the data set. The section continues with the estimation of the distance between the aircraft and the different cloud fields using the method of the optical flow (Section

9.3.2).

However, predicting the cloudiness from the webcam images is challenging due to the complexity of the different considered scenes. The images not only contain white clouds and blue sky, but also comprise segments of land, rain forest or ocean. Furthermore, the colour of the clouds is influenced by the presence of shadows or changes in the sunlight intensity. Additionally, the webcam might have moved during the campaign due to hot and humid conditions in the open hangar or due to shaking during turbulences in the air. It is important to note that in the webcam images reflections of the aircraft window are sometimes visible. These reflections can lead to possible restrictions for the different cloud detection concepts.

9.3.1 Determination of the mini-DOAS FOV in the webcam images

The webcam features a horizontal FOV of $\alpha_h = 39 \pm 1°$ and a vertical FOV of $\alpha_v = 29.5 \pm 1°$ (Section 7.1). The FOV of the mini-DOAS instrument is much smaller with a horizontal FOV of approximately $\alpha_h = 2 - 3°$ and a vertical FOV of $\alpha_v = 0.2 - 0.3°$(Section 7.2.1). Thus, the mini-DOAS instrument only covers a very small part of the webcam images. In order to study the influence of different spatial arrangements of the cloud cover on the DOAS data, it is necessary to exactly know the area in the webcam images to which the mini-DOAS telescopes pointed to. One approach to find the mini-DOAS FOV within the webcam images is studying the best correlation between the time series of the average intensities recorded by the mini-DOAS instrument and the time series of the grey and RGB values of the webcam images. This algorithm has already been used to calibrate SO_2 cameras with a DOAS system (Lübcke, 2010, 2014). The algorithm for this study is provided by Peter Lübcke (Institute of Environmental Physics, Heidelberg, personal communication, March 2013).

However, in the case of Lübcke (2010), the situation is less complex since the SO_2 camera and the DOAS system have the same wavelength interval and the correlation is based on the same measured quantities, i.e. the SO_2 absorption. This is not the case for this data set, since the webcam images cover the whole visible spectrum whereas the mini-DOAS instrument only covers a certain wavelength range within the visible spectrum (λ = 408.9 - 533.4 nm). For the DOAS data, the average intensities as well as the O_4 dSCDs of the USB spectrograph in the visible wavelength range are used. In order to improve the correlation with the webcam images, the average DOAS intensities are further convoluted with the blue colour matching function when comparing the intensities (Figure C.1). Furthermore, the webcam images are smoothed with the approximate size and form of the DOAS FOV. It is important to note that a correlation of the grey and RGB values of the webcam images and the DOAS O_4 dSCDs is not straightforward since two different quantities are compared. The O_4 dSCDs are analysed in a certain wavelength range (λ = 462 - 486 nm) where one O_4 absorption band is located with the peak wavelength being at 477.1 nm. The RGB values cover a larger wavelength range between approximately 400 and 700 nm. The O_4 dSCDs and the RGB values do not necessarily have to correlate, e.g. in the presence of a cloud that is very close to the observer, the O_4 dSCDs rather decrease whereas the intensity rather increases.

The total exposure time of the mini-DOAS spectra is five seconds and the webcam images are recorded with a time interval of also five seconds. The acquisition times of both measurements, however, were not synchronised. Therefore, the time series of the webcam images is interpolated to match the time series of the DOAS spectra or vice versa. For the DOAS spectra, the mean time of the start and stop time of each spectrum is used. Next, the linear correlation between the webcam image time series and the DOAS intensity time series is calculated. The mean correlation coefficients of each pixel are depicted in a correlation map, where the maximum correlation coefficient marks the FOV of the mini-DOAS instrument. As mentioned above, the alignment and viewing direction of the webcam might have changed slightly during the SHIVA campaign due to hot and humid conditions or due to shaking of the aircraft during turbulences in the air. Therefore, the correlation has to be repeated for each single flight.

Figure 9.16 shows the maps of the correlation coefficients for sortie 7 on 26 November 2011a.

For the correlation between the webcam image and the DOAS average intensities, maximum correlation coefficients of > 50 % are found within a narrow but long band between a row number of approximately 155 and 175 and between a column number of approximately 70 and 225. For the correlation with the DOAS O_4 dSCDs, the maximum correlation coefficients show a slightly different shape with a longer band stretched across the total width of the image having no pronounced area with maximum values.

Figure 9.17a shows the correlation coefficients for sortie 1 on 16 November 2011. This sortie includes a section in which the Falcon aircraft was flying at low altitudes in the MBL and another part in which the Falcon ascended to the upper troposphere and descended again passing several large varying cloud fields. This sortie further contains several turns. The correlation coefficients show further maxima below the position of the major maximum. If both the flight section at higher altitudes and turns are excluded from the analysis, these features disappear (Figure 9.17b) and a rather thin band of maximum correlation coefficients remains, which identifies the DOAS FOV. Obviously, the correlation of the webcam images with the DOAS O_4 dSCDs does not lead to the same FOV pattern as the intensities. Since the O_4 absorption is strongest close to the ground, the grey and RGB values of the webcam image do not necessarily have to correlate.

The stretched shape of the maximum correlation coefficients might be due to the exposure time of the mini-DOAS spectra of five seconds, whereas the effective exposure time of the webcam images is much shorter. The exposure time of the webcam images is obviously shorter than one second. Unfortunately, the exact exposure time of the webcam images is not known, since the read-out of the exposure time was not possible to control. Since the aircraft moves forward during the exposure time of one spectrum, the mini-DOAS spectra are integrated over a larger temporal and also spatial interval than the webcam images.

The correlation for a varying cloud field is not always unambiguous, since several cloudy pixel in the webcam image might resemble the pixel area where the DOAS FOV pointed to. Sections where a dense cloud cover occurs can degrade the correlations. Turns of the aircraft can further degrade the correlations, especially during left turns when the mini-DOAS has a viewing direction towards the ground/ocean.

The incomplete knowledge about the exact exposure time of the webcam is the major restriction of this method. Furthermore, the time resolution of the recorded images was restricted during the SHIVA campaign in order to reduce the processor load of the controller. For future applications it is recommended to use a professional webcam for which the exposure time can be logged. Similar to the DOAS intensities, the intensities of the webcam images can then be divided by the exposure time. In addition to that, images should be recorded with a high time resolution to avoid possible time offsets in the correlation.

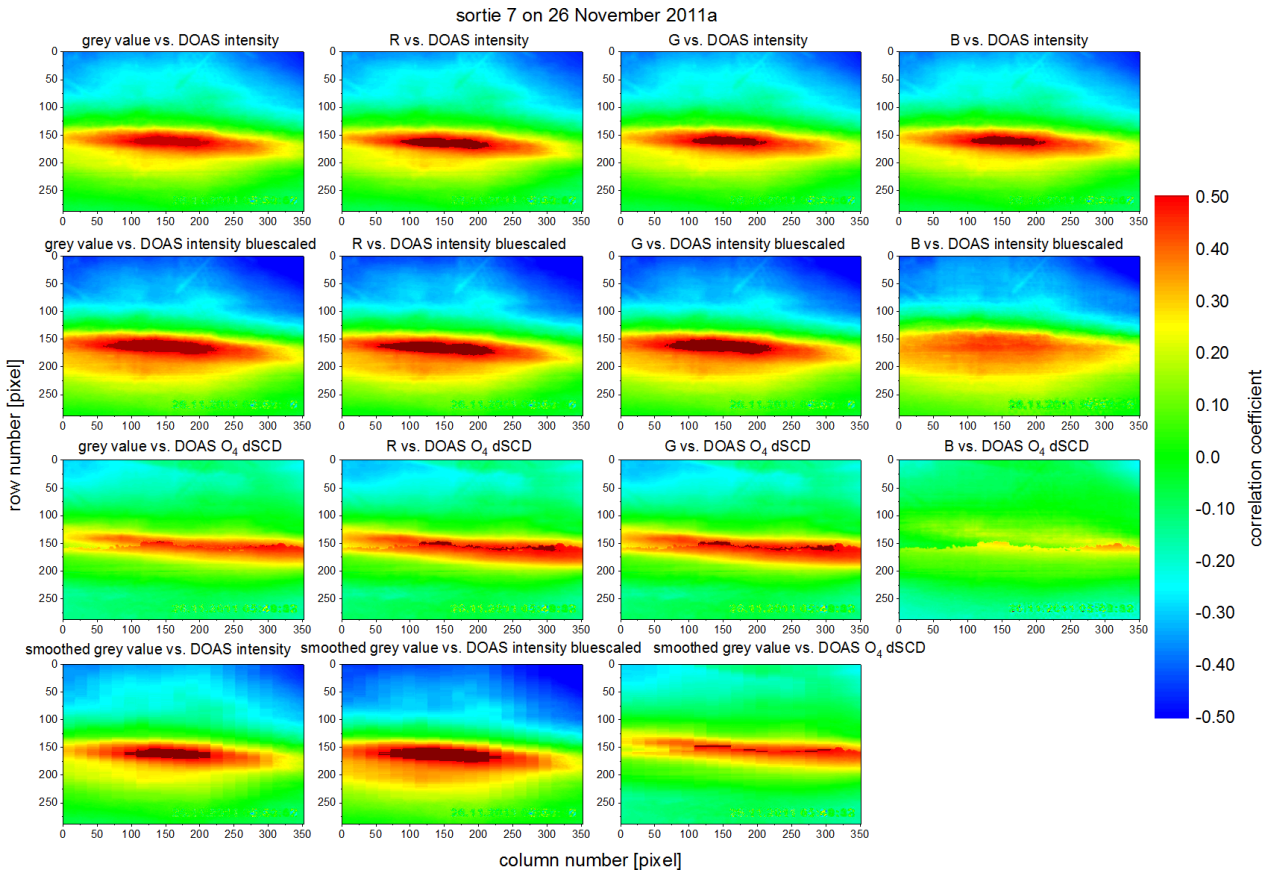

Figure 9.16: Correlation coefficients of the webcam images and the DOAS data for sortie 7 on 26 November 2011a. For the webcam images either the grey, R, G, or B values are used for the correlation, whereas for the DOAS data either the average intensity, the average blue-scaled intensity or the O_4 dSCDs in the visible wavelength range are used. The coordinates of the largest correlation coefficients denote the position of the DOAS FOV in the webcam images.

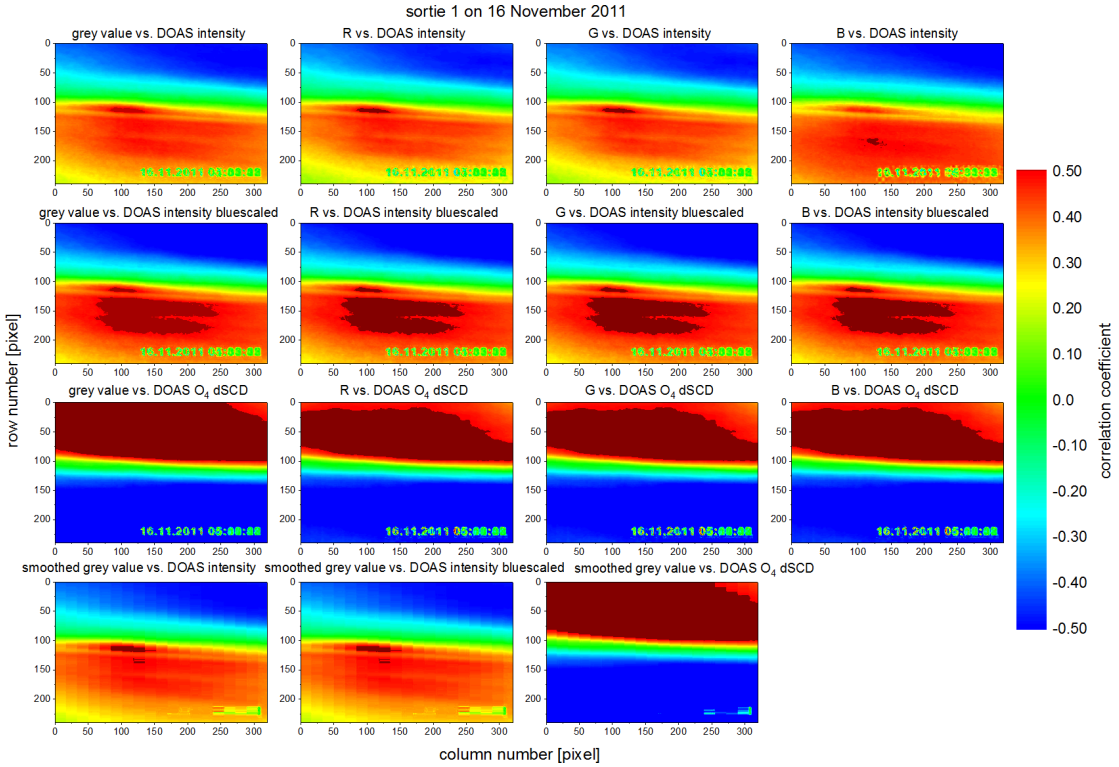

(a)

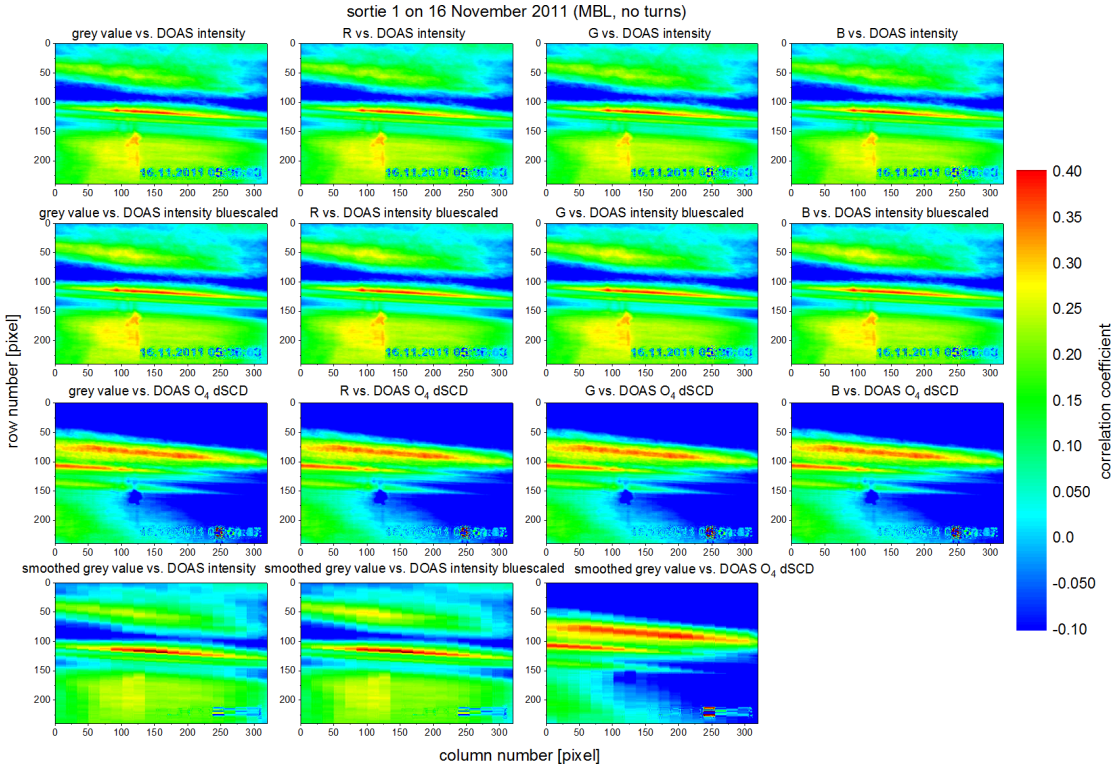

(b)

Figure 9.17: As Figure 9.16, but for (a) sortie 1 on 16 November 2011 and for (b) the low level part of sortie 1 on 16 November 2011 where the Falcon aircraft was flying within MBL; turns of the aircraft are excluded in the latter panel.

9.3.2 Determination of the cloud distance using optical flow methods

In this section, the distance between the aircraft and the clouds is estimated using optical flow methods. The algorithm used in this study is kindly provided by Angelika Klein (Institute of Environmental Physics, Heidelberg, June 2014). The optical flow describes the independent estimation of motion at each pixel (Szeliski, 2011). The currently available optical flow methods are mainly based on the original formulation by (Horn and Schunck, 1981). They developed a regularisation-based framework to simultaneously minimise over all flow vectors the brightness or colour difference between corresponding pixels summed over the image (Szeliski, 2011). An overview of optical flow estimation and its principles is for example given by Sun et al. (2010). Recently developed algorithms can, for example, be found on `http://vision.middlebury.edu/flow/`. Sun et al. (2010) provide an optical flow MATLAB code, which is publicly available at `http://www.cs.brown.edu/people/dqsun/`, and used for this analysis. Details on this technique are not presented in this study.

In the following discussion, it is assumed that the movement of the clouds is negligible relative to the movement of the Falcon aircraft, i.e. the velocity of the clouds is much smaller than the velocity of the Falcon aircraft ($v_{clouds} \ll v_F$). The minimum distance between the observer, i.e. the Falcon aircraft, and the cloud objects is referred to as d_{ref}. The distance s between two consecutive webcam images is given by $s = v_F \cdot t$, with v_F being the velocity of the aircraft and with t being the temporal difference between two webcam images ($t = 5$ s). Furthermore, the FOV of the webcam is needed, which is $\mathrm{FOV_h} = 39 \pm 1°$ in horizontal direction and $\mathrm{FOV_v} = 29.5 \pm 1°$ in vertical direction (Section 7.1). The displacement of an object in two consecutive webcam images can be divided into the displacement u in x-direction and the displacement v in y-direction. The maximum displacement in x-direction that can be resolved by the webcam is the image width (i.e. 320 and 352 pixel, respectively), whereas the maximum displacement in y-direction is given by the image height (i.e. 240 and 288 pixel, respectively). The webcam images have different sizes since the image size was changed during the campaign from a resolution of 320 x 240 pixel (16 - 19 November 2011) to 352 x 288 (21 November - 11 December 2011) (see Section 7.1). The total displacement in x- and y-direction is given by $D = \sqrt{u^2 + v^2}$. The displacement in x- and y-direction is estimated by the optical flow Matlab code provided by Sun et al. (2010).

The problem of determining the 3D position of a point from a set of corresponding image locations and known camera positions is known as triangulation (e.g. Szeliski, 2011). The derivation of the distance d to a point is based on trigonometrical relations. Figure 9.18 illustrates the geometrical situation, where d represents the unknown cloud distance. The following geometrical relations can be deduced from Figure 9.18:

$$\tan\beta = \frac{s/2}{d} \tag{9.3}$$

$$\tan\beta = \frac{s'/2}{d_{ref}} \tag{9.4}$$

$$\tan\frac{\mathrm{FOV_h}}{2} = \frac{s}{d_{ref}}. \tag{9.5}$$

The process of determining the distance via trigonometrical relations is also known as triangulation Solving Equation 9.3 for the unknown quantity d and inserting $\tan\beta$ from Equation 9.4 and the reference distance d_{ref} from Equation 9.5 leads to the following equation:

$$d = \frac{s \cdot s}{2 \cdot s' \cdot \tan\frac{\mathrm{FOV_h}}{2}}. \tag{9.6}$$

One pixel in the webcam image is given by: 1 pixel $= \frac{s}{\text{image width}} = \frac{v \cdot t}{\text{image width}}$, with the image width given in pixel. Thus, the ratio of s/s' can be expressed as:

$$\frac{s}{s'} = \frac{\text{image width} \cdot \frac{\mathrm{v \cdot t}}{\text{image width}}}{D \cdot \frac{v \cdot t}{\text{image width}}} = \frac{\text{image width}}{D}, \tag{9.7}$$

with D being the displacement. The unknown cloud distance d can therefore be derived according to the following equation:

$$d = \frac{\text{image width} \cdot v_F \cdot t}{2 \cdot D \cdot \tan \frac{FOV_h}{2}}. \tag{9.8}$$

In this case, it is assumed that the webcam is not tilted and is parallel to the horizon line. In reality, however, both the webcam and the aircraft have a roll, pitch and yaw angle, respectively. Thus, the image width has to be extended to the effective image width according to:
$\sqrt{\text{image width}^2 + (\text{image width} \cdot \tan\gamma)^2}$, with γ being the pitch angle of the aircraft.

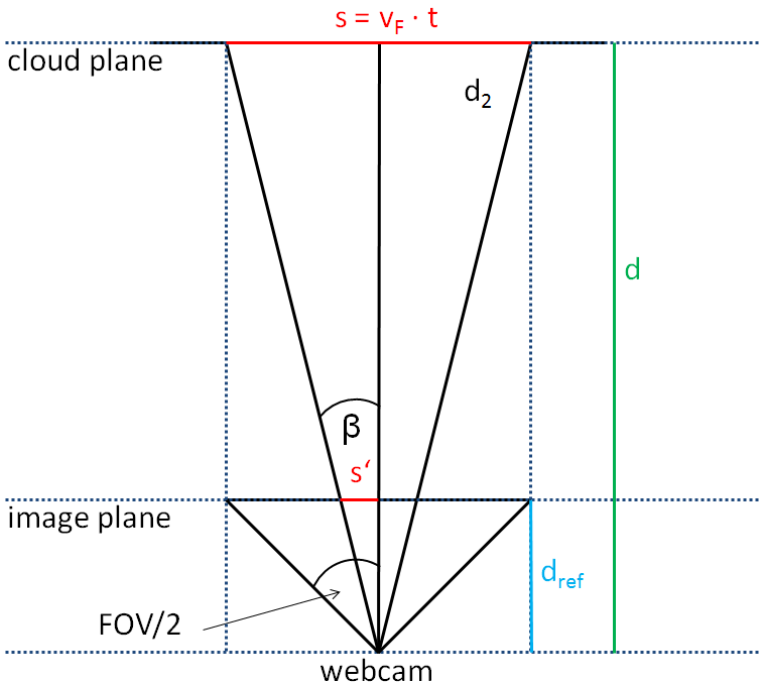

Figure 9.18: Sketch of the geometrical situation for the determination of the cloud distance.

Equation 9.8 is verified for a simple example. Figure 9.19 shows two consecutive webcam images recorded during sortie 1 on 16.11.2011 where a runway close to the coast of Borneo can be clearly identified. The ending points P_1 and P_2 of this object are marked manually in each image, respectively. The displacement results in approximately $D = 125 \pm 5$ pixel. Using Equation 9.8, a distance between the aircraft and the runway of approximately $d = 2.2 \pm 0.1$ km can be calculated. The distance between the aircraft and the runway can be further determined using Google Earth (Figure 9.19) and results in approximately $d = 2.3 \pm 0.1$ km. It can be concluded that Equation 9.8 leads to reasonable distances.

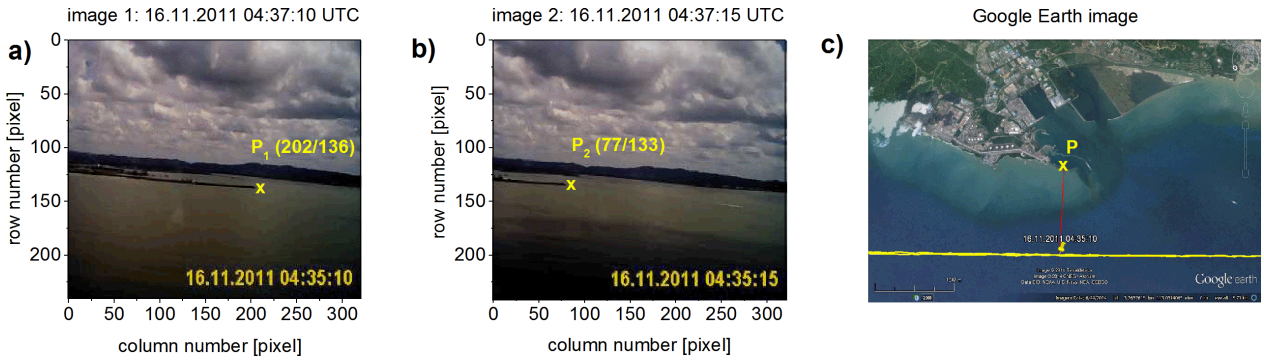

Figure 9.19: a) and b) Two consecutive webcam images recorded during sortie 1 on 16.11.2011. The yellow cross marks the ending points of the runway, respectively. The displacement of these ending points is used to calculate the distance d between the aircraft and the runway. c) Map adapted from Google Earth (September 2014) showing the flight track (yellow line) and the ending point of the runway (yellow cross). The red line corresponds to the distance between the aircraft and the ending point of the runway.

In the following, the optical flow MATLAB algorithm is used to determine the displacement automatically. For distinctive cloud features the performance of this algorithm can be checked manually as described in the simple example before.

The cloud distance d is determined for four situations occurring during the descent of sortie 7 on 26.11.2011 using the optical flow MATLAB algorithm for the determination of the displacement. If the displacement for distinctive features at the border of the clouds is determined manually as described in the simple example before, similar cloud distances can be derived as compared to the optical flow algorithm. Figure 9.20 shows the colour index, the brightness, and the O_4 dSCDs in the UV and visible wavelength range. Figure 9.21 shows the webcam images of these four situations together with the cloud distance d inferred for two consecutive webcam images, respectively. The FOV of the mini-DOAS instrument for this sortie of the Falcon aircraft is approximately located at (140±50/160±10) pixel and is highlighted with a black circle (Figure 9.16). Different assumptions are made to explain the behaviour of the colour index, the brightness, and the O_4 dSCDs in the presence of clouds with different distances to the aircraft.

In case a) and b) an enhancement in the colour index and brightness can be observed, whereas the O_4 dSCDs do not change significantly, i.e. this cloud field has no significant influence on the O_4 dSCDs. In case a) the cloud has a distance to the aircraft of approximately 60 to 90 km. According to the simulations in Section 9.2.3, a cloud with a distance between 60 and 90 km at an altitude between 7 and 8 km would already have an impact on the O_4 dSCDs. This can be possibly due to the FOV of the mini-DOAS instrument covering both cloudy and cloud-free pixels in the webcam images. The increase in the colour index and brightness could possibly be caused by the cloud layer below.

In case c) a decrease in the colour index, the brightness, and the O_4 dSCDs in the visible wavelength appears, whereas for the O_4 dSCDs in the UV this decrease is very small and hardly visible. The cloud seems to have a distance to the aircraft of approximately 100 to 150 km. According to the simulations in Section 9.2.3 for an observer altitude of approximately 3 km, a cloud with a distance of 100 km can still lead to small changes in the O_4 dSCDs in the visible wavelength range. The O_4 dSCDs in the UV wavelength range are not affected by this cloud as the relevant cloud distance, where changes in the O_4 dSCDs occur, is much smaller in the UV than in the visible wavelength range.

In case d) a strong decrease in the O_4 dSCDs can be observed, whereas the colour index and the brightness are slightly enhanced. The Falcon aircraft is flying very close to a cloud. The cloud distance inferred for this situation yields approximately between 5 and 10 km in the region of the

DOAS FOV. According to the simulations in Section 9.2.1, a cloud distance of less than 10 km at an observer altitude of 0.1 km can lead to changes in the O_4 dSCDs of up to approximately 75 % in the UV and 100 % in the visible wavelength range. However, this value decreases in the presence of aerosols.

In summary, the optical flow or triangulation method is an important tool to estimate the distance of clouds using webcam images. Equation 9.8 can be validated using fixed objects detected in the webcam images, which can be simultaneously detected by Google Earth. However, the interpretation of the observed brightness, colour index, or O_4 dSCDs in combination with the inferred cloud distance is not always unambiguous. In order to validate the performance of the optical flow algorithm with respect to complex objects such as clouds, cloud LIDAR measurements are required, which were not available during the SHIVA campaign. Furthermore, it is recommended to record webcam images in the raw image format in order to avoid any camera corrections, such as colour grading or white balancing, since these effects might degrade the determination of the displacement by optical flow methods.

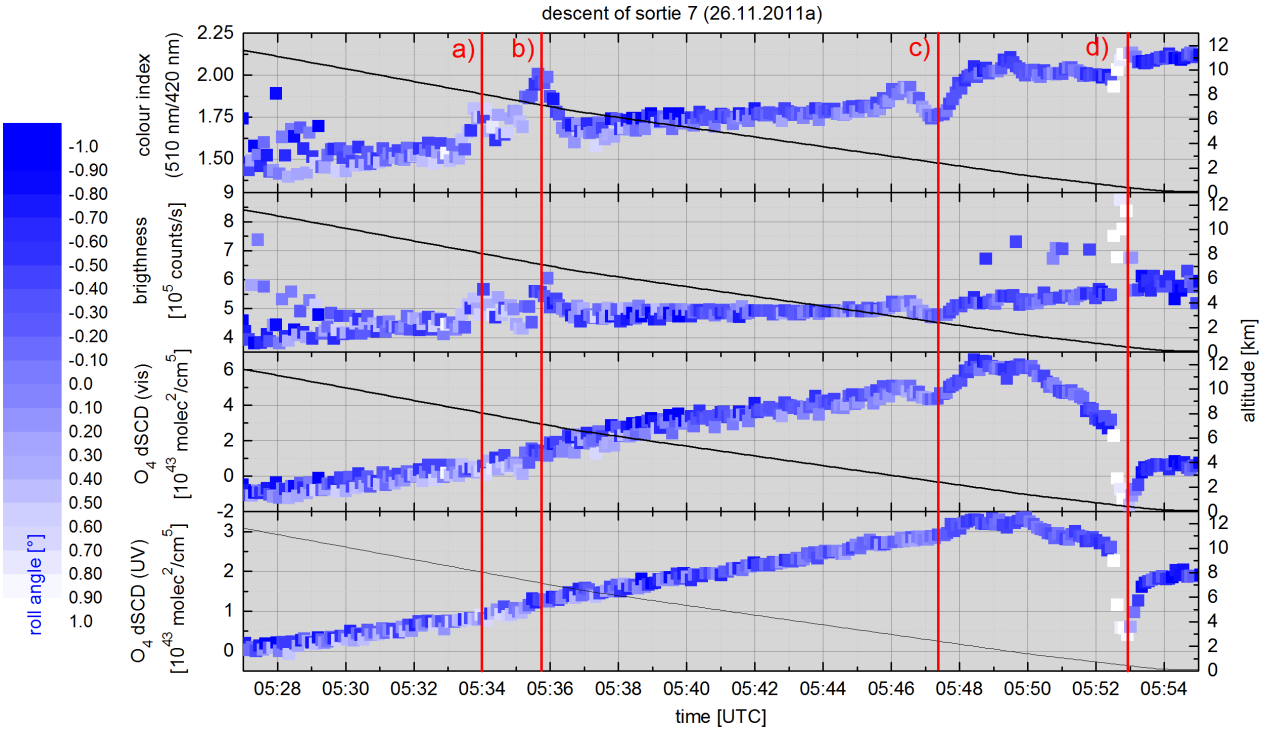

Figure 9.20: The colour index (510 nm/ 420 nm), the brightness, and the O_4 dSCDs in the visible and UV wavelength range colour-coded with the roll angle during the descent of sortie 7 on 26 November 2011.

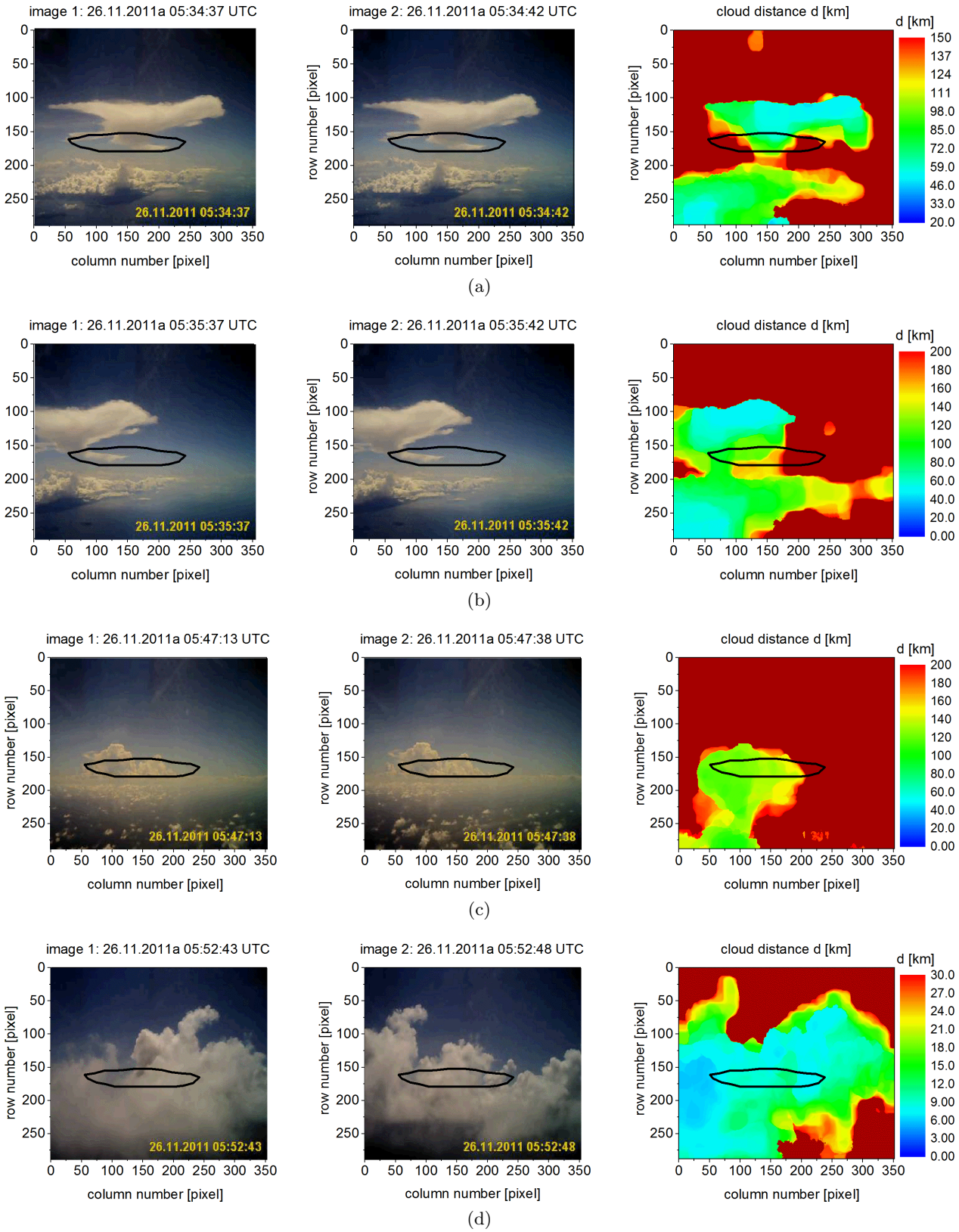

Figure 9.21: Cloud distance in km calculated from two consecutive webcam images for four different sections recorded during sortie 7 on 26 November 2011a. The black ellipse highlights the DOAS FOV determined in Figure 9.16.

10. Retrieval of tropospheric trace gas abundances

Knowledge of the atmospheric light path length is essential for the derivation of concentrations of the targeted trace gases from the measured dSCDs. As described in Chapter 9, clouds can significantly influence the light path length and thus the interpretation of DOAS measurements. Additional information regarding the cloud parameters, such as their optical properties or their spatial distribution, are required in order to accurately simulate the radiative transfer. This additional knowledge can be provided by collocated measurements by other instruments deployed on the same aircraft, e.g. from LIDAR (Light detection and ranging) measurements. However, during the SHIVA campaign none of these cloud properties were measured.
This chapter presents two different methods and their limitations in order to derive mixing ratios and vertical profiles of traces gases measured with the DOAS technique under the complex atmospheric conditions during the SHIVA campaign. Section 10.1 describes the scaling method with a gas of known profile, which is used as a proxy gas. This method represents a rough estimation and the inferred mixing ratios can be rather regarded as a lower limit. In this study, the method is based on the fact that the profile of the O_2-O_2 collision complex O_4 is known since it is proportional to the square of the profile of O_2 and only depends on meteorological parameters, such as temperature and pressure (Section 2.4.5). O_4 absorption can be derived from the DOAS measurements. Since the profile shapes of the trace gas of interest and O_4 are not identical, an additional correction factor (henceforth called α) must be calculated using RT simulations. If simultaneous in situ measurements of O_3 are available, O_3 can also be used as a proxy gas (Raecke, 2013). Since for the O_3 DOAS measurements in this study a separation of the tropospheric and stratospheric signal is not possible, the inferred O_3 dSCDs are not used as a proxy gas.
In Section 10.2, the HEIPRO retrieval described in Section 5.5 is used to infer vertical profiles for several selected ascents and descents of the Falcon aircraft. Profile information is only available from the different ascents and descents of the Falcon aircraft since during the horizontal legs at one fixed flight altitude the mini-DOAS instrument did not perform any elevation angle scans due to a missing connection to the online flight attitude data of the Falcon aircraft. The retrieved vertical profiles are further compared to the results of the scaling method with a gas of known profile and to in situ measurements of water vapour (Section 10.3). The respective error sources and uncertainties are characterised in each section.

10.1 Scaling method with a gas of known profile

In order to infer the approximate mixing ratios in the MBL and free troposphere from the measured dSCDs, the scaling method with a gas of known profile can be applied. This method is henceforth referred to as the O_4 scaling method since O_4 is used as a proxy gas in this study.
This section starts with the basic concept of this method (Section 10.1.1) and continues with the estimation of the reference SCDs S_{ref} (Section 10.1.2), which are required to convert the measured dSCDs into absolute SCDs. O_4 SCDs can be directly determined using a Kurucz spectrum as a FRS (Section 8.1). S_{ref_x} and thus the SCD_x of the different trace gases are not known. For a few

trace gases, it can be assumed that $S_{ref_{\mathrm{x}}}$ of the trace gas x is very small for the high altitudes where the FRS is recorded, i.e. $\mathrm{SCD_x} \approx \mathrm{dSCD_x}$. For other trace gases $S_{ref_{\mathrm{x}}}$ has to be determined using radiative transfer calculations, in order to account for the overhead absorption.
In Section 10.1.3 it is assumed that the trace gas x has the same profile shape as O_4. The errors resulting from this assumption are estimated using the example of HCHO. Since the profile shapes of the trace gas x and O_4 are different, a correction factor α is implemented, in order to account for the different profile shapes. This correction factor is calculated using radiative transfer simulations. The O_4 scaling method assumes similar radiative transfer at both the O_4 wavelength ($\lambda_{UV} = 360.8$ nm, $\lambda_{vis} = 477.1$ nm) and the wavelength region where the trace gas x shows its major absorption features. Section 10.1.4 discusses the validity of this assumption. In the last Section 10.1.5 the error of the O_4 scaling method is estimated.

10.1.1 Basic concept

In general, the SCD S of the trace gas of interest x and the proxy trace gas y can be modelled by:

$$S_x = \sum_i [\mathrm{x}]_i \cdot B_{\mathrm{x}_i} \cdot z_i \tag{10.1}$$

$$S_y = \sum_i [\mathrm{y}]_i \cdot B_{\mathrm{y}_i} \cdot z_i, \tag{10.2}$$

with $[\mathrm{x}]_i$ and $[\mathrm{y}]_i$ being the concentration of x and y in the layer i with the layer height z_i, and B_{x_i} and B_{y_i} representing the Box-AMFs in this layer (Equation 4.46), respectively. The concentrations $[\mathrm{x}]_j$ and $[\mathrm{y}]_j$ in a certain layer j can therefore be determined according to:

$$[\mathrm{x}]_j = \frac{S_x - \sum_{i \neq j} [\mathrm{x}]_i \cdot B_{\mathrm{x}_i} \cdot z_i}{B_{\mathrm{x}_j} \cdot z_j} \tag{10.3}$$

$$[\mathrm{y}]_j = \frac{S_y - \sum_{i \neq j} [\mathrm{y}]_i \cdot B_{\mathrm{y}_i} \cdot z_i}{B_{\mathrm{y}_j} \cdot z_j}. \tag{10.4}$$

The ratio of these two equations yields:

$$\frac{[\mathrm{x}]_j}{[\mathrm{y}]_j} = \frac{\frac{S_x - \sum_{i \neq j} [\mathrm{x}]_i \cdot B_{\mathrm{x}_i} \cdot z_i}{B_{x_j} \cdot z_j}}{\frac{S_y - \sum_{i \neq j} [\mathrm{y}]_i \cdot B_{\mathrm{y}_i} \cdot z_i}{B_{y_j} \cdot z_j}} = \frac{B_{y_j}}{B_{x_j}} \cdot \left(\frac{S_x - \sum_{i \neq j} [\mathrm{x}]_i \cdot B_{\mathrm{x}_i} \cdot z_i}{S_y - \sum_{i \neq j} [\mathrm{y}]_i \cdot B_{\mathrm{y}_i} \cdot z_i} \right). \tag{10.5}$$

In the following, a dimensionless factor α is introduced according to:

$$\alpha_{\mathrm{x}_j} = \frac{S_x - \sum_{i \neq j} [\mathrm{x}]_i \cdot B_{\mathrm{x}_i} \cdot z_i}{S_x} = \frac{[\mathrm{x}]_j \cdot B_{\mathrm{x}_j} \cdot z_j}{\sum_i [\mathrm{x}]_i \cdot B_{\mathrm{x}_i} \cdot z_i}, \tag{10.6}$$

$$\alpha_{\mathrm{y}_j} = \frac{S_y - \sum_{i \neq j} [\mathrm{y}]_i \cdot B_{\mathrm{y}_i} \cdot z_i}{S_y} = \frac{[\mathrm{y}]_j \cdot B_{\mathrm{y}_j} \cdot z_j}{\sum_i [\mathrm{y}]_i \cdot B_{\mathrm{y}_i} \cdot z_i}. \tag{10.7}$$

α_{x} describes the relative signal contribution of the SCD S_{x_j} of one model altitude layer j with the Box-AMF B_{x_j} to the total SCD S_{x} measured at the detector altitude (Raecke, 2013). It is assumed that the measured ratio of α_{x} and α_{y} is equal to the modelled ratio:

$$\left. \frac{\alpha_x}{\alpha_y} \right|_{\mathrm{meas}} = \left. \frac{\alpha_x}{\alpha_y} \right|_{\mathrm{model}}. \tag{10.8}$$

Solving Equation 10.5 for $[\mathrm{x}]_j$ and including the α factors results in the following equation:

$$[\mathrm{x}]_j = \frac{B_{y_j}}{B_{x_j}} \cdot \frac{\alpha_{x_j}}{\alpha_{y_j}} \cdot \frac{S_x}{S_y} \cdot [\mathrm{y}]_j = \frac{\alpha^*_{x_j}}{\alpha^*_{y_j}} \cdot \frac{S_x}{S_y} \cdot [\mathrm{y}]_j, \tag{10.9}$$

with $\alpha^*_{x_j}$ being the ratio of α_{x_j} and B_{x_j}, and $\alpha^*_{y_j}$ being the ratio of α_{y_j} and B_{y_j}, respectively:

$$\alpha^*_{x_j} = \frac{\alpha_{x_j}}{B_{\mathrm{x}_j}} = \frac{[\mathrm{x}]_j \cdot z_j}{\sum_i [\mathrm{x}]_i \cdot B_{\mathrm{x}_i} \cdot z_i} \tag{10.10}$$

$$\alpha^*_{y_j} = \frac{\alpha_{y_j}}{B_{\mathrm{y}_j}} = \frac{[\mathrm{y}]_j \cdot z_j}{\sum_i [\mathrm{y}]_i \cdot B_{\mathrm{y}_i} \cdot z_i}. \tag{10.11}$$

$$\tag{10.12}$$

For the simple case, it is assumed that the profile shape of the trace gas x is similar to the profile shape of the proxy gas y, i.e. the profiles are proportional to each other. In this case, $\alpha^*_{x_j}$ is equal to $\alpha^*_{y_j}$, i.e. $\frac{\alpha^*_{x_j}}{\alpha^*_{y_j}} = 1$, and Equation 10.9 simplifies to:

$$[\mathrm{x}]_{j,\mathrm{basic}} = \frac{S_x}{S_y} \cdot [\mathrm{y}]_j, \tag{10.13}$$

i.e. all radiative transfer effects would ideally cancel out and no radiative transfer simulations are required. In the following, this simple case is referred to as basic scaling method. However, in general, the profile shapes of the different trace gases are dissimilar to the profile shape of the proxy gas y. Thus, the ratio of α^*_x/α^*_y has to be determined using radiative transfer calculations in the majority of cases.
In this study, O_4 is used as a proxy gas y. The concentration of O_4 is proportional to the square of the O_2 concentration and hence decreases exponentially with altitude (see Section 2.4.5). The O_2 concentration can be calculated according to Equation 2.30 using the actual pressure and temperature measured by the Falcon aircraft sensors. Since in this study O_4 is used as proxy gas y, the method is henceforth referred to as O_4 scaling method. In this case, Equation 10.9 can be expressed by:

$$[\mathrm{x}]_j = \frac{\alpha^*_{x_j}}{\alpha^*_{O_4 j}} \cdot \frac{S_x}{S_{\mathrm{O}_4}} \cdot [\mathrm{O}_2]^2_j. \tag{10.14}$$

In order to determine volume mixing ratios (VMRs) of a particular trace gas x in the layer j, the resulting equation of the O_4 scaling method leads to:

$$\mathrm{VMR}_{\mathrm{x}_j} = \frac{[\mathrm{x}]_j \cdot T_j \cdot R}{p_j \cdot N_A} = \frac{\alpha^*_{x_j}}{\alpha^*_{O_4 j}} \cdot \frac{S_x}{S_{\mathrm{O}_4}} \cdot \frac{0.21^2 \cdot p_j \cdot N_A}{R \cdot T_j}, \tag{10.15}$$

with p_j and T_j being the respective pressure and temperature in the layer j, with N_A being the Avogadro number, and R the gas constant. Several error sources and uncertainties propagate into the total error of the O_4 scaling method such as the error of the measured dSCDs or the uncertainties due to the input parameters of the RT model when calculating the α^* correction factor. In the following, the details of the O_4 scaling method are specified.

10.1.2 Estimation of the reference SCD

Knowledge about the reference SCD S_{ref} is required when applying the O_4 scaling method, in order to convert the measured dSCDs dS into SCDs S according to:

$$S_{\mathrm{x}} = dS_{\mathrm{x}} + S_{ref_{\mathrm{x}}}. \tag{10.16}$$

O_4 SCDs can be directly determined using a Kurucz spectrum as a FRS (Section 8.1). Thus, the O_4 reference SCD S_{ref} does not need to be calculated. If a particular trace gas x is evaluated in the UV wavelength region, the O_4 SCDs of the O_4 absorption band at 360 nm are chosen. For trace gases analysed in the visible wavelength range the O_4 band at 477 nm is used instead, in order to

reduce parts of the wavelength dependence of Rayleigh and Mie scattering. The inferred O_4 SCDs for the UV and visible wavelength range are shown in Figure 8.7 for each flight, respectively.
However, if in-flight spectra are used as FRS for the DOAS spectral analysis of the different trace gases x, the reference SCD S_{ref_x} is 'a priori' not known. Since the in-flight FRS are taken from the highest altitude of each sortie, for some trace gases x it can be assumed that $SCD_x \approx dSCD_x$. This assumption likely leads to smaller VMRs since the S_{ref_x} is not accounted for.
In the following, the S_{ref_x} is estimated using 3D radiative transfer simulations for representative trace gas profiles. Since the cloud cover during the recording of the FRS is quite variable for the different sorties (Figure 8.5), different synthetic 3D cloud fields are implemented in McArtim, similar to the cloud sensitivity studies in Section 9.2. These cloud fields comprise a horizontal cumulus cloud layer located at an altitude of h = 0.5-1.0 km with a chequerboard structure and an extinction of $\epsilon = 60$ km^{-1}. In the simulations the distance between the single chequerboard cells is varied between 2 km, 4 km, and 10 km. Furthermore, cirrus cloud layers are included at different altitudes (h = 10.0-10.5 km, 11.0-11.5 km, 12.5-13.0 km, 13.0-13.5 km) with an extinction of $\epsilon = 1$ km^{-1}. Model runs are performed for all possible combinations of these cloud fields, including the cloud-free case. S_{ref_x} is simulated for the different cloud scenarios using the observation geometries of the FRS (SZA, SRAA, height, roll angle) chosen for each sortie of the Falcon aircraft (Table 8.2). The latitude and longitude of the different FRS is set to a fixed value of 4 °N and 112 °E, respectively, in order to keep the computation time low. These values correspond to the centre of the horizontal model grid. The atmosphere is modelled from the ground to an altitude of 30 km with an altitude grid size of 0.5 km below 13 km and a coarser grid size between 13 km and 30 km. The albedo is set to 5 % both for the UV and visible wavelength range.
S_{ref_x} is determined for HCHO at $\lambda = 347$ nm, NO_2 at $\lambda = 450$ nm, H_2O at $\lambda = 450$ nm, CHOCHO at $\lambda = 455$ nm, and for IO at $\lambda = 427$ nm. The input profiles of the model atmosphere are shown in Figure 10.1. The temperature, pressure, and O_3 profiles are taken from an ascent of an ozone sonde launched aboard the RV Sonne on 26.11.2011. The O_4 profile is calculated using these temperature and pressure profiles. An exponentially decreasing aerosol profile with an AOT of 0.1 is assumed. The input profiles of HCHO and NO_2 are derived from the TOMCAT model for the descent of sortie 7 on 26.11.2011. In order to account for the stratospheric NO_2, the NO_2 profile is further extended up to 30 km using a profile retrieved from ballon-borne DOAS measurements in Teresina, Brasil in March 2004 (Butz, 2006). The H_2O profile is derived from the absolute humidity measured by the Falcon sensor during the descent of sortie 7 on 26.11.2011 and continued to 30 km by a SAGE II profile. The same profiles are assumed for HCHO and CHOCHO but for CHOCHO the profile is scaled to a VMR of approximately 50 ppt at the ground. The IO profile is derived from the HEIPRO retrieval (Section 10.2.2) for the descent of sortie 7 on 26.11.2011.

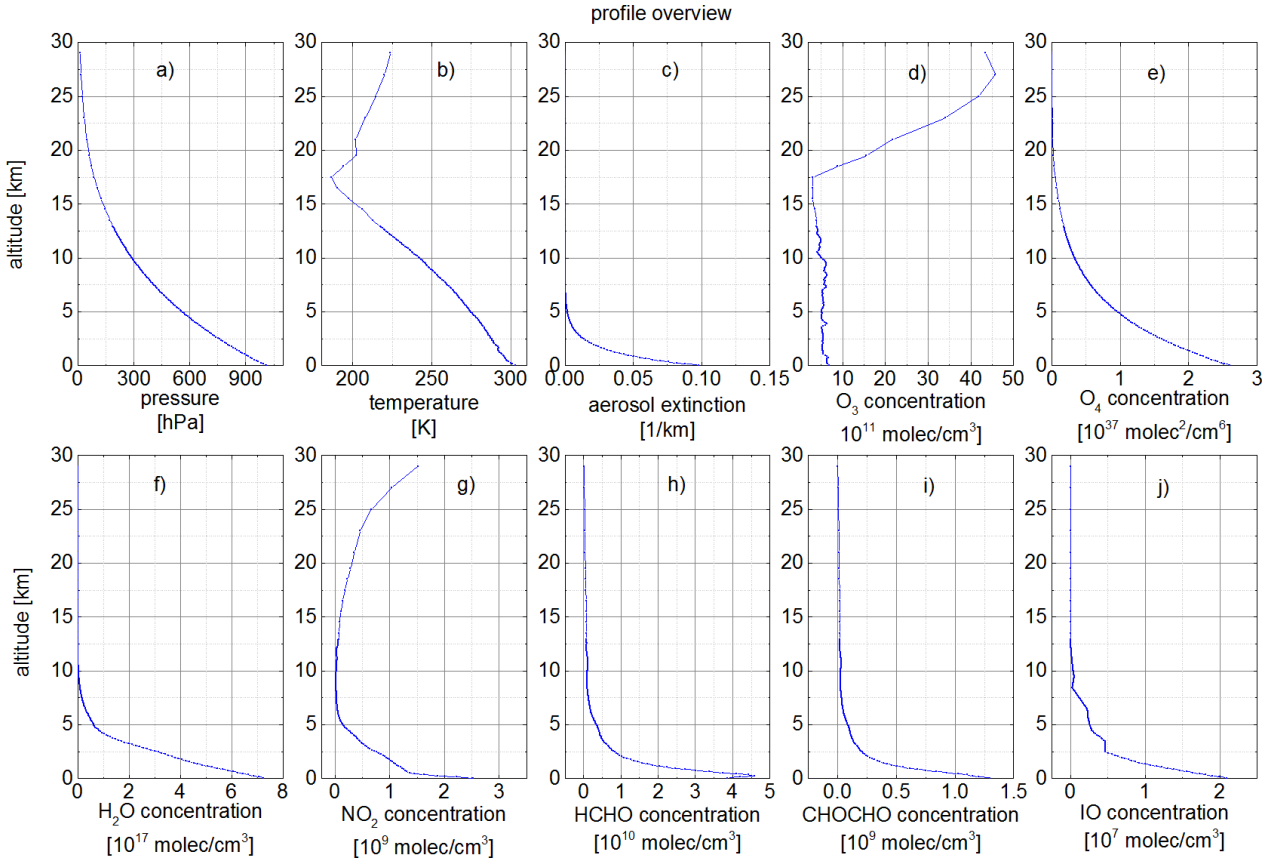

Figure 10.1: Overview of the profiles used as input for the model atmosphere in McArtim. The origin of these profiles is described in the text.

The resulting S_{ref_x} is averaged over the different model runs for each FRS. Table 10.1 summarises the resulting mean S_{ref_x} simulated for the different trace gases x for each flight of the Falcon aircraft together with their standard deviation. As an example, Figure 10.2 shows the histograms of the simulated $S_{ref_{O_4}}$ and $S_{ref_{HCHO}}$ for each flight, respectively. In order to validate the inferred S_{ref_x}, the $S_{ref_{O_4}}$ estimated using these 3D radiative transfer simulations can be compared to the $S_{ref_{O_4}}$ determined using a Kurucz spectrum as a FRS. Table 10.2 and Figure 10.3 summarise the simulated and measured $S_{ref_{O_4}}$ for each sortie of the Falcon aircraft. The measured $S_{ref_{O_4}}$ are larger than the simulated $S_{ref_{O_4}}$, especially for the UV wavelength range. This difference could be due to uncertainties in the input parameters of the model atmosphere, such as the 3D cloud fields, which may incorrectly represent the actual atmospheric conditions prevailing during the measurements. However, it might also be due to an O_4-specific problem. In several studies (e.g. Clémer et al., 2010) an O_4 scaling factor of 1.25 is introduced, which is applied to the O_4 absorption cross-section of Hermans et al. (1999) to achieve a better agreement between measured and simulated O_4 SCDs. However, the reason for this discrepancy remains unclear. As a further validation, the simulated reference SCDs of H_2O are compared to the $S_{ref_{H_2O}}$ determined using a Kurucz spectrum as a FRS (Figure 10.4). It has to be noted that the H_2O SCDs determined using a Kurucz spectrum as a FRS have to be treated with care and are only used for validation purposes. The spectral analysis using a Kurucz spectrum as a FRS is only reasonable for strong absorbers with broad absorption bands, such as O_4 (Section 8.1). The measured $S_{ref_{H_2O}}$ are larger than the simulated $S_{ref_{H_2O}}$. However, they still lie within the error bars. Since the measured $S_{ref_{H_2O}}$ are approximately 40 % larger than simulated $S_{ref_{H_2O}}$, the inferred VMRs might be underestimated.

Table 10.1: Overview of the mean reference SCDs S_{ref_x} simulated for different trace gases x for each flight of the Falcon aircraft. For sortie 4 the FRS from sortie 5 is used and for sortie 14 the FRS from sortie 13 is used (see Table 8.2). During sortie 10 no Falcon data, i.e. temperature and pressure, is available due to a failure in the data storing process. Thus, the O_4 scaling method can not be applied for this sortie. The respective errors correspond to the standard deviation of the mean S_{ref_x}.

sortie	date	altitude [km]	SZA [°]	$S_{ref_{HCHO}}$ $[10^{16}\frac{\text{molec}}{\text{cm}^2}]$	$S_{ref_{NO_2}}$ $[10^{15}\frac{\text{molec}}{\text{cm}^2}]$	$S_{ref_{H_2O}}$ $[10^{23}\frac{\text{molec}}{\text{cm}^2}]$	$S_{ref_{CHOCHO}}$ $[10^{14}\frac{\text{molec}}{\text{cm}^2}]$	$S_{ref_{IO}}$ $[10^{12}\frac{\text{molec}}{\text{cm}^2}]$
1	16.11.2011	12.9	49	1.00±0.13	2.49±0.31	1.60±0.50	3.81±0.78	4.05±1.12
2	19.11.2011a	8.4	26	1.09±0.07	1.67±0.11	2.53±0.44	4.42±0.47	7.55±1.04
3	19.11.2011b	12.9	82	1.12±0.20	6.58±0.18	1.17±0.40	4.61±1.55	3.44±1.32
5	22.11.2011	5.8	27	1.53±0.08	2.15±0.11	5.29±0.47	6.99±0.44	18.4±1.06
6	23.11.2011	8.8	26	1.08±0.07	1.66±0.08	2.43±0.32	4.31±0.26	7.47±0.78
7	26.11.2011a	12.1	29	1.04±0.09	1.89±0.08	1.64±0.50	4.28±0.63	5.12±1.08
8	26.11.2011b	9.1	80	1.37±0.05	5.68±0.08	2.14±0.33	5.44±0.33	7.76±0.76
9	02.12.2011	12.9	71	0.85±0.18	3.69±0.44	1.09±0.33	2.98±0.72	2.67±0.76
11	07.12.2011b	12.6	54	1.04±0.08	2.62±0.18	1.79±0.68	4.15±0.49	4.72±1.76
12	08.12.2011	12.7	31	1.00±0.11	1.94±0.14	1.77±0.57	3.96±0.77	4.92±1.22
13	09.12.2011a	11.4	29	1.12±0.07	1.88±0.08	1.61±0.39	4.54±0.32	5.41±1.00
16	11.12.2011b	10.7	66	1.20±0.06	3.09±0.10	1.76±0.44	4.67±0.37	5.77±1.16

Table 10.2: Overview of the mean reference SCDs $S_{ref_{O_4}}$ simulated at 360.8 nm and 477.1 nm and derived from the spectral analysis using a Kurucz spectrum as FRS. The error of the simulated $S_{ref_{O_4}}$ corresponds to the standard deviation of the mean $S_{ref_{O_4}}$, whereas the error of the measured $S_{ref_{O_4}}$ corresponds to the DOAS spectral fit error.

sortie	date	altitude [km]	SZA [°]	UV simulated $S_{ref_{O_4}}$ $[10^{43}\frac{\text{molec}^2}{\text{cm}^5}]$	UV measured $S_{ref_{O_4}}$ $[10^{43}\frac{\text{molec}^2}{\text{cm}^5}]$	vis simulated $S_{ref_{O_4}}$ $[10^{43}\frac{\text{molec}^2}{\text{cm}^5}]$	vis measured $S_{ref_{O_4}}$ $[10^{43}\frac{\text{molec}^2}{\text{cm}^5}]$
1	16.11.2011	12.9	49	2.18±0.35	2.52±0.64	3.07±0.71	3.06±0.43
2	19.11.2011a	8.4	26	3.40±0.22	4.48±0.54	6.29±0.53	3.61±0.47
3	19.11.2011b	12.9	82	2.11±0.56	2.81±0.54	3.89±1.69	2.34±0.46
5	22.11.2011	5.8	27	4.24±0.21	6.03±0.53	8.41±0.43	7.99±0.50
6	23.11.2011	8.8	26	3.38±0.19	5.62±0.53	6.18±0.20	6.69±0.50
7	26.11.2011a	12.1	29	2.45±0.31	4.25±0.54	3.95±0.75	4.81±0.51
8	26.11.2011b	9.1	80	3.67±0.16	5.67±0.55	6.40±0.36	5.79±0.51
9	02.12.2011	12.9	71	1.60±0.35	2.93±0.53	2.12±0.51	2.77±0.50
11	07.12.2011b	12.6	54	2.37±0.23	3.42±0.53	3.64±0.53	2.96±0.53
12	08.12.2011	12.7	31	2.32±0.34	2.22±0.53	3.59±0.88	1.61±0.51
13	09.12.2011a	11.4	29	2.63±0.20	3.94±0.53	4.22±0.32	3.43±0.52
16	11.12.2011b	10.7	66	2.77±0.20	3.49±0.56	4.24±0.43	2.80±0.50

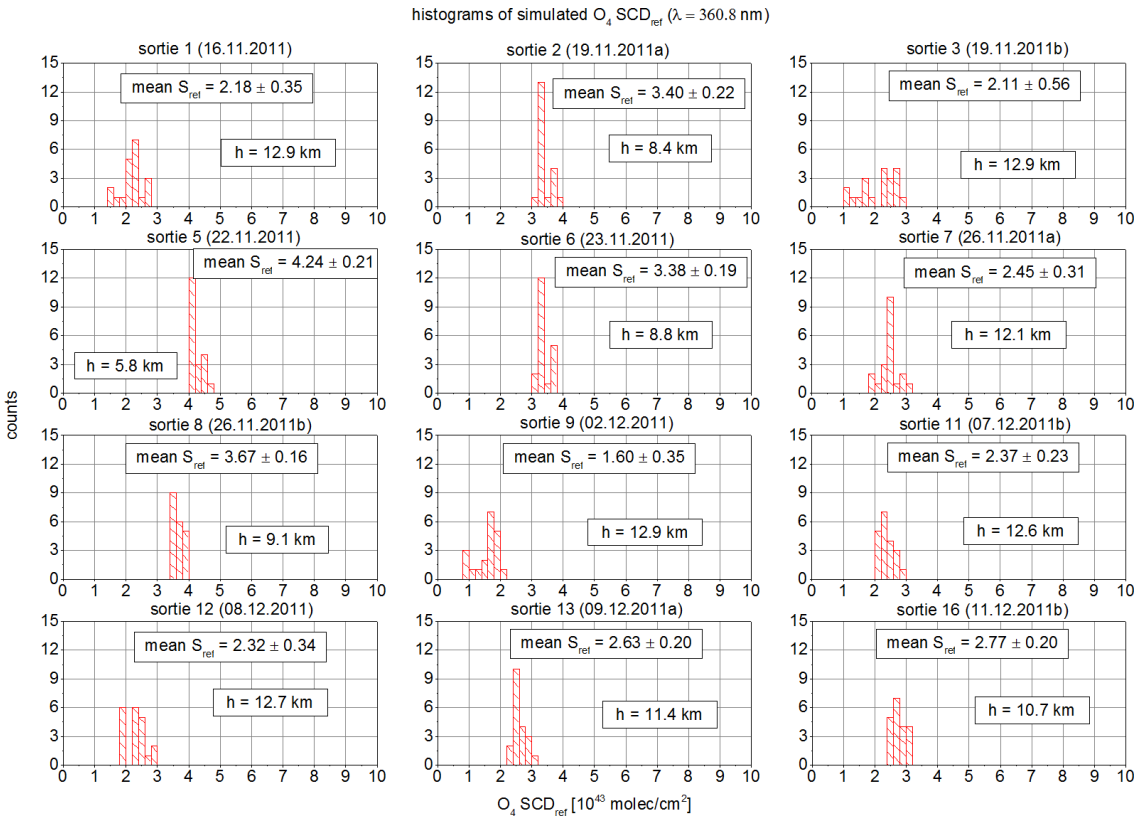

(a)

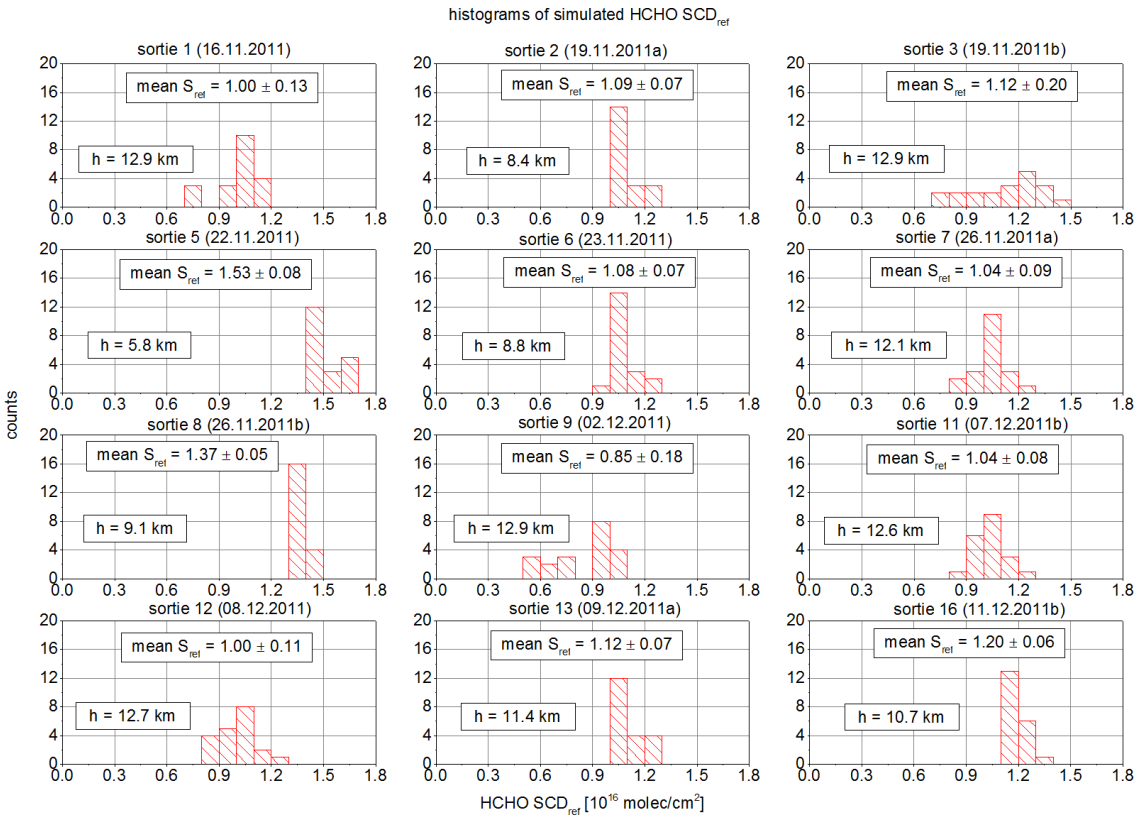

(b)

Figure 10.2: Histograms of the reference SCDs of (a) O_4 at 360.8 nm and of (b) HCHO at 347 nm simulated for different cloud scenarios for each flight, respectively.

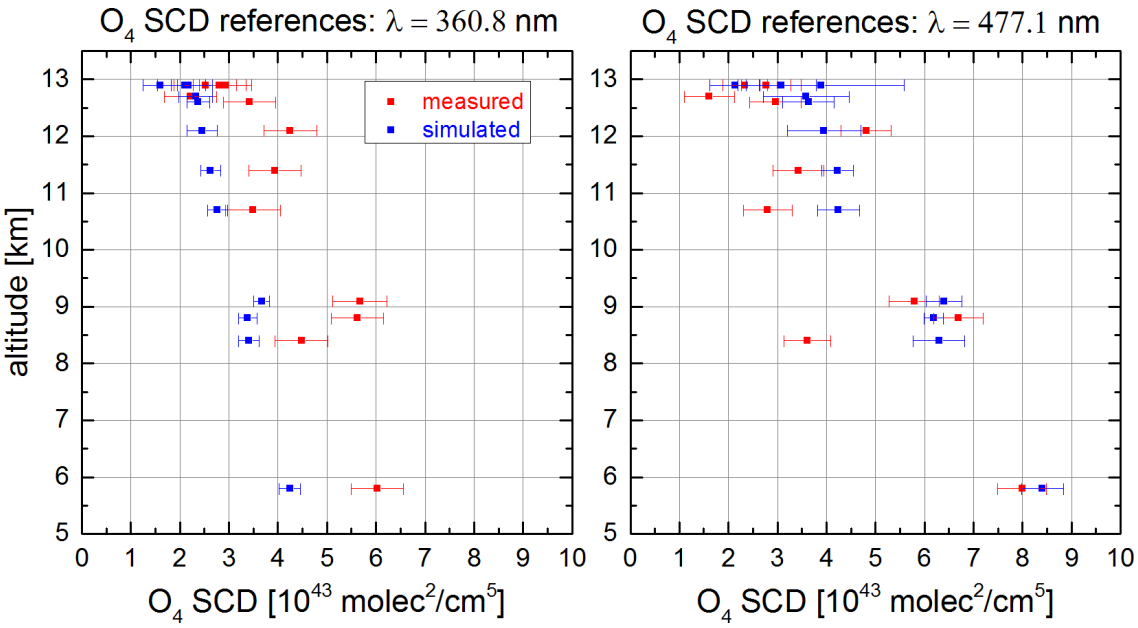

Figure 10.3: Simulated mean $S_{ref_{O4}}$ and measured $S_{ref_{O4}}$ for each flight of the Falcon aircraft. The error bars of the simulated $S_{ref_{O_4}}$ correspond to the standard deviation of the mean $S_{ref_{O_4}}$, whereas the error bars of the measured $S_{ref_{O_4}}$ represent the DOAS spectral fit error.

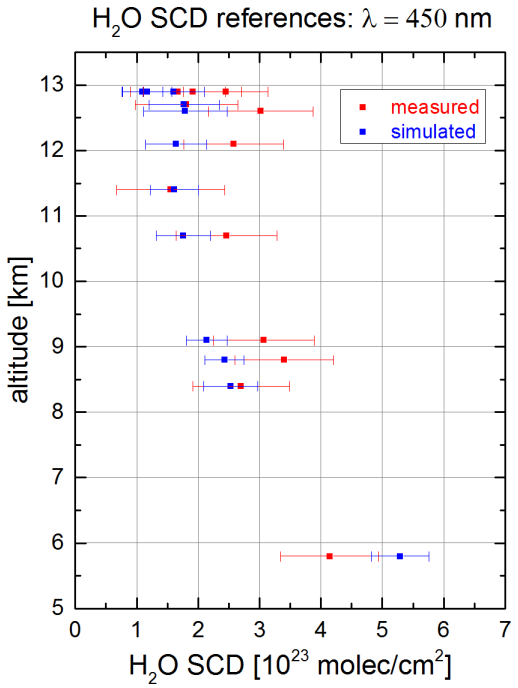

Figure 10.4: Simulated mean $S_{ref_{H_2O}}$ and measured $S_{ref_{H_2O}}$ for each flight of the Falcon aircraft. The error bars of the simulated $S_{ref_{H_2O}}$ correspond to the standard deviation of the mean $S_{ref_{H_2O}}$, whereas the error bars of the measured $S_{ref_{H_2O}}$ represent the DOAS spectral fit error.

10.1.3 Influence of the profile shape

Assumption of a similar profile shape

In the basic O_4 scaling method it is assumed that the trace gas x has the same profile shape as that of O_4 (Equation 10.10). In the following, the uncertainty of this assumption is investigated for HCHO for the aircraft descent on 26 November 2011. For this study different scenarios are simulated in McArtim for a wavelength of 347 nm, which corresponds to the centre wavelength of the HCHO analysis wavelength interval (Section 8.2.3). The model height grid has a vertical resolution of 0.2 km. The pressure and temperature profiles are extracted from the Falcon data measured during that descent. The O_4 concentration is calculated from the corresponding pressure and temperature profiles whereas the profiles of O_3 and NO_2 are based on standard SAGE II profiles. Three different aerosols extinction profiles are assumed: (a) a box profile with a height of 0.2 km and less aerosols (AOT = 0.07), (b) an exponentially decreasing profile with an AOT of 1.2 and (c) a profile with an AOT of 3.3 retrieved with SCIATRAN from the descent on 26 November 2011. Additionally, different HCHO concentration profiles are tested: An O_4 profile scaled to ≈ 1 ppb of HCHO at the ground, which is a typical background value of the continental boundary layer (Harder et al., 1997), a linear decreasing profile with ≈ 1 ppb of HCHO at the ground, a smoothed box profile with a height of 1 km and ≈ 1 ppb of HCHO at the ground, and two exponentially decreasing profiles with different scale heights z_s. These two HCHO profiles are proportional to $e^{-\frac{z}{z_s}}$, whereas the O_4 profile is proportional to $e^{-\frac{2z}{z_s}}$. The number of photons is set to 30000 for all model runs. Figure 10.5 shows the different aerosol and HCHO profiles as well as the results for the ratio $\frac{\alpha^*_{x_j}}{\alpha^*_{y_j}}$. As expected, for a HCHO profile that has the same shape as the O_4 profile (black) the ratio $\frac{\alpha^*_{x_j}}{\alpha^*_{y_j}}$ almost equals 1 for all three aerosol profiles. The strongest deviation from $\frac{\alpha^*_{x_j}}{\alpha^*_{y_j}} = 1$ can be found for a HCHO box profile with a deviation in the MBL of ≈ -50 % for less aerosols, ≈ -100 % for an exponentially decreasing aerosol profile with an AOT of 1.2 and ≈ -150 % for an aerosol profile with a AOT of 3.3. The large deviations between 10 and 12 km are possibly due to a lack of stratospheric information above 12 km. As an exponentially decreasing HCHO profile shape is most realistic, the deviations yield in the MBL: (a) ≈ 50 % for less aerosols, (b) ≈ 85 % for aerosols with an AOT of 1.2 and (c) ≈ 100 % for aerosols with an AOT of 3.3.

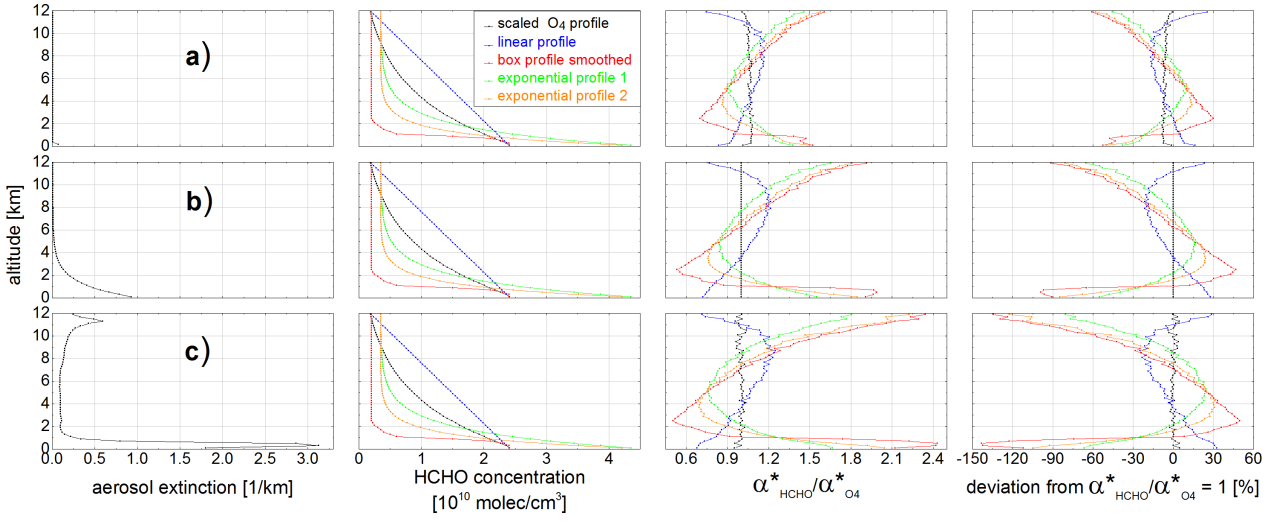

Figure 10.5: Simulation of the ratio of $\frac{\alpha^*_{x_j}}{\alpha^*_{y_j}}$ for different aerosol extinction profiles: (a) box profile with less aerosols, (b) exponentially decreasing profile and (c) a profile retrieved from a descent on 26 November 2011 with SCIATRAN for different HCHO profiles (different colours), respectively.

The deviations due to the assumption of a similar profile shape can thus be quite large. Therefore, a correction factor α^* has to be calculated for each trace gas for each measurement geometry, respectively.

Determination of the correction factor to account for different profile shapes

The correction factor α^* is determined according to Equation 10.10 using 1D RT simulations with the model McArtim. For the model atmosphere the same input profiles are used as shown in Figure 10.1. The ground albedo is set to 5 %. The altitude grid size is changed to a finer resolution of 100 m, in order to avoid discretisation problems. α^* is calculated for each measurement geometry of each sortie. Figure 10.6 shows α^*_x for the different trace gases as well as the ratio $\alpha^*_x/\alpha^*_{O_4}$ for sortie 1 on 16.11.2011. α^*_x is highly variable, which is possibly due to varying roll angles. This variation is reduced when calculating the ratio $\alpha^*_x/\alpha^*_{O_4}$ of a trace gas x and O_4 at the respective wavelength. α^*_x is increased between 05:15 and 05:25 UTC. For this period the Falcon aircraft was flying at a very low altitude of approximately 0.03 km. The Box-AMFs strongly decrease close to the ground, leading to an enhanced α^*_x. The values of $\alpha^*_{HCHO}/\alpha^*_{O_4}$ are larger than for the other trace gases. The error of α^*_x highly depends on the chosen model input parameters and has to be estimated with sensitivity studies (Section 10.1.5).

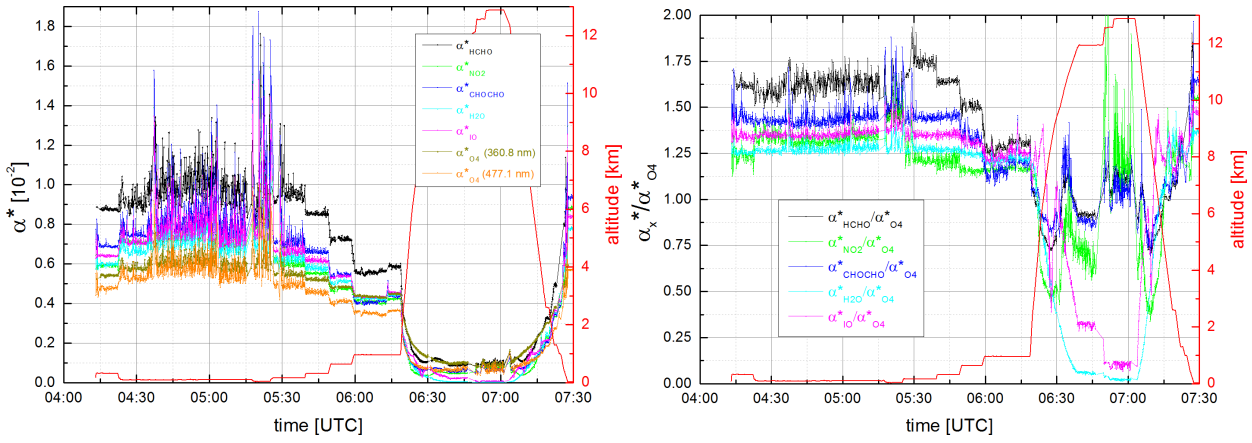

(a) (b)

Figure 10.6: (a) Simulated α^* correction factors for HCHO (347 nm), NO_2 (450 nm), CHOCHO (450 nm), H_2O (450 nm), IO (427 nm), and O_4 (360.8 nm, 477.1 nm), and (b) the ratio of α^*_x and $\alpha^*_{O_4}$ for sortie 1 on 16.11.2011.

Figures 10.7 and 10.8 show the inferred VMRs of HCHO, NO_2, CHOCHO, H_2O, and IO for sortie 1 on 16.11.2011. The plots include the basic O_4 scaling method, the basic O_4 scaling method including the estimation of S_{ref}, and the basic O_4 scaling method including the estimation of S_{ref} and the correction factor. Including S_{ref} in the calculation leads to approximately 15 to 30 % larger HCHO VMRs in the MBL than without considering S_{ref}. The HCHO VMRs further increase by approximately 60 to 120 % when the correction factor is included in the calculation. The resulting increase is consistent with the deviation between the O_4 and HCHO profile shape estimated in the previous section.

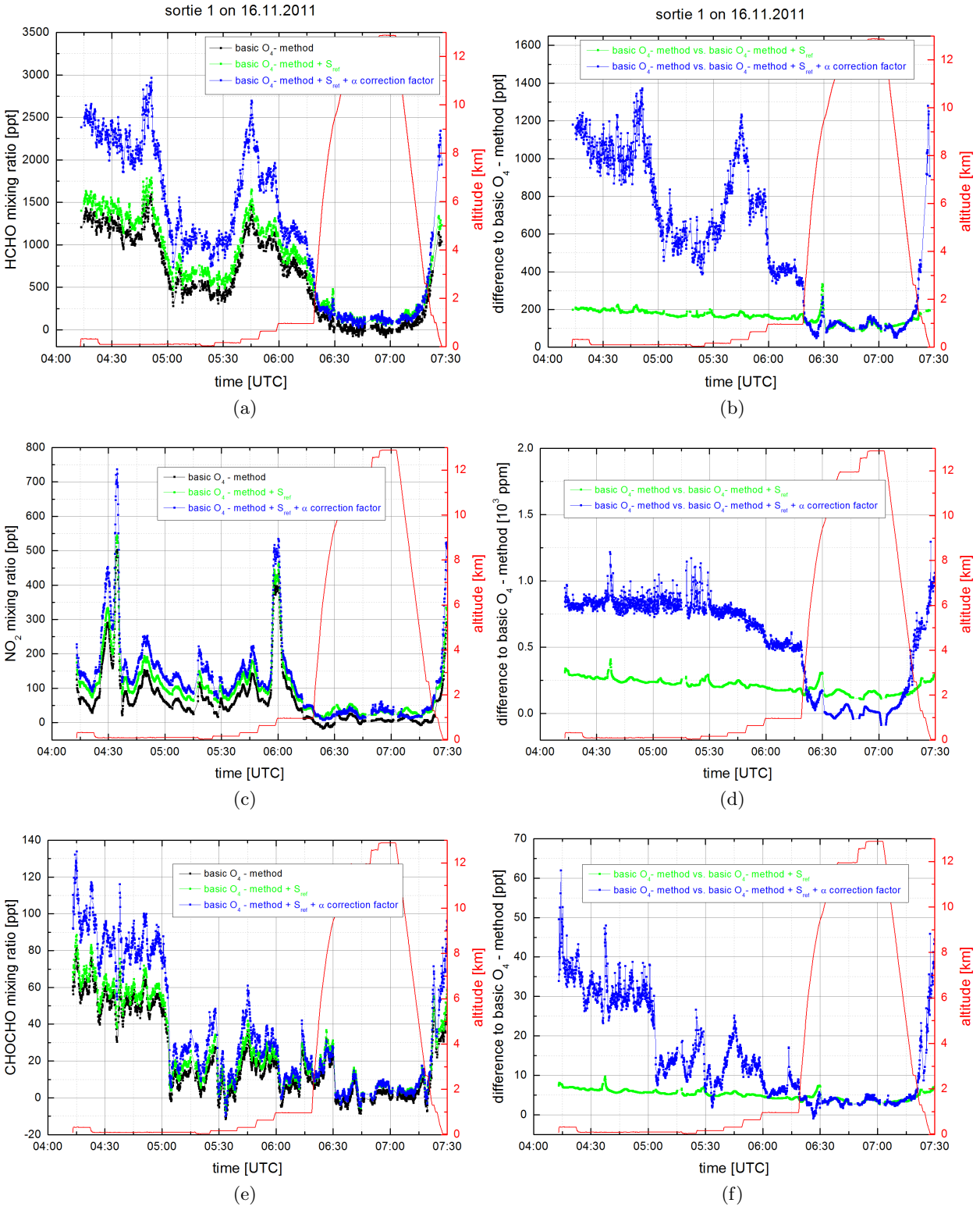

Figure 10.7: Left panels: VMRs of HCHO, NO_2, and CHOCHO derived with the basic O_4 scaling method (black), including S_{ref_x} (green), and including S_{ref_x} and the correction factor (blue); right panels: Absolute difference to the basic O_4 scaling method (no RT simulations).

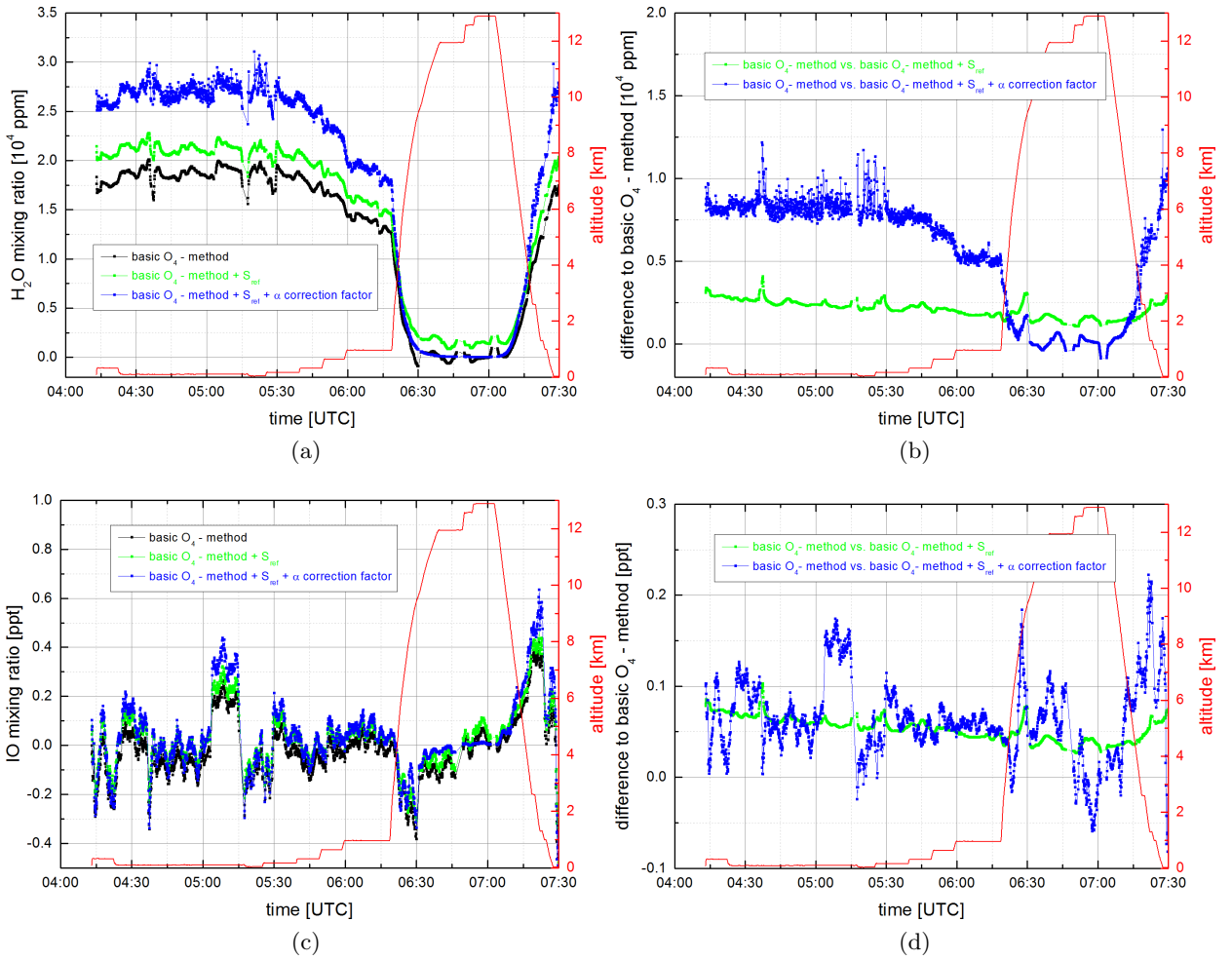

Figure 10.8: Left panels: VMRs of H_2O and IO derived with the basic O_4 scaling method (black), including S_{ref_x} (green), and including S_{ref_x} and the correction factor (blue); right panels: Absolute difference to the basic O_4 scaling method (no RT simulations).

10.1.4 Influence of the wavelength dependency of the aerosol extinction

For the above-described simulations different wavelengths are used. O_4 is for example simulated at a wavelength of 360.8 nm whereas HCHO is calculated at a wavelength of 347 nm. It is assumed that the radiative transfer is similar both for the O_4 wavelength and for the wavelength region where the absorption of trace gas x occurs, e.g. the aerosol extinction profiles are similar for both wavelengths. In order to investigate the influence of the wavelength-dependent aerosol extinction profiles, O_4 SCDs are simulated at a wavelength of 347 nm for three different aerosol extinction profiles. The wavelength-dependency of the aerosol extinction is accounted for by using Equation 3.20 with an Ångström exponent of 1.3 and $\lambda_0 = 360.8$ nm. The resulting aerosol extinction at 347 nm is approximately 5 % larger than at $\lambda_0 = 360.8$ nm. The absorption cross-section of O_4 at 347 nm is scaled to the value at 360.8 nm, since at 347 nm no O_4 absorption band is present.
Figure 10.9a shows the O_4 SCDs simulated for the different aerosol extinction profiles. The wavelength-dependent deviation in the aerosol extinction profiles of approximately 5 % does not lead to a significant change in the O_4 SCDs. The O_4 SCDs vary by less than ± 2 %. This value is comparable to the size of the Monte Carlo noise, which is between 1 and 2 % for a number of 30000 photons. For increasing aerosol extinctions, the deviation between the O_4 SCDs increases to approximately ± 4 %.
In order to investigate the influence of the wavelength-dependent aerosol extinction in the visible

wavelength range, the same test as above is performed but for O_4 SCDs simulated at a wavelength of 427 nm. The wavelength at 427 nm represents the middle wavelength of the IO dSCD evaluation range. The aerosol extinction profiles are scaled with an Ångström exponent of 1.3 and $\lambda_0 = 477.1$ nm. The difference of the two chosen visible wavelengths ($\lambda_0 = 477.1$ nm, $\lambda = 427$ nm) is with 50 nm larger than the wavelength difference of 13 nm chosen for the UV runs. The resulting aerosol extinction at 427 nm is approximately 15.5 % larger than at $\lambda_0 = 477.1$ nm. Figure 10.9b shows the simulated O_4 SCDs for different aerosol profiles. For a lower aerosol extinction, the wavelength-dependent change in the aerosol extinction profiles of approximately 15.5 % leads to a change in the O_4 SCDs by up to -2 %. For increasing aerosol loads, the deviation between O_4 SCDs increases to approximately ± 6 %, which is slightly larger than for the smaller wavelength difference in the UV.

It can be concluded that the wavelength dependency of the aerosol extinction has a small influence on the simulated O_4 SCDs. The size of the wavelength-dependent changes is comparable to the size of the Monte Carlo noise. The differences due to wavelength-dependent aerosol extinction profiles can be neglected in comparison to the uncertainties derived for example from the calculation of α^*.

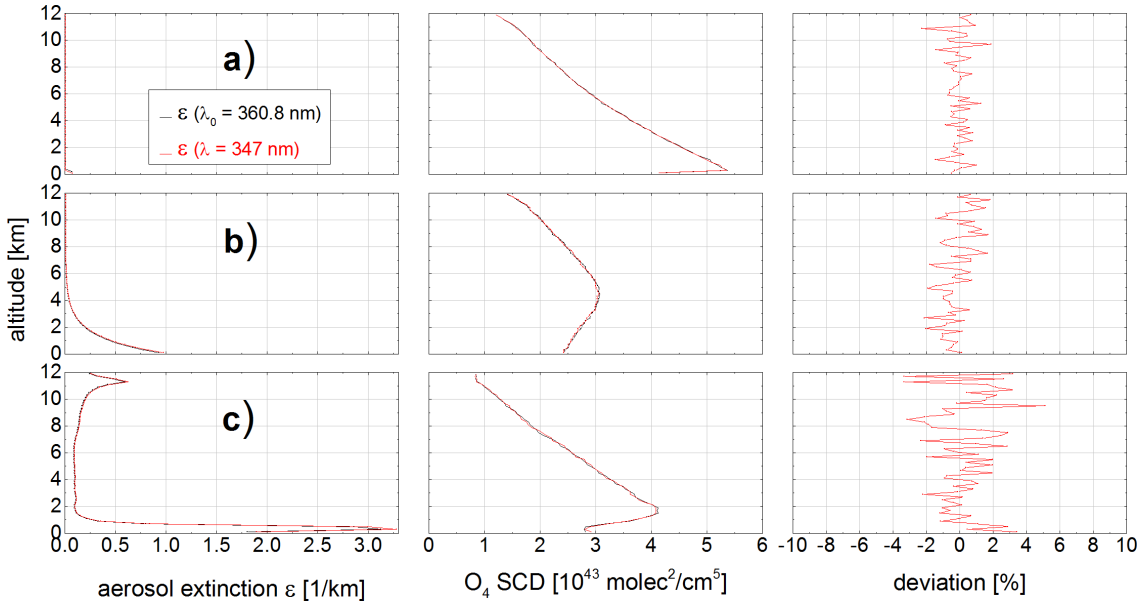

(a)

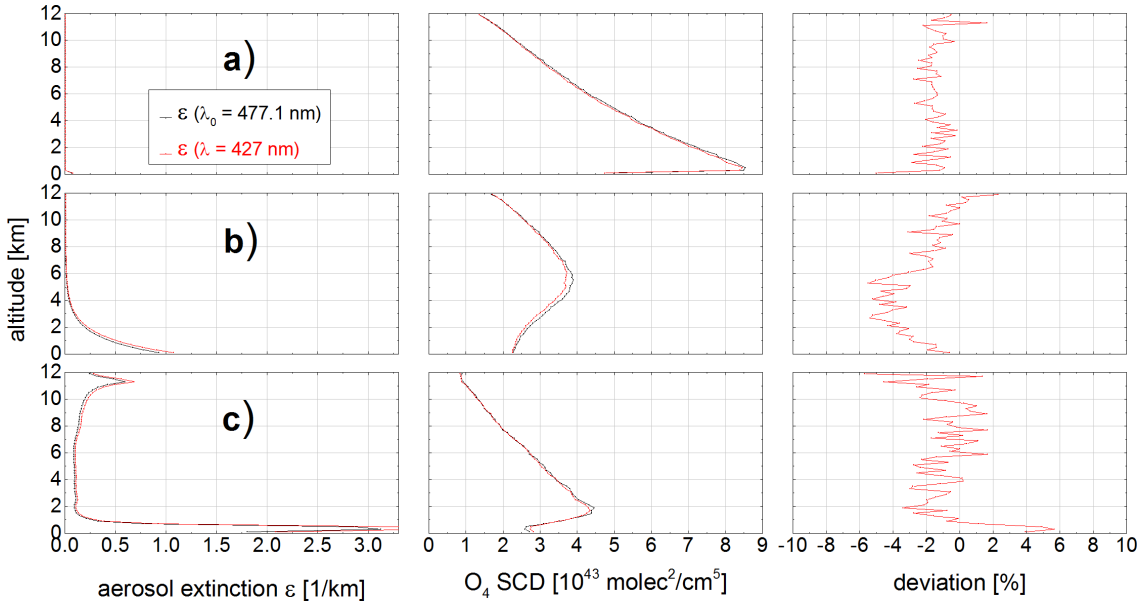

(b)

Figure 10.9: O_4 SCDs simulated for a wavelength in the (a) UV (λ = 347 nm) and in the (b) visible wavelength range (λ = 427 nm) for different wavelength-dependent aerosol extinction profiles, respectively: (a) box profile with less aerosols, (b) exponentially decreasing profile and (c) a profile retrieved from a descent on 26 November 2011 with SCIATRAN, respectively. The deviation refers to the relative deviation between the O_4 SCDs simulated using an aerosol extinction profile at λ_0 and λ, respectively.

10.1.5 Error estimation

The total uncertainty of the VMRs inferred with the O_4 scaling method according to Equation 10.15 is comprised of several parts: The errors in the measured SCDs of the different trace gases, the uncertainty arising from the calculation of the ratio $\alpha^*_x/\alpha^*_{O_4}$, and the error of the atmospheric pressures p and temperatures T. The total error of the VMRs inferred with the O_4 scaling method

can be determined according to the following formula:

$$\Delta \mathrm{VMR}_{\mathrm{x}_j} = \sqrt{\begin{array}{l}\left(\frac{\Delta S_x}{S_{\mathrm{O}_4}} \cdot \frac{\alpha_x^*}{\alpha_{\mathrm{O}_4}^*} \cdot \frac{0.21^2 \cdot p \cdot N_A}{R \cdot T}\right)^2 + \left(-\frac{S_x \cdot \Delta S_{\mathrm{O}_4}}{S_{\mathrm{O}_4}^2} \cdot \frac{\alpha_x^*}{\alpha_{\mathrm{O}_4}^*} \cdot \frac{0.21^2 \cdot p \cdot N_A}{R \cdot T}\right)^2 \\ + \left(\frac{S_x}{S_{\mathrm{O}_4}} \cdot \Delta\left(\frac{\alpha_x^*}{\alpha_{\mathrm{O}_4{}^*}}\right) \cdot \frac{0.21^2 \cdot p \cdot N_A}{R \cdot T}\right)^2 + \left(\frac{S_x}{S_{\mathrm{O}_4}} \cdot \frac{\alpha_x^*}{\alpha_{\mathrm{O}_4}^*} \cdot \frac{0.21^2 \cdot \Delta p \cdot N_A}{R \cdot T}\right)^2 \\ + \left(-\frac{S_x}{S_{\mathrm{O}_4}} \cdot \frac{\alpha_x^*}{\alpha_{\mathrm{O}_4}^*} \cdot \frac{0.21^2 \cdot p \cdot N_A \cdot \Delta T}{R \cdot T^2}\right)^2.\end{array}} \tag{10.17}$$

In the following, the different errors and uncertainties are specified. The dSCD errors ΔdS of the measured trace gases correspond to the DOAS spectral fit error as given by the WinDOAS programme (Section 8.3). Systematic dSCD errors are not taken into account in this error estimation. ΔdS typically varies between 5 and 20 %, depending on the trace gas. The SCD errors ΔS of the O_4 SCDs determined using a Kurucz spectrum as a FRS are also given by the DOAS spectral fit error and typically vary between 10 and 15 % for the UV and between 5 and 10 % for visible wavelength range. The uncertainty of S_{ref_x} of the different trace gases estimated using different 3D cloud scenarios is given by the standard deviation of the mean S_{ref_x} (Table 10.1). The resulting error of the SCD S_x of a trace gas x can be calculated according to:

$$\Delta S_x = \sqrt{\Delta dS_x^2 + \Delta S_{ref_x}^2}. \tag{10.18}$$

The temperature and pressure sensors of the Falcon aircraft are calibrated by the DLR flight department. The final error in the static pressure measurement is $\Delta p \approx 0.5$ hPa, whereas the accuracy of the static temperature yields $\Delta T \approx 0.5$ K (`http://www.dlr.de/fb/en/desktopdefault.aspx/tabid-3718/`). However, it is important to note that when flying within clouds or precipitation events the sensing elements can get wet, possibly leading to inaccurate measurements.
The major uncertainty that propagates into the total error of the inferred VMRs is caused by the uncertainty in the determination of the correction factor α^*. In the following, sensitivity studies are performed in order to estimate the uncertainty of the ratio $\alpha_{\mathrm{x}}^*/\alpha_{\mathrm{O}_4}^*$. Sensitivity studies are performed for HCHO for sortie 1 on 16.11.2011. Figure 10.10 shows α_{HCHO}^*, $\alpha_{\mathrm{O}_4}^*$, and the ratio $\alpha_{\mathrm{HCHO}}^*/\alpha_{\mathrm{O}_4}^*$ for the base run described in Section 10.1.3 as well as for different RT settings. These different RT settings include changes in the aerosol extinction profile, in the ground albedo, and in the roll angle of the Falcon aircraft. An aerosol profile with an extinction that is twice the extinction of the base run is assumed. Furthermore, a cloud layer is implemented between 0.5 and 1 km with an extinction of 20 km^{-1}. The albedo is changed from 0.05 in the base run to 1 in order to account for bright clouds. Since the assignment of the roll angle of the aircraft to the DOAS spectra can be erroneous, $\pm 1\,^\circ$ is added/subtracted from the assigned roll angle. The different RT settings lead to large differences in α_{HCHO}^* and $\alpha_{\mathrm{O}_4}^*$ as compared to the base run. However, these differences decrease when calculating the ratio $\alpha_{\mathrm{HCHO}}^*/\alpha_{\mathrm{O}_4}^*$, i.e. the ratio is less influenced by changes in the RT settings than the single α^* factors. Overall, the deviations of the ratio $\alpha_{\mathrm{HCHO}}^*/\alpha_{\mathrm{O}_4}^*$ from the base run in the MBL are smaller than $\pm(15-20)$ %. Exceptions are the scenario including a cloud layer between 0.5 and 1 km with an extinction of 20 km^{-1} and the scenario with an albedo of 1. If the flight altitude corresponds to the altitude of the cloud, the deviation of the ratio $\alpha_{\mathrm{HCHO}}^*/\alpha_{\mathrm{O}_4}^*$ from the base run increases to approximately 40 %. When the albedo is set to 1 the deviation reaches values of approximately -40 % in the free troposphere. However, flight sections within clouds or very close to a cloud layer can be identified with the colour index, the brightness, and the O_4 dSCDs as described in Section 9.1.

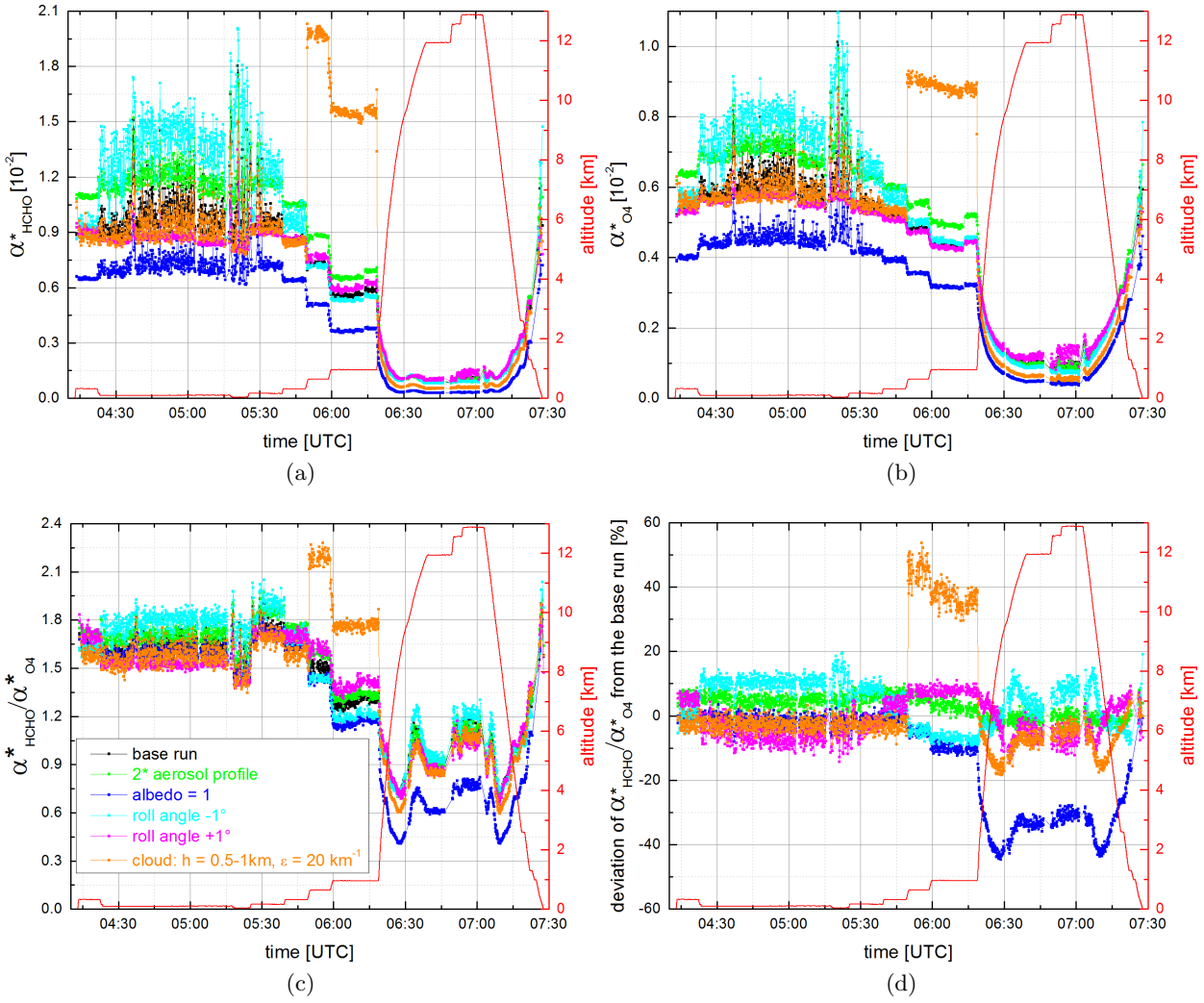

Figure 10.10: (a) α^*_{HCHO}, (b) $\alpha^*_{\mathrm{O_4}}$, (c) $\alpha^*_{\mathrm{HCHO}}/\alpha^*_{\mathrm{O_4}}$, and (d) the deviation of the ratio $\alpha^*_{\mathrm{HCHO}}/\alpha^*_{\mathrm{O_4}}$ from the base run for different RT settings for sortie 1 on 16.11.2011.

Further uncertainties can arise from the choice of the assumed trace gas profiles. Thus, different artificial HCHO profiles are generated to investigate their influence on α^*_{HCHO}. These profiles include a linearly decreasing profile, a smoothed box-shaped profile, and two exponentially decreasing profiles with different exponential decay constants (Figure 10.11a). Overall, for the range of the assumed HCHO profiles deviations in α^*_{HCHO} of approximately up to ±80 % can be observed relative to the base run. However, a linearly decreasing HCHO profile seems to be rather unrealistic. In order to receive a more realistic estimation of the typical variability of the HCHO profiles encountered during the SHIVA campaign, the variability in the HCHO profiles is estimated from the TOMCAT profiles simulated for each sortie of the Falcon aircraft. Figure 10.11b shows an overview of the different TOMCAT HCHO profiles. The maximum and minimum profiles that constitute the total range of the HCHO concentration are extracted and extended up to 30 km (Figure 10.11a). Overall, the maximum and minimum TOMCAT profiles lead to a deviation of α^*_{HCHO} and thus to a deviation of the ratio $\alpha^*_{\mathrm{HCHO}}/\alpha^*_{\mathrm{O_4}}$ from the base run of up to approximately ±40 % (Figure 10.12). The standard deviation of the average deviation corresponds to approximately 20 % for both the maximum and minimum TOMCAT profiles, respectively.
In the following, the uncertainty of the ratio $\alpha^*_{\mathrm{HCHO}}/\alpha^*_{\mathrm{O_4}}$ is set to a fixed value of 40 % in order to completely cover the different possible uncertainties arising from different RT settings or from the choice of the input profile. This value represents a rough estimation. In extreme cases, this value

might be too small or even too large. It is further assumed that the uncertainties of the other trace gases show a similar behaviour as HCHO.

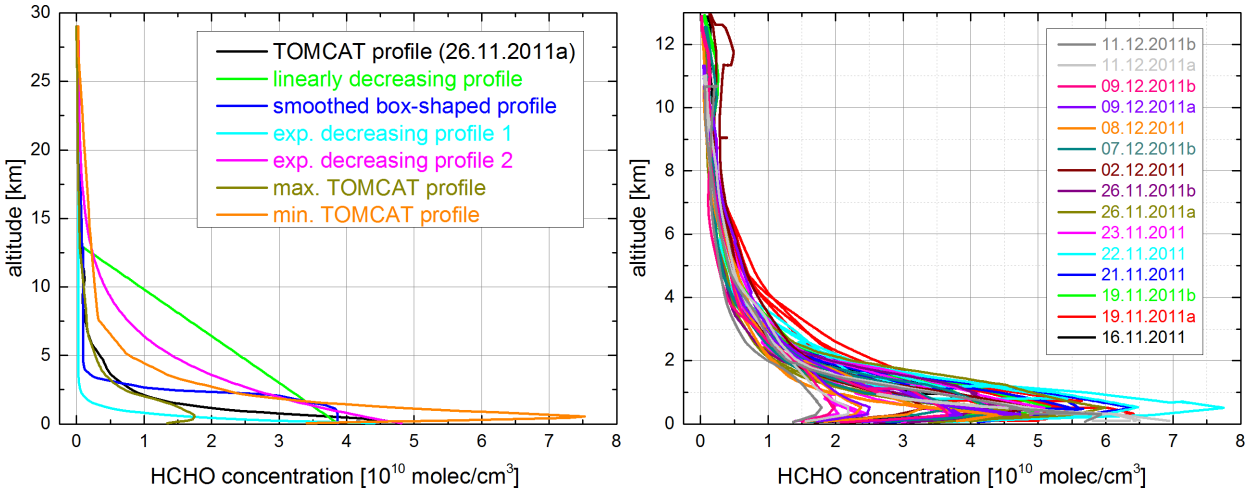

(a) (b)

Figure 10.11: (a) Overview of the different HCHO profiles used for the sensitivity study. The TOMCAT profile from the descent of sortie 1 on 26.11.2011 is used as an input profile for the base run. (b) Overview of the different profiles derived from TOMCAT simulations for each flight of the SHIVA campaign.

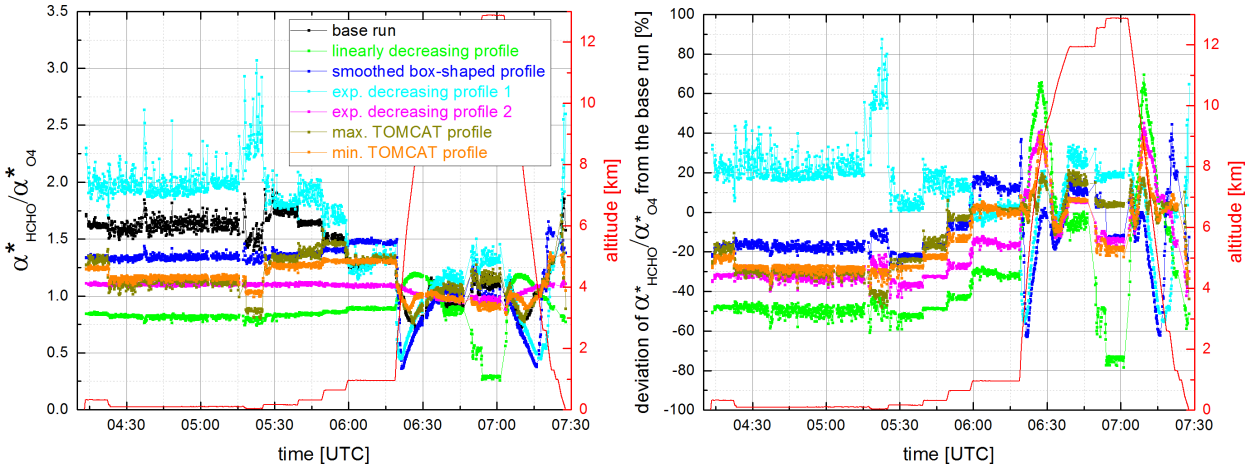

(a) (b)

Figure 10.12: (a) The ratio $\alpha^*_{\mathrm{HCHO}}/\alpha^*_{\mathrm{O_4}}$ and (b) the deviation of the ratio $\alpha^*_{\mathrm{HCHO}}/\alpha^*_{\mathrm{O_4}}$ from the base run assuming different HCHO profiles for sortie 1 on 16.11.2011.

10.2 Vertical profiles

In order to retrieve vertical profiles from DOAS measurements, different retrieval steps are required (Section 5.5). This retrieval procedure is valid in a 1D atmosphere where the atmospheric parameters only change in vertical direction. However, in reality the cloud fields are not only changing vertically but also horizontally, i.e. they have a 3D structure. As clouds vary in three dimensions, the problem needs to be mapped from 3D to 1D. It is therefore essential to assess the influence of 3D clouds on

a 1D retrieval (Section 10.2.1). Section 10.2.2 shows the results of the HEIPRO retrieval, which is used to infer vertical profiles of HCHO, CHOCHO, NO_2, H_2O, and IO. The results of two exemplary descents are presented, which show the overall performance and limitations of the 1D retrieval in a cloudy atmosphere. Sensitivity studies of both the non-linear and the linear profile retrievals are shown in Section 10.2.3. In order to validate the performance of the retrieval, the inferred vertical profiles are compared to in situ measurements that were conducted simultaneously to the DOAS measurements aboard the Falcon aircraft.
It is important to note, that the retrieved vertical profiles have a large horizontal gradient as the aircraft is moving on the scale of several kilometres during the ascents and descents. The time interval for one ascent or descent is typically between 20 and 30 minutes. Depending on the aircraft speed, the covered distance of one ascent or descent lies approximately between 200 and 300 km.

10.2.1 Influence of horizontally varying cloud structures

In order to assess the influence of 3D cloud structures on a 1D profile retrieval, dSCDs are simulated for a 3D atmosphere including 3D cloud fields. These simulated dSCDs are further used as input dSCDs for a 1D profile retrieval. Since for this study a 3D RT model is required, McArtim is used to simulate the 3D atmosphere. SCIATRAN calculates the radiation field in a 1D atmosphere. For consistency the MaRS retrieval (Bodo Werner, personal communication, 2014) is used, not the HEIPRO retrieval, since the MaRS retrieval uses McArtim as a forward model.
Two exemplary 3D cloud fields are generated in McArtim with a varying horizontal distribution (Figure 10.13).

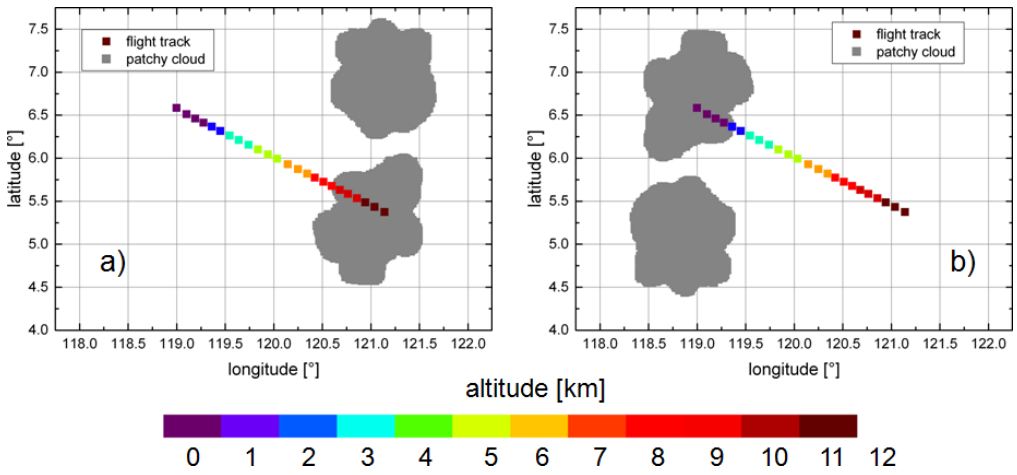

Figure 10.13: Top view of synthetic 3D cloud fields for a patchy cloud layer (grey) at an altitude between 0.5 km and 2.5 km and with an extinction of 20 km^{-1}. The flight track (descent) is colour-coded with the flight altitude. In case (a), the aircraft overflies the patchy cloud layer at high altitudes, whereas in case (b), the aircraft flies within the cloud at a low altitude.

The synthetic 3D patchy cloud field is located at an altitude between 0.5 km and 2.5 km and has an extinction of 20 km^{-1}. Synthetic geometries are created that represent a descent from 12 km down to ground level over the coastline of Borneo (similar to the descent on 26 November 2011 a). The instrument viewing direction is to the left side orthogonal to the heading direction of the aircraft. In case (a), the aircraft overflies the patchy cloud layer at high altitudes whereas in case (b), the aircraft flies within the cloud at a low altitude. The elevation angle is set to zero. The model atmosphere in McArtim is set up with the same adjustments used in the cloud sensitivity studies in Section 9.2. The height grid has a vertical resolution of 0.5 km and the horizontal grid has a size of 400 x 400 km with a resolution of 1 x 1 km for each cell. The upper panels in Figure 10.14 show

the profiles of the aerosol extinction and the HCHO concentration implemented in the McArtim atmosphere. The aerosol extinction profile is exponentially decreasing with altitude having an AOT of 0.1. The HCHO profile is simulated with the chemical transport model TOMCAT for the descent on 26 November 2011 a) (Section 6.2.4) and interpolated on the model grid. For these two cloud fields, synthetic dSCDs of O_4 and HCHO are calculated in McArtim at a wavelength of 360 nm and 347 nm, respectively (Figure 10.14 lower panels). The number of photons is set to 30000. In case (a), the dSCDs of both O_4 and HCHO decrease relative to the cloud-free case. In case (b), the dSCDs correspond to the cloud-free case until the flight track lies within the cloud. Within the cloud, the dSCDs almost decrease to zero.

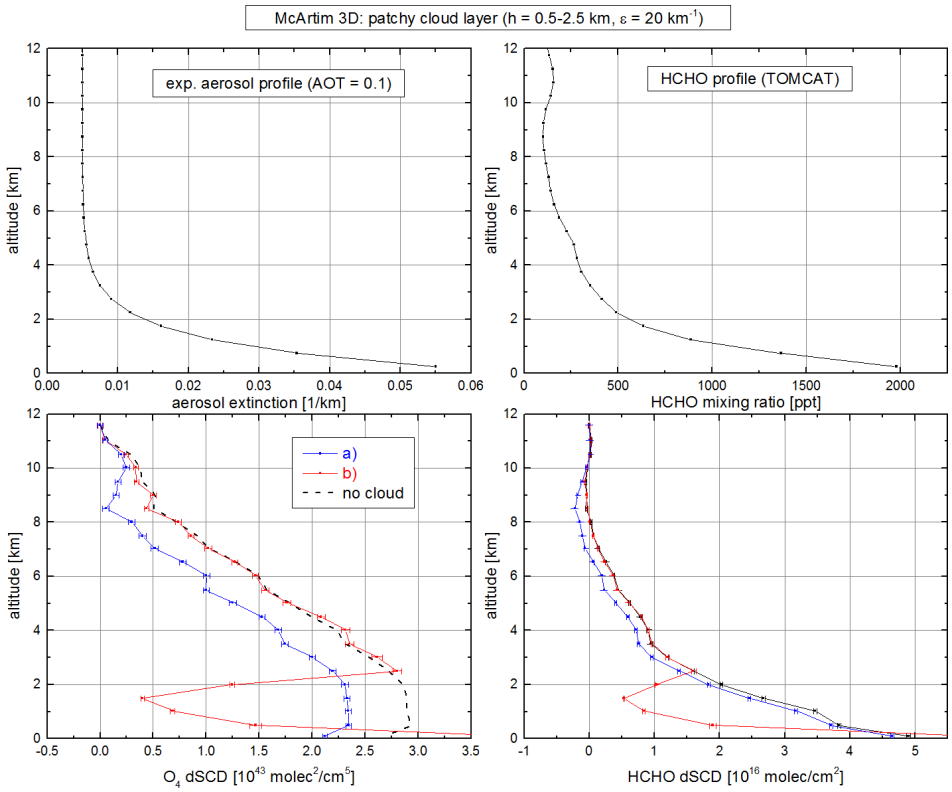

Figure 10.14: Upper panels: Profiles of the assumed aerosol extinction (left) and the HCHO concentration profiles (right). Lower panels: Simulated O_4 and HCHO dSCDs for a cloud free atmosphere (black dashed line) and for the two cloud scenarios from Figure 10.13 (red and blue line).

In a next step, the simulated dSCDs for O_4 and HCHO are used as an input for the MaRS retrieval (Bodo Werner, personal communication, 2014). An exponentially decreasing aerosol profile is assumed as an a priori, whereas for the retrieval of HCHO, the profile from TOMCAT is used as an a priori profile. The a priori error is set to 100 %. Figure 10.15 shows the results of the MaRS retrieval for case (a) and (b) for the non-linear retrieval of the particle extinction profile and for the linear retrieval of the HCHO profile, respectively. For case (a), the inferred O_4 and HCHO dSCDs are in good agreement with the input dSCDs that have seen a 3D cloud. The final particle extinction profile results in an AOT of approximately 0.4. The MaRS retrieval is further able to reproduce the HCHO profile from TOMCAT, which has been originally assumed in McArtim to calculate the dSCDs with a light path that has intercepted a 3D cloud. The averaging kernels are close to one for almost every altitude cluster, both for the non-linear and linear retrieval. Although case (b) describes an extreme case where the aircraft is flying within the cloud, the MaRS retrieval is able to reproduce the original HCHO profile. Consequently, it can be concluded that, for dedicated 3D cloud fields, it is justified to use a 1D profile retrieval.

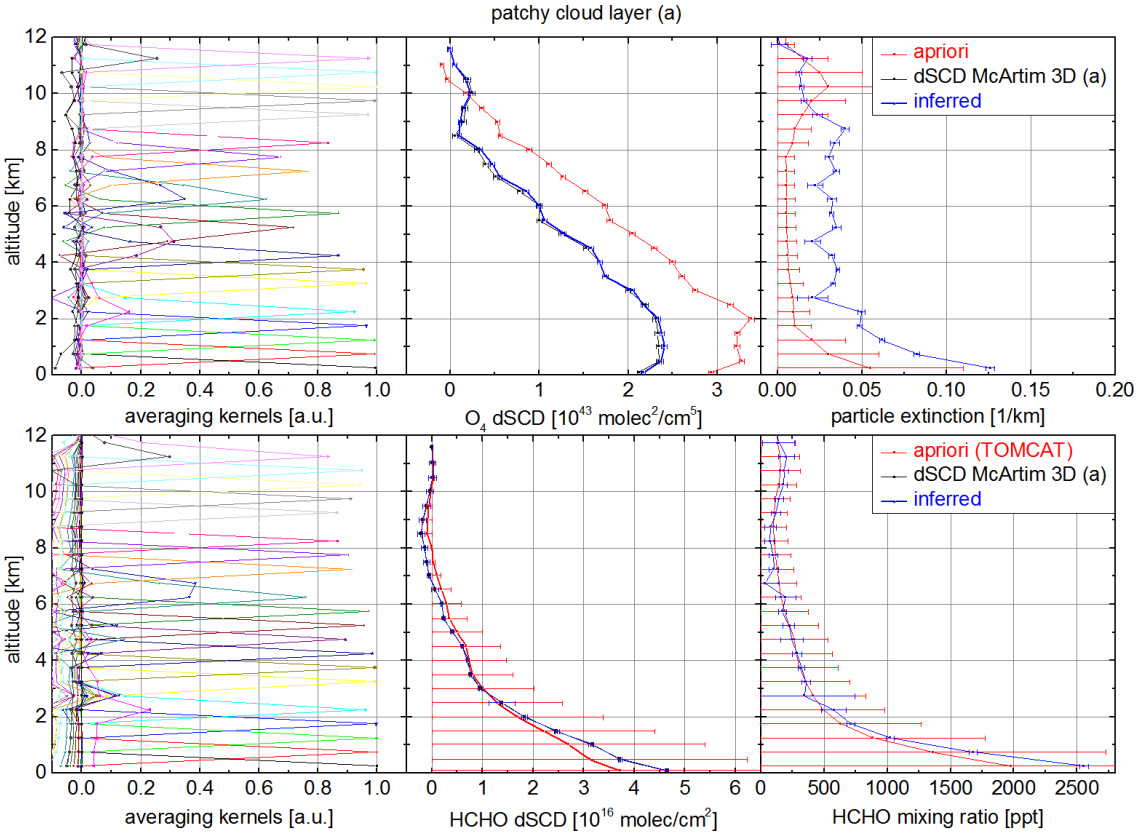

(a)

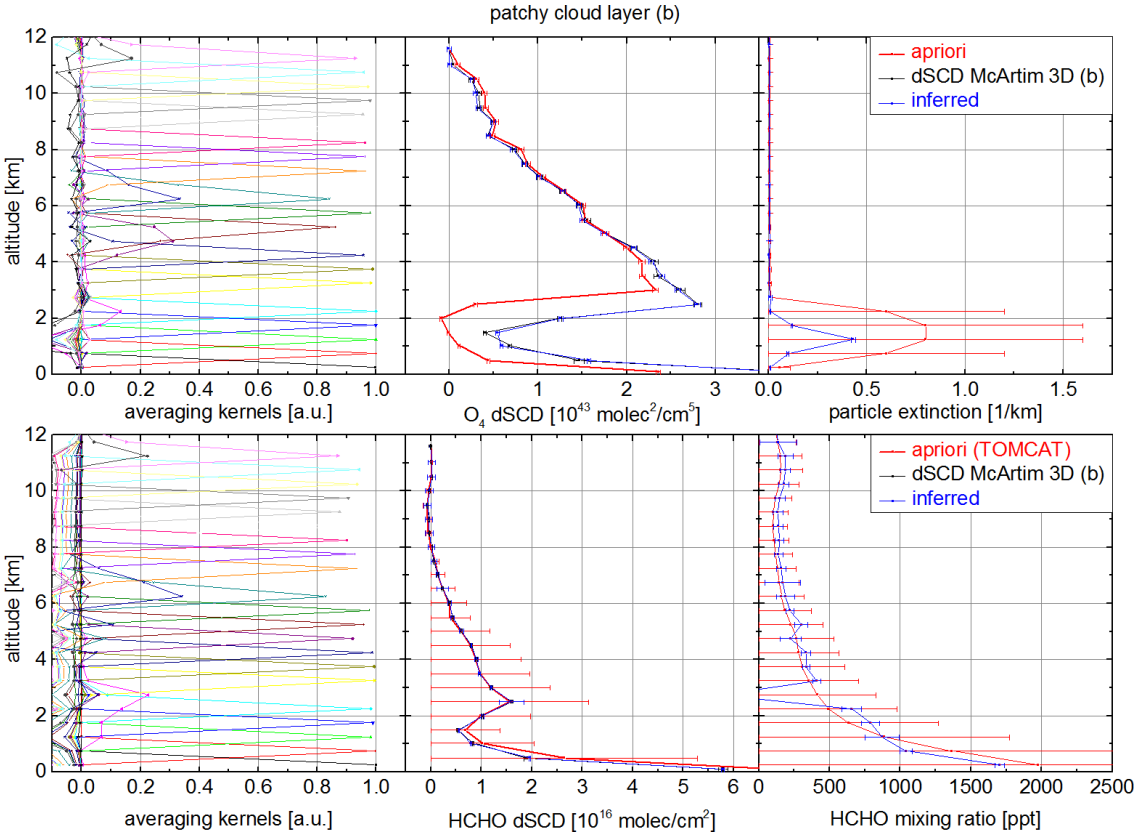

(b)

Figure 10.15: Results of the 1D MaRS profile retrieval showing the averaging kernels (left panels), the dSCDs (middle panels) and the inferred aerosol and HCHO profiles for case (a) and (b), respectively.

10.2.2 Profile selection

The SHIVA data set consists of 16 sorties each having at least two vertical profiles, i.e. one ascent and one descent. Most of the ascents and descents started and ended at the airports of Miri, Sandakan or Tawau. Only some profile flights were conducted away from airports, e.g. the descent on 26 November 2011a, which started and ended over the ocean with a total distance of approximately 100 km from the coast (see Figure A.1 and A.2 for the different flight tracks). Furthermore, most of the profiles include several turns of the aircraft where the roll angle reaches values up to $\pm 30\,^{\circ}$. Turns are very difficult to deal with without an active elevation angle control since during turns the geometries are changing quickly and the mini-DOAS might have recorded spectra of the ocean or land surface. Thus, it is recommended to exclude ascents or descents from the retrieval data that contain any turns. By visual inspection of the webcam images or by investigation of the colour index, the brightness, and the O_4 dSCDs, it can be concluded that the Falcon aircraft was frequently flying within clouds. In order to avoid strong gradients, for example in the O_4 dSCDs due to an enhanced light path, these sections of the flight are not further dealt with in the following.
These sections should be avoided in the 1D profile retrieval. For certain ascents or descents, the 1D profile retrieval shows promising results, whereas for several ascents and descents problems remain due to different reasons. In the following, two descents of the SHIVA data set are chosen to test the applicability of the 1D HEIPRO retrieval.

Basic settings of the HEIPRO retrieval

Forward simulations with the RT model SCIATRAN are performed in a spherical geometry, i.e. light is scattered in a spherical atmosphere. In this case, a Henyey-Greenstein parameterisation of the aerosol phase function is implemented. Using a plane-parallel atmosphere is not recommended for limb measurements as the light path length at an elevation angle of $0\,^{\circ}$ is expected to be so large that the Earth's curvature becomes relevant for the RT simulations. A scattering mode of fully multiple scattering is chosen in the SCIATRAN control settings. The altitude grid has to be adjusted to the expected vertical resolution. If the altitude grid cells are too large information can be lost since fine-scale variations are not resolved. If the grid cells are too small the computation time will increase but the information content will not further increase.
In this study, the altitude grid is equally divided into layers of 100 m up to an altitude of 12 km resulting in 120 different altitude layers. A fix weighting function is selected, which is not re-calculated for each iteration step. Temperature and pressure profiles from the MPI standard files are used according to the month and location of the measurements. MPI profiles are available for each month of the year at latitudes between $5\,^{\circ}$, $15\,^{\circ}$, $^{\circ}25$ ... $85\,^{\circ}$ for each hemisphere, respectively. For the base run, the temperature and pressure profiles at a latitude of $5\,^{\circ}$ N are chosen. A scaling factor of 1.25 is not applied to the O_4 absorption cross-section as for example proposed by Clémer et al. (2010). The O_4 dSCDs inferred from the absorption band at 360.8 nm and 477.1 nm serve as measurement vector for the non-linear profile retrieval. For aerosol scattering, the SSA is set to 0.99 and a Henyey-Greenstein phase function with an asymmetry parameter of 0.72 is assumed. An overview of the Ångström exponent determined by the AERONET station at the airport of Kuching for November and December 2011 is given in Figure 10.16 for the different available data levels. For data level 2, the Ångström exponent varies between 0.75 and 1.75 for the different wavelength ranges. For the HEIPRO retrieval, an Ångström exponent of 1.36 is selected. For the standard run, an albedo of 5 % is chosen, representative for open ocean conditions. The effect of including a bidirectional reflectance distribution function is examined using a pre-calculated data base for different surface types. In this study, surface types representative for the ocean and tropical forest conditions are used. The aerosol a priori profile is assumed to exponentially decrease with altitude with an extinction of 0.1 km^{-1} at the ground and a scale height of 1.5 km. The AOT of the a priori profile yields approximately 0.15. The a priori error is set to 300 %. An iterative a priori is used as described in Section 5.6, i.e. the retrieved state serves as a priori during each iteration to

account for high extinctions due to aerosol and cloud layers. Profiles from the chemistry transport model TOMCAT (Section 6.2.4) are used for the trace gas a priori profiles and are interpolated on the model grid for each ascent and descent. TOMCAT profiles are available for HCHO, O_3, and NO_2. For the profile retrieval of CHOCHO, an a priori profile in mixing ratios is assumed that exponentially decreases with altitude with a mixing ratio of 50 ppt at the ground. For water vapour, a linearly with altitude decreasing a priori profile is chosen.

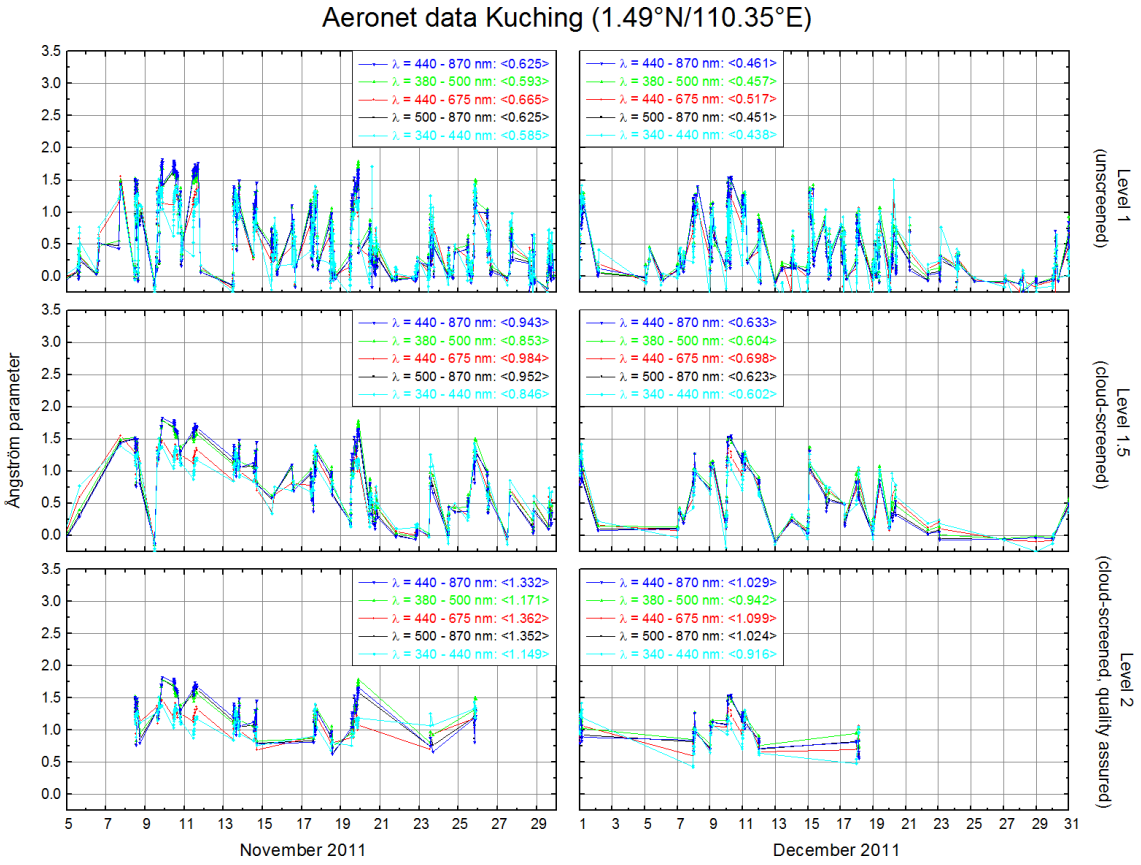

Figure 10.16: Ångström exponent from an AERONET (`http://aeronet.gsfc.nasa.gov/`) station in Kuching (1.45 °N/110.35 °E) for November and December 2011. The sun photometer of the site of Kuching is mounted on the observation tower of Kuching Meteorological Station located at the Kuching International Airport, Sarawak.

Descent of sortie 7 on 26 November 2011a

The descent of sortie 7 on 26.11.2011a represents a good example to test the performance of the profile retrieval as the descent does not include any turns and took place over the ocean away from the influence of airports (Figure 10.17).

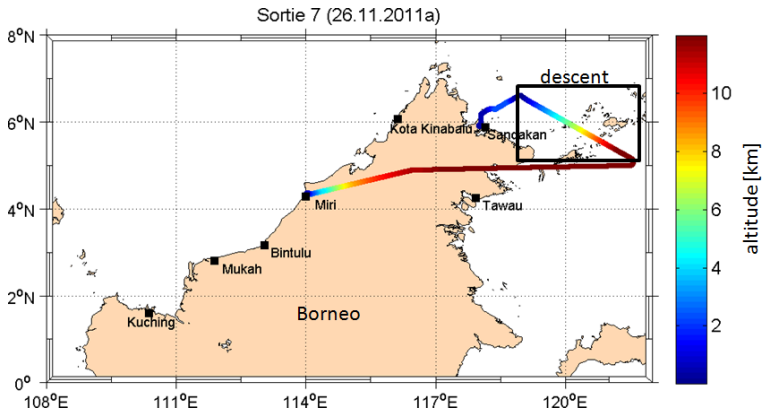

Figure 10.17: Flight track of sortie 7 on 26 November 2011a. The black box marks the location of the descent of the Falcon aircraft chosen for the profile retrieval.

Figure 10.18 shows a selection of webcam images of the different cloud conditions present during this descent. The clouds seem to be far away, except for the clouds at 05:34 UTC and 05:52 UTC. The latter is obviously located very close to the aircraft.

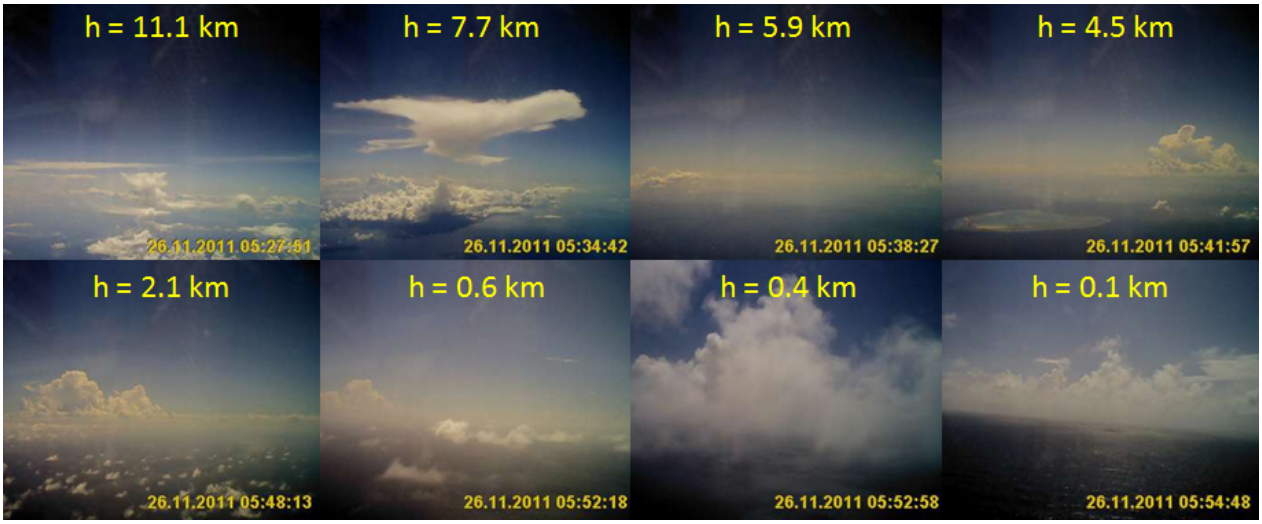

Figure 10.18: Selection of webcam images of the different cloud scenes during the descent on 26 November 2011a.

Figure 10.19 depicts the colour index, the brightness and the O_4 dSCDs for the descent described in Section 9.1. The clouds mentioned above can be clearly identified as the colour index and the brightness are increased at that time. The cloud at 05:34 UTC has less influence on the O_4 dSCDs whereas for the cloud at 05:52 UTC the O_4 dSCDs strongly decrease, leading to the assumption that the cloud at 05:34 UTC is further away from the instrument than the cloud at 05:52 UTC.

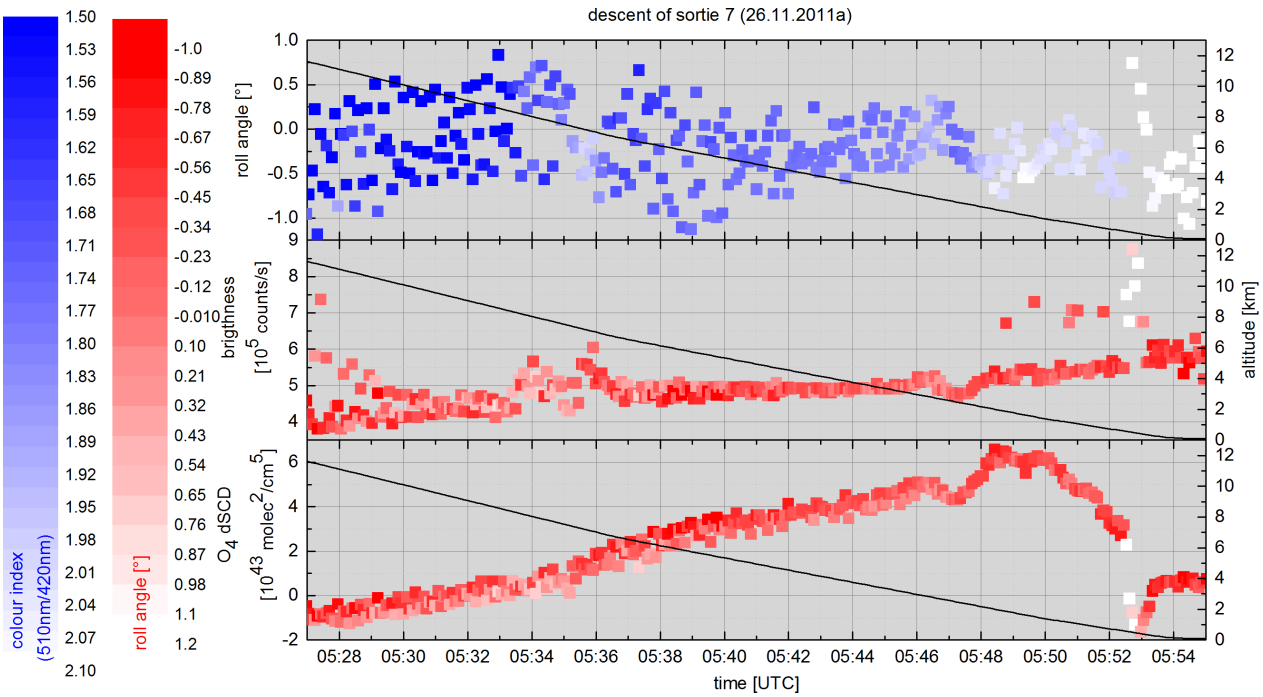

Figure 10.19: The roll angle colour-coded with the colour index (510 nm/ 420 nm), the brightness and O_4 dSCDs colour-coded with the roll angle during the descent of sortie 7 on 26 November 2011a.

The results of the non-linear profile retrieval in the UV and visible wavelength range, respectively, are displayed in Figure 10.20. The AOTs of the inferred particle extinction profiles result in $\tau = 0.20$ at 360.8 nm and $\tau = 0.22$ at 477.1 nm, respectively. These AOTs are in good agreement with the average AOT detected by the sun photometer at the AERONET station in Kuching during November and December 2011 (Figure 9.14), which approximately adds up to 0.2 for the Level 2 data. Higher AOTs of up to three or four can be occasionally found in the unscreened Level 1 AERONET data where no cloud correction is applied. The averaging kernels quantify the sensitivity of the profile retrieval towards particular altitude levels. For this descent, the averaging kernels reach values close to one up to an altitude of approximately 4 km and decrease for higher altitudes. That means that for altitudes above 4 km the fraction of a priori information in the solution vector increases for increasing altitudes. If the altitude grid size is gradually enlarged with increasing altitude, the averaging kernels will also reach values close to one. However, in the HEIPRO only a fixed altitude grid size can be chosen. The degrees of freedom (DOFs), which determine the number of independent pieces of information, add up to $d_s = 59$ and $d_s = 69$ for the UV and visible wavelength range, respectively. A good agreement between measured and modelled O_4 dSCDs is achieved (Figure 10.21) with a Pearson correlation coefficient of $R = 0.98$ at 360.8 nm and $R = 0.97$ at 477.1 nm. This shows, that the HEIPRO retrieval is able to reproduce the measurements with the chosen assumptions. For the chosen settings, the profile retrieval for this descent approximately requires seven hours of computation time.

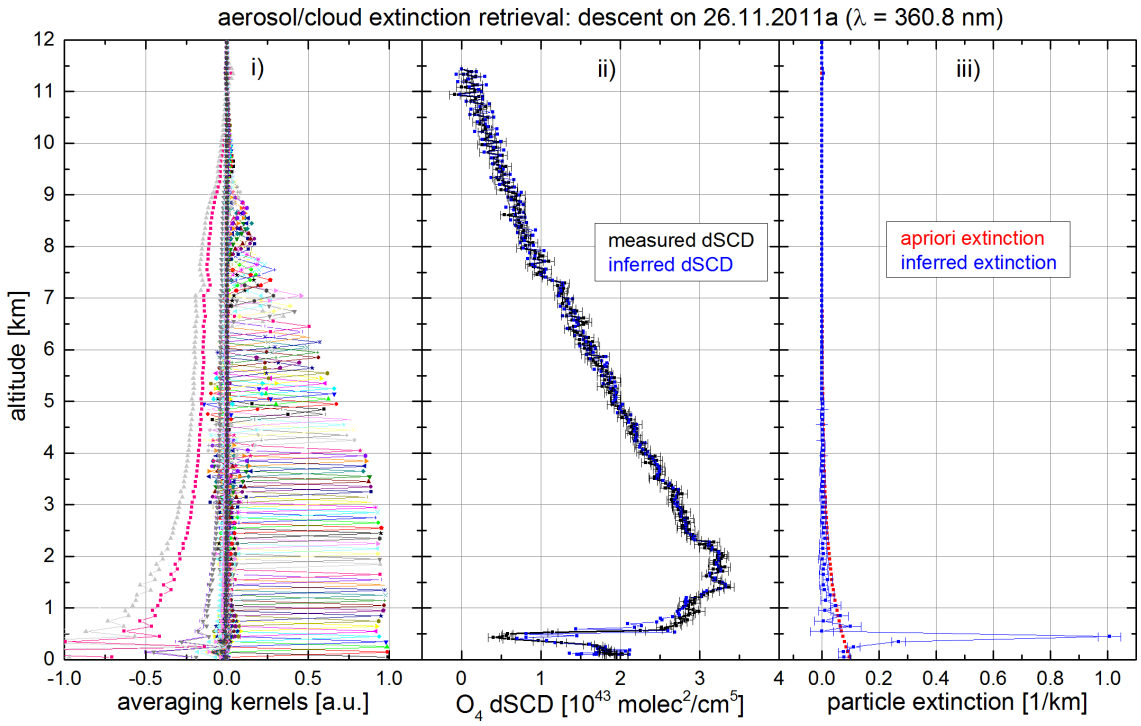

(a)

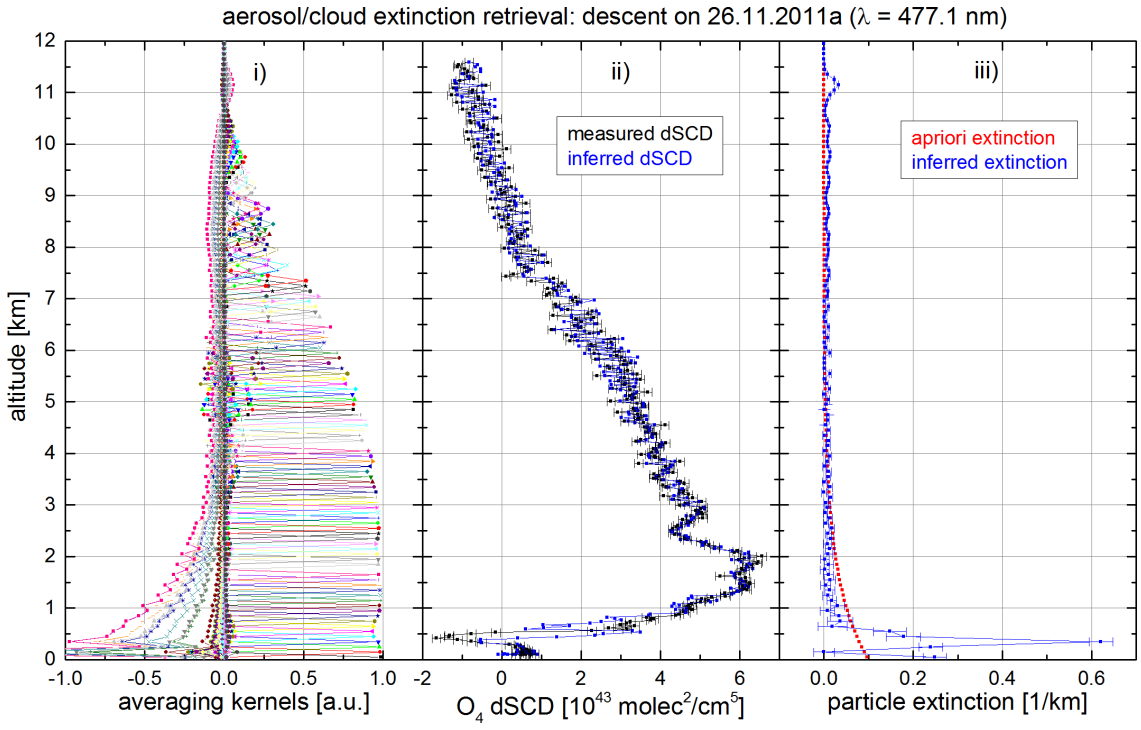

(b)

Figure 10.20: Non-linear profile retrieval of the descent of sortie 7 on 26 November 2011a at a wavelength of (a) 360.8 nm and (b) 477.1 nm, respectively: (i) averaging kernels, (ii) measured and inferred O_4 dSCDs and (iii) a priori and inferred particle extinction profile.

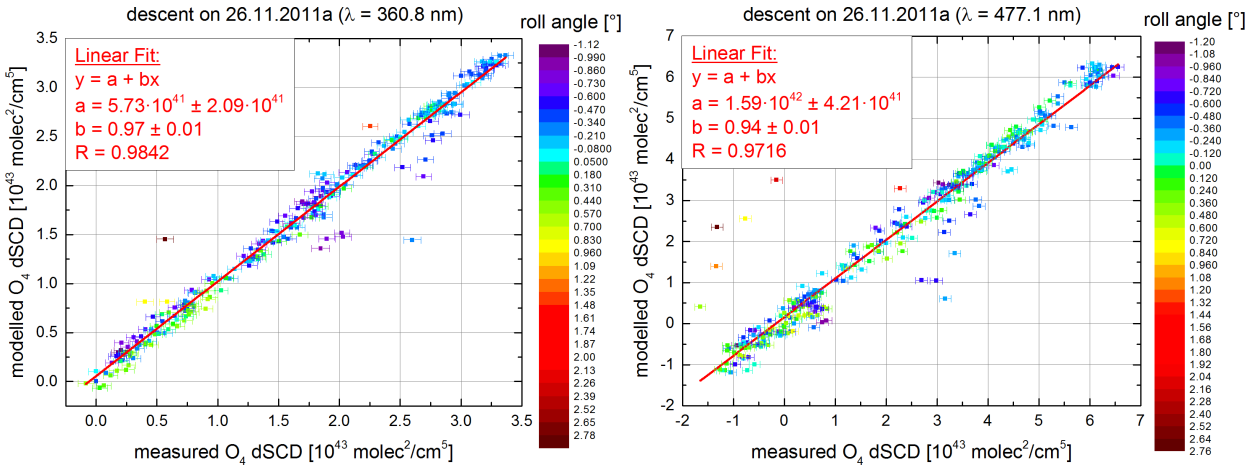

(a) (b)

Figure 10.21: Correlation of the measured and inferred O_4 dSCDs for the descent of sortie 7 on 26 November 2011a at a wavelength of (a) 360.8 nm and (b) 477.1 nm, respectively. The red line represents a linear fit with a Pearson correlation coefficient of R = 0.9842 at 360.8 nm and R = 0.9716 at 477.1 nm.

Results of the linear retrievals of HCHO, CHOCHO and NO_2 are shown in Figure 10.22 and of H_2O and IO in Figure 10.23. The measured and inferred dSCDs show a good agreement for the different trace gases with a Pearson correlation coefficient between 0.97 and 0.98 (Figure 10.24).
Figure 10.25 shows a summary of all inferred profiles for this descent together with the results from the O_4 scaling method from Section 10.1. The O_4 scaling method reproduces the profile shape of the profiles inferred with the HEIPRO retrieval very well and the VMRs lie within the error bars of the HEIPRO retrieval. It can be concluded that for this descent the O_4 scaling method and the HEIPRO retrieval lead to similar results. Thus, the O_4 scaling method can be used to infer VMRs.

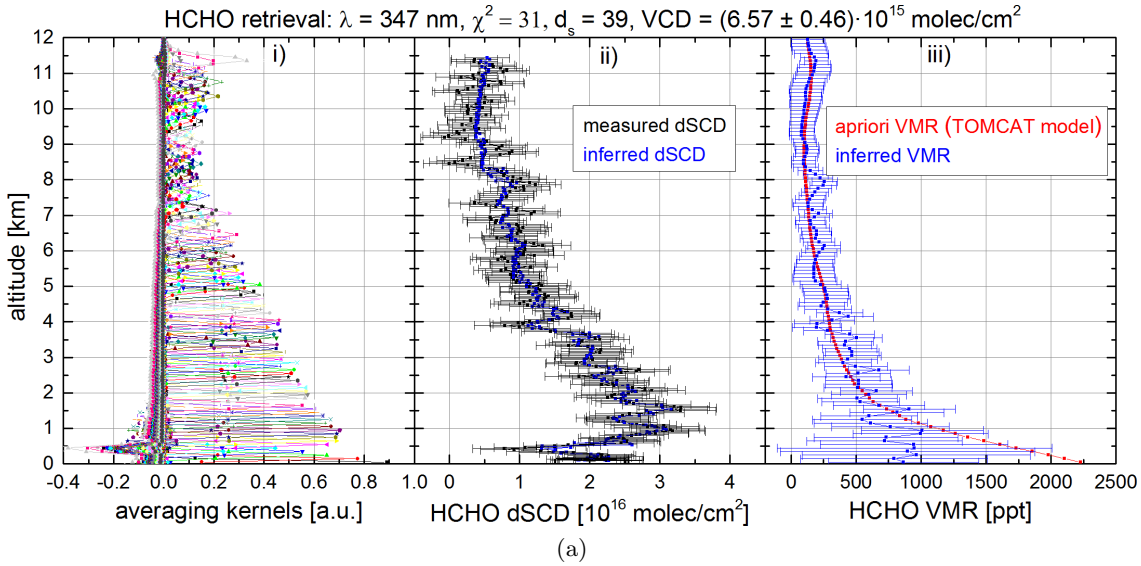

(a)

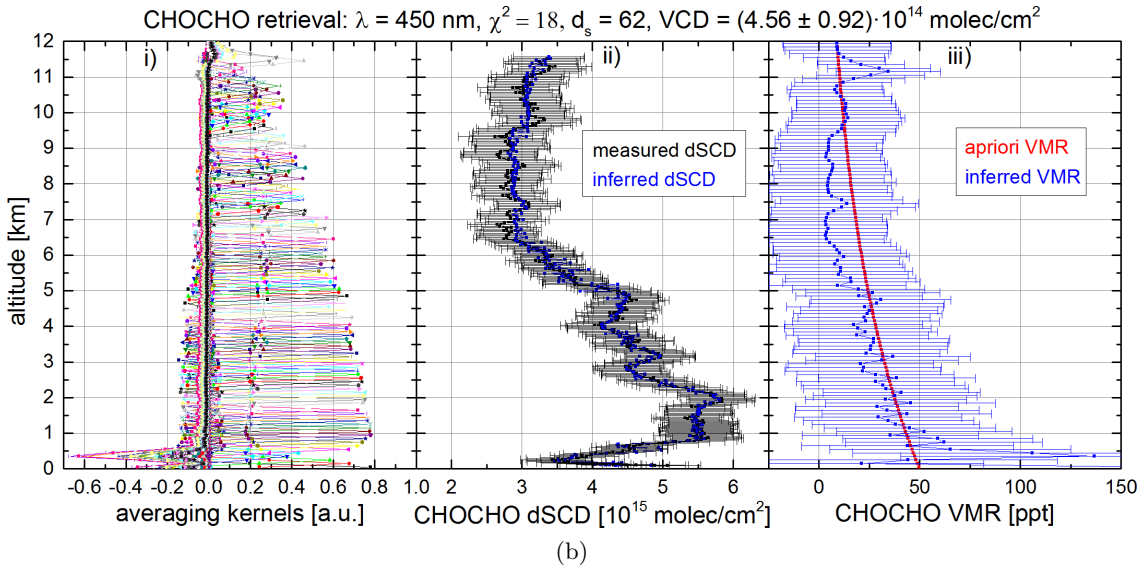

(b)

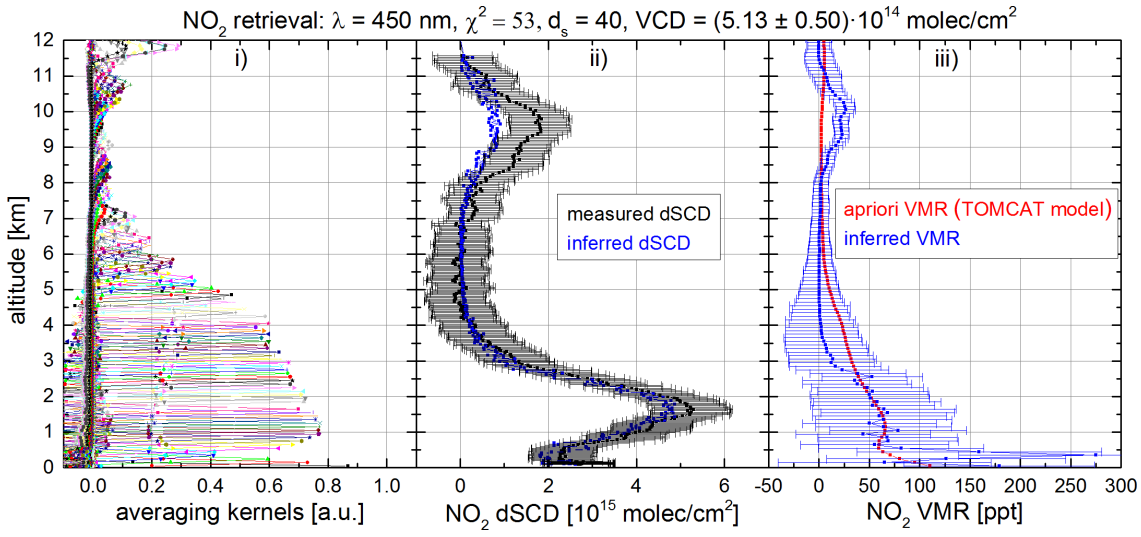

(c)

Figure 10.22: Linear profile retrieval of the descent of sortie 7 on 26 November 2011a for (a) HCHO at 347 nm, (b) CHOCHO at 455 nm and (c) NO_2 at 450 nm: (i) averaging kernels, (ii) measured and inferred dSCDs and (iii) a priori and inferred vertical profile.

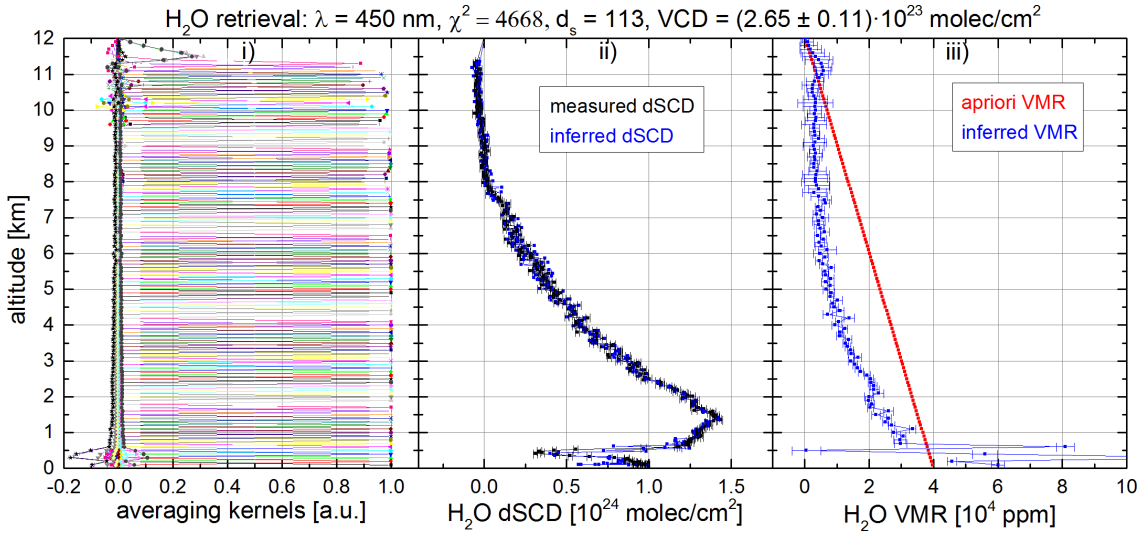

(a)

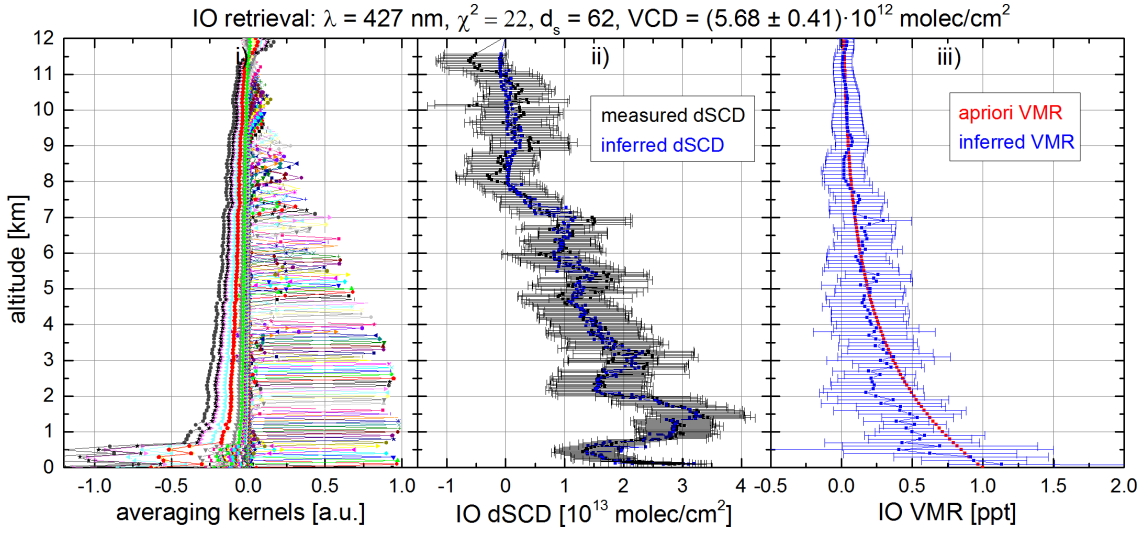

(b)

Figure 10.23: Linear profile retrieval of the descent of sortie 7 on 26 November 2011a for (a) H_2O at 450 nm and for IO at 427 nm: (i) averaging kernels, (ii) measured and inferred dSCDs and (iii) a priori and inferred vertical profile.

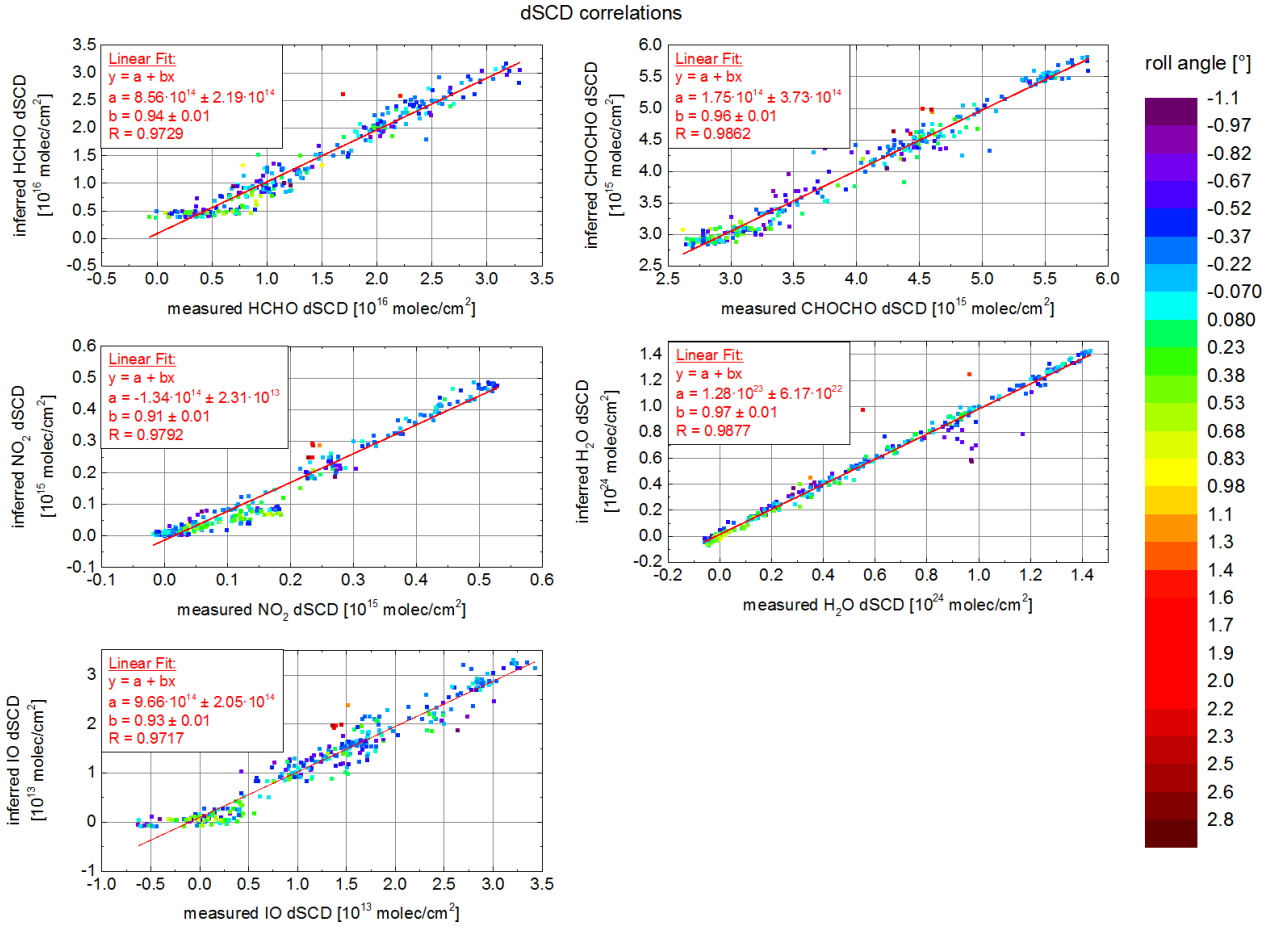

Figure 10.24: Correlation plots of the measured and inferred dSCDs of HCHO, CHOCHO, NO_2, H_2O and O_3 in the UV and visible wavelength range and of IO, respectively. The red lines corresponds to a linear fit with the fit parameters given in the box in the upper left corner of each panel.

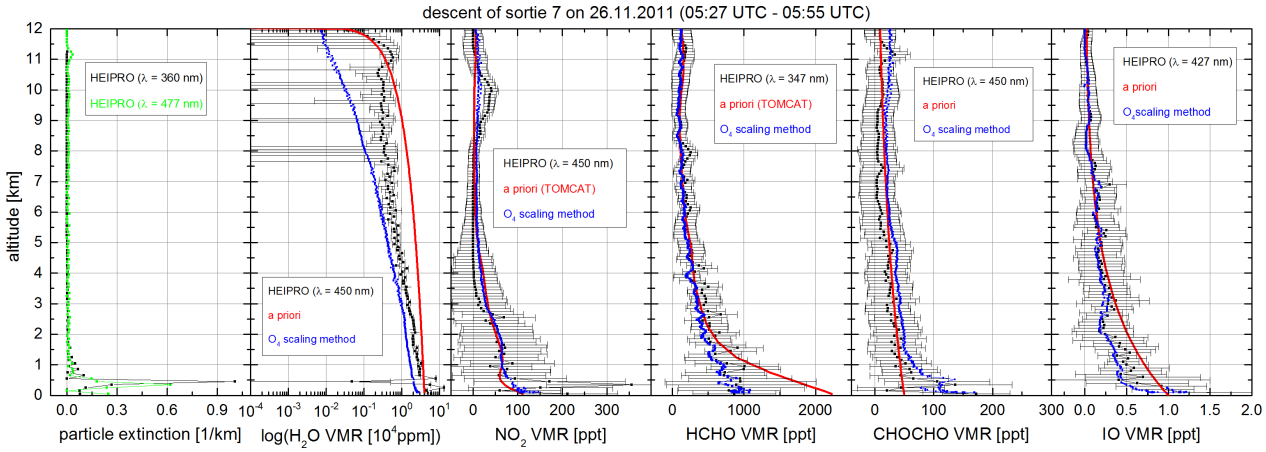

Figure 10.25: Vertical profiles for the descent on 26 November 2011 inferred with the HEIPRO retrieval (black) and with the O_4 scaling method from Section 10.1 (blue).The red lines represent the a priori profiles. For reasons of clarity, the error bars of the particle extinction profiles and the O_4 scaling method are not included.

Descent of sortie 1 on 16 November 2011

The descent of sortie 1 on 16.11.2011 represents a typical descent of the Falcon aircraft during the SHIVA campaign to the airport of Miri including a turn before landing (Figure 10.26). Figure 10.27 shows a selection of webcam images of the different cloud conditions present during this descent. Figure 10.28 further depicts the colour index, the brightness and the O_4 dSCDs for this descent. In the first part of the sortie the clouds seem to be far away. For the measurement at 07:16 UTC and an altitude of approximately 4 km the O_4 dSCDs strongly decrease due to a cloud that is obviously very close to the aircraft. Below an altitude of 4 km different cumulus clouds occur, leading to variations in the O_4 dSCDs. For the observation at 07:23 UTC the aircraft turned and the mini-DOAS instrument was pointing towards the ocean. Since the HEIPRO retrieval is not able to reproduce turns, the lowermost kilometre of the profile is excluded from the profile retrieval.
Figure 10.29 shows the inferred profiles for this descent. The O_4 scaling method reproduces the profile shape of H_2O, HCHO, and CHOCHO inferred with the HEIPRO retrieval very well and the VMRs lie within the error bars of the HEIPRO retrieval. For NO_2 and IO a bias between these two methods is discernable, but the VMRs inferred with the O_4 scaling method still lie within the error bars of the HEIPRO retreival.
Obviously, the VMRs inferred with the HEIPRO retrieval are more sensitive to heterogeneous cloud layers , i.e. if clouds are not correctly represented by the non-linear profile retrieval, remaining features will propagate into the linear retrieval of the trace gases. The VMRs inferred with the O_4 scaling method have less artefacts than the VMRs inferred with the HEIPRO retrieval. Thus, it can be concluded, that the O_4 scaling method leads to more robust results than the HEIPRO retrieval since uncertainties in the RT partly cancel out.

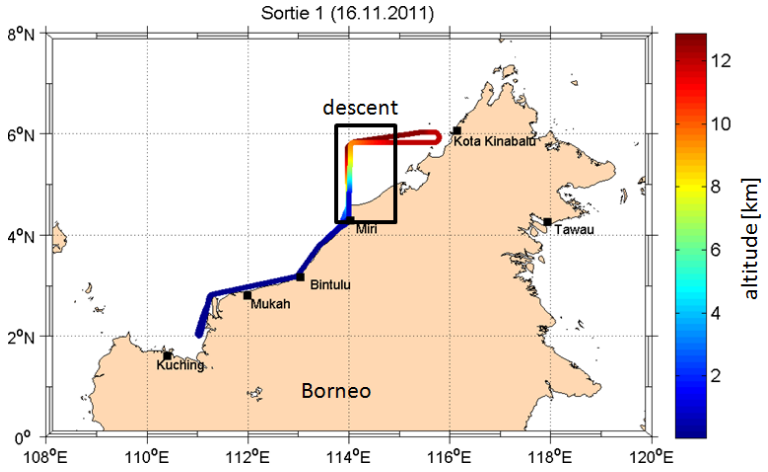

Figure 10.26: Flight track of sortie 7 on 26 November 2011a. The black box marks the location of the descent of the Falcon aircraft chosen for the profile retrieval.

Figure 10.27: Selection of webcam images of the different cloud scenes during the descent on 16 November 2011.

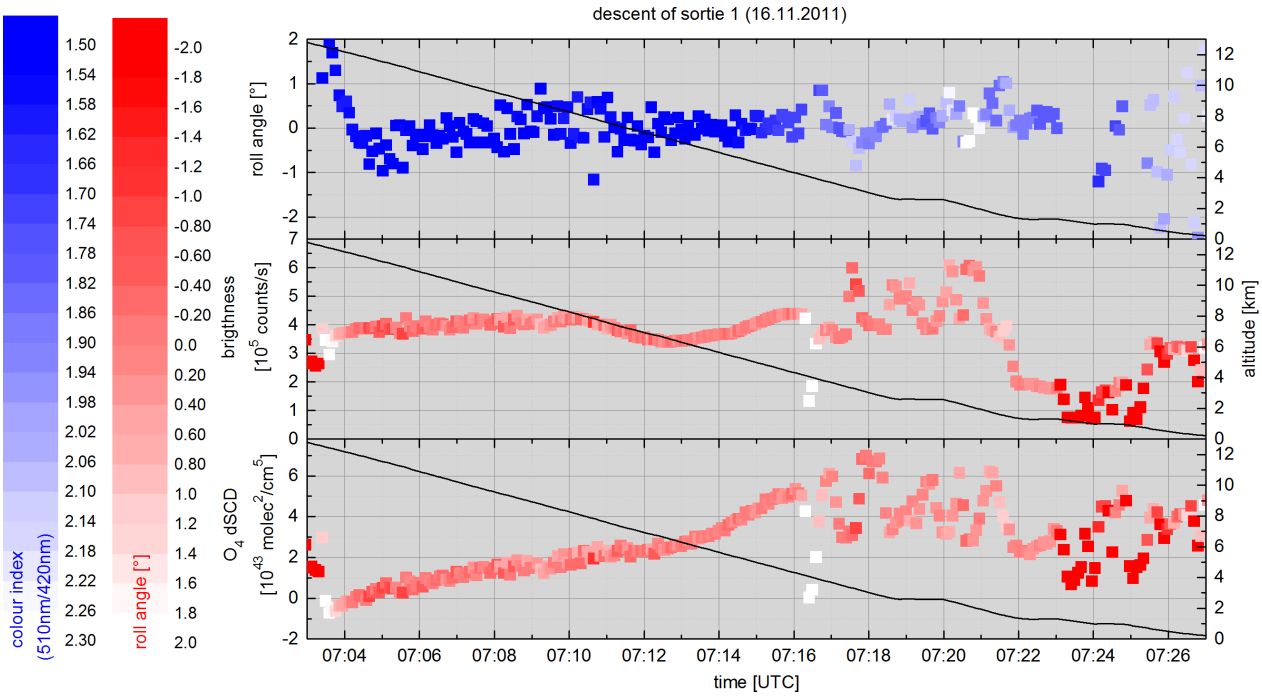

Figure 10.28: The roll angle colour-coded with the colour index (510 nm/ 420 nm), the brightness and O_4 dSCDs colour-coded with the roll angle during the descent of sortie 1 on 16 November 2011.

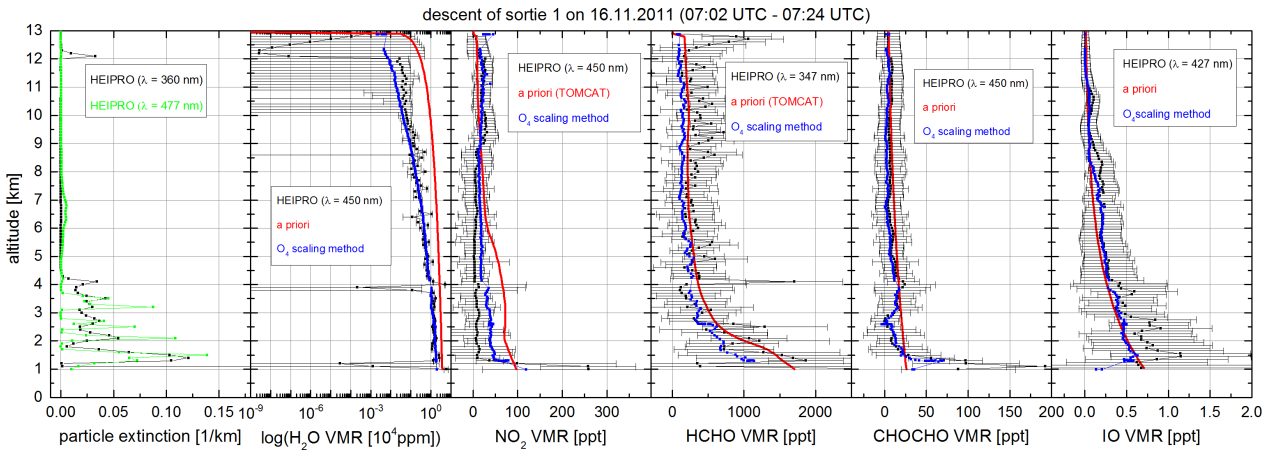

Figure 10.29: Vertical profiles for the descent on 26 November 2011 inferred with the HEIPRO retrieval (black) and with the O_4 scaling method from Section 10.1 (blue).The red lines represent the a priori profiles. For reasons of clarity, the error bars of the particle extinction profiles and the O_4 scaling method are not included.

10.2.3 Error characterisation

The total uncertainty of the HEIPRO profile retrieval is comprised of several error sources. Firstly, systematic errors due to the spectral DOAS analysis (described in Section 8.3) contribute to the total error. Furthermore, several assumptions are made, for example the 1D profile retrieval assumes that the aerosol and trace gas air masses are horizontally homogeneous. However, in reality, aerosols and trace gases change spatially and with time. Since the retrieval procedure further averages the trace gas concentration for each altitude cluster cell, average trace gas profiles are inferred. Apart from this averaging process, the results of the profile retrieval may largely depend on the chosen model input parameters.

In this section, the sensitivity of the profile retrieval to several input parameters is explored. Sensitivity studies are performed for the descent on 26 November 2011 for a set of different parameters, both for the non-linear and the linear profile retrieval. HCHO is used as a test gas for the linear profile retrieval. The particle extinction and HCHO profiles of the base run described in the previous section are displayed in Figure 10.30 including the error bars of the retrieval error, the smoothing error and the noise error. The retrieval error represents the largest error followed by the smoothing error with the noise error being the smallest error source. However, the noise error is larger than the smoothing error for retrieved particle extinction below 4 km. The mean relative HCHO error averaged over the vertical profile is approximately 73 % for the retrieval error, 64 % for smoothing error and 33 % for the noise error, respectively. The noise error decreases for higher altitudes. Table 10.3 shows an overview of the different parameters that are varied compared to the base run described in the previous section. The resulting particle extinction and HCHO profiles are displayed in Figure 10.31. In the following, the influences of the different parameters on the retrieval results are examined.

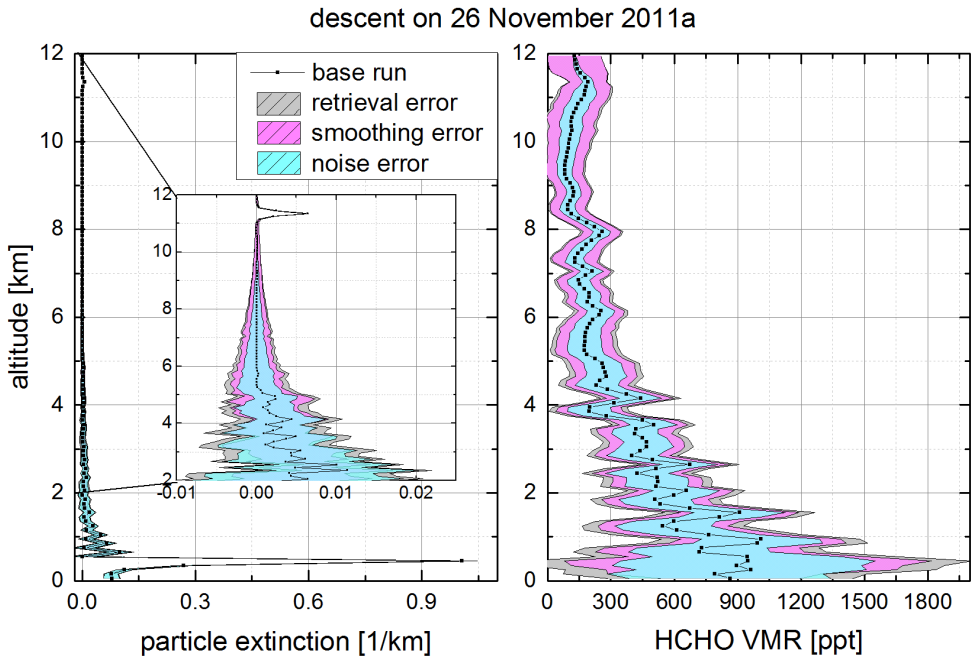

Figure 10.30: Inferred particle extinction profile (left panel) and HCHO profile of the base run for the descent on 26 November 2011a. The grey-shaded area represents the retrieval error, the pink-shaded area smoothing error and the turquoise-shaded area the noise error. For clarity, the insert in the left panel shows the particle extinction between 2 and 12 km.

Table 10.3: Overview of the retrieval results of the different sensitivity runs. The resulting retrieval parameters of the base run are given in the first row. The parameters that are changed in comparison to the base run are specified in the first column. R represents the Pearson correlation coefficient between the measured and inferred dSCDs.

	non-linear	profile	retrieval		linear	profile	retrieval	
run	AOT ± error	χ^2	d_s	R	VCD ± error	χ^2	d_s	R
base run	0.200 ± 0.003	1017	59	0.9842	6.572 ± 0.459	31	39	0.9729
aerosol apriori: box profile	0.170 ± 0.003	1234	28	0.9833	6.421 ± 0.541	31	39	0.9729
base aerosol profile · 2	0.390 ± 0.003	-	-	-	7.405 ± 0.526	29	37	0.9749
base aerosol profile / 2	0.100 ± 0.003	-	-	-	6.065 ± 0.410	34	39	0.9691
base aerosol profile + error	0.270 ± 0.003	-	-	-	7.065 ± 0.479	30	37	0.9732
height grid: 200 m	0.210 ± 0.003	2377	32	0.9712	6.661 ± 0.503	43	31	0.9596
height grid: 500 m	0.112 ± 0.003	3364	13	0.9455	6.799 ± 0.564	62	19	0.9407
albedo: 30 %	0.145 ± 0.003	1172	59	0.9817	6.359 ± 0.435	32	39	0.9718
albedo: 60 %	0.111 ± 0.003	1330	59	0.9791	6.222 ± 0.423	33	39	0.9708
SSA: 0.8	0.188 ± 0.003	1161	58	0.9819	6.552 ± 0.457	31	39	0.9719
SSA: 0.6	0.190 ± 0.003	1323	57	0.9792	6.618 ± 0.463	33	39	0.9707
g: 0.6	0.154 ± 0.003	1135	62	0.9822	6.485 ± 0.445	32	39	0.9715
g: 0.78	0.235 ± 0.003	1002	57	0.9850	6.443 ± 0.456	30	39	0.9729
roll angle + 1 °	0.337 ± 0.003	567	50	0.9924	6.633 ± 0.486	34	28	0.9704
roll angle - 1 °	0.220 ± 0.003	1447	46	0.9777	7.033 ± 0.508	42	24	0.9617
BRDF ocean	0.212 ± 0.002	897	59	0.9866	6.531 ± 0.460	31	39	0.9727
O_4 scaling factor 1.25	0.287 ± 0.002	897	62	0.9860	7.125 ± 0.486	31	37	0.9724
O_4 scaling factor 0.75	0.163 ± 0.004	2027	55	0.9782	6.088 ± 0.423	32	39	0.9719

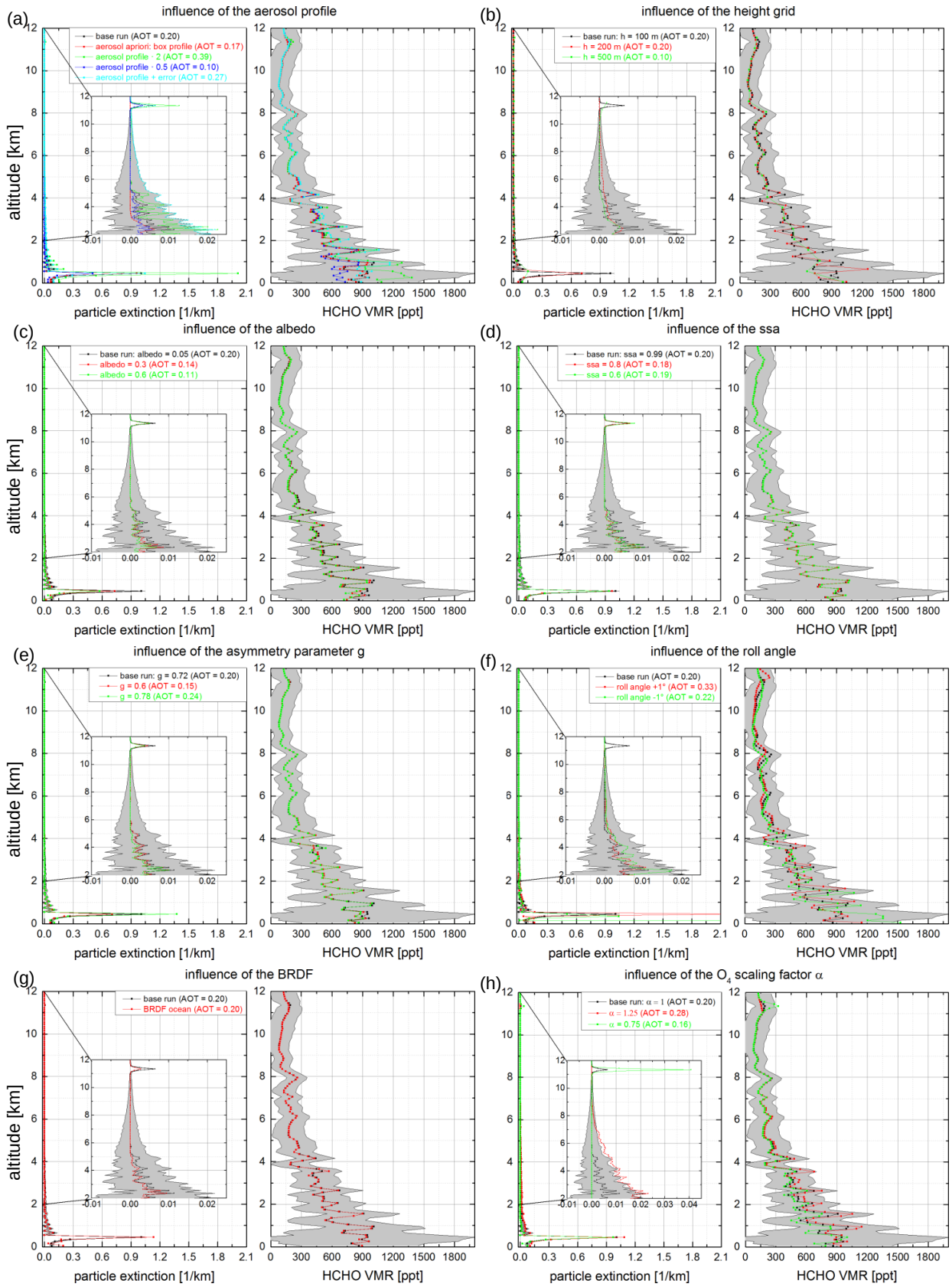

Figure 10.31: Sensitivity study for the non-linear and linear profile retrieval: Influence of (a) the aerosol profile, (b) the height grid, (c) the albedo, (d) the SSA, (e) the asymmetry parameter g, (f) the roll angle, (g) the BRDF, (h) the O_4 scaling factor.

Influence of the aerosol a priori and aerosol profile shape

In order to single out the influence of the a priori profile, the retrieval is performed assuming different a priori profiles. Assuming an a priori profile with a relatively unrealistic smoothed box shape with a height of 1.5 km and an extinction of 0.1 km^{-1} at the ground results in a different aerosol profile as compared to the base run with almost no aerosol extinction above the box altitude. However, implementing this aerosol profile into the linear retrieval of HCHO leads to a change in the HCHO mixing ratios of only 3 % or less. If the aerosol extinction profile of the base run is doubled/divided by two, the resulting HCHO mixing ratios increase/decrease by approximately 30 % in the boundary layer and 1 - 3 % in the free troposphere and above. Adding the retrieval error on the aerosol extinction profiles results in a deviation in the HCHO mixing ratios of up to 15 % relative to the base run. Overall, these systematic errors remain smaller than the retrieval error of the base run.

Influence of the height grid resolution

The influence of the resolution of the height grid on the profile retrieval is tested for height grids with a resolution of 50 m, 100 m and 500 m, with a resolution of 100 m representing the standard case. For a larger resolution than 500 m, the measured dSCDs have to be averaged, otherwise there are too many measurement points for one layer. The resulting profiles using a coarser grid than 100 m still show a similar profile as the base run. However, their shape is slightly smoothed leading to deviations in the HCHO mixing ratios of ±20% and less. For a coarser grid than 100 m, the correlation coefficient between measured and inferred dSCDs becomes smaller (Table 10.3). Ideally, a height grid with a variable height grid size should be chosen with a fine grid size for lower altitudes and with a coarser grid for higher altitudes. However, the HEIPRO retrieval only supports fixed altitude grid cells.

Influence of the albedo

In order to test the sensitivity to changes in the surface albedo, the albedo of the base run (5 %) is arbitrarily changed to 30 % and 60 %. The resulting HCHO mixing ratios show a deviation of less than 3 % for an albedo of 30 % and less than 5 % for an albedo of 60 % as compared to the base run.

Influence of SSA

Figure 10.32 (left panel) shows the aerosol single scattering albedo inferred from the AERONET station at the airport of Kuching during November and December 2011. The SSA varies between 0.6 and 0.99 with an average value of 0.96 for the smallest available wavelength of 441 nm. Assuming a smaller SSA (SSA = 0.8 and 0.6) than used for the base run (SSA = 0.99) leads to very small deviations in the HCHO profile of less than 2 % compared to the base run.

Influence of the asymmetry parameter g

In Figure 10.32 (right panel) the asymmetry parameter g is shown for the AERONET station at the airport of Kuching during November and December 2011. For a wavelength of 441 nm, g varies between 0.65 and 0.78 with an average value of 0.71. For the sensitivity study, asymmetry parameters of 0.6, 0.72 and 0.78 are chosen, where 0.72 corresponds to the base run asymmetry parameter. The difference between the respective retrieved HCHO profiles is small. The deviation in the HCHO mixing ratios in comparison to the base run is smaller than 5 % below an altitude of 5 km and smaller than 1 % at altitudes above 5 km. Thus, reasonable variations in the chosen values of SSA and g do not appear to significantly alter the retrieved profile.

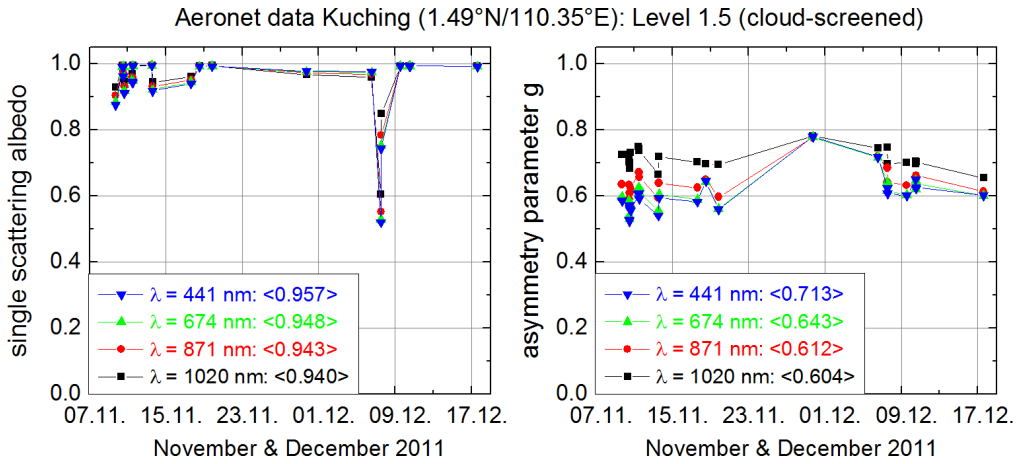

Figure 10.32: Single scattering albedo (left panel) and asymmetry parameter g (right panel) for different wavelengths from an AERONET (`http://aeronet.gsfc.nasa.gov/`) station in Kuching (1.45 °N/110.35 °E) for November and December 2011. The sun photometer of the site of Kuching is mounted on the observation tower of Kuching Meteorological Station located at the Kuching International Airport, Sarawak.

Influence of the roll angle

For each recorded spectrum, a roll angle is assigned. As the roll angle of the Falcon aircraft varies during the integration time of one spectrum, the assigned roll angle can have an error. In order to examine this error, a roll angle of $\pm 1\,^\circ$ is added to the assigned roll angle. As it can be seen from Figure 10.31 (f), the maxima in the HCHO mixing ratios slightly shift to higher altitudes for a systematic roll angle $+1\,^\circ$ and decrease for a roll angle $-1\,^\circ$. The changes from the base case may reach values up to 40 % in the inferred HCHO profile.

Influence of the BRDF

The surface albedo has a complex dependence on the incident and outgoing direction of light, which is expressed as the Bidirectional Reflectance Distribution Function (BRDF), and can have an influence on the retrieval of tropospheric trace gases from satellite measurements (Noguchi et al., 2014). SCIATRAN offers the possibility to use a BRDF for different surface types. In order to study the impact of the BRDF, a BRDF for the surface type 'ocean' is implemented in the HEIPRO retrieval. For the aerosol profile, deviations occur in comparison to the base run where no BRDF is used. However, the deviations in the HCHO profile are very small and amount to approximately 3 % for altitudes below 5 km and less than 3 % for higher altitudes.

Influence of an O_4 scaling factor

There are uncertainties associated with the O_4 literature absorption cross-sections. In several studies (e.g. Clémer et al., 2010) a scaling factor of 1.25 is introduced, which is applied to the O_4 absorption cross-section to reach a better agreement between measured and inferred O_4 dSCDs. In order to estimate the influence of these possible uncertainties, the O_4 absorption cross-section is scaled by a factor of 0.75 and 1.25. Although the resulting aerosol profile is strongly reduced/enhanced for an O_4 scaling factor of 0.75/1.25, the inferred HCHO profile only changes by less than 20 % from the base run for altitudes below 5 km, and less than 5 % for altitudes above 5 km.

Influence of different a priori profiles on the trace gas profile

A set of different a priori profiles is chosen in order to test the influence of the HCHO a priori profile on the inferred HCHO profile (Figure 10.33, left panel). In all cases the a priori error is set to 100 %. Below 4 km, the inferred HCHO mixing ratios may change between 10 and 40 % from the base run. For higher altitudes, this deviation increases up to values of 100 % and more. This is due to the decreasing averaging kernels for a fixed altitude grid (Figure 10.22a). Above 5 km, the averaging kernels drop down to values of approximately 0.2 so that for a fixed altitude grid most of the information is derived from the a priori for those altitudes. For lower altitudes the inferred profile is more independent from the a priori and can be derived more from the measurements. It can be concluded that the a priori shape within the lowermost 5 km of the profile only has a minor impact on the inferred HCHO profile whereas the a priori shape above 5 km can strongly influence the inferred profile. Thus, the choice of a priori profile, and/or the chosen altitude grid is essential for altitudes above 5 km. For this study, a priori profiles from the model TOMCAT are used, which are available for HCHO, O_3 and NO_2 for each ascent and descent, respectively.

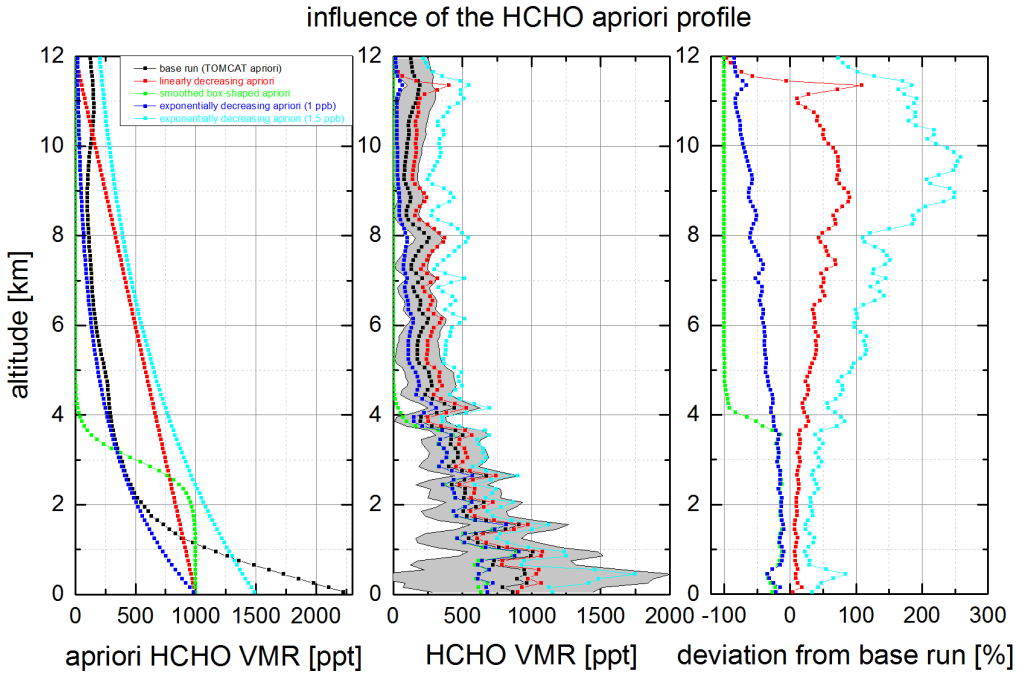

Figure 10.33: Influence of the HCHO a priori profile on the inferred HCHO profile: Left panel: Different HCHO a priori profiles, middle panel: Inferred HCHO profile, and right panel: Deviation of the different inferred HCHO profiles from the base run. The black line marks the base run.

In summary, the sensitivity studies show that the uncertainties in the retrieval results are dominated by the choice of the a priori profile. A further dominant uncertainty is the roll angle. A change in the other input parameters leads to deviations of less than 10 %.

10.3 Comparison of retrieval results to in situ data

In order to validate the O_4 scaling method and the results of the HEIPRO retrieval, the inferred H_2O VMRs can be compared to in situ water vapour measurements from the basic sensors of the Falcon aircraft or from the ascents of the radiosondes that were released aboard the RV Sonne. However, it has to be noted, that the DOAS technique is a remote-sensing method. That means that the mini-DOAS instrument might have observed a different air mass several kilometres away

from the aircraft compared to the in situ instruments that probe air masses directly at the position of the aircraft. Raecke (2013) used in situ O_3 mixing ratios measured by the NOAA instrument to infer the effective photon path length for the observations of the mini-DOAS instrument deployed aboard the Global Hawk. As the Global Hawk mini-DOAS has a viewing direction in flight direction, the in situ measured O_3 mixing ratios are averaged for every measurement point of the mini-DOAS instrument using a line-of-flight weighting function. Unfortunately, this is not possible for the DOAS measurements during the SHIVA campaign as the mini-DOAS instrument aboard the Falcon has a viewing direction perpendicular to the flight direction and does not necessarily observe the air mass the aircraft is flying through. Thus, the results of a direct comparison of the DOAS with the in situ measurements must be interpreted carefully. However, in comparison to mid-latitudes, where cold and warm front occur, the ocean and presumably the land surface around Borneo have similar temperatures. Thus, in tropical regions large gradients in the H_2O profile are not expected to occur. It is well-known that the humidity measurements recorded by radiosondes contain sensor-dependent errors with temporal and spatial variations (e.g. Antón et al., 2014, and references therein). For the water vapour measurements aboard the Falcon, three different sensors are used, located at the front part of the aircraft with each having its own advantages and disadvantages: A Lyman-alpha absorption instrument (Buch Research, Boulder), a slightly modified capacitive sensor (HUMICAP, Vaisala) and a commercial dew point hygrometer developed for aircraft applications (GE 1011B, General Eastern) (for further information on the Falcon humidity sensors see `http://www.dlr.de/fb/en/desktopdefault.aspx/tabid-3718/5796_read-8410/`). The main sensor is a Lyman-alpha instrument, which measures the absorption of water vapour at a wavelength of 121 nm. A possible drift is divided out through a comparison with the much slower HUMICAP sensor. A further consistency check is a comparison with the dew point hygrometer, which also has a slow time response. Hence, the water vapour profiles from the Falcon sensors receive their temporal solution from the Lyman-alpha sensor whereas the baseline is mainly due to the HUMICAP sensor. However, for the ascents and descents of the aircraft, the temperature dependency especially of the HUMICAP sensor and dew point hygrometer can degrade the accuracy as their time response decreases with decreasing temperature. That means that during aircraft descents the humidity inlet at high altitudes is cold and warms up much slower than the altitude change of the aircraft would require. When flying through clouds, small cloud droplets can enter the humidity inlet where they evaporate. This enhanced humidity values within clouds do not represent the steam mass fraction of the ambient air but are instead part of the liquid water content (personal communication Volker Dreiling, DLR flight department, May 2014). According to the DLR flight department who processes and calibrates the humidity data from the Falcon sensors, the accuracy of the humidity data is approximately 5 % of the measured value in the lower third of the atmosphere (`http://www.dlr.de/fb/en/desktopdefault.aspx/tabid-3718/5796_read-8410/`).

Figure 10.34 shows a flight-by-flight comparison of the H_2O VMRs inferred from the absolute humidity of the Falcon sensor and retrieved from the mini-DOAS measurements using the O_4 scaling method. The H_2O VMRs inferred from the mini-DOAS measurements show a similar distribution as compared to the VMRs derived from the Falcon sensor. However, the mini-DOAS H_2O VMRs are smaller than the VMRs inferred from the absolute humidity of the Falcon sensor. This difference can be for example due to the uncertainty of $S_{ref_{H_2O}}$ estimated using different 3D cloud scenarios. According to Figure 10.4, the simulated $S_{ref_{H_2O}}$ are 40 % smaller than the measured $S_{ref_{H_2O}}$. Thus, the VMRs inferred with the O_4 scaling method are likely underestimated by approximately 40 %. Nevertheless, in most cases, the VMRs inferred from the absolute humidity of the Falcon sensor lie within the error bars of the O_4 scaling method.

Figure 10.35 shows a comparison of the H_2O profiles for the descent on 26 November 2011 and on 16 November 2011 inferred with the HEIPRO retrieval, retrieved with the O_4 scaling method, measured by the Falcon sensor, and measured by a radiosonde that was released aboard the RV Sonne at 06:00 UTC on the respective day. The agreement of all four methods is better for sortie 1 than for sortie 7. For sortie 1 the H_2O VMRs all lie within the error bars of the O_4 scaling

method. For the descent of sortie 7 the O_4 scaling method leads to much lower H_2O VMRs than the HEIPRO retrieval (≈ 50 - 60 %) and the in situ measurements (≈ 30 - 40 %). As mentioned above, this might be due to the uncertainty in the determination of $S_{ref_{H_2O}}$. Obviously, for sortie 1 the estimation of $S_{ref_{H_2O}}$ seems to be more realistic than for sortie 7.

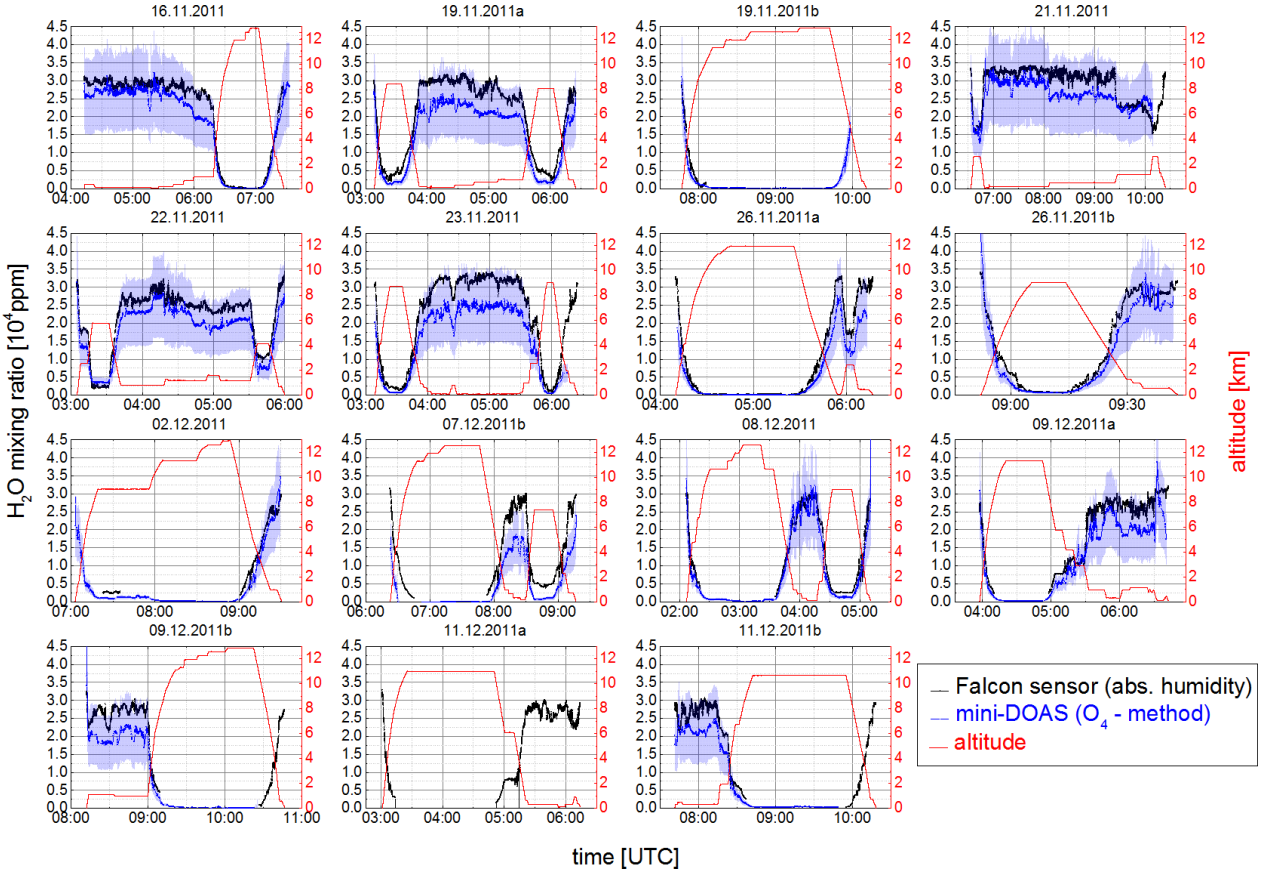

Figure 10.34: H_2O VMRs inferred from the absolute humidity of the Falcon sensor (black line) and retrieved from the mini-DOAS measurements using the O_4 scaling method (blue line) for the different sorties of the Falcon aircraft. The red line represents the height. Since for sortie 10 on 07.12.2011a no pressure and temperature data is available due to a failure in th recording of the standard aircraft parameters, VMRs can not be inferred for this sortie. For sortie 15 on 11.12.2011a no mini-DOAS data is available. Mini-DOAS data points with a roll angle larger than ±2° are excluded.

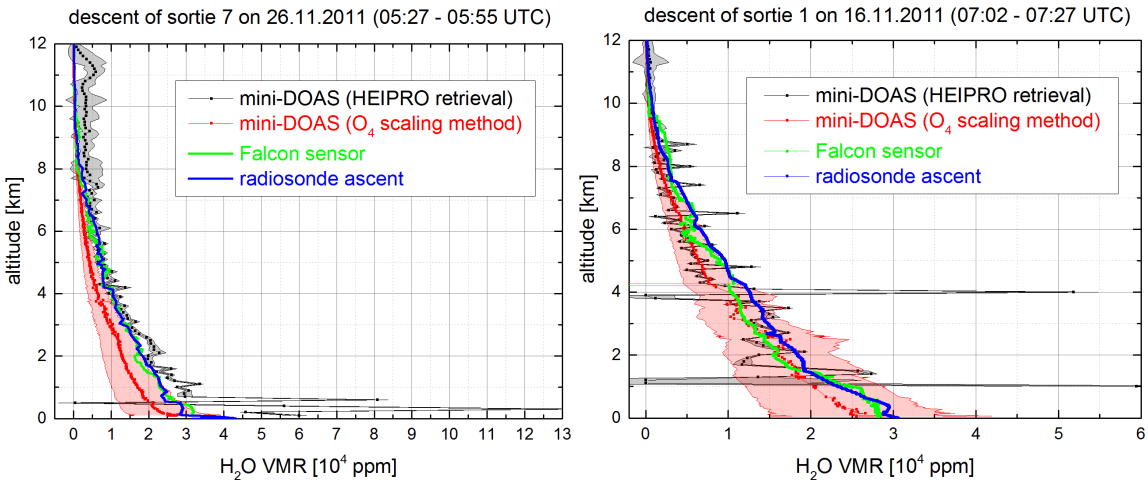

(a) (b)

Figure 10.35: H_2O profiles for the descent on (a) 26 November 2011 and on (b) 16.11.2011 inferred with the HEIPRO retrieval (black), retrieved with the O_4 scaling method (red), measured by the Falcon sensor (blue) and measured by a radiosonde that was released from the RV Sonne at 06:00 UTC on the respective day (green).

11. Implications of the airborne DOAS measurements for the tropospheric photochemistry around Borneo

This chapter discusses the major observations made by the mini-DOAS instrument during the SHIVA aircraft campaign over Borneo in November and December 2011. The structure of this chapter is based on the specific objectives of the aircraft-borne DOAS measurements defined in Section 6.1. Firstly, the findings related to the abundances of the halogenated very short-lived product gases BrO and IO are discussed (Section 11.1) and compared to previous measurements. The chapter continues with the interpretation of the measurements of HCHO, CHOCHO, and NO_2 and their possible influence on the oxidation capacity of the atmosphere (Section 11.2). Furthermore, the inferred HCHO and NO_2 VMRs are compared to simulated VMRs using the global chemical transport model TOMCAT (Section 6.2.4) and the regional chemical transport model CCATT-BRAMS (Section 6.2.5). The different possible emission sources of HCHO, CHOCHO, and NO_2 are presented in Section 11.2.3. In the final Section 11.3 the chemical composition of air masses in the outflow of a meso-scale convective cloud system is analysed and the OH concentration is estimated.

11.1 Abundance of halogenated compounds

Reactive halogen species (RHS) play an important role in atmospheric chemistry (Section 2.4.9). The following section presents the results of the DOAS measurements of BrO and IO during the SHIVA aircraft campaign. Furthermore, these results are compared to the shipborne and ground-based measurements during the SHIVA campaign as well as to previous measurements. Finally, potential sources and sinks are analysed.

11.1.1 Bromine monoxide

Observations

During the DOAS analysis of all sorties of the Falcon aircraft, BrO dSCDs never exceeded the detection limit of approximately $S_{det} = 5{\cdot}10^{13}$ molec cm^{-2} in the MBL. Assuming a light path of 10 km, this would correspond to a BrO VMR of approximately 2 ppt.
During the SHIVA campaign, shipborne MAX-DOAS measurements were performed both onboard the RV Sonne and at the ground in the north-eastern part of Borneo close to Semporna. In the case of the shipborne measurements, BrO never exceeded the detection limit of approximately 1 ppt during the whole cruise (Folkard Wittrock and Enno Peters, IUP Bremen, personal communication, July 2012). For the ground-based instrument, measurements in the UV wavelength range were not possible due to an instrument failure, i.e. no measurements of BrO were available (Peters, 2013).

Over the tropical open ocean, typical BrO mixing ratios of 0.5 - 3 ppt were reported with maximum values in the morning and approximately 1 ppt at noon (Read et al., 2008; Tschritter, 2013; Lampel, 2014). Thus, an upper limit of 2 ppt observed during the SHIVA campaign is not contradictory to previous measurements.

Discussion of the findings

In the following, the inferred upper limit of the BrO concentration in the MBL is discussed regarding the possible production and loss terms. The concentration of reactive bromine in steady state can be derived according to:

$$[\mathrm{Br}] = \frac{\text{Production rate}}{\text{Lifetime}}. \tag{11.1}$$

Sources of reactive bromine in the MBL are the heterogeneous bromine activation on aerosol surfaces, such as on sea-salt aerosols (e.g. Fickert et al., 1999) or the emission from brominated halocarbons, such as bromoform ($CHBr_3$) or dibromomethane (CH_2Br_2) (Section 2.4.9).
Pyle et al. (2011a) detected bromoform ($CHBr_3$) mixing ratios with occasional peaks reaching 10s of ppt at a coastal site in Sabah, Borneo during the OP3 campaign in 2008. Atmospheric concentrations of brominated halocarbons were further measured during a research cruise in the Strait of Malacca, the South China, and Sulu-Sulawesi Seas in June and July 2009 (Mohd Nadzir et al., 2014). During these measurements, the mixing ratios of $CHBr_3$ ranged between 1 and 2 ppt with the highest mixing ratios detected in the Strait of Malacca (4–5 ppt). During the SHIVA campaign aboard the Falcon aircraft, $CHBr_3$ measurements yielded a mean mixing ratio of 1.43 ppt with a variability of 37 % and a maximum mixing ratio of 3.42 ppt in the MBL (Sala et al., 2014b). According to Sala et al. (2014b), the atmospheric variability in the different altitude intervals of the Falcon aircraft increased with decreasing lifetime of the brominated halocarbons. Thus, as shorter is the lifetime of the halocarbons so stronger is the decrease in the VMRs between the MBL and the FT. $CHBr_3$ has, with approximately 24 days, the shortest free tropospheric lifetime of all brominated halocarbons (Table 2.2). In contrast, CH_2Br_2 is rather long-lived with a typical free tropospheric lifetime of approximately 123 days (Table 2.2).
Hepach et al. (2014) reported sea-to-air fluxes of $CHBr_3$ and CH_2Br_2 of up to $F_{CHBr_3} \approx 1.0 \cdot 10^8$ molec cm^{-2} s^{-1} and $F_{CH_2Br_2} \approx 2.5 \cdot 10^7$ molec cm^{-2} s^{-1} for the Mauritanian coastal upwelling region. In this region enhanced BrO VMRs of up to 10 ppt were observed (Martin et al., 2009; Tschritter, 2013). In order to obtain a flux for Br, F_{CHBr_3} is multiplied by a factor of 3 and $F_{CH_2Br_2}$ by 2. This results in Br fluxes of $F_{Br} = 3.0 \cdot 10^8$ molec cm^{-2} s^{-1} and $F_{Br} = 5.0 \cdot 10^7$ molec cm^{-2} s^{-1}, respectively.

In the region where the SHIVA campaign took place, interactions between marine and polluted urban air masses are likely. Reactive bromine species can interact with these air masses for example via the Reactions 2.53, 2.54, and 2.55.
In the following, the lifetime and the flux of Br are estimated for the reaction with HCHO. In Equation 2.55 Br reacts with HCHO forming hydrobromic acid (HBr), CO and HO_2 (Wagner et al., 2002). The reaction rate coefficient for this reaction yields $k_{Br+HCHO}(298K) = 1.2 \cdot 10^{-12}$ cm^{3}molec^{-1}s^{-1} (Sander et al., 2011b). This provides a lifetime for Br of $\tau_{Br} = \frac{1}{k_{Br+HCHO} \cdot [HCHO]} \approx 120$ s using a HCHO mixing ratio of approximately 300 ppt (i.e. $[HCHO] \approx 7.39 \cdot 10^9$ molec cm^{-3}) as measured during the SHIVA campaign. During daytime, BrO and Br are assumed to be in a steady state according to the following equation (Hansen et al., 1999):

$$\mathrm{Br} + \mathrm{O_3} \longrightarrow \mathrm{BrO} + \mathrm{O_2}, \tag{11.2}$$

i.e. the ratio between [BrO] and [Br] can be expressed as:

$$\frac{[\mathrm{BrO}]}{[\mathrm{Br}]} = \frac{k_{Br+HCHO}(298K) \cdot [\mathrm{O_3}]}{J_{BrO}}, \tag{11.3}$$

with a reaction rate coefficient of $k_{\mathrm{Br+HCHO}}(298\mathrm{K}) = 1.2 \cdot 10^{-12}$ cm^{3}molec^{-1}s^{-1} (Sander et al., 2011b). Assuming an O_3 mixing ratio of 25 ppb, i.e. $[O_3] \approx 6.2 \cdot 10^{11}$ molec cm^{-3}, and a photolysis rate for BrO of $J_{\mathrm{BrO}} = 5{\cdot}10^{-2}$ s^{-1}, the lifetime of $\mathrm{Br_x}$ ($\mathrm{Br_x} = \mathrm{BrO} + \mathrm{Br}$) results in $\tau_{\mathrm{Br_x}} = \tau_{\mathrm{Br}} \cdot \frac{[\mathrm{BrO}]}{[\mathrm{Br}]} \approx$ 1785 s $\approx$ 30 min. Further minor sinks for reactive bromine species are the following reactions:

$$\mathrm{BrO} + \mathrm{HO_2} \longrightarrow \mathrm{HBr} + \mathrm{O_3} \tag{11.4}$$

$$\mathrm{Br} + \mathrm{HO_2} \longrightarrow \mathrm{HBr} + \mathrm{O_2}, \tag{11.5}$$

with $k_{\mathrm{BrO+HO_2}}(298\mathrm{K}) = 2.1{\cdot}10^{-11}$ cm^{3}molec^{-1}s^{-1} and $k_{\mathrm{Br+HO_2}}(298\mathrm{K}) = 1.7{\cdot}10^{-12}$ cm^{3}molec^{-1}s^{-1} (Sander et al., 2011b). Assuming a daily mean concentration of $[\mathrm{HO_2}] = 10^7$ molec cm^{-3}, the lifetime of BrO and Br results in 1.3 hours and 18.5 hours, respectively. Thus, HBr can effectively act as a sink for reactive bromine in the troposphere.
The concentration of Br can be calculated using Equation 11.3 with the reaction rate coefficient and O_3 concentration mentioned above. The flux can be estimated from the capacity, i.e. the reservoir in the MBL, divided by the lifetime. The necessary flux F to maintain the concentration of Br in the MBL is thus determined according to:

$$F_{\mathrm{Br}} = \frac{[\mathrm{Br}] \cdot h}{\tau_{\mathrm{Br}}}, \tag{11.6}$$

being h the height of the MBL. In order to simulate a situation comparable to the conditions observed during the SHIVA campaign, a BrO VMR of 2 ppt is assumed, i.e. a BrO concentration of $[\mathrm{BrO}] \approx 4.9 \cdot 10^7$ molec cm^{-3}, and a well-mixed MBL with a height of 500 m (Table 6.2). For the reaction with HCHO ($\tau_{\mathrm{Br}} = 120$ s), the flux of Br results in $F_{\mathrm{Br}} \approx 1.4 \cdot 10^9$ molec cm^{-2} s^{-1}.
Accordingly, the loss processes (Reactions 2.53, 2.54, and 2.55) are more efficient than the formation of inorganic bromine from its organic precursors. In consequence, in steady state and assuming reactivation of HBr and HOBr on aerosols does no play a significant role, BrO would be hardly detectable in the MBL. In the chemical cocktail as given in the MBL around Borneo, BrO rapidly reacts for example with HCHO. However, it has to be noted that these estimations do not include the recycling of HBr on aerosol particles, which would reduce the necessary flux to maintain 1–3 ppt of BrO in the MBL.

11.1.2 Iodine monoxide

Observations

Figures 11.1, 11.2, and 11.3 show the measured IO dSCDs along the flight track for seven sorties of the Falcon aircraft over Borneo. Time series of the inferred IO dSCDs for the different sorties can be found in the flight by flight analysis in Appendix A. During seven sorties of the aircraft the IO signal occasionally exceeded the detection limit in the MBL and middle troposphere. The detection limit S_{det} depends on each single flight and lies approximately between 1 and $1.5 \cdot 10^{13}$ molec cm^{-2}. It has to be noted that this detection limit is rather a well-tempered detection limit ignoring any remaining systematic structures in the residual (Section 8.3.2).
During sortie 1 on 16.11.2011 (Figure 11.1a and 11.1b), sortie 2 on 19.11.2011 (Figure 11.1c and 11.1d), and sortie 11 on 07.12.2011 (Figure 11.2e and 11.2f) IO is detected in the MBL with maximum dSCDs of up to approximately $(6.0 \pm 0.7) \cdot 10^{13}$ molec cm^{-2} at altitudes between 0.1 and 0.7 km when the Falcon aircraft was flying in or close to Kuching Bay. Furthermore, IO exceeded the detection limit during the descents back to Miri. During sortie 5 on 22.11.2011 (Figure 11.1e and 11.1f) IO was detected with maximum dSCDs of up to approximately $(4.2 \pm 0.5) \cdot 10^{13}$ molec cm^{-2} when the Falcon aircraft was flying at an altitude of 0.8 km from the open ocean towards the coast. The IO signal disappeared as soon as the flight track entered the land. During sortie 6 on 23.11.2011 (Figure 11.2a and 11.2b) IO was observed above the detection limit during a short section of approximately 13 minutes at the north-eastern coast of Borneo with IO dSCDs of up

to approximately $(3.3 \pm 0.5) \cdot 10^{13}$ molec cm^{-2}. During this section the viewing direction of the mini-DOAS instrument was pointing towards the open ocean and not towards the land as compared to the rest of this sortie.

Figure 11.4 shows the mean chlorophyll-a (Chl-a) concentrations inferred from the satellite sensor MERIS averaged over five days between 20.11.2011 and 25.11.2011. Chl-a represents the biomass of phytoplankton, i.e. free-floating microalgae. If seaweed is present in the ocean, enhanced nutrient amounts can likely be found, leading to an increase in the growth of phytoplankton. Enhanced Chl-a concentrations were observed at the same location where the IO dSCDs were increased. During this flight, IO was also detected close to the city of Sandakan with dSCDs reaching approximately $(2.9 \pm 0.5) \cdot 10^{13}$ molec cm^{-2}, where the Falcon was again flying above enhanced Chl-a concentrations. The region close to Sandakan was again probed during sortie 7 on 26.11.2011 (Figure 11.2c and 11.2d), where IO exceeded the detection limit during the descent of the Falcon aircraft into Sandakan. Here in the MBL, maximum dSCDs of approximately $(5.6 \pm 0.9) \cdot 10^{13}$ molec cm^{-2} were observed. During sortie 13 on 09.12.2011 (Figure 11.3a and 11.3b) IO was detected both during the ascent and the descent of the Falcon aircraft. During the descent along the north-eastern part of Borneo the Falcon aircraft flew several times back and forth from an altitude of 11.4 km down to 0.33 km. Every time the mini-DOAS instrument was viewing towards the open ocean, IO increased, whereas for the viewing direction towards the land IO decreased below the detection limit. In addition to the enhanced IO concentrations seen in the MBL, during this sortie increased IO dSCDs were observed above the MBL in the mid-troposphere at altitudes of 5.8 km (IO dSCD $\approx (3.5 \pm 0.3) \cdot 10^{13}$ molec cm^{-2}) and 2.5 km (IO dSCD $\approx (5.4 \pm 0.5) \cdot 10^{13}$ molec cm^{-2}).

In summary, IO was observed both in the MBL and in the lowermost free troposphere, especially around the north coast of Borneo but also in Kuching Bay. Particularly in the north-eastern part of Sabah and the archipelagos between Sabah and the Philippines, areas with enhanced seaweed farming exist (Section 6.3). Furthermore, IO was observed if the viewing direction of the mini-DOAS instrument was pointing to the ocean and not to the land and disappeared as soon as the flight track entered the land. The retrieved IO dSCDs reached a maximum value of $(6.0 \pm 0.7) \cdot 10^{13}$ molec cm^{-2}.

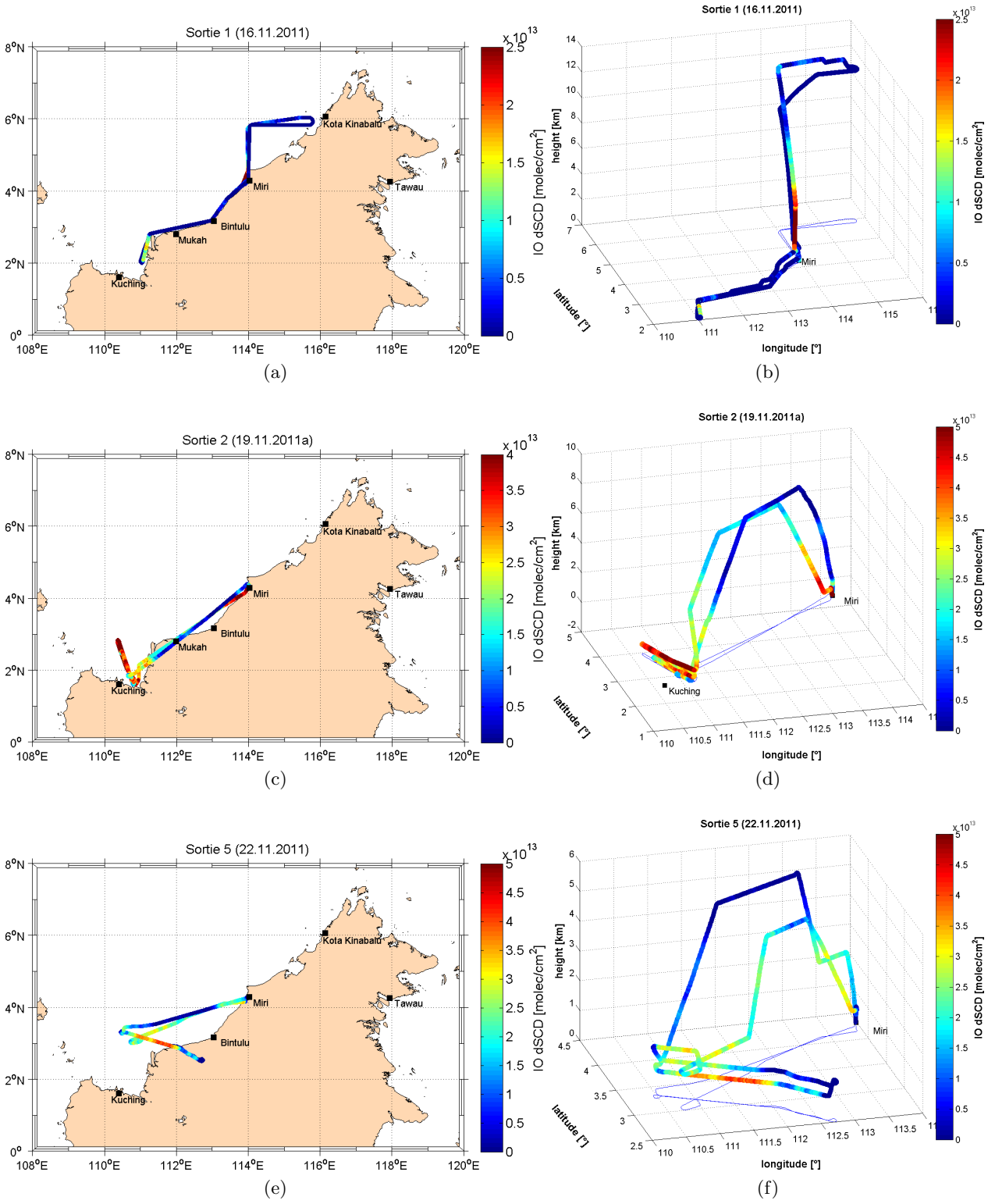

Figure 11.1: IO dSCDs inferred along the flight track for different sorties (sortie 1, 2, and 5) of the Falcon aircraft illustrated by a 2D (left panels) and a 3D perspective (right panels). Note that the colour scale is different for each flight.

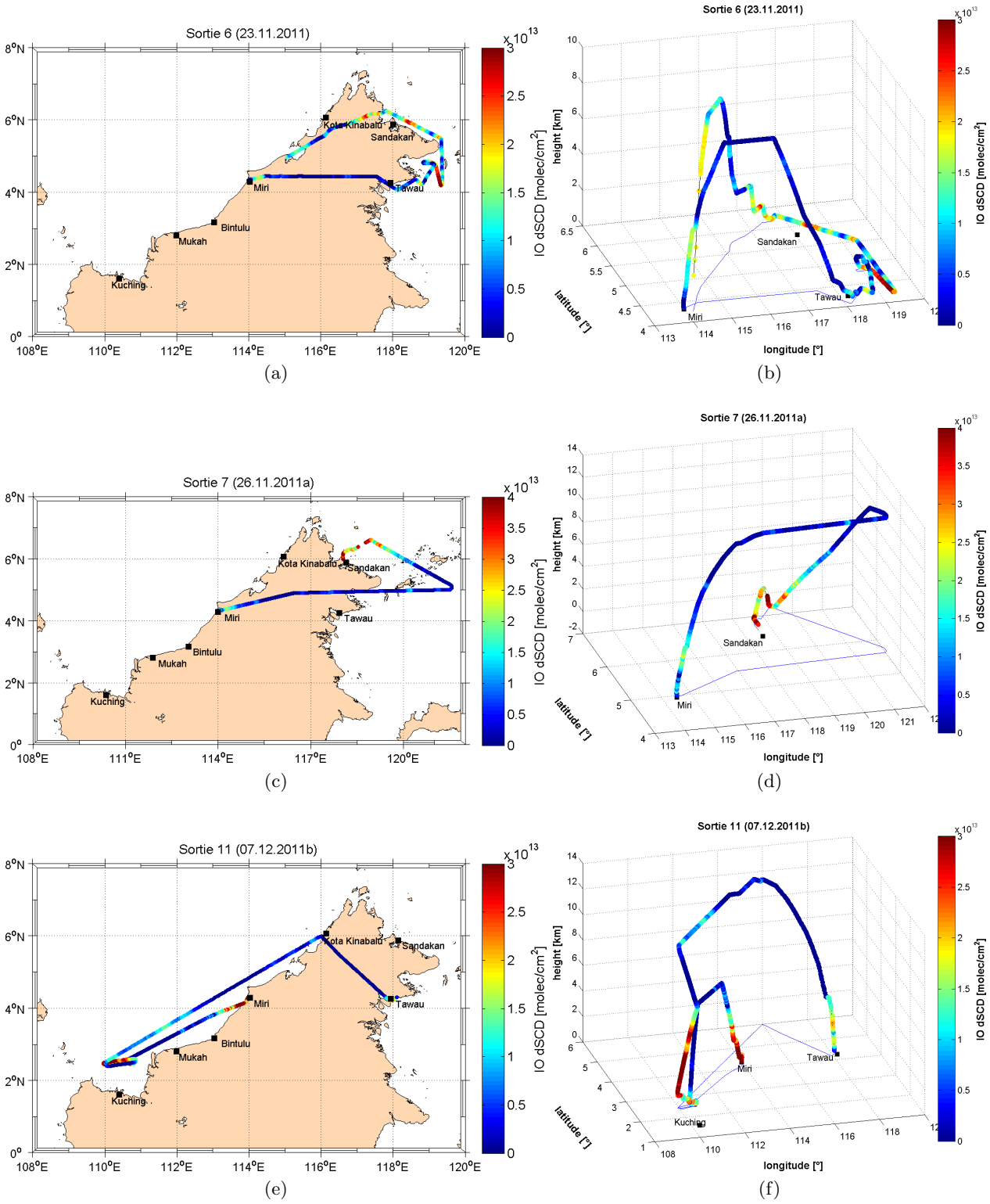

Figure 11.2: IO dSCDs inferred along the flight track for different sorties (sortie 6, 7, and 11) of the Falcon aircraft illustrated by a 2D (left panels) and a 3D perspective (right panels). Note that the colour scale is different for each flight.

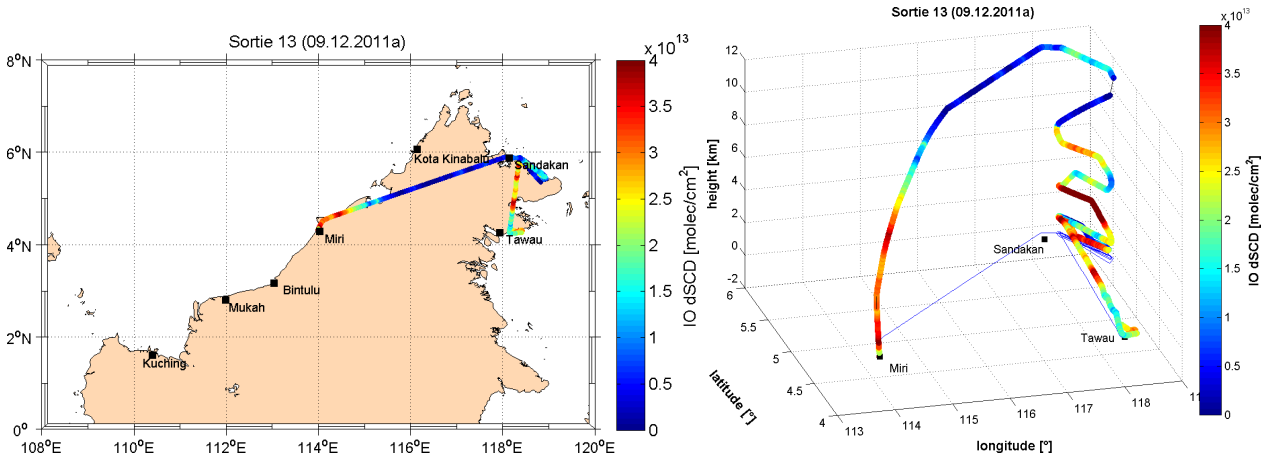

Figure 11.3: IO dSCDs inferred along the flight track for sortie 13 of the Falcon aircraft illustrated by a 2D (left panels) and a 3D perspective (right panels).

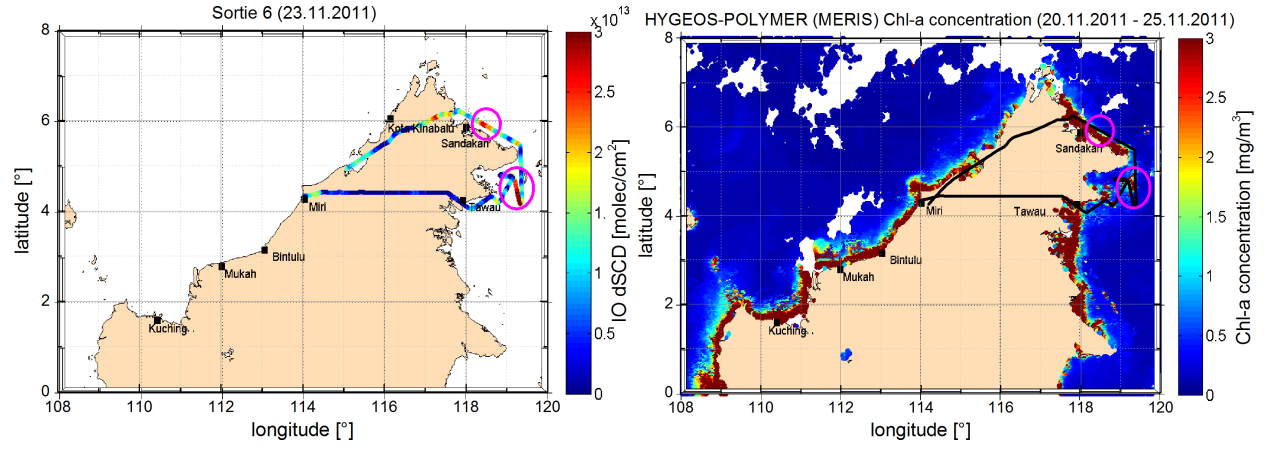

Figure 11.4: (a) IO dSCDs inferred along the flight track for sortie 13 of the Falcon aircraft and (b) the mean chlorophyll-a (Chl-a) concentration (20.11.2011-25.11.2011) inferred from the sensor MERIS onboard the satellite ENVISAT. The Chl-a data is retrieved via the POLYMER algorithm of HYGEOS gridded at 0.2 ° x 0.2 ° (Steinmetz et al., 2011). Data kindly provided by the Phytooptics group (Astrid Bracher and Tilman Dinter, AWI Bremerhaven/ IUP Bremen, personal communication, September 2014). The circles highlight the areas where both enhanced IO dSCDs and Chl-a concentrations were observed.

IO VMRs

Figure 11.5 shows the inferred IO VMRs using the O_4 scaling method for these seven sorties of the Falcon aircraft. The IO VMRs range between 0.3 and 1.5 ppt in the MBL. In the MBL, the detection limit lies approximately between 0.3 and 0.8 ppt depending on each single flight.

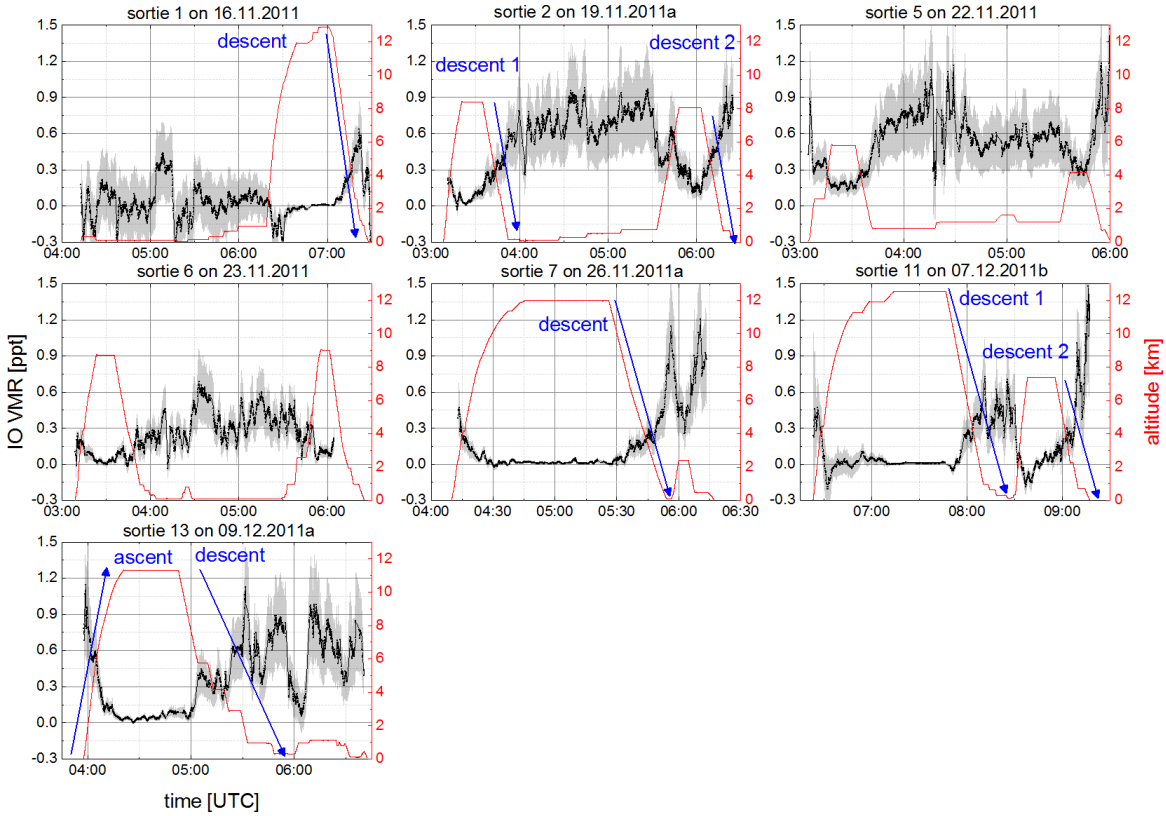

Figure 11.5: Inferred IO VMRs using the O_4 scaling method for seven sorties of the Falcon aircraft. The blue arrows mark the eight ascents and descents from which the data is chosen for the following study.

In the following, the IO VMRs inferred from the aircraft-borne DOAS measurements are compared to the shipborne and ground-based measurements of IO, which were simultaneously conducted during the SHIVA campaign.
During the SHIVA RV Sonne cruise IO was measured by a Laser-Induced Fluorescence (LIF) instrument, a MAX-DOAS instrument, and a Cavity-Enhanced DOAS (CE-DOAS) instrument. Details on the different instruments can be found in Walker (2013), Peters (2013), and in Lampel (2014). The IO detection limits of the LIF, the MAX-DOAS, and the CE-DOAS instrument were 0.35–1.25 ppt, 0.3–0.7 ppt, and 1 ppt, respectively (Walker, 2013; Lampel, 2014). The IO concentrations of the CE-DOAS instrument never exceeded its detection limit (Walker, 2013; Lampel, 2014). A reasonable agreement between the IO VMRs inferred from the LIF and the MAX-DOAS instrument was found with mean daytime VMRs of 0.8 ppt and 0.7 ppt, respectively and maximum VMRs between 2.3 and 2.4 ppt observed in the Sulu Sea (Walker, 2013).
Figure 11.6 shows the IO VMRs along the cruise track of the RV Sonne detected by the LIF instrument. Along the coastline of Borneo, the shipborne IO VMRs are lower than the ones detected in the Sulu Sea. Along the coastline between Miri and Kuching, IO VMRs of less than 0.5 ppt were observed in Kuching Bay and close to Mukah. Between Miri and Sandakan, the IO VMRs ranged between 1 and 2 ppt. The before-mentioned maximum VMRs of 2.3 and 2.4 ppt were observed in the Sulu Sea more than 100 km off the coast of Borneo. The maximum distance of the Falcon flight tracks from the north-eastern coast of Borneo was approximately 100 km during sortie 7 on 26.11.2011. These maximum IO VMRs observed in the Sulu Sea could not be confirmed by the observations from the Falcon aircraft due to a lacking permission to fly over the Sulu Sea.

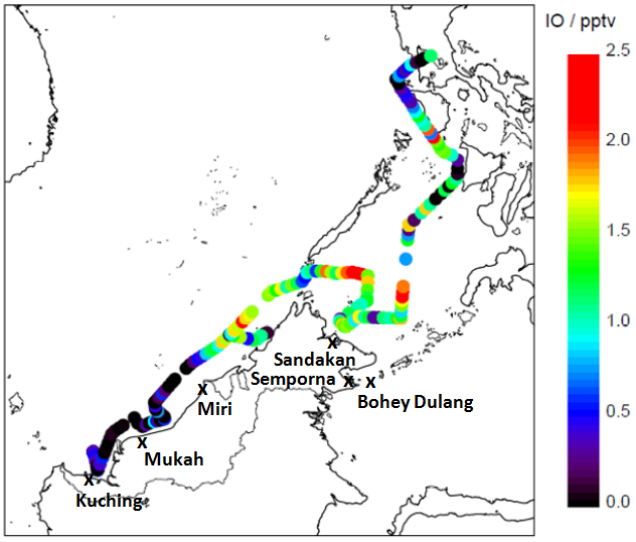

Figure 11.6: IO VMRs measured by the LIF instrument along the cruise track of the RV Sonne during the SHIVA project (Figure adapted from Walker (2013)). The black crosses mark the location of the cities of Kuching, Mukah, Miri, Sandakan, as well as the island of Bohey Dulang, where the ground-based MAX-DOAS were performed.

Furthermore, ground-based MAX-DOAS measurements of IO were performed in the north-eastern part of Borneo close to Semporna on the island of Bohey Dulang. The island is located approximately 20 km off the coast (Figure 11.6). The measurement site was located in the vicinity of a commercial seaweed field, where underwater macroalgae are cultivated (Peters, 2013). Details on the measurements and instrumental set-up can be found in Peters (2013). The inferred IO VMRs ranged between 1 and 4 ppt for a detection limit of approximately 0.9 ppt. The inferred IO VMRs from the ground-based measurements were occasionally slightly higher as compared to the shipborne and aircraft-borne IO measurements during the SHIVA campaign. This is conceivable due to the proximity of the measurements to the source of iodine, i.e. seeweeds (e.g. Carpenter et al., 2013; Leedham et al., 2013; Keng et al., 2013).
Thus, it can be concluded that the different measurements of IO during the SHIVA campaign lead to a highly consistent picture. During the ground-based measurements near seaweed fields maximum IO VMRs were observed, i.e. close to a possible source of organic iodine precursors. For the sections of the Sonne cruise track, which were also monitored during the Falcon flights, the ship-, and airborne IO measurements show comparable concentrations in the MBL.
Furthermore, our findings are in good agreement with recent measurements of IO in the Pacific region. Mahajan et al. (2012) observed a daily mean IO VMR of 0.9 ppt and a maximum of 1.2 ppt in the Eastern Pacific. IO measurements performed during the TransBrom-Sonne cruise in the Western Pacific region yield a daily mean VMR of approximately 1.5 ppt with a maximum VMR of 2.2 ppt (Großmann et al., 2013). In the global MBL, IO VMRs typically range between 0.5 and 1.5 ppt (e.g. Lampel, 2014; Prados-Roman et al., 2014).

Vertical profiles of IO

Vertical profile information can be gained from the measurements during the different ascents and descents of the Falcon aircraft. Overall, seven descents and one ascent are available where IO concentrations exceeded the detection limit (see blue arrows in Figure 11.5). Figure 11.7 shows a comparison of the different vertical profiles of IO. The overall shape is similar for the different profiles with 0.5 - 1.5 ppt IO in the MBL and a decrease by about a factor of five to 0.1–0.3 ppt in the FT. Integrating the profiles from Figure 11.7 results in VCDs between approximately (3-4) $\cdot 10^{12}$ molec cm^{-2}. For some profiles the VCDs range between (6–8) $\cdot 10^{12}$ molec cm^{-2}.

Puentedura et al. (2012) inferred vertical profiles of IO by performing MAX-DOAS measurements from a mountain top at Izaña, Canary Islands at an altitude of 2.4 km, with the majority of IO being located in the MBL, but also small amounts of 0.2–0.4 ppt in the overlying free troposphere. These findings are further comparable to Dix et al. (2013) who reported IO vertical profiles from airborne measurements over the Pacific Ocean with two-thirds of the total column above the MBL. Balloon-borne measurements in the tropics further indicated IO upper limits of 0.1 ppt in the tropical upper troposphere and stratosphere (Bösch et al., 2003; Butz et al., 2009).

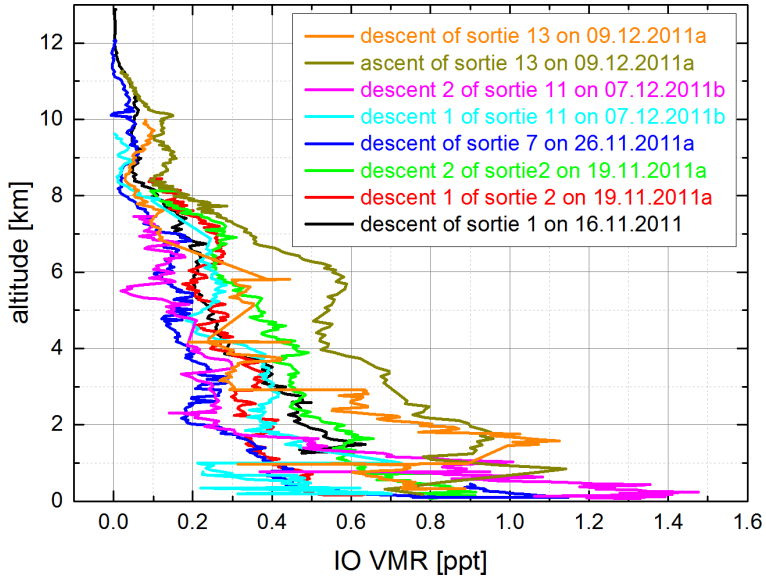

Figure 11.7: Inferred vertical profiles of IO VMRs for eight different ascents and descents of the Falcon aircraft over Borneo in fall 2011. For ease of visual comparison, the error bars are not included.

In the past, IO has also been detected on a global scale from satellite-based DOAS measurements (Schönhardt et al., 2008, 2012). Satellite-based measurements of IO from the SCIAMACHY instrument (Section 6.2.3) indicate IO VCDs of approximately $3 \cdot 10^{12}$ molec cm^{-2} around the coastline of Borneo for monthly averaged maps collected in November and December 2011 (Figure 11.8). These values are at or close to the detection limit of approximately (0.5 - 2)$\cdot 10^{12}$ molec cm^{-2}, depending on the averaging period. Thus, the aircraft-borne IO VCDs generally agree with the satellite-based measurements, but show occasionally larger VCDs. However, the IO satellite observations have to be treated with caution, since the retrieved VCD are subject to large uncertainties due to the poor signal-to-noise ratio of the retrieval and thus a high sensitivity to the chosen spectral fitting procedure (Schönhardt et al., 2008). Furthermore, the SCIAMACHY overpass time across the Equator is at about 10:00 LT in the morning, whereas the sorties of the Falcon aircraft generally took place between 12:00 and 18:00 LT. Due to the before-mentioned uncertainties, the satellite measurements are less sensitive to the detection of IO than the aircraft-borne measurements. Thus, it can be concluded that the satellite-based measurements of IO do not necessarily lead to a contradiction with the IO observations made during this study.

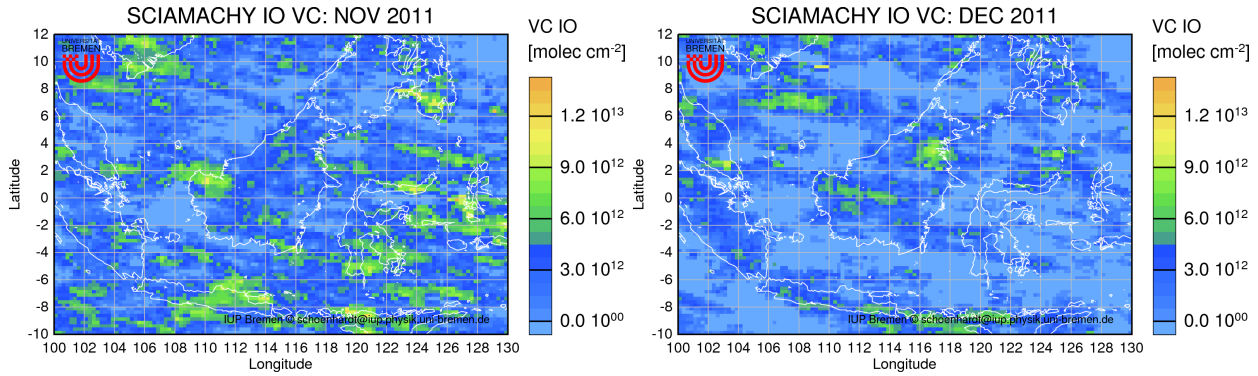

(a) (b)

Figure 11.8: IO VCDs inferred from the SCIAMACHY satellite instrument averaged for (a) November and (b) December 2011. The maps are kindly provided by Anja Schönhardt (IUP Bremen, personal communication, January 2013).

Enhanced IO occasionally occurred in the mid troposphere (see Figure 11.7). This enhancement might indicate influences of convective outflow. In order to study the influence of rapid vertical transport on the IO signal, in situ measurements of CO are used (Catoire et al., 2015). Although the sources of IO are completely distinct and likely to be different than those of CO, the main sources of both species are near or at the surface. Thus, enhancements of CO at higher altitudes can be likely associated with signatures of rapid vertical transport, i.e. entrainment of CO rich air from the boundary layer into the free troposphere by shallow convective clouds. The enhancements of CO in the mid-troposphere are therefore indicative for vertical mixing. In the following, the single IO profiles are compared to the in situ profiles of CO in order to detect signatures of convective outflow. Figure 11.9 shows a comparison of the vertical profiles of IO and CO for the ascent and descent of sortie 13 on 09.12.2011.
It can be clearly seen that IO and CO show enhancements at similar altitudes, e.g. at an altitude of approximately 6 km in both profiles. However, it has to be again noted, that the DOAS technique is a remote-sensing method. That means that the mini-DOAS instrument observes a different air mass several kilometres away from the aircraft compared to the in situ instruments, which probe air masses directly at the position of the aircraft. Furthermore, the air masses, which are entrained from the MBL, have a limited horizontal dimension. The light path detected by the mini-DOAS instrument can occasionally be larger than the horizontal dimension of the entrained air mass. Typically, the horizontal dimension of a Cb cloud is approximately of the order of 10 km (Kraus, 2006a). According to Inoue et al. (2008), who simulated deep convective cloud systems over the tropical Western Pacific, the horizontal dimension of meso-scale synoptic systems typically ranges between 20 and 100 km, but can also reach a dimension of more than 300 km. Moreover, since the photochemical lifetime of CO is of the order of a few weeks (Holloway et al., 2000), which is much longer than that of IO, both gases do not necessarily show a similar behaviour. Nevertheless, the visual inspection confirms that IO and CO show enhancements in similar altitude regions. Thus, these elevated layers of IO can possibly be associated with entrainment of IO rich air from the MBL into the free troposphere by shallow convective clouds. Figure 11.10 shows the correlation between IO and CO VMRs for both the ascent and descent of this sortie. Different regions can be identified, e.g. regions where an enhancement in CO is observed but no concomitant increase in the IO VMRs is detected. Further, a concomitant increase of CO and IO is not expected since the aircraft is moving on the scale of several kilometres during the ascents and descents, i.e. the vertical profiles have a large horizontal gradient. During one single descent, different convective cells can possibly pass, each containing a different amount of entrained air from the MBL. For regions where an enhancement in CO is observed but no change in IO is detected, IO was likely at or below the

detection limit in the MBL.

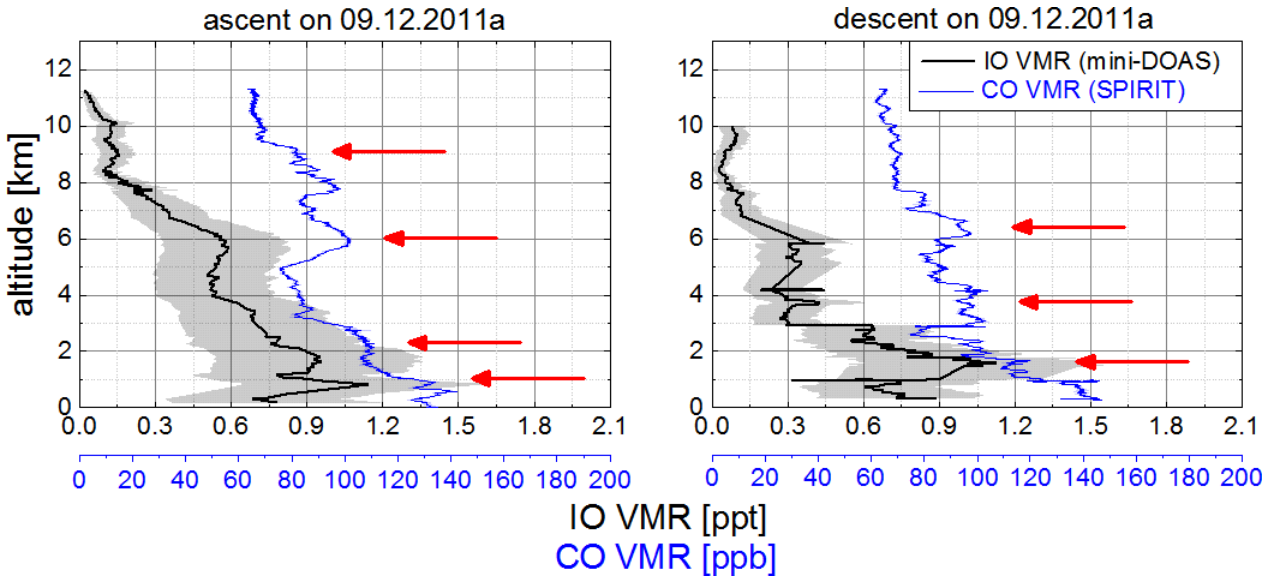

Figure 11.9: Vertical profiles of IO and CO VMRs for the ascent (left panel) and descent (right panel) of sortie 13 on 09.12.2011a. The red arrows mark the altitude where a simultaneous enhancement in CO and IO can be observed.

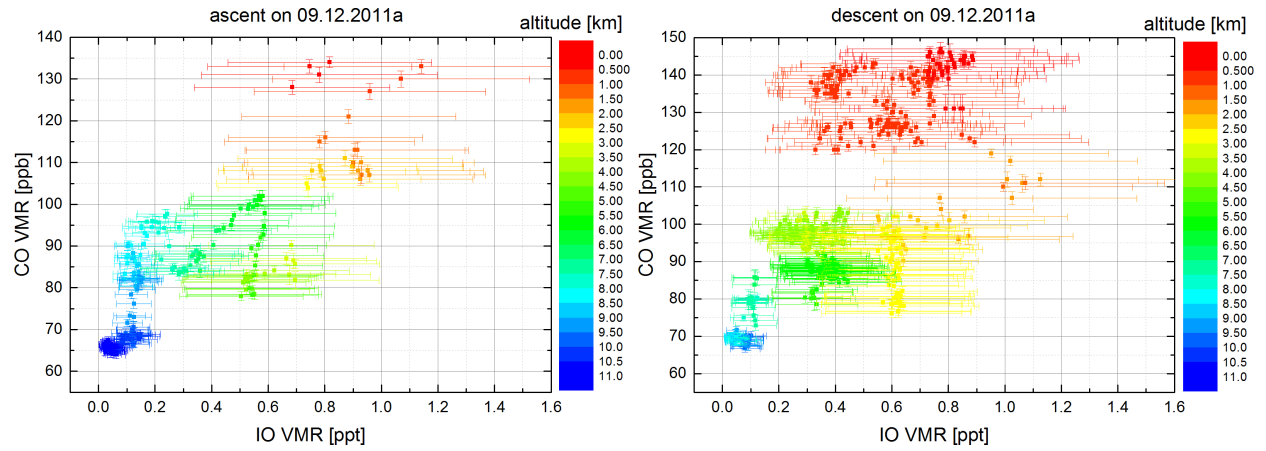

(a) (b)

Figure 11.10: Correlation of IO and CO VMRs for (a) the ascent and for (b) the descent of sortie 13 on 09.12.2011a colour-coded with the altitude in km.

Fate of atmospheric IO

The findings of the present study together with results of previous investigations indicate the following on atmospheric IO:

1. During the SHIVA campaign, the measurements of IO typically indicated mixing ratios of 0.5–1.5 ppt in the MBL, which is in good agreement with previous IO measurements in the MBL (e.g. Mahajan et al., 2012; Großmann et al., 2013; Lampel, 2014; Prados-Roman et al., 2014). The major atmospheric source of iodine is the sea-air exchange of gaseous

organic and inorganic iodine (Carpenter et al., 2012). Macroalgae are known to produce iodine containing precursor species, such as I_2 or iodocarbons, which can further react to form IO (e.g. Carpenter et al., 2012; Leedham et al., 2013). The kelp *Laminaria* and related brown macroalgae thereby represent the strongest iodine source in coastal regions (Küpper et al., 1998). Further, the reaction of O_3 and iodide at the ocean surface can further lead to the production of I_2 and hypoiodous acid (HOI) (Martino et al., 2009; Carpenter et al., 2013; MacDonald et al., 2014). At daytime, I_2 and HOI quickly photolyse and release iodine atoms, which further react with O_3 finally forming IO. In addition to the iodocarbon fluxes of methyl iodide (CH_3I), diiodomethane (CH_2I_2), chloroiodomethane (CH_2ClI), and bromoiodomethane (CH_2BrI), Großmann et al. (2013) estimated an additional flux of I_2 of the order of 1 to 1.8 $\cdot 10^8$ molec cm^{-2} s^{-1} to reproduce the amounts of IO of 1–2 ppt typically detected in the MBL. Recent studies suggest that the main source of IO in the MBL is represented by inorganic iodine species, such as I_2 and HOI, which can explain approximately 75 % and thus the majority of the observed IO concentrations in the MBL (e.g. Carpenter et al., 2013; MacDonald et al., 2014).

2. As indicated in this study, MBL IO is likely to be transported by shallow convection from the near surface into the mid-troposphere. Typically, the horizontal dimension of convective clouds is of the order of 10 km (Kraus, 2006a) and can reach a dimension of more than 100 km in deep convective cloud systems over the tropical Western Pacific (Inoue et al., 2008). However, due to their short lifetime (Table 2.3), the organic source gases for inorganic iodine already photolytically decay within the MBL.

   Only rather long-lived iodocarbons are likely to be transported into the mid- and upper troposphere by means of tropical deep convection (Dix et al., 2013). As the iodine-containing di-halocarbons, such as CH_2I_2, CH_2ClI, or CH_2BrI, are mainly photolysed within the MBL, CH_3I with a lifetime of several days is the predominant iodocarbon species that is present in the FT (Saiz-Lopez et al., 2014). Figure 11.11 shows the vertical profiles of IO together with CH_3I measured simultaneously by the GhOST-MS instrument aboard the Falcon aircraft (Sala, 2014a). IO and CH_3I show similar atmospheric profiles. CH_3I can be observed with VMRs between 0.3 and 0.8 ppt in the MBL occasionally with a maximum VMR of 1.2 ppt. In the FT the CH_3I VMRs decrease to approximately 0.1 to 0.15 ppt.

3. Since the process of entrainment has a typical time scale which lasts several hours (Kraus, 2006a), the impact of IO on the free troposphere is likely limited by the dimension of the entrained air mass package. Further, IO was neither detected in the boundary layer nor in the free troposphere over land. Thus, efficient photochemical processes may exist, preventing IO from being transported over a wider horizontal range or from even reaching the upper troposphere or stratosphere.

4. Possible sinks of IO include for example the self-reaction of IO, leading to the formation of new particles by polymerisation (Hoffmann et al., 2001; O'Dowd et al., 2002). This loss process dominates for large IO concentrations since the formation of higher iodine oxides (I_xO_y) is proportional to $[IO]^2$ due to the nature of the IO self-reaction. According to model calculations by Sommariva et al. (2012), the self-reaction of IO is not a dominant loss process for typical MBL concentrations of IO below 2 ppt. However, beyond qualitative observations, further information on the higher iodine oxides in the gas phase is not available (e.g. Saiz-Lopez et al., 2012, and references therein). Another possible sink for reactive iodine is the reaction with aerosols and rain drops (e.g. Murphy et al., 1997; Gilfedder et al., 2008). Gilfedder et al. (2008) detected iodine particularly in organic aerosols. For tropical Atlantic aerosol, the iodine content in marine aerosol was for example found to be much higher than the seawater iodine content (Baker et al., 2000; Baker, 2004). Iodine is also abundant in aerosols located in the free troposphere and stratosphere (Murphy et al., 1998, 2014). However, the

interactions of iodine and organic matter represent the most significant uncertainty in aerosol iodine chemistry (Saiz-Lopez et al., 2012).

In summary, atmospheric IO originates from organic (i.e. iodocarbons) and inorganic iodine precursor species (i.e. HOI and I_2) emitted by the ocean and is distributed by vertical mixing in the MBL. Occasionally, IO can reach the mid-troposphere via MBL air masses subject to convection as indicated by elevated concentrations of CO. There, IO has a limited lifetime due to a yet unknown loss mechanisms, preventing inorganic iodine from reaching the TTL and stratosphere.
In order to further examine possible sinks of iodine, chemical models are required. The global chemistry transport model TOMCAT (Section 6.2.4) is used to simulate IO and CH_3I (Ryan Hossaini, Institute for Climate and Atmospheric Science, School of Earth and Environment, University of Leeds, personal communication, August 2014). Figure 11.12 shows a preliminary comparison between the measured and simulated vertical profiles of CH_3I and IO VMRs for the descent of sortie 7 on 26.11.2011. The measured and simulated CH_3I VMRs are in a good agreement. However, close to the surface, the simulated IO VMRs are much lower than the measured IO VMRs. Since HOI and I_2 are not included in the current model run, the IO VMRs close to the surface are underestimated by the model. In further model runs, the emission mechanism of HOI and I_2 from Carpenter et al. (2013) will be included. However, this analysis is still ongoing and is thus subject to future studies.

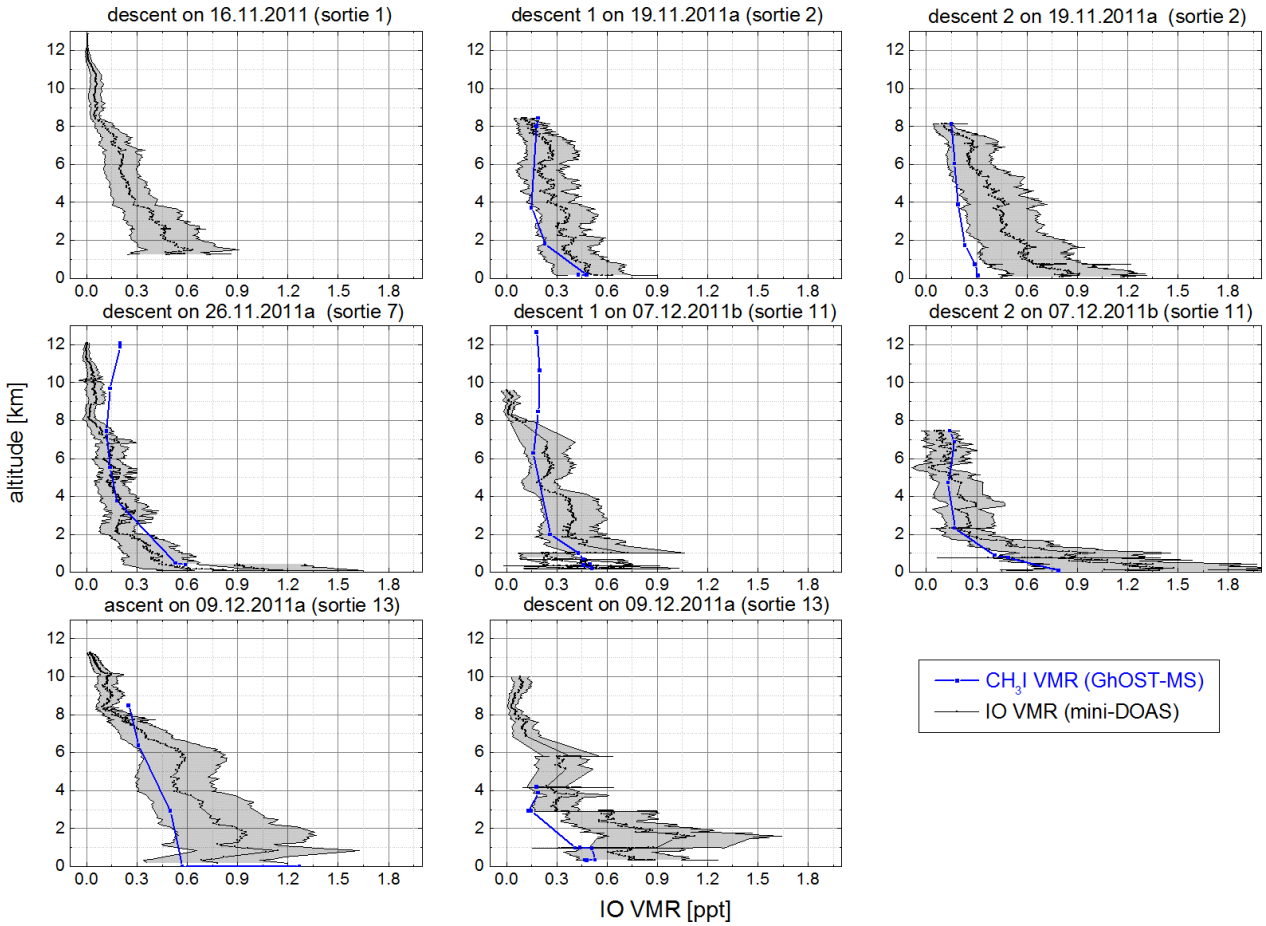

Figure 11.11: Vertical profiles of IO and CH_3I VMRs for eight different ascents and descents of the Falcon aircraft. For sortie 1 on 16.11.2011 no GhOST-MS data is available.

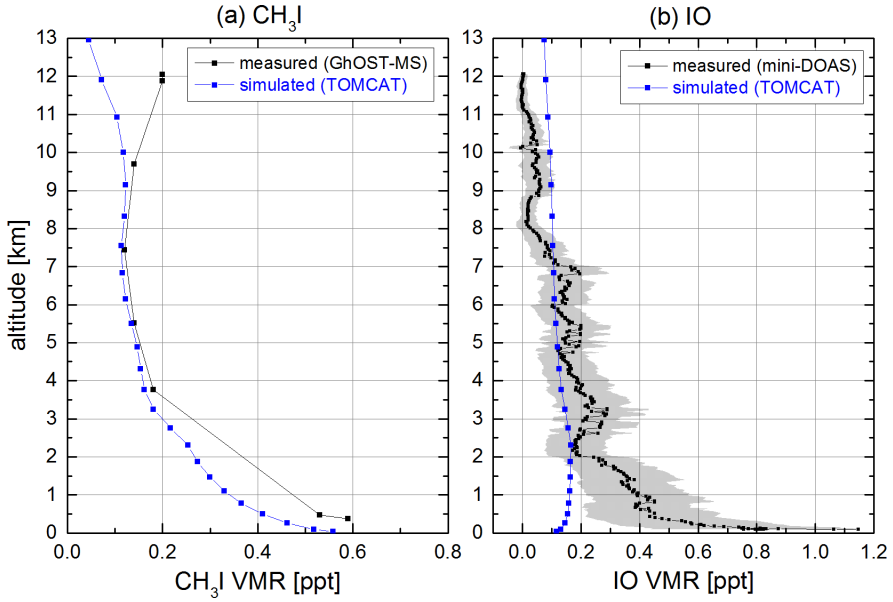

Figure 11.12: Measured and TOMCAT simulated vertical profiles of (a) CH_3I and (b) IO VMRs for the descent of sortie 7 on 26.11.2011a.

11.2 Constraining the oxidation capacity over Borneo

Tropical rain forests represent a large source of volatile organic compounds (VOCs) with isoprene being the most abundant biogenic VOC naturally emitted into the atmosphere (e.g. Guenther et al., 1995, 2006). Isoprene rapidly reacts with the hydroxyl radical OH. Its organic intermediates may enhance the formation of tropospheric ozone in polluted areas and can also lead to the formation of secondary organic aerosols (SOA), which can act as cloud condensation nuclei (CCN) (Kiendler-Scharr et al., 2009; Robinson et al., 2011) (Section 6.3). Measurements of VOC oxidation products, such as HCHO and CHOCHO, can provide useful information about the degradation of VOCs and in particular of isoprene, in air above the terrestrial tropical troposphere.

11.2.1 Observations of HCHO, CHOCHO, and NO_2 over Borneo

Molecular absorption of HCHO, CHOCHO, and NO_2 was observed during all sorties of the Falcon aircraft over Borneo in November and December 2011. The dSCDs of the respective trace gases inferred for each flight are shown flightwise in Appendix A. Table 11.1 shows an overview of the detection limits S_{det} (assumed to be 2σ, Section 8.3.2) of HCHO, CHOCHO, and NO_2 averaged for each sortie of the Falcon aircraft, respectively. The mean detection limits of HCHO, CHOCHO, and NO_2 column densities were approximately $1 \cdot 10^{16}$ molec cm^{-2}, $1 \cdot 10^{15}$ molec cm^{-2}, and $1.2 \cdot 10^{15}$ molec cm^{-2}, respectively, depending on the circumstance of each flight.

Table 11.1: Overview of mean detection limits S_{det} of HCHO, CHOCHO, and NO_2 for the different sorties of the Falcon aircraft during the SHIVA campaign.

sortie	date	S_{det} HCHO [10^{16} molec cm^{-2}]	S_{det} CHOCHO [10^{15} molec cm^{-2}]	S_{det} NO_2 [10^{15} molec cm^{-2}]
1	16.11.11	1.0	1.2	1.5
2	19.11.11a	0.7	0.8	1.1
3	19.11.11b	1.2	1.0	1.3
4	21.11.11	0.9	1.2	1.7
5	22.11.11	0.7	0.9	1.3
6	23.11.11	0.9	0.8	1.2
7	26.11.11a	0.8	0.9	1.1
8	26.11.11b	1.5	1.2	1.6
9	02.12.11	0.9	0.7	0.9
10	07.12.11a	0.7	0.6	0.9
11	07.12.11b	0.8	0.9	1.2
12	08.12.11	0.7	0.7	1.0
13	09.12.11a	0.7	0.8	1.0
14	09.12.11b	1.2	1.1	1.4
16	11.12.11b	1.0	0.8	1.0

Figure 11.13 shows an overview of the HCHO, CHOCHO, and NO_2 VMRs inferred using the O_4 scaling method for all sorties of the Falcon aircraft during the SHIVA campaign. In the MBL, the detection limits of HCHO, CHOCHO, and NO_2 ranged between approximately 100 and 150 ppt, 20 and 30 ppt, and 50 and 100 ppt, respectively.

Typically, the HCHO VMRs ranged between 500 and 2500 ppt in the MBL and decreased to about 100 ppt in the upper troposphere (10–13 km). CHOCHO VMRs ranged between 20 and 180 ppt in the lowermost kilometre and decreased to VMRs at or below the detection limit in the upper troposphere.

In the remote marine atmosphere, global background HCHO VMRs range between 0.2 and 1 ppb at the surface, which is mainly caused by the oxidation of methane (Weller et al., 2000; Peters et al., 2012; Lampel, 2014). Airborne measurements further indicated HCHO VMRs between 0.5 and 2 ppb in the altitude range between 0 and 1 km over the Amazon rain forest in October 2005 (Stickler et al., 2007). CHOCHO was observed under open ocean condition during several ship campaigns (Mahajan et al., 2014), showing a large variability in the inferred VMRs (approximately between 25 and 140 ppt). However, observations of CHOCHO, especially above the open ocean, have to be treated with care due to interfering absorptions caused by liquid water or vibrational Raman scattering, which could mimic absorption of CHOCHO (Lampel, 2014). As an example, Sinreich et al. (2010) reported CHOCHO mixing ratios of up to 140 ppt over the open ocean of the Eastern Pacific, whereas recent measurements above the equatorial Pacific showed lower mixing ratios between 25 and 80 ppt (Coburn et al., 2014).

In contrast to the remote marine atmosphere, maximum concentrations of HCHO of up to 4.5 ppb and CHOCHO concentrations of up to 1.6 ppb were observed in DOAS measurements directly above a rain forest canopy in Danum Valley, Sabah, Borneo during the OP3 campaign in 2008 (MacDonald et al., 2012). According to their modelling studies, the enhanced concentrations of HCHO and CHOCHO can be explained by oxidation of isoprene due to OH (MacDonald et al., 2012). Further detailed chemical modelling indicated consistency with isoprene as their main source above the forest canopy. However, their measurement site was located directly above a rain forest canopy, i.e. directly above the source, whereas during the SHIVA campaign, the Falcon aircraft generally probed air masses near the coastal region of Borneo.

During the SHIVA aircraft campaign, the NO_2 VMRs typically ranged between 100 and 1000 ppt in

the MBL. The NO_2 VMRs decreased below the detection limit at altitudes between 10 and 13 km. In the remote marine atmosphere, NO_2 VMRs of approximately 50 ppt were detected (Peters et al., 2012). During the SHIVA RV Sonne cruise, cavity-enhanced DOAS measurements showed mean and maximum NO_2 VMRs of 0.59 ppb and 21.5 ppb, respectively, with typical VMRs between 100 and 400 ppt (Walker, 2013).
Obviously, the air masses encountered during the SHIVA campaign were occasionally influenced, for example by emissions from ships cruising in the South China Sea, by emissions from oil and gas production facilities along the coastline of Borneo, or by emissions due to industrial fossil fuel combustion on land.

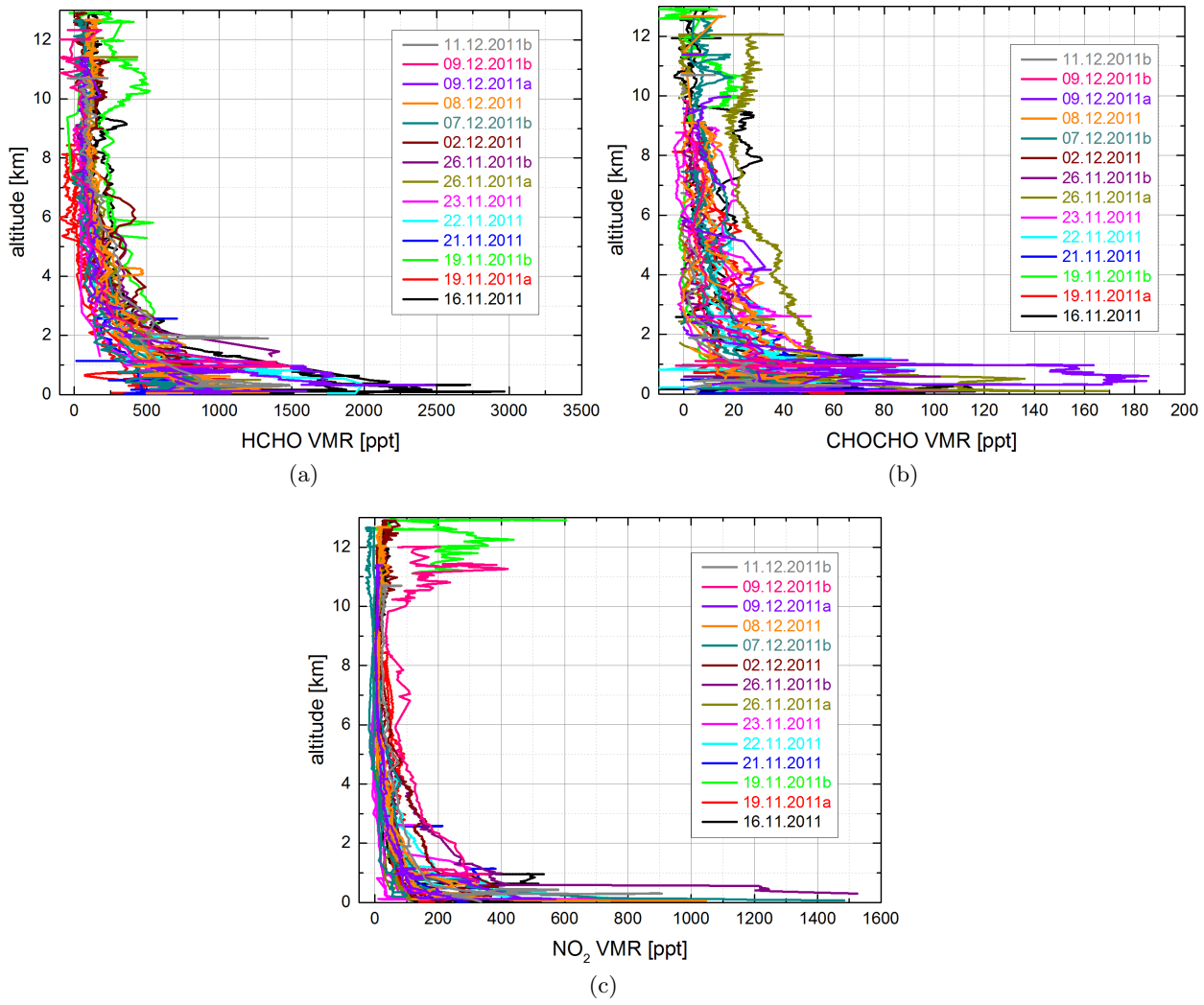

(a) (b) (c)

Figure 11.13: Overview of the (a) HCHO, (b) CHOCHO, and (c) VMR profiles inferred using the O_4 scaling method for all sorties of the Falcon aircraft over Borneo during fall 2011.

11.2.2 Comparison to model simulations

In this section, the measured trace gases are compared to simulations using the chemistry transport models TOMCAT (e.g. Hossaini et al., 2013) and CCATT-BRAMS (e.g. Hamer et al., 2013). The basics of the TOMCAT and CCATT-BRAMS models are presented in Section 6.2.4 and 6.2.5, respectively.
Figures 11.14 shows the flight by flight comparison of the measured and simulated VMRs of HCHO and NO_2. Unfortunately, simulations of CHOCHO are not yet included neither in the TOMCAT

nor in the CCATT-BRAMS model and thus simulated results can not be shown in this context. In the MBL, the HCHO VMRs simulated with TOMCAT and CCATT-BRAMS are generally larger than the measured ones, with the CCATT-BRAMS VMRs being occasionally more than twice larger than the TOMCAT simulations. The background concentrations of NO_2 agree both for the model simulations and the measurements. Typically, the measured background NO_2 concentration ranges between 50 and 100 ppt in the MBL whereas the simulated ones are slightly lower. These background NO_2 concentrations can be reached via a steady state between NO_2 and nitric acid (HNO_3) if HNO_3 is not largely removed via rain-out or dry deposition:

$$NO_2 + OH + M \longrightarrow HNO_3 + M \tag{11.7}$$

$$HNO_3 + OH \longrightarrow H_2O + NO_3 \tag{11.8}$$

$$NO_3 + h\nu \longrightarrow NO_2 + O(^3P). \tag{11.9}$$

HNO_3 can further react with OH forming H_2O and NO_3 (Equation 11.9). However, a minor contribution from a channel producing H_2O_2 and NO_2 cannot be ruled out (Finlayson-Pitts and Pitts Jr., 2000). In the measurements, peaks in the NO_2 VMRs occasionally occur obviously due to local NO_x emissions, such as emissions from exhaust plumes of ships, or emissions from oil and gas production facilities along the coastline of Borneo, or emissions from biomass burning. Since these local emissions are likely not captured by the model, it is not expected that the simulated and measured NO_2 concentrations for these emission plumes may agree.

Figure 11.15a further shows the flight by flight comparison of the CO VMRs measured by the SPIRIT instrument (Catoire et al., 2015) and simulated by TOMCAT and CCATT-BRAMS. Figure 11.15b shows the isoprene VMRs measured by the WASP instrument (David Oram and Graham Mills, School of environmental Sciences, University of East Anglia, Norwich, personal communication, November 2012) and simulated by TOMCAT and CCATT-BRAMS. It has to be noted that CCATT-BRAMS does not directly provide simulations of isoprene but rather a lumped chemical species called 'BIO', which mostly contains isoprene plus some other terpenes. The detection limit of the isoprene data from the WASP instrument was 10 ppt and measurements for altitudes larger than 3 km were not possible. Except for a few events (e.g. at 04:10 UTC on 22.11.2011), the measured isoprene is mostly at or below the detection limit. In contrast to the isoprene measurements, the model simulates isoprene VMRs of up to approximately 6 ppb in the MBL. The lumped species BIO of the CCATT-BRAMS model even simulates VMRs up tp 30 ppb for sortie 6 on 23.11.2011. Such large isoprene VMRs were not measured by WASP during SHIVA, nor were they reported from Danum Valley during the OP3 campaign (MacDonald et al., 2012).

For CO, the agreement between model simulations and observations is of variable quality for the different flights. Similar to HCHO, the CO VMRs simulated by the CCATT-BRAMS model are occasionally twice larger than the TOMCAT simulations.

Figure 11.16 further shows the mean percentage difference (MPD) between the CO VMRs measured by the SPIRIT instrument and simulated with the TOMCAT model. MPD is calculated according to the following formula:

$$\mathrm{MPD} = |100 \cdot (\mathrm{VMR_{model}} - \mathrm{VMR_{meas}})/\mathrm{VMR_{meas}}|. \tag{11.10}$$

Except for some flights, the mean deviation between the CO VMRs simulated with TOMCAT and measured by the SPIRIT instrument is typically around 20 %. A large discrepancy between the model and the measurements occurs for sortie 2 on 19.11.2011a and for sortie 9 on 02.12.2011 where the MPD occasionally reaches values of up to 100 %. Figure 11.17 shows simulated CO from the FLEXPART model (Section 6.2.1), which originates from fire plumes. During sortie 2 on 19.11.2011a the Falcon aircraft was flying around Kuching Bay where a fire plume was passed at 03:45 UTC and again on the way back at 05:30 UTC. In addition to a short section during sortie 5 on 22.11.2011, the sortie 9 on 02.12.2011 was the only flight during the SHIVA campaign where the flight track of the Falcon aircraft was almost completely over land. According to the FLEXPART

simulations, CO enhancements originating from fire plumes occurred at approximately 07:40 UTC as well as during the descent to Miri at approximately 09:10 UTC. The maximum deviations in the MPD of CO for both sorties occur at the same time as the fire plumes. This gives rise to speculate as to whether direct emissions of CO are overestimated in the TOMCAT model. Noteworthy is that, according to FLEXPART simulations, fires plumes occurred during almost every sortie of the Falcon aircraft (Table 6.3).

In summary, both the global chemistry transport model TOMCAT and the regional chemistry transport model CCATT-BRAMS overestimate the VMRs of HCHO, CO, and isoprene measured during the SHIVA campaign over Borneo in November and December 2011. The modelled isoprene VMRs even exceed the measured isoprene VMRs of 2 to 3 ppb, which were measured directly above a forest canopy in Danum Valley, Sabah, Borneo during the OP3 campaign in 2008 (MacDonald et al., 2012). The fact that the species HCHO, CO, and isoprene are overestimated by the models, gives rise to speculate that the emission inventories are too large in both models.

A decrease in the VOC concentrations in particular of isoprene has several consequences for the atmospheric oxidation capacity. Since the VOC oxidation is mainly initiated by OH, which is primarily formed through the photodissociation of O_3 (e.g. Levy, 1971; Lelieveld et al., 2008), changes in the O_3 production or the OH concentrations might occur. Further, the oxidation of VOCs emitted by the rain forest leads to the formation of secondary organic aerosols (SOA), which serve as nuclei for clouds and precipitation (e.g. Pöschl et al., 2010; Ehn et al., 2014). However, it is important to note that the isoprene oxidation over remote tropical forests efficiently recycles OH, thus acting both as a source and sink for the OH radical (Taraborrelli et al., 2012).

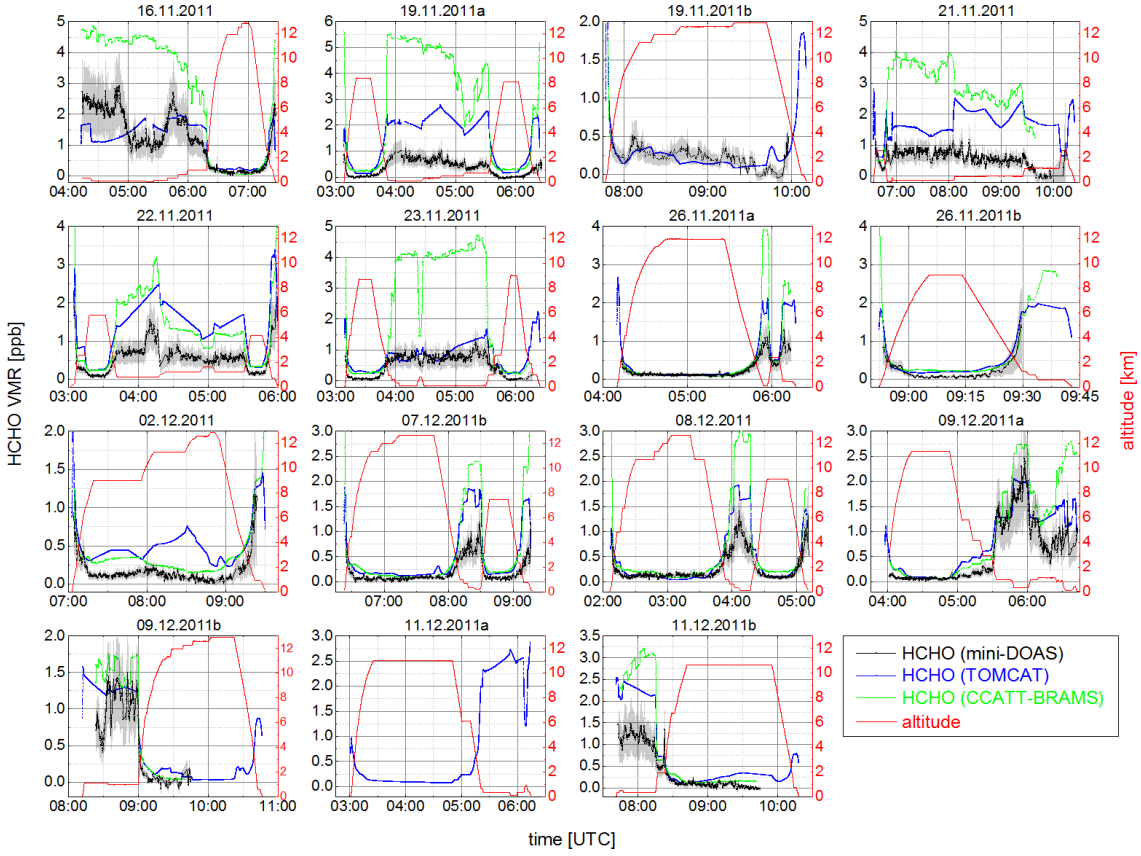

(a)

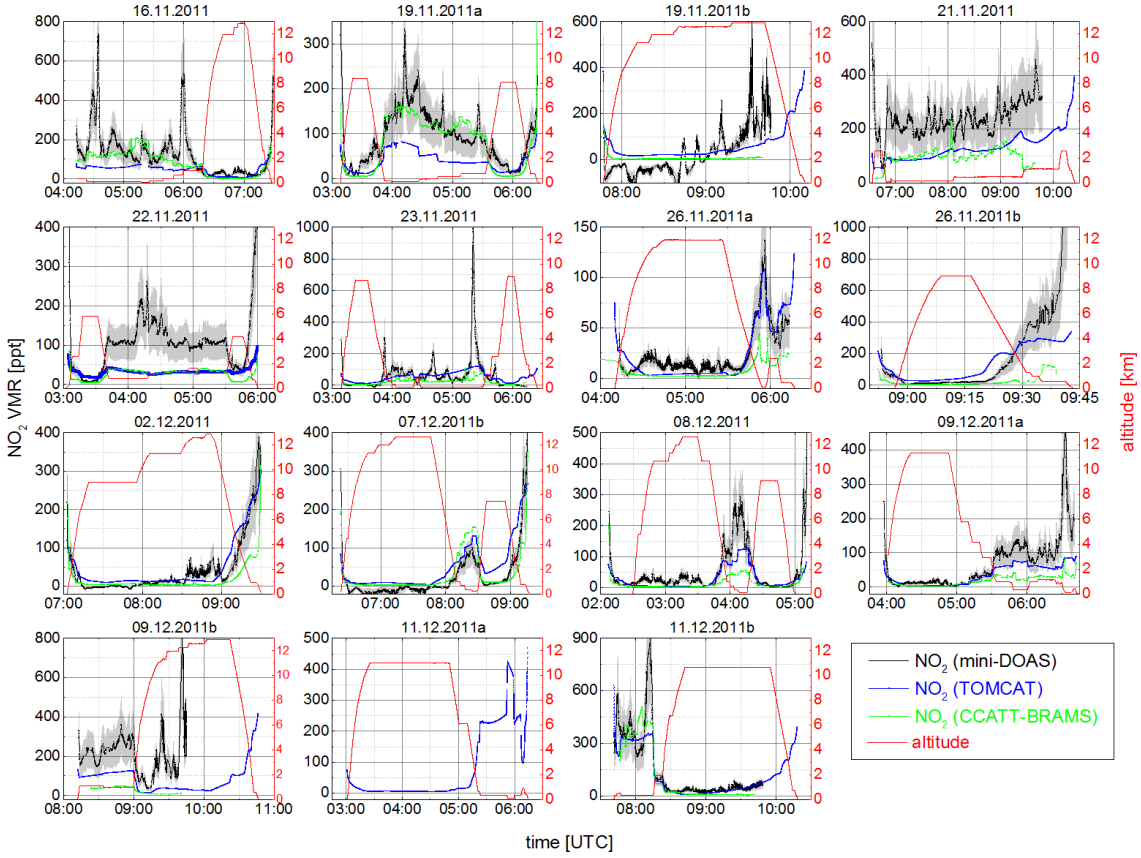

(b)

Figure 11.14: Flight by flight comparison of measured and simulated (a) HCHO and (b) NO_2 VMRs simulated with TOMCAT and CCATT-BRAMS and inferred from the mini-DOAS instrument using the O_4 scaling method (Section 10.1). For sortie 15 no mini-DOAS and CCATT-BRAMS data are available. Mini-DOAS data points with a roll angle larger than $\pm 2\,^\circ$ are excluded.

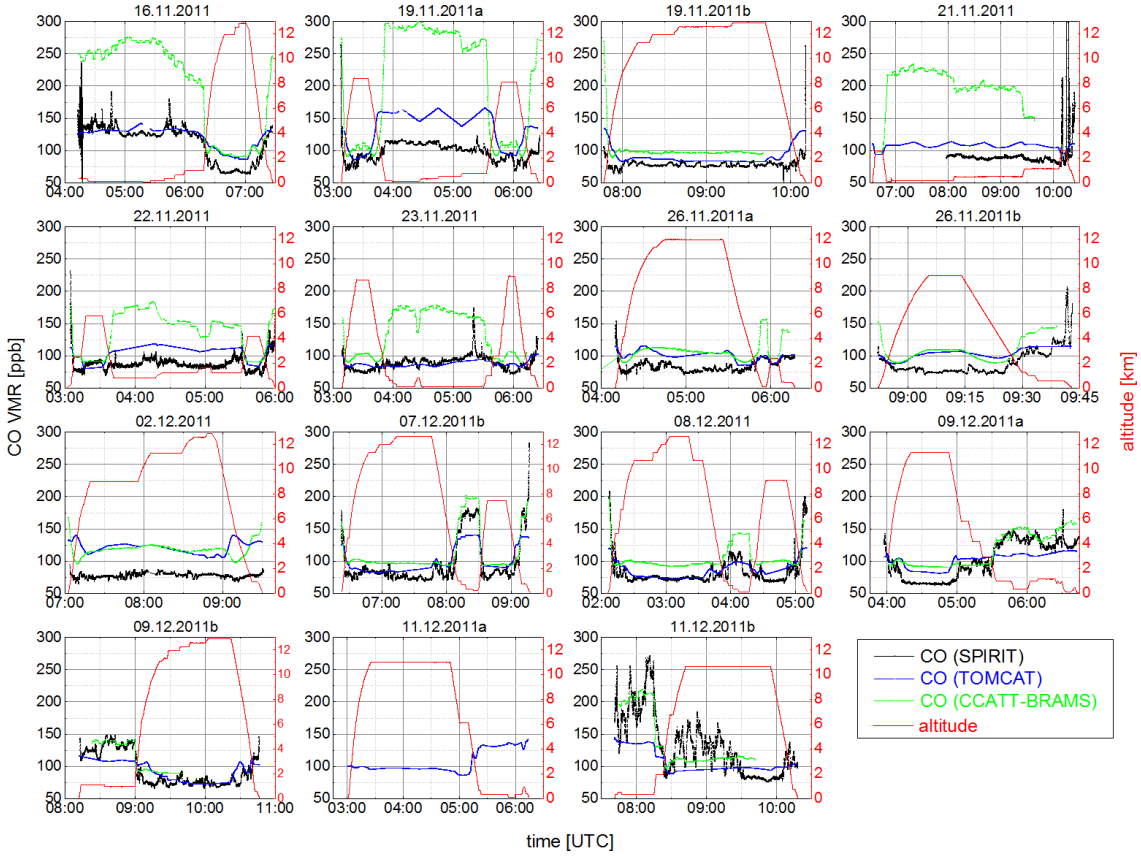

(a)

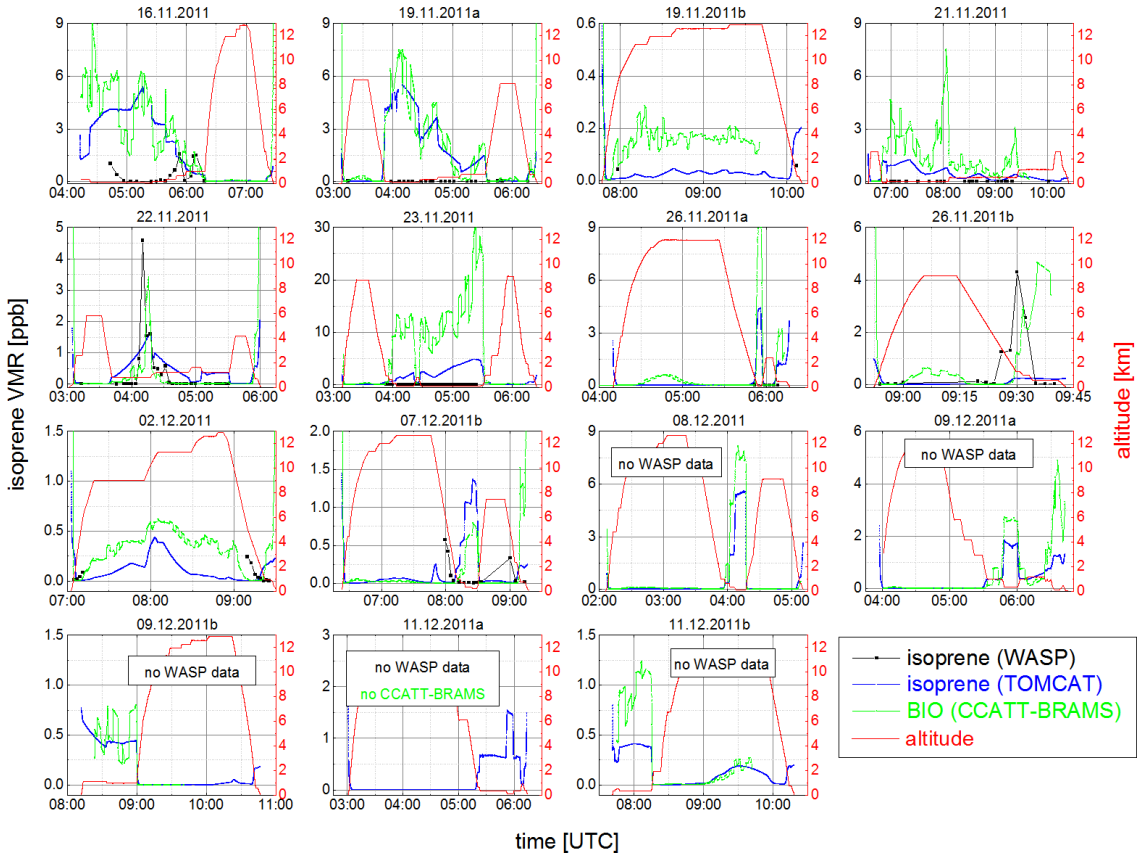

(b)

Figure 11.15: Flight by flight comparison of measured and simulated (a) CO and (b) isoprene VMRs simulated with TOMCAT and CCATT-BRAMS and measured by the SPIRIT and by the WASP instrument, respectively. For sortie 15 no mini-DOAS and CCATT-BRAMS data are available. 'BIO' is a lumped chemical species, which mostly contains isoprene plus some other terpenes.

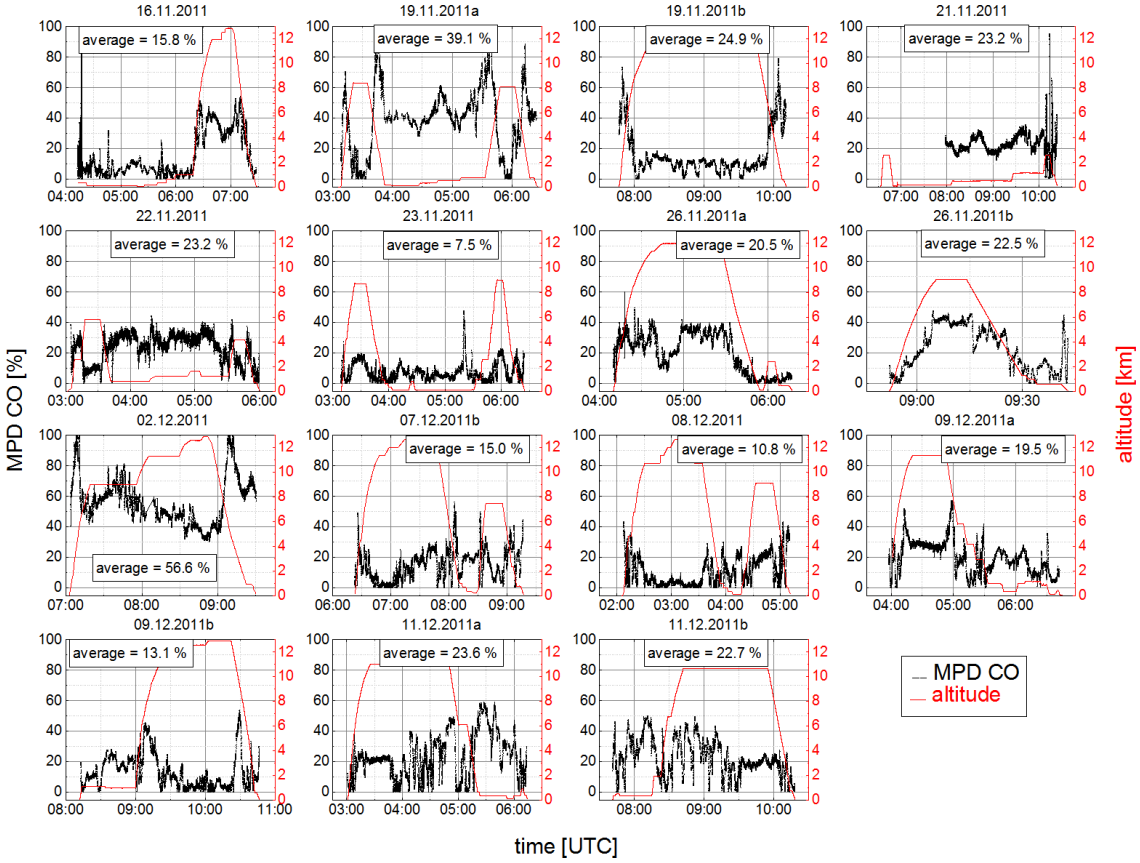

Figure 11.16: Mean percentage difference (MPD) (Equation 11.10) between the CO VMRs measured by the SPIRIT instrument and simulated with the TOMCAT model.

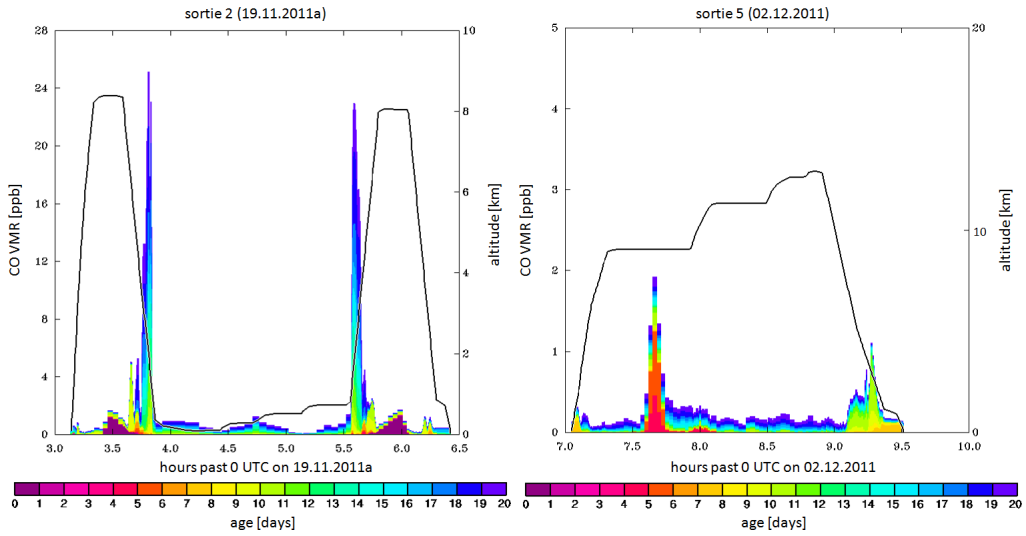

(a) (b)

Figure 11.17: FLEXPART simulations (Section 6.2.1) of CO originating from fire plumes for (a) sortie 2 on 19.11.2011a and (b) sortie 9 on 02.12.2011. The colour bar corresponds to the emission age in days.

11.2.3 Attribution of major emission sources of HCHO, CHOCHO, and NO_2

Regional air pollution

In order to identify the different emission sources, different trace gases with different sources and loss processes have to be analysed. Table 11.2 summarises the different emission sources and their composition, e.g. if biomass is burned, CO, NO_2 and HCHO will simultaneously increase (e.g. Allen et al., 2004; Miller et al., 2008).

Table 11.2: Identifying different emission sources according to the composition of trace gases. Table compiled according to Holzinger et al. (1999); Allen et al. (2004); Beirle et al. (2004); TCEQ (2007); Miller et al. (2008); Marbach et al. (2009); Reiter (2012), and references therein.

biomass burning	volcanic emissions	oil rigs	ship emissions	anthropogenic emissions
CO	-	CO?	CO	CO
NO_2	-	NO_2	NO_2	NO_2
HCHO	-	HCHO	HCHO	HCHO
CHOCHO	-	CHOCHO	CHOCHO	CHOCHO
-	SO_2	SO_2	SO_2	SO_2
-	-	-	-	HONO

In the following, one exemplary sortie (sortie 1 on 16.11.2011) is discussed with regard to the different possible emission sources. Figure 11.18 shows the flight track of this sortie. The aircraft started in Miri and cruised south-westward along the coast of Borneo passing Bintulu to Kuching Bay on a constant flight altitude of 100 m. In Kuching Bay the aircraft turned at 05:15 UTC and headed back towards Miri on the same way, however on different flight levels. Back over Miri, the aircraft climbed northward following a loop with a maximum altitude of 12.8 km.

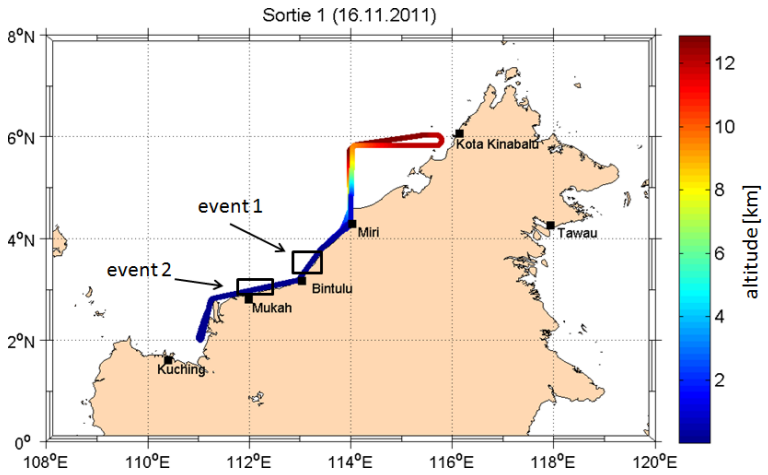

Figure 11.18: Flight track of sortie 7 on 26 November 2011a. The black boxes highlight the area of the pollution events 1 and 2.

Figure 11.19 shows an overview of the inferred VMRs of the trace gases measured during sortie 1 on 16.11.2011. Along the low level parts of the flight (04:10 - 06:15 UTC) NO_2 occasionally peaks at the same locations both for the forward and return track. The NO_2 enhancement detected around 04:30 UTC (event 1a) is also seen on the return track around 06:00 UTC (event 1b), and at the

same location HCHO, CO, O_3, SO_2, and isoprene were elevated too. According to the emission fingerprint provided in Table 11.2, this plume is most likely due to emissions from oil rigs, ships, or anthropogenic combustion. In this area, the Falcon aircraft passed several ships, heading towards the industrial area near Bintulu (3.3 °N/113.1 °E) (Figure 11.20). Furthermore, along the coastline of Borneo many oil rigs are located (Figure 6.6).
A smaller plume in NO_2 and HCHO occurred at around 04:45 UTC (event 2a) and around 05:45 UTC (event 2b) again at the same location on the forward and return leg of the flight. This increase in pollutants occurs close to the cities of Sibu (2.3 °N/111.8 °E), and Mukah (2.9 °N/112.1 °E) and thus might be linked to anthropogenic emissions from these cities. However, it has to be noted that event 1a consists of 2 individual peaks, whereas event 1b only consists of a single peak (Figure 11.21). A similar behaviour can be observed for event 2, where during the forward flight leg one peak occurred and during the return flight leg two peaks occurred.
Figure 11.22 shows the source region of the air masses simulated with FLEXPART. The air masses mainly originate from the south-western direction travelling along the coastline of Borneo. Thus, the air masses might be influenced by emissions from the land. Figure 11.23 further shows 48-hours backward trajectories calculated with HYSPLIT (Section 6.2.2). It can be seen that the air masses travel along the coastline of Borneo moving towards the sea and back to the land due to a change from sea to land breeze during the course of the day. This changes in wind direction decreases for increasing altitude, in this case for an altitude of 500 m.

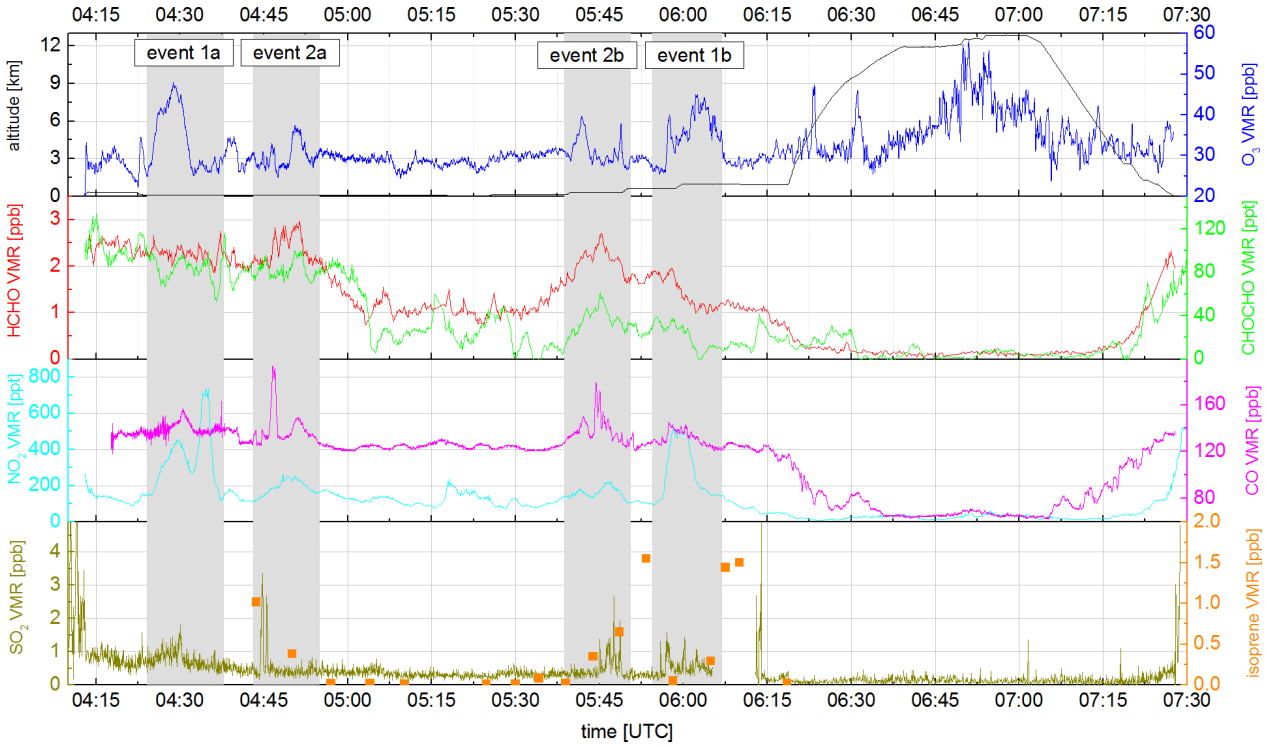

Figure 11.19: Inferred trace gas VMRs during sortie 1 on 16.11.2011: Altitude (black) from the Falcon dataset, in situ O_3 VMRs (blue) measured by the ozone monitor (Hans Schlager, IPA DLR, Oberpfaffenhofen, personal communication, June 2012), HCHO (red), CHOCHO (green), and NO_2 (turquoise) VMRs measured by the mini-DOAS instrument, in situ CO VMRs (pink) measured by the SPIRIT instrument (Catoire et al., 2015), in situ SO_2 VMRs (dark yellow) measured by the IT-CIMS instrument (Reiter, 2012), and isoprene VMRs (orange) measured by the WASP instrument (David Oram and Graham Mills, School of environmental Sciences, University of East Anglia, Norwich, personal communication, November 2012).

Figure 11.20: Webcam images of some ships detected with the webcam on the portside of the Falcon aircraft during the flight on 16 November 2011.

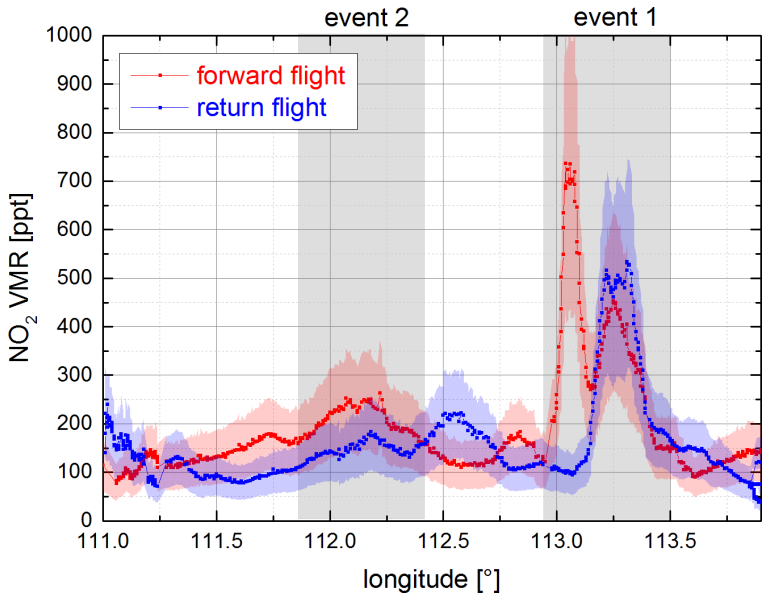

Figure 11.21: NO_2 VMRs along the longitude for the low level part of sortie 1 on 16 November 2011. The grey boxes highlight the area of the events 1 and 2.

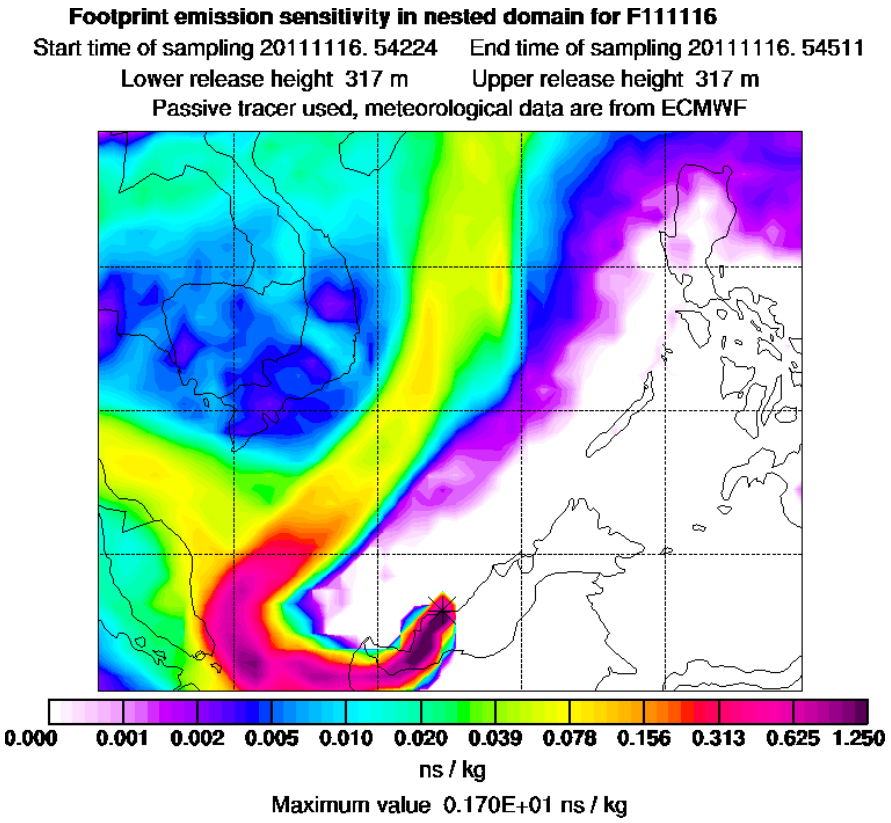

Figure 11.22: Local footprint emission sensitivity calculated with FLEXPART (Section 6.2.1) for sortie 1 on 16 November 2011.

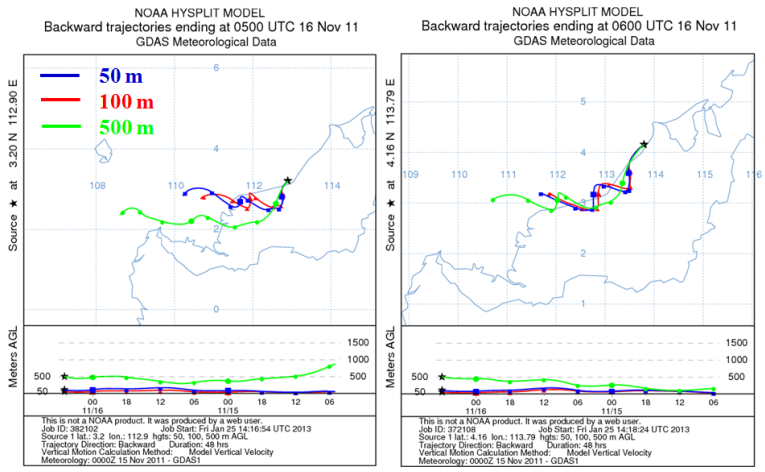

Figure 11.23: HYSPLIT 48-hours backward trajectories (Section 6.2.2) for the sortie on 16 November 2011.

Satellite maps of tropospheric HCHO, CHOCHO, and NO_2 VCDs can be further used to validate the aircraft-borne DOAS measurements (or vice versa) and to identify spots where regularly elevated VCDs occurred. Figure 11.24 shows GOME-2 maps of tropospheric VCDs of HCHO, CHOCHO, and NO_2 for November and December 2011, kindly provided by F. Hendrick, I. DeSmedt, Y. Huan, and C. Lerot (IASB-BIRA, Brussels, Belgium, personal communications, July 2013). A short description of the GOME-2 satellite instrument can be found in Section 6.2.3. The satellite maps show spatially variable patterns. Inferred HCHO VCDs range from (5–10) $\cdot 10^{15}$ molec cm^{-2}, for CHOCHO from

(1–2) $\cdot 10^{14}$ molec cm^{-2}, and for NO_2 from (1–3) $\cdot 10^{15}$ molec cm^{-2} near the coastline of Borneo. It can be seen that in the region of events 1 and 2 NO_2 is enhanced. However, due to their noisy spatial pattern, enhancements of HCHO and CHOCHO VCDs can hardly be distinguished.

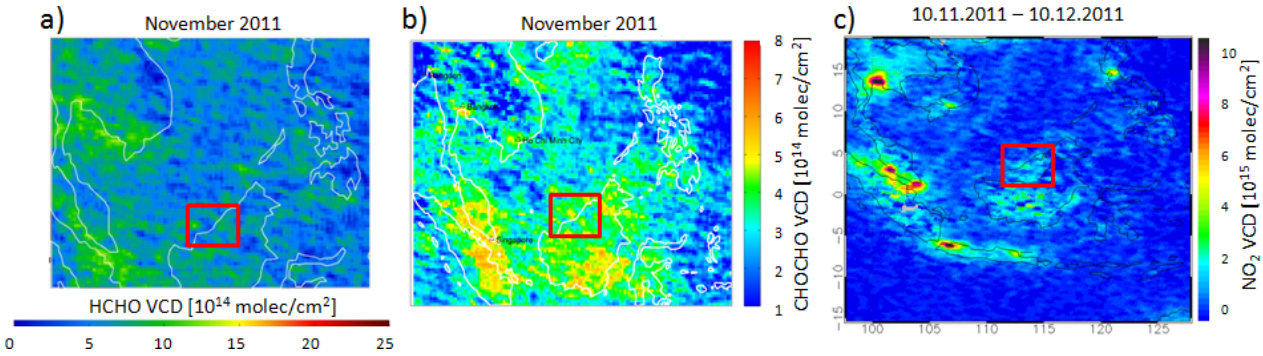

Figure 11.24: GOME-2 maps of monthly mean tropospheric VCDs of (a) HCHO, (b) CHOCHO, and (c) NO_2 over Borneo for a cloud fraction smaller than 40 %. GOME-2 data kindly provided by F. Hendrick, I. DeSmedt, Y. Huan, and C. Lerot (IASB-BIRA, Brussels, Belgium, personal communications, July 2013). The red boxes highlight the region where the events 1 and 2 occurred.

The CHOCHO/HCHO ratio

Satellite measurements indicate enhanced concentrations of both HCHO and CHOCHO over areas where large abundances of isoprene occur (Wittrock et al., 2006). According to these satellite measurements, the ratio of CHOCHO and HCHO indicates whether the sources of both species are of biogenic or of anthropogenic origin. The ratio R_{GF} of CHOCHO and HCHO has been further used by Vrekoussis et al. (2010) on a global scale in order to classify the sources according to biogenic and/or anthropogenic emissions of the precursors. Ratios R_{GF} between 0.04 and 0.06 are thereby indicative for biogenic emissions, whereas ratios below 0.04 point to anthropogenic emissions during high levels of NO_2 (Vrekoussis et al., 2010). MacDonald et al. (2012) detected much higher ratios with an average value of 0.2 for ground-based measurements directly above a rain forest canopy in Danum Valley, Sabah, Borneo. GOME-2 measurements yield a ratio of approximately 0.06 for the island of Borneo (Vrekoussis et al., 2010). Noteworthy is that the ratio R_{GF} derived from satellite measurements is an average over the troposphere. Furthermore, the GOME-2 crossing time over the Equator is at about 09:30 am LT, whereas the sorties of the Falcon aircraft generally took place between 03:00 and 10:00 UTC, i.e. 11:00 and 18:00 LT.

Figure 11.25 shows the CHOCHO and HCHO VMRs for sortie 1 on 16.11.2011 and for sortie 5 on 22.11.2011 as well as the ratio R_{GF}, respectively. The error of the ratio R_{GF} is calculated via error propagation using the error of the CHOCHO and HCHO VMRs, respectively. During the first part of sortie 1 on 16.11.2011 at an altitude of 100 m (04:10 - 05:00 UTC), the ratio R_{GF} varies between approximately 0.03 and 0.06 with a decrease to 0.03 at 04:35 UTC and 04:45 UTC where the pollution events 1 and 2 are located. Between 05:00 and 05:30 UTC the aircraft was flying in Kuching Bay and the CHOCHO VMRs decrease to 20 and 30 ppt, i.e. to values at or below the detection limit. At 05:15 UTC the Falcon aircraft headed backward to Miri on the same flight leg but at higher flight levels. The HCHO VMRs are slightly decreased during the return flight relative to the forward flight, and the CHOCHO VMRs show even a stronger decrease. This results in a ratio R_{GF} between 0.01 and 0.02. This decrease in both HCHO and CHOCHO might eventually be due to the lower HCHO and CHOCHO VMRs at higher flight levels relative to the forward flight at a lower flight level. This decrease can be caused by the different viewing directions of the mini-DOAS instrument for the out- and inbound legs of the flight. During the forward flight to Kuching Bay, the viewing direction pointed towards the coast, i.e. towards the source region, whereas during the

return flight the viewing direction was to the ocean. The lifetime of CHOCHO in the atmosphere is about 1.3 hours for overhead sun conditions in urban air (Volkamer et al., 2005a), and 2 to 3 hours on a global scale (Fu et al., 2008; Myriokefalitakis et al., 2008). The average lifetime of HCHO results in approximately 5 hours in the troposphere (Arlander et al., 1995; De Smedt et al., 2008). Thus, it can be assumed that either CHOCHO shows a stronger decrease with altitude than HCHO or that CHOCHO decreases more quickly with increasing distance from the sources than HCHO.
Between 04:10 and 04:40 UTC during sortie 5 on 22.11.2011 the Falcon aircraft flew over land. The flight track of this sortie is shown in Appendix in Figure A.1. During this section the ratio R_{GF} varies between approximately 0.04 and 0.1, i.e. the ratio is increased relative to the ratio observed above the ocean close to the coast.
However, since during the different sorties of the Falcon aircraft several parameters change simultaneously, such as the altitude, the location, or the viewing direction of the instrument, it is difficult to draw any firm conclusions about the varying behaviour of the ratio R_{GF}. Furthermore, CHOCHO is regularly at or close to the detection limit.

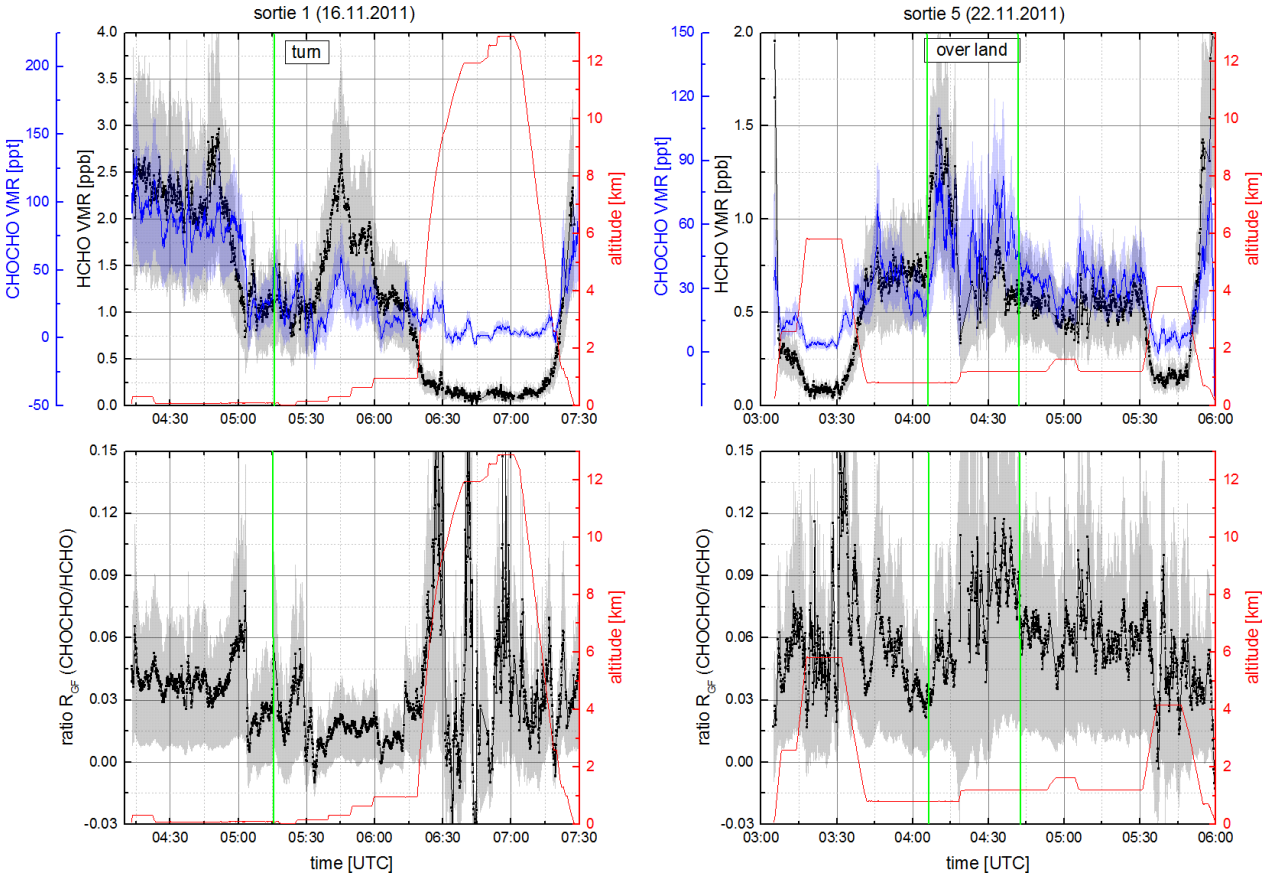

Figure 11.25: Upper panels: CHOCHO and HCHO VMRs inferred with the O_4 scaling method for sortie 1 on 16.11.2011 (left panel) and sortie 5 on 22.11.2011 (right panel). Lower panels: Ratio R_{GF} of the CHOCHO and HCHO VMRs from the upper panels.

11.2.4 The impact of NO_2 and VOCs on the O_3 production

The formation of tropospheric ozone is driven by a complex non-linear function of NO_x and VOCs, i.e. reductions in the emissions of NO_x and VOCs can alter the ozone production rate (e.g. Sillman, 1999; Finlayson-Pitts and Pitts Jr., 2000). The relation between these species is illustrated in Figure 11.26, which shows a peak in the O_3 production as a function of NO_x and VOC VMRs. It is therefore possible to identify two regimes with different sensitivities for the O_3 production as a

function of NO_x and VOC VMRs. The straight line in Figure 11.26 distinguishes the NO_x-limited from the VOC-limited regime. In the NO_x-limited regime with low NO_x and large VOC VMRs, O_3 almost linearly increases with increasing NO_x, and changes less for increasing VOC concentrations. This regime typically occurs in suburban, rural, and downwind areas (Finlayson-Pitts and Pitts Jr., 2000). In the VOC-limited or NO_x- saturated regime in steady state, O_3 decreases with increasing NO_x and increases with increasing VOCs due to titration of O_3 by the following reactions (Section 2.4.2):

$$NO + O_3 \longrightarrow NO_2 + O_2 \tag{11.11}$$

$$NO_2 + O_3 \longrightarrow NO_3 + O_2 \tag{11.12}$$

$$NO_2 + NO_3 + M \longrightarrow N_2O_5 + M \tag{11.13}$$

$$N_2O_5 + H_2O \longrightarrow 2\ HNO_3. \tag{11.14}$$

In addition to the the hydrolysis of N_2O_5 (Equation 11.14), which is catalysed by surfaces, further loss processes of N_2O_5 exist, such as the reaction with aerosols (Finlayson-Pitts and Pitts Jr., 2000). The behaviour described above is also known as the 'weekend effect' (e.g. Cleveland et al., 1974), i.e. in urban regions it appears that the O_3 concentrations are slightly higher on weekends relative to weekdays.

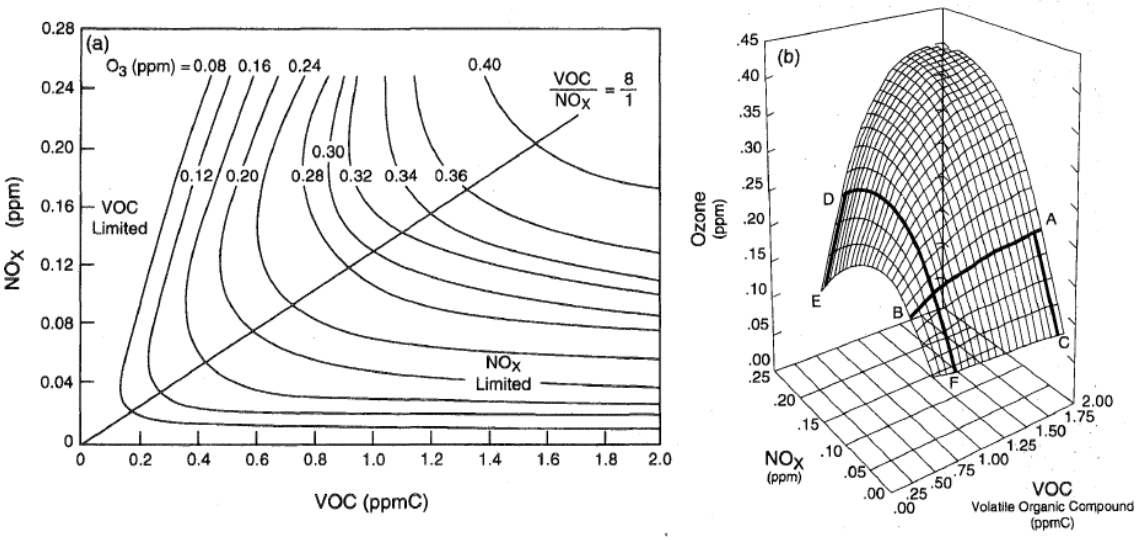

Figure 11.26: Typical peak ozone production isopleths generated from initial mixtures of VOCs and NO_x in air using the EKMA (Empirical Kinetic Modelling Approach) model depicted in (a) two dimensions and in (b) three dimensions. The VOC-limited regime, e.g. point D, can be found in polluted urban areas, Figure adapted from Finlayson-Pitts and Pitts Jr. (1993).

However, the sensitivities for the O_3 production as a function of NO_x and VOC VMRs highly depends on the individual location. Chameides et al. (1992) investigated the relationship between the concentrations of O_3, NO_x, and VOCs in a variety of different tropospheric locations. Figure 11.27 shows the range of NO_x and OH-reactivity adjusted VOCs for different regions. Chameides et al. (1992) thereby converted the VOCs to reactivity-based concentrations by adjusting for the individual VOC reactivities with OH. They expressed the OH-reactivity adjusted VOCs relative to propene. Although this approach may overestimate the reactivity of highly reactive species relative to organics, it is a useful step in comparing VOC reactivities from different regions (Finlayson-Pitts and Pitts Jr., 1993). The four regions comprise urban and suburban areas, rural areas, as well as the remote tropical Brazilian forests, and the remote marine boundary layer. Figure 11.27 shows the range of NO_x and OH-reactivity adjusted VOCs, i.e. expressed relative to propene. As discussed by

Chameides et al. (1992), the reactivity-adjusted VOC concentrations increase by almost two orders of magnitude from the remote marine region to the tropical forests, but O_3 remains approximately constant. Thus, in remote and in rural regions, the O_3 formation is most sensitive to NO_x whereas in polluted urban and suburban regions, it can be sensitive to either NO_x, or VOC control depending on the particular conditions (Finlayson-Pitts and Pitts Jr., 2000).
During the SHIVA aircraft campaign, enhanced concentrations of oxygenated VOCs were observed as compared to the classified remote marine regions, whereas O_3 rather remained constant. Accordingly, O_3 is most sensitive to the NO_x concentrations. Thus, in the region around Borneo the O_3 formation is likely dominated by a NO_x-limited regime. However, in order to gain a more detailed understanding about the sensitivity of O_3 production as a function of NO_x and VOC VMRs over Borneo, photochemical modelling would be required.

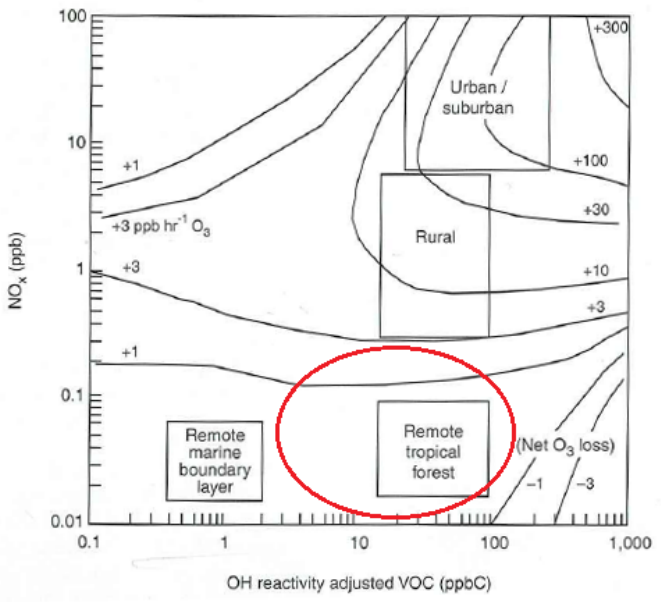

Figure 11.27: Observed NO_x and OH-reactivity-adjusted VOC (expressed as propene) for different regions of the troposphere. The isopleths depict the midday rates of O_3 production in ppb per hour calculated using a box model, Figure adapted from Chameides et al. (1992). The red circle highlights the likely position of the region around and above Borneo.

11.3 Composition of air masses in a meso-scale convective cloud system

In thunderstorm clouds, chemically inert trace gas species, such as CO, or even chemically reactive but poorly soluble gases, such as HCHO, can be rapidly transported from the boundary layer to the upper troposphere, thus having a major influence on the composition of the atmosphere (Dickerson et al., 1987). Furthermore, several studies indicate that lightning-induced NO_x production is the dominating source of NO_x in the upper troposphere, particularly in the tropics (e.g. Schumann and Huntrieser, 2007, and references therein). The production of NO by lightning follows the Zel'dovich mechanism (Zel'dovich and Raizer, 1967), which describes the dissociation of O_2 and N_2 and the subsequent production of NO in the hot lightning stroke according to the following reactions:

$$O_2 + M \longrightarrow O + O + M \tag{11.15}$$
$$O + N_2 \longrightarrow NO + N \tag{11.16}$$
$$N + O_2 \longrightarrow NO + O. \tag{11.17}$$

Equation 11.16 has a large activation energy of 318 $\frac{\text{kJ}}{\text{mol}}$ and is only efficient at temperatures larger than 2000 K. Due to the larger bond dissociation energy of N_2 of 0.94 MJ mol^{-1} relative to that of O_2 (0.5 MJ mol^{-1}) (Howard and Rees, 1996), O_2 readily dissociates. In addition to the formation of NO_2 by the reaction of O_3 and NO, NO_2 can also be produced by lightning, with the $[NO_2]/[NO]$ ratio being strongly dependent on the water content of the air (Stark et al., 1996). According to Schumann and Huntrieser (2007), the NO production rate of lightning strokes ranges between (2 - 40)$\cdot 10^{25}$ NO molecules per flash with an average value of $15 \cdot 10^{25}$ NO molecules per flash. According to simulations by Bhetanabhotla et al. (1985), lightning strokes not only produce NO_x, but also HONO and OH. Within the lightning radical channel, the OH concentration can even increase up to approximately $4 \cdot 10^8$ molec cm^{-3} in the first milliseconds directly after the flash (Bhetanabhotla et al., 1985).
Recently, Bozem et al. (2014) proposed that corona discharge associated with lightning strokes appears to be a likely source of enhanced ozone in the outflow of a cumulonimbus (Cb) cloud over the tropical rain forest in Suriname. They further deduced a production rate of $5.12 \cdot 10^{28}$ molec O_3 $flash^{-1}$.
In the following, a meso-scale convective system probed over Borneo on 19 November 2011 is examined to study the composition of air masses in its outflow. The following analysis and assumptions are based on the studies performed by Heue et al. (2014), who examined the intersection of the CARIBIC (Civil Aircraft for the Regular Investigation of the atmosphere based on an Instrument Container) flying laboratory with a large thunderstorm cloud over the Caribbean Sea in August 2011.

11.3.1 Observations

The outflow of a meso-scale convective cell was investigated for the afternoon of 19 November 2011, when a large thunderstorm cloud is formed at the north-east coast of Borneo. The Falcon aircraft penetrated the outflow of the cumulonimbus cloud several times at a flight altitude between 11.3 and 12.9 km. For this sortie, Hamer et al. (2013) discusses the meteorology and transport processes in detail. Figure 11.28a shows the flight track of sortie 3 on 19.11.2011 together with the lightning activity during the time of the sortie (07:45 - 10:15 UTC) according to data from the World Wide Lightning Location Network (`http://wwwlln.net`, August 2014). An increased number of flashes was detected close to the flight track. In analogy to Hamer et al. (2013), two regions are defined. Region 1 defines the area where the convective signatures occur and region 2 indicates the convective source region for the outflow observed in region 1, where an increased number of flashes was detected. As indicated in the radar image (Figure 11.28b), rainfall above 10 mm/hour occurred only in region 2.

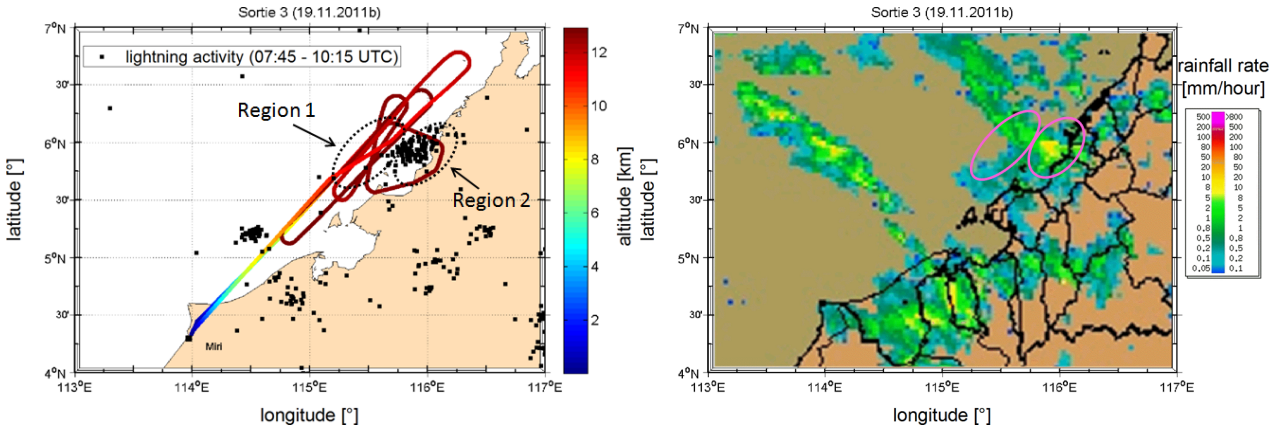

(a) (b)

Figure 11.28: (a) Flight track and location of observed flashes during sortie 3 on 19.11.2011. Each black point represents one registered flash. The lightning location data are kindly provided by the World Wide Lightning Location Network (`http://wwlln.net`), a collaboration among over 50 universities and institutions. (b) Radar image of the rainfall rate at 08:40:10 UTC on 19.11.2011, adapted from the Malaysian Meteorological Department (MMD).

Figure 11.29 shows the time series of the DOAS and in situ measurements of this sortie. Each time the Falcon aircraft penetrated the outflow of the Cb cloud plume, dSCDs of HCHO, HONO, and NO_2 as well as in situ CO VMRs were increased as compared to ambient air concentrations. An increase in the O_4 dSCDs was also observed inside the cloud indicating an elevated light path mainly due to multiple Mie scattering within the cloud. The red bars in Figure 11.29 highlight the five sections (cloud penetration events 1 to 5) when elevated HONO dSCDs above the detection limit of approximately $1 \cdot 10^{15}$ molec cm^{-2} occurred. Figure 11.30 shows the webcam images directly taken before, during, and after each intersection of the aircraft with the cloud. These intersections are collocated with the maxima of the measured HCHO, HONO, and NO_2 dSCDs, as well as with the maxima of the in situ measured CO VMRs.
Figure 11.31 indicates simultaneous increases of the dSCDs of HCHO, HONO, and NO_2, as well as the CO VMRs along the flight track. Inside the cloud, CO shows elevated VMRs of 80 to 85 ppb relative to the ambient air concentrations of approximately 75 ppb at flight altitude (between 11.3 km and 12.9 km).

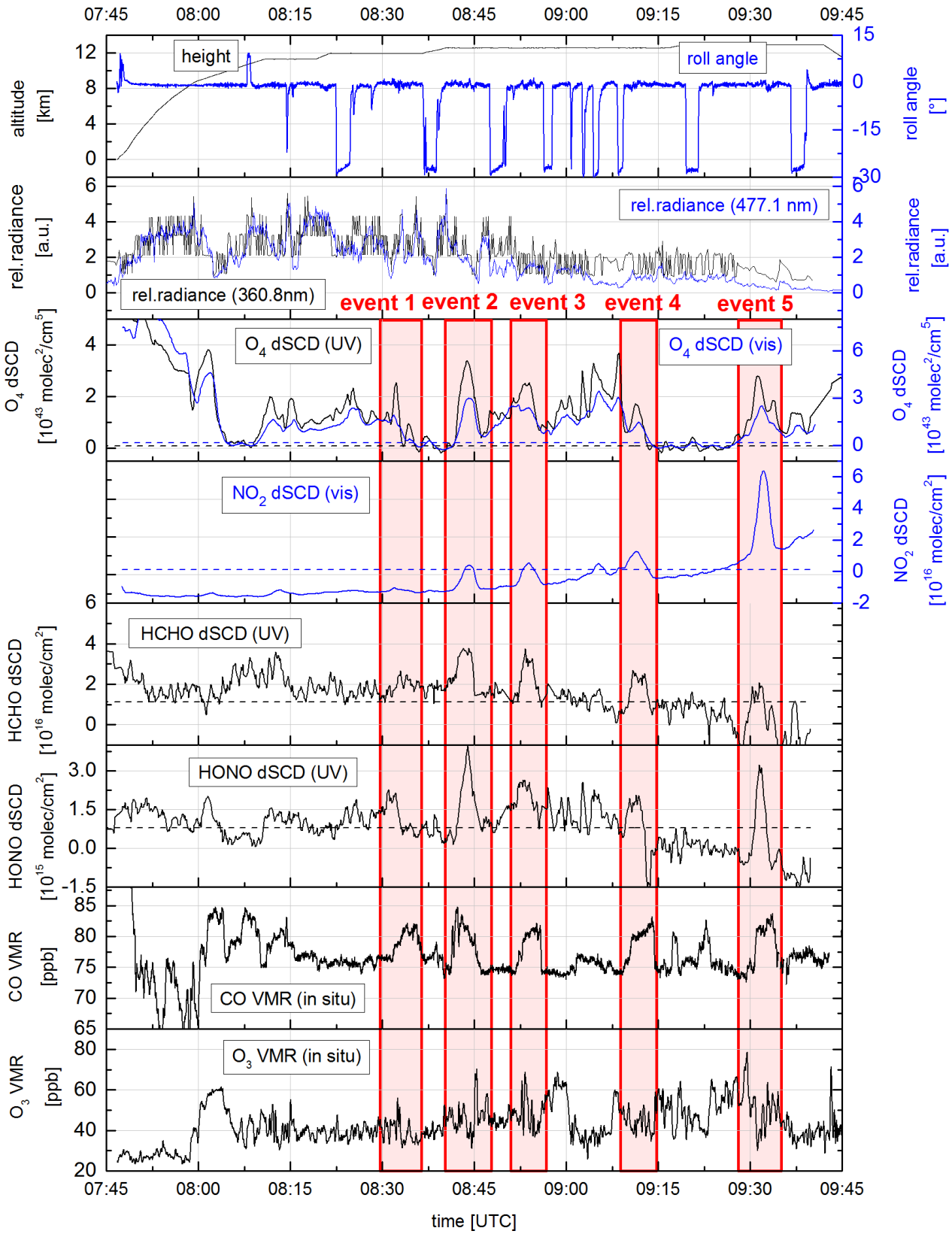

Figure 11.29: Overview of the measurements during the sortie on 19 November 2011 b. The uppermost panel shows the altitude (black) and the roll angle (blue) of the Falcon aircraft. The dSCDs retrieved in the UV spectral range are shown by a black line and the dSCDs retrieved in the visible wavelength range by a blue line. The respective average 2 σ detection limits of the dSCDs are illustrated by dashed lines. The lowermost two panels show the in situ CO and O_3 VMRs measured by the SPIRIT instrument (Krysztofiak, 2013; Catoire et al., 2015) and the ozone monitor (Hans Schlager, IPA, DLR, Oberpfaffenhofen, personal communication, June 2012), respectively. The red boxes mark the five cloud penetration events used for the analysis in this study.

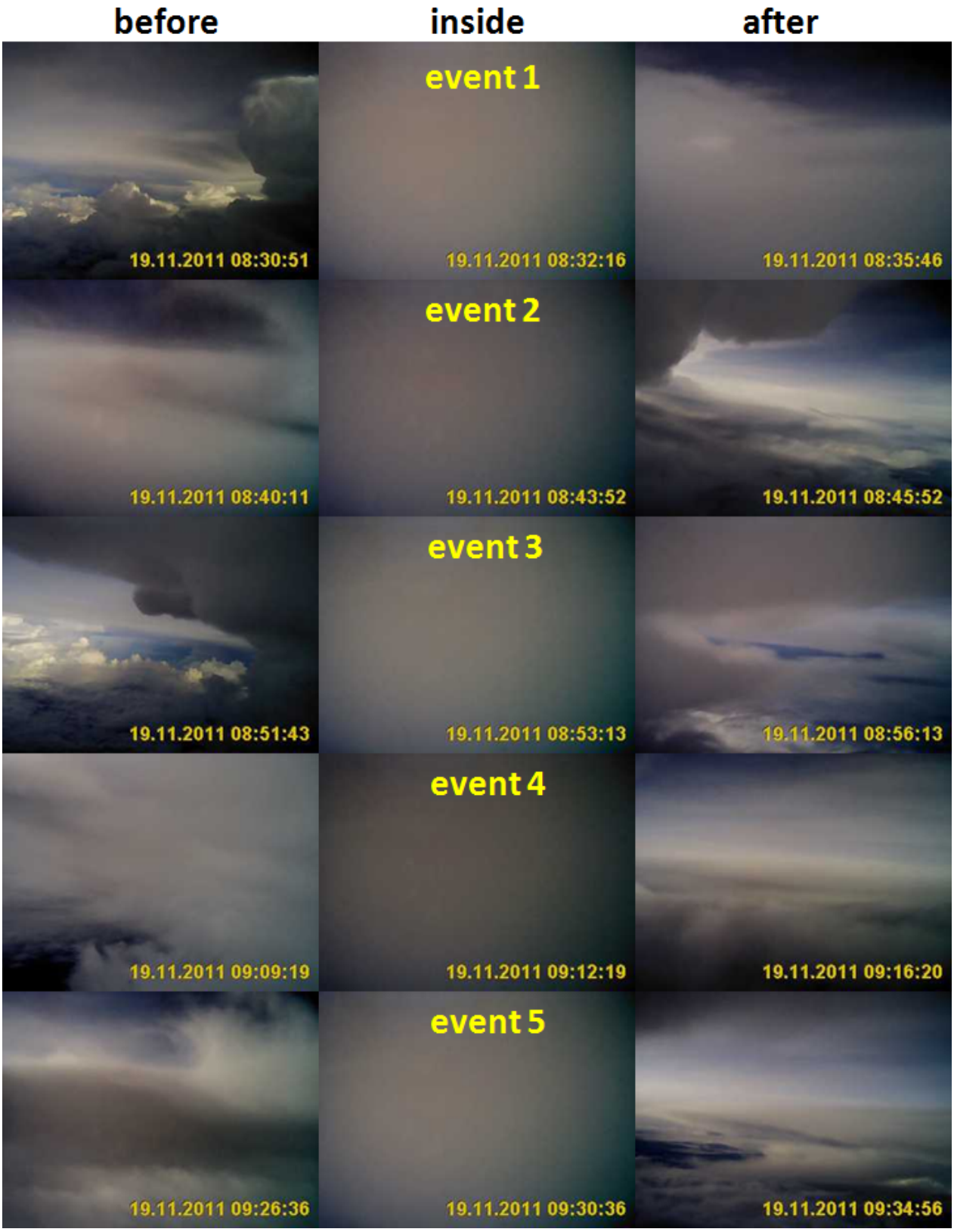

Figure 11.30: Webcam images directly taken before (left panels), inside (middle panels) and directly after (right panels) the Cb cloud on 19 November 2011b. The five cloud penetration events are highlighted in red in Figure 11.29. Inside the Cb cloud, HONO, NO_2 as well HCHO were elevated, whereas outside the cloud, the trace gases reached background dSCDs.

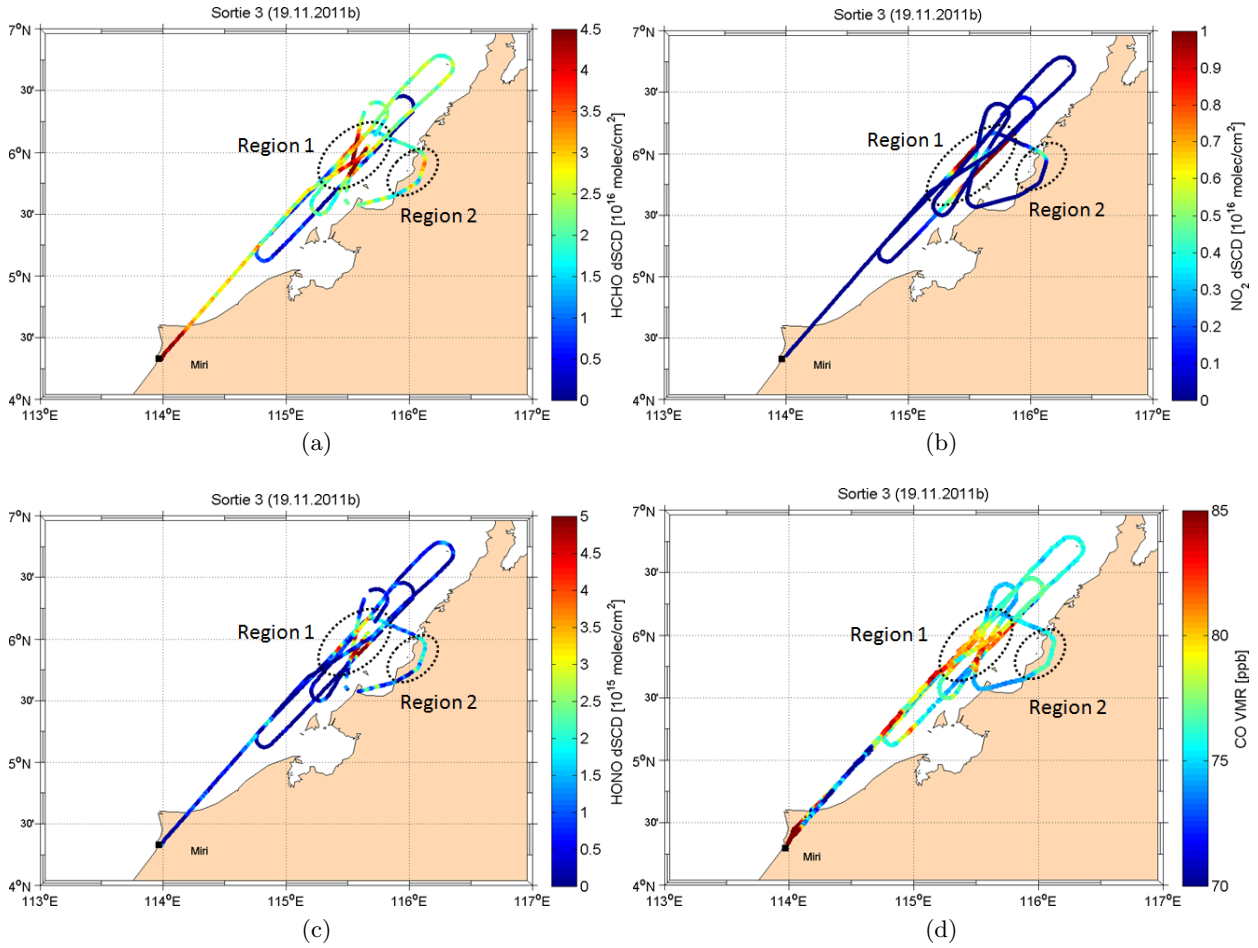

Figure 11.31: Measured dSCDs of (a) HCHO, (b) NO_2 and (c) HONO, and (d) in situ CO VMRs along the flight track. For ease of visual comparison, the increase in the NO_2 dSCDs due to an increasing SZA is subtracted from the NO_2 dSCDs in panel (b).

11.3.2 Trace gas concentrations inside the cloud anvil

In this study, the VMRs of the maximum dSCD of each peak are estimated using the O_4 scaling method described in Section 10.1. Prior to the application of the O_4 scaling method, the background dSCDs are subtracted from each peak in order to calculate the enhanced signal inside the cloud. The determination of the reference SCD can be neglected since for this study only the enhancement inside the cloud is considered. It is further assumed, that the ratio of $\alpha^*_x/\alpha^*_{O_4}$ of the trace gas x and O_4 is approximately one inside the thunderstorm cloud since the absorption attributed to the photon diffusion within the cloud is likely not significantly influenced by anything outside the cloud. Thus, the basic O_4 scaling method according to Equation 10.13 can be applied, i.e. no radiative transfer calculations are required.

Using this basic O_4 scaling method, the inferred VMRs of HONO, HCHO, and NO_2 yield concentrations of 25 to 48 ppt, 216 to 462 ppt, and 54 to 917 ppt, respectively, depending on the cloud penetration events 1 to 5 (Table 11.3). The VMRs of NO_2 and HCHO increase with increasing cloud penetration event number. This increase could not be observed by Heue et al. (2014), because there, the convective system was only passed once.

The inferred VMRs are comparable to the VMRs inferred by Heue et al. (2014). The NO_2 VMRs of approximately 200 ppt estimated by Heue et al. (2014) seem to be lower than those of the present study. The thunderstorm cloud probed by Heue et al. (2014) occurred above rather clean marine air, where pollution is assumed to be low. The convective cloud system in this study is located close

to the coast of Borneo (Figure 11.31), where an updraught of polluted air seems to be possible.

Table 11.3: Overview of the measured trace gases for the five cloud penetration events during sortie 3 on 19.11.2011b.

	event 1	event 2	event 3	event 4	event 5
time [UTC]	08:30-08:33	08:41-08:46	08:48-08:55	09:09-09:12	09:29-09:33
altitude [km]	11.97	12.60	12.60 km	12.60	12.91
latitude [°N]	6.20	5.95	6.01	5.96	5.94
longitude [°E]	115.69	115.59	115.56	115.46	115.64
HONO dSCD [10^{15} molec cm^{-2}]	1.74±0.39	3.81±0.41	2.04±0.41	1.95±0.38	4.00±0.49
HONO VMR [ppt]	36.25	27.04	25.91	33.72	48.08
HONO concentration [10^8 molec cm^{-3}]	2.28	1.61	1.54	1.99	2.73
HCHO dSCD [10^{16} molec cm^{-2}]	1.04±0.58	3.99±0.61	3.56±0.64	2.67±0.54	3.50±0.78
HCHO VMR [ppt]	216.22	282.67	451.77	462.70	420.75
HCHO concentration [10^9 molec cm^{-3}]	1.36	1.69	2.68	2.74	2.39
light path L_{UV} [km]	76.11	236.11	132.73	97.61	146.52
NO_2 dSCD [10^{16} molec cm^{-2}]	0.24±0.06	1.55±0.06	1.63±0.06	1.05±0.06	5.56±0.10
NO_2 VMR [ppt]	54.42	158.98	335.26	615.34	916.77
NO_2 concentration [10^9 molec cm^{-3}]	3.42	9.50	1.99	3.64	5.23
light path L_{vis} [km]	69.23	163.50	81.98	28.86	106.34

11.3.3 Sources of the different trace gases inside the cloud anvil

Inside the Cb cloud, the studied trace gases HONO, HCHO, NO_2, and CO show enhanced VMRs as compared to ambient air (Figure 11.29 and 11.31). The simultaneous enhancement of these gases possibly indicates a rapid uplift of near-surface pollution to the upper troposphere. An enhancement of CO of approximately 10 ppb is indicative for an entrainment of CO rich air from the boundary layer into the FT by convective transport. An uplift of HCHO from the MBL is possible since the solubility of HCHO in water is low. Henry's law constant of HCHO is small (Staudinger and Roberts, 2001) and thus, the wet deposition is slow. The dimensionless air-to-water concentration ratio of HCHO corresponds to $H_{cc} = 8.6 \cdot 10^{-6}$ for T = 293 K, which is much smaller than for example the ratio for CH_3Br with $H_{cc} = 2.0 \cdot 10^{-1}$ (Staudinger and Roberts, 2001).
In the following, the fraction f_{conv} of MBL air contained in the convective outflow is determined for HCHO, assuming that a statistically unbiased sampling of both the boundary layer and free troposphere was conducted (Bertram et al., 2007). The fraction f_{conv} of MBL air present in the convective outflow can be determined according to:

$$f_{\text{conv}} = \frac{[\text{x}]_{\text{conv}} - [\text{x}]_{\text{UT}}}{[\text{x}]_{\text{MBL}} - [\text{x}]_{\text{UT}}}, \tag{11.18}$$

with the mean mixing ratio $[\text{x}]_{\text{conv}}$ of trace gas x in the convective outflow, the mean mixing ratio $[\text{x}]_{\text{UT}}$ of x in the upper troposphere (UT), and the mean mixing ratio $[\text{x}]_{\text{MBL}}$ of x in the MBL. However, the MBL directly below the convective cloud system was not probed during the sortie examined in this study.
Typically, the HCHO VMRs range between 500 and 2500 ppt in the MBL and decrease to approximately 100 ppt for altitudes between 10 km and 13 km (Figure 11.13a). In order to estimate the fraction f_{conv} for this study, the mean HCHO VMR observed in the MBL is used, which is approximately 1500 ppt. The mean HCHO VMR observed in the convective outflow results in approximately 370 ppt, whereas the mean background VMRs in the UT corresponds to approximately 100 ppt. Thus, the average fraction of MBL air in convective outflow results in approximately $f_{\text{conv}} = 0.19$. Calculating the fraction f_{conv} using the CO measurements, results in $f_{\text{conv}} = 0.21$

(Krysztofiak, 2013). These estimates of f_{conv} are consistent with the observations by Bertram et al. (2007), who calculated an average fraction of $f_{conv} = 0.17$ for a convective system observed over the eastern United States and Canada during summer. These estimations further agree with the range of Ray et al. (2004), who determined a fraction of mid-latitude tropospheric air in convective plumes over the central and eastern United States between 0.1 and 0.4. However, the inferred fraction depends on the HCHO VMRs observed in the MBL, which strongly vary for different locations.
Since HONO dSCDs are below the detection limit during all sorties of the Falcon aircraft in the MBL, it is not likely that the enhanced HONO dSCDs observed in the convective cloud originate from the MBL. Furthermore, since the lifetime of HONO is typically 10 min at noon (Alicke et al., 2003), a transport of HONO over a long distance is therefore not very likely. Thus, for HONO and also NO_x, in situ production due to lightning processes is most likely.
The in situ O_3 VMRs vary between approximately 30 ppb and 65 ppb during this sortie (Figure 11.29). A simultaneous enhancement in the O_3 VMRs inside the cloud, as observed by Bozem et al. (2014), can not be clearly identified.

11.3.4 Estimation of the OH concentration inside the cloud

Measurements of OH were not available during the SHIVA aircraft campaign. In the following, the enhancement of OH inside the cloud relative to the background concentrations outside the cloud is estimated based on the measurements of HONO. In analogy to Heue et al. (2014), several assumptions are made in order to calculate the OH concentrations inside the cloud. It is assumed that HONO, NO, and OH are in a photo-stationary state and that the photolysis of HONO is the only source of OH. The concentration of OH can be calculated using the Reactions 2.48, 2.50, and 2.51 according to the following equation:

$$[\mathrm{OH}] = \frac{J_{\mathrm{HONO}} \cdot [\mathrm{HONO}]}{k_{\mathrm{NO+OH}} \cdot [\mathrm{NO}] + k_{\mathrm{HONO+OH}} \cdot [\mathrm{HONO}]}. \tag{11.19}$$

Since NO was not measured from aboard the Falcon aircraft during the SHIVA campaign, it needs to be estimated. Here, the concentration of NO is estimated under the assumption that NO and NO_2 are in a photo-stationary state given by the *Leighton ratio L* (Equation 2.19). Thus, the NO concentration can be approximated by:

$$[\mathrm{NO}] = \frac{J_{\mathrm{NO_2}} \cdot [\mathrm{NO_2}]}{[\mathrm{O_3}] \cdot k_{\mathrm{NO+O_3}}}. \tag{11.20}$$

The assumption that NO and NO_2 are in a photo-stationary state rather represents an upper limit for the NO concentration, since further reactions are missing, in particular the reaction NO + OH. Further missing reactions include for example the loss of O_3 due to the reaction of O_3 with HO_2. Including Equation 11.20 into Equation 11.19 results in:

$$[\mathrm{OH}] = \frac{J_{\mathrm{HONO}} \cdot [\mathrm{HONO}]}{\frac{k_{\mathrm{NO+OH}} \cdot J_{\mathrm{NO_2}} \cdot [\mathrm{NO_2}]}{[\mathrm{O_3}] \cdot k_{\mathrm{NO+O_3}}} + k_{\mathrm{HONO+OH}} \cdot [\mathrm{HONO}]}. \tag{11.21}$$

Here, the reaction rate coefficients of Sander et al. (2011b) are used (Appendix D). The mean temperature inside the cloud was assumed to be 240 K, which corresponds to the temperature at flight altitude given by the aircraft sensors. The reaction rate coefficients result in $k_{\mathrm{NO+O_3}} = 5.965 \cdot 10^{-15}$ cm^3 molec^{-1} s^{-1}, $k_{\mathrm{HONO+OH}} = 7.386 \cdot 10^{-12}$ cm^3 molec^{-1} s^{-1}, $k_{\mathrm{NO+OH+M}} = 4.390 \cdot 10^{-12}$ cm^3 molec^{-1} s^{-1}.
The photolysis frequencies of HONO and NO_2 are derived with the quick Tropospheric Ultraviolet and Visible (TUV) Radiation model calculator (`http://cprm.acd.ucar.edu`) assuming an overhead O_3 column of 250 DU. The surface albedo is set to 1 in order to account for the high reflectivity of optically thick clouds. Furthermore, the latitude, longitude, and altitude are specified for each cloud penetration event. The simulated photolysis frequencies of J_{HONO} and $J_{\mathrm{NO_2}}$ are given in Table 11.4.

It has to be noted that these simulated photolysis rates are valid for cloud-free situations. According to simulations by Madronich (1987), the total actinic flux and consequently the photolysis frequency can be enhanced by a factor of up to five at the top edge of a cloud. The photolysis frequency of NO_2 inside a cloud is enhanced by a factor of approximately 2.5 as compared to the cloud-free value. The enhancement of J_{HONO} might be less than for J_{NO_2}, since the two molecules absorb at different wavelength ranges (Brasseur et al., 2002). HONO absorbs in the UV wavelength range whereas NO_2 absorbs in the visible wavelength range. Furthermore, light in the UV is more absorbed than light in the visible wavelength range. Brasseur et al. (2002) states that the ratio of cloudy to cloud-free air for J_{HCHO} results in 2 for the same scenario where the J_{NO_2} ratio yields 2.5. Since HCHO and HONO absorb at a comparable wavelength region, a cloud enhancement of the actinic flux by a factor of 2 may equally apply for both species. However, possible uncertainties in the photolysis frequencies of HONO and NO_2 almost cancel out, since they are divided by each other in Equation 11.21.

The inferred NO VMRs range between 0.48 and 3.47 ppb and the Leighton ratio ranges between 3.68 and 8.65, depending on the number of the penetration event (Table 11.4). The mean in situ NO VMR inside the cloud system measured by Heue et al. (2014) results in 1.48±1 ppb with several sharp peaks up to mixing ratios of 4 to 5 ppb. Thus, for the penetration events 1 to 3 the NO mixing ratios determined in this study are comparable to the mixing ratios observed by Heue et al. (2014). The penetration events 4 and 5 show much larger NO_2 mixing ratios and thus larger NO mixing ratios than for the penetration events 1 to 3.

Heue et al. (2014) estimated a production rate of approximately $5 \cdot 10^{25}$ NO molecules per flash based on NO VMRs simulated with the CAABA box model and based on the observed mean lightning density of 6.3 flashes/(100 km^2 h). They further concluded that a lightning density of approximately 6 flashes/(100 km^2 h) is sufficient to explain the observed NO VMRs of 1.48 ppb inside the cloud. Figure 11.32 shows the flash density calculated for region 2 using the registered flashes from Figure 11.28a. A maximum flash density of approximately 8 flashes/(100 km^2 h) is observed during the flight.

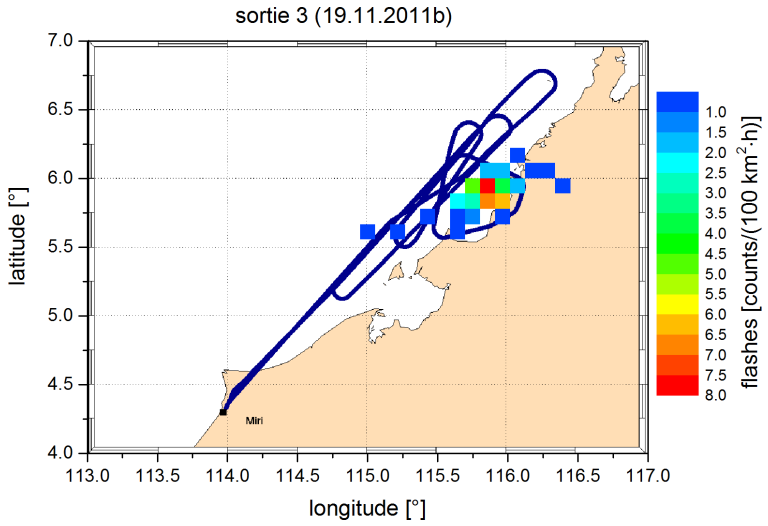

Figure 11.32: Flash density in flashes per 100 km^2 and hour for region 2 calculated using the registered flashes from Figure 11.28a.

The calculated OH concentrations range between 0.29 to 4.09 $\cdot 10^7$ molec cm^{-3}, which correspond to VMRs between 0.49 and 6.86 ppt (Table 11.4). The OH concentration estimated by Heue et al. (2014) is 1.5 $\cdot 10^7$ molec cm^{-3}, or 2.3 ppt at flight altitude. It has to be noted that for this estimation

additional HONO sources are omitted, such as outgassing during freezing according to:

$$NO_2 + HO_2 + M \longrightarrow HO_2NO_2 + M \quad (11.22)$$

$$HO_2NO_2 + \text{aerosol} \longrightarrow HONO + H_2O, \quad (11.23)$$

possibly leading to an underestimation of the inferred OH concentration. Furthermore, only one production term and two loss terms are assumed for OH but in reality several production and loss terms for OH exist. However, model studies with the CAABA box model by Heue et al. (2014) even result in larger OH VMRs of 4.8 ppt inside the cloud.
In the following, the OH concentrations inferred inside the Cb cloud are compared to OH concentrations typically observed in the remote atmosphere. Airborne measurements of OH were, for example, performed during the PEM-Tropics B campaign in the remote tropical Pacific region between March and April 1999 (Tan et al., 2001). Four geographical regions were selected and the mean OH VMRs were determined for three altitude ranges ($<$ 2 km, 2–8 km, and $>$ 8 km). The mean OH VMR for altitudes smaller than 2 km ranged between 0.10 and 0.24 ppt for the four different geographical Pacific regions, respectively. At altitudes between 2 and 8 km, OH ranged between 0.20 and 0.23 ppt, and for altitudes higher than 8 km, the mean OH VMRs ranged between 0.23 and 0.32 ppt for the four regions, respectively.
Obviously, the OH concentrations inside the cloud system estimated in this study are strongly enhanced in comparison to typical ambient OH concentrations for example observed in the remote Pacific region.

Table 11.4: Estimation of the OH concentration at flight altitude for the five cloud penetration events observed during sortie 3 on 19.11.2011.

	event 1	event 2	event 3	event 4	event 5
time [UTC]	08:30-08:33	08:41-08:46	08:48-08:55	09:09-09:12	09:29-09:33
altitude [km]	11.97	12.60	12.60 km	12.60	12.91
latitude [°N]	6.20	5.95	6.01	5.96	5.94
longitude [°E]	115.69	115.59	115.56	115.46	115.64
O_3 VMR [ppt]	37.5	37.2	57.9	37.8	36.3
O_3 concentration [10^{11} molec cm^{-3}]	2.36	2.22	3.43	2.24	2.06
J_{HONO} [10^{-3} s^{-1}]	2.57	2.32	2.10	1.62	0.92
J_{NO_2} [10^{-3} s^{-1}]	11.82	10.74	9.75	7.61	4.52
NO concentration [10^9 molec cm^{-3}]	2.87	7.70	9.49	20.7	19.2
NO VMR [ppt]	481	1290	1589	3472	3224
Leighton ratio	8.40	8.65	4.77	5.69	3.68
OH concentration [10^6 molec cm^{-3}]	**40.92**	**10.36**	**7.55**	**3.48**	**2.92**
OH VMR [ppt]	**6.86**	**1.72**	**1.26**	**0.58**	**0.49**

Table 11.5 summarises the results of this study and of Heue et al. (2014). The VMRs inferred in this study are compatible with the results of Heue et al. (2014), indicating that HONO and NO_x should be observable inside all lightning-affected thunderstorm clouds.
However, for a further study, at least simultaneous measurements of NO are needed. Model simulations for example with the CAABA box model (Sander et al., 2011a) are further required in order to estimate the source strengths of the different trace gases. The inferred source strengths can then be combined with the flash density to estimate the lightning emission factor according to Heue et al. (2014). Since the HCHO VMRs observed in the MBL strongly vary for different locations, for future aircraft missions, it is further recommended to sample the boundary layer prior to measurements in the outflow of the Cb cloud.

Table 11.5: Comparison of the HCHO, NO_2, HONO, NO, and OH VMRs inferred in this study and determined by Heue et al. (2014). The flash density is calculated using the number of registered flashes according to the World Wide Lightning Location Network (`http://wwlln.net`). The VMR ranges correspond to the five cloud penetration events observed in this study whereas the VMRs of Heue et al. (2014) correspond to the average VMRs.

	HCHO VMR [ppb]	NO_2 VMR [ppb]	HONO VMR [ppt]	NO VMR [ppb]	OH VMR [ppt]	max. flash density [flashes/(100 km^2 h)]
this study	0.22–0.46	0.05–0.92	26–48	0.48–3.47	0.49–6.86	8
Heue et al. (2014)	0.47	0.21	37	1.48	2.3	11

12. Summary and Outlook

12.1 Summary

The present thesis examines the influence of BrO and IO (i.e. product gases of marine VSLS) on the photochemistry of the troposphere and stratosphere. Furthermore, the thesis investigates the abundance of different atmospheric trace gases (HCHO, CHOCHO, NO_2, and HONO) and their implications for the photochemistry in a region of strong convective transport.
Airborne DOAS (Platt and Stutz, 2008) measurements were performed aboard the DLR-Falcon research aircraft during the SHIVA field campaign at Miri, Borneo, in November and December 2011. The sixteen different flights covered legs in the boundary layer as well as in the free troposphere to study the emissions and sources of several trace gases that are crucial for the composition of the TTL and stratosphere, such as halogenated sources gases, halogen and nitrogen oxides, or the intermediates of hydrocarbon oxidation.
The main challenge of the remote-sensing DOAS method is the retrieval of trace gas concentrations from the measured differential slant column densities (dSCDs), since a photon path length has to be attributed to each measurement. This is particularly complicated in a cloudy atmosphere. The complex atmospheric conditions in tropical regions with both horizontally and vertically varying clouds pose a further challenge to airborne DOAS measurements.
In order to overcome these difficulties, cloud sensitivity studies are performed using the 3D radiative transfer model McArtim (Deutschmann et al., 2011). It is found that the influence of clouds on the measured O_4 SCDs is smaller for the UV than for the visible wavelength range. For a flight altitude of 0.1 km and an aerosol profile with an AOT of 0.1, which is typical for the region of Borneo, a cloud distance larger than approximately 15 km for the UV and approximately 30 km for the visible wavelength range will have no significant effect on the measured O_4 SCDs. This cloud distance increases with increasing flight altitude and decreases with increasing aerosol load. Changes in the surface albedo, the observer geometry, or the cloud properties, such as the cloud extinction or SSA, only lead to minor changes in the cloud distance that is relevant for O_4 SCDs.
The images recorded with the webcam installed aboard the Falcon aircraft are used to further assess the cloud cover during the SHIVA campaign. The position of the mini-DOAS FOV within the webcam images is determined via the maximum correlation coefficients between the DOAS intensity and the colour values of the webcam images. This tool gives a first idea as to which part of the webcam image is most relevant for the analysis of the data set. Next, the distance between the aircraft and the clouds is estimated using a triangulation method. The inferred distance can be used as an input for 3D radiative transfer calculations to support the interpretation of cloudy conditions.
Within this thesis, two different methods are applied to infer trace gas mixing ratios from the measured dSCDs: The O_4 scaling method and a modified optimal estimation method. The O_4 scaling method is based on the fact that the profile of O_4 only depends on meteorological parameters, such as temperature and pressure, and can therefore be used as a proxy for the light path length. Optimal estimation is an inversion method described by Rodgers (2000) and is implemented in the HEIPRO retrieval code developed by (Yilmaz, 2012). The retrieval procedure consists of two steps, i.e. the non-linear inversion of the aerosol extinction profile and the linear inversion of the different

trace gas profiles. In general, the VMRs inferred with the HEIPRO retrieval are more sensitive to heterogeneous cloud layers, whereas the VMRs inferred using the O_4 scaling method have less systematic artefacts than the VMRs inferred using the HEIPRO retrieval. The O_4 scaling method leads to more robust results than the HEIPRO retrieval since uncertainties in the RT partly cancel out. Therefore, the O_4 scaling method is used for the further data analysis. In the following, the major scientific findings of this thesis are summarised.

Abundance of the halogenated product gases IO and BrO over Borneo

An atmospheric picture of IO is deduced from the measurements, which is highly consistent with previous studies. IO was detected during several sorties of the Falcon aircraft with VMRs ranging between 0.5 and 1.5 ppt in the MBL, which is in good agreement with previous IO measurements in the global marine boundary layer (e.g. Mahajan et al., 2012; Großmann et al., 2013; Lampel, 2014; Prados-Roman et al., 2014). The measurements provide further evidence that IO is transported from the MBL to the mid-troposphere by shallow convection, often in coincidence with elevated concentrations of CO. The IO loss processes act on time scales which are comparable to the time scales of vertical and horizontal transport, preventing IO from being transported over a wider horizontal range or from even reaching the upper troposphere or stratosphere. These loss processes include for example the self-reaction of IO, leading to the formation of new particles by polymerisation (e.g. Hoffmann et al., 2001; O'Dowd et al., 2002) or the reaction with organic aerosols and rain drops (e.g. Murphy et al., 1997; Gilfedder et al., 2008). This finding confirms that the iodine concentrations in the TTL and lowermost stratosphere are low, i.e. inorganic iodinated product gases do not reach the stratosphere in significant amounts. According to Butz et al. (2009) and Tegtmeier et al. (2013), these low iodine concentrations are too low to be significant for stratospheric ozone loss. Information regarding the vertical distribution of IO is sparse. Only few measurements of vertical profiles of IO exist (e.g. Dix et al., 2013), which are confirmed by the profiles inferred in this thesis. The concentrations of IO measured during the field work for this thesis already have a significant influence on the oxidation capacity of the troposphere through the catalytic destruction of ozone and changes in the ratio $[HO_2]/[OH]$ (e.g. Saiz-Lopez et al., 2012; Dix et al., 2013).

During all sorties of the Falcon aircraft, the inorganic product gas BrO did not exceed the detection limit of approximately 2 ppt in the MBL. This upper limit of 2 ppt is in agreement with previous measurements, which typically report BrO VMRs between 0.5 and 3 ppt in the MBL (e.g. Read et al., 2008; Lampel, 2014). These measurements are also consistent with estimations of the Br production and loss fluxes, indicating that BrO and Br would be hardly detectable around Borneo since they rapidly react for example with HCHO, forming the stable compounds HOBr or HBr. Thus, rather organic bromine species are likely transported from the MBL to the stratosphere since inorganic brominated PGs do not reach the stratosphere in significant amounts. The SHIVA observations of brominated VSLS as well as long-lived halons give weak indications of enhanced source gas injection of organic bromine into the stratosphere in the region around and above Borneo relative to other tropical regions (Sala et al., 2014b).

Constraining the oxidation capacity over Borneo

During the different sorties of the Falcon aircraft, the VOC oxidation products CHOCHO and HCHO were frequently detected at larger concentrations than background concentrations in the MBL. These observations indicate an efficient photochemistry since HCHO and CHOCHO are mainly produced by the oxidation of VOCs emitted from the tropical forests in Borneo and also from anthropogenic sources. The air masses encountered during the SHIVA campaign were occasionally influenced by anthropogenic sources, such as emissions from ships, from oil and gas production facilities along the coastline of Borneo, or emissions due to industrial fossil fuel combustion on land. The ratio of CHOCHO and HCHO shows whether the emission sources of both species are of biogenic or of

anthropogenic origin.
For the first time, the chemical transport models TOMCAT (Hossaini et al., 2013) and CCATT-BRAMS (Hamer et al., 2013) were validated against measurements of HCHO. The comparison shows that the emission scenarios of VOCs are too large in both models and have to be adjusted. A decrease in the VOC concentrations has several consequences for the atmospheric oxidation capacity, leading for example to changes in the O_3 production or concentration of OH (e.g. Lelieveld et al., 2008). This can further affect the formation of secondary organic aerosol (SOA), which is closely coupled with the oxidation of VOCs (Pöschl et al., 2010; Ehn et al., 2014).

Composition of air masses in a meso-scale convective cloud system

The outflow of a meso-scale convective cell was investigated for a large thunderstorm cloud north of Brunei. Inside the Cb cloud, HONO, HCHO, NO_2, and CO show enhanced VMRs as compared to ambient air. The simultaneous enhancement of HCHO and CO suggests a rapid uplift of polluted air originating from near the surface to the upper troposphere. The fraction of MBL air contained in the convective outflow of $f_{\mathrm{conv}} \approx 0.19$ is in good agreement with previous measurements (e.g. Bertram et al., 2007). An enhancement of NO_2 and HONO inside the cloud is due to in situ production by lightning and photochemistry. According to model simulations by Heue et al. (2014), a lightning density of approximately 6 flashes/(100 km^2 h) is sufficient to explain the enhanced NO VMRs inside the Cb cloud. In this study, a maximum flash density of approximately 8 flashes/(100 km^2 h) was observed during the flight.
The OH concentration inside the cloud is estimated assuming that HONO, NO, and OH are in a photo-stationary state. The calculated OH VMRs range between 0.49 and 6.86 ppt. The OH concentrations inside the cloud system estimated in this study are enhanced by a factor of approximately 50 to 200 % relative to typical ambient OH concentrations observed in the remote Pacific region (Tan et al., 2001).
This indicates that flashes are an important source of NO_x and HO_x, which further leads to an enhanced chemical production of HONO. This confirms the findings of earlier studies (e.g. Dix et al., 2009; Heue et al., 2014). The precise knowledge of lightning-induced NO_x and HO_x is essential for the understanding of the atmospheric oxidation capacity as well as the lifetime of trace gases, which are destroyed by reactions with OH (e.g. Schumann and Huntrieser, 2007).

12.2 Outlook

In addition to instrumental improvements recommended for future applications (Appendix E), several open scientific issues remain for airborne DOAS applications, such as aboard the DLR-HALO aircraft or the NASA Global Hawk or during balloon-borne measurements. Regarding the different findings summarised in the previous section, the following issues could be examined.

a) The abundance of reactive halogen species (BrO and IO) in the upper troposphere and stratosphere should be examined in order to further confirm that inorganic bromine and iodine hardly make it from the MBL into the TTL and lowermost tropical stratosphere. Furthermore, their possible loss processes should be determined.

b) The oxidation capacity over tropical rain forests can be further analysed using simultaneous measurements of NO, NO_2, HCHO, CHOCHO, isoprene, OH, and HO_2. This comprehensive dataset can possibly explain the current discrepancies between HO_x measurements and models, which occur under low NO_x conditions, especially in the presence of large amounts of VOCs as in tropical rain forests (e.g. Lelieveld et al., 2008; Kubistin et al., 2010; Edwards et al., 2013).

c) In order to improve the knowledge about the production of NO_x and HONO in thunderstorm clouds simultaneous measurements of at least NO_x, HONO, OH, and HO_2 are required. Model

simulations are needed in order to estimate the source strengths of the different trace gases. It is further recommended to sample the boundary layer prior to measurements in the outflow of the Cb cloud in order to analyse the fraction of near surface air that is contained in the convective outflow.

In general, these issues require a multi-sensor and model approach in order to take advantage of the synergy of simultaneously measured data in combination with model studies. This approach can improve the data interpretation, leading to a more comprehensive picture of the atmosphere.

A. Appendix A: Flight by flight analysis

In this chapter the 16 different sorties of the SHIVA aircraft campaign are specified. The sorties started in Miri, Sarawak, except for the days with a refuelling stopover, which were in Sandakan, Sabah (26.11.2011), Tawau, Sabah (07.12.2011, 09.12.2011) and Singapore (11.12.2011). The flight tracks of the 16 different sorties are shown in Figure A.1 and A.2. For the analysis, only data points with an RMS smaller than $1{\cdot}10^{-3}$ are used.

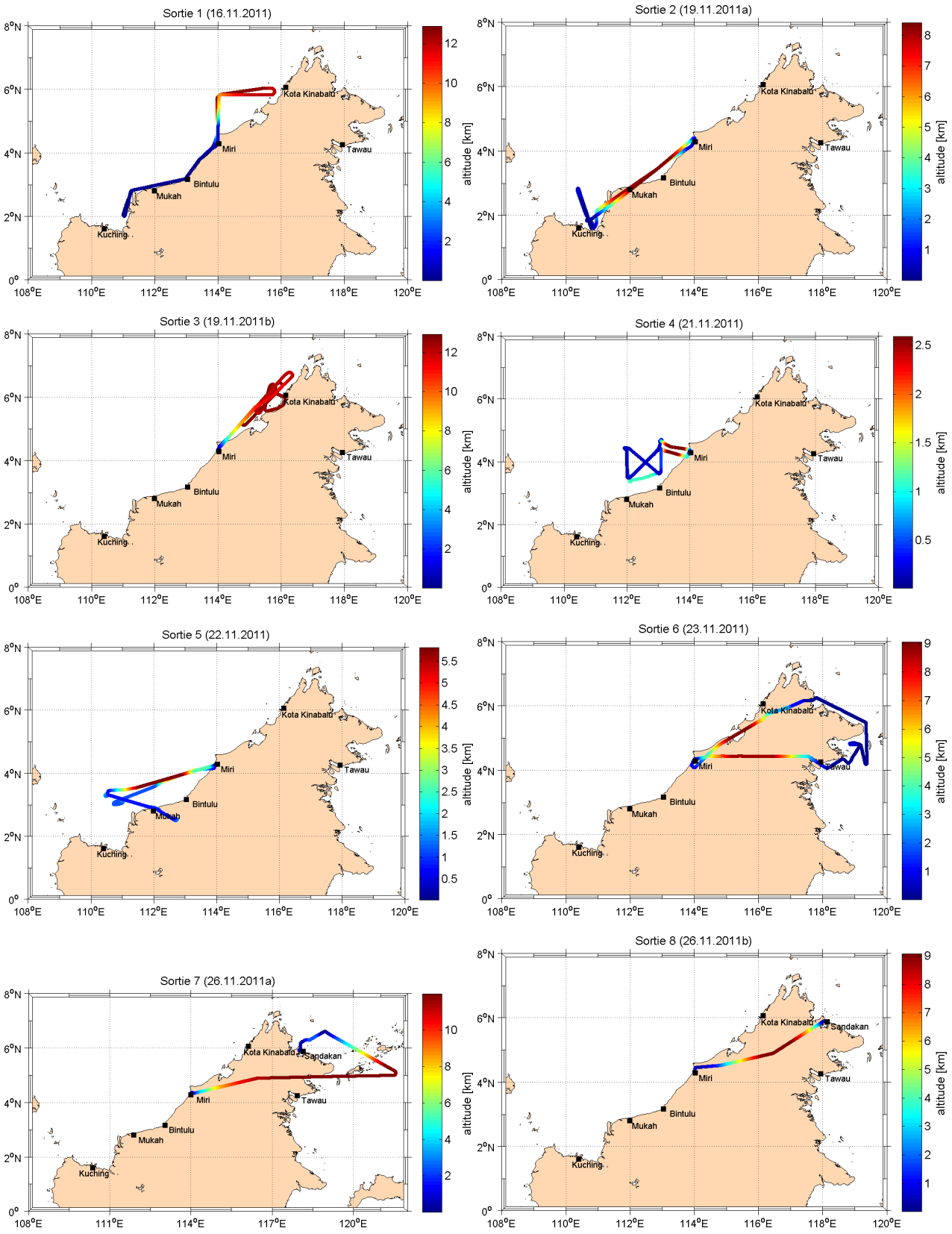

Figure A.1: Flight tracks of the different sorties during the SHIVA aircraft campaign in November 2011. The colour bar indicates the altitude in kilometres.

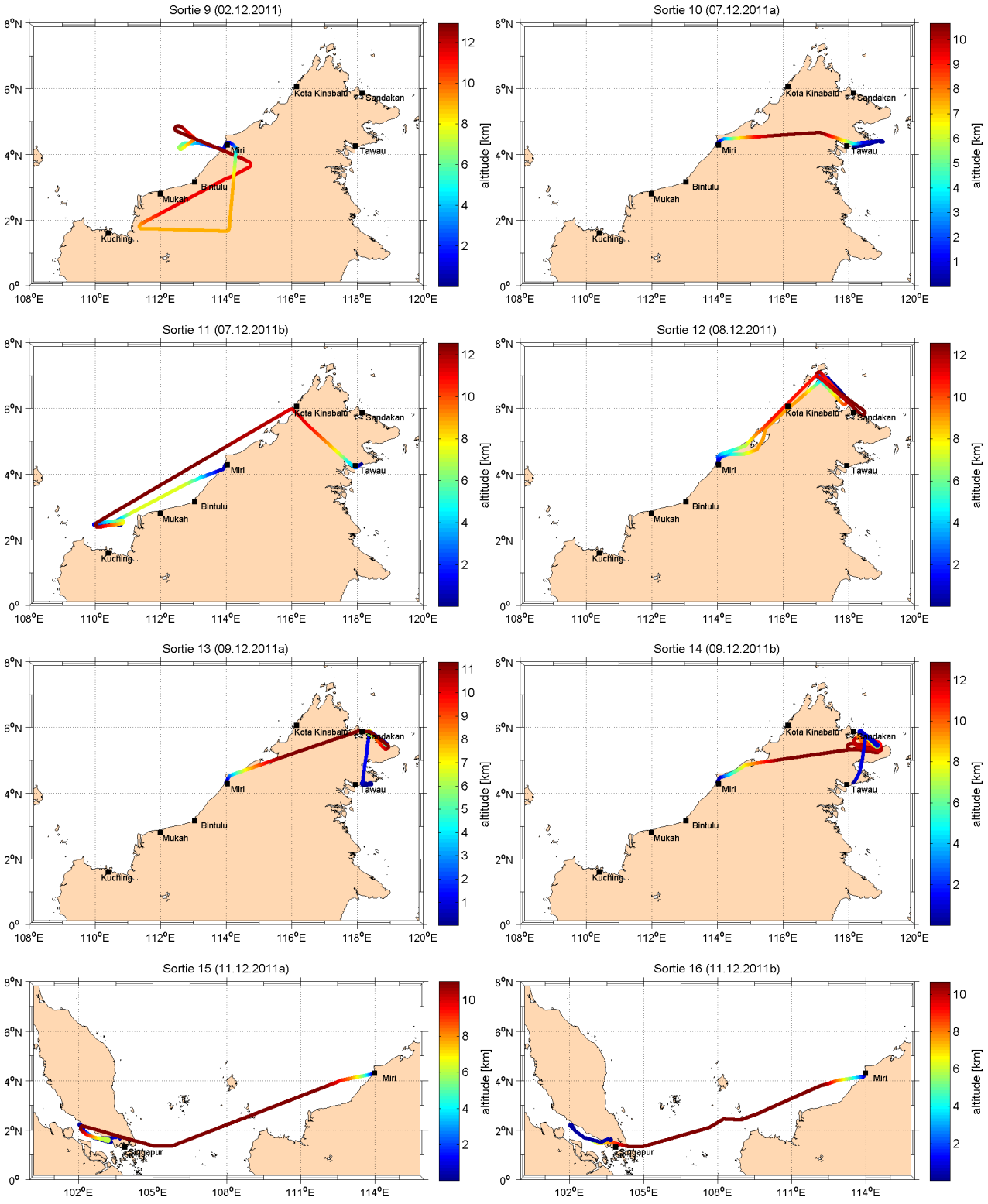

Figure A.2: Flight tracks of the different sorties during the SHIVA aircraft campaign in December 2011. The colour bar indicates the altitude in kilometres.

Sortie 1 (16 November 2011)

The first measurement flight was a combination of a survey in the MBL and upper troposphere and lower stratosphere (UT/LS). The Falcon aircraft cruised from Miri in a southwestward direction

along the coast of Borneo passing Bintulu to Kuching Bay on a constant flight altitude of 100 m. In Kuching Bay (05:15 UTC) the aircraft turned and headed back towards Miri on the same way, however on different flight levels (160 m, 320 m, 640 m and 1000 m). Back over Miri, the aircraft climbed northward flying a loop with a maximum altitude of 12.8 km. During the flight lots of clouds were present over the land as well as over the sea including some smaller cumulonimbus clouds. Along the coastline several ships were passed (Figure 11.20). Figure A.6 shows the DOAS results of this sortie.

Sortie 2 (19 November 2011 a)

This sortie mainly took place in Kuching Bay where the Falcon aircraft passed the RV Sonne several times at different flight levels (110 m, 300 m, 530 m, 750 m). The transfer to Kuching Bay and back was on a constant flight altitude of approximately 8.4 km and 8.1 km, respectively. Figure A.7 shows the DOAS results of this sortie.

Sortie 3 (19 November 2011 b)

The outflow of a meso-scale convective cell was investigated on the afternoon of 19 November 2011, when a large thunderstorm cloud north of Brunei was probed. The Falcon aircraft penetrated the outflow of the cumulonimbus cloud several times at a flight altitude between 11.3 and 12.9 km. In Hamer et al. (2013) the meteorology and transport processes of this sortie are discussed in detail. Figure A.8 shows the DOAS results of this sortie.

Sortie 4 (21 November 2011)

This sortie was a tracer release experiment (Lagrangian experiment). The perfluorocarbon tracer (C6F12) had been released a few hours before the take-off of the Falcon aircraft from the RV Sonne. Before sampling the tracer, the aircraft passed the RV Sonne. After the rendezvous, the tracer plume was sampled during five cross-sections on three different flight levels (160 m, 490 m, 1130 m). Figure A.9 shows the DOAS results of this sortie. At 07:37 UTC an offshore oil production platform was passed (Figure A.3).

Figure A.3: Webcam image of an offshore oil production platform at a latitude of 4.39 °N and a longitude 111.63 °E at 07:37 UTC on 22 November 2011 (mini-DOAS webcam attached at the second window on the portside of the Falcon aircraft).

Sortie 5 (22 November 2011)

This sortie was the second part of the tracer release experiment from sortie 4. The tracer plume has been expected slightly south of Bintulu elongated in east-western direction and lifted up to a level

of about 1300 m. The location where the maximum concentrations of C6F12 were expected was probed three times. After having passed the C6F12 plume for the first time, the Falcon aircraft flew a short section over land. Figure A.10 shows the DOAS results of this sortie. At 04:10 UTC the aircraft encountered a biomass burning event at the portside of the aircraft (Figure A.4). However, this event can not be directly observed in the DOAS data.

Figure A.4: Webcam image of a biomass burning event close to Bintulu at 04:10 UTC on 22 November 2011 (mini-DOAS webcam attached at the second window on the portside of the Falcon aircraft).

Sortie 6 (23 November 2011)

During the transfer from Miri to Semporna the aircraft was flying at 8.8 km and descended from Semporna remaining at 930 m, 600 m and 320 m for two minutes, respectively. The aircraft then cruised along the north-eastern coast of Borneo at a constant flight altitude of 100 m. Seaweed was clearly visible in the region around Semporna (Figure 6.7). The cloud coverage during the low level part of 100 m was about 6/8 with lots of cumulus clouds. At approximately 04:20 UTC the aircraft had to climb up for 10 minutes, because the contact to the radar was lost. At the most easterly tip of northern Borneo very light rain was observed for only a few minutes. After having passed Sandakan, the aircraft slowly ascended from 100 m until 9.1 km where rain forests, lakes and the Mount Kinabalu were visible over the land on the starboard side of the Falcon. The aircraft stayed at 9.1 km until the descend to Miri airport. Figure A.11 shows the DOAS results of this sortie. NO_2 and CHOCHO are enhanced at 03:52 UTC and 05:19 UTC when the city of Tawau and Sandakan was passed, respectively.

Sortie 7 (26 November 2011 a)

This sortie was a survey flight characterising the tropospheric background composition east of Borneo during a persisting easterly wind phase. During the first flight part to the most easterly point of this sortie the Falcon aircraft stayed on constant high flight altitude of 12 km. During this time the aircraft flew above some lower convective systems. From this point to the position of the RV Sonne a detailed profile was carried out with a descent rate of 1500 feet/minutes down to an altitude of 100 m. Unfortunately, the RV Sonne was not encountered at the planned position. During the last flight part to Sandakan, the mission was to find the perfluorocarbon tracer PMCH (C7F14) that had been emitted several hours before on the RV Sonne. The aircraft stopped at the airport of Sandakan for refuelling. Figure A.12 shows the DOAS results of this sortie. Since the descent between 05:25 and 05:55 UTC is over the ocean with a quite stable roll angle ($\overline{\alpha} = -0.2 \pm 0.5$) with a cloud cover below the aircraft and an almost blue sky above, this descent might be representative for a background air flight. Therefore, it is used in the retrieval procedure (Chapter 10.2.2).

Sortie 8 (26 November 2011 b)

During this sortie it was planned to sample the released perfluorocarbon tracer PMCH (C7F14). Due to a technical problem with the Falcon aircraft, the aircraft had to return directly from Sandakan to Miri. The return flight was at a high altitude of 9.1 km with a slow descent down to Miri airport. Over land there were some high reaching clouds. Furthermore, a thunderstorm was predicted to be in this region. The sortie started very late at an SZA of 78 ° and ended at an SZA of 85 °. As the RMS becomes large during twilight, the data set is not shown here.

Sortie 9 (2 December 2011)

The main objectives during this sortie were measurements of the vertical transport of VSLS by deep convection as well as a detailed vertical profile over ocean in the south-western area of Miri mainly over land. Several tops of convective clouds (turbulence) were penetrated at 9 km, 11.1 km and 12.25 km. Thin cirrus clouds could be observed above the convective clouds. The aircraft then climbed to an altitude of 12.3 km for detailed profile down to Miri. South-east of Miri biomass burning sources were visible. However, as the return flight to Miri was during the twilight, the biomass burning event could not be observed with the mini-DOAS instrument. Figure A.13 shows the DOAS results of this sortie. Possible enhancements of HCHO and HONO within convective clouds can be observed. Since HCHO and HONO as well as CHOCHO and NO_2 are close to or below the detection limit during the whole flight, this sortie is not further analysed.

Sortie 10 (7 December 2011 a)

This sortie was a survey flight looking for elevated VSLS concentrations in the north-eastern part of Borneo. The Falcon aircraft was flying from Miri over land in the direction to Tawau at an altitude of 10.7 km. Over the land there was a uniform closed cloud coverage up to several thousand metres. Then the aircraft descended slowly (1500 ft/min) down to 100 m. From the most eastward point to Tawau the aircraft stayed at an altitude of 100 m. The Falcon landed in Tawau for refuelling. Unfortunately, for this sortie no standard aircraft parameters from the Falcon dataset are available due to a recording problem. Figure A.14 shows the DOAS results of this sortie.

Sortie 11 (7 December 2011 b)

This sortie was designed to probe the upper tropospheric chemical composition downstream of the Malaysian part of Borneo as well as again the Kuching Bay region in detail where the RV Sonne found the most elevated VSLS mixing ratios during its whole cruise. From Tawau down to Kuching Bay the aircraft was flying at an altitude of 12.7 km. In Kuching Bay a detailed profile was measured (1500 ft/min) with some additional altitude steps. There were no active convective systems, but closed cloud coverage up to several thousand metres in the northern part of the flight track, especially over the land. Figure A.15 shows the DOAS results of this sortie.

Sortie 12 (8 December 2011)

The main objectives of this sortie were measurements of the vertical transport of marine emissions by shallow and deep convection as well as sampling of marine emissions at the northern top of Borneo. The aircraft started in Miri flying at an altitude of 10 km to Kudat. The aircraft then descended down to 120 m flying several times back and forth between Kudat and Sandakan. Deep and shallow convection was visible in the measurement area and high level convective outflow was traversed multiple times. During the back transfer from Kudat to Miri smaller thunderclouds were penetrated several times. Figure A.16 shows the DOAS results of this sortie.

Sortie 13 (9 December 2011 a)

The first part of this flight started in Miri with a transfer to Sandakan at an altitude of 11.4 km. The Falcon aircraft then flew several times back and forth at different altitudes between 11.4 km down to 0.33 km along the north-eastern part of Borneo and landed in Tawau for refuelling. Only shallow convection was visible and a thin broken cloud deck was traversed at an altitude of approximately 2 and 5 km. Sea weed was clearly visible during the low level part as well as the sediment transport out of river deltas (Figure A.5).
Figure A.17 shows the DOAS results of this sortie. During the descent along the north-eastern part of Borneo (between 04:55 and 06:10 UTC) the IO and CHOCHO dSCDs are anti-correlated. Every time the mini-DOAS instrument is viewing towards the open ocean IO is elevated whereas for the viewing direction towards the land CHOCHO is elevated and IO decreases.

Figure A.5: Webcam images of sediment transport out of river deltas close to Sandakan on 9 December 2011 a.

Sortie 14 (9 December 2011 b)

The second part of this flight started in Tawau with a transfer to Sandakan at an altitude of approximately 1 km. The aircraft then ascended up to 12.6 km flying back and forth between Sandakan and the northern part of Borneo. During the return flight over land back to Miri the aircraft stayed at an altitude of 12.6 km. Several thunderstorm clouds were traversed during that flight. The sortie ended at 10:50 UTC at an SZA of 98 ° when the Sun had already set. As the RMS becomes large during twilight, the data is cut at 09:45 UTC. Figure A.18 shows the DOAS results of this sortie.

Sortie 15 (11 December 2011 a)

This sortie was a survey looking for elevated VSLS concentrations in the Strait of Malacca. The first part of the flight was a transfer from Miri to the west coast of Peninsula Malaysia along the north-western coast of Borneo at a high flight level. The aircraft then flew along the south-western coast of Peninsula Malaysia (Strait of Malacca) at a low flight level and landed in Singapore for refuelling. Unfortunately, only the first ascent ($\approx$ 20 min) is available due to a script error of the mini-DOAS instrument. Hence, the sortie is not shown here.

Sortie 16 (11 December 2011 b)

The second sortie on 11 December 2011 includes the return flight from Singapore back to Miri. During this sortie the Falcon aircraft flew at a low flight level along the Strait of Malacca and ascended up to 10.7 km for the transfer back to Miri. High convective systems were observed along

the coast of Borneo. The same thunderstorm system as in sortie 15 was probed. Figure A.19 shows the DOAS results of this sortie.

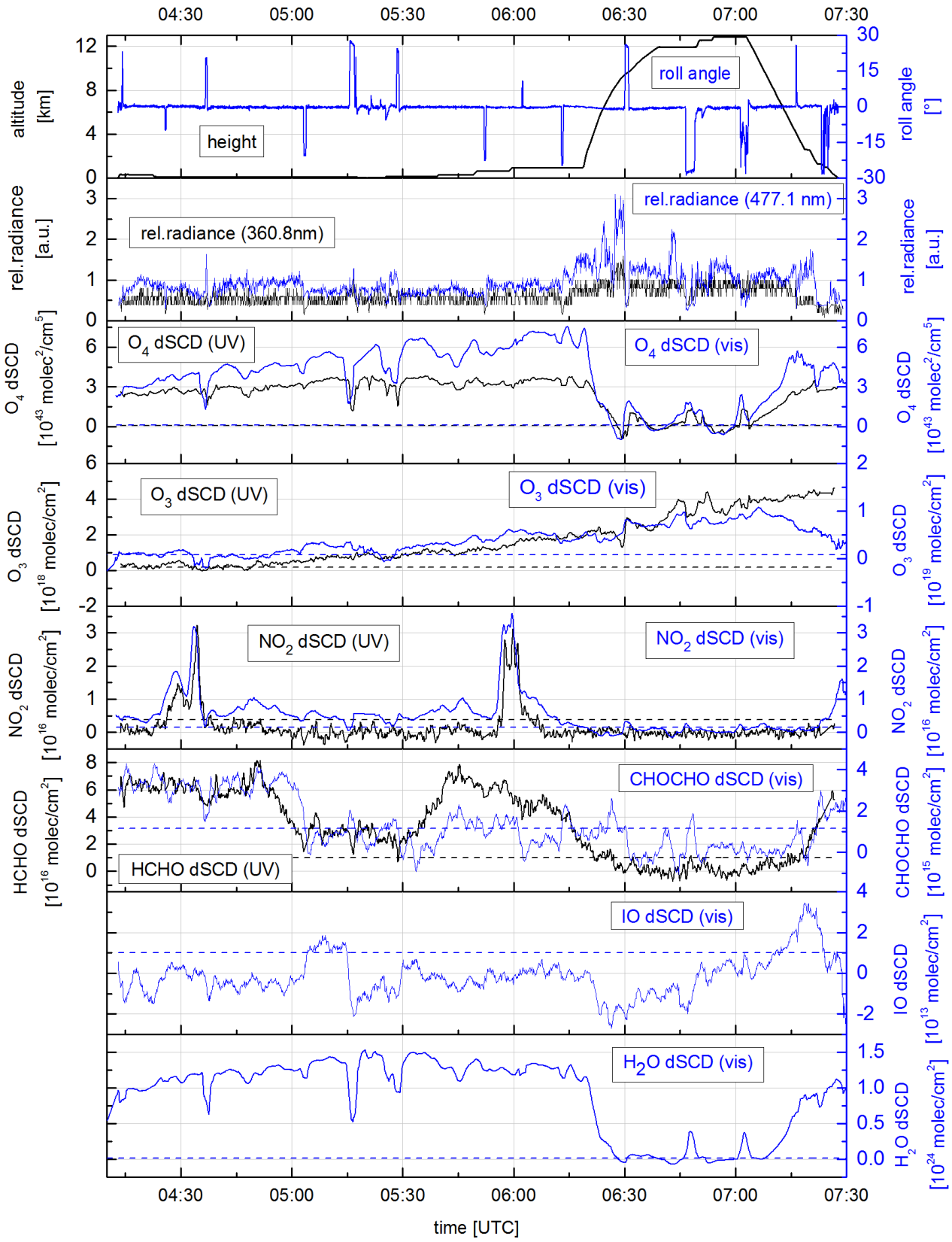

Figure A.6: Overview of the measured dSCDs during sortie 1 on 16 November 2011. The uppermost panel shows the altitude (black) and the roll angle (blue) of the Falcon aircraft. The dSCDs retrieved in the UV are represented by a black line and the dSCDs retrieved in the visible wavelength range by a blue line. The respective average detection limit (assumed to be 2 σ) is illustrated by dashed lines.

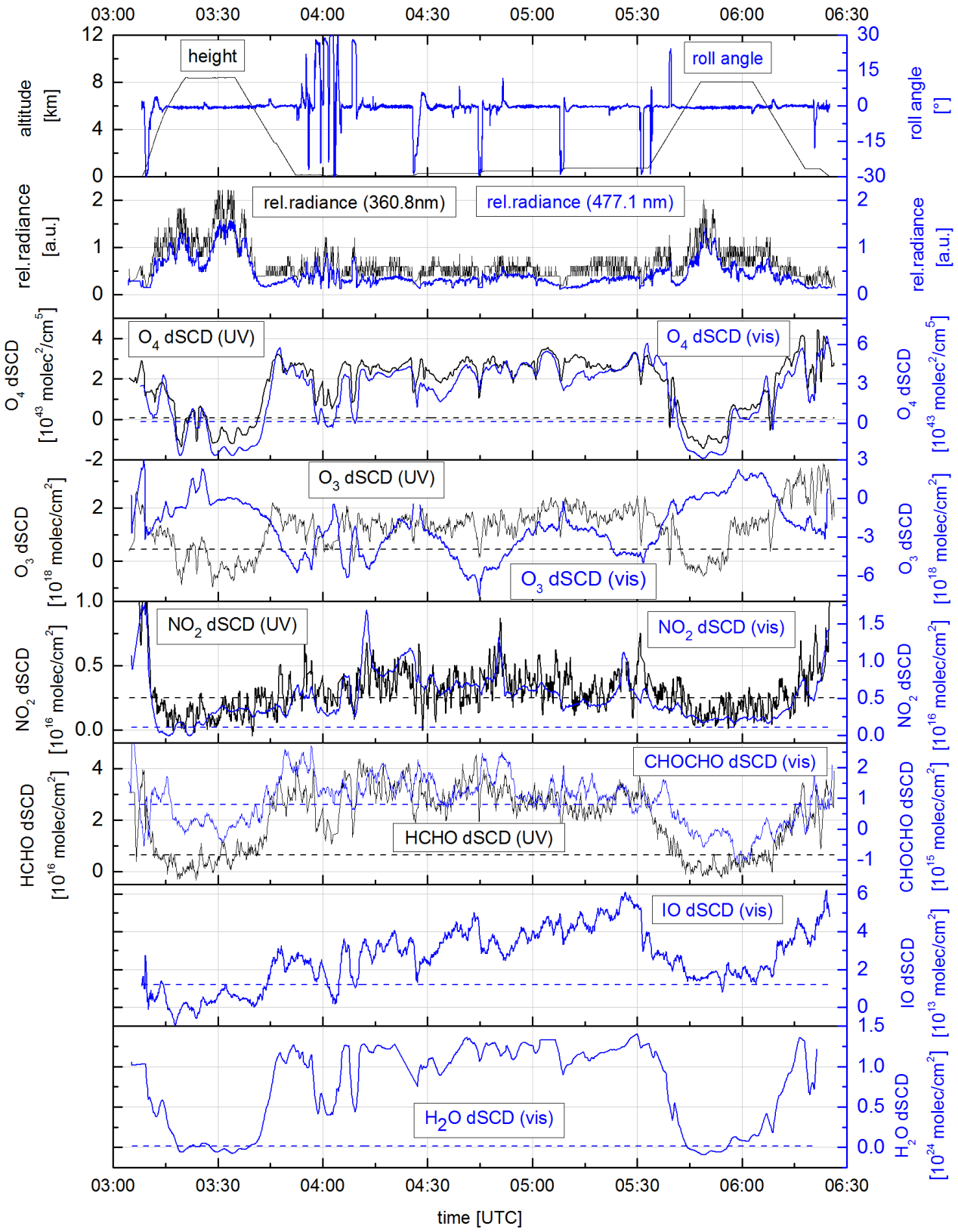

Figure A.7: Overview of the measured dSCDs during sortie 2 on 19 November 2011 a. The uppermost panel shows the altitude (black) and the roll angle (blue) of the Falcon aircraft. The dSCDs retrieved in the UV are represented by a black line and the dSCDs retrieved in the visible wavelength range by a blue line. The respective average detection limit (assumed to be 2 σ) is illustrated by dashed lines.

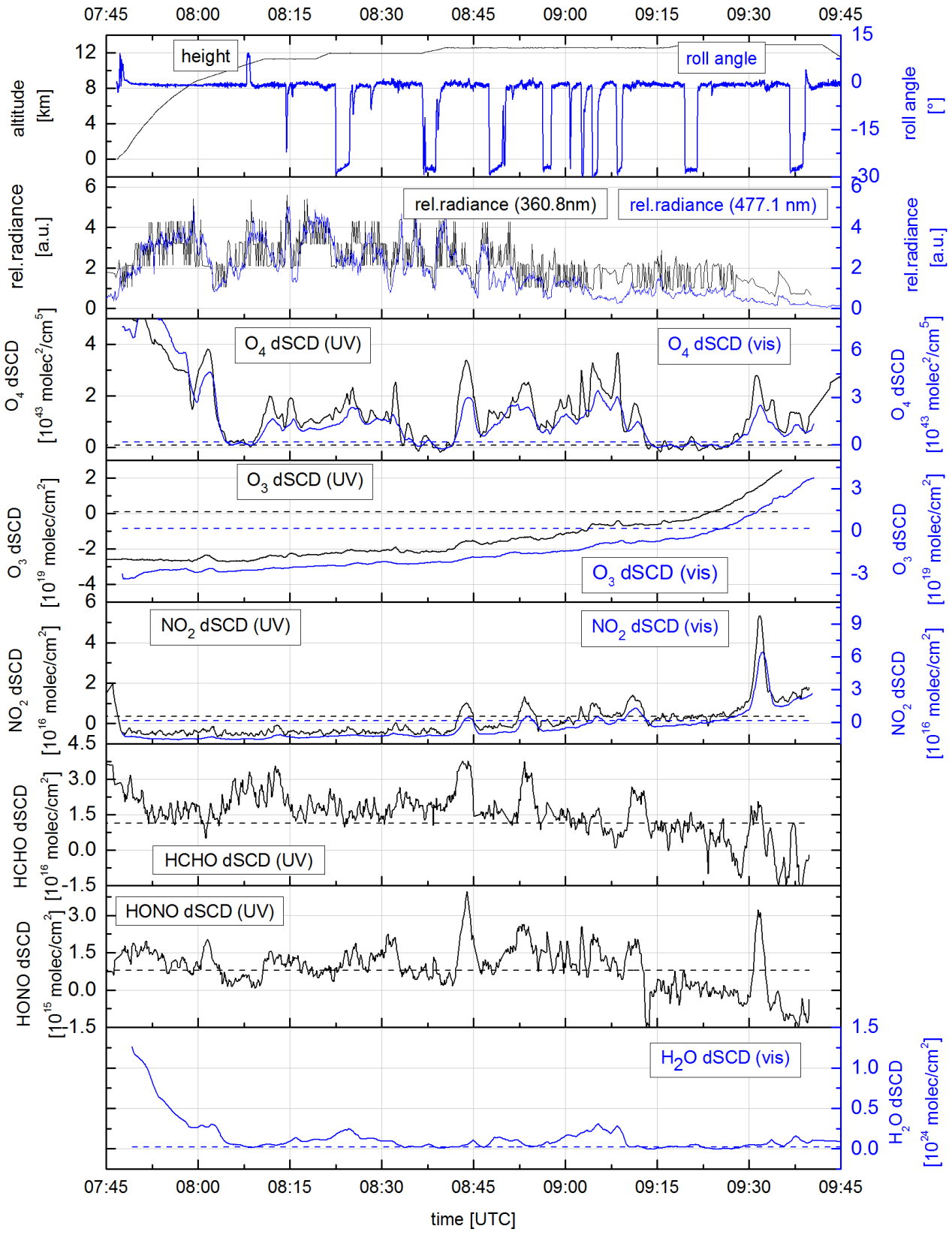

Figure A.8: Overview of the measured dSCDs during sortie 3 on 19 November 2011 b. The uppermost panel shows the altitude (black) and the roll angle (blue) of the Falcon aircraft. The dSCDs retrieved in the UV are represented by a black line and the dSCDs retrieved in the visible wavelength range by a blue line. The respective average detection limit (assumed to be 2 σ) is illustrated by dashed lines.

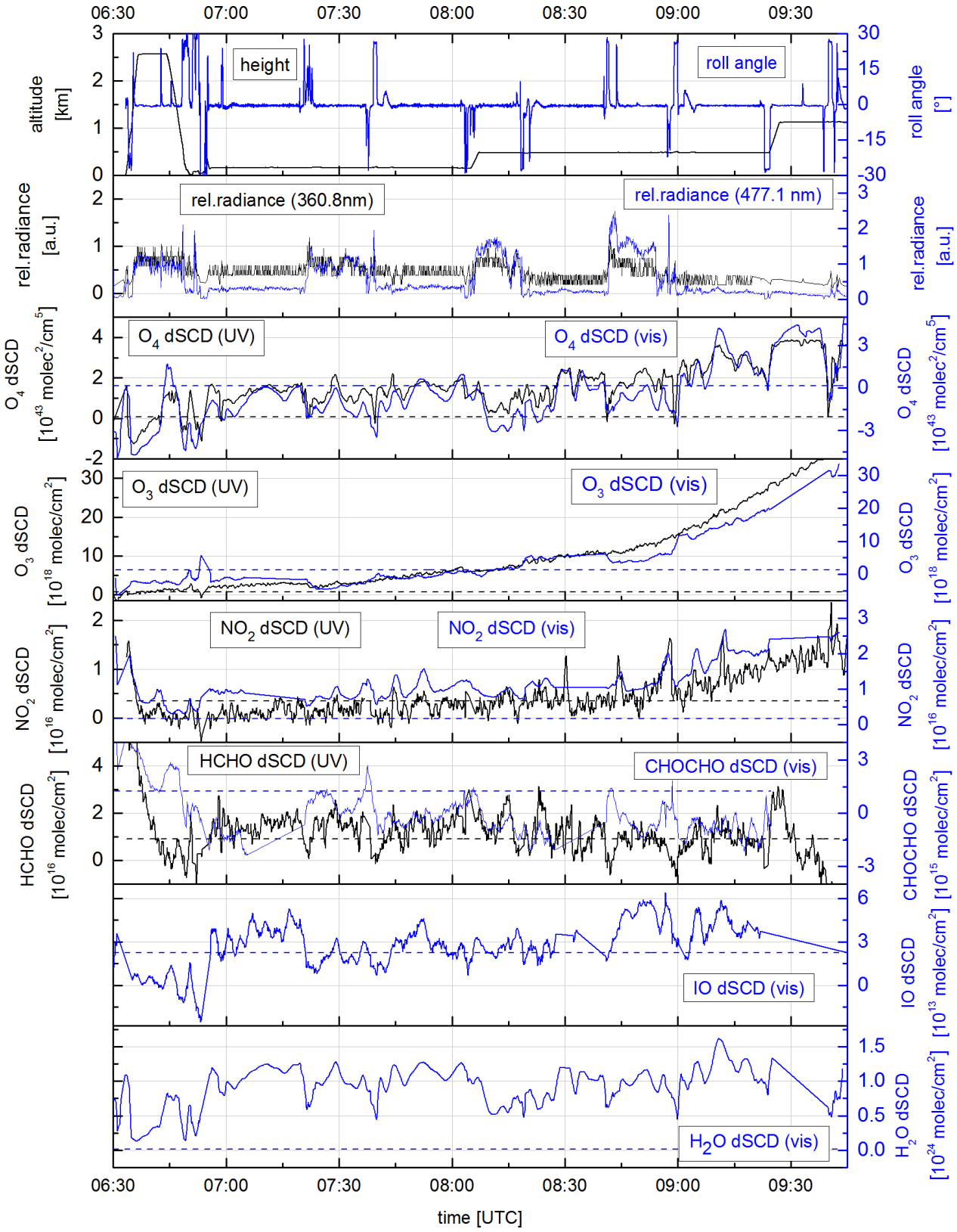

Figure A.9: Overview of the measured dSCDs during sortie 4 on 21 November 2011. The uppermost panel shows the altitude (black) and the roll angle (blue) of the Falcon aircraft. The dSCDs retrieved in the UV are represented by a black line and the dSCDs retrieved in the visible wavelength range by a blue line. The respective average detection limit (assumed to be 2 σ) is illustrated by dashed lines.

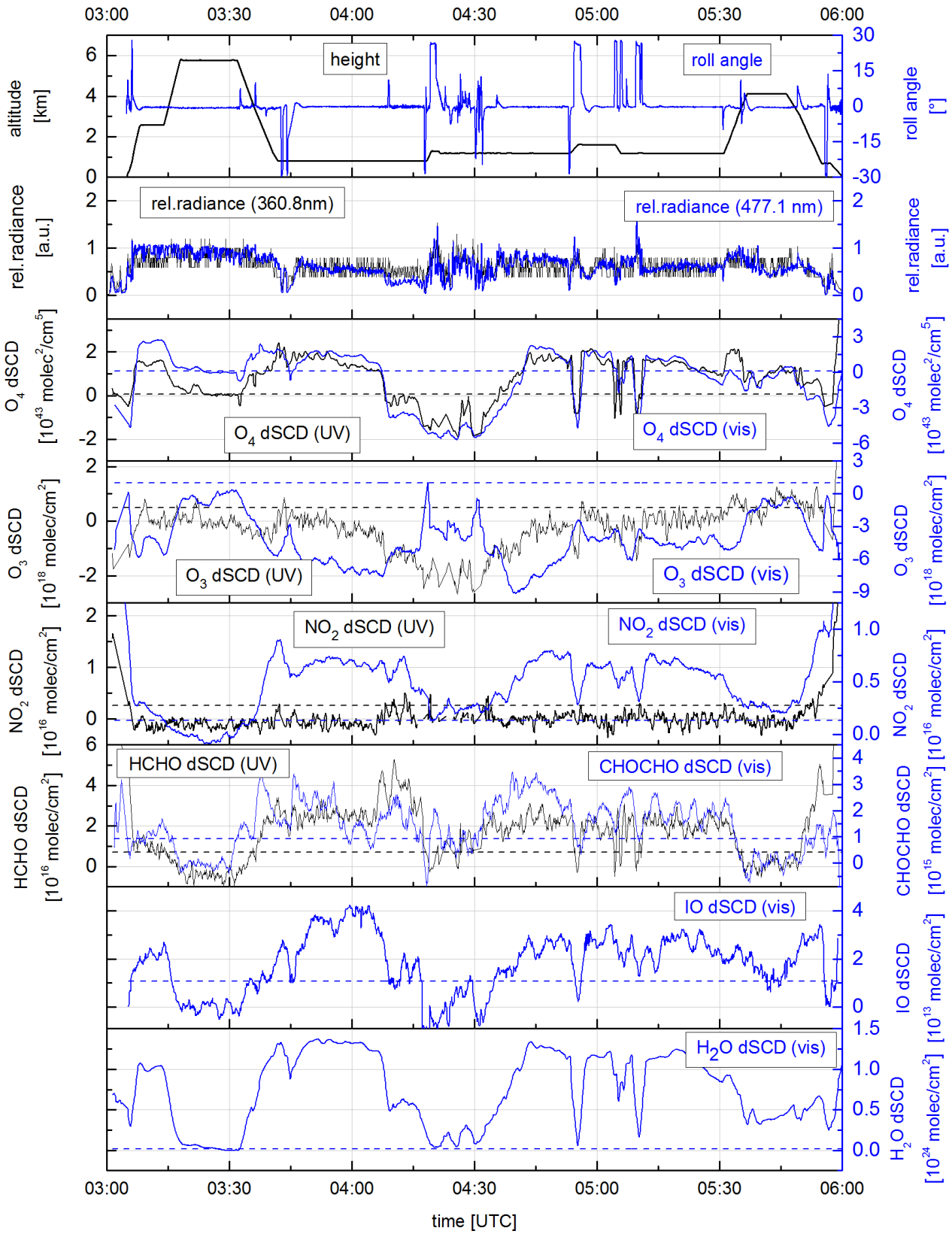

Figure A.10: Overview of the measured dSCDs during sortie 5 on 22 November 2011. The uppermost panel shows the altitude (black) and the roll angle (blue) of the Falcon aircraft. The dSCDs retrieved in the UV are represented by a black line and the dSCDs retrieved in the visible wavelength range by a blue line. The respective average detection limit (assumed to be 2 σ) is illustrated by dashed lines.

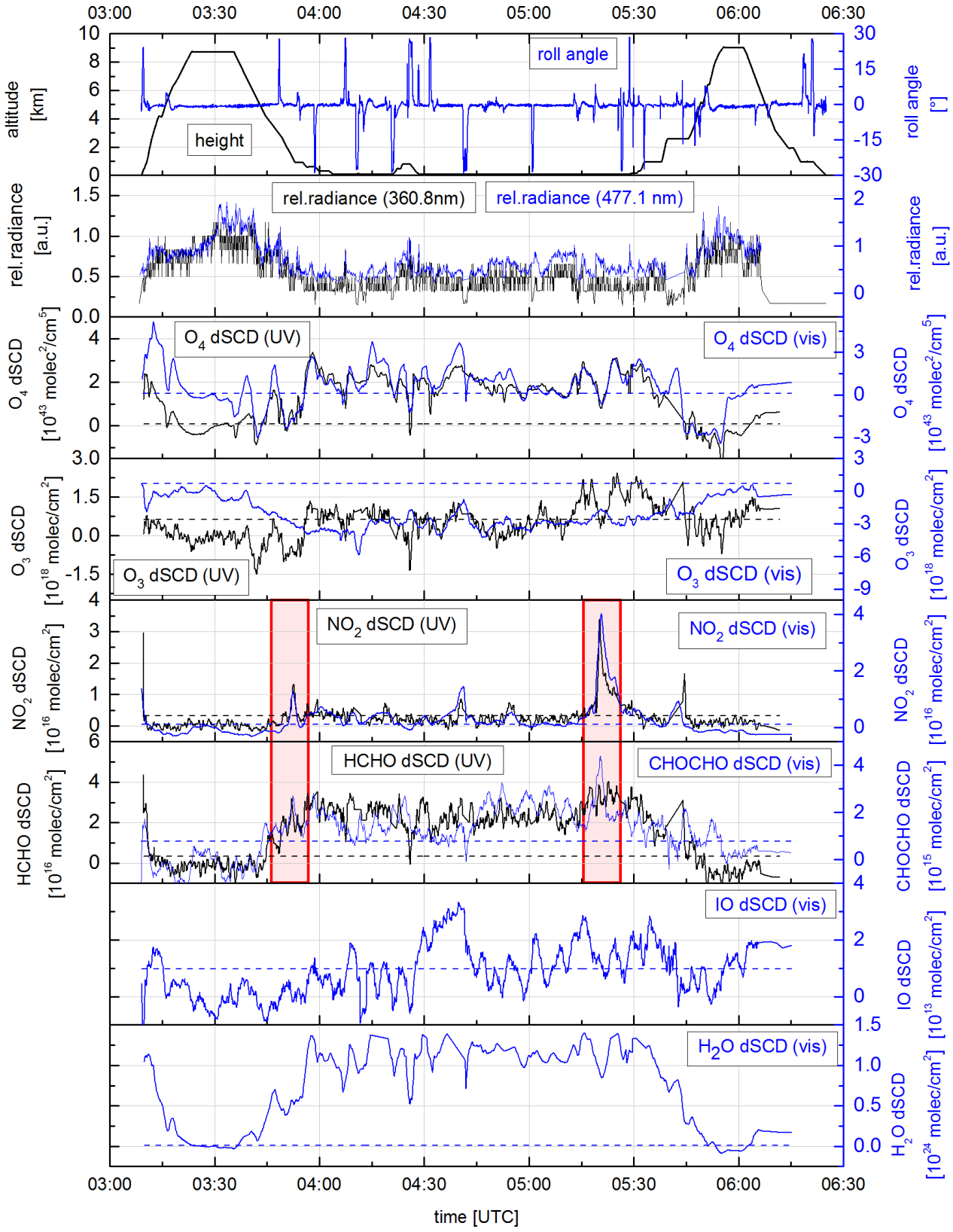

Figure A.11: Overview of the measured dSCDs during sortie 6 on 23 November 2011. The uppermost panel shows the altitude (black) and the roll angle (blue) of the Falcon aircraft. The dSCDs retrieved in the UV are represented by a black line and the dSCDs retrieved in the visible wavelength range by a blue line. The respective average detection limit (assumed to be 2 σ) is illustrated by dashed lines. The left red bar marks the location of the city of Tawau and the right red bar Sandakan.

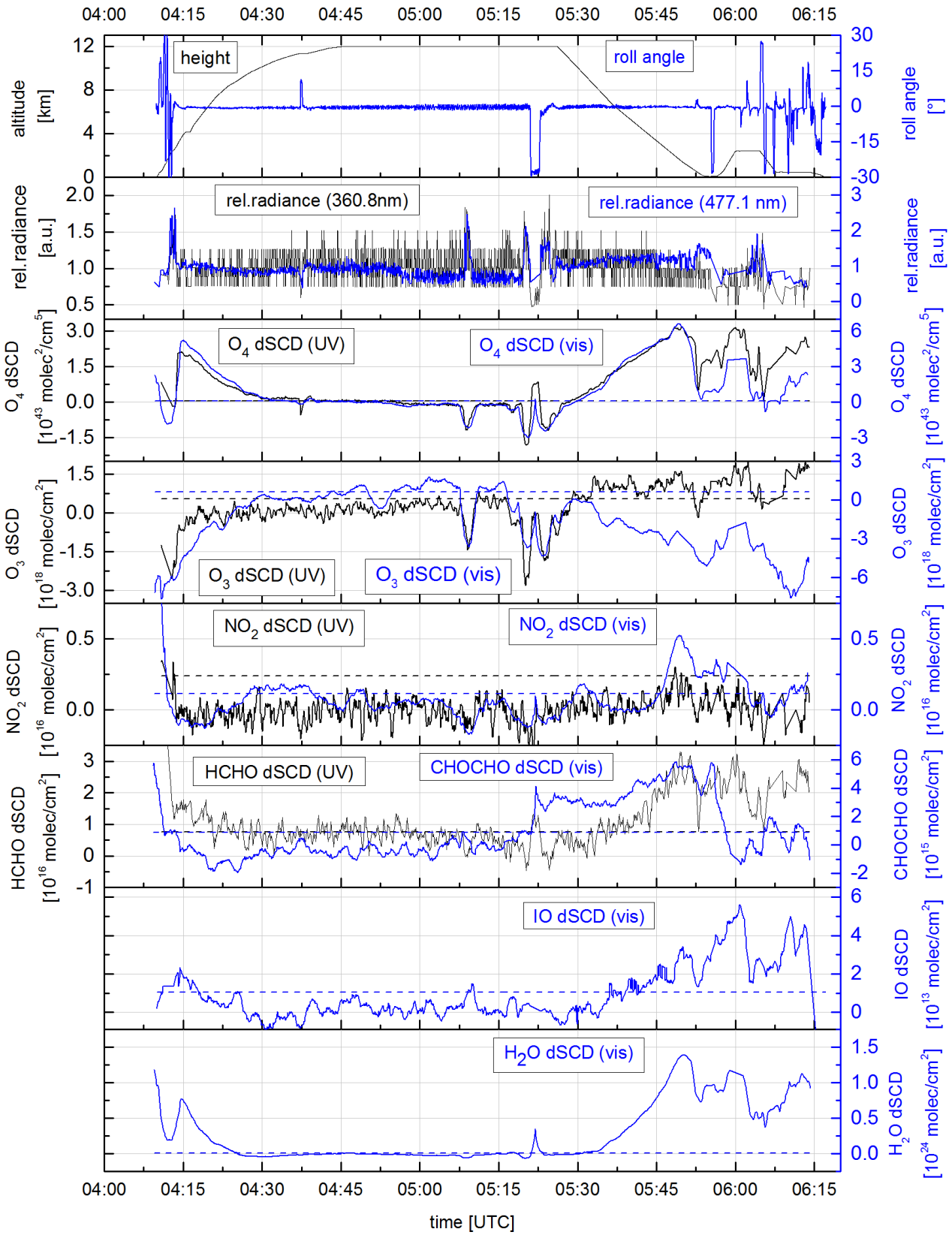

Figure A.12: Overview of the measured dSCDs during sortie 7 on 26 November 2011 a. The uppermost panel shows the altitude (black) and the roll angle (blue) of the Falcon aircraft. The dSCDs retrieved in the UV are represented by a black line and the dSCDs retrieved in the visible wavelength range by a blue line. The respective average detection limit (assumed to be 2 σ) is illustrated by dashed lines.

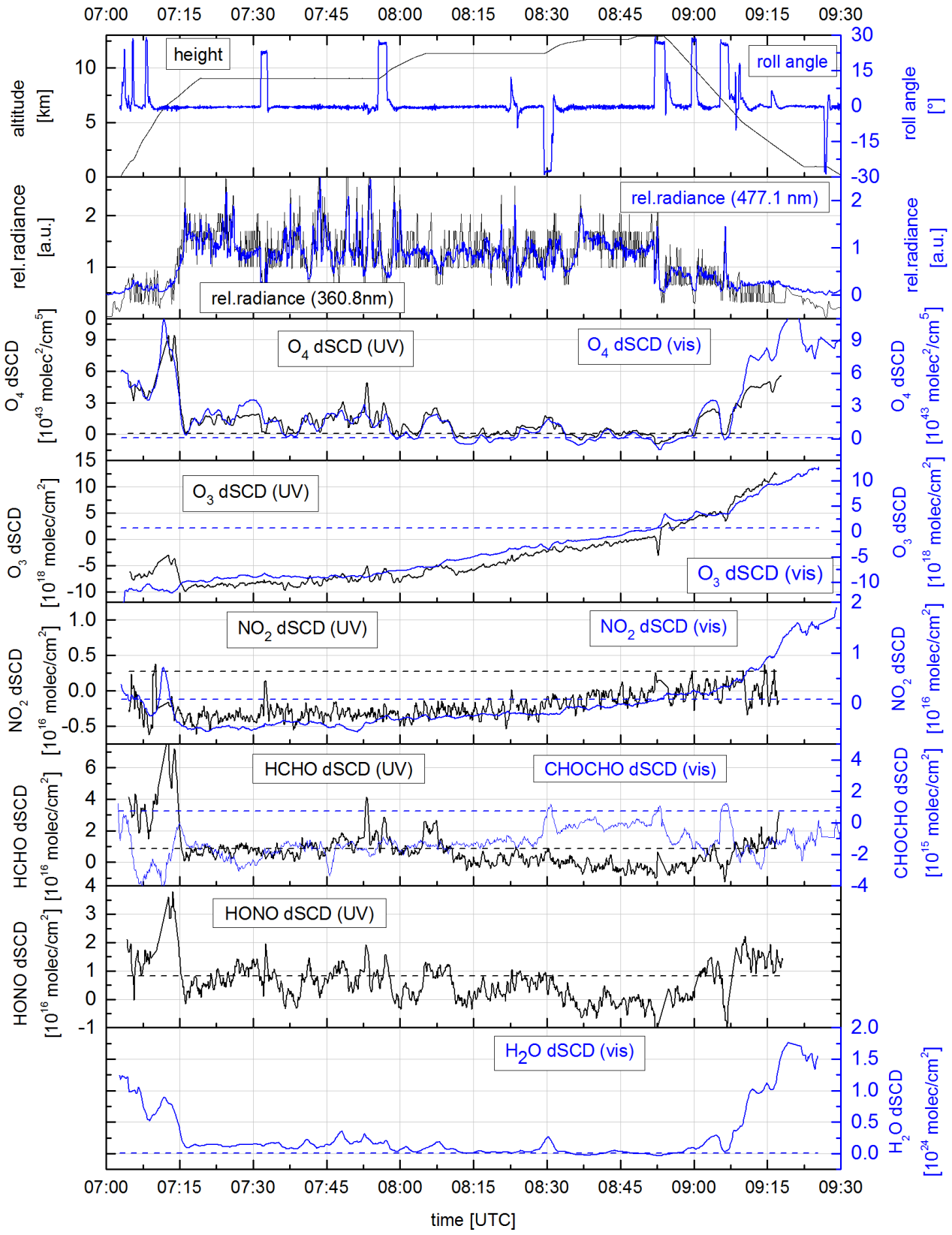

Figure A.13: Overview of the measured dSCDs during sortie 9 on 2 December 2011. The uppermost panel shows the altitude (black) and the roll angle (blue) of the Falcon aircraft. The dSCDs retrieved in the UV are represented by a black line and the dSCDs retrieved in the visible wavelength range by a blue line. The respective average detection limit (assumed to be 2 σ) is illustrated by dashed lines.

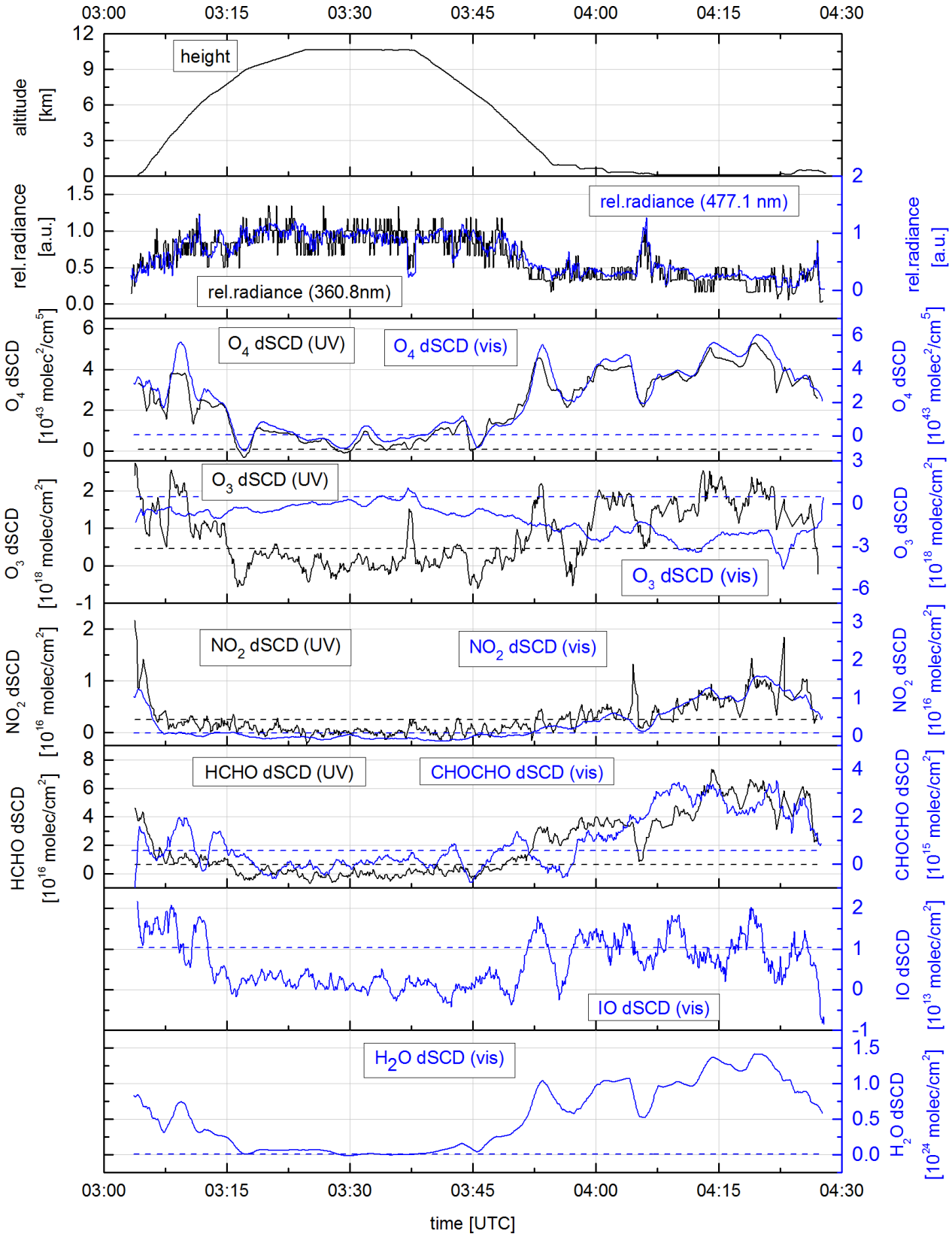

Figure A.14: Overview of the measured dSCDs during sortie 10 on 7 December 2011 a. The uppermost panel shows the altitude (black) and the roll angle (blue) of the Falcon aircraft. The dSCDs retrieved in the UV are represented by a black line and the dSCDs retrieved in the visible wavelength range by a blue line. The respective average detection limit (assumed to be 2 σ) is illustrated by dashed lines.

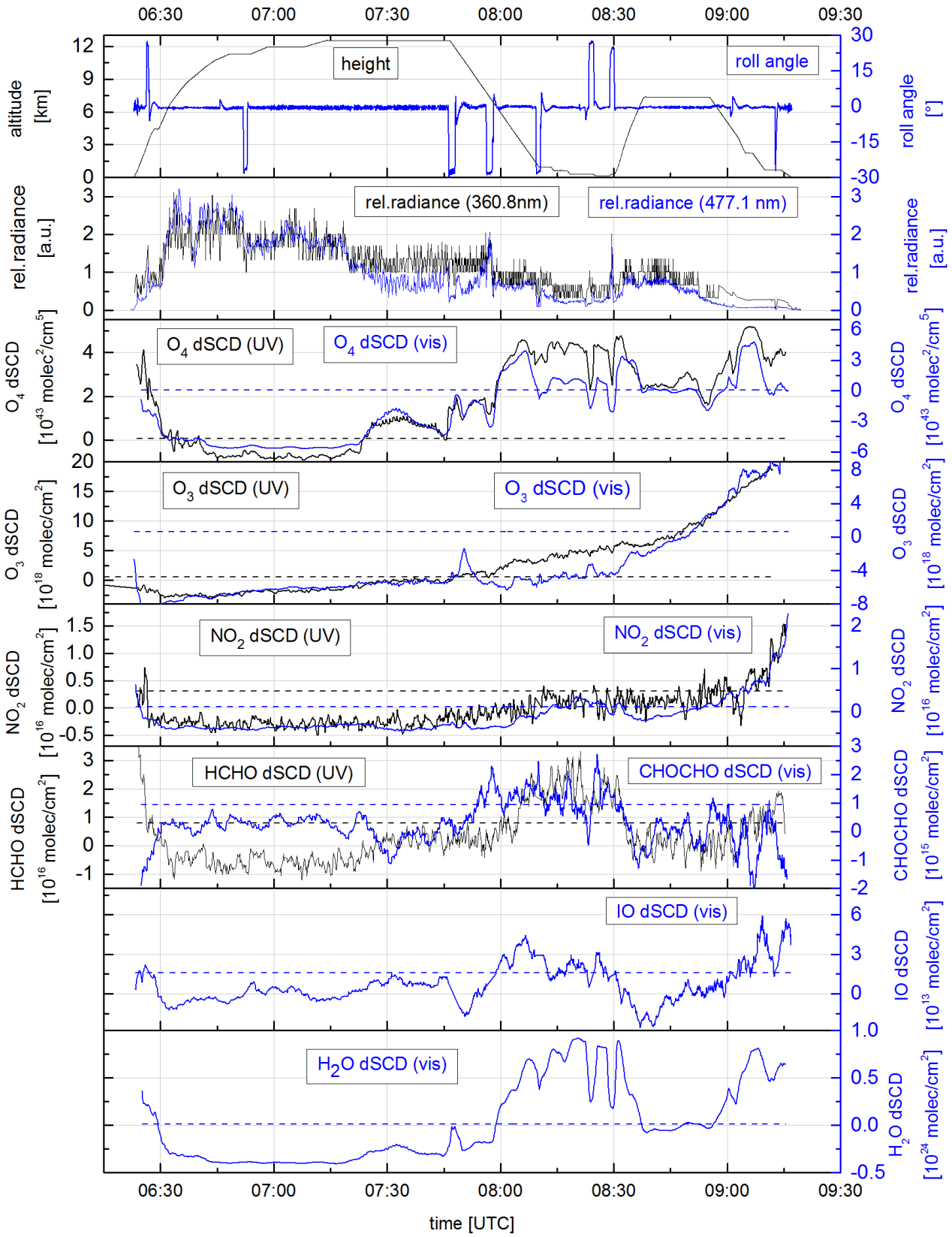

Figure A.15: Overview of the measured dSCDs during sortie 11 on 7 December 2011 b. The uppermost panel shows the altitude (black) and the roll angle (blue) of the Falcon aircraft. The dSCDs retrieved in the UV are represented by a black line and the dSCDs retrieved in the visible wavelength range by a blue line. The respective average detection limit (assumed to be 2 σ) is illustrated by dashed lines.

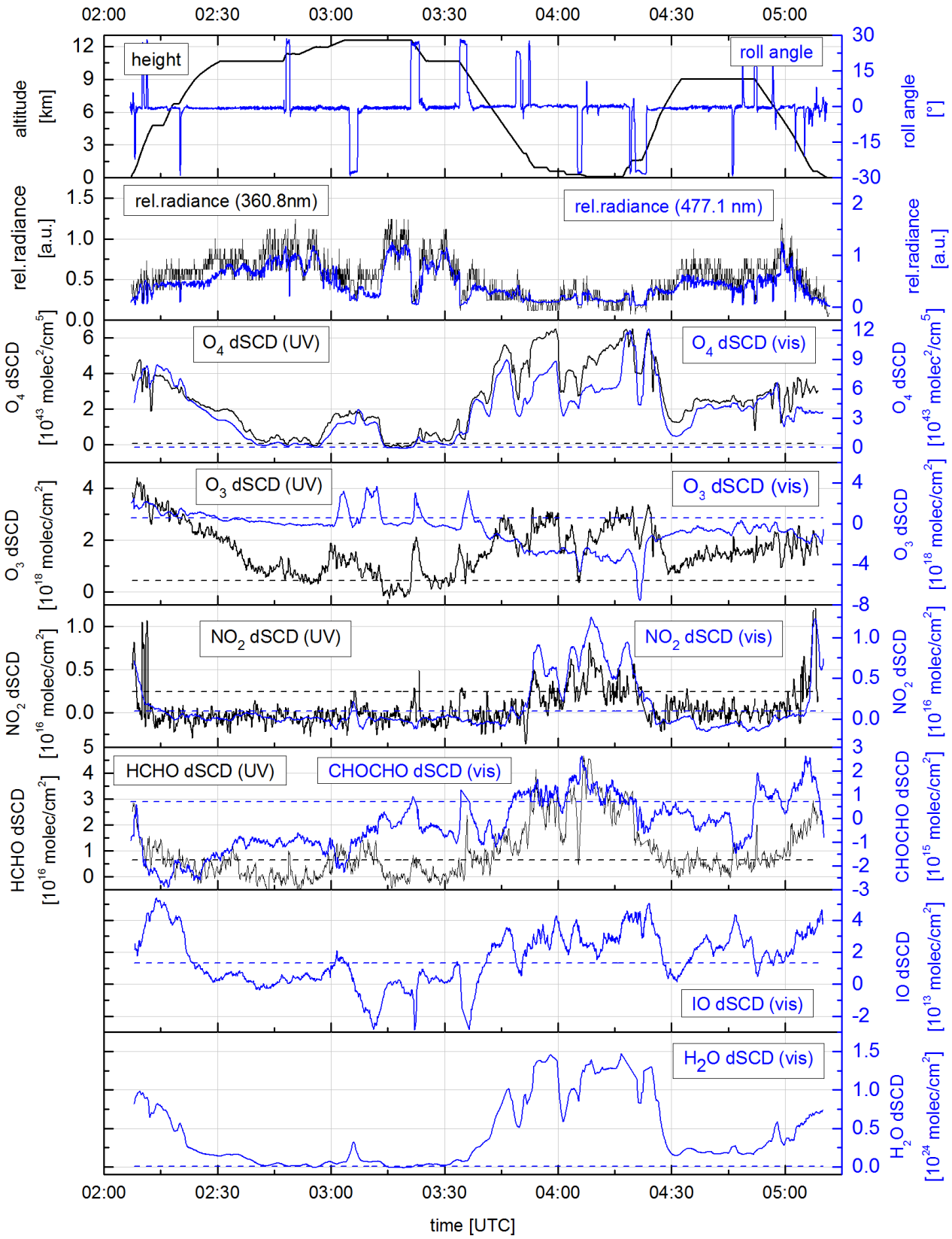

Figure A.16: Overview of the measured dSCDs during sortie 12 on 8 December 2011. The uppermost panel shows the altitude (black) and the roll angle (blue) of the Falcon aircraft. The dSCDs retrieved in the UV are represented by a black line and the dSCDs retrieved in the visible wavelength range by a blue line. The respective average detection limit (assumed to be 2 σ) is illustrated by dashed lines.

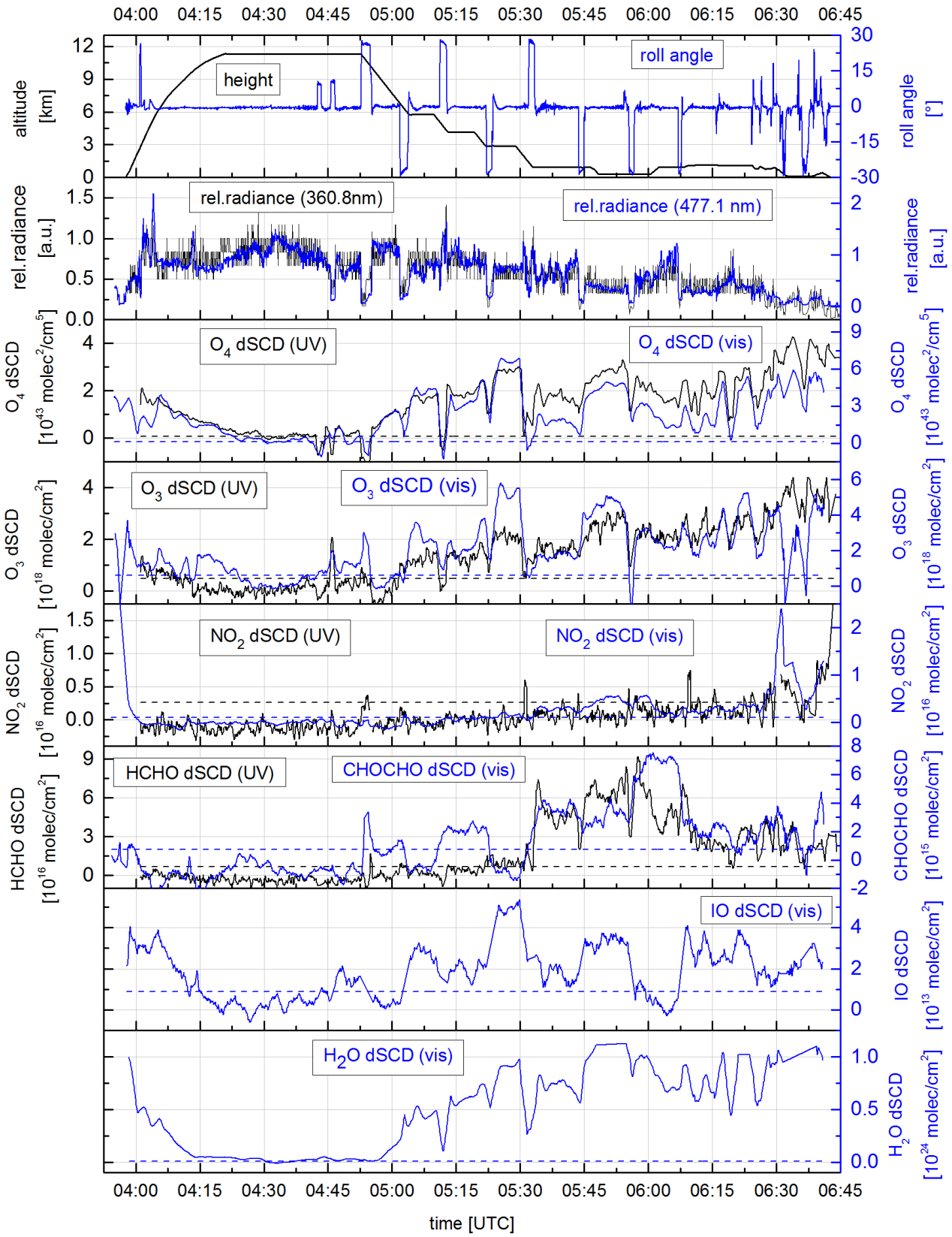

Figure A.17: Overview of the measured dSCDs during sortie 13 on 9 December 2011 a. The uppermost panel shows the altitude (black) and the roll angle (blue) of the Falcon aircraft. The dSCDs retrieved in the UV are represented by a black line and the dSCDs retrieved in the visible wavelength range by a blue line. The respective average detection limit (assumed to be 2 σ) is illustrated by dashed lines.

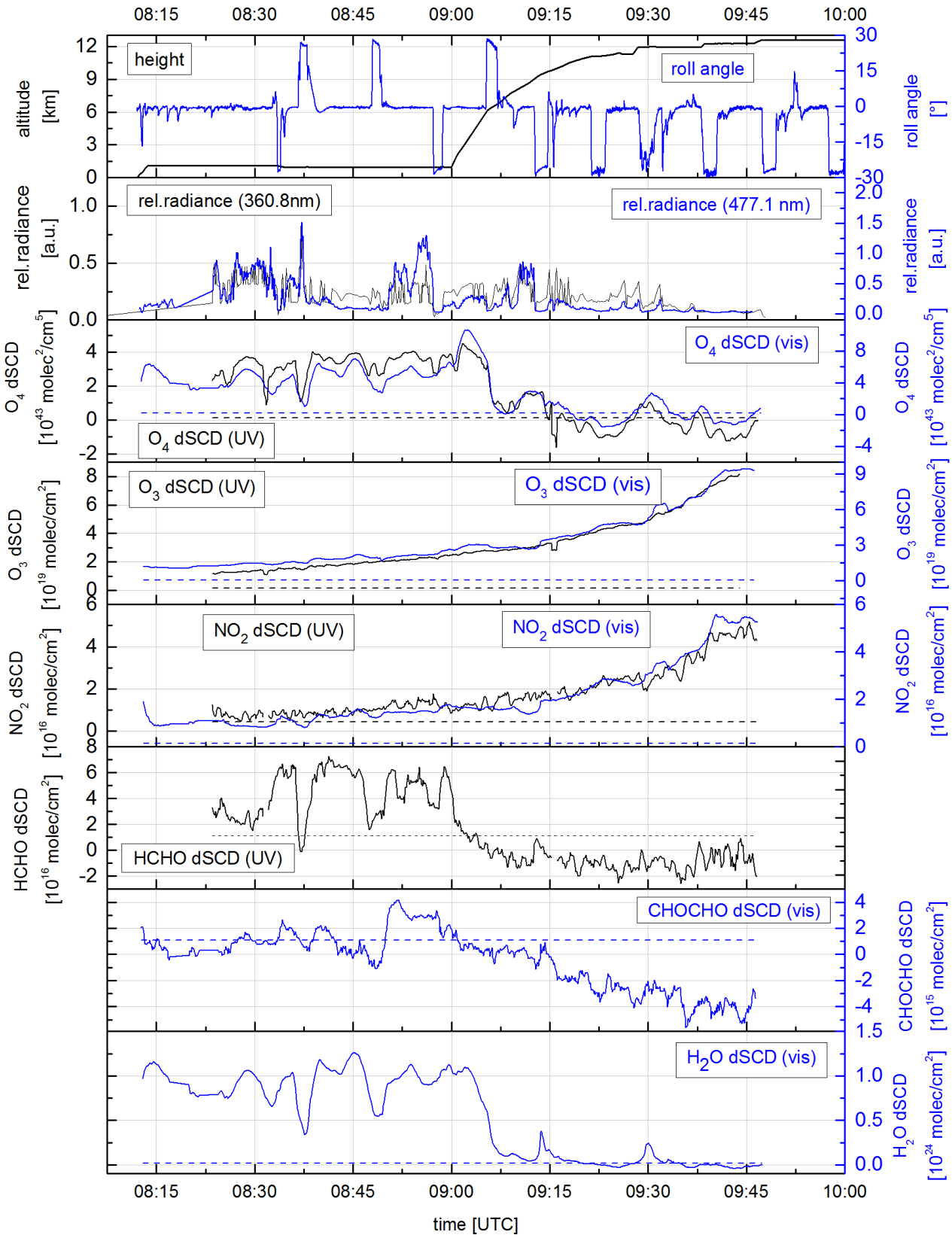

Figure A.18: Overview of the measured dSCDs during sortie 14 on 9 December 2011 b. The uppermost panel shows the altitude (black) and the roll angle (blue) of the Falcon aircraft. The dSCDs retrieved in the UV are represented by a black line and the dSCDs retrieved in the visible wavelength range by a blue line. The respective average detection limit (assumed to be 2 σ) is illustrated by dashed lines.

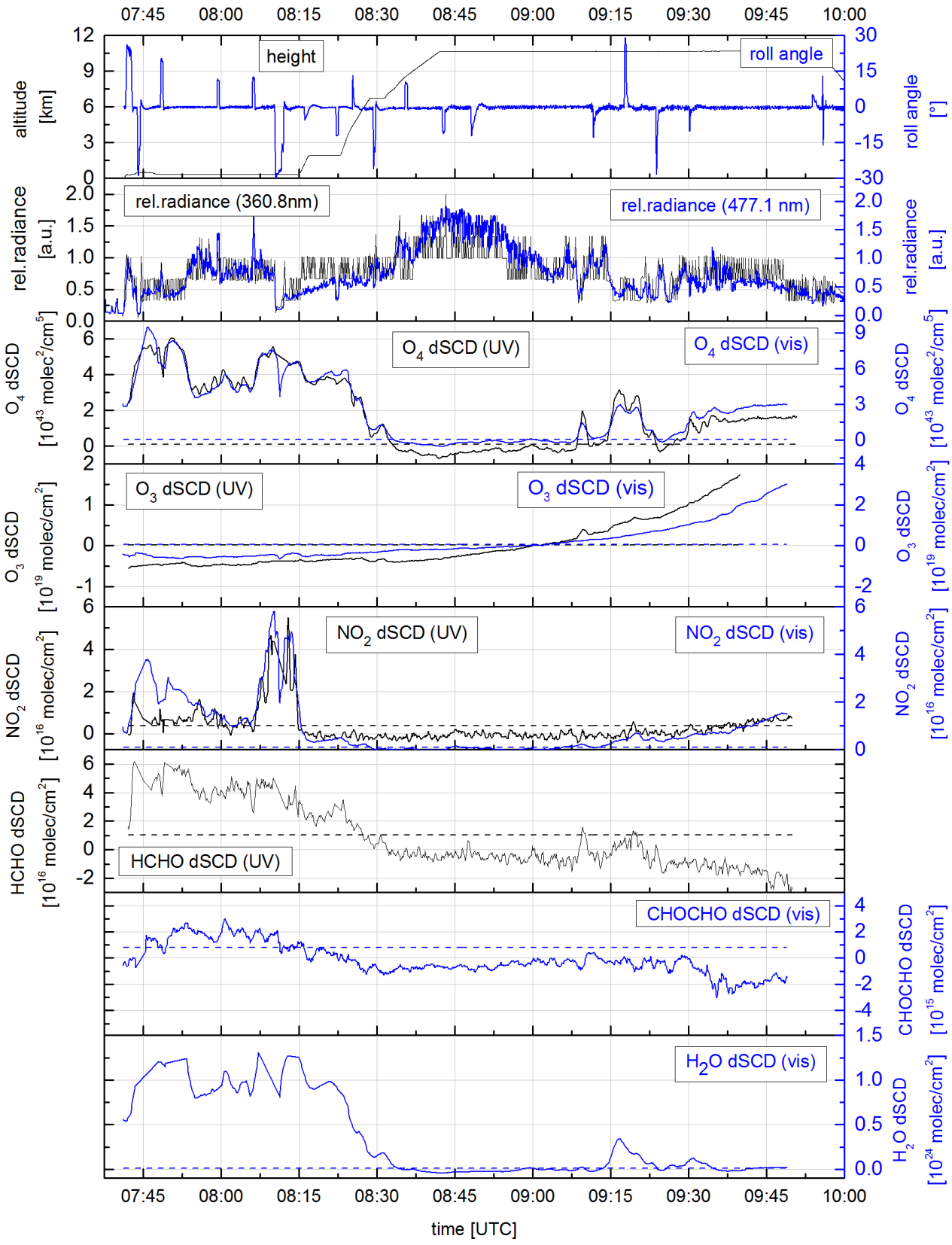

Figure A.19: Overview of the measured dSCDs during sortie 16 on 11 December 2011 b. The uppermost panel shows the altitude (black) and the roll angle (blue) of the Falcon aircraft. The dSCDs retrieved in the UV are represented by a black line and the dSCDs retrieved in the visible wavelength range by a blue line. The respective average detection limit (assumed to be 2 σ) is illustrated by dashed lines.

B. Appendix B: Estimation of the number of photons

Neglecting losses at the optical elements of the instrument, the number of photons n_{phot} can be estimated according to the following equation (General, 2014a):

$$n_{\text{phot}} = n \cdot \frac{S_{\text{counts}} \cdot C_{\text{elec}}}{C_{\text{counts}} \cdot Q}, \tag{B.1}$$

with n being the total number of co-added scans. The total number of co-added scans is $n = n_{\text{scans}} \cdot n_{\text{spectra}}$, with n_{scans} being the number of scans of one spectrum and n_{spectra} being the number of co-added spectra. S_{counts} corresponds to the average signal in counts, C_{elec} is the full-well capacity of the read-out register pixel in electrons, C_{counts} is the maximum number of counts, and Q is the quantum efficiency of the detector in the respective spectral range. Table B.1 summarises the technical details of the mini-DOAS spectrometers to calculate the number of photons.

Table B.1: Technical details of the mini-DOAS spectrometers used in this study. C_{counts} and Q adapted from Ocean Optics (`http://oceanoptics.com/wp-content/uploads/OEM-Data-Sheet-QE65000.pdf` and `http://oceanoptics.com/wp-content/uploads/USB2000-OEM-Data-Sheet.pdf`) (September 2014).

	number of scans per spectrum	number of co-added spectra	maximum number of counts	average signal	well-depth	quantum efficiency	number of photons	signal-to-noise ratio
	n_{scans}	n_{spectra}	C_{counts} [counts]	S_{counts} [counts]	C_{elec} [electrons/pixel]	Q [%]	n_{phot}	$\frac{S}{N}$
QE	≈3	20	65536	≈20000	$1.5{\cdot}10^6$	0.5	$5.5{\cdot}10^7$	7411
USB	≈60	15	4096	≈2000	$6.25{\cdot}10^4$	0.1	$2.8{\cdot}10^8$	16572

Each spectrum recorded with the QE consists of approximately 3 scans for a saturation of 75% and a total integration time of 5 sec, resulting in an average signal of approximately 20000 counts. The number of photons for one single scan results in $n_{\text{phot}_{\text{QE}}} \approx 9.2 \cdot 10^5$ and a signal-to-noise ratio of $\frac{S}{N} \approx 956$. According to Figure 8.10, the RMS of the HCHO spectral analysis of the QE spectrograph does not further decrease starting at a number of approximately 20 co-added spectra. This corresponds to a photon number of approximately $n_{\text{phot}_{\text{QE}}} \approx 5.5 \cdot 10^7$ and a signal-to-noise ratio of $\frac{S}{N} \approx 7411$.
Each spectrum recorded with the USB spectrograph consists of approximately 60 scans for a saturation of 75% and a total integration time of 5 sec, resulting in an average signal of approximately 2000 counts. The number of photons for a single scan is $n_{\text{phot}_{\text{USB}}} \approx 3.1 \cdot 10^5$ with a signal-to-noise ratio of $\frac{S}{N} \approx 552$. The RMS of the NO_2 spectral analysis does not further decrease starting at a

number of approximately 15 co-added spectra (Figure 8.10). This results in a photon number of $n_{\mathrm{phot}_{\mathrm{USB}}} \approx 2.8 \cdot 10^8$ and a signal-to-noise ratio $\frac{\mathrm{S}}{\mathrm{N}} \approx 16572$.

C. Appendix C: Determination of 3D cloud fields from 2D webcam images

This chapter presents two possible methods to derive 3D cloud fields from 2D webcam images. The first method is based on the transformation and projection of 2D webcam image in space (Appendix C.1) and the second method describes the structure from motion concept using a pre-existing software (Appendix C.2).

C.1 Spatial transformation of webcam images

One possible method to derive a 3D cloud field from the 2D webcam images is based on the transformation and projection of the 2D webcam image in space. In this section, the different steps of this method are described. Firstly, a cloud mask has to be generated, i.e. a filter that assigns the flag 'cloudy' or 'cloud-free' to each webcam pixel. This can be realised by different approaches, e.g. by defining certain threshold values for the red, green, or blue colour component of each pixel. In a next step these 2D clouds have to be transformed in space. The transformation includes a rotation of the camera coordinate system to the Falcon aircraft coordinate system and a further rotation of the Falcon aircraft coordinate system to the world coordinate system. The relation between a point P in the 3D world coordinate system and a point P' in the 2D webcam image is then given by a projection. Then, different methods can be applied to construct a 3D cloud.

Determination of a cloud mask

A cloud mask has to be determined from each image before the webcam images are transformed in space. There are several different concepts how to analyse an image to detect clouds structures:

1. RGB colour space (R = red, G = green, B = blue):
   The RGB colour model is an additive colour model, in which the three primary colours (red (R), green (G) and blue (B)) can be added to form a new colour (e.g. Jähne, 2005; Szeliski, 2011). If all three light components have an intensity of zero, the new colour is considered as black. If all three components have maximum intensity, the new colour results in white. The Commission Internationale d'Eclairage (CIE) (`http://www.cie.co.at/`) introduced standards for the RGB representation by performing colour matching experiments using the primary colours of red (R = 700 nm), green (G = 546.1 nm), and blue (B = 435.8 nm) (Szeliski, 2011). The left panel of Figure C.1 shows these standard CIE colour matching functions. The three components can be determined according to the following equations:

$$r = \frac{R}{R+G+B},\ g = \frac{G}{R+G+B},\ b = \frac{B}{R+G+B}, \tag{C.1}$$

   with $r + g + b = 1$ (Jähne, 2005). In order to avoid negative colour values, the CIE further developed a new XYZ colour space, which can be derived from a linear combination of RGB

through the following transformation (Jähne, 2005):

$$\begin{bmatrix} X \\ Y \\ Z \end{bmatrix} = \begin{bmatrix} 0.490 & 0.310 & 0.200 \\ 0.177 & 0.812 & 0.011 \\ 0.000 & 0.010 & 0.990 \end{bmatrix} \begin{bmatrix} R \\ G \\ B \end{bmatrix}. \tag{C.2}$$

Another quantity that might be useful for cloud detection is the colour index, which is defined as the ratio of B and R.

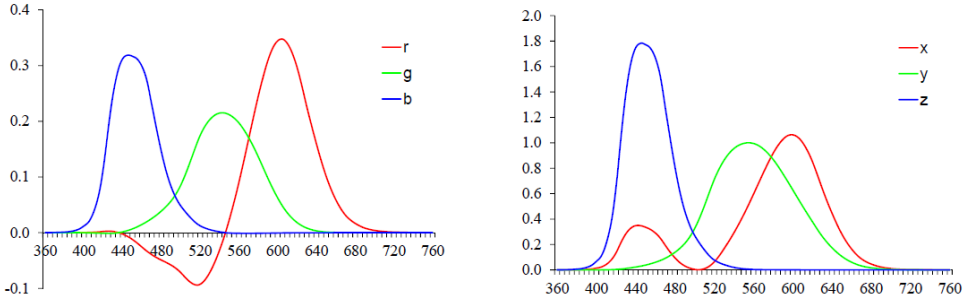

Figure C.1: Standard CIE colour matching functions: Left panel: Colour spectra of $r(\lambda)$, $g(\lambda)$, and $b(\lambda)$ from matching pure colours to the primary colours of R = 700 nm, G = 546.1 nm, and B = 435.8 nm; right panel: Colour matching functions $x(\lambda)$, $y(\lambda)$, and $z(\lambda)$, which are gained from linear combinations of the standard colour matching functions from the left panel. Figure adapted from Szeliski (2011).

2. HSV colour space (H = hue, S = saturation, V = value):
The HSV colour space represents a projection of the RGB colour cube onto a non-linear chroma angle, a radial saturation percentage, and a luminance-inspired value (Szeliski, 2011). According to Szeliski (2011), hue (H) can be defined as the direction around a wheel, the saturation (S) specifies a scaled distance from the diagonal, and value (V) yields either the mean or maximum colour value. The HSV colour space can be calculated from the RGB colour space. As a precondition of the conversion it is necessary that R, G, B lie within the interval between zero and one. In the following definitions according to Gonzalez and Woods (2002) 'max' represents the maximum and 'min' the minimum of (R, G, B), respectively:

$$H := \begin{cases} 0, & \text{if max} = \text{min} \\ 60\,^\circ \cdot (\frac{G-B}{\text{max}-\text{min}}), & \text{if max} = \text{R} \\ 60\,^\circ \cdot (2 + \frac{B-R}{\text{max}-\text{min}}), & \text{if max} = \text{G} \\ 60\,^\circ \cdot (4 + \frac{R-G}{\text{max}-\text{min}}), & \text{if max} = \text{B} \end{cases} \tag{C.3}$$

$$S := \begin{cases} 0, & \text{if max} = 0 \\ \frac{\text{max}-\text{min}}{\text{max}}, & \text{else} \end{cases} \tag{C.4}$$

$$V := \text{max}. \tag{C.5}$$

If H is smaller than $0\,^\circ$, $360\,^\circ$ have to be added to H.

3. Image gradient, variance and smoothing:
Prior to calculating the gradient, variance or smoothing of an image, the true colour RGB image has to be converted to a grey scale intensity image. In MATLAB, an RGB image is converted to grey scale by eliminating the hue and saturation information while the luminance is retained. The luminance describes the perceived relative brightness (e.g. Szeliski, 2011). If i represents the image width and j the image height in pixel, respectively, the gradient of an

image can be divided into a gradient in x direction ($G_x = p(i+1, j) - p(i, j)$) and a gradient in y direction ($G_y = p(i, j+1) - p(i, j)$). The total image gradient can be calculated according to:

$$G_{tot} = \sqrt{G_x^2 + G_y^2}. \tag{C.6}$$

The smoothing of an image in one direction is defined as $S_{smooth} = p(i+1) - 2p(i) + p(i-1)$ and the variance V_{var} describes the variance of the eight neighbouring pixel.

Each of these concepts has its advantages and disadvantages. In Figure C.2 the above-mentioned concepts are applied on an exemplary image of a cloud recorded during the SHIVA campaign on 26 November 2011 at an altitude of approximately 7.7 km. This image shows a rather simple cloud case, since the boundaries of the cloud can be easily distinguished from the dark background.
In particular, the red component and the value from the HSV colour space represent the cloud structures quite well. Cloud sections which are influenced by shadows cannot be represented by the different concepts. For the colour index, hue and saturation cases, features in the upper right corner of the image remain, which have the same value as the cloud pixel. The image gradient, variance and smoothing mark the borders of clouds very well. However, problems can occur within the cloud, where less structures are present. Thus, this concept can only be used if information about the cloud borders is sufficient. In order to detect cloudy pixels, certain constraints are selected and applied to the different concepts, i.e. certain threshold values are chosen to distinguish between two cases: 0 for a cloud-free pixel and 1 for a pixel showing a cloud fragment. A further solution is represented by the combination of the different concepts. In Figure C.3 a threshold value of 0.5 is chosen for R, G and B and combinations of two of them are shown.
In summary, different concepts can be used that lead to similar cloud masks. It is recommended to use the red component, the value from the HSV colour space, or a combination of both together with a certain threshold value as for example shown in Figure C.3.

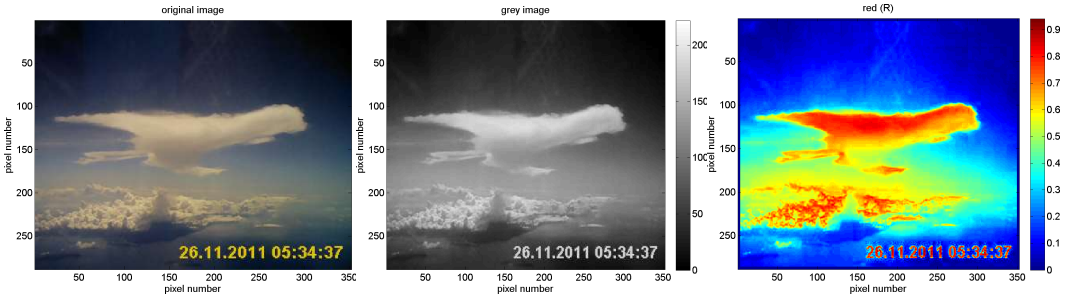

(a) original image

(b) grey image

(c) red (R)

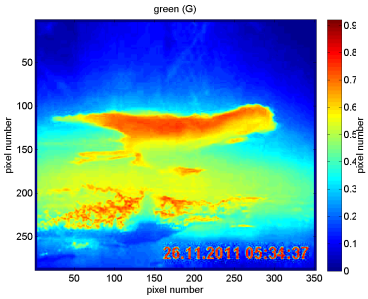

(d) green (G)

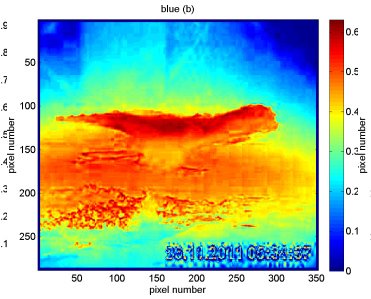

(e) blue (B)

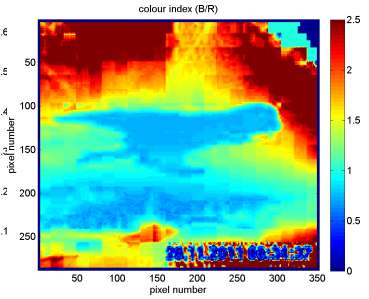

(f) colour index (B/R)

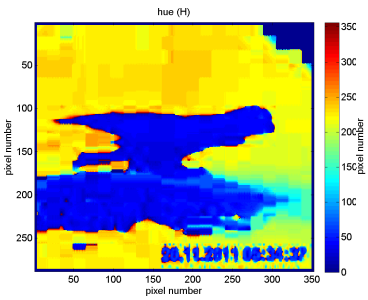

(g) hue (H)

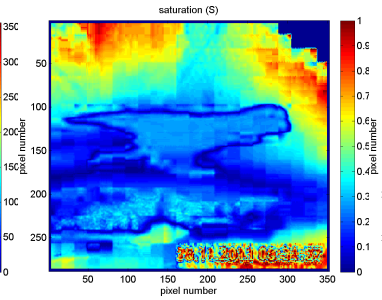

(h) saturation (S)

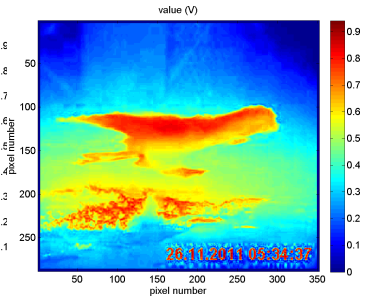

(i) value (V)

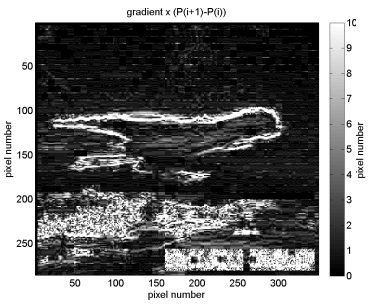

(j) gradient x

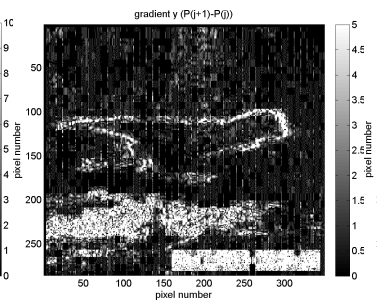

(k) gradient y

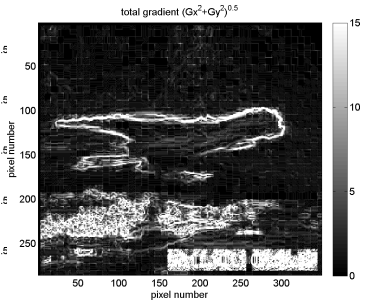

(l) total gradient

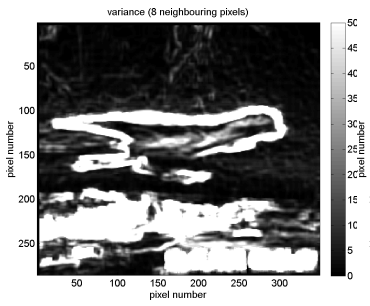

(m) variance

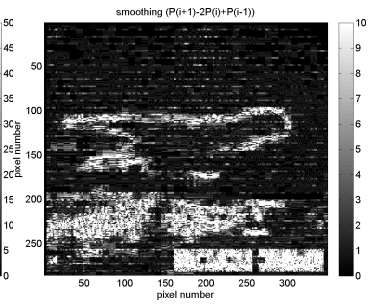

(n) smoothing

Figure C.2: Different concepts to detect clouds in a webcam image recorded during sortie 7 on 26 November 2011a at 05:34:37 UTC at an altitude of 7.7 km. The colour bars are given in arbitrary units.

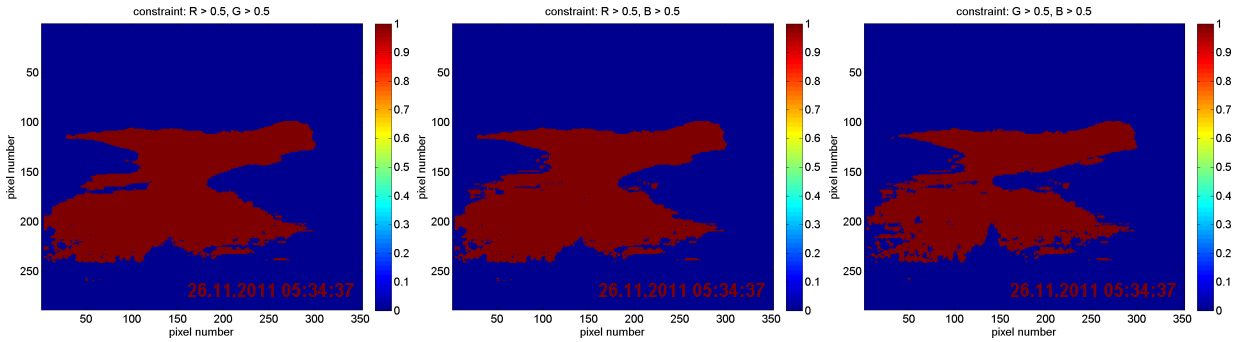

(a) R > 0.5, G> 0.5 (b) R > 0.5, B > 0.5 (c) G > 0.5, B > 0.5

Figure C.3: Different constraints to distinguish between a cloud-free (0) and a cloudy (1) pixel for a webcam image recorded during sortie 7 on 26 November 2011a on 05:34:37 UTC at an altitude of 7.7 km. The colour bars are given in arbitrary units.

Description of the different coordinate systems

Different coordinate systems have to be defined, in order to describe a position of an object in the 3D space (Jähne, 2005). Figure C.4 sketches the different left-handed coordinate systems used in this study. In the Falcon coordinate system F, the aircraft is flying along the negative x_F - axis with the right wing pointing to the positive y_F - axis and the left wing pointing to the negative y_F - axis. A rotation around the y_F - axis around the angle $roll_F$ corresponds to the roll movement of the Falcon aircraft, whereas a rotation around the negative x_F - axis around the angle $pitch_F$ corresponds to the pitch movement and a rotation around the z_F - axis around the angle yaw_F to the yaw movement or heading direction of the aircraft.
The webcam has a viewing direction along the negative x_F - axis of the aircraft. For simplicity reasons, the yaw angle of the camera is changed to $yaw_C = 90\,^\circ + yaw_C$ to avoid confusions about the different viewing directions of the camera and the aircraft. Hence, the names of the axes and rotation angles of the Falcon coordinate system F can be easily transferred to the camera coordinate system C without contradicting each other. The matrix of C can be therefore written as: C = [010, 001, -100]. In this case, the 2D webcam image is projected in the $y_F z_F$-plane of the aircraft with the z - axis corresponding to the image height and the y - axis corresponding to the image width in pixel. In the world coordinate system W, the Falcon aircraft is located at the North Pole with a viewing direction to the negative x_W - axis.

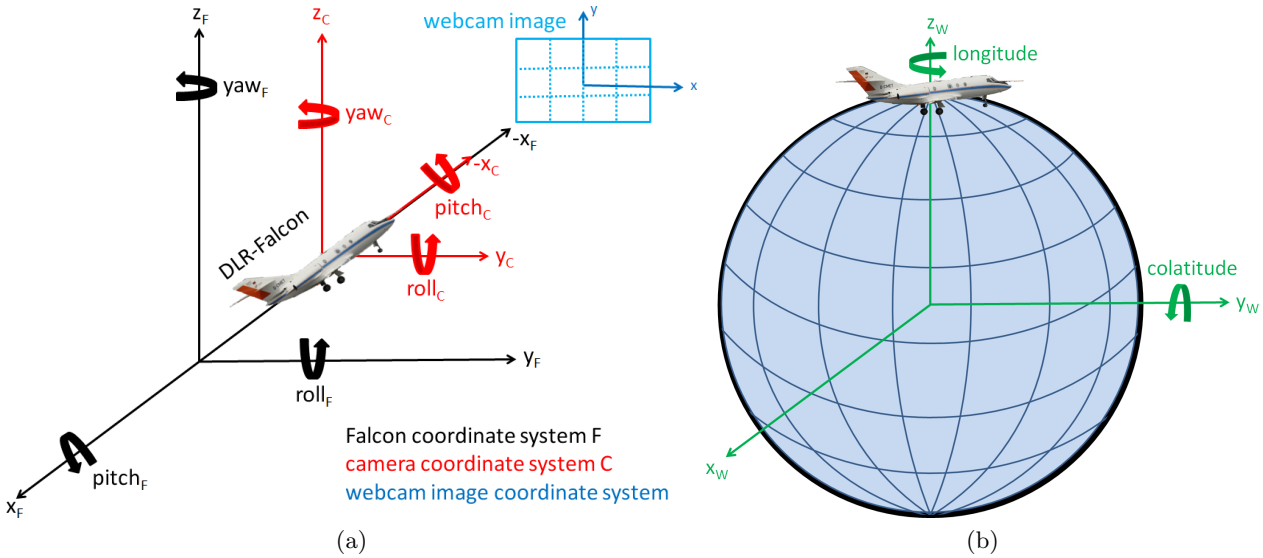

(a) (b)

Figure C.4: (a) Falcon aircraft coordinate system F (black), camera coordinate system C (red) and the 2D webcam image coordinate system (blue). (b) World coordinate system W (green) with the Falcon aircraft located at the North Pole with a viewing direction to the east.

Determination of the camera angles

The webcam was not orientated perfectly within the Falcon aircraft. Therefore, the roll, pitch and yaw angle of the camera ($roll_C$, $pitch_C$, yaw_C) are not equal to zero. Hence, the rotation of the camera has to be determined. This can be done by calculating the horizon line from the aircraft data (time, colatitude, longitude, height, $roll_F$, $pitch_F$, yaw_F) and comparing it to the horizon in the images. $roll_C$, $pitch_C$ and yaw_C are then changed until the calculated horizon and the actual horizon agree with each other. The final angles of the camera are: $roll_C = 0.7\,°$, $pitch_C = 0.7\,°$, $yaw_C = 90\,° + 1\,° = 91\,°$ (sortie 1 on 16.11.2011). The camera position has to be checked for each sortie, separately.

Rotation of the camera coordinate system C to the Falcon coordinate system F

As a first step, C is transformed in F. The basic transformation of a coordinate system into another consists of a translation, which moves every point in space by a fixed distance in the same direction and a rotation, which is performed by spinning the coordinate system around different axes in the right order. As the webcam is located within the aircraft, no translation is necessary. The general rotation matrices can be written as:

$$R_x = [1\ 0\ 0\ ;0\ \ \cos(a)\ \ -\sin(a)\ ;\ 0\ \sin(a)\ \cos(a)] \quad \text{(C.7)}$$

$$R_y = [\cos(a)\ 0\ \sin(a)\ ;\ 0\ 1\ 0\ ;\ -\sin(a)\ 0\ \cos(a)] \quad \text{(C.8)}$$

$$R_z = [\cos(a)\ \ -\sin(a)\ 0\ ;\ \sin(a)\ \cos(a)\ 0\ ;\ 0\ 0\ 1]. \quad \text{(C.9)}$$

The three rotations do not permute: (i) rotation around the y_C - axis around $roll_C$ (R_y), (ii) rotation around the x_C - axis around $pitch_C$ (R_x) and (iii) rotation around the z_C - axis around yaw_C (R_z). Hence, F_0 can be calculated in the following way:

$$F_0 = R_z(yaw_C) \cdot R_x(pitch_C) \cdot R_y(roll_C) \cdot C. \quad \text{(C.10)}$$

The camera coordinate system is now transformed to the Falcon coordinate system.

Rotation of the Falcon coordinate system F to the world coordinate system W

In order to transform F to W the Falcon coordinate system has to be rotated in the same order:

$$F = R_z(yaw_F) \cdot R_x(pitch_F) \cdot R_y(roll_F) \cdot F_0. \tag{C.11}$$

In the next step, the aircraft is projected onto the globe, i.e. rotating F around colatitudes and longitude.

$$F_W = R_z(\text{longitude}) \cdot R_y(\text{colatitude}) \cdot F. \tag{C.12}$$

The camera is now orientated in the world coordinate system. The total rotation matrix results in:

$$\begin{aligned} F_{geo} = R_z(\text{longitude}) \cdot R_y(\text{colatitude}) \cdot R_z(yaw_F) \cdot R_x(pitch_F) \\ \cdot R_y(roll_F) \cdot R_z(yaw_C) \cdot R_x(pitch_C) \cdot R_y(roll_C) \cdot C. \end{aligned} \tag{C.13}$$

This transformation corresponds to a rotation of a point P_C in the camera coordinate system to the point P_W in the world coordinate system. A back transformation is realised by transposing the rotation matrices or by reversing the order of the single rotation matrices and changing the sign of the rotation angles. The transpose matrix of F_{geo} yields:

$$\begin{aligned} {F_{geo}}' = R_y(-roll_C) \cdot R_x(-pitch_C) \cdot R_z(-yaw_C) \cdot R_y(-roll_F) \\ \cdot R_x(-pitch_F) \cdot R_z(-yaw_F) \cdot R_y(-\text{colatitude}) \cdot R_z(-\text{longitude}) \cdot C. \end{aligned} \tag{C.14}$$

The individual components of P_C are:

$$P_{x_C} = {F_{geo}}' \cdot [0\ 1\ 0] \tag{C.15}$$

$$P_{y_C} = {F_{geo}}' \cdot [0\ 0\ 1] \tag{C.16}$$

$$P_{z_C} = {F_{geo}}' \cdot [-1\ 0\ 0]. \tag{C.17}$$

Projection of a point P in space to the point P' in the webcam image

Figure C.5 displays the geometric relations between the point P in the world and the respective point P' in the webcam image.

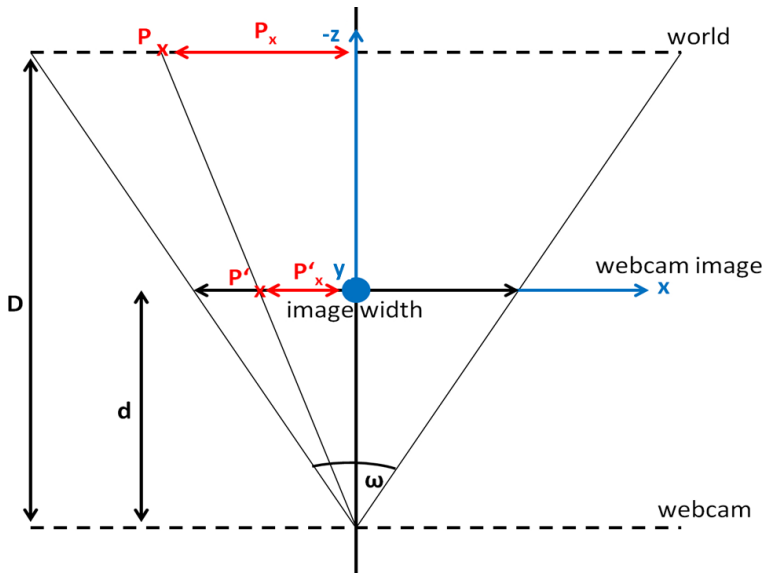

Figure C.5: Sketch of the top view of a webcam image.

The distance d_x between the position of the webcam and the webcam image in horizontal direction can be calculated according to the following equation:

$$d_x = \frac{\text{Image width}}{2 \cdot \tan(\omega/2)}. \tag{C.18}$$

Respectively, the distance d_y in vertical direction yields:

$$d_y = \frac{\text{Image height}}{2 \cdot \tan(\omega/2)}, \tag{C.19}$$

The average value of d_x and d_y is:

$$d = 0.5 \cdot (d_x + d_y). \tag{C.20}$$

The intercept theorem yields the following equations:

$$P_x{}' = d \cdot \frac{P_x}{P_z} \tag{C.21}$$

$$P_y{}' = d \cdot \frac{P_y}{P_z} \tag{C.22}$$

$$P_z{}' = -d, \tag{C.23}$$

with P_x, P_y and P_z corresponding to P_{xC}, P_{yC} and P_{zC}, respectively. Consequently, with this algorithm single webcam pixels can now be transformed in space.
With this knowledge, different methods can be applied to infer 3D cloud structures from the webcam images (Tim Deutschmann, IUP Heidelberg, personal communication, September 2013). One method spatially transforms the 2D cloud mask: Firstly, it should be checked whether the projected point P in space lies within the webcam image. If the point P lies within the webcam image and the respective webcam pixel shows a distinct cloud feature retrieved with one of the cloud mask methods from above, the point P is marked with a certain number k. This procedure is repeated as long as the point P in space is visible in the subsequent webcam images. If the sum over k exceeds a certain value, it can be concluded that the point P in space will represent a part of a cloud. Another method to infer 3D cloud structures from the webcam images could be for example the ray tracing technique. The basic idea of ray tracing is to send individual rays from the webcam across multiple bounces towards the light source. Thereby, a light ray is associated with each pixel in the webcam image and its intersection with the nearest surface is determined (e.g. Szeliski, 2011, and references therein). Additional rays can be cast towards a specific scene in order to calculate the colour of the object.

C.2 Structure from motion

Structure from motion (SfM) (Ullman, 1979) is a technique, that is able to provide the simultaneous recovery of 3D camera motion and 3D scene structures from a sequence of 2D images (Szeliski, 2011). Details on this technique are not presented in this study. A detailed description can for example be found in Szeliski (2011) and in references therein. The GUI application VisualSFM, developed by Changchang Wu (`http://ccwu.me/vsfm/`), provides a 3D reconstruction tool using the SfM method. In principal, VisualSFM automatically detects distinct features in an image and runs a pairwise image matching algorithm. In a next step, a sparse 3D reconstruction is performed in order to obtain the 3D points. Optionally, VisualSFM supports different dense reconstruction tools. To improve the 3D reconstruction, it is recommended to calibrate and rectify the images before implementing them into the software.

Calibration of the webcam

All webcam images have to be distorted before they are further processed. The camera calibration toolbox for MATLAB (`http://www.vision.caltech.edu/bouguetj/calib_doc/`) provides an easy software to calibrate the webcam. Several images of a planar chequerboard plate (chequerboard size: 100 mm x 100 mm) in different perspectives are recorded (Figure C.6).
The four main outer grid corners of this plate are marked by hand in each image. The calibration software then automatically extracts all chequerboard corners of each image and calculates the distortion factor with a non-linear optimisation method. Figure C.7 shows the resulting distortions of the two applied image sizes. For both image sizes the principal point p is with a difference of Δp = 24 pixels slightly shifted to the left. For the image resolution of 320x240 the principal point p is located at the pixel number 136 instead of 160, whereas for the image resolution of 352x288 p is at the pixel number 152 instead of 160. The focal length of the smaller image size results in 456 pixel and for the larger image size in 501 pixel. All in all, the complete distortion is quite small. For an image size of 320x240 the distortion is smaller than 1.4 pixel and for the image size of 352x288 smaller than 2 pixel. The main distortion prevails rather in the right part of the images, whereas the left parts are almost completely rectified without any distortions. As the mini-DOAS FOV is located in the upper left part of the webcam images (Section 9.3.1), the distortion of the images can be neglected here. However, for the application in the VisualSFM software, rectifying the images and using a fixed calibration is essential to improve the 3D reconstruction.

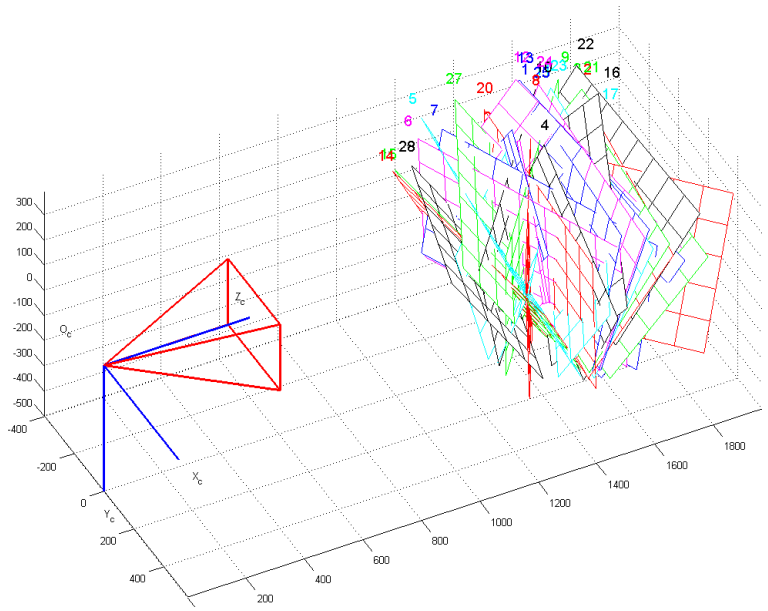

Figure C.6: Sketch of the position of the planar chequerboard plate in order to calibrate the webcam. Figure provided by the MATLAB camera calibration toolbox.

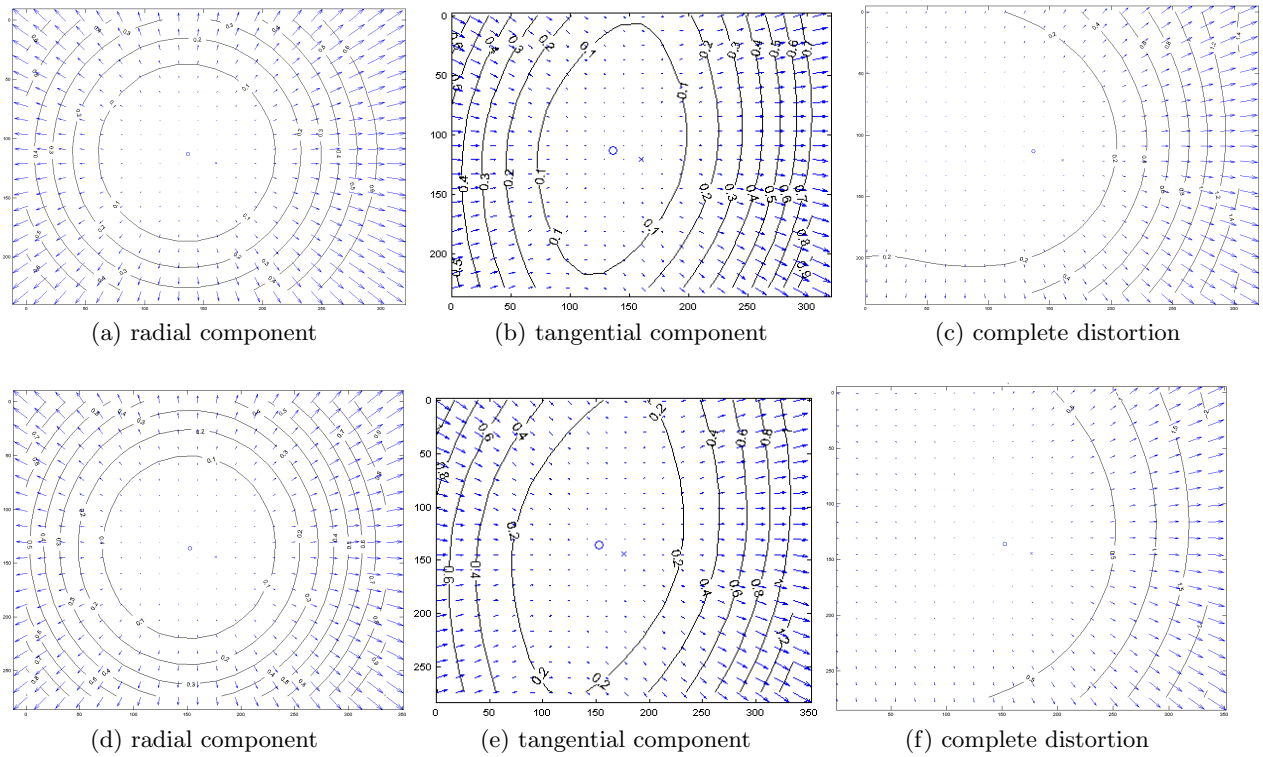

(a) radial component (b) tangential component (c) complete distortion

(d) radial component (e) tangential component (f) complete distortion

Figure C.7: Radial, tangential and complete distortion of the webcam images for an image size of 320x240 pixel ((a) - (c)) and for a size of 352x288 pixel ((d) - (f)). The values at the contour lines correspond to the shift in pixel.

Results of VisualSFM

After the images have been rectified, they are implemented in the VisualSFM software. The calibration is fixed using the principal points and focal lengths of the calibration determined in the previous section. A sequence of 30 webcam image of the cloud scene from Figure C.2 recorded during sortie 7 on 26 November 2011 is selected in order to test the SfM method.
Figure C.8 shows the results of this image selection. In general, the contour lines of the cloud are roughly visible. However, one major restriction of this method is that the number of reconstructed 3D points is small. Inside the cloud, where less structures occur, too little feature matches are found and thus an insufficient number 3D points are generated. Furthermore, not only cloud features are reconstructed by the software, but also other parts of the images where specific structures occur.
For future applications, sensitivity studies for very simple cloud fields have to be performed. The cloud fields that were prevailing during the SHIVA campaign are too complex for a further processing. Furthermore, not only the spatial structure and position of a cloud are relevant for the radiative transfer in the atmosphere, but also the properties of a cloud, such the extinction, SSA or, droplet size.

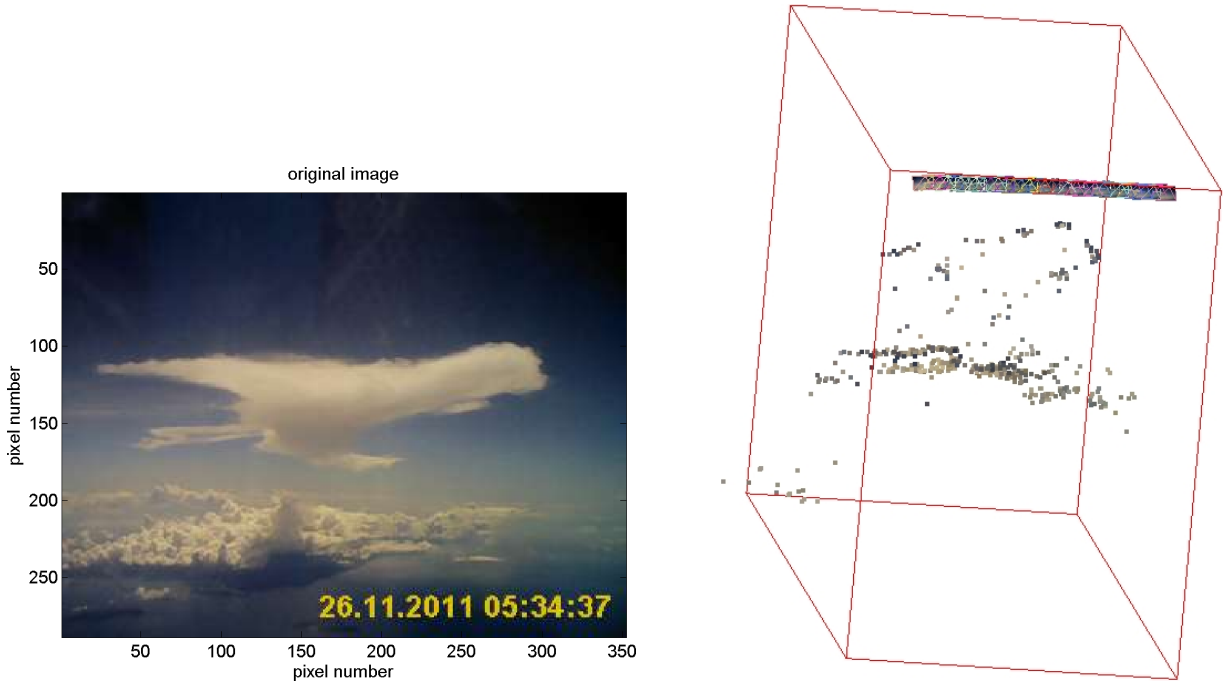

(a) (b)

Figure C.8: (a) Webcam image of the cloud scence from Figure C.2 recorded during sortie 7 on 26 November 2011. (b) Results of the VisualSFM software for a sequence of 30 webcam images including image (a). The red box marks the reconstructed model. The position of the webcam and thus the 3D flight track is illustrated by the small single webcam images at the upper edge of the red box. The reconstructed 3D points are represented by small rectangles colour-coded with the respective colour of the webcam image pixel.

D. Appendix D: Determination of reaction rate coefficients

In the following, the reactions rate coefficients of the reactions are determined, which are required for the estimation of the OH concentration in Section 11.3.4. The derivation of the different reaction rate coefficients follows the description of Sander et al. (2011b).
The reaction rate coefficient $k_{\mathrm{NO+O_3}}$ for Reaction 2.21 is given by:

$$k_{\mathrm{NO+O_3}} = 1.4 \cdot 10^{-12} e^{\frac{-1310}{\mathrm{T}}} \mathrm{cm^3 molec^{-1} s^{-1}}. \tag{D.1}$$

The mean temperature inside the cloud was assumed to be 240 K, which corresponds to the temperature at flight altitude given by the aircraft sensors. This results in $k_{\mathrm{NO+O_3}} = 5.965 \cdot 10^{-15}$ cm^3 molec^{-1} s^{-1}. The reaction rate coefficient $k_{\mathrm{HONO+OH}}$ for Reaction 2.51 is given by:

$$k_{\mathrm{HONO+OH}} = 2.5 \cdot 10^{-12} e^{\frac{260}{T}} \mathrm{cm^3 molec^{-1} s^{-1}}, \tag{D.2}$$

leading to a reaction rate coefficient of $k_{\mathrm{HONO+OH}} = 7.386 \cdot 10^{-12}$ cm^3 molec^{-1} s^{-1} for a temperature of T = 240 K. Reaction 2.50 is a termolecular reaction, i.e. a three-body-collision reaction, which can be pressure dependent. For termolecular reactions, a low-pressure-limiting rate constant and a high-pressure-limiting-rate constant have to be determined. The low-pressure-limiting rate constant is given in the form:

$$k_0(T) = 7.0 \cdot 10^{-31} \left(\frac{\mathrm{T}}{300} \right)^{-2.6} \mathrm{cm^6 molec^{-2} s^{-1}}, \tag{D.3}$$

whereas the high-pressure-limiting-rate constant can be expressed as:

$$k_\infty(T) = 3.6 \cdot 10^{-11} \left(\frac{\mathrm{T}}{300} \right)^{-0.1} \mathrm{cm^3 molec^{-1} s^{-1}}. \tag{D.4}$$

In order to obtain the effective second order rate constant for the termolecular reaction (2.50), the following formula can be applied:

$$k([\mathrm{M}], T) = \left(\frac{k_0(T) \cdot [\mathrm{M}]}{1 + \frac{k_0(T) \cdot [\mathrm{M}]}{k_\infty(T)}} \right) 0.6^{\left(1 + \left(log_{10}\left(\frac{k_0(T) \cdot [\mathrm{M}]}{k_\infty(T)}\right)\right)^2\right)^{-1}}, \tag{D.5}$$

with $[\mathrm{M}] = \frac{p \cdot N_A}{R \cdot T}$. For T = 240 K and p = 197 mbar, the final reaction rate coefficient results in $k_{\mathrm{NO+OH+M}} = 4.39 \cdot 10^{-12}$ cm^3 molec^{-1} s^{-1}.

E. Appendix E: Recommendations for future applications

Based on the experience gained during the SHIVA campaign, several restrictions can be identified that limit the analysis and interpretation of the data set presented in this study. These restrictions comprise instrument-related topics as well as missing additional information, which is needed for an interpretation of the data. In the following, the different restrictions are listed together with recommendations for future applications.

1. **Stable instrument**:
   Having a stable instrument temperature is a fundamental feature in DOAS applications. In order to guarantee a stable instrument temperature, which varies less than $\pm 0.1\,^{\circ}\mathrm{C}$, a passive cooling system, such as the ice-water mixture is not sufficient. Thus, besides the ice-water cooling, an additional active cooling system, such as Peltier elements, should be included, which does not heat up with increasing cabin temperature and which compensates for the melting of the ice.

2. **Improvement of the signal-to-noise ratio**:
   During the SHIVA campaign, weak absorbers, such as IO and CHOCHO, were regularly close to or at the detection limit of the mini-DOAS instrument. For future deployments, spectrometers with a better signal-to-noise ratio and thus a lower detection limit are required in order to further investigate weak absorbers. This can be achieved in combination with point (1.) and an increased number of photons, e.g. a smaller f-number.

3. **Connection to the attitude data of the aircraft**:
   An active pointing of the telescopes is absolutely essential, in order to reach a sufficient altitude resolution and to ensure an accurate knowledge of the viewing direction. Due to a missing connection to the attitude data of the aircraft during the flights, no direct compensation of the roll and pitch movement of the aircraft was possible during the SHIVA campaign, leading to a loss in the achievable altitude resolution. Meanwhile, aboard the HALO aircraft (Kenntner, 2013) as well as aboard the NASA Global Hawk (Raecke, 2013) it is already possible to directly read in the aircraft position data with a high frequency and thus being able to directly compensate for the roll and pitch movement of the aircraft while scanning.

4. **Additional knowledge about the state of the atmosphere**:
   For radiative transfer simulations that represent the actual atmosphere in an appropriate way, additional knowledge about the state of the atmosphere is needed, which can be provided by collocated measurements of other instruments deployed on the same vehicle or from satellites. Particularly for this study, knowledge about the prevailing cloud field and its properties as e.g. the optical depth, the altitude or the horizontal distribution of the clouds is very crucial. During the SHIVA campaign, none of the before-mentioned cloud properties were available. Information about the cloud height can e.g. be provided by LIDAR (Light detection and ranging) measurements as realised aboard the Global Hawk (Raecke, 2013). For future applications, it is highly recommended to have at least a cloud LIDAR in addition to DOAS

measurements to be able to adjust the forward model in a realistic way. Space-borne high resolution spectrometers probing the O_2 A-band, such as the GOSAT and OCO-2 satellites, can already simultaneously retrieve several cloud parameters, such as optical thickness, top height and droplet size (Sanghavi et al., 2014).

5. **Instrument viewing direction in flight direction**:
   During the SHIVA campaign, the mini-DOAS instrument was integrated on the port side of the Falcon aircraft, having a viewing direction orthogonal to the flight direction. Thus, a direct comparison to in situ data as is not unambiguous, as the mini-DOAS instrument might have observed a different air mass than the in situ measurements. If a direct comparison with in situ data is requested, it is recommended to use forward looking DOAS telescopes in future applications as realised aboard the Global Hawk (Raecke, 2013).

6. **Using a high quality webcam**:
   For future applications, it is recommended to use a high quality webcam, for which the exposure time can be logged. This likely improves the localisation of the DOAS FOV in the webcam images. Similar to the DOAS intensities, the intensities of the webcam images can then be divided by the exposure time. In addition to that, images should be recorded in the raw image format in order to avoid any camera corrections, such as colour grading or white balancing.

7. **High-temporal-resolution radiative transfer simulations**:
   For highly variable geometries it is suggested to perform high-resolution radiative transfer simulations, i.e. using the geometries with the highest possible resolution that is provided by the aircraft standard parameters for RT calculations and then averaging the results according to the integration time of each spectrum. Using this approach implicates that turns of the aircraft, where large roll angle changes occur, can be included in radiative transfer simulations. However, this method requires additional computation power.

8. **Application of 3D cloud reconstruction**:
   3D cloud fields can be derived from 2D webcam images. The implementation of these 3D cloud fields in 3D RT models can provide useful information on the interpretation of spatially variable clouds on DOAS measurements.

Publications

- **Prados-Roman et al., 2014:**
  Prados-Roman, C., Cuevas, C. A., Hay, T., Fernandez, R. P., Mahajan, A. S., Royer, S.-J., Gali, M., Simo, R., Dachs, J., Großmann, K., Kinnison, D. E., Lamarque, J.-F., and Saiz-Lopez, A.: Iodine oxide in the global marine boundary layer, Atmospheric Chemistry and Physics Discussions, 14, 22217–22243, doi:10.5194/acpd-14-22217-2014, URL http://www.atmos-chem-phys-discuss.net/14/22217/2014/, 2014

- **Mahajan et al., 2014:**
  Mahajan, A. S., Prados-Roman, C., Hay, T. D., Lampel, J., Pöhler, D., Großmann, K., Tschritter, J., Frieß, U., Platt, U., Johnston, P., Kreher, K., Wittrock, F., Burrows, J. P., Plane, J. M., and Saiz-Lopez, A.: Glyoxal observations in the global marine boundary layer, Journal of Geophysical Research: Atmospheres, 119, 6160–6169, doi:10.1002/2013JD021388, URL http://dx.doi.org/10.1002/2013JD021388, 2014

- **Großmann et al., 2013b:**
  Großmann, K., Dorf, M., Kenntner, M., Catoire, V., Schlager, H., Hendrick, F., DeSmedt, I., Huan, Y. , Pfeilsticker, K.: DOAS observations over Borneo during the SHIVA aircraft campaign, Malaysian Journal of Science, Vol. 32, South China Sea Special Issue, Proceedings Of The 2Nd Conference For Regional Cooperation In Ocean And Earth Science Research In The South China Sea, 21-24 October 2012, 259–266, 2013

- **Großmann et al., 2013a:**
  Großmann, K., Frieß, U., Peters, E., Wittrock, F., Lampel, J., Yilmaz, S., Tschritter, J., Sommariva, R., von Glasow, R., Quack, B., Krüger, K., Pfeilsticker, K., and Platt, U.: Iodine monoxide in the Western Pacific marine boundary layer, Atmos. Chem. Phys., 13, 3363-3378, doi:10.5194/acp-13-3363-2013, URL http://www.atmos-chem-phys.net/13/3363/2013/, 2013

- **Peters et al., 2012:**
  Peters, E., Wittrock, F., Großmann, K., Frieß, U., Richter, A., and Burrows, J. P.: Formaldehyde and nitrogen dioxide over the remote western Pacific Ocean: SCIAMACHY and GOME-2 validation using ship-based MAX-DOAS observations, Atmos. Chem. Phys., 12, 11179–11197, doi:10.5194/acp-12-11179-2012, URL http://www.atmos-chem-phys.net/12/11179/2012/, 2012

- **Piters et al., 2012:**
  Piters, A. J. M., Boersma, K. F., Kroon, M., Hains, J. C., Van Roozendael, M., Wittrock, F., Abuhassan, N., Adams, C., Akrami, M., Allaart, M. A. F., Apituley, A., Beirle, S., Bergwerff, J. B., Berkhout, A. J. C., Brunner, D., Cede, A., Chong, J., Clémer, K., Fayt, C., Frieß, U., Gast, L. F. L., Gil-Ojeda, M., Goutail, F., Graves, R., Griesfeller, A., Großmann, K., Hemerijckx, G., Hendrick, F., Henzing, B., Herman, J., Hermans, C., Hoexum, M., van der Hoff, G. R., Irie, H., Johnston, P. V., Kanaya, Y., Kim, Y. J., Klein Baltink, H., Kreher, K., de Leeuw, G., Leigh, R., Merlaud, A., Moerman, M. M., Monks, P. S., Mount, G. H., Navarro-Comas,

M., Oetjen, H., Pazmino, A., Perez-Camacho, M., Peters, E., du Piesanie, A., Pinardi, G., Puentedura, O., Richter, A., Roscoe, H. K., Schönhardt, A., Schwarzenbach, B., Shaiganfar, R., Sluis, W., Spinei, E., Stolk, A. P., Strong, K., Swart, D. P. J., Takashima, H., Vlemmix, T., Vrekoussis, M., Wagner, T., Whyte, C., Wilson, K. M., Yela, M., Yilmaz, S., Zieger, P., and Zhou, Y.: The Cabauw Intercomparison campaign for Nitrogen Dioxide measuring Instruments (CINDI): design, execution, and early results, Atmos. Meas. Tech., 5, 457-485, doi:10.5194/amt-5-457-2012, URL `http://www.atmos-meas-tech.net/5/457/2012/`, 2012

- **Roscoe et al., 2010:**
  Roscoe, H. K. and Van Roozendael, M. and Fayt, C. and du Piesanie, A. and Abuhassan, N. and Adams, C. and Akrami, M. and Cede, A. and Chong, J. and Clémer, K. and Frieß, U. and Gil Ojeda, M. and Goutail, F. and Graves, R. and Griesfeller, A. and Großmann, K. and Hemerijckx, G. and Hendrick, F. and Herman, J. and Hermans, C. and Irie, H. and Johnston, P. V. and Kanaya, Y. and Kreher, K. and Leigh, R. and Merlaud, A. and Mount, G. H. and Navarro, M. and Oetjen, H. and Pazmino, A. and Perez-Camacho, M. and Peters, E. and Pinardi, G. and Puentedura, O. and Richter, A. and Schönhardt, A. and Shaiganfar, R. and Spinei, E. and Strong, K. and Takashima, H. and Vlemmix, T. and Vrekoussis, M. and Wagner, T. and Wittrock, F. and Yela, M. and Yilmaz, S. and Boersma, F. and Hains, J. and Kroon, M. and Piters, A. and Kim, Y. J.: Intercomparison of slant column measurements of NO_2 and O_4 by MAX-DOAS and zenith-sky UV and visible spectrometers, Atmos. Meas. Tech., 3, 1629–1646, doi:10.5194/ amt-3-1629-2010, URL `http://www.atmos-meas-tech.net/3/1629/2010/`, 2010

Bibliography

Akima, H.: A New Method of Interpolation and Smooth Curve Fitting Based on Local Procedures, J. ACM, 17, 589–602, doi:10.1145/321607.321609, URL http://doi.acm.org/10.1145/321607.321609, 1970.

Alicke, B., Platt, U., and Stutz, J.: Impact of nitrous acid photolysis on the total hydroxyl radical budget during the Limitation of Oxidant Production/Pianura Padana Produzione di Ozono study in Milan, Journal of Geophysical Research: Atmospheres, 107, LOP 9–1–LOP 9–17, doi:10.1029/2000JD000075, URL http://dx.doi.org/10.1029/2000JD000075, 2002.

Alicke, B., Geyer, A., Hofzumahaus, A., Holland, F., Konrad, S., Pätz, H. W., Schäfer, J., Stutz, J., Volz-Thomas, A., and Platt, U.: OH formation by HONO photolysis during the BERLIOZ experiment, Journal of Geophysical Research: Atmospheres, 108, PHO 3–1–PHO 3–17, doi:10.1029/2001JD000579, URL http://dx.doi.org/10.1029/2001JD000579, 2003.

Aliwell, S. R., Roozendael, M. V., Johnston, P. V., Richter, A., Wagner, T., Arlander, D. W., Burrows, J. P., Jones, D. J., Tornkvist, K. K., Lambert, J.-C., Pfeilsticker, K., and Pundt, I.: Analysis for BrO in Zenith-sky spectra: An intercomparision exercise for analysis improvement, J. Geophys. Res., 107, 10.1029/2001JD000 329, 2002.

Allen, D., Pickering, K., and Fox-Rabinovitz, M.: Evaluation of pollutant outflow and CO sources during TRACE-P using model-calculated, aircraft-based, and Measurements of Pollution in the Troposphere (MOPITT)-derived CO concentrations, Journal of Geophysical Research: Atmospheres, 109, doi:10.1029/2003JD004250, URL http://dx.doi.org/10.1029/2003JD004250, 2004.

Alvarado, L. M. A., Richter, A., Vrekoussis, M., Wittrock, F., Hilboll, A., Schreier, S. F., and Burrows, J. P.: An improved glyoxal retrieval from OMI measurements, Atmospheric Measurement Techniques Discussions, 7, 5559–5599, doi:10.5194/amtd-7-5559-2014, URL http://www.atmos-meas-tech-discuss.net/7/5559/2014/, 2014.

Andrews, E., Sheridan, P. J., Fiebig, M., McComiskey, A., Ogren, J. A., Arnott, P., Covert, D., Elleman, R., Gasparini, R., Collins, D., Jonsson, H., Schmid, B., and Wang, J.: Comparison of methods for deriving aerosol asymmetry parameter, Journal of Geophysical Research: Atmospheres, 111, doi:10.1029/2004JD005734, URL http://dx.doi.org/10.1029/2004JD005734, 2006.

Angström, A.: On the atmospheric transmission of sun radiation, II, Geogr. Ann. Stockholm, 12, 130–159, 1930.

Antón, M., Loyola, D., Román, R., and Vömel, H.: Validation of GOME-2/MetOp-A total water vapour column using reference radiosonde data from GRUAN network, Atmospheric Measurement Techniques Discussions, 7, 9573–9601, doi:10.5194/amtd-7-9573-2014, URL http://www.atmos-meas-tech-discuss.net/7/9573/2014/, 2014.

Aquilanti, V., Ascenzi, D., Bartolomei, M., Cappelletti, D., Cavalli, S., de Castro Vitores, M., and Pirani, F.: Molecular Beam Scattering of Aligned Oxygen Molecules. The Nature of the Bond in the O2-O2 Dimer, Journal of the American Chemical Society, 121, 10 794–10 802, doi: 10.1021/ja9917215, URL http://pubs.acs.org/doi/abs/10.1021/ja9917215, 1999.

Arlander, D., Brüning, D., Schmidt, U., and Ehhalt, D.: The tropospheric distribution of formaldehyde during TROPOZ II, Journal of Atmospheric Chemistry, 22, 251–269, doi:10.1007/BF00696637, URL http://dx.doi.org/10.1007/BF00696637, 1995.

Aschmann, J., Sinnhuber, B.-M., Atlas, E. L., and Schauffler, S. M.: Modeling the transport of very short-lived substances into the tropical upper troposphere and lower stratosphere, Atmospheric Chemistry and Physics, 9, 9237–9247, doi:10.5194/acp-9-9237-2009, URL http://www.atmos-chem-phys.net/9/9237/2009/, 2009.

Ashfold, M. J., Harris, N. R. P., Atlas, E. L., Manning, A. J., and Pyle, J. A.: Transport of short-lived species into the Tropical Tropopause Layer, Atmospheric Chemistry and Physics, 12, 6309–6322, doi:10.5194/acp-12-6309-2012, URL http://www.atmos-chem-phys.net/12/6309/2012/, 2012.

Ashworth, S. H., Allan, B. J., and Plane, J. M. C.: High resolution spectroscopy of the OIO radical: Implications for the ozone-depleting potential of iodine, Geophys. Res. Lett., 29, doi:10.1029/2001GL013851, 2002.

Atkinson, R., Baulch, D. L., Cox, R. A., Crowley, J. N., Hampson, R. F., Hynes, R. G., Jenkin, M. E., Rossi, M. J., and Troe, J.: Evaluated kinetic and photochemical data for atmospheric chemistry: Volume I - gas phase reactions of O_x, HO_x, NO_x and SO_x species, Atmospheric Chemistry and Physics, 4, 1461–1738, doi:10.5194/acp-4-1461-2004, URL http://www.atmos-chem-phys.net/4/1461/2004/, 2004.

Baidar, S., Oetjen, H., Coburn, S., Dix, B., Ortega, I., Sinreich, R., and Volkamer, R.: The CU Airborne MAX-DOAS instrument: vertical profiling of aerosol extinction and trace gases, Atmospheric Measurement Techniques, 6, 719–739, doi:10.5194/amt-6-719-2013, URL http://www.atmos-meas-tech.net/6/719/2013/, 2013.

Baker, A., Thompson, D., Campos, M., Parry, S., and Jickells, T.: Iodine concentration and availability in atmospheric aerosol, Atmospheric Environment, 34, 4331 – 4336, doi:http://dx.doi.org/10.1016/S1352-2310(00)00208-9, URL http://www.sciencedirect.com/science/article/pii/S1352231000002089, 2000.

Baker, A. R.: Inorganic iodine speciation in tropical Atlantic aerosol, Geophysical Research Letters, 31, doi:10.1029/2004GL020144, URL http://dx.doi.org/10.1029/2004GL020144, 2004.

Barker, H. W., Marshak, A., Szyrmer, W., Blanchet, J.-P., Trishchenko, A., and Li, Z.: Inference of Cloud Optical Depth from Aircraft-Based Solar Radiometric Measurements, J. Atmos. Sci., 59, 2093–2111, doi:10.1175/1520-0469(2002)059⟨2093:IOCODF⟩2.0.CO;2, URL http://dx.doi.org/10.1175/1520-0469(2002)059<2093:IOCODF>2.0.CO;2, 2002.

Battaglia, A., Westbrook, C. D., Kneifel, S., Kollias, P., Humpage, N., Löhnert, U., Tyynelä, J., and Petty, G. W.: G band atmospheric radars: new frontiers in cloud physics, Atmospheric Measurement Techniques, 7, 1527–1546, doi:10.5194/amt-7-1527-2014, URL http://www.atmos-meas-tech.net/7/1527/2014/, 2014.

Beirle, S., Platt, U., von Glasow, R., Wenig, M., and Wagner, T.: Estimate of nitrogen oxide emissions from shipping by satellite remote sensing, Geophysical Research Letters, 31, n/a–n/a, doi:10.1029/2004GL020312, URL http://dx.doi.org/10.1029/2004GL020312, 2004.

Bell, N., Hsu, L., Jacob, D. J., Schultz, M. G., Blake, D. R., Butler, J. H., King, D. B., Lobert, J. M., and Maier-Reimer, E.: Methyl iodide: Atmospheric budget and use as a tracer of marine convection in global models, J. Geophys. Res., 107, 4340–, 2002.

Bertram, T. H., Perring, A. E., Wooldridge, P. J., Crounse, J. D., Kwan, A. J., Wennberg, P. O., Scheuer, E., Dibb, J., Avery, M., Sachse, G., Vay, S. A., Crawford, J. H., McNaughton, C. S., Clarke, A., Pickering, K. E., Fuelberg, H., Huey, G., Blake, D. R., Singh, H. B., Hall, S. R., Shetter, R. E., Fried, A., Heikes, B. G., and Cohen, R. C.: Direct Measurements of the Convective Recycling of the Upper Troposphere, Science, 315, 816–820, doi:10.1126/science.1134548, URL http://www.sciencemag.org/content/315/5813/816.abstract, 2007.

Bhetanabhotla, M., Crowell, B., Coucouvinos, A., Hill, R., and Rinker, R.: Simulation of trace species production by lightning and corona discharge in moist air, Atmospheric Environment (1967), 19, 1391 – 1397, doi:http://dx.doi.org/10.1016/0004-6981(85)90276-8, URL http://www.sciencedirect.com/science/article/pii/0004698185902768, 1985.

Bloss, W. J., Lee, J. D., Johnson, G. P., Sommariva, R., Heard, D. E., Saiz-Lopez, A., Plane, J. M. C., McFiggans, G., Coe, H., Flynn, M., Williams, P., Rickard, A. R., and Fleming, Z. L.: Impact of halogen monoxide chemistry upon boundary layer OH and HO2 concentrations at a coastal site, Geophysical Research Letters, 32, doi:10.1029/2004GL022084, URL http://dx.doi.org/10.1029/2004GL022084, 2005.

Bobrowski, N., Honninger, G., Galle, B., and Platt, U.: Detection of bromine monoxide in a volcanic plume, Nature, 423, 273–276, doi:10.1038/nature01625, URL http://dx.doi.org/10.1038/nature01625, 2003.

Bogumil, K., Orphal, J., and Burrows, J. P.: Temperature-dependent absorption cross-sections of O_3, NO_2, and other atmospheric trace gases measured with the SCIAMACHY spectrometer, in: Proceedings of the ERS-Envisat Symposium, Gothenburg, Sweden, 2000.

Bonazzola, M. and Haynes, P.: A trajectory-based study of the tropical tropopause region, J. Geophys. Res., 109, D20 112, doi:10.1029/2003JD004356, 2004.

Bönisch, H., Engel, A., Birner, T., Hoor, P., Tarasick, D. W., and Ray, E. A.: On the structural changes in the Brewer-Dobson circulation after 2000, Atmospheric Chemistry and Physics, 11, 3937–3948, doi:10.5194/acp-11-3937-2011, URL http://www.atmos-chem-phys.net/11/3937/2011/, 2011.

Bösch, H., Camy-Peyret, C., Chipperfield, M. P., Fitzenberger, R., Harder, H., Platt, U., and Pfeilsticker, K.: Upper limits of stratospheric IO and OIO inferred from center-to-limb-darkening-corrected balloon-borne solar occultation visible spectra: Implications for total gaseous iodine and stratospheric ozone, Journal of Geophysical Research: Atmospheres, 108, doi:10.1029/2002JD003078, URL http://dx.doi.org/10.1029/2002JD003078, 2003.

Bozem, H., Fischer, H., Gurk, C., Schiller, C. L., Parchatka, U., Koenigstedt, R., Stickler, A., Martinez, M., Harder, H., Kubistin, D., Williams, J., Eerdekens, G., and Lelieveld, J.: Influence of corona discharge on the ozone budget in the tropical free troposphere: a case study of deep convection during GABRIEL, Atmospheric Chemistry and Physics, 14, 8917–8931, doi:10.5194/acp-14-8917-2014, URL http://www.atmos-chem-phys.net/14/8917/2014/, 2014.

Braesicke, P., See Hai, O., and Abu Samah, A.: Properties of strong off-shore Borneo vortices: a composite analysis of flow pattern and composition as captured by ERA-Interim, Atmospheric Science Letters, 13, 128–132, doi:10.1002/asl.372, URL http://dx.doi.org/10.1002/asl.372, 2012.

Brasseur, A.-L., Ramaroson, R., Delannoy, A., Skamarock, W., and Barth, M.: Three-Dimensional Calculation of Photolysis Frequencies in the Presence of Clouds and Impact on Photochemistry, Journal of Atmospheric Chemistry, 41, 211–237, doi:10.1023/A:1014952630482, URL http://dx.doi.org/10.1023/A%3A1014952630482, 2002.

Brühl, C. and Crutzen, P. J.: MPIC two-dimensional model, in: The Atmospheric Effect of Stratospheric Aircraft, edited by: Prather, M. J. and Remsberg, E. E., NASA Ref. Publications, 1292, 103–104, 1993.

Bussemer, M.: Der Ring- Effekt: Ursachen und Einfluss auf die spektroskopische Messung stratosphärischer Spurenstoffe, Diploma thesis, University of Heidelberg, Heidelberg, Germany, 1993.

Butz, A.: Case Studies of Stratospheric Nitrogen, Chlorine, and Iodine Photochemistry Based on Balloon-borne UV/visible and IR Absorption Spectroscopy, Ph.D. thesis, Institute of Environmental Physics, University of Heidelberg, 2006.

Butz, A., Bösch, H., Camy-Peyret, C., Chipperfield, M. P., Dorf, M., Kreycy, S., Kritten, L., Prados-Roman, C., Schwärzle, J., and Pfeilsticker, K.: Constraints on inorganic gaseous iodine in the tropical upper troposphere and stratosphere inferred from balloon-borne solar occultation observations, Atmos. Chem. Phys., 9, 7229–7242, doi:10.5194/acp-9-7229-2009, 2009.

Callies, J., Corpaccioli, E., Eisinger, M., Hahne, A., , and Lefebvre, A.: GOME-2- Metop's second-generation sensor for operational ozone monitoring, ESA Bulletin, 102, 28–36, URL http://www.esa.int/esapub/bulletin/bullet102/Callies102.pdf, 2000.

Carpenter, L., Archer, S. D., and Beale, R.: Ocean-atmosphere trace gas exchange, Chem. Soc. Rev., 41, 6473–6506, doi:10.1039/C2CS35121H, 2012.

Carpenter, L., MacDonald, S. M., Shaw, M. D., Kumar, R., Saunders, R. W., Parthipan, R., Wilson, J., and Plane, J. M. C.: Atmospheric iodine levels influenced by sea surface emissions of inorganic iodine, Nature, 6, 108–111, doi:10.1038/ngeo1687, 2013.

Catoire, V., Krystofiak, G., Robert, C., and Chartier, M.: Airborne infrared laser spectrometry for in-situ trace gas measurements: convection case studies as an example of application, to be submitted to Atmospheric Measurement Techniques Discussions, 2015.

Chameides, W. L. and Davis, D. D.: Iodine: Its Possible Role in Tropospheric Photochemistry, J. Geophys. Res., 85, 7383–7398, 1980.

Chameides, W. L., Fehsenfeld, F., Rodgers, M. O., Cardelino, C., Martinez, J., Parrish, D., Lonneman, W., Lawson, D. R., Rasmussen, R. A., Zimmerman, P., Greenberg, J., Mlddleton, P., and Wang, T.: Ozone precursor relationships in the ambient atmosphere, Journal of Geophysical Research: Atmospheres, 97, 6037–6055, doi:10.1029/91JD03014, URL http://dx.doi.org/10.1029/91JD03014, 1992.

Chance, K. and Kurucz, R.: An improved high-resolution solar reference spectrum for earth's atmosphere measurements in the ultraviolet, visible, and near infrared, Journal of Quantitative Spectroscopy &Radiative Transfer, 111, 1289–1295, doi:10.1016/j.jqsrt.2010.01.036, 2010.

Chance, K. and Spurr, R. J. D.: Ring effect studies; Rayleigh scattering, including molecular parameters for rotational Raman scattering and the Fraunhofer spectrum, Appl. Opt., 36, 5224–5230, 1997.

Chapman, S.: On ozone and atomic oxygen in the upper atmosphere, Philos. Mag., 10, 369–383, 1930.

Chipperfield, M. P.: New version of the TOMCAT/SLIMCAT off-line chemical transport model: Intercomparison of stratospheric tracer experiments, Quarterly Journal of the Royal Meteorological Society, 132, 1179–1203, doi:10.1256/qj.05.51, URL http://dx.doi.org/10.1256/qj.05.51, 2006.

Chuck, A. L., Turner, S. M., and Liss, P. S.: Oceanic distributions and air-sea fluxes of biogenic halocarbons in the open ocean, Journal of Geophysical Research: Oceans, 110, doi:10.1029/2004JC002741, URL http://dx.doi.org/10.1029/2004JC002741, 2005.

Clémer, K., Van Roozendael, M., Fayt, C., Hendrick, F., Hermans, C., Pinardi, G., Spurr, R., Wang, P., and De Mazière, M.: Multiple wavelength retrieval of tropospheric aerosol optical properties from MAXDOAS measurements in Beijing, Atmos. Meas. Tech., 3, 111–145, 2010.

Cleveland, W. S., Graedel, T. E., Kleiner, B., and Warner, J. L.: Sunday and Workday Variations in Photochemical Air Pollutants in New Jersey and New York, Science, 186, 1037–1038, doi:10.1126/science.186.4168.1037, URL http://www.sciencemag.org/content/186/4168/1037.abstract, 1974.

Coburn, S., Ortega, I., Thalman, R., Blomquist, B., Fairall, C. W., and Volkamer, R.: Measurements of diurnal variations and Eddy Covariance (EC) fluxes of glyoxal in the tropical marine boundary layer: description of the Fast LED-CE-DOAS instrument, Atmospheric Measurement Techniques Discussions, 7, 6245–6285, doi:10.5194/amtd-7-6245-2014, URL http://www.atmos-meas-tech-discuss.net/7/6245/2014/, 2014.

Commane, R., Seitz, K., Bale, C. S. E., Bloss, W. J., Buxmann, J., Ingham, T., Platt, U., Pöhler, D., and Heard, D. E.: Iodine monoxide at a clean marine coastal site: observations of high frequency variations and inhomogeneous distributions, Atmos. Chem. Phys., 11, 6721–6733, doi:10.5194/acp-11-6721-2011, 2011.

Crutzen, P. J.: The influence of nitrogen oxide on the atmospheric ozone content, Q.J.R. Meteorol. Soc., 96, 320–325, doi:10.1002/qj.49709640815, URL http://dx.doi.org/10.1002/qj.49709640815, 1970.

David, A. and Marshak, A.: Space-Time Characteristics of Light Transmitted through Dense Clouds: A Greenâ€™s Function Analysis, J. Atmos. Sci, 59, 2713–2727, doi:10.1175/1520-0469(2002)059⟨2713:STCOLT⟩2.0.CO;2, URL http://dx.doi.org/10.1175/1520-0469(2002)059<2713:STCOLT>2.0.CO;2, 2002.

De Smedt, I.: Long-Term Global Observations of Tropospheric Formaldehyde Retrieved from Spaceborne Nadir UV Sensors, Ph.D. thesis, Laboratoire de Chimie Quantique et Photophysique, Université libre de Bruxelles, 2011.

De Smedt, I., Müller, J.-F., Stavrakou, T., van der A, R., Eskes, H., and Van Roozendael, M.: Twelve years of global observations of formaldehyde in the troposphere using GOME and SCIAMACHY sensors, Atmospheric Chemistry and Physics, 8, 4947–4963, doi:10.5194/acp-8-4947-2008, URL http://www.atmos-chem-phys.net/8/4947/2008/, 2008.

De Smedt, I., Stavrakou, T., Müller, J.-F., van der A, R. J., and Van Roozendael, M.: Trend detection in satellite observations of formaldehyde tropospheric columns, Geophysical Research Letters, 37, doi:10.1029/2010GL044245, URL http://dx.doi.org/10.1029/2010GL044245, 2010.

De Smedt, I., Van Roozendael, M., Stavrakou, T., Müller, J.-F., Lerot, C., Theys, N., Valks, P., Hao, N., and van der A, R.: Improved retrieval of global tropospheric formaldehyde columns from GOME-2/MetOp-A addressing noise reduction and instrumental degradation issues, Atmospheric Measurement Techniques, 5, 2933–2949, doi:10.5194/amt-5-2933-2012, URL http://www.atmos-meas-tech.net/5/2933/2012/, 2012.

Demtröder, W.: Experimentalphysik 3 - Atome, Moleküle und Festkörper, 3.Auflage, Springer-Verlag, Heidelberg, doi:10.1007/978-3-642-03911-9, 2010.

Deutschmann, T.: Atmospheric radiative transfer modelling using Monte Carlo methods, Diploma thesis, University of Heidelberg, 2008.

Deutschmann, T., Beirle, S., Frieß, U., Grzegorski, M., Kern, C., Kritten, L., Platt, U., Prados-Roman, C., Pukite, J., Wagner, T., Werner, B., and Pfeilsticker, K.: The Monte Carlo atmospheric radiative transfer model McArtim: Introduction and validation of Jacobians and 3D features, Journal of Quantitative Spectroscopy &Radiative Transfer, p. 19, 2011.

Dickerson, R. R., Huffman, G. J., Luke, W. T., Nunnermacker, L., Pickering, K., Leslie, A., Lindsey, C., Slinn, W., Kelly, T., Daum, P., Delany, A., Greenberg, J., Zimmerman, P., Boatman, J., Ray, J., and Stedman, D.: Thunderstorms: An important mechanism in the transport of air pollutants, Science, 235, 460–465, URL http://www.atmos.umd.edu/~russ/thunder1987.pdf, 1987.

DiGangi, J. P., Boyle, E. S., Karl, T., Harley, P., Turnipseed, A., Kim, S., Cantrell, C., Maudlin III, R. L., Zheng, W., Flocke, F., Hall, S. R., Ullmann, K., Nakashima, Y., Paul, J. B., Wolfe, G. M., Desai, A. R., Kajii, Y., Guenther, A., and Keutsch, F. N.: First direct measurements of formaldehyde flux via eddy covariance: implications for missing in-canopy formaldehyde sources, Atmospheric Chemistry and Physics, 11, 10 565–10 578, doi:10.5194/acp-11-10565-2011, URL http://www.atmos-chem-phys.net/11/10565/2011/, 2011.

Dinter, T.: Modellierung ozeanischer Rückstreuung unter Einbeziehung von Vibrations-Raman-Streuung und die Auswertung anhand von Satellitendaten, Master's thesis, Institute of Environmental Physics, Bremen, 2005.

Dix, B., Brenninkmeijer, C. A. M., Frieß, U., Wagner, T., and Platt, U.: Airborne multi-axis DOAS measurements of atmospheric trace gases on CARIBIC long-distance flights, Atmospheric Measurement Techniques, 2, 639–652, doi:10.5194/amt-2-639-2009, URL http://www.atmos-meas-tech.net/2/639/2009/, 2009.

Dix, B., Baidar, S., Bresch, J. F., Hall, S. R., Schmidt, K. S., Wang, S., and Volkamer, R.: Detection of iodine monoxide in the tropical free troposphere, Proceedings of the National Academy of Sciences, doi:10.1073/pnas.1212386110, URL http://www.pnas.org/content/early/2013/01/22/1212386110.abstract, 2013.

Draxler, R. and Rolph, G.: HYSPLIT (HYbrid Single-Particle Lagrangian Integrated Trajectory) Model access via NOAA ARL READY Website (http://ready.arl.noaa.gov/HYSPLIT.php), NOAA Air Resources Laboratory, Silver Spring, MD, 2013.

Edwards, P. M., Evans, M. J., Furneaux, K. L., Hopkins, J., Ingham, T., Jones, C., Lee, J. D., Lewis, A. C., Moller, S. J., Stone, D., Whalley, L. K., and Heard, D. E.: OH reactivity in a South East Asian tropical rainforest during the Oxidant and Particle Photochemical Processes (OP3) project, Atmospheric Chemistry and Physics, 13, 9497–9514, doi:10.5194/acp-13-9497-2013, URL http://www.atmos-chem-phys.net/13/9497/2013/, 2013.

Ehn, M., Thornton, J. A., Kleist, E., Sipila, M., Junninen, H., Pullinen, I., Springer, M., Rubach, F., Tillmann, R., Lee, B., Lopez-Hilfiker, F., Andres, S., Acir, I.-H., Rissanen, M., Jokinen, T., Schobesberger, S., Kangasluoma, J., Kontkanen, J., Nieminen, T., Kurten, T., Nielsen, L. B., Jorgensen, S., Kjaergaard, H. G., Canagaratna, M., Maso, M. D., Berndt, T., Petaja, T., Wahner, A., Kerminen, V.-M., Kulmala, M., Worsnop, D. R., Wildt, J., and Mentel, T. F.: A large source of low-volatility secondary organic aerosol, Nature, 506, 476–479, doi:10.1038/nature13032, URL http://dx.doi.org/10.1038/nature13032, 2014.

Enell, C.-F., Steen, Å., Wagner, T., Frieß, U., Pfeilsticker, K., Platt, U., and Fricke, K.-H.: Occurrence of polar stratospheric clouds at Kiruna, Annales Geophysicae, 17, 1457–1462, doi: 10.1007/s00585-999-1457-7, URL http://www.ann-geophys.net/17/1457/1999/, 1999.

Erle, F., Pfeilsticker, K., and Platt, U.: On the influence of tropospheric clouds on zenith-scattered-light measurements of stratospheric species, Geophysical Research Letters, 22, 2725–2728, doi: 10.1029/95GL02789, URL http://dx.doi.org/10.1029/95GL02789, 1995.

Fahey, D. and Hegglin, M.: Twenty Questions and answers about the ozone layer: 2010 Update, Scientific Assessment of Ozone Depletion: 2010; World Meteorological Organization Global Ozone Research and Monitoring Project - Report No. 52, p. 72, URL http://ozone.unep.org/Assessment_Panels/SAP/Scientific_Assessment_2010/SAP-2010-FAQs-update.pdf, 2010.

Farman, J. C., Gardiner, B. G., and Shanklin, J. D.: Large losses of total ozone in Antarctica reveal seasonal ClO_x/NO_x interaction, Nature, 315, 207–210, 1985.

Fickert, S., Adams, J. W., and Crowley, J. N.: Activation of Br2 and BrCl via uptake of HOBr onto aqueous salt solutions, Journal of Geophysical Research: Atmospheres, 104, 23 719–23 727, doi:10.1029/1999JD900359, URL http://dx.doi.org/10.1029/1999JD900359, 1999.

Finlayson-Pitts, B. J. and Pitts Jr., J. N.: Volatile Organic Compounds: Ozone Formation, Alternative Fuels, and Toxics, Chem. Ind., October 18, 796–800, 1993.

Finlayson-Pitts, B. J. and Pitts Jr., J. N.: Chemistry of the upper and lower atmosphere: Theory, experiments and applications, Academic Press, San Diego, doi:http://dx.doi.org/10.1016/B978-012257060-5/50000-9, 2000.

Fishman, J. and Crutzen, P.: The origin of ozone in the troposphere, Nature, 274, 855–858, 1978.

Fowler, D., Nemitz, E., Misztal, P., Di Marco, C., Skiba, U., Ryder, J., Helfter, C., Cape, J. N., Owen, S., Dorsey, J., Gallagher, M. W., Coyle, M., Phillips, G., Davison, B., Langford, B., MacKenzie, R., Muller, J., Siong, J., Dari-Salisburgo, C., Di Carlo, P., Aruffo, E., Giammaria, F., Pyle, J. A., and Hewitt, C. N.: Effects of land use on surface-atmosphere exchanges of trace gases and energy in Borneo: comparing fluxes over oil palm plantations and a rainforest, Philosophical Transactions of the Royal Society B: Biological Sciences, 366, 3196–3209, doi:10.1098/rstb.2011.0055, URL http://rstb.royalsocietypublishing.org/content/366/1582/3196.abstract, 2011.

Fraunhofer, J.: Bestimmung des Brechungs- und des Farbenzerstreungs-Vermögens verschiedener Glasarten, in Bezug auf die Vervollkommnung achromatischer Fernröhre, Annalen der Physik, 56, 264–313, doi:10.1002/andp.18170560706, URL http://dx.doi.org/10.1002/andp.18170560706, 1817.

Frieß, U., Hollwedel, J., König-Langlo, G., Wagner, T., and Platt, U.: Dynamics and chemistry of tropospheric bromine explosion events in the Antarctic coastal region, J. Geophys. Res., 109, D06 305, 2004.

Frieß, U., Monks, P., Remedios, J., Rozanov, A., Sinreich, R., Wagner, T., and Platt, U.: MAX-DOAS O_4 measurements: A new technique to derive information on atmospheric aerosols: 2. Modeling studies, J. Geophys. Res., 111, D14 203, doi:10.1029/2005JD006618, 2006.

Frieß, U., Sihler, H., Sander, R., Pöhler, D., Yilmaz, S., and Platt, U.: The vertical distribution of BrO and aerosols in the Arctic: Measurements by active and passive differential optical absorption spectroscopy, J. Geophys. Res., 116, D00R04–, 2011.

Fu, T.-M., Jacob, D. J., Palmer, P. I., Chance, K., Wang, Y. X., Barletta, B., Blake, D. R., Stanton, J. C., and Pilling, M. J.: Space-based formaldehyde measurements as constraints on volatile organic compound emissions in east and south Asia and implications for ozone, Journal of Geophysical Research: Atmospheres, 112, doi:10.1029/2006JD007853, URL http://dx.doi.org/10.1029/2006JD007853, 2007.

Fu, T.-M., Jacob, D. J., Wittrock, F., Burrows, J. P., Vrekoussis, M., and Henze, D. K.: Global budgets of atmospheric glyoxal and methylglyoxal, and implications for formation of secondary organic aerosols, Journal of Geophysical Research: Atmospheres, 113, doi:10.1029/2007JD009505, URL http://dx.doi.org/10.1029/2007JD009505, 2008.

Fueglistaler, S., Dessler, A. E., Dunkerton, T. J., Folkins, I., Fu, Q., and Mote, P. W.: Tropical tropopause layer, Reviews of Geophysics, 47, doi:10.1029/2008RG000267, URL http://dx.doi.org/10.1029/2008RG000267, 2009.

Fuhlbrügge, S., Krüger, K., Quack, B., Atlas, E., Hepach, H., and Ziska, F.: Impact of the marine atmospheric boundary layer conditions on VSLS abundances in the eastern tropical and subtropical North Atlantic Ocean, Atmospheric Chemistry and Physics, 13, 6345–6357, doi:10.5194/acp-13-6345-2013, URL http://www.atmos-chem-phys.net/13/6345/2013/, 2013.

Garland, R. M., Yang, H., Schmid, O., Rose, D., Nowak, A., Achtert, P., Wiedensohler, A., Takegawa, N., Kita, K., Miyazaki, Y., Kondo, Y., Hu, M., Shao, M., Zeng, L. M., Zhang, Y. H., Andreae, M. O., and Pöschl, U.: Aerosol optical properties in a rural environment near the mega-city Guangzhou, China: implications for regional air pollution, radiative forcing and remote sensing, Atmospheric Chemistry and Physics, 8, 5161–5186, doi:10.5194/acp-8-5161-2008, URL http://www.atmos-chem-phys.net/8/5161/2008/, 2008.

General, S.: Development of the Heidelberg Airborne Imaging DOAS Instrument (HAIDI): A novel remote sensing device for the investigation of two-and three-dimensional trace gas distributions in the troposphere, Ph.D. thesis, Institute of Environmental Physics, University of Heidelberg, 2014a.

General, S., Pöhler, D., Sihler, H., Bobrowski, N., Frieß, U., Zielcke, J., Horbanski, M., Shepson, P. B., Stirm, B. H., Simpson, W. R., Weber, K., Fischer, C., and Platt, U.: The Heidelberg Airborne Imaging DOAS Instrument (HAIDI) - a novel Imaging DOAS device for 2-D and 3-D imaging of trace gases and aerosols, Atmospheric Measurement Techniques Discussions, 7, 2187–2257, doi:10.5194/amtd-7-2187-2014, URL http://www.atmos-meas-tech-discuss.net/7/2187/2014/, 2014b.

Gettelman, A., Salby, M. L., and Sassi, F.: Distribution and influence of convection in the tropical tropopause region, Journal of Geophysical Research: Atmospheres, 107, ACL 6–1–ACL 6–12, doi:10.1029/2001JD001048, URL http://dx.doi.org/10.1029/2001JD001048, 2002.

Gielen, C., Van Roozendael, M., Hendrick, F., Pinardi, G., Vlemmix, T., De Bock, V., De Backer, H., Fayt, C., Hermans, C., Gillotay, D., and Wang, P.: A simple and versatile cloud-screening method for MAX-DOAS retrievals, Atmospheric Measurement Techniques Discussions, 7, 5883–5920, doi:10.5194/amtd-7-5883-2014, URL http://www.atmos-meas-tech-discuss.net/7/5883/2014/, 2014.

Giglio, L.: MODIS Collection 5 Active Fire Product User's Guide Version 2.4, Science Systems and Applications, Inc. University of Maryland, Department of Geography, p. 61, 2010.

Giglio, L., Descloitres, J., Justice, C. O., and Kaufman, Y. J.: An Enhanced Contextual Fire Detection Algorithm for MODIS, Remote Sensing of Environment, 87, 273 – 282, doi:http://dx.doi.org/10.1016/S0034-4257(03)00184-6, URL http://www.sciencedirect.com/science/article/pii/S0034425703001846, 2003.

Gilfedder, B. S., Lai, S. C., Petri, M., Biester, H., and Hoffmann, T.: Iodine speciation in rain, snow and aerosols, Atmospheric Chemistry and Physics, 8, 6069–6084, doi:10.5194/acp-8-6069-2008, URL http://www.atmos-chem-phys.net/8/6069/2008/, 2008.

Gonzalez, R. C. and Woods, R. E.: Digital Image Processing, Prentice-Hall Press, Inc., New Jersey, 2002.

Grainger, J. and Ring, J.: Anomalous Fraunhofer line profiles, Nature, 193, 762, 1962.

Gray, D. F.: The Inferred Color Index of the Sun, Astronomical Society of the Pacific, 104, 1035–1038, URL http://articles.adsabs.harvard.edu/cgi-bin/nph-iarticle_query?1992PASP..104.1035G&data_type=PDF_HIGH&whole_paper=YES&type=PRINTER&filetype=.pdf, 1992.

Greenblatt, G. D., Orlando, J. J., Burkholder, J. B., and Ravishankara, A. R.: Absorption measurements of oxygen between 330 and 1140 nm, Journal of Geophysical Research: Atmospheres, 95, 18 577–18 582, doi:10.1029/JD095iD11p18577, URL http://dx.doi.org/10.1029/JD095iD11p18577, 1990.

Großmann, K., Frieß, U., Peters, E., Wittrock, F., Lampel, J., Yilmaz, S., Tschritter, J., Sommariva, R., von Glasow, R., Quack, B., Krüger, K., Pfeilsticker, K., and Platt, U.: Iodine monoxide in the Western Pacific marine boundary layer, Atmospheric Chemistry and Physics, 13, 3363–3378, doi:10.5194/acp-13-3363-2013, URL http://www.atmos-chem-phys.net/13/3363/2013/, 2013.

Guenther, A., Hewitt, C. N., Erickson, D., Fall, R., Geron, C., Graedel, T., Harley, P., Klinger, L., Lerdau, M., Mckay, W. A., Pierce, T., Scholes, B., Steinbrecher, R., Tallamraju, R., Taylor, J., and Zimmerman, P.: A global model of natural volatile organic compound emissions, Journal of Geophysical Research: Atmospheres, 100, 8873–8892, doi:10.1029/94JD02950, URL http://dx.doi.org/10.1029/94JD02950, 1995.

Guenther, A., Karl, T., Harley, P., Wiedinmyer, C., Palmer, P. I., and Geron, C.: Estimates of global terrestrial isoprene emissions using MEGAN (Model of Emissions of Gases and Aerosols from Nature), Atmospheric Chemistry and Physics, 6, 3181–3210, doi:10.5194/acp-6-3181-2006, URL http://www.atmos-chem-phys.net/6/3181/2006/, 2006.

Guimbaud, C., Catoire, V., Gogo, S., Robert, C., Chartier, M., Laggoun-Defarge, F., Grossel, A., Alberic, P., Pomathiod, L., Nicoullaud, B., and Richard, G.: A portable infrared laser spectrometer for flux measurements of trace gases at the geosphere-atmosphere interface, Measurement Science and Technology, 22, 075 601, URL http://stacks.iop.org/0957-0233/22/i=7/a=075601, 2011.

Haken, H. and Wolf, H. C.: Atom- und Quantenphysik, Springer-Verlag Berlin Heidelberg, 2004.

Haken, H. and Wolf, H. C.: Molekülphysik und Quantenchemie, Springer-Verlag Berlin Heidelberg, 2006.

Hamann, U., Walther, A., Baum, B., Bennartz, R., Bugliaro, L., Derrien, M., Francis, P. N., Heidinger, A., Joro, S., Kniffka, A., Le Gléau, H., Lockhoff, M., Lutz, H.-J., Meirink, J. F., Minnis, P., Palikonda, R., Roebeling, R., Thoss, A., Platnick, S., Watts, P., and Wind, G.: Remote sensing of cloud top pressure/height from SEVIRI: analysis of ten current retrieval algorithms, Atmospheric Measurement Techniques, 7, 2839–2867, doi:10.5194/amt-7-2839-2014, URL http://www.atmos-meas-tech.net/7/2839/2014/, 2014.

Hamer, P. D., Marécal, V., Hossaini, R., Pirre, M., Warwick, N., Chipperfield, M., Samah, A. A., Harris, N., Robinson, A., Quack, B., Engel, A., Krüger, K., Atlas, E., Subramaniam, K., Oram, D., Leedham, E., Mills, G., Pfeilsticker, K., Sala, S., Keber, T., Bönisch, H., Peng, L. K.,

Nadzir, M. S. M., Lim, P. T., Mujahid, A., Anton, A., Schlager, H., Catoire, V., Krysztofiak, G., Fühlbrügge, S., Dorf, M., and Sturges, W. T.: Modelling the chemistry and transport of bromoform within a sea breeze driven convective system during the SHIVA Campaign, Atmospheric Chemistry and Physics Discussions, 13, 20 611–20 676, doi:10.5194/acpd-13-20611-2013, URL http://www.atmos-chem-phys-discuss.net/13/20611/2013/, 2013.

Hansen, J. C., Li, Y., Francisco, J. S., and Li, Z.: On the Mechanism of the BrO + CH2O Reaction, The Journal of Physical Chemistry A, 103, 8543–8546, doi:10.1021/jp991757j, URL http://pubs.acs.org/doi/abs/10.1021/jp991757j, 1999.

Harder, J. W., Fried, A., Sewell, S., and Henry, B.: Comparison of tunable diode laser and long-path ultraviolet/visible spectroscopic measurements of ambient formaldehyde concentrations during the 1993 OH Photochemistry Experiment, Journal of Geophysical Research: Atmospheres, 102, 6267–6282, doi:10.1029/96JD01731, URL http://dx.doi.org/10.1029/96JD01731, 1997.

Heard, D. and Pilling, M.: Measurement of OH and HO2in the Troposphere, Chem. Rev., 103, 5163–5198, 2003.

Heinle, A., Macke, A., and Srivastav, A.: Automatic cloud classification of whole sky images, Atmospheric Measurement Techniques, 3, 557–567, doi:10.5194/amt-3-557-2010, URL http://www.atmos-meas-tech.net/3/557/2010/, 2010.

Held, I. M. and Soden, B. J.: Water vapour feedback and global warming, Annu. Rev. Energ. Env., 25, 441–475, 2000.

Henyey, L. and Greenstein, J.: Diffuse radiation in the Galaxy, Astrophysical Journal, 93, 70–83, doi:10.1086/144246, 1941.

Hepach, H., Quack, B., Ziska, F., Fuhlbrügge, S., Atlas, E. L., Krüger, K., Peeken, I., and Wallace, D. W. R.: Drivers of diel and regional variations of halocarbon emissions from the tropical North East Atlantic, Atmospheric Chemistry and Physics, 14, 1255–1275, doi:10.5194/acp-14-1255-2014, URL http://www.atmos-chem-phys.net/14/1255/2014/, 2014.

Hermans, C., Vandaele, A. C., Carleer, M., Fally, S., Colin, R., Jenouvrier, A., Coquart, B., and Mérienne, M.-F.: Absorption Cross-Sections of Atmospheric Constituents: NO_2, O_2, and H_2O, Environ. Sci. & Pollut. Res., 6, 151–158, 1999.

Heue, K.-P., Riede, H., Walter, D., Brenninkmeijer, C. A. M., Wagner, T., Frieß, U., Platt, U., Zahn, A., Stratmann, G., and Ziereis, H.: CARIBIC DOAS observations of nitrous acid and formaldehyde in a large convective cloud, Atmospheric Chemistry and Physics, 14, 6621–6642, doi:10.5194/acp-14-6621-2014, URL http://www.atmos-chem-phys.net/14/6621/2014/, 2014.

Hewitt, C. N., Lee, J. D., MacKenzie, A. R., Barkley, M. P., Carslaw, N., Carver, G. D., Chappell, N. A., Coe, H., Collier, C., Commane, R., Davies, F., Davison, B., DiCarlo, P., Di Marco, C. F., Dorsey, J. R., Edwards, P. M., Evans, M. J., Fowler, D., Furneaux, K. L., Gallagher, M., Guenther, A., Heard, D. E., Helfter, C., Hopkins, J., Ingham, T., Irwin, M., Jones, C., Karunaharan, A., Langford, B., Lewis, A. C., Lim, S. F., MacDonald, S. M., Mahajan, A. S., Malpass, S., McFiggans, G., Mills, G., Misztal, P., Moller, S., Monks, P. S., Nemitz, E., Nicolas-Perea, V., Oetjen, H., Oram, D. E., Palmer, P. I., Phillips, G. J., Pike, R., Plane, J. M. C., Pugh, T., Pyle, J. A., Reeves, C. E., Robinson, N. H., Stewart, D., Stone, D., Whalley, L. K., and Yin, X.: Overview: oxidant and particle photochemical processes above a south-east Asian tropical rainforest (the OP3 project): introduction, rationale, location characteristics and tools, Atmospheric Chemistry and Physics, 10, 169–199, doi:10.5194/acp-10-169-2010, URL http://www.atmos-chem-phys.net/10/169/2010/, 2010.

Hoffmann, T., O'Dowd, C. D., and Seinfeld, J. H.: IO homogeneous nucleation: An explanation for coastal new particle formation, Geophys. Res. Lett., 28, 1949–1952, 2001.

Holla, R.: Reactive Halogen Species above Salt Lakes and Salt Pans, Ph.D. thesis, Institute of Environmental Physics, University of Heidelberg, 2013.

Holloway, T., Levy, H., and Kasibhatla, P.: Global distribution of carbon monoxide, Journal of Geophysical Research: Atmospheres, 105, 12 123–12 147, doi:10.1029/1999JD901173, URL http://dx.doi.org/10.1029/1999JD901173, 2000.

Holzinger, R., Warneke, C., Hansel, A., Jordan, A., Lindinger, W., Scharffe, D. H., Schade, G., and Crutzen, P. J.: Biomass burning as a source of formaldehyde, acetaldehyde, methanol, acetone, acetonitrile, and hydrogen cyanide, Geophysical Research Letters, 26, 1161–1164, doi:10.1029/1999GL900156, URL http://dx.doi.org/10.1029/1999GL900156, 1999.

Hönninger, G.: Halogen Oxide Studies in the Boundary layer by Multi Axis Differential Optical Absorption Spectroscopy and Active longpath-DOAS, Phd thesis, Heidelberg University, Germany, 2002.

Hönninger, G., von Friedeburg, C., and Platt, U.: Multi axis differential optical absorption spectroscopy (MAX-DOAS), Atmos. Chem. Phys., 4, 231–254, 2004.

Horn, B. K. and Schunck, B. G.: Determining optical flow, Artificial Intelligence, 17, 185 – 203, doi:http://dx.doi.org/10.1016/0004-3702(81)90024-2, URL http://www.sciencedirect.com/science/article/pii/0004370281900242, 1981.

Hossaini, R., Mantle, H., Chipperfield, M. P., Montzka, S. A., Hamer, P., Ziska, F., Quack, B., Krüger, K., Tegtmeier, S., Atlas, E., Sala, S., Engel, A., Bönisch, H., Keber, T., Oram, D., Mills, G., Ordóñez, C., Saiz-Lopez, A., Warwick, N., Liang, Q., Feng, W., Moore, F., Miller, B. R., Marécal, V., Richards, N. A. D., Dorf, M., and Pfeilsticker, K.: Evaluating global emission inventories of biogenic bromocarbons, Atmospheric Chemistry and Physics, 13, 11 819–11 838, doi:10.5194/acp-13-11819-2013, URL http://www.atmos-chem-phys.net/13/11819/2013/, 2013.

Houze, R., Geotis, S.G.and Marks, F., and West, A.: Winter Monsoon Convection in the Vicinity of North Borneo, Part 1: Structure and Time Variation of theClouds and Precipitation, American Meteorological Society, 109, 8, 1981.

Howard, J. B. and Rees, D. C.: Structural Basis of Biological Nitrogen Fixation, Chem. Rev., 96, 2965–2982, 1996.

Huang, R.-J., Seitz, K., Buxmann, J., Pöhler, D., Hornsby, K. E., Carpenter, L. J., Platt, U., and Hoffmann, T.: In situ measurements of molecular iodine in the marine boundary layer: the link to macroalgae and the implications for O_3, IO, OIO and NO_x, Atmospheric Chemistry and Physics, 10, 4823–4833, doi:10.5194/acp-10-4823-2010, URL http://www.atmos-chem-phys.net/10/4823/2010/, 2010.

Hüneke, T.: Aufbau und Charakterisierung eines sechsfach-miniDOAS Spektrographen für das Forschungsflugzeug DLR-HALO, Diploma thesis, University of Heidelberg, Heidelberg, Germany, 2011.

Inoue, T., Satoh, M., Miura, H., and Mapes, B.: Characteristics of Cloud Size of Deep Convection Simulated by a Global Cloud Resolving Model over the Western Tropical Pacific, Journal of the Meteorological Society of Japan, 86A, 1–15, URL http://157.82.240.167/vl/presentation/data/86A_1.pdf, 2008.

IPCC: Climate Change 2013: The Physical Science Basis, Working Group I Contribution to the Fifth Assessment Report of the Intergovernmental Panel on Climate Change, Working Group I Technical Support Unit, Cambridge University Press, p. 1552, URL https://www.ipcc.ch/report/ar5/wg1/, 2013.

Jacob, D. J.: Introduction to Atmospheric Chemistry, Princeton University Press, Princeton, URL http://acmg.seas.harvard.edu/people/faculty/djj/book/, 1999.

Jaenicke, R.: Aerosol Physics and Chemistry, In: Landolt-Börnstein Numerical Data and Functional Relationships in Science and Technology New Series Group V: Geophysics and Space Research Volume 4 Meteorology Subvolume b, edited by G.Fischer,Physical and Chemical Properties of the Air, pp. 391–457, 2007.

Jähne, P. D. B.: Digitale Bildverarbeitung, Springer-Verlag Berlin Heidelberg, URL http://download.springer.com/static/pdf/786/bfm%253A978-3-540-27384-4%252F1.pdf?auth66=1404286697_18a537de31d20bf15dcc07b236fe737e&ext=.pdf, 2005.

John, R. P., Anisha, G., Nampoothiri, K. M., and Pandey, A.: Micro and macroalgal biomass: A renewable source for bioethanol, Bioresource Technology, 102, 186 – 193, doi:http://dx.doi.org/10.1016/j.biortech.2010.06.139, URL http://www.sciencedirect.com/science/article/pii/S0960852410011429, 2011.

Johnston, H. S.: Reduction of stratospheric ozone by nitrogen oxide catalysts from supersonic transport exhaust, Science, 173, 517–522, doi:10.1126/science.173.3996.517, 1971.

Joseph, B., Bhatt, B. C., Koh, T. Y., and Chen, S.: Sea breeze simulation over the Malay Peninsula in an intermonsoon period, Journal of Geophysical Research: Atmospheres, 113, doi:10.1029/2008JD010319, URL http://dx.doi.org/10.1029/2008JD010319, 2008.

Junkermann, W., Platt, U., and Volz-Thomas, A.: A photoelectric detector for the measurement of photolysis frequencies of ozone and other atmospheric molecules, Journal of Atmospheric Chemistry, 8, 203–227, doi:10.1007/BF00051494, URL http://dx.doi.org/10.1007/BF00051494, 1989.

Kaufman, Y. J., Tanre, D., and Boucher, O.: A satellite view of aerosols in the climate system, Nature, 419, 215–223, doi:10.1038/nature01091, URL http://dx.doi.org/10.1038/nature01091, 2002.

Keng, F.-L., Phang, S.-M., Rahman, N., Leedham, E., Hughes, C., Robinson, A., Harris, N., Pyle, J., and Sturges, W.: Volatile halocarbon emissions by three tropical brown seaweeds under different irradiances, Journal of Applied Phycology, 25, 1377–1386, doi:10.1007/s10811-013-9990-x, URL http://dx.doi.org/10.1007/s10811-013-9990-x, 2013.

Kenntner, M.: A Novel Limb and Nadir DOAS Optical Spectrometer for the the German research aircraft HALO - Feasibility and Validation, Diploma thesis, University of Heidelberg, 2013.

Kiendler-Scharr, A., Wildt, J., Maso, M. D., Hohaus, T., Kleist, E., Mentel, T. F., Tillmann, R., Uerlings, R., Schurr, U., and Wahner, A.: New particle formation in forests inhibited by isoprene emissions, Nature, 461, 381–384, doi:10.1038/nature08292, 2009.

Kim, S., Kim, S.-Y., Lee, M., Shim, H., Wolfe, G. M., Guenther, A. B., He, A., Hong, Y., and Han, J.: Urban-rural interactions in a South Korean forest: uncertainties in isoprene-OH interactions limit understanding of ozone and secondary organic aerosols production, Atmospheric Chemistry and Physics Discussions, 14, 16 691–16 729, doi:10.5194/acpd-14-16691-2014, URL http://www.atmos-chem-phys-discuss.net/14/16691/2014/, 2014.

Kirchhoff, G.: Ueber die Fraunhofer'schen Linien, Annalen der Physik, 185, 148–150, doi:10.1002/andp.18601850115, URL http://dx.doi.org/10.1002/andp.18601850115, 1860a.

Kirchhoff, G.: Ueber das Verhältniss zwischen dem Emissionsvermögen und dem Absorptionsvermögen der Körper für Wärme und Licht, Annalen der Physik, 185, 275–301, doi:10.1002/andp.18601850205, URL http://dx.doi.org/10.1002/andp.18601850205, 1860b.

Klebe, D. I., Blatherwick, R. D., and Morris, V. R.: Ground-based all-sky mid-infrared and visible imagery for purposes of characterizing cloud properties, Atmospheric Measurement Techniques, 7, 637–645, doi:10.5194/amt-7-637-2014, URL http://www.atmos-meas-tech.net/7/637/2014/, 2014.

Kleffmann, J., Gavriloaiei, T., Hofzumahaus, A., Holland, F., Koppmann, R., Rupp, L., Schlosser, E., Siese, M., and Wahner, A.: Daytime formation of nitrous acid: A major source of OH radicals in a forest, Geophysical Research Letters, 32, doi:10.1029/2005GL022524, URL http://dx.doi.org/10.1029/2005GL022524, 2005.

Koseki, S., Koh, T.-Y., and Teo, C.-K.: Borneo vortex and mesoscale convective rainfall, Atmospheric Chemistry and Physics, 14, 4539–4562, doi:10.5194/acp-14-4539-2014, URL http://www.atmos-chem-phys.net/14/4539/2014/, 2014.

Kramida, A., Ralchenko, Y., Reader, J., and NIST ASD Team: NIST Atomic Spectra Database (ver. 5.2), [Online]. Available: http://physics.nist.gov/asd National Institute of Standards and Technology, Gaithersburg, MD., 2014.

Kraus, H.: Die Atmosphäre Der Erde: Eine Einführung in Die Meteorologie, Springer, URL http://books.google.de/books?id=oAXtzWRQARYC, 2006a.

Kraus, S. G.: DOASIS: A Framework Design for DOAS, Ph.D. thesis, University of Mannheim, 2006b.

Kreycy, S.: Investigation of the Stratospheric Bromine Chemistry by Balloon-Borne Spectroscopic Observations and Photochemical Modelling: A Case Study of J($BrONO_2$)/$k_{BrO+NO2}$, Ph.D. thesis, Institute of Environmental Physics, University of Heidelberg, 2012.

Kritten, L., Butz, A., Dorf, M., Deutschmann, T., Kühl, S., Prados-Roman, C., Pukite, J., Rozanov, A., Schofield, R., and Pfeilsticker, K.: Time dependent profile retrieval of UV/vis absorbing radicals from balloon-borne limb measurements - a case study on NO_2 and O_3, Atmospheric Measurement Techniques, 3, 933–946, doi:10.5194/amt-3-933-2010, URL http://www.atmos-meas-tech.net/3/933/2010/, 2010.

Krüger, K., Tegtmeier, S., and Rex, M.: Long-term climatology of air mass transport through the Tropical Tropopause Layer (TTL) during NH winter, Atmos. Chem. Phys., 8, 813–823, doi:10.5194/acp-8-813-2008, 2008.

Krysztofiak, G.: Transport et chimie d'espèces soufrées et bromées dans la haute troposphère et basse stratosphere diagnostiqués par des mesures sous ballon et en avion et par modélisation, Ph.D. thesis, Laboratoire de Physique et Chimie de l'Environnement et de l'Espace (LPC2E), Université d'Orléans, 2013.

Kubistin, D., Harder, H., Martinez, M., Rudolf, M., Sander, R., Bozem, H., Eerdekens, G., Fischer, H., Gurk, C., Klüpfel, T., Königstedt, R., Parchatka, U., Schiller, C. L., Stickler, A., Taraborrelli, D., Williams, J., and Lelieveld, J.: Hydroxyl radicals in the tropical troposphere over the Suriname rainforest: comparison of measurements with the box model MECCA, Atmospheric Chemistry and Physics, 10, 9705–9728, doi:10.5194/acp-10-9705-2010, URL http://www.atmos-chem-phys.net/10/9705/2010/, 2010.

Küpper, F. C., Schweigert, N., Ar Gall, E., Legendre, J.-M., Vilter, H., and Kloareg, B.: Iodine uptake in Laminariales involves extracellular, haloperoxidase-mediated oxidation of iodide, Planta, 207, 163–171, doi:10.1007/s004250050469, URL http://dx.doi.org/10.1007/s004250050469, 1998.

Kurokawa, J., Ohara, T., Morikawa, T., Hanayama, S., Janssens-Maenhout, G., Fukui, T., Kawashima, K., and Akimoto, H.: Emissions of air pollutants and greenhouse gases over Asian regions during 2000â€“2008: Regional Emission inventory in ASia (REAS) version 2, Atmospheric Chemistry and Physics, 13, 11 019–11 058, doi:10.5194/acp-13-11019-2013, URL http://www.atmos-chem-phys.net/13/11019/2013/, 2013.

Kurucz, R. L., Furenlid, I., Brault, J., and Testerman, L.: Solar flux atlas from 296 to 1300nm, Tech. rep., National Solar Observatory, 1984.

Kuttippurath, J., Godin-Beekmann, S., Lefèvre, F., Nikulin, G., Santee, M. L., and Froidevaux, L.: Record-breaking ozone loss in the Arctic winter 2010/2011: comparison with 1996/1997, Atmospheric Chemistry and Physics, 12, 7073–7085, doi:10.5194/acp-12-7073-2012, URL http://www.atmos-chem-phys.net/12/7073/2012/, 2012.

Lampel, J.: Ship-borne MAX-DOAS Measurements of Tropospheric Halogen Oxides on Atlantic Transects, Master's thesis, University of Heidelberg, 2010.

Lampel, J.: Measurements of reactive trace gases in the marine boundary layer using novel DOAS methods, Ph.D. thesis, Institute of Environmental Physics, University of Heidelberg, 2014.

Lee, D., Kühler, I., Grobler, E., Rohrer, F., Sausen, R., Gallardo-Klenner, L., Olivier, J., Dentener, F., and Bouwman, A.: Estimates of Global NOx Emissions and their Uncertainties, Atmospheric Environment, 31, 1735–1749, 1997.

Leedham, E. C., Hughes, C., Keng, F. S. L., Phang, S.-M., Malin, G., and Sturges, W. T.: Emission of atmospherically significant halocarbons by naturally occurring and farmed tropical macroalgae, Biogeosciences, 10, 3615–3633, doi:10.5194/bg-10-3615-2013, URL http://www.biogeosciences.net/10/3615/2013/, 2013.

Leighton, P.: Photochemistry of air pollution, Academic Press, New York, 1961.

Lelieveld, J., Peters, W., Dentener, F. J., and Krol, M. C.: Stability of tropospheric hydroxyl chemistry, Journal of Geophysical Research: Atmospheres, 107, ACH 17–1–ACH 17–11, doi:10.1029/2002JD002272, URL http://dx.doi.org/10.1029/2002JD002272, 2002.

Lelieveld, J., Dentener, F. J., Peters, W., and Krol, M. C.: On the role of hydroxyl radicals in the self-cleansing capacity of the troposphere, Atmospheric Chemistry and Physics, 4, 2337–2344, doi:10.5194/acp-4-2337-2004, URL http://www.atmos-chem-phys.net/4/2337/2004/, 2004.

Lelieveld, J., Butler, T. M., Crowley, J. N., Dillon, T. J., Fischer, H., Ganzeveld, L., Harder, H., Lawrence, M. G., Martinez, M., Taraborrelli, D., and Williams, J.: Atmospheric oxidation capacity sustained by a tropical forest, Nature, 452, 737–740, doi:10.1038/nature06870, URL http://www.nature.com/nature/journal/v452/n7188/suppinfo/nature06870_S1.html, 2008.

Levenberg, K.: A method for the solution of certain non-linear problems in least squares, Quart. Appl., Math., 2, 164–168, 1944.

Levy, H.: Normal Atmosphere: Large Radical and Formaldehyde Concentrations Predicted, Science, 173, 141–143, doi:10.1126/science.173.3992.141, URL http://www.sciencemag.org/content/173/3992/141.abstract, 1971.

Lewis, G. N.: THE MAGNETISM OF OXYGEN AND THE MOLECULE O4, Journal of the American Chemical Society, 46, 2027–2032, doi:10.1021/ja01674a008, URL http://dx.doi.org/10.1021/ja01674a008, 1924.

Li, X., Rohrer, F., Hofzumahaus, A., Brauers, T., Häseler, R., Bohn, B., Broch, S., Fuchs, H., Gomm, S., Holland, F., Jäger, J., Kaiser, J., Keutsch, F. N., Lohse, I., Lu, K., Tillmann, R., Wegener, R., Wolfe, G. M., Mentel, T. F., Kiendler-Scharr, A., and Wahner, A.: Missing Gas-Phase Source of HONO Inferred from Zeppelin Measurements in the Troposphere, Science, 344, 292–296, doi:10.1126/science.1248999, URL http://www.sciencemag.org/content/344/6181/292.abstract, 2014.

Lim, J. and Samah, A.: Weather and climate of Malaysia, University of Malaya Press, URL http://books.google.de/books?id=ZGwcAQAAMAAJ, 2004.

Liou, K.: An Introduction to Atmospheric Radiation, Second Edition, Academic Press, An imprint of Elsevier Science, Department of Atmospheric Sciences, University of California, Los Angeles, California, USA, 2002.

Longo, K. M., Freitas, S. R., Pirre, M., Marécal, V., Rodrigues, L. F., Panetta, J., Alonso, M. F., Rosário, N. E., Moreira, D. S., Gácita, M. S., Arteta, J., Fonseca, R., Stockler, R., Katsurayama, D. M., Fazenda, A., and Bela, M.: The Chemistry CATT-BRAMS model (CCATT-BRAMS 4.5): a regional atmospheric model system for integrated air quality and weather forecasting and research, Geoscientific Model Development, 6, 1389–1405, doi:10.5194/gmd-6-1389-2013, URL http://www.geosci-model-dev.net/6/1389/2013/, 2013.

Lübcke, P.: Development of a new SO_2 camera for volcanic gas flux measurements, Master's thesis, Institute of Environmental Physics, University of Heidelberg, 2010.

Lübcke, P.: Optical remote sensing measurements of bromine and sulphur emissions: Investigating their potential as tracers of volcanic activity, Ph.D. thesis, Institute of Environmental Physics, University of Heidelberg, 2014.

Luecken, D., Hutzell, W., Strum, M., and Pouliot, G.: Regional sources of atmospheric formaldehyde and acetaldehyde, and implications for atmospheric modeling, Atmospheric Environment, 47, 477 – 490, doi:http://dx.doi.org/10.1016/j.atmosenv.2011.10.005, URL http://www.sciencedirect.com/science/article/pii/S1352231011010508, 2012.

MacDonald, S. M., Oetjen, H., Mahajan, A. S., Whalley, L. K., Edwards, P. M., Heard, D. E., Jones, C. E., and Plane, J. M. C.: DOAS measurements of formaldehyde and glyoxal above a south-east Asian tropical rainforest, Atmospheric Chemistry and Physics, 12, 5949–5962, doi:10.5194/acp-12-5949-2012, URL http://www.atmos-chem-phys.net/12/5949/2012/, 2012.

MacDonald, S. M., Gómez Martín, J. C., Chance, R., Warriner, S., Saiz-Lopez, A., Carpenter, L. J., and Plane, J. M. C.: A laboratory characterisation of inorganic iodine emissions from the sea surface: dependence on oceanic variables and parameterisation for global modelling, Atmospheric Chemistry and Physics, 14, 5841–5852, doi:10.5194/acp-14-5841-2014, URL http://www.atmos-chem-phys.net/14/5841/2014/, 2014.

MacKenzie, A. R., Langford, B., Pugh, T. A. M., Robinson, N., Misztal, P. K., Heard, D. E., Lee, J. D., Lewis, A. C., Jones, C. E., Hopkins, J. R., Phillips, G., Monks, P. S., Karunaharan, A., Hornsby, K. E., Nicolas-Perea, V., Coe, H., Gabey, A. M., Gallagher, M. W., Whalley, L. K., Edwards, P. M., Evans, M. J., Stone, D., Ingham, T., Commane, R., Furneaux, K. L., McQuaid, J. B., Nemitz, E., Seng, Y. K., Fowler, D., Pyle, J. A., and Hewitt, C. N.: The atmospheric chemistry of trace gases and particulate matter emitted by different land uses

in Borneo, Philosophical Transactions of the Royal Society B: Biological Sciences, 366, 3177–3195, doi:10.1098/rstb.2011.0053, URL http://rstb.royalsocietypublishing.org/content/366/1582/3177.abstract, 2011.

Madronich, S.: Photodissociation in the atmosphere: 1. Actinic flux and the effects of ground reflections and clouds, Journal of Geophysical Research: Atmospheres, 92, 9740–9752, doi:10.1029/JD092iD08p09740, URL http://dx.doi.org/10.1029/JD092iD08p09740, 1987.

Mahajan, A. S., Gómez Martín, J. C., Hay, T. D., Royer, S.-J., Yvon-Lewis, S., Liu, Y., Hu, L., Prados-Roman, C., Ordóñez, C., Plane, J. M. C., and Saiz-Lopez, A.: Latitudinal distribution of reactive iodine in the Eastern Pacific and its link to open ocean sources, Atmospheric Chemistry and Physics, 12, 11 609–11 617, doi:10.5194/acp-12-11609-2012, URL http://www.atmos-chem-phys.net/12/11609/2012/, 2012.

Mahajan, A. S., Prados-Roman, C., Hay, T. D., Lampel, J., Pöhler, D., Groß mann, K., Tschritter, J., Frieß, U., Platt, U., Johnston, P., Kreher, K., Wittrock, F., Burrows, J. P., Plane, J. M., and Saiz-Lopez, A.: Glyoxal observations in the global marine boundary layer, Journal of Geophysical Research: Atmospheres, 119, 6160–6169, doi:10.1002/2013JD021388, URL http://dx.doi.org/10.1002/2013JD021388, 2014.

Mak, M. K. and Walsh, J. E.: On the Relative Intensities of Sea and Land Breezes, Journal of the Atmospheric Sciences, 33, 242–251, doi:10.1175/1520-0469(1976)033⟨0242:OTRIOS⟩2.0.CO;2, 1976.

Marais, E. A., Jacob, D. J., Kurosu, T. P., Chance, K., Murphy, J. G., Reeves, C., Mills, G., Casadio, S., Millet, D. B., Barkley, M. P., Paulot, F., and Mao, J.: Isoprene emissions in Africa inferred from OMI observations of formaldehyde columns, Atmospheric Chemistry and Physics, 12, 6219–6235, doi:10.5194/acp-12-6219-2012, URL http://www.atmos-chem-phys.net/12/6219/2012/, 2012.

Marbach, T., Beirle, S., Frankenberg, C., Platt, U., and Wagner, T.: Identification of tropospheric trace gas sources: synergistic use of HCHO and other satellite observations, ESA Publication SP-636, 2007.

Marbach, T., Beirle, S., Platt, U., Hoor, P., Wittrock, F., Richter, A., Vrekoussis, M., Grzegorski, M., Burrows, J. P., and Wagner, T.: Satellite measurements of formaldehyde linked to shipping emissions, Atmospheric Chemistry and Physics, 9, 8223–8234, doi:10.5194/acp-9-8223-2009, URL http://www.atmos-chem-phys.net/9/8223/2009/, 2009.

Marquardt, D. W.: An algorithm for least-squares estimation of nonlinear parameters, J. Soc. Indust. Math., 11, 431–441, 1963.

Marshak, A. and Davis, A.: 3D Radiative Transfer in Cloudy Atmospheres, Springer-Verlag, Heidelberg, 2005.

Martin, M., Pöhler, D., Seitz, K., Sinreich, R., and Platt, U.: BrO measurements over the Eastern North-Atlantic, Atmospheric Chemistry and Physics, 9, 9545–9554, 2009.

Martino, M., Mills, G. P., Woeltjen, J., and Liss, P. S.: A new source of volatile organoiodine compounds in surface seawater, Geophys. Res. Lett., 36, L01 609, doi:10.1029/2008GL036334, 2009.

McFarlane, N. and Pendlebury, D.: Report on the 14th Session of the SPARC Scientific Steering Group, SPARC Newsletter No 28, 28, 28, URL http://www.sparc-climate.org/fileadmin/customer/6_Publications/Newsletter_PDF/28_SPARCnewsletter_Jan2007.pdf, 2007.

McFiggans, G., Plane, J. M. C., Allan, B. J., and Carpenter, L. J.: A modeling study of iodine chemistry in the marine boundary layer, J. Geophys. Res., 105, 14 371–14 385, doi: 10.1029/1999JD901187, 2000.

McHugh, D.: A guide to the seaweed industry. Food and Agriculture Organisation (FAO), Report, School of Chemistry, University College, University of New South Wales and Australian Defence Force Academy Canberra Australia, URL http://www.fao.org/docrep/006/y4765e/y4765e00.HTM, 2003.

Meller, R. and Moortgat, G.: Temperature dependence of the absorption cross sections of formaldehyde between 223 and 323 K in the wavelength range 225-375 nm, J. Geophys. Res., D 105, 7089-7101, 2000.

Merlaud, A., Van Roozendael, M., Theys, N., Fayt, C., Hermans, C., Quennehen, B., Schwarzenboeck, A., Ancellet, G., Pommier, M., Pelon, J., Burkhart, J., Stohl, A., and De Mazière, M.: Airborne DOAS measurements in Arctic: vertical distributions of aerosol extinction coefficient and NO_2 concentration, Atmospheric Chemistry and Physics, 11, 9219–9236, doi: 10.5194/acp-11-9219-2011, URL http://www.atmos-chem-phys.net/11/9219/2011/, 2011.

Miettinen, J., Hooijer, A., Tollenaar, D., Page, S., Malins, C., Vernimmen, R., Shi, C., and Liew, S. C.: Historical Analysis and Projection of Oil Palm Plantation Expansion on Peat- land in Southeast Asia, White Paper 17, The International Council on Clean Transportation, pp. 29 554,29 560,29 584, URL www.theicct.org, 2012a.

Miettinen, J., Shi, C., Tan, W. J., and Liew, S. C.: 2010 land cover map of insular Southeast Asia in 250-m spatial resolution, Remote Sensing Letters, 3, 11–20, doi:10.1080/01431161.2010.526971, URL http://www.tandfonline.com/doi/abs/10.1080/01431161.2010.526971, 2012b.

Miller, S. M., Matross, D. M., Andrews, A. E., Millet, D. B., Longo, M., Gottlieb, E. W., Hirsch, A. I., Gerbig, C., Lin, J. C., Daube, B. C., Hudman, R. C., Dias, P. L. S., Chow, V. Y., and Wofsy, S. C.: Sources of carbon monoxide and formaldehyde in North America determined from high-resolution atmospheric data, Atmospheric Chemistry and Physics, 8, 7673–7696, doi: 10.5194/acp-8-7673-2008, URL http://www.atmos-chem-phys.net/8/7673/2008/, 2008.

Mohd Nadzir, M. S., Phang, S. M., Abas, M. R., Abdul Rahman, N., Abu Samah, A., Sturges, W. T., Oram, D. E., Mills, G. P., Leedham, E. C., Pyle, J. A., Harris, N. R. P., Robinson, A. D., Ashfold, M. J., Mead, M. I., Latif, M. T., Khan, M. F., Amiruddin, A. M., Banan, N., and Hanafiah, M. M.: Bromocarbons in the tropical coastal and open ocean atmosphere during the 2009 Prime Expedition Scientific Cruise (PESC-09), Atmospheric Chemistry and Physics, 14, 8137–8148, doi:10.5194/acp-14-8137-2014, URL http://www.atmos-chem-phys.net/14/8137/2014/, 2014.

Molina, M. J. and Rowland, F. S.: Stratospheric sink for chlorofluoromethanes: chlorine atomcatalysed destruction of ozone, Nature, 249, 810–812, doi:10.1038/249810a0, 1974.

Montzka, S., Reimann, S., Engel, A., Krüger, K., O'Doherty, S., Sturges, W. T., Blake, D., Dorf, M., Fraser, P., Froidevaux, L., Jucks, K., Kreher, K., Kurylo, M. J., Mellouki, A., Miller, J., Nielsen, O.-J., Orkin, V. L., Prinn, R. G., Rhew, R., Santee, M. L., and Verdonik, D.: Ozone-Depleting Substances (ODSs) and Related Chemicals, Chapter 1 in Scientific Assessment of Ozone Depletion: 2010, Global Ozone Research and Monitoring Project-Report No. 52, World Meteorological Organization, Geneva, Switzerland, 516 pp., 2011.

Mössinger, J. C., E. Shallcross, D., and Anthony Cox, R.: UV-VIS absorption cross-sections and atmospheric lifetimes of CH_2Br_2, CH_2I_2 and CH_2BrI, J. Chem. Soc., Faraday Trans., 94, 1391–1396, 1998.

Murphy, D. M., Thomson, D. S., and Middlebrook, A. M.: Bromine, iodine, and chlorine in single aerosol particles at Cape Grim, Geophysical Research Letters, 24, 3197–3200, doi: 10.1029/97GL03195, URL http://dx.doi.org/10.1029/97GL03195, 1997.

Murphy, D. M., Thomson, D. S., and Mahoney, M. J.: In Situ Measurements of Organics, Meteoritic Material, Mercury, and Other Elements in Aerosols at 5 to 19 Kilometers, Science, 282, 1664–1669, doi:10.1126/science.282.5394.1664, URL http://www.sciencemag.org/content/282/5394/1664.abstract, 1998.

Murphy, D. M., Froyd, K. D., Schwarz, J. P., and Wilson, J. C.: Observations of the chemical composition of stratospheric aerosol particles, Quarterly Journal of the Royal Meteorological Society, 140, 1269–1278, doi:10.1002/qj.2213, URL http://dx.doi.org/10.1002/qj.2213, 2014.

Myriokefalitakis, S., Vrekoussis, M., Tsigaridis, K., Wittrock, F., Richter, A., Brühl, C., Volkamer, R., Burrows, J. P., and Kanakidou, M.: The influence of natural and anthropogenic secondary sources on the glyoxal global distribution, Atmospheric Chemistry and Physics, 8, 4965–4981, doi:10.5194/acp-8-4965-2008, URL http://www.atmos-chem-phys.net/8/4965/2008/, 2008.

Nakajima, T. and King, M. D.: Determination of the Optical Thickness and Effective Particle Radius of Clouds from Reflected Solar Radiation Measurements. Part I: Theory, J. Atmos. Sci, 47, 1878–1893, doi:doi:10.1175/1520-0469(1990)047⟨1878:DOTOTA⟩2.0.CO;2, 1990.

Nakajima, T., King, M. D., Spinhirne, J., and Radke, L.: Determination of the optical thickness and effective particle radius of clouds from reflected solar radiation measurements. Part II: Marine stratocumulus observations, J. Atmos. Sci, 48, 728–750, 1991.

Nasse, J.-M.: Retrieval of aerosol and trace gas vertical profiles in the Antarctic troposphere using helicopter- and ship-borne MAX-DOAS measurements, Master thesis, Institute of Environmental Physics, University of Heidelberg, Heidelberg, Germany, 2014.

Newell, R. E. and Gould-Stewart, S.: A Stratospheric Fountain?, Journal of the Atmospheric Sciences, 38, 2789–2796, doi:10.1175/1520-0469(1981)038⟨2789:ASF⟩2.0.CO;2, URL http://dx.doi.org/10.1175/1520-0469(1981)038<2789:ASF>2.0.CO;2, 1981.

Noguchi, K., Richter, A., Rozanov, V., Rozanov, A., Burrows, J. P., Irie, H., and Kita, K.: Effect of surface BRDF of various land cover types on the geostationary observations of tropospheric NO_2, Atmospheric Measurement Techniques Discussions, 7, 3443–3469, doi:10.5194/amtd-7-3443-2014, URL http://www.atmos-meas-tech-discuss.net/7/3443/2014/, 2014.

O'Brien, K.: Application of a novel air-borne mini-DOAS instrument for UV/visible limb observations during the POLARCAT GRACE 2008 research campaign, Diploma thesis, Institute of Environmental Physics, University of Heidelberg, 2008.

O'Dowd, C., Jimenez, J. L., Bahreini, R., Flagan, R. C., Seinfeld, J. H., Hämeri, K., Pirjola, L., ans S. G. Jennings, M. K., and Hoffmann, T.: Marine aerosol formation from biogenic iodine emissions, Nature, 417, 632–636, 2002.

Palancar, G. G., Shetter, R. E., Hall, S. R., Toselli, B. M., and Madronich, S.: Ultraviolet actinic flux in clear and cloudy atmospheres: model calculations and aircraft-based measurements, Atmospheric Chemistry and Physics, 11, 5457–5469, doi:10.5194/acp-11-5457-2011, URL http://www.atmos-chem-phys.net/11/5457/2011/, 2011.

Paquette, J., Wren, J., Sunder, S., and Ford, B.: The disproportionation of iodine (I), Proceedings of OECD Iodine Workshop, Harwell, (AERE-R–11974),Potter, P.E. (Ed.), United Kingdom, pp. 29–45, 1986.

Pearson, K.: On Lines and Planes of Closest Fit to Systems of Points in Space, Philosophical Magazine, 2, 559–572, 1901.

Penndorf, R.: Tables of the Refractive Index for Standard Air and the Rayleigh Scattering Coefficient for the Spectral Region between 0.2 and 20.0 μ and Their Application to Atmospheric Optics, J. Opt. Soc. Am., 47, 176–182, doi:10.1364/JOSA.47.000176, URL http://www.opticsinfobase.org/abstract.cfm?URI=josa-47-2-176, 1957.

Perner, D. and Platt, U.: Detection of Nitrous Acid in the Atmosphere by Differential Optical Absorption, Geophys. Res. Lett., 6, 917–920, doi:10.1029/GL006i012p00917, URL http://dx.doi.org/10.1029/GL006i012p00917, 1979.

Perovich, D. K., Roesler, C. S., and Pegau, W. S.: Variability in Arctic sea ice optical properties, Journal of Geophysical Research: Oceans, 103, 1193–1208, doi:10.1029/97JC01614, URL http://dx.doi.org/10.1029/97JC01614, 1998.

Peters, E.: Improved MAX-DOAS measurements and retrievals focused on the marine boundary layer, Ph.D. thesis, Institute of Environmental Physics, University of Bremen, 2013.

Peters, E., Wittrock, F., Großmann, K., Frieß, U., Richter, A., and Burrows, J. P.: Formaldehyde and nitrogen dioxide over the remote western Pacific Ocean: SCIAMACHY and GOME-2 validation using ship-based MAX-DOAS observations, Atmospheric Chemistry and Physics, 12, 11 179–11 197, doi:10.5194/acp-12-11179-2012, URL http://www.atmos-chem-phys.net/12/11179/2012/, 2012.

Peters, E., Wittrock, F., Richter, A., Alvarado, L. M. A., Rozanov, V. V., and Burrows, J. P.: Liquid water absorption and scattering effects in DOAS retrievals over oceans, Atmospheric Measurement Techniques Discussions, 7, 5027–5073, doi:10.5194/amtd-7-5027-2014, URL http://www.atmos-meas-tech-discuss.net/7/5027/2014/, 2014.

Pfeilsticker, K.: The SHIVA Western Pacific campaign in November and December 2011 Post-campaign Activity Report, Report, University of Heidelberg, URL http://shiva.iup.uni-heidelberg.de/dl/SHIVA_campaign_report.pdf, 2012.

Pfeilsticker, K. and Platt, U.: Airborne measurements during the Arctic Stratospheric Experiment: Observation of O3 and NO2, Geophysical Research Letters, 21, 1375–1378, doi:10.1029/93GL01870, URL http://dx.doi.org/10.1029/93GL01870, 1994.

Pfeilsticker, K., Erle, F., Funk, O., Veitel, H., and Platt, U.: First geometrical pathlengths probability density function derivation of the skylight from spectroscopically highly resolving oxygen A-band observations: 1. Measurement technique, atmospheric observations and model calculations, Journal of Geophysical Research: Atmospheres, 103, 11 483–11 504, doi:10.1029/98JD00725, URL http://dx.doi.org/10.1029/98JD00725, 1998.

Pfeilsticker, K., Erle, F., Funk, O., Marquard, L., Wagner, T., and Platt, U.: Optical path modifications due to tropospheric clouds: Implications for zenith sky measurements of stratospheric gases, Journal of Geophysical Research: Atmospheres, 103, 25 323–25 335, doi:10.1029/98JD01803, URL http://dx.doi.org/10.1029/98JD01803, 1998a.

Pfeilsticker, K., Bösch, H., Camy-Peyret, C., Fitzenberger, R., Harder, H., and Osterkamp, H.: First atmospheric profile measurements of UV/visible O4 absorption band intensities: Implications for the spectroscopy, and the formation enthalpy of the O2-O2 dimer, Geophysical Research Letters, 28, 4595–4598, doi:10.1029/2001GL013734, URL http://dx.doi.org/10.1029/2001GL013734, 2001.

Pfister, G., McKenzie, R. L., Liley, J. B., Thomas, A., Forgan, B. W., and Long, C. N.: Cloud Coverage Based on All-Sky Imaging and Its Impact on Surface Solar Irradiance, Journal of Applied Meteorology, 42, 1421–1434, doi:http://dx.doi.org/10.1175/1520-0450(2003)042⟨1421:CCBOAI⟩2.0.CO;2, 2003.

Phang, S. M.: Seaweed resources in Malaysia: Current status and future prospects, Aquatic Ecosystem Health and Management, 9, 185–202, doi:10.1080/14634980600710576, URL http://www.tandfonline.com/doi/abs/10.1080/14634980600710576, 2006.

Pillar, E. A., Guzman, M. I., and Rodriguez, J. M.: Conversion of Iodide to Hypoiodous Acid and Iodine in Aqueous Microdroplets Exposed to Ozone, Environmental Science & Technology, 47, 10 971–10 979, doi:10.1021/es401700h, URL http://dx.doi.org/10.1021/es401700h, pMID: 23987087, 2013.

Pinardi, G., Van Roozendael, M., Abuhassan, N., Adams, C., Cede, A., Clémer, K., Fayt, C., Frieß, U., Gil, M., Herman, J., Hermans, C., Hendrick, F., Irie, H., Merlaud, A., Navarro Comas, M., Peters, E., Piters, A. J. M., Puentedura, O., Richter, A., Schönhardt, A., Shaiganfar, R., Spinei, E., Strong, K., Takashima, H., Vrekoussis, M., Wagner, T., Wittrock, F., and Yilmaz, S.: MAX-DOAS formaldehyde slant column measurements during CINDI: intercomparison and analysis improvement, Atmospheric Measurement Techniques, 6, 167–185, doi:10.5194/amt-6-167-2013, URL http://www.atmos-meas-tech.net/6/167/2013/, 2013.

Platt, U. and Stutz, J.: Differential optical absorption spectroscopy, Springer Verlag, 2008.

Platt, U., Perner, D., Harris, G. W., Winer, A. M., and Pitts, J. N.: Observations of nitrous acid in an urban atmosphere by differential optical absorption, Nature, 285, 312–314, doi:10.1038/285312a0, 1980.

Platt, U., Marquard, L., Wagner, T., and Perner, D.: Corrections for Zenith Scattered Light DOAS, Geophys. Res. Letters, 24, 1759–1762, 1997.

Pöschl, U., Martin, S. T., Sinha, B., Chen, Q., Gunthe, S. S., Huffman, J. A., Borrmann, S., Farmer, D. K., Garland, R. M., Helas, G., Jimenez, J. L., King, S. M., Manzi, A., Mikhailov, E., Pauliquevis, T., Petters, M. D., Prenni, A. J., Roldin, P., Rose, D., Schneider, J., Su, H., Zorn, S. R., Artaxo, P., and Andreae, M. O.: Rainforest Aerosols as Biogenic Nuclei of Clouds and Precipitation in the Amazon, Science, 329, 1513–1516, doi:10.1126/science.1191056, URL http://www.sciencemag.org/content/329/5998/1513.abstract, 2010.

Prados-Roman, C., Butz, A., Deutschmann, T., Dorf, M., Kritten, L., Minikin, A., Platt, U., Schlager, H., Sihler, H., Theys, N., Van Roozendael, M., Wagner, T., and Pfeilsticker, K.: Airborne DOAS limb measurements of tropospheric trace gas profiles: case study on the profile retrieval of O_4 and BrO, Atmospheric Measurement Techniques, 3, 3925–3969, doi:10.5194/amtd-3-3925-2010, URL http://www.atmos-meas-tech-discuss.net/3/3925/2010/, 2011.

Prados-Roman, C., Cuevas, C. A., Hay, T., Fernandez, R. P., Mahajan, A. S., Royer, S.-J., Galí, M., Simó, R., Dachs, J., Großmann, K., Kinnison, D. E., Lamarque, J.-F., and Saiz-Lopez, A.: Iodine oxide in the global marine boundary layer, Atmospheric Chemistry and Physics Discussions, 14, 22 217–22 243, doi:10.5194/acpd-14-22217-2014, URL http://www.atmos-chem-phys-discuss.net/14/22217/2014/, 2014.

Puentedura, O., Gil, M., Saiz-Lopez, A., Hay, T., Navarro-Comas, M., Gómez-Pelaez, A., Cuevas, E., and Iglesias, J.: Iodine monoxide in the north subtropical free troposphere, Atmos. Chem. Phys., 11, 27 833–27 860, doi:10.5194/acpd-11-27833-2011, 2012.

Pyle, J., Warwick, N. J., Harris, N. R. P., Abas, M. R., Archibald, A. T., Ashfold, M. J., Ashworth, K., Barkley, M. P., G. D. Carver, G. D., Chance, K., Dorsey, J. R., Fowler, D., Gonzi, S., Gostlow, B., Hewitt, C. N., Kurosu, T. P., Lee, J. D., Langford, S. B., Mills, G., Moller, S., MacKenzie, A. R., Manning, A. J., Misztal, P., Nadzir, M. S. M., Nemitz, E., Newton, H. M., O'Brien, L. M., Ong, S., Oram, D., Palmer, P. I., Peng, L. K., Phang, S. M., Pike, R., Pugh, T. A. M., Rahman, N. A., Robinson, A. D., Sentian, J., Samah, A. A., Skiba, U., Ung, H. E., Yong, S. E., and Young, P. J.: The impact of local surface changes in Borneo on atmospheric composition at wider spatial scales: coastal processes, land-use change and air quality, Phil Trans R Soc B, 366, 3210–3224, doi:10.1098/rstb.2011.0060, 2011.

Pyle, J. A., Ashfold, M. J., Harris, N. R. P., Robinson, A. D., Warwick, N. J., Carver, G. D., Gostlow, B., O'Brien, L. M., Manning, A. J., Phang, S. M., Yong, S. E., Leong, K. P., Ung, E. H., and Ong, S.: Bromoform in the tropical boundary layer of the Maritime Continent during OP3, Atmospheric Chemistry and Physics, 11, 529–542, doi:10.5194/acp-11-529-2011, URL `http://www.atmos-chem-phys.net/11/529/2011/`, 2011a.

Quack, B. and Wallace, D. W. R.: Air-sea flux of bromoform: Controls, rates, and implications, Global Biogeochemical Cycles, 17, doi:10.1029/2002GB001890, URL `http://dx.doi.org/10.1029/2002GB001890`, 2003.

Raecke, R.: Atmospheric spectroscopy of trace gases and water vapor in the tropical tropopause layer from the NASA Global Hawk, Master thesis, Institute of Environmental Physics, University of Heidelberg, Heidelberg, Germany, 2013.

Raman, C.: A new radiation, Indian Journal of Physics, 2, 387–398, URL `http://hdl.handle.net/2289/2135`, 1928.

Ramanathan, V., Cess, R. D., Harrison, E. F., Minnis, P., Barkstrom, B. R., Ahmad, E., and Hartmann, D.: Cloud-Radiative Forcing and Climate: Results from the Earth Radiation Budget Experiment, Science, 243, 57–63, doi:10.1126/science.243.4887.57, URL `http://www.sciencemag.org/content/243/4887/57.abstract`, 1989.

Randel, W. J. and Jensen, E. J.: Physical processes in the tropical tropopause layer and their roles in a changing climate, Nature Geoscience, 6, 169–176, doi:10.1038/ngeo1733, URL `http://dx.doi.org/10.1038/ngeo1733`, 2013.

Rattigan, O. V., E. Shallcross, D., and Anthony Cox, R.: UV absorption cross-sections and atmospheric photolysis rates of CF_3I, CH_3I, C_2H_5I and CH_2ICl, J. Chem. Soc., Faraday Trans., 93, 2839–2846, 1997.

Ray, E. A., Rosenlof, K. H., Richard, E. C., Hudson, P. K., Cziczo, D. J., Loewenstein, M., Jost, H.-J., Lopez, J., Ridley, B., Weinheimer, A., Montzka, D., Knapp, D., Wofsy, S. C., Daube, B. C., Gerbig, C., Xueref, I., and Herman, R. L.: Evidence of the effect of summertime midlatitude convection on the subtropical lower stratosphere from CRYSTAL-FACE tracer measurements, Journal of Geophysical Research: Atmospheres, 109, doi:10.1029/2004JD004655, URL `http://dx.doi.org/10.1029/2004JD004655`, 2004.

Read, K. A., Mahajan, A. S., Carpenter, L. J., Evans, M. J., Faria, B. V. E., Heard, D. E., Hopkins, J. R., Lee, J. D., Moller, S. J., Lewis, A. C., Mendes, L., McQuaid, J. B., Oetjen, H., Saiz-Lopez, A., Pilling, M. J., and Plane, J. M. C.: Extensive halogen-mediated ozone destruction over the tropical Atlantic Ocean., Nature, 453, 1232–1235, doi:10.1038/nature07035, 2008.

Reiter, A.: First airborne SO_2 Measurements in the West Pacific using IT-CIMS: Analysis of Regional Distribution, Sources and Transport, Master's thesis, Meteorological Institute Munich, Ludwig-Maximilians-University Munich (LMU), 2012.

Rex, M., Wohltmann, I., Ridder, T., Lehmann, R., Rosenlof, K., Wennberg, P., Weisenstein, D., Notholt, J., Krüger, K., Mohr, V., and Tegtmeier, S.: A tropical West Pacific OH minimum and implications for stratospheric composition, Atmospheric Chemistry and Physics, 14, 4827–4841, doi:10.5194/acp-14-4827-2014, URL http://www.atmos-chem-phys.net/14/4827/2014/, 2014.

Riipinen, I., Yli-Juuti, T., Pierce, J. R., Petaja, T., Worsnop, D. R., Kulmala, M., and Donahue, N. M.: The contribution of organics to atmospheric nanoparticle growth, Nature Geoscience, 5, 453–458, doi:10.1038/ngeo1499, URL http://dx.doi.org/10.1038/ngeo1499, 2012.

Robinson, A. D., Harris, N. R. P., Ashfold, M. J., Gostlow, B., Warwick, N. J., O'Brien, L. M., Beardmore, E. J., Nadzir, M. S. M., Phang, S. M., Samah, A. A., Ong, S., Ung, H. E., Peng, L. K., Yong, S. E., Mohamad, M., and Pyle, J. A.: Long-term halocarbon observations from a coastal and an inland site in Sabah, Malaysian Borneo, Atmospheric Chemistry and Physics, 14, 8369–8388, doi:10.5194/acp-14-8369-2014, URL http://www.atmos-chem-phys.net/14/8369/2014/, 2014.

Robinson, N. H., Hamilton, J. F., Allan, J. D., Langford, B., Oram, D. E., Chen, Q., Docherty, K., Farmer, D. K., Jimenez, J. L., Ward, M. W., Hewitt, C. N., Barley, M. H., Jenkin, M. E., Rickard, A. R., Martin, S. T., McFiggans, G., and Coe, H.: Evidence for a significant proportion of Secondary Organic Aerosol from isoprene above a maritime tropical forest, Atmospheric Chemistry and Physics, 11, 1039–1050, doi:10.5194/acp-11-1039-2011, URL http://www.atmos-chem-phys.net/11/1039/2011/, 2011.

Rodgers, C. D.: Inverse methods for atmospheric sounding, theory and practice, Series on Atmospheric, Oceanic and Planetary Physics, World Scientific, 2000.

Roedel, W.: Physik unserer Umwelt: Die Atmosphäre, Springer Verlag, Heidelberg, 2000.

Rohrer, F. and Berresheim, H.: Strong correlation between levels of tropospheric hydroxyl radicals and solar ultraviolet radiation, Nature, 442, 184 – 187, doi:http://dx.doi.org/10.1038/nature04924, URL http://www.nature.com/nature/journal/v442/n7099/suppinfo/nature04924_S1.html, 2006.

Rolph, G.: Real-time Environmental Applications and Display sYstem (READY) Website (http://ready.arl.noaa.gov), NOAA Air Resources Laboratory, Silver Spring, MD, 2013.

Roscoe, H. K., Van Roozendael, M., Fayt, C., du Piesanie, A., Abuhassan, N., Adams, C., Akrami, M., Cede, A., Chong, J., Clémer, K., Friess, U., Gil Ojeda, M., Goutail, F., Graves, R., Griesfeller, A., Grossmann, K., Hemerijckx, G., Hendrick, F., Herman, J., Hermans, C., Irie, H., Johnston, P. V., Kanaya, Y., Kreher, K., Leigh, R., Merlaud, A., Mount, G. H., Navarro, M., Oetjen, H., Pazmino, A., Perez-Camacho, M., Peters, E., Pinardi, G., Puentedura, O., Richter, A., Schönhardt, A., Shaiganfar, R., Spinei, E., Strong, K., Takashima, H., Vlemmix, T., Vrekoussis, M., Wagner, T., Wittrock, F., Yela, M., Yilmaz, S., Boersma, F., Hains, J., Kroon, M., Piters, A., and Kim, Y. J.: Intercomparison of slant column measurements of NO_2 and O_4 by MAX-DOAS and zenith-sky UV and visible spectrometers, Atmos. Meas. Tech., 3, 1629–1646, doi:10.5194/amt-3-1629-2010, 2010.

Rosenfeld, D., Lohmann, U., Raga, G. B., O'Dowd, C. D., Kulmala, M., Fuzzi, S., Reissell, A., and Andreae, M. O.: Flood or Drought: How Do Aerosols Affect Precipitation?, Science, 321, 1309–1313, doi:10.1126/science.1160606, URL http://www.sciencemag.org/content/321/5894/1309.abstract, 2008.

Rothman, L., Gordon, I., Barbe, A., Chris Benner, D., Bernath, P., Birk, M., Boudon, V., Brown, L., Campargue, A., Champion, J.-P., Chance, K., Coudert, L., Dana, V., Devi, V., Fally, S., Flaud, J.-M., Gamache, R., Goldman, A., Jacquemart, D., Kleiner, I., Lacome, N., Lafferty, W., Mandin,

J.-Y., Massie, S., Mikhailenko, S., Miller, C., Moazzen-Ahmadi, N., Naumenko, O., Nikitin, A., Orphal, J., Perevalov, V., Perrin, A., Predoi-Cross, A., Rinsland, C., Rotger, M., Simeckova, M., Smith, M., Sung, K., Tashkun, S., Tennyson, J., Toth, R., Vandaele, A., and Vander Auwera, J.: The HITRAN 2008 molecular spectroscopic database, Journal of Quantitative Spectroscopy and Radiative Transfer, 110, 533 – 572, doi:10.1016/j.jqsrt.2009.02.013, 2009.

Rothman, L., Gordon, I., Babikov, Y., Barbe, A., Chris Benner, D., Bernath, P., Birk, M., Bizzocchi, L., Boudon, V., Brown, L., Campargue, A., Chance, K., Cohen, E., Coudert, L., Devi, V., Drouin, B., Fayt, A., Flaud, J.-M., Gamache, R., Harrison, J., Hartmann, J.-M., Hill, C., Hodges, J., Jacquemart, D., Jolly, A., Lamouroux, J., Le Roy, R., Li, G., Long, D., Lyulin, O., Mackie, C., Massie, S., Mikhailenko, S., Müller, H., Naumenko, O., Nikitin, A., Orphal, J., Perevalov, V., Perrin, A., Polovtseva, E., Richard, C., Smith, M., Starikova, E., Sung, K., Tashkun, S., Tennyson, J., Toon, G., Tyuterev, V., and Wagner, G.: The HITRAN 2012 molecular spectroscopic database, Journal of Quantitative Spectroscopy and Radiative Transfer, 130, 4 – 50, doi:http://dx.doi.org/10.1016/j.jqsrt.2013.07.002, 2013.

Rozanov, A.: User's Guide for the Software Package SCIATRAN (Radiative Transfer Model and Retrieval Algorithm) - Version 2.2 -, Institute of Remote Sensing University of Bremen, Germany, URL http://www.iup.uni-bremen.de/~alex/sciatran/free_downloads/users_guide_sciatran_v2-1.pdf, 2007.

Rozanov, A., Rozanov, V., and Burrows, J.: A numerical radiative transfer model for a spherical planetary atmosphere: combined differential-integral approach involving the Picard iterative approximation, Journal of Quantitative Spectroscopy and Radiative Transfer, 69, 491 – 512, doi:http://dx.doi.org/10.1016/S0022-4073(00)00100-X, URL http://www.sciencedirect.com/science/article/pii/S002240730000100X, 2001.

Rozanov, A., Rozanov, V., Buchwitz, M., Kokhanovsky, A., and Burrows, J.: SCIATRAN 2.0: A new radiative transfer model for geophysical applications in the 175-2400 nm spectral region, Advances in Space Research, 36, 1015 – 1019, doi:http://dx.doi.org/10.1016/j.asr.2005.03.012, URL http://www.sciencedirect.com/science/article/pii/S0273117705002887, atmospheric Remote Sensing: Earth's Surface, Troposphere, Stratosphere and Mesosphere- I, 2005.

Rozanov, A. V., Rozanov, V. V., and Burrows, J. P.: Combined differential-integral approach for the radiation field computation in a spherical shell atmosphere: Nonlimb geometry, Journal of Geophysical Research: Atmospheres, 105, 22 937–22 942, doi:10.1029/2000JD900378, URL http://dx.doi.org/10.1029/2000JD900378, 2000.

Saiz-Lopez, A. and von Glasow, R.: Reactive halogen chemistry in the troposphere, Chem. Soc. Rev., 41, 6448–6472, doi:10.1039/C2CS35208G, URL http://dx.doi.org/10.1039/C2CS35208G, 2012.

Saiz-Lopez, A., Plane, J. M. C., Baker, A. R., Carpenter, L. J., von Glasow, R., Gómez Martín, J. C., McFiggans, G., and Saunders, R. W.: Atmospheric Chemistry of Iodine, Chem. Rev., 112, 1773–1804, doi:10.1021/cr200029u, 2012.

Saiz-Lopez, A., Fernandez, R. P., Ordóñez, C., Kinnison, D. E., Gómez Martín, J. C., Lamarque, J.-F., and Tilmes, S.: Iodine chemistry in the troposphere and its effect on ozone, Atmospheric Chemistry and Physics Discussions, 14, 19 985–20 044, doi:10.5194/acpd-14-19985-2014, URL http://www.atmos-chem-phys-discuss.net/14/19985/2014/, 2014.

Sala, S.: Entwicklung und Einsatz eines flugzeuggetragenen GC/MS - Systems zum Nachweis halogenierter Kohlenwasserstoffe in der Atmosphäre, Ph.D. thesis, Goethe University Frankfurt, 2014a.

Sala, S., Bönisch, H., Keber, T., Oram, D. E., Mills, G., and Engel, A.: Deriving an atmospheric budget of total organic bromine using airborne in situ measurements from the western Pacific area during SHIVA, Atmospheric Chemistry and Physics, 14, 6903–6923, doi:10.5194/acp-14-6903-2014, URL http://www.atmos-chem-phys.net/14/6903/2014/, 2014b.

Saliba, N. A., Moussa, S. G., and El Tayyar, G.: Contribution of airborne dust particles to HONO sources, Atmospheric Chemistry and Physics Discussions, 14, 4827–4839, doi:10.5194/acpd-14-4827-2014, URL http://www.atmos-chem-phys-discuss.net/14/4827/2014/, 2014.

Sander, R., Baumgaertner, A., Gromov, S., Harder, H., Jöckel, P., Kerkweg, A., Kubistin, D., Regelin, E., Riede, H., Sandu, A., Taraborrelli, D., Tost, H., and Xie, Z.-Q.: The atmospheric chemistry box model CAABA/MECCA-3.0, Geoscientific Model Development, 4, 373–380, doi:10.5194/gmd-4-373-2011, URL http://www.geosci-model-dev.net/4/373/2011/, 2011a.

Sander, S., Friedl, R. R., Barkern, J., Golden, D., Kurylo, M., Wine, P., Abbat, J., Burkholder, J., Kolb, C., Moortgat, G., Huie, R., and Orkin, V.: Chemical Kinetics and Photochemical Data for Use in Atmospheric Studies, Evaluation No. 17, JPL Publication 10-6, Jet Propulsion Laboratory, Pasadena, URL http://jpldataeval.jpl.nasa.gov/, 2011b.

Sanghavi, S.: An efficient Mie theory implementation to investigate the influence of aerosols on radiative transfer, Diploma thesis, Institute of Environmental Physics, University of Heidelberg, 2003.

Sanghavi, S., Lebsock, M., and Stephens, G.: Probing the sensitivity of polarimetric O_2 A-band measurements to clouds with emphasis on potential OCO-2 and GOSAT retrievals, Atmospheric Measurement Techniques Discussions, 7, 9603–9671, doi:10.5194/amtd-7-9603-2014, URL http://www.atmos-meas-tech-discuss.net/7/9603/2014/, 2014.

Sansonetti, C. J., Salit, M. L., and Reader, J.: Wavelengths of spectral lines in mercury pencil lamps, Appl. Opt., 35, 74–77, doi:10.1364/AO.35.000074, URL http://ao.osa.org/abstract.cfm?URI=ao-35-1-74, 1996.

Saunders, R. W., Kumar, R., Gomez Martin, J. C., Mahajan, A. S., Murray, B. J., and Plane, J. M. C.: Studies of the Formation and Growth of Aerosol from Molecular Iodine Precursor, Zeitschrift für Physikalische Chemie International journal of research in physical chemistry and chemical physics, 224, 7–8, doi:10.1524/zpch.2010.6143, URL http://www.degruyter.com/view/j/zpch.2010.224.issue-7-8/zpch.2010.6143/zpch.2010.6143.xml, 2010.

Schlager, H., Konopka, P., Schulte, P., Schumann, U., Ziereis, H., Arnold, F., Klemm, M., Hagen, D. E., Whitefield, P. D., and Ovarlez, J.: In situ observations of air traffic emission signatures in the North Atlantic flight corridor, Journal of Geophysical Research: Atmospheres, 102, 10 739–10 750, doi:10.1029/96JD03748, URL http://dx.doi.org/10.1029/96JD03748, 1997.

Schönhardt, A., Richter, A., Wittrock, F., Kirk, H., Oetjen, H., Roscoe, H. K., and Burrows, J. P.: Observations of iodine monoxide columns from satellite, Atmos. Chem. Phys., 8, 637–653, 2008.

Schönhardt, A., Begoin, M., Richter, A., Wittrock, F., Kaleschke, L., Gómez Martín, J. C., and Burrows, J. P.: Simultaneous satellite observations of IO and BrO over Antarctica, Atmos. Chem. Phys., 11, 33 651–33 688, doi:10.5194/acpd-11-33651-2011, 2012.

Schumann, U. and Huntrieser, H.: The global lightning-induced nitrogen oxides source, Atmospheric Chemistry and Physics, 7, 3823–3907, doi:10.5194/acp-7-3823-2007, URL http://www.atmos-chem-phys.net/7/3823/2007/, 2007.

Seibert, P., Beyrich, F., Gryning, S.-E., Joffre, S., Rasmussen, A., and Tercier, P.: Review and intercomparison of operational methods for the determination of the mixing height, Atmospheric

Environment, 34, 1001 – 1027, doi:http://dx.doi.org/10.1016/S1352-2310(99)00349-0, URL http://www.sciencedirect.com/science/article/pii/S1352231099003490, 2000.

Seinfeld, J. H. and Pandis, S. N.: Atmospheric Chemistry and Physics - From Air Pollution to Climate Change, 2nd Edition, John Wiley and Sons, Inc., Hoboken, New Jersey, 2006.

Seitz, K., Buxmann, J., Pöhler, D., Sommer, T., Tschritter, J., Neary, T., O'Dowd, C., and Platt, U.: The spatial distribution of the reactive iodine species IO from simultaneous active and passive DOAS observations, Atmos. Chem. Phys., 10, 2117–2128, 2010.

Shields, J. E., Johnson, R. W., Karr, M. E., Burden, A. R., and Baker, J. G.: Daylight visible/NIR whole-sky imagers for cloud and radiance monitoring in support of UV research programs, Proc. SPIE, 5156, 155–166, doi:10.1117/12.509062, URL http://dx.doi.org/10.1117/12.509062, 2003.

Sillman, S.: The relation between ozone, {NOx} and hydrocarbons in urban and polluted rural environments, Atmospheric Environment, 33, 1821 – 1845, doi:http://dx.doi.org/10.1016/S1352-2310(98)00345-8, URL http://www.sciencedirect.com/science/article/pii/S1352231098003458, 1999.

Simmes, B.: Development of a Novel Aircraft-borne DOAS Instrument for UV/visible Limb Observations, Diploma thesis, Institute of Environmental Physics, University of Heidelberg, Heidelberg, Germany, 2007.

Sinreich, R., Frieß U., and Platt, U.: Multi axis differential optical absorption spectroscopy (MAX-DOAS) of gas and aerosol distributions, Faraday Discuss., 130, 153–164, doi:10.1039/b419274p, 2005.

Sinreich, R., Coburn, S., Dix, B., and Volkamer, R.: Temperature-dependent cross sections of O_2-O_2 collision-induced absorption resonances at 477 and 577nm, J. Quant. Spectrosc. Ra., 98, 405–424, doi:10.1016/j.jqsrt.2005.06.004, 2006.

Sinreich, R., Coburn, S., Dix, B., and Volkamer, R.: Ship-based detection of glyoxal over the remote tropical Pacific Ocean, Atmospheric Chemistry and Physics, 10, 11 359–11 371, doi:10.5194/acp-10-11359-2010, URL http://www.atmos-chem-phys.net/10/11359/2010/, 2010.

Sinreich, R., Ortega, I., and Volkamer, R.: Sensitivity Study of Glyoxal Retrievals at Different Wavelength Ranges (Poster), 2013 International DOAS Workshop, URL http://www.colorado.edu/chemistry/volkamer/IDW-2013/poster-images/Sinreich_etal_poster_DOASWS_2013_glyx.pdf, 2013.

Smirnov, A., Holben, B., Kaufman, Y., Dubovik, O., Eck, T., Slutsker, I., Pietras, C., and Halthore, R.: Optical Properties of Atmospheric Aerosol in Maritime Environments, American Meteorological Society, 2001.

Solomon, S.: Stratospheric ozone depletion: A review of concepts and history, Reviews of Geophysics, 37, 275–316, doi:10.1029/1999RG900008, URL http://dx.doi.org/10.1029/1999RG900008, 1999.

Sommariva, R., Bloss, W., and von Glasow, R.: Uncertainties in gas-phase atmospheric iodine chemistry, Atmospheric Environment, 57, 219–232, 2012.

Sörgel, M., Regelin, E., Bozem, H., Diesch, J.-M., Drewnick, F., Fischer, H., Harder, H., Held, A., Hosaynali-Beygi, Z., Martinez, M., and Zetzsch, C.: Quantification of the unknown HONO daytime source and its relation to NO_2, Atmospheric Chemistry and Physics, 11, 10 433–10 447, doi:10.5194/acp-11-10433-2011, URL http://www.atmos-chem-phys.net/11/10433/2011/, 2011.

Souza-Echer, M. P., Pereira, E. B., Bins, L. S., and Andrade, M. A. R.: A Simple Method for the Assessment of the Cloud Cover State in High-Latitude Regions by a Ground-Based Digital Camera, Journal of Atmospheric and Oceanic Technology, 23, 437–447, doi:10.1175/JTECH1833.1, 2006.

Speidel, M., Nau, R., Arnold, F., Schlager, H., and Stohl, A.: Sulfur dioxide measurements in the lower, middle and upper troposphere: Deployment of an aircraft-based chemical ionization mass spectrometer with permanent in-flight calibration, Atmospheric Environment, 41, 2427–2437, doi:10.1016/j.atmosenv.2006.07.047, 2007.

Spietz, P., Martin, J., and Burrows, J. P.: Spectroscopic studies of the I2/O3 photochemistry. Part 2. Improved spectra of iodine oxides and analysis of the IO absorption spectrum, J. Photochem. Photobiol. A: Chem., 176, 50 – 67, 2005.

Stark, M. S., Harrison, J. T. H., and Anastasi, C.: Formation of nitrogen oxides by electrical discharges and implications for atmospheric lightning, Journal of Geophysical Research: Atmospheres, 101, 6963–6969, doi:10.1029/95JD03008, URL http://dx.doi.org/10.1029/95JD03008, 1996.

Staudinger, J. and Roberts, P. V.: A critical compilation of Henry's law constant temperature dependence relations for organic compounds in dilute aqueous solutions, Chemosphere, 44, 561 – 576, doi:http://dx.doi.org/10.1016/S0045-6535(00)00505-1, URL http://www.sciencedirect.com/science/article/pii/S0045653500005051, 2001.

Stavrakou, T., Müller, J.-F., De Smedt, I., Van Roozendael, M., van der Werf, G. R., Giglio, L., and Guenther, A.: Evaluating the performance of pyrogenic and biogenic emission inventories against one decade of space-based formaldehyde columns, Atmospheric Chemistry and Physics, 9, 1037–1060, doi:10.5194/acp-9-1037-2009, URL http://www.atmos-chem-phys.net/9/1037/2009/, 2009a.

Stavrakou, T., Müller, J.-F., De Smedt, I., Van Roozendael, M., Kanakidou, M., Vrekoussis, M., Wittrock, F., Richter, A., and Burrows, J. P.: The continental source of glyoxal estimated by the synergistic use of spaceborne measurements and inverse modelling, Atmospheric Chemistry and Physics, 9, 8431–8446, doi:10.5194/acp-9-8431-2009, URL http://www.atmos-chem-phys.net/9/8431/2009/, 2009b.

Stavrakou, T., Müller, J.-F., De Smedt, I., Van Roozendael, M., van der Werf, G. R., Giglio, L., and Guenther, A.: Global emissions of non-methane hydrocarbons deduced from SCIAMACHY formaldehyde columns through 2003-2006, Atmospheric Chemistry and Physics, 9, 3663–3679, doi:10.5194/acp-9-3663-2009, URL http://www.atmos-chem-phys.net/9/3663/2009/, 2009c.

Stavrakou, T., Müller, J.-F., Bauwens, M., De Smedt, I., Van Roozendael, M., Guenther, A., Wild, M., and Xia, X.: Isoprene emissions over Asia 1979-2012: impact of climate and land-use changes, Atmospheric Chemistry and Physics, 14, 4587–4605, doi:10.5194/acp-14-4587-2014, URL http://www.atmos-chem-phys.net/14/4587/2014/, 2014.

Steinmetz, F., Deschamps, P.-Y., and Ramon, D.: Atmospheric correction in presence of sun glint: application to MERIS, Opt. Express, 19, 9783–9800, doi:10.1364/OE.19.009783, URL http://www.opticsexpress.org/abstract.cfm?URI=oe-19-10-9783, 2011.

Stickler, A., Fischer, H., Bozem, H., Gurk, C., Schiller, C., Martinez-Harder, M., Kubistin, D., Harder, H., Williams, J., Eerdekens, G., Yassaa, N., Ganzeveld, L., Sander, R., and Lelieveld, J.: Chemistry, transport and dry deposition of trace gases in the boundary layer over the tropical Atlantic Ocean and the Guyanas during the GABRIEL field campaign, Atmospheric Chemistry and Physics, 7, 3933–3956, doi:10.5194/acp-7-3933-2007, URL http://www.atmos-chem-phys.net/7/3933/2007/, 2007.

Stockwell, W. R. and Calvert, J. G.: The near ultraviolet absorption spectrum of gaseous {HONO} and {N2O3}, Journal of Photochemistry, 8, 193 – 203, doi:http://dx.doi.org/10.1016/0047-2670(78)80019-7, URL http://www.sciencedirect.com/science/article/pii/0047267078800197, 1978.

Stohl, A., Forster, C., Frank, A., Seibert, P., and Wotawa, G.: Technical note: The Lagrangian particle dispersion model FLEXPART version 6.2, Atmospheric Chemistry and Physics, 5, 2461–2474, doi:10.5194/acp-5-2461-2005, URL http://www.atmos-chem-phys.net/5/2461/2005/, 2005.

Stone, D., Whalley, L. K., and Heard, D. E.: Tropospheric OH and HO2 radicals: field measurements and model comparisons, Chem. Soc. Rev., 41, 6348–6404, doi:10.1039/C2CS35140D, URL http://dx.doi.org/10.1039/C2CS35140D, 2012.

Stutz, J. and Platt, U.: Numerical Analysis and Estimation of the Statistical Error of Differential Optical Absorption Spectroscopy Measurements with Least-Squares methods, Appl. Opt., 35, 6041–6053, 1996.

Stutz, J., Kim, E. S., Platt, U., Bruno, P., Perrino, C., and Febo, A.: UV-visible absorption cross sections of nitrous acid, Journal of Geophysical Research: Atmospheres, 105, 14 585–14 592, doi:10.1029/2000JD900003, URL http://dx.doi.org/10.1029/2000JD900003, 2000.

Sun, D., Roth, S., and Black, M.: Secrets of optical flow estimation and their principles, in: Computer Vision and Pattern Recognition (CVPR), 2010 IEEE Conference on, pp. 2432–2439, doi:10.1109/CVPR.2010.5539939, 2010.

Szeliski, D. R.: Computer Vision: Algorithms and Applications, Springer-Verlag London, doi:10.1007/978-1-84882-935-0, URL http://szeliski.org/Book/, 2011.

Takashima, H., Irie, H., Kanaya, Y., Shimizu, A., Aoki, K., and Akimoto, H.: Atmospheric aerosol variations at Okinawa Island in Japan observed by MAX-DOAS using a new cloud-screening method, J. Geophys. Res., 114, D18 213, doi:10.1029/2009JD011939, URL http://dx.doi.org/10.1029/2009JD011939, 2009.

Tan, D., Faloona, I., Simpas, J. B., Brune, W., Olson, J., Crawford, J., Avery, M., Sachse, G., Vay, S., Sandholm, S., Guan, H.-W., Vaughn, T., Mastromarino, J., Heikes, B., Snow, J., Podolske, J., and Singh, H.: OH and HO2 in the tropical Pacific: Results from PEM-Tropics B, Journal of Geophysical Research: Atmospheres, 106, 32 667–32 681, doi:10.1029/2001JD900002, URL http://dx.doi.org/10.1029/2001JD900002, 2001.

Tangang, F. T., Juneng, L., Salimun, E., Vinayachandran, P. N., Seng, Y. K., Reason, C. J. C., Behera, S. K., and Yasunari, T.: On the roles of the northeast cold surge, the Borneo vortex, the Madden-Julian Oscillation, and the Indian Ocean Dipole during the extreme 2006/2007 flood in southern Peninsular Malaysia, Geophysical Research Letters, 35, doi:10.1029/2008GL033429, URL http://dx.doi.org/10.1029/2008GL033429, 2008.

Taraborrelli, D., Lawrence, M. G., Crowley, J. N., Dillon, T. J., Gromov, S., Grosz, C. B. M., Vereecken, L., and Lelieveld, J.: Hydroxyl radical buffered by isoprene oxidation over tropical forests, Nature, 5, 190–193, doi:10.1038/ngeo1405, URL http://www.nature.com/ngeo/journal/v5/n3/abs/ngeo1405.html#supplementary-information, 2012.

TCEQ: Emissions from oil and gas production facilities, prepared for: Mr. Bertie Fernando, P.E., Texas Commission on Environmental Quality Air Quality Division, prepared by: Eastern Research Group, Inc., Technical Report, p. 90, URL http://www.tceq.texas.gov/assets/public/implementation/air/am/contracts/reports/ei/5820784003FY0701-20090831-ergi-ei_from_old_gas_facilities.pdf, 2007.

Tegtmeier, S., Krüger, K., Quack, B., Atlas, E., Blake, D. R., Boenisch, H., Engel, A., Hepach, H., Hossaini, R., Navarro, M. A., Raimund, S., Sala, S., Shi, Q., and Ziska, F.: The contribution of oceanic methyl iodide to stratospheric iodine, Atmospheric Chemistry and Physics, 13, 11 869–11 886, doi:10.5194/acp-13-11869-2013, URL http://www.atmos-chem-phys.net/13/11869/2013/, 2013.

Thalman, R. and Volkamer, R.: Temperature dependent absorption cross-sections of O2-O2 collision pairs between 340 and 630 nm and at atmospherically relevant pressure, Phys. Chem. Chem. Phys., pp. –, doi:10.1039/C3CP50968K, URL http://dx.doi.org/10.1039/C3CP50968K, 2013.

Tie, X., Madronich, S., Walters, S., Zhang, R., Rasch, P., and Collins, W.: Effect of clouds on photolysis and oxidants in the troposphere, Journal of Geophysical Research: Atmospheres, 108, doi:10.1029/2003JD003659, URL http://dx.doi.org/10.1029/2003JD003659, 2003.

Trick, S.: Formation of Nitrous Acid on Urban Surfaces- A Physical-Chemical Perspective, Ph.D. thesis, University of Heidelberg, 2004.

TRIPOLI, G. J.: The Colorado State University three-dimensional cloud/mesoscale model-1982 Part I : General theoretical framework and sensitivity experiments, J. Rech. Atmos., 16, 185–219, URL http://ci.nii.ac.jp/naid/80001546675/en/, 1982.

Tschritter, J.: Untersuchung mariner Halogenemissionen im tropischen Atlantik, Ph.D. thesis, Institute of Environmental Physics, University of Heidelberg, 2013.

Ullman, S.: The Interpretation of Structure from Motion, Proceedings of the Royal Society of London. Series B. Biological Sciences, 203, 405–426, doi:10.1098/rspb.1979.0006, URL http://rspb.royalsocietypublishing.org/content/203/1153/405.abstract, 1979.

van de Hulst, H. C.: Light scattering by small particles, Dover Publications, Inc. 1981, New York, 1981.

Van Roozendael, M. and Fayt, C.: WinDOAS 2.1. Software User Manual, IASB/BIRA Uccle, Belgium, 2001.

Vandaele, A. C., Hermans, C., Simon, P. C., Carleer, M., Colin, R., Fally, S., Mérienne, M. F., Jenouvrier, A., and Coquart, B.: Measurements of the NO_2 absorption cross-section from 42,000 cm^{-1} to 10,000 cm^{-1} (238-1000 nm) at 220 K and 294 K., J. of Quant. Spectrosc. and Rad. Transfer, 59, 171–184, doi:10.1016/S0022-4073(97)00168-4, 1998.

Varnai, T., Marshak, A., and Yang, W.: Multi-satellite aerosol observations in the vicinity of clouds, Atmospheric Chemistry and Physics, 13, 3899–3908, doi:10.5194/acp-13-3899-2013, URL http://www.atmos-chem-phys.net/13/3899/2013/, 2013.

Veitel, H., Funk, O., Kurz, C., Platt, U., and Pfeilsticker, K.: Geometrical path length probability density functions of the skylight transmitted by midlatitude cloudy skies: Some case studies, Geophysical Research Letters, 25, 3355–3358, doi:10.1029/98GL02506, URL http://dx.doi.org/10.1029/98GL02506, 1998.

Vogel, L., Sihler, H., Lampel, J., Wagner, T., and Platt, U.: Retrieval interval mapping: a tool to visualize the impact of the spectral retrieval range on differential optical absorption spectroscopy evaluations, Atmospheric Measurement Techniques, 6, 275–299, doi:10.5194/amt-6-275-2013, URL http://www.atmos-meas-tech.net/6/275/2013/, 2013.

Vogt, R., Sander, R., von Glasow, R., and Crutzen, P. J.: Iodine Chemistry and its Role in Halogen Activation and Ozone Loss in the Marine Boundary Layer: A Model Study, J. Atmos. Chem., 32, 375–395, doi:10.1023/A:1006179901037, 1999.

Volkamer, R., Platt, U., and Wirtz, K.: Primary and Secondary Glyoxal Formation from Aromatics: Experimental Evidence for the Bicycloalkyl-Radical Pathway from Benzene, Toluene and p-Xylene, J. Phys. Chem., 105, 7865–7874, 2001.

Volkamer, R., Molina, L. T., Molina, M. J., Shirley, T., and Brune, W. H.: DOAS measurement of glyoxal as an indicator for fast VOC chemistry in urban air, Geophysical Research Letters, 32, doi:10.1029/2005GL022616, URL http://dx.doi.org/10.1029/2005GL022616, 2005a.

Volkamer, R., Spietz, P., Burrows, J. P., and Platt, U.: High-resolution absorption cross-section of Glyoxal in the UV/vis and IR spectral ranges, J. Photoch. Photobio. A: Chemistry, 172, 35 – 46, 2005b.

Volkamer, R., San Martini, F., Molina, L. T., Salcedo, D., Jimenez, J. L., and Molina, M. J.: A missing sink for gas-phase glyoxal in Mexico City: Formation of secondary organic aerosol, Geophysical Research Letters, 34, doi:10.1029/2007GL030752, URL http://dx.doi.org/10.1029/2007GL030752, 2007.

von Clarmann, T.: Smoothing error pitfalls, Atmospheric Measurement Techniques, 7, 3023–3034, doi:10.5194/amt-7-3023-2014, URL http://www.atmos-meas-tech.net/7/3023/2014/, 2014.

Vountas, M., Richter, A., Wittrock, F., and Burrows, J. P.: Inelastic scattering in ocean water and its impact on trace gas retrievals from satellite data, Atmos. Chem. Phys., 3, 1365–1375, doi:10.5194/acp-3-1365-2003, 2003.

Vrekoussis, M., Wittrock, F., Richter, A., and Burrows, J. P.: Temporal and spatial variability of glyoxal as observed from space, Atmospheric Chemistry and Physics, 9, 4485–4504, URL http://www.atmos-chem-phys.net/9/4485/2009/, 2009.

Vrekoussis, M., Wittrock, F., Richter, A., and Burrows, J. P.: GOME-2 observations of oxygenated VOCs: what can we learn from the ratio glyoxal to formaldehyde on a global scale?, Atmospheric Chemistry and Physics, 10, 10 145–10 160, doi:10.5194/acp-10-10145-2010, URL http://www.atmos-chem-phys.net/10/10145/2010/, 2010.

Wagner, T., Erle, F., Marquard, L., Otten, C., Pfeilsticker, K., Senne, T., Stutz, J., and Platt, U.: Cloudy sky optical paths as derived from differential optical absorption spectroscopy observations, Journal of Geophysical Research: Atmospheres, 103, 25 307–25 321, doi:10.1029/98JD01021, URL http://dx.doi.org/10.1029/98JD01021, 1998.

Wagner, T., Chance, K., Frieß, U., Gil, M., Goutail, F., Hönninger, G., Johnston, P., Karlsen-Tornkvist, K., Kostadinov, I., Leser, H., Petritoli, A., Richter, A., Van Roozendael, M., and Platt, U.: Correction of the Ring effect and I0 - effect for DOAS observations of scattered sunlight, ESA Technical Report, URL http://satellite.mpic.de/pdf_dateien/RING4.pdf, 2002c.

Wagner, T., Dix, B., von Friedeburg, C., Frieß, U., Sanghavi, S., Sinreich, R., and Platt, U.: MAX-DOAS O_4 measurements: A new technique to derive information on atmospheric aerosols - principles and information content, J. Geophys. Res., 109, D22 205, doi:10.1029/2004JD004904, 2004.

Wagner, T., Beirle, S., and Deutschmann, T.: Three-dimensional simulation of the Ring effect in observations of scattered sun light using Monte Carlo radiative transfer models, Atmos. Meas. Tech., 2, 113–124, URL http://www.atmos-meas-tech.net/2/113/2009/, 2009.

Wagner, T., Beirle, S., Brauers, T., Deutschmann, T., Frieß, U., Hak, C., Halla, J. D., Heue, K. P., Junkermann, W., Li, X., Platt, U., and Pundt-Gruber, I.: Inversion of tropospheric

profiles of aerosol extinction and HCHO and NO_2 mixing ratios from MAX-DOAS observations in Milano during the summer of 2003 and comparison with independent data sets, Atmospheric Measurement Techniques, 4, 2685–2715, doi:10.5194/amt-4-2685-2011, URL http://www.atmos-meas-tech.net/4/2685/2011/, 2011.

Wagner, T., Andreae, M. O., Beirle, S., Dörner, S., Mies, K., and Shaiganfar, R.: MAX-DOAS observations of the total atmospheric water vapour column and comparison with independent observations, Atmospheric Measurement Techniques, 6, 131–149, doi:10.5194/amt-6-131-2013, URL http://www.atmos-meas-tech.net/6/131/2013/, 2013a.

Wagner, T., Beirle, S., Sihler, H., and Mies, K.: A feasibility study for the retrieval of the total column precipitable water vapour from satellite observations in the blue spectral range, Atmospheric Measurement Techniques, 6, 2593–2605, doi:10.5194/amt-6-2593-2013, URL http://www.atmos-meas-tech.net/6/2593/2013/, 2013b.

Wagner, T., Apituley, A., Beirle, S., Dörner, S., Friess, U., Remmers, J., and Shaiganfar, R.: Cloud detection and classification based on MAX-DOAS observations, Atmospheric Measurement Techniques, 7, 1289–1320, doi:10.5194/amt-7-1289-2014, URL http://www.atmos-meas-tech.net/7/1289/2014/, 2014.

Wagner, V., von Glasow, R., Fischer, H., and Crutzen, P. J.: Are CH2O measurements in the marine boundary layer suitable for testing the current understanding of CH4 photooxidation?: A model study, Journal of Geophysical Research: Atmospheres, 107, ACH 3–1–ACH 3–14, doi:10.1029/2001JD000722, URL http://dx.doi.org/10.1029/2001JD000722, 2002.

Wahner, A., Callies, J., Dorn, H.-P., Platt, U., and Schiller, C.: Near UV atmospheric absorption measurements of column abundances during Airborne Arctic Stratospheric Expedition, January - February 1989: 3. BrO observations, Geophysical Research Letters, 17, 517–520, doi:10.1029/GL017i004p00517, URL http://dx.doi.org/10.1029/GL017i004p00517, 1990.

Walker, H. M.: Field Measurements and Analysis of Reactive Tropospheric Species using the FAGE technique, Ph.D. thesis, University of Leeds, 2013.

Walko, R. L., Band, L. E., Baron, J., Kittel, T. G. F., Lammers, R., Lee, T. J., Ojima, D., Pielke, R. A., Taylor, C., Tague, C., Tremback, C. J., and Vidale, P. L.: Coupled Atmosphereâ€“Biophysicsâ€“Hydrology Models for Environmental Modeling, J. Appl. Meteor., 39, 931–944, doi:10.1175/1520-0450(2000)039⟨0931:CABHMF⟩2.0.CO;2, URL http://dx.doi.org/10.1175/1520-0450(2000)039<0931:CABHMF>2.0.CO;2, 2000.

Wang, H., Liu, X., Chance, K., González Abad, G., and Chan Miller, C.: Water vapor retrieval from OMI visible spectra, Atmospheric Measurement Techniques, 7, 1901–1913, doi:10.5194/amt-7-1901-2014, URL http://www.atmos-meas-tech.net/7/1901/2014/, 2014.

Warwick, N. J., Archibald, A. T., Ashworth, K., Dorsey, J., Edwards, P. M., Heard, D. E., Langford, B., Lee, J., Misztal, P. K., Whalley, L. K., and Pyle, J. A.: A global model study of the impact of land-use change in Borneo on atmospheric composition, Atmospheric Chemistry and Physics, 13, 9183–9194, doi:10.5194/acp-13-9183-2013, URL http://www.atmos-chem-phys.net/13/9183/2013/, 2013.

Weller, R., Schrems, O., Boddenberg, A., Gäb, S., and Gautrois, M.: Meridional distribution of hydroperoxides and formaldehyde in the marine boundary layer of the Atlantic (48Â°N-35Â°S) measured during the Albatross campaign, Journal of Geophysical Research: Atmospheres, 105, 14 401–14 412, doi:10.1029/1999JD901145, URL http://dx.doi.org/10.1029/1999JD901145, 2000.

Werner, B.: Case Study of Stratospheric Limb Measurements of O_3, NO_2 and BrO in the Polar Summer, Diploma thesis, Institute of Environmental Physics, University of Heidelberg, Heidelberg, Germany, 2009.

Wilbur Kaye, Beckman Instruments, I.: Pen-Ray Rare Gas Lamp Spectra, Ultra-Violet Products, p. 29, URL http://www.uvp.com/pdf/spectra.pdf, 1997.

Williams, J., Gros, V., Atlas, E., Maciejczyk, K., Batsaikhan, A., Schöler, H., Forster, C., Quack, B., Yassa, N., Sander, R., and Van Dingenen, R.: Possible evidence for a connection between methyl iodide emissions and Sahara dust, J. Geophys. Res., 112, D07 302, doi:10.1029/205JD006702, 2007.

Wilmouth, D. M., Hanisco, T. F., Donahue, N. M., and Anderson, J. G.: Fourier transform ultraviolet spectroscopy of the $A^2\Pi_{3/2} \leftarrow X^2\Pi_{3/2}$ transition of BrO, J. Phys. Chem. A, 103, 8935–8945, doi:10.1021/jp991651o, 1999.

Wittrock, F., Richter, A., Oetjen, H., Burrows, J. P., Kanakidou, M., Myriokefalitakis, S., Volkamer, R., Beirle, S., Platt, U., and Wagner, T.: Simultaneous global observations of glyoxal and formaldehyde from space, GEOPHYSICAL RESEARCH LETTERS, 33, 5, doi: 10.1029/2006GL026310, 2006.

WMO: World Meteorological Organization, International Cloud Atlas, Volume I, revised edition 1975, Manual on the Observation of Clouds and other Meteors, 1975.

WMO: World Meteorological Organization, International Cloud Atlas, Volume II, 1987.

WMO: World Meteorological Organization, Scientific Assessment of Ozone Depletion: 1998, Global Ozone Research and Monitoring Project-Report No.44, Geneva, Switzerland, 1999.

WMO: World Meteorological Organization, Scientific Assessment of Ozone Depletion: 2006, Global Ozone Research and Monitoring Project-Report No.50, 516 pp., Geneva, Switzerland, 2007.

WMO: World Meteorological Organization, Scientific Assessment of Ozone Depletion: 2010, Global Ozone Research and Monitoring Project-Report No.52, 516 pp., Geneva, Switzerland, 2011.

Yilmaz, S.: Retrieval of Atmospheric Aerosol and Trace Gas Vertical Profiles using Multi-Axis Differential Optical Absorption Spectroscopy, Ph.D. thesis, Institute of Environmental Physics, University of Heidelberg, 2012.

Yokelson, R. J., Burling, I. R., Gilman, J. B., Warneke, C., Stockwell, C. E., de Gouw, J., Akagi, S. K., Urbanski, S. P., Veres, P., Roberts, J. M., Kuster, W. C., Reardon, J., Griffith, D. W. T., Johnson, T. J., Hosseini, S., Miller, J. W., Cocker III, D. R., Jung, H., and Weise, D. R.: Coupling field and laboratory measurements to estimate the emission factors of identified and unidentified trace gases for prescribed fires, Atmospheric Chemistry and Physics, 13, 89–116, doi:10.5194/acp-13-89-2013, URL http://www.atmos-chem-phys.net/13/89/2013/, 2013.

Zel'dovich, Y. and Raizer, W. D., eds.: Physics of Shock Waves and High-Temperature Hydrodynamic Phenomena, Academic Press, San Diego, California, doi:http://dx.doi.org/10.1016/B978-0-12-395672-9.50001-1, URL http://www.sciencedirect.com/science/article/pii/B9780123956729500011, 1967.

Zender, C. S., Krolewski, A. G., Tosca, M. G., and Randerson, J. T.: Tropical biomass burning smoke plume size, shape, reflectance, and age based on 2001-2009 MISR imagery of Borneo, Atmospheric Chemistry and Physics, 12, 3437–3454, doi:10.5194/acp-12-3437-2012, URL http://www.atmos-chem-phys.net/12/3437/2012/, 2012.

Acknowledgements

Ganz zum Schluss möchte ich mich noch bei allen bedanken, die mich während der Arbeit unterstützt haben. Vielen Dank an:

- Prof. Dr. Klaus Pfeilsticker, für das Ermöglichen dieser Arbeit, die vielen Anregungen zur Auswertung und Interpretation der Daten
- Prof. Dr. Thomas Leisner, für die spontane Übernahme des Zweitgutachtens
- alle Korrekturleser (Sebastian, Zoe, Udo, Peter, Bodo, 2 x Johannes, Holger, Katja, 2 x Marcel, Martin, Lisa, Tilman, Nicole, Stefan, Annick, Klaus-Peter)
- die gesamte Luftchem-Arbeitsgruppe, für die vielen Diskussionen, die Fragen und Antworten, die gute Zusammenarbeit, die vielen Vorschläge und die Geduld, insbesondere an Tim, Bodo, Udo, Peter, Angelika, Johannes, Matthias, Steffen, Martin, Henning und Rasmus
- Daniel und Paul für die Einführung in die verschiedenen Methoden der Bildverarbeitung, sowie für die Bereitstellung der Schachbrettmusterplatte zur Kalibrierung der Webcam
- das ganze SHIVA-Team, für die Unterstützung während der Kampagne, die Diskussionen während der SHIVA Meetings, sowie die Bereitstellung verschiedener Vergleichsdaten
- Ryan Hossaini und Paul Hamer für die TOMCAT und CCATT-BRAMS Modellierungen und für die zahlreichen Diskussionen und Fragen und Antworten per Email
- Gisèle Krystofiak und Valery Catoire für die Bereitstellung der CO Daten
- Stefan Sala für die Bereitstellung der CH_3I Daten
- Francois Hendrick, Isabelle DeSmedt, Yu Huan und Christophe Lerot für die Bereitstellung der Satellitenkarten von NO_2, HCHO und CHOCHO, sowie an Anja Schönhardt für die IO Satellitenkarten von Borneo
- die Phytooptics Gruppe (Astrid Bracher and Tilman Dinter, AWI Bremerhaven/ IUP Bremen) und an F. Steinmetz für die Bereitstellung der Chl-a Daten von Borneo
- Hans Schlager und das IPA Team für die Bereitstellung der O_3 und SO_2 Daten
- David Oram und Graham Mills für die Bereitstellung der Isoprendaten
- Zoe und Katja, für die vielen guten Englischtipps
- Tobias, für die Aufmunterung und Unterstützung in den letzten Wochen vor der Abgabe
- David, sowie an meine Familie und Freunde, dass sie während der ganzen Zeit für mich da waren!